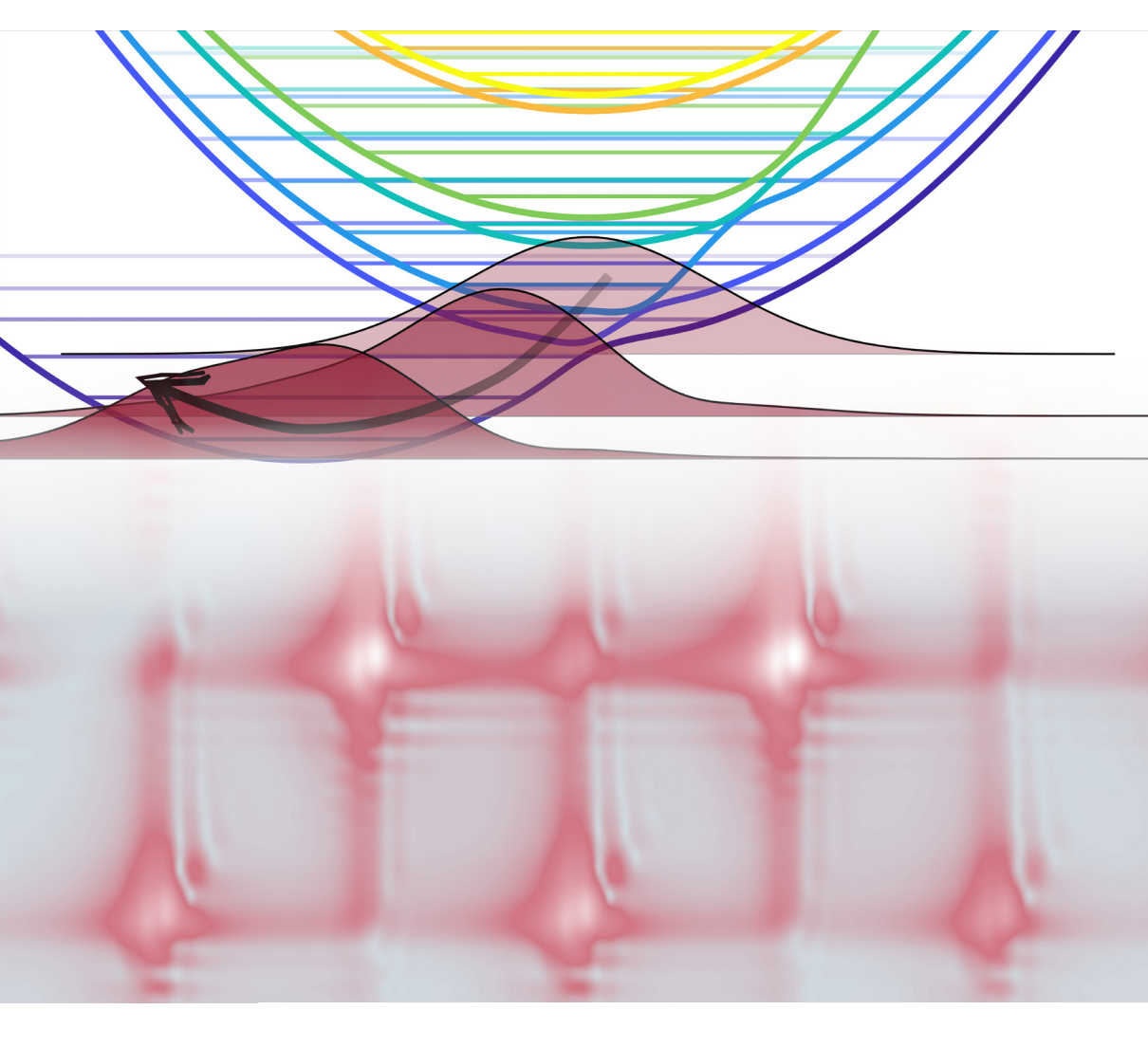
Quantum Dynamics and Spectroscopy of Functional Molecular Materials and Biological Photosystems

Les Houches Summer School 2023

Edited by Irene Burghardt, Jeffrey Cina, Jérémie Léonard





Quantum Dynamics and Spectroscopy of Functional Molecular Materials and Biological Photosystems

Les Houches Summer School 2023

Edited by
Irene Burghardt, Jeffrey Cina, Jérémie Léonard

This volume presents a collection of lectures at the frontier between ultrafast spectroscopy and molecular quantum science, which were held in 2023 as part of a summer school at the Ecole de Physique at Les Houches, France. In the first four chapters, a combined experimental and theoretical perspective is developed, including the concepts of ultrafast optics and two-dimensional electronic spectroscopy, along with the theoretical interpretation of nonlinear spectroscopic signals relying on state-of-the-art simulation approaches in quantum molecular dynamics. The next two chapters present an overview of applications to light harvesting in photosynthesis and excitonic processes in organic photovoltaics. The two final chapters pedagogically summarize the material of computational exercises on quantum dynamical simulations and the computation of linear and nonlinear spectroscopic signals, with Jupyter notebooks made available together with this volume.

Irene Burghardt, Professor of Theoretical Chemistry at Goethe University Frankfurt, Germany, and Jeffrey Cina, Professor of Theoretical Physical Chemistry at the University of Oregon, USA, initiated the workshop series on the topic «Quantum Dynamics and Spectroscopy of Functional Molecular Materials and Biological Photosystems». Jérémie Léonard, Directeur de Recherche at the Institut de Physique et Chimie des Matériaux de Strasbourg, CNRS & Université de Strasbourg, France, is part of the current organizer team.



ISBN: 978-2-7598-3761-8 979-10-344-0248-9

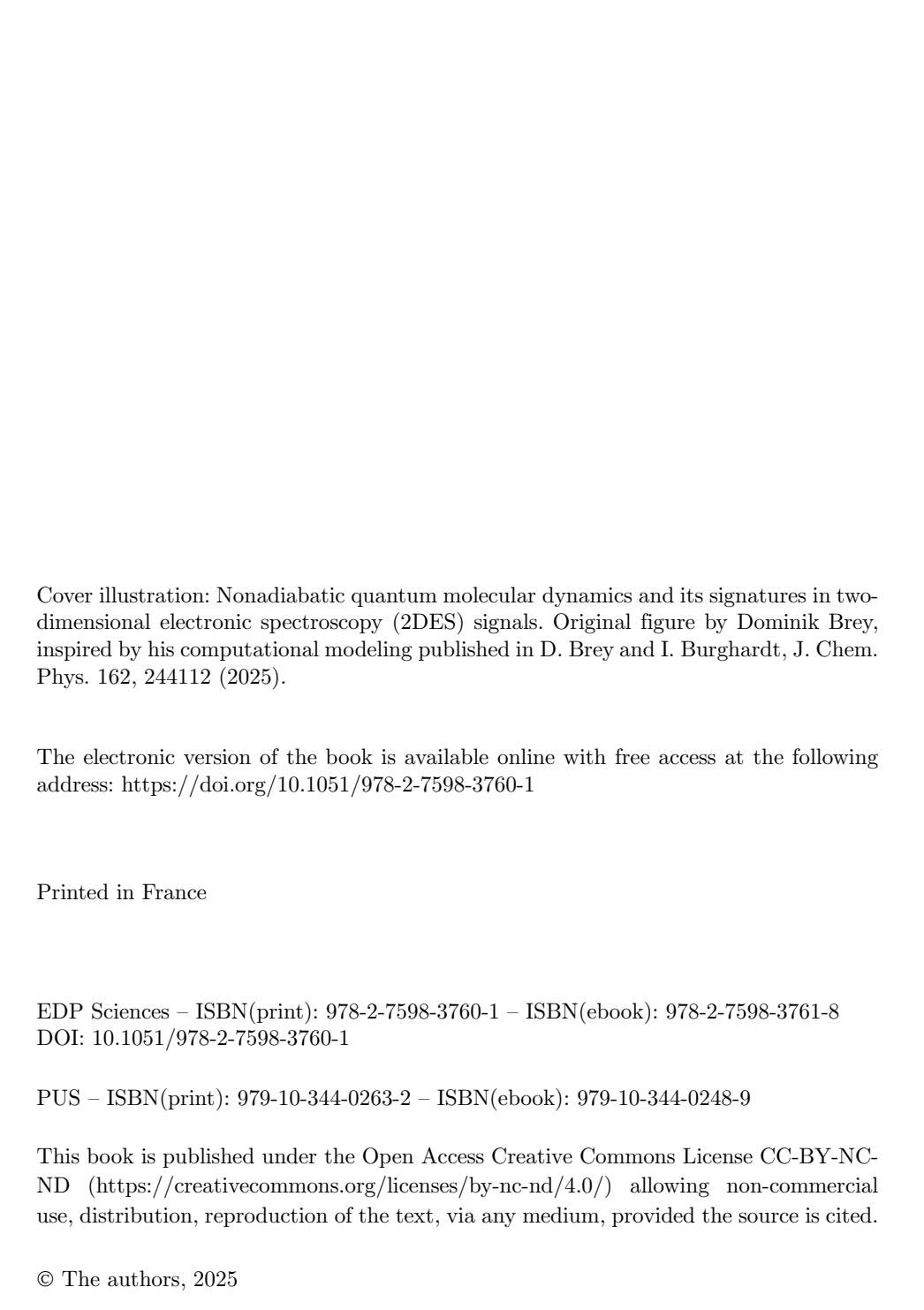
Irene BURGHARDT, Jeffrey CINA and Jérémie LÉONARD, Eds

Quantum Dynamics and Spectroscopy of Functional Molecular Materials and Biological Photosystems

Les Houches Summer School 2023







Editorial

This volume presents a collection of lectures on the topic "Quantum Dynamics and Spectroscopy of Functional Molecular Materials and Biological Photosystems" that were held during the 2023 edition of a summer school accompanying a workshop on the same theme. The event took place at the École de Physique at Les Houches, France, in August/September 2023, as part of a biennial series of meetings. Within this series, 2023 marks the first time that a combined school and workshop event was organized, and it also marks the 10th anniversary of a workshop series that arose from the spontaneous initiative of two of us.

To briefly sketch out the history of the event, Jeff Cina and Irene Burghardt met at an ACS meeting in Denver in 2011 and raised the idea of submitting a proposal for a Telluride Science and Research Center (TSRC) workshop on a theme that would combine experimental and computational state-of-the-art methodology in the study of elementary energy and charge transfer events in molecular materials and biosystems. At that time, the exploration of molecular systems by ultrafast spectroscopies had extended to molecular aggregates and various nanoscale materials, and diverse spectroscopic techniques were available, from multidimensional electronic and vibrational spectroscopies to emergent time-resolved X-ray techniques for structural dynamics. In parallel, tangible progress was made in quantum dynamical simulations for modeling ultrafast vibronic and transport phenomena. As two theorists, we were keen to establish an interaction platform between spectroscopists and theorists in an informal, discussion-oriented environment.

A first workshop took place in summer 2013 at the TSRC and clearly exceeded our expectations. A second TSRC workshop on the same theme followed in 2015, and it turned out that a significant number of participants expressed interest in the continuation of the event. At this point, Irene Burghardt suggested to explore the possibility of an alternative venue in Europe and contacted the director of the École

¹See the 2023 event website at https://www.theochem.uni-frankfurt.de/LesHouches2023/.

de Physique at Les Houches. Molecular science was not prominent within the Les Houches program at that time, so we considered ourselves lucky to be offered a slot for our workshop in 2017. Les Houches turned out as perfect a venue as Telluride, which made us consider alternating between the two venues. To account for the international flavor of our event, we expanded the co-organizer team from two to six organizers from five countries. In 2019, we returned to the TSRC, and in 2021, we offered an online version of the event due to the pandemic. Finally, 2023 saw our return to Les Houches, this time with a combination of school and workshop events. One of the new co-organizers (Jérémie Léonard) especially promoted the addition of a school, in line with the tradition of the École de Physique. In 2025, this combination was continued, and it might well turn into the new paradigm of the biennial event.

Against this background, the contributions of the present volume very much reflect the general philosophy of the event, which combines spectroscopic, theoretical, and computational perspectives. The first four chapters summarize contributions by the main lecturers of the 2023 summer school, followed by two chapters on more specialized topics, and two final chapters accompanying the computational exercises that were offered at the school.

In chapter 1, Giulio Cerullo and Cristian Manzoni address the basic concepts of ultrafast optics, *i.e.*, the generation and propagation of ultrafast light pulses. In chapter 2, Elisa Palacino-González and David Picconi present a broad overview of theoretical and computational methods for photoinduced molecular quantum dynamics, from state-of-the-art tensor network methods to trajectory-based approaches. Chapter 3 by Tobias Kramer focuses on open quantum system dynamics, from Markovian to non-Markovian approaches, and the computation of two-dimensional electronic spectroscopy (2DES) signals, notably within a GPU-based implementation of the Hierarchical Equations of Motion (HEOM) method. Chapter 4 by Pavel Malý presents an overview of the response function formalism in a density matrix setting, focusing on the comparison between coherent detection vs. fluorescence detection of ultrafast four-wave mixing and six-wave mixing 2DES signals.

Next, chapters 5 and 6 address two application areas that are of central interest. In chapter 5, Thomas Renger addresses light harvesting in photosynthesis, while chapter 6 by Irene Burghardt focuses on excitonic processes in organic photovoltaics. Even though exciton transport and the formation of charge-separated states are the unifying themes in both instances, significant differences arise from the respective parameter regimes, raising intriguing questions on structure-function relations.

Finally, chapters 7 and 8 presented jointly by Dominik Brey and James Green, accompany computational exercises on quantum dynamical simulations and their application to the computation of linear and nonlinear spectroscopic signals. Both chapters combine theoretical background with detailed explanations relating to the Python scripts that were employed in the computational exercises. The corresponding Jupyter notebooks are made available together with these chapters.

From the very positive feedback that was received throughout the summer school, we believe that the level of theory and of the computational exercises was adequate

Editorial V

and motivating. While being far from comprehensive, the present lectures should provide a combined experimental and theoretical spotlight on the molecular-level investigation of light-induced processes in biological systems and nanostructured materials. We hope that this collection will inspire future experiment-theory connections at this frontier between molecular and nanoscale quantum phenomena.

We would like to express our sincere gratitude to the Lecturers for joining this book project with the aspiration to present their work in a clear and pedagogical style. Furthermore, we thank our co-organizers, *i.e.*, Jessica Anna (University of Pennsylvania, USA), Thomas Renger (University of Linz, Austria), and Young Min Rhee (KAIST, South Korea), for their role in making the summer school and workshop a success. Finally, we are grateful to the École de Physique des Houches, the Université Franco-Allemande, the Institut de Physique et Chimie des Matériaux de Strasbourg, and the Interdisciplinary Thematic Institute for Quantum Science and nanoMaterials (QMat), Strasbourg University, for supporting the event, and we thank the editorial teams at EDP Sciences and Presses Universitaires de Strasbourg (PUS) for their invaluable assistance with publishing this volume.

Irene Burghardt, Goethe University Frankfurt, Germany Jérémie Léonard, University of Strasbourg, France Jeffrey Cina, University of Oregon, USA

Contents

Editorial		III	
Line	TER 1 and Nonlinear Propagation of Ultrashort Light Pulses		1
1.1	Introduction		1
1.2	Linear Propagation of Ultrashort Pulses: Dispersion and its Compensation		2
Refe	Parametric Amplifiers		15 25
Phot and	TER 2 Induced Molecular Quantum Dynamics: Theory Induced Molecular Quantum Dynamics (Induced No. 1997) Induced Molecul		27
2.1	Introduction		27
2.2	Molecular Quantum Dynamics		28
	2.2.1 Electronic States and Time-Dependent Schrödinger Equation	n	29
	2.2.2 The Adiabatic Representation		32
	2.2.3 The Diabatic Representation		34
	2.2.4 Examples of Diabatic States		36
	2.2.5 Vibronic Coupling Models for Diabatic PESs		38
	2.2.6 Conical Intersections		40
2.3	Connection Between Quantum Dynamics and Linear		
	Absorption Spectroscopy		42
	2.3.1 Sum-Over-States Expression for the Linear		
	Absorption Spectrum		44
2.4	Numerical Methods: Quantum Wave Packets		46
	2.4.1 The Time-Dependent Variational Principle		46
	2.4.2 Expansion in a Finite Time-Independent Basis		48
	2.4.3 Mitigating the Curse of Dimensionality:		
	The Multi-Configurational Time-Dependent Hartree Metho	d	52

VIII Contents

	2.4.4	An Alternative Tensor Decomposition: Tensor Trains	60
	2.4.5	Towards Direct Dynamics: Variational Multi-Configurational	
		Gaussian Wave Packets	62
2.5	Nume	rical Methods: Quantum-Classical Approximations	67
	2.5.1	Gaussian Wave Packets Moving Classically	67
	2.5.2	Spawning Techniques for Trajectory Basis Functions	68
	2.5.3	Fully Independent Trajectories: The Surface Hopping	
		Approach	71
	2.5.4	The Phase Space View on Nuclear Quantum Effects	73
	2.5.5	Mapping Discrete Electronic States to Phase Space Variables	75
	2.5.6	Quantum-Classical Approaches vs. Numerically Exact	
		Quantum Dynamics	80
	2.5.7	What Else Do We Have?	83
Refer	ences .		83
CHA	PTER	3	
Open	Quant	um System Simulation of Time and Frequency	
Reso	lved Sp	ectroscopy	89
Tobia	as Kran	ner	
3.1	Introd	luction	89
3.2		Quantum System Dynamics	90
3.3	-	vs. Approximate Solution	91
0.0	3.3.1	Weak Coupling Limit: Redfield Equations	92
	3.3.2	Strong Coupling Limit: Förster Energy Transfer and Rate	32
	0.0.2	Equations	94
	3.3.3	Decoherence, Dephasing, and Relaxation Dynamics	96
3.4		uting Optical Spectra	98
0.1	3.4.1	Linear Absorption Spectra	100
	3.4.2	Two-Dimensional Electronic Spectroscopy (2DES)	100
3.5		able Averages	102
0.0	3.5.1	Isotropic Average	102
	3.5.2	Static Disorder	103
3.6		HEOM for Quantum Dynamics	103
0.0	3.6.1	Populations and Coherences	104
	3.6.2	Two-Dimensional Spectra.	104
3.7	0.0	tary	108
-			108
100101			100
СНА	PTER	4	
		and Fluorescence-Detected Ultrafast Spectroscopy	111
	l Malý	The second secon	
4.1		luction	111
4.2		near Spectroscopy as Measurement of Perturbation Theory	112
	4.2.1	Microscopic Interaction with Light	112
	4.2.2	Perturbative Expansion	113

Contents

	4.2.3 Production of the Overall Macroscopic Signal	115
	4.2.4 Signal Separation by Phase and Wave Vector	118
4.3	Wave Mixing on a Heterodimer	119
	4.3.1 Squaraine Dimers with Increasing Coupling	120
	4.3.2 Two-Wave Mixing: Linear Absorption	121
	4.3.3 Four-Wave Mixing	124
4.4	Overview: Fluorescence vs. Polarization	137
Refer	rences	139
СНА	APTER 5	
Light	t Harvesting in Photosynthesis: From Structure to Function	141
Thor	mas Renger	
5.1	Overview	141
$5.1 \\ 5.2$	Frenkel Exciton Hamiltonian and Parameterization	141
5.2	5.2.1 Electronic Degrees of Freedom	141
		$143 \\ 152$
۳.0	0.2.0 1 0.10.11.00.11.01 0.1 0.10 1 1.10 1 1.00.11.	154
5.3	Quantum Dynamics	156
- ,	5.3.1 Energy Transfer in the FMO Protein	162
5.4	Light-Harvesting Efficiency of the Core of Green Sulfur Bacteria	163
5.5	Photosynthetic Light Conversion as a Blueprint	
	for Organic Solar Cells?	169
Refe	rences	171
OTT 1	DEED A	
	APTER 6	
_	unic Photovoltaics – Excitons at Work	175
Irene	e Burghardt	
6.1	Introduction	175
6.2	Key Elementary Steps	177
6.3	Theoretical Approaches	179
	6.3.1 First-Principles Parametrized Lattice Hamiltonians	180
	6.3.2 Vibronic Coupling Effects	182
	6.3.3 Multiconfigurational Quantum Dynamics	187
6.4	Coherent Effects in Exciton Dynamics: Case Studies	187
0.1	6.4.1 Exciton Dissociation at Donor-Acceptor Interfaces	187
	6.4.2 Intra-Chain Exciton Diffusion	190
6.5	Brief Excursion to 2D Electronic Spectroscopy	190
		192 195
6.6	Discussion and Outlook	
Reiei	rences	196
OTT A	DITED 7	
	PTER 7	100
	putational Exercise: Introduction to Quantum Dynamical Simulations	199
Dom	inik Brey and James A. Green	
7.1	Conventions in this Chapter	199

X Contents

	7.1.1 Initial Conditions	200
	7.1.2 Atomic Units	201
	7.1.3 Python Packages	201
7.2	Solving the Time-Dependent Schrödinger Equation	202
	7.2.1 Numerical Perspective	203
7.3	Single-State Systems	205
7.4	Imaginary Time Propagation	214
7.5	Multiple Electronic States	219
	7.5.1 Density Matrix	220
7.6	Autocorrelation Function	222
7.7	Excitonic Dimer	226
	7.7.1 Uncoupled Dimer	229
7.8	Coupled Dimer	238
7.9	Final Remarks	244
Refer	rences	244
_	PTER 8	
	putational Exercise: Ultrafast Spectroscopy of Complex	
Mole	cular Systems	247
Jame	s A. Green and Dominik Brey	
8.1	Introduction	247
0.1	8.1.1 Background and Theory	249
8.2	Setup of System	252
J	8.2.1 Setup Notebook and Python Libraries	252
	8.2.2 Define Parameters for System	252
	8.2.3 Input to UFSS	254
8.3	Ultrafast Laser Pulse and Absorption Spectrum	256
	8.3.1 Absorption Spectrum	259
	8.3.2 Inhomogeneous Broadening	262
8.4	Transient Absorption	264
	8.4.1 Peak Monitoring	267
8.5	2D Electronic Spectroscopy (2DES)	269
	8.5.1 Rephasing, Non-Rephasing and Absorptive Spectra	269
	8.5.2 Peak Monitoring	275
	8.5.3 Inhomogeneous Broadening	276
8.6	Feynman Diagrams	278
	8.6.1 Generating Feynman Diagrams	279
	8.6.2 Assigning Feynman Diagrams	281
	8.6.3 Separating Spectral Components by Diagram	282
	8.6.4 Time Ordering	284
8.7	Where Do We Go From Here?	285
	rences	285

Chapter 1

Linear and Nonlinear Propagation of Ultrashort Light Pulses

Giulio Cerullo^{1,*} and Cristian Manzoni²

¹Dipartimento di Fisica, Politecnico di Milano, Piazza L. da Vinci 32, 20133 Milano, Italy

²Istituto di Fotonica e Nanotecnologie - CNR, Piazza L. da Vinci 32, 20133 Milano, Italy

*e-mail: giulio.cerullo@polimi.it

1.1 Introduction

Ultrafast optical spectroscopy is a very powerful technique for the investigation of non-equilibrium time-dependent processes in molecules and solids. It is used by an interdisciplinary group of physicists, chemists and biologists to study problems ranging from charge carrier relaxation in semiconductors and their nanostructures to photosynthetic light harvesting in plants to the making and breaking chemical bonds during chemical reactions. This variety of experiments has been enabled by spectacular developments in ultrafast laser technology in the last three decades. Nowadays, it is possible to generate powerful femtosecond light pulses with high stability and reliability using mature primary laser sources, such as Ti:sapphire and Ytterbium lasers, working in the near-infrared range. Furthermore, it is possible to tune the frequency of the ultrashort laser pulses almost continuously, from the mid-infrared to the ultraviolet, using nonlinear optical frequency conversion processes.

With respect to the early times of femtosecond laser technology, when the generation of the ultrashort pulses was an experiment in itself, in which the researchers invested a lot of time and effort, nowadays, ultrafast laser systems have become increasingly turnkey. On the one hand, this gives the researchers the opportunity to perform sophisticated experiments and concentrate on the physicochemical processes of interest. On the other hand, however, some of the knowledge on the

DOI: 10.1051/978-2-7598-3760-1.c001 © The authors, 2025 properties of ultrashort pulses and their linear and nonlinear interaction with matter, which was previously necessary in order to be able to generate the ultrashort light pulses, may have been lost. This chapter aims to fill this gap by reviewing linear and nonlinear propagation of ultrashort pulses in transparent media. Due to space limitations, it does not cover all the essential topics of ultrafast optics, which include techniques for the generation and the temporal characterization of ultrashort pulses. It instead focuses on the linear propagation of femtosecond pulses, with the effects of dispersion and the techniques for its compensation (section 1.2) and the propagation in second-order nonlinear media, with an emphasis on the optical parametric amplification process, which allows tuning the frequency of ultrashort pulses (section 1.3). This chapter aims to present a self-consistent treatment, starting from Maxwell's wave propagation equations in the scalar and plane wave approximations.

1.2 Linear Propagation of Ultrashort Pulses: Dispersion and its Compensation

The electric field of an ultrashort light pulse can be written as:

$$E_0(t) = \frac{1}{2} \{ A(t) \exp[i(\omega_0 t + \varphi)] + \text{c.c.} \} = \Re\{ A(t) \exp[i(\omega_0 t + \varphi)] \}$$
 (1)

where A(t) is the complex pulse envelope and $\exp[i(\omega_0 t + \varphi)]$ is the traveling optical carrier, where ω_0 is the carrier angular frequency and φ is the carrier-envelope phase. In the following, whenever linear operators are involved, we will consider the complex field:

$$E(t) = A(t) \exp[i(\omega_0 t + \varphi)] \tag{2}$$

and extract the real part only as a final step. The Fourier transform of the complex field E(t) is

$$\tilde{E}(\omega) = \tilde{A}(\omega - \omega_0) = |\tilde{A}(\omega - \omega_0)| \exp[i\phi(\omega - \omega_0)]$$
(3)

where $|\tilde{A}(\omega)|$ is the spectral amplitude and $\phi(\omega)$ is the spectral phase of the Fourier transform of the complex envelope A(t), whereas the Fourier transform of the real field is $\tilde{E}_0(\omega) = 1/2 \left[\tilde{A}(\omega - \omega_0) + \tilde{A}^*(-\omega - \omega_0) \right]$. Both the spectral amplitude and the spectral phase of $\tilde{A}(\omega - \omega_0)$ are crucial for the generation of an ultrashort pulse. According to the Fourier transform theorem, a short pulse in the time domain corresponds to a broad spectrum in the frequency domain, so an ultrashort pulse necessarily has a polychromatic spectrum, which contains different frequency components. However, having a broadband spectrum is insufficient for having an ultrashort pulse. One also needs to control the spectral phase, which determines the relative arrival times of the different frequency components of the pulse. In the following, we will describe the linear propagation of an ultrashort pulse in a transparent medium, showing how it affects its duration and spectral phase.

We start from Maxwell's wave equation for an electromagnetic wave propagating in a medium with a polarization \mathbf{P} , which can be written for the electric field vector $\mathbf{E}(x, y, z, t)$ as:

$$\nabla^2 \mathbf{E} = \mu_0 \varepsilon_0 \frac{\partial^2 \mathbf{E}}{\partial t^2} + \mu_0 \frac{\partial^2 \mathbf{P}}{\partial t^2} \tag{4}$$

Equation (1) is a vector equation. We first make the scalar approximation by assuming a linearly polarized pulse propagating in the z direction and considering only one component E of the electric field vector \mathbf{E} :

$$\frac{\partial^2 E}{\partial z^2} + \nabla_T^2 E = \mu_0 \varepsilon_0 \frac{\partial^2 E}{\partial t^2} + \mu_0 \frac{\partial^2 P}{\partial t^2}$$
 (5)

where

$$\nabla_T^2 E = \frac{\partial^2 E}{\partial x^2} + \frac{\partial^2 E}{\partial y^2} \tag{6}$$

is the so-called transverse Laplacian operator. We further make the plane wave approximation by neglecting any transverse variation of the electric field and assuming that:

$$E = E(z, t) \tag{7}$$

so that the propagation equation becomes:

$$\frac{\partial^2 E}{\partial z^2} - \frac{1}{c_0^2} \frac{\partial^2 E}{\partial t^2} = \mu_0 \frac{\partial^2 P}{\partial t^2} \tag{8}$$

where $c_0 = 1/\sqrt{\epsilon_0 \mu_0}$ is the speed of light in vacuum. Equation (5) already allows a first physical insight into the propagation of an electromagnetic (e.m.) wave into a medium with polarization P. The polarization is on the right-hand side of the equation and thus acts as a driving term for the electric field, modifying it during propagation. Let us now consider a plane wave of the form:

$$E(t) = A(z, t) \exp[i(\omega_0 t - k_0 z)] = |A(z, t)| \exp\{i[\omega_0 t - k_0 z + \phi(z, t)]\}$$
(9)

where A(z, t) is the complex field envelope, $\phi(z, t)$ is its temporal phase, ω_0 is the carrier angular frequency and $k_0 = \frac{\omega_0}{c(\omega_0)} = \frac{\omega_0 n(\omega_0)}{c_0}$ is the wave number.

The polarization is a function of the incident electric field and can be decomposed in the sum of a linear (P_L) and a nonlinear (P_{NL}) component:

$$P(z,t) = P_L(z,t) + P_{NL}(z,t)$$
(10)

Similarly to equation (9), the polarization can be written as:

$$P(z,t) = p(z,t) \exp[i(\omega_0 t - k_p z)]$$
(11)

where the wavevector of the polarization is generically indicated as k_p and can be different from that of the electric field k_0 ; in section 1.3, we will treat the nonlinear case and calculate the exact value of k_p .

For the remainder of this section, instead, we will consider only the linear component:

$$P_L(z,t) = \varepsilon_0 \chi E(z,t) = \varepsilon_0 \chi A(z,t) \exp[i(\omega_0 t - k_0 z)] = p_L(z,t) \exp[i(\omega_0 t - k_0 z)]$$
(12)

where χ is the dielectric susceptibility; note that for the linear component k_p is exactly k_0 . In this case, equation (8) becomes:

$$\frac{\partial^2 E}{\partial z^2} - \frac{1}{c_0^2} \frac{\partial^2 E}{\partial t^2} = \mu_0 \frac{\partial^2 P_L}{\partial t^2}$$
 (13)

Equation (13) is more easily solved in the frequency domain by introducing the Fourier transform:

$$\tilde{E}(z,\omega) = \Im[E(z,t)] = \int_{-\infty}^{+\infty} E(z,t) \exp(-i\omega t) dt$$
 (14)

which can be expressed as:

$$\tilde{E}(z,\omega) = \tilde{A}(z,\omega - \omega_0) \exp(-ik_0 z)$$
(15a)

Similarly, the Fourier transform of the polarization can be expressed as:

$$\tilde{P}_L(z,\omega) = \tilde{p}_L(z,\omega - \omega_0) \exp(-ik_0 z)$$
(15b)

where $A(z, \omega) = \Im[A(z, t)]$. By taking the Fourier transform of (13) and recalling the derivative rule for the Fourier transform:

$$\Im\left[\frac{d^n F(t)}{dt^n}\right] = (i\omega)^n \tilde{F}(\omega) \tag{16}$$

we obtain:

$$\frac{\partial^2 \tilde{E}}{\partial z^2} + \frac{\omega^2}{c_0^2} \tilde{E} = -\mu_0 \omega^2 \tilde{P}_L \tag{17}$$

We can express the derivatives with respect to the longitudinal propagation coordinate z as follows:

$$\frac{\partial \tilde{E}}{\partial z} = \left(\frac{\partial \tilde{A}}{\partial z} - ik_0\tilde{A}\right) \exp(-ik_0z)$$
 (18a)

$$\frac{\partial^2 \tilde{E}}{\partial z^2} = \left(\frac{\partial^2 \tilde{A}}{\partial z^2} - 2ik_0 \frac{\partial \tilde{A}}{\partial z} - k_0^2 \tilde{A}\right) \exp(-ik_0 z) \tag{18b}$$

By plugging (18b) into (17) we obtain:

$$\frac{\partial^2 \tilde{A}}{\partial z^2} - 2ik_0 \frac{\partial \tilde{A}}{\partial z} - k_0^2 \tilde{A} + \frac{\omega^2}{c_0^2} \tilde{A} = -\mu_0 \omega^2 \tilde{p}_L \tag{19}$$

We now make the Slowly Varying Envelope Approximation (SVEA), which consists of assuming that $\frac{\partial^2 \tilde{A}}{\partial z^2} \ll k_0 \frac{\partial \tilde{A}}{\partial z}$; this corresponds to neglecting variations of the envelope over propagation lengths of the order of the wavelength and breaks down only for extreme focusing conditions (down to the diffraction limit). With this assumption, we obtain:

$$-2ik_0\frac{\partial\tilde{A}}{\partial z} - k_0^2\tilde{A} + \frac{\omega^2}{c_0^2}\tilde{A} = -\mu_0\omega^2\tilde{p}_L \tag{20}$$

For a monochromatic wave, the linear polarization can be expressed as:

$$\tilde{P}_L(\omega) = \varepsilon_0 \chi^{(1)}(\omega) E(\omega) \tag{21}$$

where $\chi^{(1)}(\omega)$ is the linear (first-order) dielectric susceptibility. By recalling the definition of linear complex refractive index $n_L(\omega) = \sqrt{1 + \chi^{(1)}(\omega)}$, we obtain:

$$\tilde{p}_L(\omega) = \varepsilon_0 \left[n_L^2(\omega) - 1 \right] \tilde{A}(\omega) \tag{22}$$

We finally obtain:

$$-2ik_0\frac{\partial\tilde{A}}{\partial z} - k_0^2\tilde{A} + \frac{\omega^2}{c_0^2}\tilde{A} = -\frac{\omega^2}{c_0^2} \left[n_L^2(\omega) - 1\right]\tilde{A}$$
 (23)

which simplifies to:

$$2ik_0 \frac{\partial \tilde{A}}{\partial z} = \left[k^2(\omega) - k_0^2\right] \tilde{A}$$
 (24)

with $k(\omega) = \frac{\omega}{c_0} n(\omega)$. In a dispersive medium, the refractive index is a function of frequency, and the wavevector thus becomes a nonlinear function of ω . We can write:

$$k^{2}(\omega) - k_{0}^{2} = [k(\omega) - k_{0}][k(\omega) + k_{0}] \approx 2k_{0}[k(\omega) - k_{0}]$$
(25)

where the approximation holds for a small bandwidth around ω_0 . By a Taylor expansion of $k(\omega)$ around ω_0 :

$$k(\omega) = k_0 + \left(\frac{dk}{d\omega}\right)_{\omega_0} (\omega - \omega_0) + \frac{1}{2} \left(\frac{d^2k}{d\omega^2}\right)_{\omega_0} (\omega - \omega_0)^2 + \frac{1}{6} \left(\frac{d^3k}{d\omega^3}\right)_{\omega_0} (\omega - \omega_0)^3 + \dots$$
(26)

Usually, an expansion up to the third order (or to the second order for moderate pulse bandwidths) is sufficient. By substituting (25) and (26) into (24), we obtain:

$$i\frac{\partial \tilde{A}(\omega - \omega_0)}{\partial z} \cong k_0'(\omega - \omega_0)\tilde{A} + \frac{1}{2}k_0''(\omega - \omega_0)^2\tilde{A} + \frac{1}{6}k_0'''(\omega - \omega_0)^3\tilde{A}$$
 (27)

In particular, it can be shown that $k_0' = \left(\frac{dk}{d\omega}\right)_{\omega_0} = \frac{1}{v_{g0}}$, where v_{g0} is the group velocity at the carrier angular frequency; similarly $k_0'' = \left(\frac{d^2k}{d\omega^2}\right)_{\omega_0} = \text{GVD}$ is known as Group Velocity Dispersion (GVD) and $k_0''' = \left(\frac{d^3k}{d\omega^3}\right)_{\omega_0}$ is the third-order dispersion. We can now transform (24) back to the time domain. Recalling the rule:

$$\mathfrak{I}^{-1}\left[\omega^n \tilde{F}(\omega)\right] = (-i)^n \frac{d^n F(t)}{dt^n} \tag{28}$$

we obtain:

$$\frac{\partial A(z,t)}{\partial z} + \frac{1}{v_{c0}} \frac{\partial A}{\partial t} - \frac{i}{2} k_0'' \frac{\partial^2 A}{\partial t^2} + \frac{1}{6} k_0''' \frac{\partial^3 A}{\partial t^3} = 0$$
 (29)

Equation (29) can be simplified by changing to a temporal frame of reference that moves with the group velocity of the carrier wave: z' = z, $\tau = t - \frac{z}{v_{g0}}$. We obtain:

$$\frac{\partial}{\partial t} = \frac{\partial}{\partial \tau}; \frac{\partial^n}{\partial t^n} = \frac{\partial^n}{\partial \tau^n}; \frac{\partial}{\partial z} = \frac{\partial}{\partial z'} - \frac{1}{v_{\sigma 0}} \frac{\partial}{\partial \tau}$$
(30)

In this new frame of reference, equation (29) becomes:

$$\frac{\partial A}{\partial z'} - \frac{i}{2} k_0'' \frac{\partial^2 A}{\partial \tau^2} + \frac{1}{6} k_0''' \frac{\partial^3 A}{\partial \tau^3} = 0$$
 (31)

In this case, often satisfied in practice for moderate pulse bandwidths, in which one assumes $k_0''' \cong 0$, equation (31) further simplifies to:

$$\frac{\partial A}{\partial z} - \frac{i}{2} k_0'' \frac{\partial^2 A}{\partial \tau^2} = 0 \tag{32}$$

Equation (32), also known as the parabolic equation, captures the main physics of linear propagation of ultrashort pulses in dispersive media.

Let us study the propagation of a pulse with a known envelope at z=0, $A(0,t)=A_0(t)$. We start with the simplified case of a non-dispersive medium, in which the refractive index is constant with frequency: $n(\omega)=n(\omega_0)=$ const. In this case, $k(\omega)=\frac{\omega}{c_0}n(\omega_0)$ is a linear function of frequency and $k_0''=0$. We then have: $\frac{\partial A(z,\tau)}{\partial z}=0$ which gives $A(L,\tau)=$ const. $=A_0(\tau)=A_0\left(t-\frac{L}{v_{g0}}\right)$. We thus have a pulse that moves with the group velocity of the carrier frequency (so that its peak position shifts linearly with time) but maintains its shape unaltered. Note that, strictly speaking, only the vacuum is a non-dispersive medium. According to the properties of the Fourier transform operator, the spectrum of the time-shifted pulse after propagation acquires a linear phase:

$$\tilde{A}(L,\omega) = \tilde{A}(0,\omega) \exp\left(-i\frac{L}{v_{g0}}\omega\right) = \tilde{A}(0,\omega) \exp\left(-i\tau_{g0}\omega\right)$$
(33)

where $\tau_{g0} = \frac{L}{v_{g0}}$ is called the group delay at the carrier frequency and is the delay of the pulse envelope upon propagation in a non-dispersive medium.

We now turn to a dispersive medium; equation (32) can be solved by taking a Fourier transform with respect to time:

$$\frac{\partial \tilde{A}(z,\omega)}{\partial z} + \frac{i}{2}\omega^2 z k_0'' \tilde{A} = 0 \tag{34}$$

Note that now we are working in the so-called baseband, *i.e.*, with envelope A, which is a slowly varying function of time. Equation (34) can be easily solved by separation of variables:

$$\tilde{A}(L,\omega) = \tilde{A}(0,\omega) \exp\left(-\frac{i}{2}D_2\omega^2\right)$$
 (35)

where we have defined $D_2 = k_0''L$ as the second-order dispersion or Group Delay Dispersion (GDD). It should be noted that, since the phase shift induced by propagation through a length L can be expressed as $\varphi(\omega) = k(\omega)L$, one can write $D_2 = \left(\frac{d^2\phi}{d\omega^2}\right)_{co}$. We can now go back to the time domain and obtain:

$$A(L,t) = \frac{1}{2\pi} \int_{-\infty}^{+\infty} \tilde{A}(0,\omega) \exp\left(-\frac{i}{2}D_2\omega^2\right) \exp(i\omega t) d\omega$$
 (36)

Equation (36) can be numerically solved for any input pulse; we can see that the effect of propagation in a dispersive medium is to add to the spectrum a **quadratic phase**. An analytical solution of (36) is possible only in the special case of a Gaussian pulse shape:

$$A_0(\tau) = A_0 \, \exp\left(-\frac{\tau^2}{2\tau_p^2}\right) \tag{37}$$

This pulse shape, although it may not necessarily represent the realistic shape of an ultrashort laser pulse, is amenable to analytical calculation because the Fourier transform of a Gaussian function is also Gaussian. The parameter τ_p defines the pulse duration; for an ultrashort pulse, in particular, one usually specifies the duration as the Full Width at Half Maximum (FWHM) of intensity, which is given by $\tau_{\rm FWHM} = \sqrt{2\log 2}\tau_p$. Recalling that:

$$\Im\left[\exp\left(-at^2\right)\right] = \sqrt{\frac{\pi}{a}}\exp\left(-\frac{\omega^2}{4a}\right) \tag{38}$$

And putting $a = 1/2\tau_p^2$, we obtain:

$$\tilde{A}_0(\omega) = \sqrt{2\pi}\tau_p A_0 \exp\left(-\frac{\tau_p^2 \omega^2}{2}\right)$$
 (39)

and, after propagation:

$$\tilde{A}(L,\omega) = \sqrt{2\pi}\tau_p A_0 \exp\left[-\frac{\tau_p^2}{2}\omega^2 \left(1 + i\frac{D_2}{\tau_p^2}\right)\right]$$
(40)

Transforming back to the time domain, we obtain:

$$A(L,t) = \frac{A_0 \tau_p}{\sqrt{\tau_p^2 + jD_2}} \exp\left[-\frac{\tau^2}{2\left(\tau_p^2 + iD_2\right)}\right]$$
$$= \frac{A_0 \tau_p}{\sqrt{\tau_p^2 + jD_2}} \exp\left(-\frac{\tau^2}{2\tau_{\text{out}}^2}\right) \exp[i\phi(\tau)]$$
(41)

where:

$$\tau_{\text{out}}^2 = \tau_p^2 + \frac{D_2^2}{\tau_p^2} = \tau_p^2 \left[1 + \left(\frac{D_2}{\tau_p^2} \right)^2 \right]$$
(42a)

and:

$$\phi(\tau) = \frac{D_2 \tau^2}{2(\tau_p^4 + D_2^2)}$$
 (42b)

By recalling that $D_2 = k_0''L$ and defining a "dispersion length" $L_D = \frac{\tau_p^2}{k_0''} = \frac{\tau_p^2}{\text{GVD}}$, equation (42a) can be rewritten as:

$$\tau_{\text{out}} = \tau_p \sqrt{1 + \left(\frac{L}{L_D}\right)^2} \tag{43}$$

Equation (43) provides a physical insight into the mechanism of dispersive pulse broadening. For short propagation lengths, $L \ll L_D$, the pulse width remains basically unchanged upon propagation, while for long propagation, $L \gg L_D$, we get a linear broadening with distance, $\tau_{\rm out} = \frac{\tau_p}{L_D} L$. It is important to notice that the dispersion length is inversely proportional to the GVD of the medium and directly proportional to the square of the pulse duration. Therefore, shorter pulses start to broaden for a much shorter propagation length, *i.e.*, they are intrinsically more fragile. We will better understand the physical reasons for this in the following section.

In passing, we note that the temporal spreading of the Gaussian pulse due to dispersion has the same expression as the spatial spreading of a Gaussian beam due to diffraction:

$$w(z) = w_0 \sqrt{1 + \left(\frac{z}{z_R}\right)^2} \tag{44}$$

where the Rayleigh range, defined as $z_R = \frac{n\pi w_0^2}{\lambda}$, plays a similar role to the dispersion length L_D .

Let us now consider the time-dependent temporal phase. By recalling that the ultrashort pulse is written as

$$E(\tau) = |A(z,\tau)| \exp\{i[\omega_0 \tau - k_0 z + \phi(z,\tau)]\}$$
(45)

The instantaneous pulse angular frequency becomes:

$$\omega_i(\tau) = \omega_0 + \frac{d\phi}{d\tau} = \omega_0 + \frac{2D_2\tau}{2(\tau_p^4 + D_2^2)}$$
 (46)

Therefore, in the most general case, its frequency is not constant but displays a linear temporal variation, or "chirp". In particular, for $D_2 > 0$, the frequency increases with time, *i.e.*, the leading edge of the pulse is composed of low-frequency components ("positive chirp" or "up-chirp"); on the contrary, for $D_2 < 0$, the frequency decreases with time, hence the leading edge of the pulse is composed of high-frequency components ("negative chirp" or "down-chirp").

To understand this behavior, let us recall that $D_2 = \frac{d}{d\omega} \frac{dk}{d\omega} = \frac{d}{d\omega} \left(\frac{1}{v_g(\omega)}\right)$ so that $D_2 > 0$ means that v_g decreases with frequency (and vice versa for $D_2 < 0$). For $D_2 > 0$, therefore, the higher frequencies (blue components of the spectrum) move at a lower speed with respect to the lower frequencies (red components of the spectrum) and become delayed. When the pulse propagates in a dispersive medium with $D_2 > 0$, the pulse thus acquires a further up-chirp. The opposite holds for the case of a down-chirp. Figure 1.1 shows examples of pulses with a positive and a negative chirp.

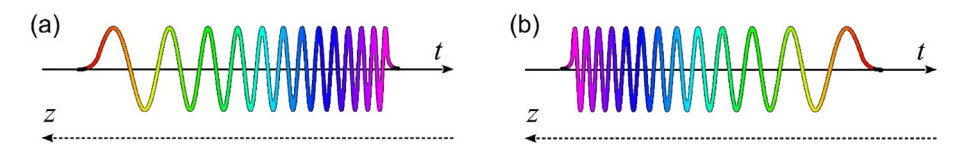


Fig. 1.1 – Temporal profiles of pulses with a positive (a) and with a negative frequency chirp (b). Both the time and propagation axes are given.

We can, therefore, conclude that linear propagation of an ultrashort pulse in a dispersive medium has two effects: i) it broadens its temporal profile; ii) it introduces a frequency chirp, *i.e.*, a time-dependent carrier frequency. The two effects are strictly related since the temporal broadening is due precisely to the different propagation velocities of the spectral components of the ultrashort pulse. This also explains why shorter pulses are more fragile: since, due to the Fourier theorem, they have broader bandwidths, their frequency components will be more separated and will, therefore, experience more relative delay upon propagation. To illustrate this

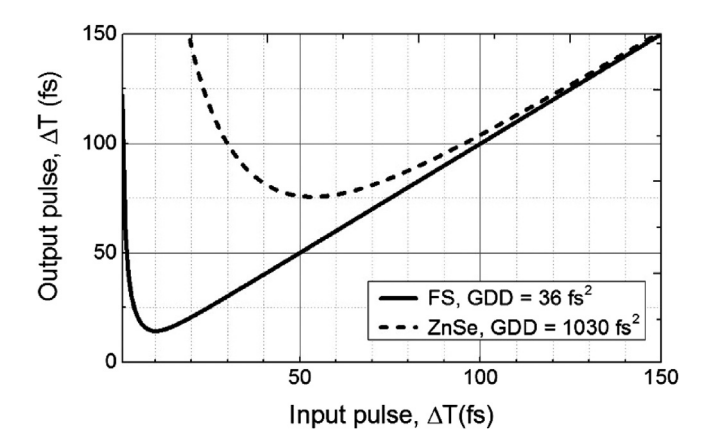


Fig. 1.2 – Output pulse duration as a function of input pulse duration upon propagation in a 1-mm-thick plate of fused silica (FS) and zinc selenide (ZnSe). The dispersion is evaluated at carrier wavelength $\lambda = 800$ nm. The durations are calculated at FWHM of the pulse intensity.

effect, figure 1.2 shows the calculated output pulse duration upon propagation of a femtosecond pulse through 1 mm of fused silica (FS) and ZnSe glass (a situation quite common in an ultrafast spectroscopy experiment) as a function of the input pulse duration ΔT , calculated as FWHM of the pulse intensity. One can see that, for input pulse durations longer than 100 fs, in both glasses, there is hardly any effect of dispersive propagation. On the other hand, for input pulses shorter than 50 fs in ZnSe, the effect becomes dramatic and for a pulse duration of 10 fs, the output pulse is lengthened to more than 200 fs.

To further understand dispersive pulse broadening, let us express the laser pulse like an inverse Fourier transform (or Fourier integral):

$$E(t) = \frac{1}{2\pi} \int_{-\infty}^{+\infty} \left| \tilde{E}(\omega) \right| \exp[-i\phi(\omega)] \exp[i\omega t] d\omega \tag{47}$$

Let us now slice from the pulse spectrum a narrow interval of frequencies around a given angular frequency $\overline{\omega}$:

$$E_{\overline{\omega}}(t) = \frac{1}{2\pi} \int_{\overline{\omega} - \Delta\omega}^{\overline{\omega} + \Delta\omega} |\tilde{E}(\omega)| \exp[-i\phi(\omega)] \exp[i\omega t] d\omega$$
 (48)

By expanding $\phi(\omega)$ in a Taylor series around $\overline{\omega}$, we obtain:

$$E_{\overline{\omega}}(t) = \frac{1}{2\pi} \exp[i\overline{\omega}t] \int_{\overline{\omega} - \Delta\omega}^{\overline{\omega} + \Delta\omega} |\tilde{E}(\omega)| \exp\left[-i\phi(\overline{\omega}) - i\left(\frac{d\phi}{d\omega}\right)_{\overline{\omega}}(\omega - \overline{\omega})\right] \exp[i(\omega - \overline{\omega})t] d\omega$$
$$= \frac{1}{2\pi} \exp[i(\overline{\omega}t - \phi(\overline{\omega}))] \int_{\overline{\omega} - \Delta\omega}^{\overline{\omega} + \Delta\omega} |\tilde{E}(\omega)| \exp\left[i(\omega - \overline{\omega})\left(t - \left(\frac{d\phi}{d\omega}\right)_{\overline{\omega}}\right)\right] d\omega \qquad (49)$$

One can easily see that the right-hand side of the equation is maximum when the argument of the exponential is zero, *i.e.* when:

$$t = \tau_g(\overline{\omega}) = \left(\frac{d\phi}{d\omega}\right)_{\overline{\omega}} \tag{50}$$

The derivative of the spectral phase with respect to frequency, or group delay τ_g , is thus the relative arrival time of a given frequency wavepacket within the pulse. By a Taylor expansion of the spectral phase:

$$\phi(\omega) = \phi(\omega_0) + \left(\frac{d\phi}{d\omega}\right)_{\omega_0} (\omega - \omega_0) + \frac{1}{2} \left(\frac{d^2\phi}{d\omega^2}\right)_{\omega_0} (\omega - \omega_0)^2 + \frac{1}{6} \left(\frac{d^3\phi}{d\omega^3}\right)_{\omega_0} (\omega - \omega_0)^3 + \dots$$

$$= \phi(\omega_0) + \tau_{g0}(\omega - \omega_0) + \frac{1}{2} D_2(\omega - \omega_0)^2 + \frac{1}{6} D_3(\omega - \omega_0)^3 + \dots$$
(51)

where $D_3 = \left(\frac{d^3\phi}{d\omega^3}\right)_{\omega_0}$ is called third-order dispersion (TOD). One can thus write:

$$\tau_g(\omega) = \frac{d\phi(\omega)}{d\omega} = \tau_{g0} + D_2(\omega - \omega_0) + \frac{1}{2}D_3(\omega - \omega_0)^2 + \dots$$
(52)

Equation (52) shows that for $D_2 = D_3 = 0$, all the frequency components of the pulse arrive simultaneously so that it is called Transform-Limited (TL), while in all other cases, the different frequency components arrive at different times, and the pulse becomes chirped. In particular, if the D_2 term is dominant (quadratic chirp) then the group delay varies linearly with frequency, meaning that the instantaneous frequency is swept within the pulse envelope (from red to blue for positive chirp and from blue to red for negative chirp, see figure 1.1).

When an ultrashort pulse propagates in a dispersive optical medium (which is any medium except vacuum), its refractive index depends on the wavelength, n = n (ω), giving rise to dispersion. Propagation through a block of material with thickness L changes the spectral phase according to the expression:

$$\phi_{\text{out}}(\omega) = \phi_{\text{in}}(\omega) + Ln(\omega)\omega/c \tag{53}$$

and introduces the following GDD:

$$D_2 = \lambda^3 / (2\pi c^2) d^2 n / d\lambda^2 L \tag{54}$$

where we have used the expression of the refractive index as a function of wavelength, $n = n(\lambda)$, also known as Sellmeier's equation.

Nearly all materials in the visible and near-infrared range have $d^2n/d\lambda^2 > 0$ so they introduce a positive GDD, which corresponds to an up-chirp. In an ultrafast spectroscopy experiment, therefore, the optical elements on the beam path (lenses, polarizers, birefringent plates, cryostat windows,...) introduce a positive dispersion which lengthens the pulses and degrades the temporal resolution. To reverse this effect and retrieve a TL pulse duration, one needs an optical system that introduces negative dispersion, known in ultrafast optics as a pulse compressor. To understand

the effect of a pulse compressor on the spectral phase, let us consider an input pulse with a spectrum:

$$\tilde{E}_{\rm in}(\omega) = |\tilde{E}_{\rm in}(\omega)| \exp[i\varphi_{\rm in}(\omega)] \tag{55}$$

and a lossless linear optical system, the pulse compressor, which only introduces a spectral phase with a transmission function:

$$T(\omega) = \exp\left[i\varphi_{\text{comp}}(\omega)\right] \tag{56}$$

The transmitted field can then be written as:

$$\tilde{E}_{\text{out}}(\omega) = \tilde{E}_{\text{in}}(\omega) T(\omega) = \left| \tilde{E}_{\text{in}}(\omega) \left| \exp \left\{ i \left[\varphi_{\text{in}}(\omega) + \varphi_{\text{comp}}(\omega) \right] \right\} \right.$$
 (57)

so that the GDD and the TOD of the output pulse can be expressed as:

$$D_{2\text{out}} = D_{2\text{in}} + D_{2\text{comp}} \tag{58}$$

$$D_{3\text{out}} = D_{3\text{in}} + D_{3\text{comp}} \tag{59}$$

where $D_{2\text{comp}} = \left[\frac{d^2 \varphi_{\text{comp}}(\omega)}{d\omega^2}\right]_{\omega_0}$ and $D_{3\text{comp}} = \left[\frac{d^3 \varphi_{\text{comp}}(\omega)}{d\omega^3}\right]_{\omega_0}$. An ideal pulse compressor should, therefore, introduce a GDD and a TOD, which precisely cancel those of the input pulse. Figure 1.3 summarizes the most common pulse compressors used in ultrafast optics.

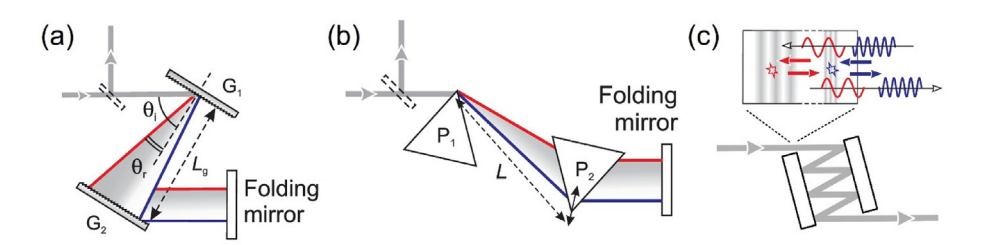


Fig. 1.3 – Pulse compressors most commonly used in ultrafast optics. (a) Grating compressor. (b) Prism compressor. (c) Chirped mirrors, with a detail on the reflection of long-wavelength (red) and low-wavelength (blue) waves.

Figure 1.3a shows the grating compressor, which consists of a pair of parallel and identical gratings [1]. For a wavelength λ incident at an angle θ_i on the grating, the reflected beam direction is given by the grating equation: $\sin \theta_r = \sin \theta_i + m \frac{\lambda}{d}$, where d is the grating period, and m is the diffraction order. For m = -1, the red frequencies travel a longer path with respect to the blue ones and are, therefore, more delayed, resulting in negative dispersion. The GDD can be expressed as

$$D_2 = -\frac{\lambda^3 L_g}{\pi^2 c^2 d^2} \frac{1}{\left[1 - (\sin\theta_i - \lambda/d)^2\right]^{3/2}}$$
 (60)

where L_g is the distance between the gratings. A single pass in the grating pair produces a spatial separation of the different frequency components of the pulse, which is known as spatial chirp. This effect can, however, be removed by a double pass on the gratings pair after reflection from a folding mirror. The negative GDD introduced by the grating pair depends on the design (grating period d, incidence angle θ_i) and on the distance L_g between the gratings. One should note that the grating pair compressor introduces a positive TOD ($D_3 > 0$), which, therefore, adds up to the one introduced by the dispersive medium. It is, therefore, not possible, using only a grating pair, to completely cancel the positive dispersion introduced by propagation in a medium.

Figure 1.3b shows the prism compressor, which consists of a pair of prisms at distance L, aligned in such a way as to be at minimum deviation for the incident beam [2, 3]. The angular dispersion of the first prism creates a longer path through the second prism material for the red wavelengths with respect to the blue ones, thus providing negative dispersion. To achieve a negative GDD, the prism distance L must be sufficiently large to compensate for the positive dispersion induced by propagation in the prism material itself. The GDD of the prism pair can be coarsely adjusted by setting the prisms distance L, and finely tuned by translating one of the prisms along a direction perpendicular to its base, thus varying its insertion and the positive material dispersion. Similarly to the grating pair, also the prism pair introduces a spatial chirp on the transmitted beam, which is removed by reflecting it on a folding mirror and passing it again through the prism sequence. With respect to the grating pair, the prism pair has the advantage of higher transmission: if the prisms have an apex angle cut such that at minimum deviation, the angle of incidence is Brewster's angle, there is virtually no reflection for the correct linear polarization (TM or p polarization) and the system is essentially loss-free. On the other hand, this compressor introduces not only a negative GDD but also a large negative TOD, which cannot be independently controlled; if the prism pair GDD is set to compensate for that of the material, then the overall dispersion of the system is dominated by the large negative TOD introduced by the prism pair. Since both GDD and TOD are proportional to the prism separation L, the ratio TOD/GDD depends on the prisms material and the wavelength and can be minimized by choosing materials with low dispersion (such as fused silica, MgF_2 , or CaF_2). In this case, however, the prism distance required to achieve a given value of D_2 increases. In summary, the prism pair is a very simple compressor but cannot be used with very short pulses (with a duration shorter than 15–20 fs in the visible) due to the residual TOD. In principle, a prism pair/grating pair combination with suitably chosen distances $L_{\text{grating}}/L_{\text{prism}}$ provides enough degrees of freedom to control both the GDD and the TOD of the output pulses [4], according to the equations:

$$D_{2\text{out}} = D_{2\text{in}} + D_{2\text{grating}} \left(L_{\text{grating}} \right) + D_{2\text{prism}} \left(L_{\text{prism}} \right) = 0 \tag{61a}$$

$$D_{3\text{out}} = D_{3\text{in}} + D_{3\text{grating}} \left(L_{\text{grating}} \right) + D_{3\text{prism}} \left(L_{\text{prism}} \right) = 0 \tag{61b}$$

A finer control on both GDD and TOD can be achieved by using the so-called chirped mirrors [5], shown in figure 1.3c. These mirrors are inspired by the multilayer Bragg dielectric mirrors, commonly used to achieve high reflectivity. Such mirrors consist of a large number (≈ 50) of thin films of alternating high (n_H) and low (n_L) refractive index materials with thickness $d = \lambda/4n_{H/L}$, which provide constructive interference between multiple reflections and thus high reflectivity at the wavelength λ . Chirped mirrors are designed in such a way that the layer thickness increases from the surface going towards the substrate. In this way, the high-frequency (short wavelength) components of the laser spectrum are reflected first, while the low frequency (long wavelength) components penetrate more deeply into the multilayer, thus acquiring an additional group delay. Suitable computer optimisation allows to avoid spurious resonances and design a custom-tailored frequency-dependent negative GDD/TOD, which compensates for the GDD/TOD introduced by propagation in one or more optical materials. Often, the obtained frequency-dependent GDD from a chirped mirror presents rather large oscillations around the design values; this problem can be overcome by using matched chirped mirror pairs in which the oscillations introduced by the two coupled mirrors cancel out [6]. When used with a specific optical system introducing a dispersion which is well characterized and stable in time, chirped mirrors can, therefore, compensate for both GDD and TOD and retrieve a TL pulse duration even for broadband pulses.

Chirped mirrors have several advantages: the dispersion can be arbitrarily controlled over very broad bandwidths (exceeding one octave), they have very high energy throughput, and they are particularly insensitive to misalignment, facilitating day-to-day operation. On the other hand, their fabrication is not trivial, since very high precision on the layer thickness is required, achievable only by sophisticated techniques such as ion beam sputtering. In addition, the negative GDD obtainable from a single bounce is typically rather small ($\approx -50 \text{ fs}^2$), so many bounces are generally required. Finally, using chirped mirrors, the GDD can only be varied in discrete steps by adding or removing a bounce pair; to achieve better control, one can add a pair of SiO₂ glass wedges, which allow one to finely vary the material dispersion by their controlled insertion.

In conclusion, after discussing the linear propagation of ultrashort pulses, a few general considerations can be drawn:

- i) Ultrashort pulses propagating in any medium (except vacuum) undergo dispersion, which results in a lengthening of their duration and in a frequency chirp, with the instantaneous carrier frequency varying with time; the effects of dispersion become more severe for very short pulses, due to their broad bandwidths.
- ii) When designing an ultrafast spectroscopy experiment, one should try to minimize dispersion by using only the strictly necessary amount of material. For example, it is better to use curved mirrors instead of lenses to collimate and focus the beams, and when glass windows are unavoidable (such as, for example, in the entrance windows of cryostats) one should try to minimize their thickness. In this way, one relaxes the requirements on the compressor and allows overall better dispersion compensation.

iii) To compensate for the unavoidable dispersion, one should use pulse compressors which introduce a negative dispersion to minimize the pulse duration at the plane of the sample. Whenever possible, one should use chirped mirrors, or else prism pairs made of materials with low TOD/GDD ratio.

1.3 Nonlinear Propagation of Ultrashort Pulses: Optical Parametric Amplifiers

Now we go back to the propagation of an ultrashort pulse in a nonlinear medium. We start with the equation:

$$\frac{\partial^2 E}{\partial z^2} - \frac{1}{c_0^2} \frac{\partial^2 E}{\partial t^2} = \mu_0 \frac{\partial^2 P_L}{\partial t^2} + \mu_0 \frac{\partial^2 P_{NL}}{\partial t^2}$$
 (62)

where the polarization has been split into a linear and a nonlinear term (see equation (11)). In this case, the nonlinear polarization can be expressed as:

$$\tilde{P}_{NL}(\omega) = \varepsilon_0 \chi^{(2)}(\omega) \tilde{E}^2(\omega) + \varepsilon_0 \chi^{(3)}(\omega) \tilde{E}^3(\omega) + \dots$$
 (63a)

where $\chi^{(n)}$ is the *n*-th order nonlinear susceptibility. \tilde{P}_{NL} becomes comparable to linear polarization when the intensity of the light field is higher than 10^9 W/cm^2 . Similarly to the approach used for equation (12) for the linear term, also the nonlinear polarization can be expressed as:

$$P_{NL}(z,t) = p_{NL}(z,t) \exp\left[i(\omega_0 t - k_p z)\right]$$
(63b)

As will be shown later, we emphasize that the wavenumber k_p of the nonlinear polarization at angular frequency ω_0 is different from that of the linear polarization and of the electric field, k_0 . The second derivative of the nonlinear polarization can be expressed as:

$$\frac{\partial^2 P_{NL}}{\partial t^2} = \left(\frac{\partial^2 p_{NL}}{\partial t^2} + 2i\omega_0 \frac{\partial p_{NL}}{\partial t} - \omega_0^2 p_{NL}\right) \exp\left[i(\omega_0 t - k_p z)\right]$$
(64)

We now make the approximation that the envelope p_{NL} varies slowly over the timescale of an optical cycle, so that

$$\frac{\partial^2 p_{NL}}{\partial t^2}, \omega_0 \frac{\partial p_{NL}}{\partial t} \ll \omega_0^2 p_{NL} \tag{65}$$

Equation (64) then becomes:

$$\frac{\partial^2 P_{NL}}{\partial t^2} \cong -\omega_0^2 p_{NL} \exp\left[i\left(\omega_0 t - k_p z\right)\right] \tag{66}$$

By plugging (66) into equation (62) and using the SVEA made in section 1.2 to derive equation (20), we obtain:

$$-2ik_0\frac{\partial A}{\partial z} - 2\frac{ik_0}{v_{o0}}\frac{\partial A}{\partial t} - k_0k_0''\frac{\partial^2 A}{\partial t^2} = -\mu_0\omega_0^2 p_{NL} \exp[-i\Delta kz]$$
 (67)

where $\Delta k = k_p - k_0$ is the so-called "wave-vector mismatch" between the nonlinear polarization and the field. Equation (67), recalling that $\omega_0/k_0 = c/n_0$, can be rewritten as:

$$\frac{\partial A}{\partial z} + \frac{1}{v_{a0}} \frac{\partial A}{\partial t} - \frac{i}{2} k_0'' \frac{\partial^2 A}{\partial t^2} = -i \frac{\mu_0 \omega_0 c}{2n_0} p_{NL} \exp[-i\Delta kz]$$
 (68)

We will now discuss the propagation of light pulses in a second-order nonlinear medium, with a non-zero second-order susceptibility, $\chi^{(2)} \neq 0$. Let us consider the superposition of three monochromatic and collinear waves, at frequencies ω_1, ω_2 and ω_3 :

$$E(z,t) = \frac{1}{2} \{ A_1(z,t) \exp[i(\omega_1 t - k_1 z)] + A_2(z,t) \exp[i(\omega_2 t - k_2 z)] + A_3(z,t) \exp[i(\omega_3 t - k_3 z)] + \text{c.c.} \}$$
(69)

satisfying the condition $\omega_1 + \omega_2 = \omega_3$. Note that in this case, we are using the real notation introduced in equation (1): this is mandatory since we are considering a nonlinear interaction in a medium with a second-order response:

$$P_{NL}(z,t) = \varepsilon_0 \chi^{(2)} E^2(z,t) \tag{70}$$

in which the interaction depends on the square of the electric field.

This situation is known as three-wave mixing or nonlinear second-order parametric interaction and corresponds to an exchange of energy between the three fields by means of second-order nonlinearity. By inserting equation (69) into equation (70), we can calculate the nonlinear polarization. This will result in the linear combination of functions oscillating at frequencies $2\omega_1$, $2\omega_2$, $2\omega_3$, $|\omega_1 \pm \omega_2|$, $|\omega_1 \pm \omega_3|$, and $|\omega_2 \pm \omega_3|$ which are the source of a variety of nonlinear optical phenomena, such as second-harmonic generation (SHG), sum-frequency generation (SFG), difference-frequency generation (DFG) and optical parametric amplification (OPA).

Let's now assume that only the interaction which mixes the fields at frequencies ω_1 , ω_2 and ω_3 is efficient, due to the phase-matching condition, which will be defined and explained later. We will hence only keep the components of the nonlinear polarization at frequencies ω_1 , ω_2 and ω_3 , which are:

$$P_{1NL}(z,t) = \frac{\varepsilon_0 \chi^{(2)}}{2} A_2^* A_3 \exp\{i[(\omega_3 - \omega_2)t - (k_3 - k_2)z] + \text{c.c.}\}$$
 (71a)

$$P_{2NL}(z,t) = \frac{\varepsilon_0 \chi^{(2)}}{2} A_1^* A_3 \exp\{i[(\omega_3 - \omega_1)t - (k_3 - k_1)z] + \text{c.c.}\}$$
 (71b)

$$P_{3NL}(z,t) = \frac{\varepsilon_0 \chi^{(2)}}{2} A_1 A_2 \exp\{i[(\omega_1 + \omega_2)t - (k_1 + k_2)z] + \text{c.c.}\}$$
 (71c)

Inserting these expressions into equation (68), we derive the following three equations for the fields at ω_1 , ω_2 and ω_3 :

$$\frac{\partial A_1}{\partial z} + \frac{1}{v_{ol}} \frac{\partial A_1}{\partial t} - \frac{i}{2} k_1'' \frac{\partial^2 A_1}{\partial t^2} = -i \frac{\mu_0 \varepsilon_0 c \omega_1}{4 n_1} \chi^{(2)} A_2^* A_3 \exp[-i(k_3 - k_2 - k_1)z] \quad (72a)$$

$$\frac{\partial A_2}{\partial z} + \frac{1}{v_{c2}} \frac{\partial A_2}{\partial t} - \frac{i}{2} k_2'' \frac{\partial^2 A_2}{\partial t^2} = -i \frac{\mu_0 \varepsilon_0 c \omega_2}{4 n_2} \chi^{(2)} A_1^* A_3 \exp[-i(k_3 - k_1 - k_2)z]$$
 (72b)

$$\frac{\partial A_3}{\partial z} + \frac{1}{v_{o3}} \frac{\partial A_3}{\partial t} - \frac{i}{2} k_3'' \frac{\partial^2 A_3}{\partial t^2} = -i \frac{\mu_0 \varepsilon_0 c \omega_3}{4 n_3} \chi^{(2)} A_1 A_2 \exp[-i(k_1 + k_2 - k_3)z]$$
 (72c)

In the following, we will define the "wave-vector mismatch" as: $\Delta k = k_3 - k_1 - k_2$. The configuration when $\Delta k = 0$ is called phase matching. The three equations are coupled nonlinear partial differential equations, are, in general, not amenable to an analytic solution and must be treated numerically. A first simplification, that captures the main physics of parametric interaction, consists of neglecting the GVD terms, *i.e.* putting $k_i'' = 0$. This is justified by considering that the three interacting pulses are propagating at very different group velocities v_{gi} . The effects of this group velocity difference (intra-pulse GVD) are much more relevant than those of group velocity dispersion between the different frequency components of a single pulse (inter-pulse GVD). The coupled equations then become:

$$\frac{\partial A_1}{\partial z} + \frac{1}{v_{q1}} \frac{\partial A_1}{\partial t} = -i\kappa_1 A_2^* A_3 \exp[-i\Delta kz]$$
 (73a)

$$\frac{\partial A_2}{\partial z} + \frac{1}{v_{q2}} \frac{\partial A_2}{\partial t} = -i\kappa_2 A_1^* A_3 \exp[-i\Delta kz]$$
 (73b)

$$\frac{\partial A_3}{\partial z} + \frac{1}{v_{g3}} \frac{\partial A_3}{\partial t} = -i\kappa_3 A_1 A_2 \exp[i\Delta kz]$$
 (73c)

with the nonlinear coupling constants defined as: $\kappa_i = \frac{\omega_i \chi^{(2)}}{4cn_i}$. They can be simplified by moving to a frame of reference translating with the group velocity of the field at ω_3 : $t' = t - \frac{z}{v_{o3}}$. The equations then become:

$$\frac{\partial A_1}{\partial z} + \delta_{13} \frac{\partial A_1}{\partial t} = -i\kappa_1 A_2^* A_3 \exp[-i\Delta kz]$$
 (74a)

$$\frac{\partial A_2}{\partial z} + \delta_{23} \frac{\partial A_2}{\partial t} = -i\kappa_2 A_1^* A_3 \exp[-i\Delta kz]$$
 (74b)

$$\frac{\partial A_3}{\partial z} = -i\kappa_3 A_1 A_2 \exp[i\Delta kz] \tag{74c}$$

where $\delta_{i3} = \frac{1}{v_{gi}} - \frac{1}{v_{g3}}$ with i = 1, 2 is the Group Velocity Mismatch (GVM) between the waves at ω_1/ω_2 and ω_3 . These are nonlinear coupled partial differential equations that can be solved numerically. To get some physical insight, we can make the approximation of quasi-monochromatic waves, *i.e.* $\frac{\partial A_i}{\partial t} = 0$. The coupled equations in this case become:

$$\frac{dA_1}{dz} = -i\kappa_1 A_3 A_2^* \exp[-i\Delta kz] \tag{75a}$$

$$\frac{dA_2}{dz} = -i\kappa_2 A_3 A_1^* \exp[-i\Delta kz] \tag{75b}$$

$$\frac{dA_3}{dz} = -i\kappa_3 A_1 A_2 \exp[+i\Delta kz] \tag{75c}$$

Note that, according to the initial boundary conditions $A_1(0)$, $A_2(0)$ and $A_3(0)$, these coupled equations describe all second-order nonlinear optical phenomena, such as SHG $(A_1(0) = A_2(0); A_3(0) = 0)$, SFG $(A_3(0) = 0)$, DFG and OPA $(A_1(0) = 0)$. In the remainder of this chapter, we will focus on the OPA process, which is important since it allows us to generate frequency tunable ultrashort light pulses. In an OPA, an intense light beam at angular frequency ω_3 (the pump beam) impinges on the nonlinear crystal together with a weak beam at frequency ω_2 (the signal beam). The OPA process can be also described as an interaction among photons occurring through virtual states, as depicted in figure 1.4: each pump photon is annihilated bringing the system to the highest virtual state; simultaneously, a signal photon stimulates a decay towards a lower state generating a signal photon together with a photon at the difference frequency $\omega_1 = \omega_3 - \omega_2$, known as the idler frequency. The OPA thus amplifies the signal beam at the expense of the pump beam, using virtual states to mediate the process and thus without depositing any energy into the gain medium.

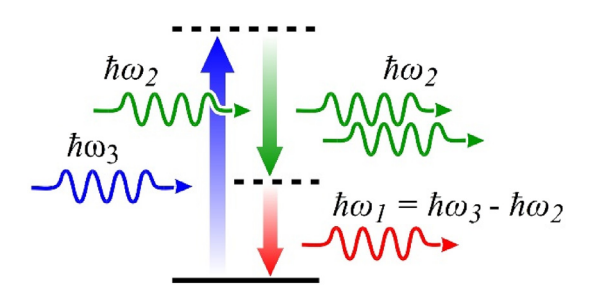


Fig. 1.4 – Scheme of the nonlinear interaction taking place in an OPA.

To discuss the OPA process, we first make the no-pump-depletion approximation, *i.e.* we assume that the conversion efficiencies are so low that $A_3 \cong A_{30} = \text{const.}$, *i.e.* the pump is not depleted, where A_{30} is the amplitude of the pump at the beginning of the interaction. We also initially make the approximation of perfect phase matching ($\Delta k = 0$), simplifying the equations to:

$$\frac{dA_1}{dz} = -i\kappa_1 A_{30} A_2^* \tag{76a}$$

$$\frac{dA_2}{dz} = -i\kappa_2 A_{30} A_1^* \tag{76b}$$

By taking the derivative of (76b) with respect to z:

$$\frac{d^2 A_2}{dz^2} = -i\kappa_2 A_{30} \frac{dA_1^*}{dz} = \kappa_1 \kappa_2 |A_{30}|^2 A_2$$
 (77)

By defining: $\Gamma^2 = \kappa_1 \kappa_2 |A_{30}|^2 = \frac{\omega_1 \omega_2 \chi^{(2)2}}{16c^2 n_1 n_2} |A_{30}|^2 = \frac{\omega_1 \omega_2 \chi^{(2)2}}{16\varepsilon_0 c^3 n_1 n_2} I_{30}$ we can write the equation:

$$\frac{d^2 A_2}{dz^2} - \Gamma^2 A_2 = 0 (78)$$

which has the solution:

$$A_2(z) = C_1 \exp(\Gamma z) + C_2 \exp(-\Gamma z)$$
(79)

By using the boundary conditions $A_2(0) = A_{20}$, $A_1(0) = 0$, which corresponds to injecting in the nonlinear crystal a pulse at the signal frequency (the so-called "seed" pulse) but no pulse at the idler frequency, we obtain:

$$A_2(z) = A_{20} \cosh(\Gamma z) \tag{80}$$

which, for large values of Γz , becomes:

$$A_2(z) \cong \frac{A_{20}}{2} \exp(\Gamma z) \tag{81}$$

At the output of a crystal with length L, the amplified signal intensity therefore becomes:

$$I_2(L) = \frac{I_{20}}{4} \exp(2\Gamma L)$$
 (82)

The weak seed beam is therefore amplified in the nonlinear crystal, with a parametric gain which is defined as:

$$G = \frac{I_2(L)}{I_{20}} = \frac{1}{4} \exp(2\Gamma L) \tag{83}$$

The parametric gain G thus depends exponentially on the propagation length L and on the coefficient Γ , which in turn depends on the nonlinear susceptibility $\chi^{(2)}$ and on the square root of the pump intensity. Using realistic values achievable with femtosecond light pulses, one can obtain parametric gains of the order of $10^3 \div 10^4$ for propagations of just a few mm in the nonlinear medium.

The idler beam amplitude can be easily obtained by integrating equation (76a) as:

$$A_1(z) = -i\kappa_1 A_{30} A_{20}^* \frac{\sinh(\Gamma z)}{\Gamma}$$
(84)

which, in the large gain limit, becomes:

$$A_1(z) = -i\kappa_1 A_{30} A_{20}^* \frac{\exp(\Gamma z)}{2\Gamma}$$
 (85)

The idler intensity is then written as:

$$I_1(L) = \frac{\kappa_1}{\kappa_2} \frac{n_1}{n_2} I_2(L) = \frac{\omega_1}{\omega_2} I_2(L)$$
 (86)

Equation (86) lends itself to a simple physical interpretation: for each signal photon generated in the OPA process there must be an idler photon, so that in the large gain limit, neglecting the initial number of signal photons, the number of signal and idler photons is equal, i.e. $\frac{I_1}{\hbar a_0} = \frac{I_2}{\hbar a_0}$.

Let us now evaluate how to get the collinear phase matching condition, i.e. $k_1 + k_2 = k_3$, which is equivalent to writing: $\omega_1 n_1 + \omega_2 n_2 = \omega_3 n_3$. It is easy to show that this condition cannot be satisfied in an isotropic bulk medium, for which $dn/d\omega > 0$. One can, however, use birefringent crystals, which are also non-centrosymmetric and thus with $\chi^{(2)} \neq 0$. We will consider the following uniaxial birefringent crystals, which are the simplest to describe and also widely used in nonlinear optics. In such a crystal one can define an axis, known as the optical axis, such that, for a propagation direction forming an angle θ with the optical axis, the two orthogonal polarizations see different refractive indexes: the ordinary index n_o , and the extraordinary index, n_e , which depends on the angle θ according to the expression:

$$\frac{1}{n_e^2(\theta)} = \frac{\cos^2(\theta)}{n_o^2} + \frac{\sin^2(\theta)}{n_e^2}$$
 (87)

According to the value of θ , therefore, $n_e(\theta)$ varies between n_o and n_e . Let us consider a negative uniaxial crystal, for which $n_e < n_o$. In this case, the phase matching condition can be achieved by polarizing ω_3 along the extraordinary direction and ω_1 , ω_2 along the ordinary direction (Type I phase matching). In this case, one can write:

$$n_e(\omega_3, \theta_m) = n_o(\omega_1) \frac{\omega_1}{\omega_3} + n_o(\omega_2) \frac{\omega_2}{\omega_3}$$
(88)

from which, with the help of equation (87), one obtains:

$$\theta_{m} = \operatorname{asin} \left[\frac{n_{e}(\omega_{3})}{n_{e}(\omega_{3}, \theta_{m})} \sqrt{\frac{n_{o}^{2}(\omega_{3}) - n_{e}^{2}(\omega_{3}, \theta_{m})}{n_{o}^{2}(\omega_{3}) - n_{e}^{2}(\omega_{3})}} \right]$$
(89)

Another type of phase-matching configuration, called Type II, is possible, in which either the signal or the idler beams have extraordinary polarizations. The discussion of the merits and drawbacks of different phase-matching configurations goes beyond the scope of this chapter [7].

So far, we have considered the case of parametric amplification in the case of perfect phase matching, which can be achieved only for a set of pump, signal and idler frequencies. If we generalize to the case of non-vanishing phase mismatch Δk , while still retaining the no pump depletion approximation, by taking the derivative of (75b) with respect to z we obtain:

$$\frac{d^2 A_2}{dz^2} = -i\kappa_2 A_{30} \left(\frac{dA_1^*}{dz} - i\Delta k A_1^*\right) \exp(-i\Delta k z) \tag{90}$$

which, with the help of (75a) and its complex conjugate, can be rewritten as:

$$\frac{d^2A_2}{dz^2} + i\Delta k \frac{dA_2}{dz} - \Gamma^2 A_2 = 0 \tag{91}$$

Equation (91) is a second-order linear differential equation which has solution of the kind: $A_2(z) = \exp(\gamma z)$, where γ are the solutions of the corresponding characteristic equation:

$$\gamma^2 + i\Delta k\gamma - \Gamma^2 = 0$$
 $\gamma = -\frac{i\Delta k}{2} \pm \sqrt{\Gamma^2 - \left(\frac{\Delta k}{2}\right)^2} = -\frac{i\Delta k}{2} \pm g$ (92a)

with

$$g = \sqrt{\Gamma^2 - \left(\frac{\Delta k}{2}\right)^2}.$$
 (92b)

We can thus write a generic solution as:

$$A_2(z) = \exp\left(-i\frac{\Delta kz}{2}\right) \left[C_1 \exp(gz) + C_2 \exp(-gz)\right]$$
(93)

which, with the usual boundary conditions $A_2(0) = A_{20}$, $A_1(0) = 0$, becomes:

$$A_2(z) = A_{20} \exp\left(-i\frac{\Delta kz}{2}\right) \left[\cosh(gz) + \frac{i\Delta k}{2g}\sinh(gz)\right]$$
(94)

The amplified signal intensity can now be written as:

$$I_2(z) = I_{20} \left[\cosh^2(gz) + \frac{\Delta k^2}{4g^2} \sinh^2(gz) \right]$$
 (95)

which, after some manipulation, becomes:

$$I_2(z) = I_{20} \left[1 + \frac{\Gamma^2}{g^2} \sinh^2(gz) \right]$$
 (96)

so that the parametric gain can be written as:

$$G(\Delta k) = 1 + \frac{\Gamma^2}{g^2} \sinh^2(gz) \tag{97}$$

or, in the large gain case $(gz \gg 1)$:

$$G(\Delta k) = \frac{\Gamma^2}{4q^2} \exp(2gL) \tag{98}$$

Since g decreases with increasing Δk , so will also the parametric gain. We now calculate the wave-vector mismatch that reduces the parametric gain to half. From equation (83) we get:

$$G(\Delta k) = \frac{G(0)}{2} = \frac{1}{2} \frac{1}{4} \exp(2\Gamma L)$$
 (99)

which corresponds to:

$$\frac{\Gamma^2}{4g^2} \exp(2gL) = \frac{1}{2} \frac{1}{4} \exp(2\Gamma L)$$
 (100)

By assuming that $\Delta k \ll 2\Gamma$, from equation (92b) we obtain that $\frac{\Gamma^2}{g^2} \cong 1$ and equation (100) results in:

$$2gL \cong 2\Gamma L - \ln 2 \tag{101}$$

The expression of g in equation (92b) g can be expanded to the first order as: $g = \Gamma - \frac{\Delta k^2}{8\Gamma}$, resulting in:

$$\Delta k \cong 2(\ln 2)^{1/2} \left(\frac{\Gamma}{L}\right)^{1/2} \tag{102}$$

In order to calculate the phase-matching bandwidth for the OPA process, let us now link the wave-vector mismatch to the frequency variation of the signal pulse. Let us assume that the phase-matching condition is rigorously satisfied for a set of frequencies $\overline{\omega}_1, \overline{\omega}_2, \overline{\omega}_3$, with $\overline{\omega}_1 + \overline{\omega}_2 = \overline{\omega}_3$, so that:

$$k(\tilde{\omega}_1) + k(\tilde{\omega}_2) = k(\tilde{\omega}_3) \tag{103}$$

We now keep ω_3 fixed and vary the signal frequency: $\omega_2 = \tilde{\omega}_2 + \Delta \omega$. The idler frequency will consequently vary as: $\omega_1 = \tilde{\omega}_1 - \Delta \omega$. The wave-vector mismatch will be:

$$\Delta k = k(\overline{\omega}_{3}) - \left[k(\overline{\omega}_{2}) + \left(\frac{\partial k}{\partial \omega} \right)_{\overline{\omega}_{2}} \Delta \omega + \frac{1}{2} \left(\frac{\partial^{2} k}{\partial \omega^{2}} \right)_{\overline{\omega}_{2}} \Delta \omega^{2} + \dots \right] - \left[k(\overline{\omega}_{1}) + \left(\frac{\partial k}{\partial \omega} \right)_{\overline{\omega}_{1}} (-\Delta \omega) + \frac{1}{2} \left(\frac{\partial^{2} k}{\partial \omega^{2}} \right)_{\overline{\omega}_{1}} (-\Delta \omega)^{2} + \dots \right]$$

$$(104)$$

In (104) we have stopped the wave-vector expansion to the second order. Taking into account equation (103), equation (104) can be rewritten as:

$$\Delta k \cong -\left(\frac{1}{v_{g2}} - \frac{1}{v_{g1}}\right) \Delta \omega - \frac{1}{2} \left(k_1'' + k_2''\right) \Delta \omega^2 \tag{105}$$

This shows that, to the first order, the wave-vector mismatch is proportional to the GVM between signal and idler pulses: $\delta_{12} = \frac{1}{v_{g2}} - \frac{1}{v_{g1}}$, $\Delta k \cong -\delta_{12}\Delta\omega$. The FWHM gain bandwidth, using equation (102), can then be written as:

$$\Delta \nu_{\text{FWHM}} \cong \frac{2(\ln 2)^{1/2}}{\pi} \left(\frac{\Gamma}{L}\right)^{1/2} \frac{1}{|\delta_{12}|} \tag{106}$$

Equation (106) shows that to achieve a broad phase-matching bandwidth, the group velocities of signal and idler frequencies should be matched (group-velocity matched OPA). In the case of $\delta_{12} = 0$, the wavevector mismatch must be expanded to the second order in $\Delta \omega$, giving:

$$\Delta \nu_{\text{FWHM}} \cong \frac{\sqrt{2}(\ln 2)^{1/4}}{\pi} \left(\frac{\Gamma}{L}\right)^{1/4} \frac{1}{\left|k_1'' + k_2''\right|^{1/2}}$$
(107)

and is thus inversely proportional to the sum of the GVDs of signal and idler pulses. In both cases, we see that the gain bandwidth increases with increasing nonlinearity Γ and decreases for increasing crystal length L, but the dependence is quite weak. To achieve broadband phase matching, it is therefore necessary to have $\delta_{12} = 0$, i.e. to achieve group velocity matching between signal and idler pulses.

One possibility is to work with type I phase matching and around the degeneracy condition, for which $\omega_1 = \omega_2 = \omega_3/2$. In this case, signal and idler have the same frequency and polarization, so their group velocities are equal and $\delta_{12} = 0$. This is called a degenerate OPA (DOPA). If, however, one works outside the degeneracy condition, in general one has $v_{g1} \neq v_{g2}$; in this case, to achieve group velocity matching, one has to exploit a non-collinear interaction geometry. Let us consider the geometry depicted in figure 1.5, in which the propagation direction of the signal beam forms an angle α with that of the pump beam. In this case, to satisfy the vectorial phase matching equation $\mathbf{k}_3 = \mathbf{k}_1 + \mathbf{k}_2$ the idler wave vector must join the tips of the pump and signal wave vectors. We call Ω the angle formed between signal and idler wave vectors. By projecting this equation along two axes parallel and perpendicular to the signal wave vector, we obtain:

$$k(\tilde{\omega}_1)\cos\Omega + k(\tilde{\omega}_2) = k(\tilde{\omega}_3)\cos\alpha$$
 (108a)

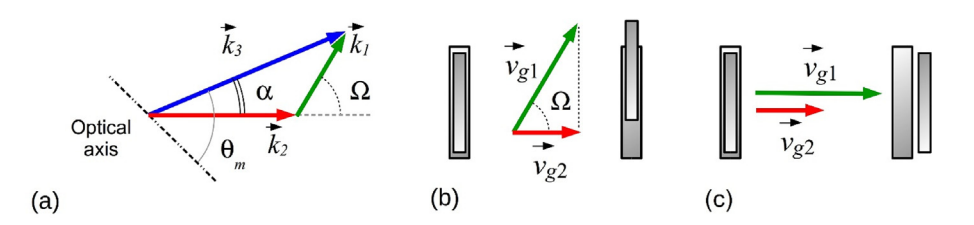


Fig. 1.5 – (a) Scheme of a non-collinear interaction geometry in an OPA. (b) Interpretation of the broadband amplification: the group velocity of the signal matches the group velocity of the idler along the signal direction. (c) For comparison: the collinear configuration, with no-matching velocities.

$$k(\tilde{\omega}_1)\sin\Omega = k(\tilde{\omega}_3)\sin\alpha \tag{108b}$$

If we now change the signal angular frequency by $\Delta\omega$ (and correspondingly the idler frequency by $-\Delta\omega$) we can calculate the wave vector mismatches in a direction parallel and perpendicular to the signal and impose that they both vanish:

$$\Delta k_{\text{par}} = -\left(\frac{dk}{d\omega}\right)_{\overline{\omega}_2} \Delta\omega + \left(\frac{dk}{d\omega}\right)_{\overline{\omega}_1} \Delta\omega \cos\Omega - k(\tilde{\omega}_1) \sin\Omega \frac{d\Omega}{d\omega} \Delta\omega = 0$$
 (109a)

$$\Delta k_{\text{per}} = \left(\frac{dk}{d\omega}\right)_{\overline{\omega}_1} \Delta \omega \sin\Omega + k(\tilde{\omega}_1) \cos\Omega \frac{d\Omega}{d\omega} \Delta\omega = 0$$
 (109b)

Multiplying equation (109a) by $\cos\Omega$ and (109b) by $\sin\Omega$ and adding them, we obtain

$$v_{g2} = v_{g1} \cos\Omega \tag{110}$$

Equation (110) lends itself to a very simple interpretation: in a non-collinear interaction geometry, broadband phase matching can be obtained when the group velocity of the signal matches the projection of the group velocity of the idler along the signal direction. This so-called non-collinear OPA (NOPA) is a very powerful tool for the generation of very short visible pulses.

In conclusion, we can draw the following general remarks on the nonlinear interactions of ultrashort pulses:

1) The nonlinear processes arise from the higher-order terms in the expansion of the polarization vector; such terms become relevant when the intensity of the light is higher than 10^9 W/cm². The second-order processes arise in a medium with a non-zero second-order susceptibility, $\chi^{(2)} \neq 0$. In his case, the nonlinear interaction may give rise to sum and difference frequency generation; one particular case of difference frequency generation is parametric amplification, in which the energy of a strong pulse is transferred to a weak beam, the signal. OPAs are used to generate, starting from, a fixed

- frequency pulse and frequency tunable femtosecond pulses and are, therefore, powerful tools in ultrafast optical spectroscopy.
- 2) The second-order nonlinear processes occur efficiently only when the so-called phase matching condition, which implies that the wave vector of the nonlinear polarization at a certain frequency matches that of the light beam, is fulfilled. This condition can be satisfied in birefringent crystals, which are also non-centrosymmetric and thus exhibit second-order nonlinearity. In such crystals, the refractive index depends on the polarization of light; the extraordinary one also depends on the direction of the propagation of light, which enables it to fulfil the phase-matching condition by properly orienting the crystal.
- 3) When dealing with pulses, it is necessary to ensure that the nonlinear interaction is occurring over a broad bandwidth. In the case of broadband OPA, the broadband field is the signal beam. Also in this case, the main parameter which influences the process efficiency is the phase mismatch: broadband operation is obtained when the phase mismatch is null or negligible over a broad bandwidth. In an OPA this condition is fulfilled when the signal and idler propagate with the same group velocity; in a non-collinear configuration, this means that the group velocity of the signal must match the projection of the group velocity of the idler along the signal direction. Non-collinear OPAs enable the amplification of broadband pulses and the generation of ultrashort visible pulses.

Conclusions

This Chapter aimed to introduce key concepts of ultrafast optics, which deals with the generation, propagation and characterization of ultrashort light pulses. Of course, we cannot provide a comprehensive coverage of the topic, for which we refer the reader to excellent books [8]. We focused on two key aspects of ultrashort pulses: their linear propagation in dispersive media, which gives rise to pulse broadening and frequency chirp, and the methods adopted for dispersion compensation; their nonlinear propagation in non-centrosymmetric crystals, which gives rise to three-wave-mixing phenomena such as optical parametric amplification, used to generate frequency tunable pulses for ultrafast spectroscopy. We believe that it is important for the multi-disciplinary experimentalist approaching ultrafast spectroscopy with scientific questions in physics, chemistry, or biology to fully master these concepts, which are essential to properly perform the experiments.

References

- Treacy E.B. (1969) Optical pulse compression with diffraction gratings, IEEE J. Quantum Electron. QE-5, 454-458.
- [2] Martinez O.E., Gordon J.P., Fork R.L. (1984) Negative group-velocity dispersion using refraction, J. Opt. Soc. Am. A 1, 1003-1006.
- [3] Fork R.L., Martinez O.E., Gordon J.P. (1984) Negative dispersion using pairs of prisms, Opt. Lett. 9, 150-152.

- [4] Fork R.L., Brito Cruz C.H., Becker P.C., Shank C.V. (1987) Compression of optical pulses to six femtoseconds by using cubic phase compensation, Opt. Lett. 12, 483–485.
- [5] Szipöcs R., Spielmann C., Krausz F., Ferencz K. (1994) Chirped multilayer coatings for broadband dispersion control in femtosecond lasers, Opt. Lett. 19, 201–203.
- [6] Kärtner F.X., Matuschek N., Schibli T., Keller U., Haus H.A., Heine C., Morf R., Scheuer V., Tilsch M., Tschudi T. (1997) Design and fabrication of double-chirped mirrors, Opt. Lett. 22, 831–833.
- [7] Manzoni C., Cerullo G. (2016) Design criteria for ultrafast optical parametric amplifiers, J. Opt. 18, 103501.
- [8] Weiner A.M. (2011) Ultrafast optics. John Wiley & Sons.

Chapter 2

Photoinduced Molecular Quantum Dynamics: Theory and Computational Methods

Elisa Palacino-González* and David Picconi**

Institute of Theoretical and Computational Chemistry Heinrich-Heine University Düsseldorf, Germany

*e-mail: elisa.palacino.gonzalez@hhu.de

**e-mail: david.picconi@hhu.de

2.1 Introduction

Many light-induced chemical and physical processes in molecular systems, such as photochemical reactions, charge transfer, and excitation energy transfer, take place on ultrafast timescales, often ranging from femtoseconds to picoseconds. Gaining a detailed understanding of these mechanisms is key to the rational design of novel functional molecular materials. This pursuit has led to the development of powerful time-resolved nonlinear spectroscopic techniques.

In ultrafast spectroscopy, a typical experiment begins with a short ultraviolet-visible (UV-vis) laser pulse that initiates a photophysical or photochemical process. The ensuing molecular dynamics is then monitored using one or more delayed probe pulses, possibly from different spectral domains (infrared, UV-vis, X-ray). Depending on the detection scheme, the interaction between the laser pulses and the molecular system gives rise to various observables – for instance, transmitted fields, photoelectron spectra, or fluorescence signals. These measured signals can potentially be very informative about the evolution of the system following photoexcitation.

However, decoding such experimental data to reconstruct the underlying molecular dynamics is far from straightforward. It requires a solid grasp of theoretical principles, including molecular quantum mechanics, quantum dynamics, and the

DOI: 10.1051/978-2-7598-3760-1.c002 © The authors, 2025 fundamentals of light-matter interaction. Without this foundation, the rich information encoded in ultrafast spectroscopic measurements remains largely inaccessible.

The goal of this chapter is to present the essential theoretical tools needed to understand and analyze light-induced processes in molecules and molecular materials. In addition, an overview is given on the various families of computational methods used to model molecular photodynamics, with a particular focus on how electronic transitions are coupled to nuclear motion, an aspect central to the photophysics and photochemistry of complex systems.

In particular, section 2.2 introduces the formalism commonly used to describe photoinduced molecular motion quantum mechanically in most applications. Section 2.3 illustrates the connection between molecular dynamics and linear absorption spectroscopy. Sections 2.4 and 2.5 focus on quantum mechanical or quantum-classical numerical approaches to simulate the coupled electronic-nuclear molecular dynamics induced by light.

2.2 Molecular Quantum Dynamics

This section introduces the quantum mechanical formalism to describe the coupled electronic and nuclear dynamics of an isolated molecular system, also referred to as a "molecule" for simplicity. The word *isolated* implies the absence of interactions between the system and the surrounding environment, so that the molecular energy is conserved. While this assumption is strictly valid only for molecules *in vacuo*, it can also be applied to processes faster than the energy exchange between the molecule and its environment. Quantum systems whose energy is not conserved during their dynamical evolution are called *open*, and their theoretical description is given in chapter 3.

The starting point for the quantum mechanical description of an isolated molecule is the molecular Hamiltonian in the non-relativistic approximation [1],

$$\hat{H} = \hat{T} + \hat{H}_{el},\tag{2.1}$$

where \hat{T} is the kinetic energy operator for the atomic nuclei and $\hat{H}_{\rm el}$ is the electronic Hamiltonian, which accounts for the kinetic energy of the electrons, as well as the Coulomb interactions between the constituent particles. Using Cartesian coordinates $\mathbf{R}_{\kappa} = (R_{\kappa x}, R_{\kappa y}, R_{\kappa z})$ and $\mathbf{r}_i = (r_{ix}, r_{iy}, r_{iz})$ to define the positions of nuclei and electrons, respectively, the operators \hat{T} and $\hat{H}_{\rm el}$ take the form

$$\hat{T} = \sum_{\kappa=1}^{N} -\frac{\hbar^2}{2M_{\kappa}} \left(\frac{\partial^2}{\partial R_{\kappa x}^2} + \frac{\partial^2}{\partial R_{\kappa y}^2} + \frac{\partial^2}{\partial R_{\kappa z}^2} \right)$$
 (2.2)

and

$$\hat{H}_{el} = \sum_{i=1}^{N_{el}} -\frac{\hbar^2}{2m_e} \left(\frac{\partial^2}{\partial r_{ix}^2} + \frac{\partial^2}{\partial r_{iy}^2} + \frac{\partial^2}{\partial r_{iz}^2} \right) + \frac{\hbar^2}{m_e a_0} \left(-\sum_{\kappa=1}^{N} \sum_{i=1}^{N_{el}} \frac{Z_{\kappa}}{|\mathbf{R}_{\kappa} - \mathbf{r}_i|} + \sum_{i \neq j}^{N_{el}} \frac{1}{|\mathbf{r}_i - \mathbf{r}_j|} + \sum_{\kappa \neq \mu}^{N} \frac{Z_{\kappa} Z_{\mu}}{|\mathbf{R}_{\kappa} - \mathbf{R}_{\mu}|} \right),$$
(2.3)

where N and $N_{\rm el}$ are the number of nuclei and electrons, respectively. M_{κ} are the atomic masses, Z_{κ} are the atomic numbers and \hbar , $m_{\rm e}$ and a_0 are fundamental constants (Planck's constant, the electron mass, and Bohr radius, all equal to one in atomic units).

The explicit form of the electronic Hamiltonian, reported for completeness in equation (2.3), is not necessary for the derivations of this chapter. However, it is worth emphasizing that $\hat{H}_{\rm el}$ is an operator acting in the Hilbert space of the electronic states, but also depends on the nuclear geometry through the coordinates \mathbf{R}_{κ} . It follows that the eigenstates and eigenvalues of $\hat{H}_{\rm el}$ – the so-called *adiabatic* states and potential energy surfaces, introduced in section 2.2.1, are also formally dependent on the geometry.

The choice of Cartesian coordinates to describe molecular geometry is not the only option. Depending on the problem, internal coordinates (e.g., bond distances, angles, torsions) or vibrational normal modes may be more appropriate. However, in the case of internal coordinates, the nuclear kinetic energy operator, \hat{T} can take on a rather complicated form [2]. In the following, nuclear coordinates will be generically denoted as \mathbf{q} and the dependence of $\hat{H}_{\rm el}$ on molecular geometry as $\hat{H}_{\rm el}(\mathbf{q})$.

2.2.1 Electronic States and Time-Dependent Schrödinger Equation

In quantum mechanics, the coupled dynamics of electrons and nuclei is described by a time-dependent wavefunction $\Psi(\mathbf{r}, \mathbf{q}, t)$, which evolves according to the time-dependent Schrödinger equation,

$$\frac{\partial \Psi(\mathbf{r}, \mathbf{q}, t)}{\partial t} = -\frac{i}{\hbar} \hat{H} \Psi(\mathbf{r}, \mathbf{q}, t), \qquad (2.4)$$

that has to be solved for a given initial condition fixed at time $t = t_0$, *i.e.* $\Psi(\mathbf{r}, \mathbf{q}, t_0) = \Psi_0(\mathbf{r}, \mathbf{q})$. Here, the vector $\mathbf{r} = (\mathbf{r}_1 s_1, \mathbf{r}_2 s_2, ...)$ collects all electronic coordinates and spin variables s_i . In the context of photochemistry and spectroscopy, typical problems involve a relatively short interaction between the molecule and an electromagnetic field, which prepares the molecule in some initial state Ψ_0 . This state is out of equilibrium and evolves in time according to equation (2.4).

The exact solution of this equation in the framework of a many-body electronic-nuclear problem is a formidable computational task that can be carried out only for systems with a very small number of electrons. Therefore, the most common approaches in photochemistry rely on some form of separation between the electronic and nuclear problems.

The first step to achieve such a separation is to assume that, at each time, the wavefunction can be expanded in a truncated basis of $N_{\rm S}$ electronic states that do not depend on time. This is known as the group Born-Oppenheimer approximation [3], and its validity is briefly discussed in section 2.2.2. Using Dirac's notation to indicate the electronic states – generally geometry-dependent – the group Born-Oppenheimer

approximation is formally obtained using the projection operator $\hat{P}_{el}(\mathbf{q}) = \sum_{\alpha=1}^{N_s} |\alpha(\mathbf{q})\rangle\langle\alpha(\mathbf{q})|$ as

$$\Psi(\mathbf{r}, \mathbf{q}, t) \simeq \hat{P}_{el}(\mathbf{q})\Psi(\mathbf{r}, \mathbf{q}, t) = \sum_{\alpha=1}^{N_S} |\alpha(\mathbf{q})\rangle \chi_{\alpha}(\mathbf{q}, t), \qquad (2.5)$$

where $\chi_{\alpha}(\mathbf{q}, t)$ are nuclear wavefunctions associated with each electronic state. Formally, they are defined as the integral $\chi_{\alpha}(\mathbf{q}, t) = \langle \alpha(\mathbf{q}) | \Psi(\mathbf{r}, \mathbf{q}, t) \rangle_{\mathbf{r}}$ performed over the electronic coordinates \mathbf{r} .

The definition of the electronic basis $\{|\alpha(\mathbf{q})\rangle\}$ used in the expansion of equation (2.5) is not unique and needs to be chosen in numerical calculations. Indeed, it is easy to verify that the total molecular wavefunction is invariant under unitary transformations

$$|\alpha(\mathbf{q})\rangle \longrightarrow |\alpha'(\mathbf{q})\rangle = \sum_{\beta=1}^{N_{S}} |\beta(\mathbf{q})\rangle U_{\beta\alpha}(\mathbf{q}),$$

$$\chi_{\alpha}(\mathbf{q}, t) \longrightarrow \chi_{\alpha}'(\mathbf{q}, t) = \sum_{\beta=1}^{N_{S}} \chi_{\beta}(\mathbf{q}, t) U_{\beta\alpha}^{*}(\mathbf{q}),$$
(2.6)

where the geometry-dependent matrix $\mathbf{U}(\mathbf{q}) = \{U_{\beta\alpha}(\mathbf{q})\}$ is unitary, *i.e.* $\mathbf{U}^{\dagger}(\mathbf{q})\mathbf{U}(\mathbf{q}) = \mathbf{U}(\mathbf{q})\mathbf{U}^{\dagger}(\mathbf{q}) = \mathbf{1}$.

For the moment we proceed without giving a precise choice for the electronic states. Replacing equation (2.5) into equation (2.4) and using the definition $\hat{H} = \hat{T} + \hat{H}_{el}(\mathbf{q})$ gives

$$\sum_{\alpha=1}^{N_{S}} |\alpha(\mathbf{q})\rangle \frac{\partial \chi_{\alpha}(\mathbf{q}, t)}{\partial t} = -\frac{i}{\hbar} \sum_{\alpha=1}^{N_{S}} (\hat{T}|\alpha(\mathbf{q})\rangle \chi_{\alpha}(\mathbf{q}, t) + \hat{H}_{el}(\mathbf{q})|\alpha(\mathbf{q})\rangle \chi_{\alpha}(\mathbf{q}, t))$$

$$= -\frac{i}{\hbar} \sum_{\alpha=1}^{N_{S}} ([\hat{T}, |\alpha(\mathbf{q})\rangle] \chi_{\alpha}(\mathbf{q}, t) + |\alpha(\mathbf{q})\rangle \hat{T} \chi_{\alpha}(\mathbf{q}, t) + \hat{H}_{el}|\alpha(\mathbf{q})\rangle \chi_{\alpha}(\mathbf{q}, t)),$$
(2.7)

where we introduced the commutator $[\hat{T}, |\alpha(\mathbf{q})\rangle] = \hat{T}|\alpha(\mathbf{q})\rangle - |\alpha(\mathbf{q})\rangle \hat{T}$. In this way, we have got a term $\hat{T}\chi_{\alpha}$, that contains the action of the nuclear kinetic energy operator on the nuclear wavefunctions. Assuming the group Born–Oppenheimer approximation, we can apply the operator \hat{P}_{el} to both sides of equation (2.7). Using the orthonormality condition $\langle \alpha(\mathbf{q})|\beta(\mathbf{q})\rangle = \delta_{\alpha\beta}$, we derive a general form of the evolutionary equations for the nuclear wavefunctions,

$$\frac{\partial \chi_{\alpha}(\mathbf{q}, t)}{\partial t} = -\frac{\mathrm{i}}{\hbar} \hat{T} \chi_{\alpha}(\mathbf{q}, t) - \frac{\mathrm{i}}{\hbar} \sum_{\beta=1}^{N_{\mathrm{S}}} \left(V_{\alpha\beta}(\mathbf{q}) \chi_{\beta}(\mathbf{q}, t) + \hat{\Lambda}_{\alpha\beta}(\mathbf{q}) \chi_{\beta}(\mathbf{q}, t) \right), \tag{2.8}$$

where we have introduced two operator matrices. One of them,

$$V_{\alpha\beta}(\mathbf{q}) = \langle \alpha(\mathbf{q}) | \hat{H}_{el}(\mathbf{q}) | \beta(\mathbf{q}) \rangle, \tag{2.9}$$

is purely multiplicative, *i.e.*, it contains diagonal potential energy surfaces and off-diagonal potential electronic couplings. The other matrix,

$$\hat{\Lambda}_{\alpha\beta}(\mathbf{q}) = \langle \alpha(\mathbf{q}) | [\hat{T}, |\beta(\mathbf{q})\rangle], \qquad (2.10)$$

contains operators that also have a differential component. In particular, the off-diagonal terms, which couple the equations of motion of different nuclear wavefunctions, are formally *kinematic couplings*, *i.e.*, they arise from the coordinate dependence of the electronic states, which prevents them from commuting with the nuclear kinetic energy operator.

From the physical viewpoint, the terms with $\alpha \neq \beta$ in equations (2.9) and (2.10) account for radiationless transitions between different electronic states of the same spin multiplicity, i.e., the phenomenon of internal conversion. It is clear from the discussion so far that nonradiative changes in the electronic structure are inherently quantum mechanical phenomena, mediated by molecular vibrational motions.

In addition, the phenomenon of intersystem crossing, involving transitions between states of different spin multiplicity, can also be accounted for within the present formalism. To this end, a relativistic spin-orbit coupling operator $\hat{H}_{SOC}(\mathbf{q})$ is added to the electronic Hamiltonian $\hat{H}_{el}(\mathbf{q})$ in equation (2.9). Nevertheless, for simplicity, the theory of this chapter focuses only on the internal conversion process, and readers interested in the theoretical description of intersystem crossing are directed to Ref. [4].

To give a mathematical shape to the kinematic couplings of equation (2.10), we need an explicit expression for the kinetic energy operator. We adopt the generic form

$$\hat{T} = \sum_{\kappa=1}^{f} \frac{\hat{p}_{\kappa}^2}{2M_{\kappa}},\tag{2.11}$$

where $\hat{p}_{\kappa} = -\mathrm{i}\hbar\partial/\partial q_{\kappa}$ is the momentum operator associated with the coordinate q_{κ} . Note that here f is the total number of coordinates used to describe the nuclear motion, rather than the number of atoms. Equation (2.11) is valid when Cartesian coordinates are used as well as for *normal modes*; in this case, since normal modes are linear combinations of mass-weighted Cartesian coordinates, the masses M_i are set to one in equation (2.11).

Replacing equation (2.11) into equation (2.10), we obtain the following expression for the kinematic couplings¹,

$$\hat{\Lambda}_{\alpha\beta}(\mathbf{q}) = -\sum_{\kappa=1}^{N} \left(\frac{\mathrm{i}\hbar}{M_{\kappa}} \left\langle \alpha(\mathbf{q}) \left| \frac{\partial}{\partial q_{\kappa}} \right| \beta(\mathbf{q}) \right\rangle \hat{p}_{\kappa} + \frac{\hbar^{2}}{2M_{\kappa}} \left\langle \alpha(\mathbf{q}) \left| \frac{\partial^{2}}{\partial q_{\kappa}^{2}} \right| \beta(\mathbf{q}) \right\rangle \right)
\equiv \sum_{\kappa=1}^{N} \left(\mathrm{i}D_{\kappa,\alpha\beta}(\mathbf{q}) \hat{p}_{\kappa} + F_{\kappa,\alpha\beta}(\mathbf{q}) \right).$$
(2.12)

¹This expression can be derived by evaluating the commutator $\left[\hat{p}_{\kappa}^{2}, |\alpha(\mathbf{q})\rangle\right]$ using the relation $\left[\hat{p}_{\kappa}, f(\mathbf{q})\right] = -\mathrm{i}\hbar\partial f/\partial q_{\kappa}$ and the operator identity $\left[\hat{A}\hat{B}, \hat{C}\right] = \hat{A}\left[\hat{B}, \hat{C}\right] + \left[\hat{A}, \hat{C}\right]\hat{B}$.

The terms $D_{\kappa,\alpha\beta}(\mathbf{q})$ are combined with the nuclear momenta, which are differential operators, therefore they are called *derivative couplings*; note that the differentiation of the orthonormality relation $\langle \alpha(\mathbf{q})|\beta(\mathbf{q})\rangle = \delta_{\alpha\beta}$ leads to the property $D_{\kappa,\alpha\beta} = -D_{\kappa,\beta\alpha}^*$, *i.e.*, the matrices \mathbf{D}_i , defined for each coordinate κ , are anti-Hermitian (or simply anti-symmetric for real electronic states, which is the most common case). The terms $F_{\kappa,\alpha\beta}(\mathbf{q})$, denoted *scalar couplings*, are instead purely multiplicative and can be added to the potential energy surfaces and couplings of equation (2.9). The kinematic couplings are weighted by the inverse of the nuclear mass, therefore, in the summation of equation (2.12), the terms associated with light atoms are likely the most important.

At this stage we have, in principle, all the formal ingredients for the quantum mechanical description of photochemical phenomena, governed by the system of Schrödinger equations given in equation (2.8). The only step which is still left, in order to compute the potential and/or the kinematic couplings, is to choose a precise definition for the electronic states $|\alpha(\mathbf{q})\rangle$. Two different choices are presented in the following sections.

2.2.2 The Adiabatic Representation

The simplest way to simplify equation (2.8) is to choose the electronic basis such that the matrix **V** is diagonal, *i.e.* $V_{\alpha\beta}(\mathbf{q}) = V_{\alpha}(\mathbf{q})\delta_{\alpha\beta}$. According to equation (2.9), this is achieved by defining the electronic states as eigenstates of the electronic Hamiltonian for each geometry **q**:

$$\hat{H}_{\rm el}(\mathbf{q})|\alpha(\mathbf{q})\rangle = V_{\alpha}(\mathbf{q})|\alpha(\mathbf{q})\rangle.$$
 (2.13)

In this case, the electronic states are called *adiabatic states*, and the functions $V_{\alpha}(\mathbf{q})$, which depend on the nuclear coordinates, are denoted as *adiabatic potential energy surfaces* (PESs). The dynamics of the nuclear wavefunctions associated to the adiabatic states is given by the coupled time-dependent Schrödinger equations

$$\frac{\partial \chi_{\alpha}(\mathbf{q}, t)}{\partial t} = -\frac{\mathrm{i}}{\hbar} \left(\hat{T} + V_{\alpha}(\mathbf{q}) \right) \chi_{\alpha}(\mathbf{q}, t) - \frac{\mathrm{i}}{\hbar} \sum_{\beta=1}^{N_{\mathrm{S}}} \hat{\Lambda}_{\alpha\beta} \chi_{\beta}(\mathbf{q}, t), \tag{2.14}$$

where the kinematic coupling terms $\hat{\Lambda}_{\alpha\beta}$ are denoted as nonadiabatic couplings. Among these terms, the derivative couplings $(iD_{\kappa,\alpha\beta}(\mathbf{q})\hat{p}_{\kappa})$ are typically the ones with the largest magnitude.

The (approximate) calculation of the adiabatic states, *i.e.*, the solution of the electronic Schrödinger equation (2.13), is carried out with the methodologies of electronic structure theory, or *quantum chemistry*, which are implemented in dedicated codes. We will not address the question of how one can choose the most appropriate electronic structure method (time-dependent density functional theory, coupled-cluster methods, algebraic diagrammatic connection, multi-configurational approaches, etc.) and set up these calculations (see Ref. [5] for an overview of different methods).

Instead, we assume that such a choice has been properly made, and we have at our disposal the code we need to compute the adiabatic electronic states, the PES, the nonadiabatic couplings, etc. With this assumption, in principle, one obtains a precise strategy to simulate a photo-initiated molecular process quantum mechanically:

- 1. The set of electronic states included in the group Born-Oppenheimer approximation is identified. For example, if the process under study is initiated by a laser pulse, one can include the states whose energies lie within the optical bandwidth of the pulse (see chapter 1).
- 2. The adiabatic potential energy surfaces V_{α} and the nonadiabatic couplings are computed using quantum chemistry codes.
- 3. The system of time-dependent Schrödinger equations (2.14) is solved to evaluate the coupled electronic-nuclear dynamics (see section 2.4), for the initial conditions specific for the process of interest. Spectroscopic observables are finally computed using quantum mechanical expressions (see section 2.3).

However, there are several difficulties with this approach. The main one is the need to compute the adiabatic PESs along all the nuclear coordinates that might be relevant for the dynamical process one wants to describe. Although a few modes are sometimes sufficient to describe the ultrafast (<100 fs) time scale, a multi-mode description becomes necessary to account for decoherence, intramolecular vibrational redistribution, and dissipation to an environment in polyatomic molecules or aggregates. This implies that high-dimensional adiabatic PESs need to be computed to solve the dynamical problem, and these functions might be rather complicated to fit to an analytic form (see section 2.2.5).

It is worth noting at this stage that this complication arises from the quantum mechanical description of nuclear motion, based on the nuclear wavefunctions $\chi_{\alpha}(\mathbf{q},t)$. In contrast, in classical mechanics, a molecule is described as a set of point masses in a well-defined configuration, and the simulation of its motion requires only the force computed at the specific molecular geometry, therefore, the construction of the entire PESs is not needed. This is one of the reasons why the description of nonadiabatic dynamics in terms of adiabatic states is more common in quantum-classical methods (section 2.5), where only the electronic states are quantized, while the nuclear coordinates follow Hamiltonian trajectories.

For the moment being, we continue with the rigorous quantum mechanical description of the coupled nuclear-electronic dynamics, according to equation (2.14). Another main difficulty of using the adiabatic states as the electronic basis is that the nonadiabatic couplings diverge when the PESs of the coupled states approach each other. To understand why, we differentiate equation (2.13) and multiply both sides from the left by $\langle \beta(\mathbf{q})|$, obtaining

$$\left\langle \beta(\mathbf{q}) \middle| \frac{\partial \hat{H}_{\text{el}}}{\partial q_{\kappa}} \middle| \alpha(\mathbf{q}) \right\rangle + \underbrace{\left\langle \beta(\mathbf{q}) \middle| \hat{H}_{\text{el}}}_{\langle \beta(\mathbf{q}) \middle| V_{\beta}(\mathbf{q})} \frac{\partial}{\partial q_{\kappa}} \middle| \alpha(\mathbf{q}) \right\rangle = \frac{\partial V_{\alpha}(\mathbf{q})}{\partial q_{\kappa}} \underbrace{\left\langle \beta(\mathbf{q}) \middle| \alpha(\mathbf{q}) \right\rangle}_{\delta_{\beta\alpha}} + V_{\alpha}(\mathbf{q}) \underbrace{\left\langle \beta(\mathbf{q}) \middle| \frac{\partial}{\partial q_{\kappa}} \middle| \alpha(\mathbf{q}) \right\rangle}_{M_{i}D_{\kappa,\beta\alpha}(\mathbf{q})/\hbar},$$
(2.15)

where the derivative couplings $D_{\kappa,\beta\alpha}(\mathbf{q})$ appear. Rearranging the terms, we obtain that, for two electronic states α and β , with $\alpha \neq \beta$,

$$D_{\kappa,\beta\alpha}(\mathbf{q}) = -\frac{\hbar}{M_{\kappa}} \frac{\left\langle \beta(\mathbf{q}) \left| \frac{\partial \hat{H}_{cl}}{\partial q_{\kappa}} \right| \alpha(\mathbf{q}) \right\rangle}{V_{\beta}(\mathbf{q}) - V_{\alpha}(\mathbf{q})}.$$
 (2.16)

which shows the divergence at the geometries where $V_{\alpha}(\mathbf{q}) \approx V_{\beta}(\mathbf{q})$.

The fact that the nonadiabatic couplings become large near the *intersections* between PESs makes the solution of the time-dependent Schrödinger equation numerically unstable. Indeed, quantum mechanical simulations in the adiabatic representation are usually performed only on reduced-dimensionality models for the nuclear motion, including 2–3 nuclear modes at most [6]. For high-dimensional problems, the experience shows that a different representation, denoted *diabatic* and discussed in section 2.2.3, is more convenient.

Equation (2.16) formalizes the intuitive notion that the group Born–Oppenheimer approximation is more valid the more separated the "group of states" is from the other electronic states. The simplest situation is when the light excitation brings the molecule to an electronic state α , which is energetically well separated from all other states. In this case, the denominator of equation (2.16) is large, implying that non-radiative transitions are so slow or unlikely that they can be reasonably neglected. This is the setup of the well-known Born-Oppenheimer approximation, whereby the dynamics are described by a nuclear wavefunction evolving on an isolated PES,

$$\frac{\partial \chi_{\alpha}(\mathbf{q}, t)}{\partial t} = -\frac{\mathrm{i}}{\hbar} \left[\hat{T} + V_{\alpha}(\mathbf{q}) \right] \chi_{\alpha}(\mathbf{q}, t) \quad \text{(Born-Oppenheimer approx.)}. \tag{2.17}$$

2.2.3 The Diabatic Representation

In high-dimensional multi-state quantum molecular dynamics, the use of the adiabatic representation makes the numerical treatment unstable. One main source of instability is the divergence of the derivative couplings $D_{\kappa,\alpha\beta}$ – the dominant electronic coupling terms – in the regions of near degeneracy between potential energy surfaces.

This suggests that a possible solution to avoid the divergence problem is to adopt a representation that minimizes, or ideally eliminates, the derivative couplings. Such representation must be obtained by mixing the adiabatic electronic states (*i.e.*, the eigenstates of the electronic Hamiltonian) via a unitary transformation to get a new set of electronic states $|\tilde{\alpha}\rangle$ denoted diabatic states,

$$|\tilde{\alpha}(\mathbf{q})\rangle = \sum_{\beta=1}^{N_{\rm S}} |\beta(\mathbf{q})\rangle U_{\beta\alpha}(\mathbf{q}),$$
 (2.18)

where $\mathbf{U}(\mathbf{q}) = \{U_{\beta\alpha}(\mathbf{q})\}$ is a $N_S \times N_S$ unitary (or, if the states are real, orthogonal) matrix that needs to be defined at each molecular geometry \mathbf{q} .

Ideally, we would like to fix the **U** matrix so that the derivative couplings in the diabatic basis vanish, *i.e.*,

$$\widetilde{D}_{i,\alpha\beta}(\mathbf{q}) = \left\langle \widetilde{\alpha}(\mathbf{q}) \middle| \frac{\partial}{\partial q_i} \middle| \widetilde{\beta}(\mathbf{q}) \right\rangle \approx 0.$$
 (2.19)

An obvious way to impose this condition is to define the diabatic states to be independent of the molecular geometry. For example, we could make them coincide with the adiabatic states at one specific reference geometry \mathbf{q}_{ref} , i.e., $|\tilde{\mathbf{x}}\rangle = |\alpha(\mathbf{q}_{\text{ref}})\rangle$. However, this choice, denoted crude diabatic representation, does not have much practical utility. The reason is that its rigorous application would require a complete (infinite!) electronic basis to re-expand the geometry-dependent states $|\alpha(\mathbf{q})\rangle$ in terms of the reference adiabatic states $|\alpha(\mathbf{q}_{\text{ref}})\rangle$.

In contrast, we would like to keep working in the group Born–Oppenheimer approximation, and construct the diabatic states by mixing only a small set of adiabatic states that we obtain from quantum chemistry codes. To this end, defining the matrices $\widetilde{\mathbf{D}}_{i}(\mathbf{q}) = \left\{ \widetilde{D}_{i,\alpha\beta}(\mathbf{q}) \right\}$ and $\mathbf{D}_{\kappa}(\mathbf{q}) = \left\{ D_{\kappa,\alpha\beta}(\mathbf{q}) \right\}$, and replacing equation (2.18) into equation (2.19), the following relation is obtained,

$$\widetilde{\mathbf{D}}_{\kappa} = \mathbf{U}^{\dagger} \mathbf{D}_{\kappa} \mathbf{U} + \mathbf{U}^{\dagger} \frac{\partial \mathbf{U}}{\partial q_{\kappa}} \approx \mathbf{0}.$$
 (2.20)

In general, it can be proved that equation (2.20) cannot be solved exactly for **U**, hence the symbol " \approx " [7]. Indeed, to be precise, a correct denomination for the resulting electronic states would be *quasi-diabatic*, however, the improper use of the simpler adjective *diabatic* has become common practice.

Several techniques exist to mix the adiabatic states according to equation (2.18) and obtain a set of states that minimally depend on geometrical changes, $\partial |\tilde{\alpha}\rangle/\partial q_{\kappa} \approx 0$, so that equation (2.20) is satisfied to a good approximation and the residual derivative couplings are negligible. Such techniques include property-based methods [8–10], global fits [11, 12], or overlap-based methods [13, 14].

The use of diabatic states allows us to neglect the kinematic couplings in the solution of the evolution equations (2.8). On the other hand, these states are not eigenstates of the electronic Hamiltonian, therefore, the potential coupling terms are present, and the diabatic equations of motion take the form

$$\frac{\partial \chi_{\alpha}(\mathbf{q}, t)}{\partial t} = -\frac{\mathrm{i}}{\hbar} \hat{T} \chi_{\alpha}(\mathbf{q}, t) - \frac{\mathrm{i}}{\hbar} \sum_{\beta=1}^{N_{\mathrm{S}}} W_{\alpha\beta}(\mathbf{q}) \chi_{\beta}(\mathbf{q}, t), \tag{2.21}$$

where the χ_{α} 's are the nuclear wavefunctions associated with the different diabatic states and $W_{\alpha\beta}(\mathbf{q}) = \langle \tilde{\alpha} | \hat{H}_{\rm el} | \tilde{\beta} \rangle$. The main disadvantage of the diabatic representation is that the surfaces $W_{\alpha\beta}(\mathbf{q})$ cannot be obtained directly as an output of electronic structure calculations, but need to be constructed, on a case-by-case basis, using one of the strategies mentioned above.

On the other hand, given that each diabatic state describes the same "type" of electronic configuration, independently of the molecular geometry, the diabatic

potentials and couplings $W_{\alpha\beta}(\mathbf{q})$ are typically smooth functions of the nuclear coordinates. This smoothness facilitates fitting the potentials to analytic functions, and greatly improves the numerical stability of quantum dynamical simulations, which are therefore preferably performed in the diabatic representation.

2.2.4 Examples of Diabatic States

Diabatic electronic states are a useful concept both for the theoretical description and the interpretation of spectroscopic experiments, because they are associated with a well-defined electronic character: different types of diabatic states differ in their optical properties, strength of interaction with polar solvents or the local environment, photochemical reactivity, etc.

Examples of coupled electronic states that can be regarded as diabatic are:

• $\pi\pi^*$ and $n\pi^*$ states in organic molecules. Molecules containing lone pair electrons for heteroatoms in conjugated chains or aromatic rings can have electronic states of $\pi\pi^*$ character, which are energetically close to $n\pi^*$ state. Examples are carbonyl or thionyl groups conjugated to benzene rings. The interplay between $\pi\pi^*$ and $n\pi^*$ states are particularly important when the conjugated π the region is not too extended, so that $\pi\pi^*$ are not too stable as compared to $n\pi^*$ states.

In biological systems, a typical example of $\pi\pi^*/n\pi^*$ interaction is that of canonical nucleobases and their thionated analogues [16, 17]. As an example, figure 2.1 depicts the orbitals involved in $n\pi^*$ and $\pi\pi^*$ excitations in the thymine molecule, as well as computed diabatic potential energy surfaces [15]. In prebiotic chemistry, given that the $\pi\pi^*$ excitation can lead to mutagenic cycloaddition reactions, the ultrafast internal conversion to the neighboring $n\pi^*$ state was a key natural selection mechanism for these biomolecules. At the mechanistic level, since the coupled diabatic states have different symmetry with respect to the molecular plane, the coupling between different diabatic states is induced by out-of-plane vibrational modes [18, 19].

The diabatic $n\pi^*$ states in nucleobases and thio-nucleobases are associated with an electron hole localized at the O or S heteroatom. Therefore, they give specific signatures in time-resolved pump-probe experiments based on X-ray probes, which induce excitation or ionization from core orbitals. This has allowed proving that the $\pi\pi^* \longrightarrow n\pi^*$ internal conversion is a primary mechanism for the photostability of nucleobases [15, 20].

• Localized Frenkel excitons in supramolecular multi-chromophoric aggregates. The character of these diabatic states is that of molecular excitations involving orbitals localized on specific chromophores of the aggregate ("site" excitations). Local excitations are coupled with each other *via* the Coulomb interaction, and the resulting adiabatic states are delocalized "excitons" which involve multiple sites of the aggregate [21–23].

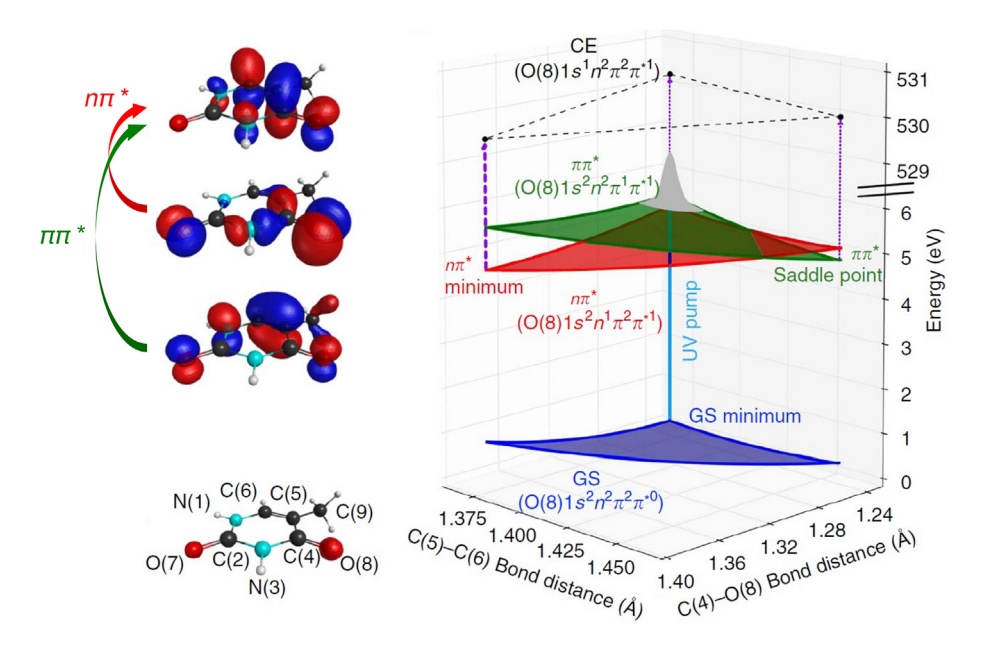


Fig. 2.1 – Diabatic $n\pi^*$ and $\pi\pi^*$ potential energy surfaces of thymine, involved in the transient X-ray absorption of thymine, presented in Ref. [15]. The electronic configuration of the two states is dominated by single excitation to the final π^* orbital. The fact that the $n\pi^*$ state is associated with a "hole" in a lone pair n orbital gives a characteristic excited state absorption band [15].

The geometry of the aggregate determines which adiabatic excitonic states are "bright" or "dark". Depending on the nature of the chromophores and their relative stacking structure, the linear absorption spectrum can be red-shifted, blue-shifted, or split with respect to the monomeric absorption band [24]. Excitonic states for a molecular dimer and their optical properties are described in more detail in chapter 4.

• Localized vs. charge transfer transitions in donor-acceptor systems. Site excitations can interact not only with each other, but also with charge-transfer states. Ideal diabatic charge-transfer states are formed by a one-electron transition from an orbital localized on one site of an aggregate (donor) to a virtual orbital localized on one acceptor site. The formation and the lifetime of charge-transfer states are critical in photocatalysis because they modify the redox potential of the donor/acceptor pair and can activate specific chemical reactions.

An illustration of diabatic potential energy surfaces of localized and charge transfer states is given in figure 2.2 for a donor-acceptor-donor triad [10, 25]. Note that the surfaces cross smoothly, and each of them is associated with a specific electronic configuration.

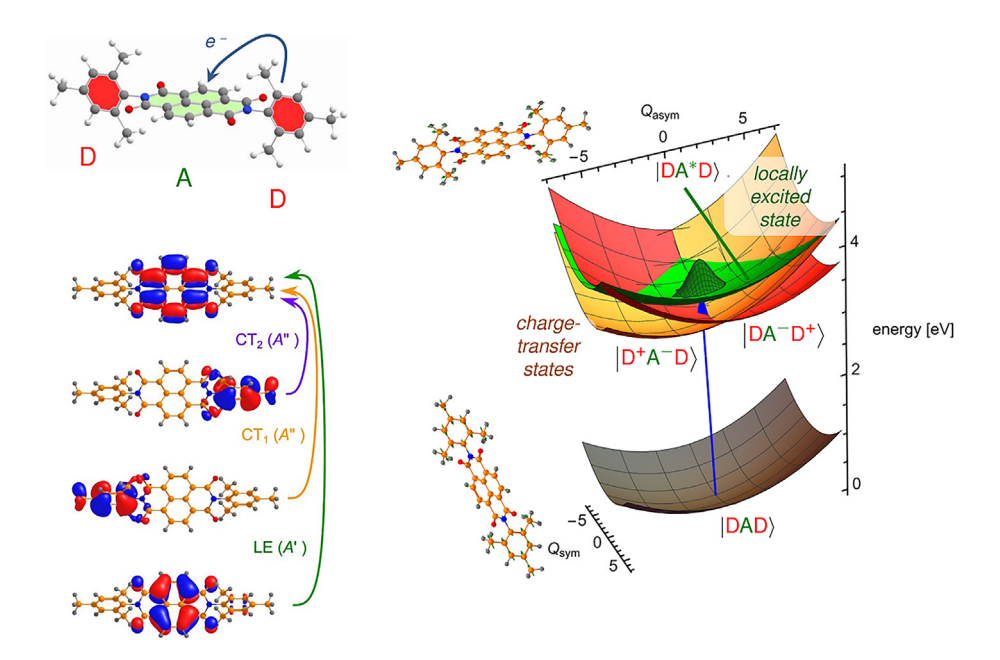


Fig. 2.2 – Calculated diabatic potential energy surfaces of the locally excited (LE) and charge-transfer (CT) states of a donor-acceptor-donor triad [10, 25]. The (CT) states, involving transitions from orbitals localized on two possible donors, are stabilized by symmetry-breaking vibrational distortions. The LE state is formed by a transition between orbitals localized in the central chromophore and is stabilized only by symmetry-conserving modes.

2.2.5 Vibronic Coupling Models for Diabatic PESs

One of the advantages of the diabatic representation is that the potential energy surfaces and couplings entering equation (2.21) can be described by smooth analytic functions of the coordinates. Specific choices for these functions define different vibronic coupling models [5].

For semi-rigid molecules, where nuclear motions are limited to small oscillations, a popular choice is the so-called *linear vibronic coupling model*, whereby the diabatic potentials are approximated as

$$W_{\alpha\beta}(\mathbf{q}) = W_0^{(\alpha\beta)} + \sum_{\kappa=1}^F W_{1,\kappa}^{(\alpha\beta)} q_{\kappa} + \delta_{\alpha\beta} \sum_{\kappa=1}^F \frac{M_{\kappa} \Omega_{\kappa}^2}{2} q_{\kappa}^2. \tag{2.22}$$

The parameters can be determined by electronic structure calculations using different strategies. This step is facilitated in the cases where the equilibrium structure of the molecule has some symmetry element, and the diabatic states α and β transform according to different irreducible representations $\Gamma_{\alpha} \neq \Gamma_{\beta}$ of the point symmetry group. In this case $W_0^{(\alpha\beta)} = 0$ by symmetry, and the only coupling modes for which $W_{1,\kappa}^{(\alpha\beta)} \neq 0$ are those associated with an irreducible representation $\Gamma_{\kappa} \subset \Gamma_{\alpha} \times \Gamma_{\beta}$.

In contrast, in the case of multi-chromophoric aggregates, such as natural light-harvesting systems, each diabatic state can be associated with an electronic excitation localized on a single chromophore. In this case, the coupling between different sites is reasonably independent of the vibrations, i.e. $W_{1,\kappa}^{(\alpha\beta)} = 0$ [22, 26, 27], and the couplings $W_0^{(\alpha\beta)}$ can be determined as the electrostatic interaction between the transition dipole moments of chromophores α and β , or – more rigorously – evaluating the Coulomb coupling between the electronic transition densities for the localized excitations [28]. The limiting case of a system with two electronic states is known in the literature as the *spin-boson model*, since it describes a two-level system (the spin) embedded into a vibrational (boson) bath.

The linear vibronic coupling model is one of the simplest Hamiltonian models, which is nevertheless capable of capturing the essential aspects of the physics of nonadiabatic transitions. In particular, it allows modelling the strong electronic-vibrational correlation at conical intersections, described in section 2.2.6.

However, the model neglects "intra-state" mode correlations, meaning that if the molecular system is in a specific diabatic state, then the different modes evolve independently of each other. Moreover, the normal modes are assumed to be the same for all diabatic states. This approximation might easily break down when the electronic structure changes significantly between different diabatic states. This is the case, for example, for transitions between localized excitons and charge-transfer states, whereby an initially neutral donor (acceptor) becomes cationic (anionic) and the reorganization energy is large. Such changes in the electronic charge distribution can lead to relatively large geometrical rearrangements as well as different vibrational frequencies [29]. Even $\pi\pi^*$ excitations strongly localized on a C=C bond might lead to large changes in the bond stretching frequency.

Within the harmonic approximation, the most general way to account for such vibronic changes is to adopt the so-called *quadratic vibronic coupling model*, where the diabatic surfaces take the general quadratic form

$$W_{\alpha\beta}(\mathbf{q}) = W_0^{(\alpha\beta)} + \sum_{\kappa=1}^F W_{1,\kappa}^{(\alpha\beta)} q_{\kappa} + \frac{1}{2} \sum_{\kappa,\mu=1}^F W_{2,\kappa\mu}^{(\alpha\beta)} q_{\kappa} q_{\mu}, \tag{2.23}$$

which accounts for changes in the normal modes between the different electronic states (the so-called Duschinsky rotation). The parametrization of these models from first principles is more involved, since it requires frequency calculations for the excited states [10, 19].

For systems where large amplitude motions need to be accounted for, the vibronic coupling models need to be extended beyond the harmonic approximation. Such anharmonic models are needed, for example, to describe the torsional dynamics in polymeric chains of chromophores [22, 30] or to model cis-trans photoisomerization [12]. As an example, figure 2.3 shows a Hamiltonian for the excitonic states of a polymeric chain with N methyl-thiophene units, where the diabatic potentials and couplings are parametrized using anharmonic functions of the inter-monomeric torsional angles, computed from electronic structure data [22].

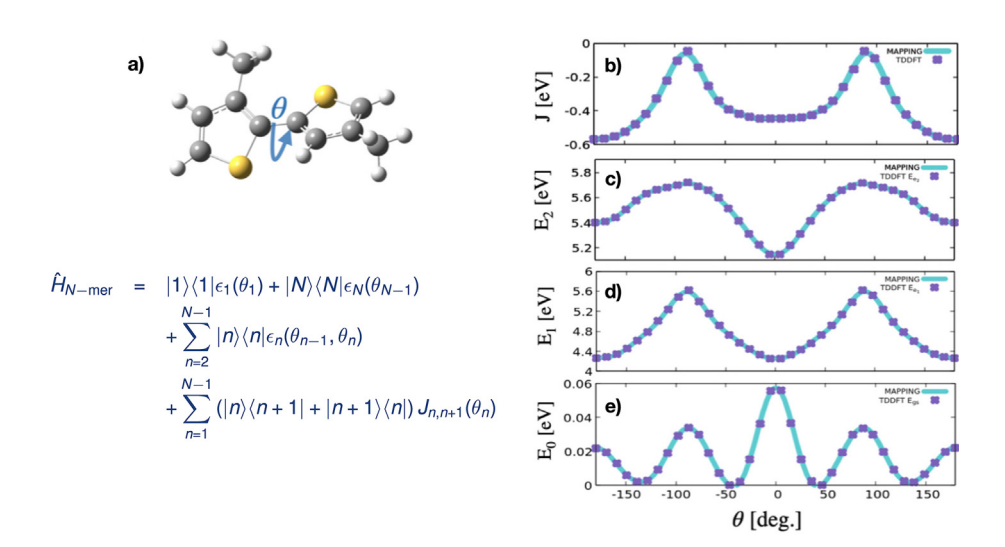


Fig. 2.3 – Excitonic Hamiltonian for a polymeric chain of chromophores with nearest-neighbor interactions, modulated by torsional angles θ , taken from Ref. [22] Panels (c–e) show the adiabatic energies for the ground (E_0) and the lowest two excited states $(E_1$ and $E_2)$ of the dimer shown in panel (a), as a function of the θ . Panel (b) depicts the inter-monomer excitonic coupling obtained upon diabatization.

To conclude this section, there are cases where only a few coordinates $\mathbf{q}_{\rm anh}$ are involved in large amplitude anharmonic motions. In this situation, a possible strategy is to construct a so-called *reaction path Hamiltonian*, making the parameters of equation (2.23) dependent on the anharmonic modes, *i.e.*

$$W_{\alpha\beta}(\mathbf{q}_{\rm anh}, \mathbf{q}) = W_0^{(\alpha\beta)}(\mathbf{q}_{\rm anh}) + \sum_{\kappa=1}^F W_{1,\kappa}^{(\alpha\beta)}(\mathbf{q}_{\rm anh}) q_{\kappa} + \frac{1}{2} \sum_{\kappa,\mu=1}^F W_{2,\kappa\mu}^{(\alpha\beta)}(\mathbf{q}_{\rm anh}) q_{\kappa} q_{\mu}. \quad (2.24)$$

As possible examples, this type of model can be used to describe photodissociation [11, 31], photoisomerization [12], or excited-state proton transfer [32] in small/medium-sized molecules.

2.2.6 Conical Intersections

Equation (2.16) for the derivative couplings shows that the transitions between different adiabatic states are most likely for molecular geometries where two adiabatic potentials are energetically close or, in the limiting case, degenerate. For a system with two electronic state, this implies the condition $V_1(\mathbf{q}) = V_2(\mathbf{q})$. Considering, in this case, the diabatic representation, the electronic Hamiltonian matrix, containing the diabatic potentials and couplings, is given as

$$\mathbf{H}_{\text{el}} = \begin{pmatrix} W_{11}(\mathbf{q}) & W_{12}(\mathbf{q}) \\ W_{12}(\mathbf{q}) & W_{22}(\mathbf{q}) \end{pmatrix}, \tag{2.25}$$

and we are assuming real electronic wavefunctions and potential energy surfaces.

The adiabatic potential energy surfaces are the eigenvalues of the matrix of equation (2.25) and can be evaluated analytically as

$$V_{1,2}(\mathbf{q}) = \frac{W_{11}(\mathbf{q}) + W_{22}(\mathbf{q})}{2} \pm \sqrt{\left(\frac{W_{11}(\mathbf{q}) - W_{22}(\mathbf{q})}{2}\right)^2 + W_{12}^2(\mathbf{q})}.$$
 (2.26)

Given the sum of two squares under the square root sign, the degeneracy condition $V_1(\mathbf{q}) = V_2(\mathbf{q})$ requires that the two equations

$$\begin{cases} W_{11}(\mathbf{q}) = W_{22}(\mathbf{q}) \\ W_{12}(\mathbf{q}) = 0 \end{cases}$$
 (2.27)

are simultaneously valid.

For one-dimensional models, which are exact for diatomic molecules, it is generally impossible to find one value of the nuclear coordinate (typically a bond distance) for which the equation (2.27) are both valid, therefore, the degeneracy can be approached but is never found. This is called the non-crossing rule and its most well-known manifestation is perhaps in the potential energy curves of alkyl halides [33, 34]. Its only exception is the so-called symmetry-allowed intersections, which are found when the two electronic states have different symmetry (e.g., g and u states of a homonuclear diatomic molecule) and thus $W_{12}(\mathbf{q})$ vanishes identically.

For high-dimensional models, which describe polyatomic molecules or aggregates, it is generally possible to encounter solutions of equation (2.27). The space of solutions (crossing seam) can be very large: for a system with F degrees of freedom, imposing two constraints leaves out F-2 coordinates for the seam space. Given a point of intersection \mathbf{q}_0 , the change in energy gap $\delta(V_2 - V_1)$ is generally linear as a function of the displacement δq_{κ} along a coordinate q_{κ} ,

$$\delta(V_2 - V_1) \approx |\delta q_{\kappa}| \sqrt{\left(\frac{\partial (W_{11} - W_{22})}{\partial q_{\kappa}}\right)_{\mathbf{q} = \mathbf{q}_0}^2 + 4\left(\frac{\partial W_{12}}{\partial q_{\kappa}}\right)_{\mathbf{q} = \mathbf{q}_0}^2}.$$
 (2.28)

Equation (2.28) describes a double-cone topography centered around the intersection point \mathbf{q}_0 . Molecular geometries exhibiting this kind of topography are referred to as *conical intersections* [35]. Due to the divergence of nonadiabatic couplings at these points, conical intersections are often described as "molecular funnels" that efficiently channel the photochemical process from one adiabatic surface to another, provided that they occur at an accessible energy.

However, it should be pointed out that such a pictorial view of molecules that "jump" to another surface after reaching conical intersection geometries is reasonably valid only within the adiabatic representation, therefore – in general – it does correlate with any specific change in the electronic character of the molecule, and should not be overinterpreted. Furthermore, for polyatomic molecules, conical intersections are not just special geometries, but large regions of the configuration space. In contrast, in the diabatic representation, the nuclear wave packets evolve on smooth potential energy surfaces that do not display double cone topographies.

Diabatic quantum transitions are therefore more correctly described as delocalized over a broad range of geometries.

A special role in radiationless transitions between adiabatic states is played by the gradients of the functions $W_{11}(\mathbf{q}) - W_{22}(\mathbf{q})$ and $W_{12}(\mathbf{q})$, which, according to equation (2.28), are the only coordinates that can lift the degeneracy at the conical intersection. These molecular motions are responsible for driving the molecule towards the intersection, so that the internal conversion is likely to happen, and then bring it away towards further vibrational relaxation.

2.3 Connection Between Quantum Dynamics and Linear Absorption Spectroscopy

The development of methods to simulate and investigate the dynamics of molecular quantum wave packets, governed by the time-dependent Schrödinger equations (2.14) or (2.21), is instrumental to the interpretation of any form of optical spectroscopy. To illustrate this concept, the simple case of linear absorption is briefly presented in this chapter.

In a standard linear absorption setup, sketched in figure 2.4, the decrease of intensity of a weak monochromatic field passing through a molecular sample is measured, and related to the absorption cross section $\sigma(\omega)$ by the Lambert–Beer law,

$$\frac{I(z)}{I(0)} = \frac{\left|\overrightarrow{E}(z,t)\right|^2}{\left|\overrightarrow{E}(0,t)\right|^2} = e^{-\sigma(\omega)\varrho_0 z},$$
(2.29)

where ϱ_0 is the number density of molecules and z is the length of the optical path. This equation can be derived from classical electrodynamical wave equations, assuming that the induced electric dipole of the molecular sample (*i.e.*, the polarization) is a linear function of the applied external field [36]. The absorption

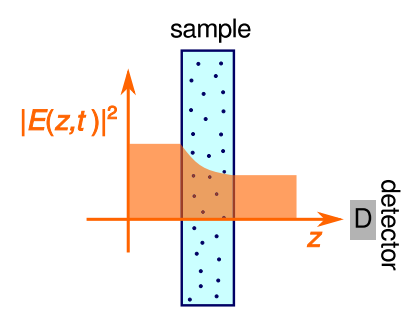


Fig. 2.4 — Linear spectroscopy experiment where an electric field radiating along the z direction crosses a molecular sample. The absorption of the sample leads to a decay of the field intensity.

cross section is related to the imaginary part of the linear susceptibility $\chi^{(1)}(\omega)$ which, in turn, is the half-Fourier transform of the linear response function $S^{(1)}(t)^2$,

$$\sigma(\omega) = \frac{4\pi\omega}{\varrho_0 c} \text{Im} \chi^{(1)}(\omega)$$

$$= \frac{4\pi\omega}{\varrho_0 c} \text{Im} \int_0^\infty S^{(1)}(t) e^{i\omega t} dt.$$
(2.30)

The response function is an intrinsic property of the molecular system (i.e., it does not depend on the applied field), and its time dependence can be formally connected to the molecular quantum dynamics induced by an ideal ultrashort light pulse. This connection can be established using time-dependent perturbation theory [37]. In particular, assuming that, before the interaction with light, the system is in a pure state $|\Psi_0\rangle$, and adopting the so-called rotating wave approximation (see chapter 4), it is found that the absorption spectrum can be computed as

$$\sigma(\omega) = \frac{4\pi\omega}{\hbar c} \operatorname{Re} \int_0^\infty C(t) e^{i\left(\frac{E_0}{\hbar} + \omega\right)t} dt, \qquad (2.31)$$

where

$$C(t) = \left\langle \Psi_0 \middle| \hat{\mu} e^{-\frac{i}{\hbar} \hat{H}_0 t} \hat{\mu} \middle| \Psi_0 \right\rangle. \tag{2.32}$$

This expression has an interesting physical interpretation, first pointed out by Heller [38]. The state $|\Phi(0)\rangle = \hat{\mu}|\Psi_0\rangle$ can be viewed as a state created at time t=0 by an instantaneous electric dipole interaction with the electric field. This state is called the doorway state, and is not an eigenstate of the molecular Hamiltonian, therefore, it evolves in time and its time evolution is represented by the time-evolution operator, i.e.

$$\begin{cases} |\Phi(0)\rangle = \hat{\mu}|\Psi_0\rangle \\ |\Phi(t)\rangle = e^{-\frac{i}{\hbar}\hat{H}_0t}|\Phi(0)\rangle \end{cases}$$
 (2.33)

The function $C(t) = \langle \Phi(0) | \Phi(t) \rangle$ is called the *autocorrelation function* of the doorway state (or the dipole-dipole autocorrelation function). It contains the overlap between the time-dependent wave packet created by the light excitation and itself at the initial time.

The oscillations in the autocorrelation function are converted, by Fourier transformation, into a progression of peaks in the absorption spectrum. An illustration of this process is given in figure 2.5 for the motion of a wave packet on a two-dimensional Morse potential. The autocorrelation function is displayed in the bottom-left panel: the maxima correspond to the recurrence times, when the wave packets go partially

²This equation assumes that the refraction index of the sample $n(\omega)$ is 1. If not, the absorption cross section should be rescaled by $n(\omega)$.

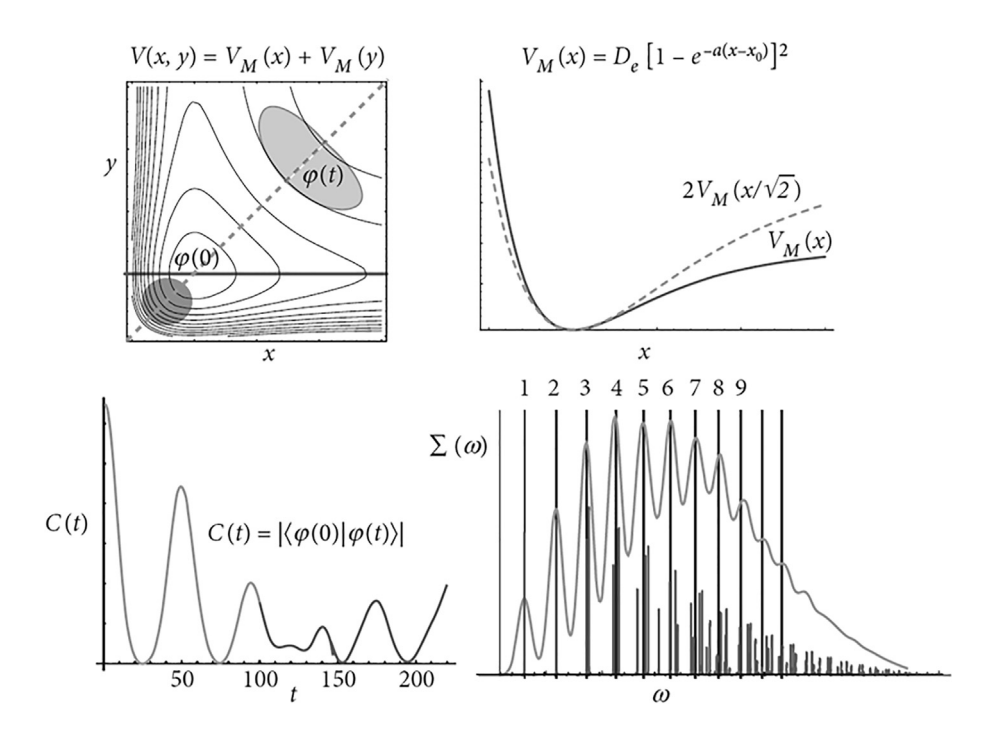


Fig. 2.5 – Motion of a quantum wave packet on a two-dimensional Morse potential, taken from Ref. [39]. The recurrences in the autocorrelation function (bottom-left panel) give rise to the vibrational structure in the linear absorption band (bottom-right panel).

back to their initial position. The Fourier analysis of these recurrences gives the vibrationally resolved absorption spectrum, shown in the bottom-right panel.

2.3.1 Sum-Over-States Expression for the Linear Absorption Spectrum

Equation (2.31) expresses the time-dependent formalism for the linear absorption spectrum, which is useful in different aspects. First, it is a good starting point to interpret multi-photon nonlinear processes, especially those involved in time-resolved spectroscopy. Second, from the computational viewpoint, it allows a simulation and interpretation of the absorption spectrum without the need of determining the energy levels of the molecule, which is a complex task in many cases, such as for highly flexible molecules (where the harmonic approximation cannot be used), photodissociation processes (where the relevant levels form a continuum) or in the presence of nonadiabatic effects (where the Born-Oppenheimer approximation is not valid). In contrast, very efficient quantum dynamical methods, described in section 2.4, are available to simulate high-dimensional multi-state wave packets.

The alternative approach to defining the linear absorption spectrum is the *time-independent formalism*, which is explicitly based on the energy levels of the

molecule. The equivalence between the time-dependent and the time-independent formalism is based on the eigenstate decomposition of the time-evolution operator,

$$e^{-\frac{i}{\hbar}\hat{H}_0 t} = \sum_{n=0}^{\infty} |\Psi_n\rangle e^{-\frac{i}{\hbar}E_n t} \langle \Psi_n|, \qquad (2.34)$$

which can be replaced into equation (2.32) to obtain

$$C(t) = \sum_{n=0}^{\infty} \underbrace{\langle \Psi_0 | \hat{\mu} | \Psi_n \rangle}_{=\mu_{n0}^*} e^{-\frac{i}{\hbar} E_n t} \underbrace{\langle \Psi_n | \hat{\mu} | \Psi_0 \rangle}_{=\mu_{n0}}$$

$$= \sum_{n=0}^{\infty} |\mu_{n0}|^2 e^{-\frac{i}{\hbar} E_n t},$$
(2.35)

where the integral $\mu_{n0} = \langle \Psi_n | \hat{\mu} | \Psi_0 \rangle$ is the transition dipole moment between the eigenstates $|\Psi_0\rangle$ and $|\Psi_n\rangle$. Equation (2.35) implies that only the excited states that have a nonzero transition dipole moment with the ground state contribute to the absorption spectrum. Replacing equation (2.35) into equation (2.31) gives

$$\sigma(\omega) = \frac{4\pi\omega}{\hbar c} \sum_{n=0}^{\infty} |\mu_{n0}|^2 \underbrace{\operatorname{Re} \int_{0}^{\infty} e^{\frac{i}{\hbar}(\hbar\omega - E_n + E_0)t} dt}_{=\pi\delta\left(\omega - \frac{E_n - E_0}{\hbar}\right)}$$

$$= \frac{4\pi^2\omega}{\hbar c} \sum_{n=0}^{\infty} |\mu_{n0}|^2 \delta\left(\omega - \frac{E_n - E_0}{\hbar}\right),$$
(2.36)

where the Dirac δ -function has been introduced to express the result of the time integral. The absorption spectrum has, in principle, the shape of a series of "sticks", each placed at a specific transition frequency; the intensity of each stick is proportional to the product between the squared transition dipole moment and the transition frequency (because of the ω prefactor). The states for which $\langle \Psi_0 | \hat{\mu} | \Psi_n \rangle = 0$ are "dark", i.e., they do not contribute any intensity to the linear absorption spectrum.

More realistic lineshapes are obtained by assuming that the final states decay by non-radiative dissipative mechanisms, due to the surroundings. In the time-dependent formalism, this process is associated with the damping of the autocorrelation function, which, in the simplest case, can be described by an exponential factor $e^{-\Gamma t}$, the same for all energy levels. This leads to the Lorentzian lineshape function,

$$L\left(\omega - \frac{E_n - E_0}{\hbar}\right) = \frac{1}{\pi} \operatorname{Re} \int_0^\infty e^{\frac{i}{\hbar}(\hbar\omega - E_n + E_0)t} e^{-\Gamma t} dt$$
$$= \frac{\Gamma}{\left(\omega - \frac{E_n - E_0}{\hbar}\right)^2 + \Gamma^2},$$
 (2.37)

which, as a function of ω , is a bell-shaped function with a maximum at $(E_n - E_0)/\hbar$. The value 2Γ coincides with the full-width at half maximum of the absorption line.

2.4 Numerical Methods: Quantum Wave Packets

This section discusses computational techniques of molecular quantum dynamics applied to photochemical and photophysical problems. These methodologies address the problem of solving the time-dependent Schrödinger equation

$$\frac{\partial |\Psi, t\rangle}{\partial t} = -\frac{i}{\hbar} \hat{H} |\Psi, t\rangle, \qquad (2.38)$$

for a generic wave packet expressed in the group Born–Oppenheimer approximation as

$$|\Psi, t\rangle = \sum_{\alpha=1}^{N_{\rm S}} |\alpha\rangle \chi_{\alpha}(\mathbf{q}, t).$$
 (2.39)

In this section, we adopt the diabatic representation, which is the most common choice for quantum dynamics due to the smoothness of the potential energy surfaces. Moreover, we consider, for simplicity, a time-independent Hamiltonian

$$\hat{H} = \hat{T} + \sum_{\alpha,\beta} |\alpha\rangle W_{\alpha\beta}(\mathbf{q})\langle\beta|. \tag{2.40}$$

The extension of the presented techniques to time-dependent Hamiltonians or to the adiabatic representation is generally straightforward, except for a few numerical caveats.

In the diabatic representation, the nuclear wavefunctions $\chi_{\alpha}(\mathbf{q}, t)$ evolve exactly according to equation (2.21). Their norms give the diabatic state *populations*,

$$p_{\alpha}(t) = \langle \chi_{\alpha}(t) | \chi_{\alpha}(t) \rangle, \tag{2.41}$$

whereas the diabatic *electronic coherences* are given by the wave packet overlaps,

$$\rho_{\alpha\beta}(t) = \langle \chi_{\alpha}(t) | \chi_{\beta}(t) \rangle. \tag{2.42}$$

2.4.1 The Time-Dependent Variational Principle

A number of methods for the numerical solution of equation (2.38) can be formulated via a variational approach. This strategy involves, as a first step, the formulation of a physically reasonable ansatz for the time-dependent wavefunction. This ansatz has a well-defined functional form, and it is made time-dependent by introducing numerical parameters $\lambda(t) = (\lambda_1(t), \lambda_2(t), ...)$ in its definition,

$$|\Psi, t\rangle \equiv |\Psi, \lambda(t)\rangle.$$
 (2.43)

In the following, we consider the common case of complex-valued parameters $\lambda_r(t)$, and a parametrization defined such that $|\Psi, t\rangle$ is a holomorphic function of the parameters, *i.e.*, does not explicitly depend on their complex conjugates,

$$\frac{\partial |\Psi, \lambda\rangle}{\partial \lambda_r^*} = 0. \tag{2.44}$$

The introduction of numerical parameters transforms the original partial differential equation into a system of ordinary differential equations for the parameters. To derive such equations, we notice that, in general, the ansatz introduces an approximation in the time evolution of the wavefunction. This is because the approximate time derivative evaluated using the chain rule,

$$\begin{aligned} \left|\dot{\Psi}\right\rangle_{\text{approx}} &= \sum_{r} \frac{\partial \left|\Psi\right\rangle}{\partial \lambda_{r}} \dot{\lambda}_{r} \\ &= \sum_{r} \left|\frac{\partial \Psi}{\partial \lambda_{r}}\right\rangle \dot{\lambda}_{r}, \end{aligned} \tag{2.45}$$

generally differs from the *exact* time derivative given by the time-dependent Schrödinger equation,

$$|\dot{\Psi}\rangle_{\rm exact} = -\frac{\mathrm{i}}{\hbar}\hat{H}|\Psi\rangle.$$
 (2.46)

This suggests that an optimal strategy to compute the evolution of the parameters is to minimize the difference between the approximate and the exact time derivatives,

$$\left\{\dot{\boldsymbol{\lambda}},\dot{\boldsymbol{\lambda}}^*\right\} = \arg \min \langle \dot{\boldsymbol{\Psi}}_{approx} - \dot{\boldsymbol{\Psi}}_{exact} \big| \dot{\boldsymbol{\Psi}}_{approx} - \dot{\boldsymbol{\Psi}}_{exact} \rangle. \tag{2.47}$$

This recipe defines the *time-dependent variational principle* (TDVP). Although its application might be complicated for complex wavefunction ansätze, it is a pretty robust strategy, independent of the specific problem, and can also be used in the case of a time-dependent Hamiltonian, *i.e.*, when the electromagnetic field is explicitly included.

To use the TDVP, the right-hand side of equation (2.47) must be differentiated with respect to the individual parameter derivatives $\dot{\lambda}_r$, and the result is set to zero. Due to the analyticity condition of equation (2.44), the resulting equations of motion take the general form

$$\left\langle \frac{\partial \Psi}{\partial \lambda_r} \middle| \dot{\Psi}_{approx} - \dot{\Psi}_{exact} \right\rangle = 0. \tag{2.48}$$

Replacing equations (2.45) and (2.46) into equation (2.48) gives, for each parameter index r,

$$\sum_{s} \left\langle \frac{\partial \Psi}{\partial \lambda_{r}} \middle| \frac{\partial \Psi}{\partial \lambda_{s}} \middle\rangle \dot{\lambda}_{s} = -\frac{i}{\hbar} \left\langle \frac{\partial \Psi}{\partial \lambda_{r}} \middle| \hat{H} \middle| \Psi \right\rangle
\Longrightarrow \dot{\lambda}_{r} = -\frac{i}{\hbar} \sum_{s} \left\{ \mathbf{M}^{-1} \right\}_{rs} \left\langle \frac{\partial \Psi}{\partial \lambda_{r}} \middle| \hat{H} \middle| \Psi \right\rangle,$$
(2.49)

where **M** is the overlap matrix between the allowed variations of the wavefunction ansatz, $M_{rs} = \langle \partial \Psi / \partial \lambda_r | \partial \Psi / \partial \lambda_s \rangle$, which needs to be formally inverted to solve the equations. Notice that in the case of linearly dependent variations, the **M** matrix becomes singular, and the equations of motion need to be regularized by introducing additional constraints between the parameters that eliminate the linear dependence.

Examples of ansätze with linearly dependent variations will be presented in the following sections.

An equivalent way to formulate the TDVP is based on the tangent space projector, which, for linearly independent variations, takes the form

$$\hat{P}_{\text{var}} = \sum_{r_s} \left| \frac{\partial \Psi}{\partial \lambda_r} \right\rangle \left\{ \mathbf{M}^{-1} \right\}_{r_s} \left\langle \frac{\partial \Psi}{\partial \lambda_s} \right|. \tag{2.50}$$

Applied to a generic wavefunction, this operator yields a linear combination of the variations, exactly as in equation (2.45). Therefore, we can derive the equations of motion for the parameters by projecting the exact time derivative onto the tangent space,

$$|\dot{\Psi}\rangle_{\rm approx} = -\frac{\mathrm{i}}{\hbar}\hat{P}_{\rm var}\hat{H}|\Psi\rangle.$$
 (2.51)

This formulation allows us to derive two formal, highly desirable properties for the methods derived from the TDVP. The first one is that if the wavefunction itself is contained in the space of variations, i.e. $\hat{P}_{\text{var}}|\Psi\rangle = |\Psi\rangle$, then the equations of motion conserve the norm,

$$\frac{\mathrm{d}}{\mathrm{d}t} \langle \Psi | \Psi \rangle = \langle \dot{\Psi} | \Psi \rangle + \langle \Psi | \dot{\Psi} \rangle
= \frac{\mathrm{i}}{\hbar} \langle \Psi | \hat{H} \hat{P}_{\mathrm{var}} | \Psi \rangle - \frac{\mathrm{i}}{\hbar} \langle \Psi | \hat{P}_{\mathrm{var}} \hat{H} | \Psi \rangle
= \frac{\mathrm{i}}{\hbar} \langle \Psi | \hat{H} | \Psi \rangle - \frac{\mathrm{i}}{\hbar} \langle \Psi | \hat{H} | \Psi \rangle
= 0.$$
(2.52)

The second property is that if the Hamiltonian does not explicitly depend on time, then the energy is also conserved:

$$\frac{\mathrm{d}}{\mathrm{d}t} \langle \Psi | \hat{H} | \Psi \rangle = \langle \dot{\Psi} | \hat{H} | \Psi \rangle + \langle \Psi | \hat{H} | \Psi \rangle
= \frac{\mathrm{i}}{\hbar} \langle \Psi | \hat{H} \hat{P}_{\mathrm{var}} \hat{H} | \Psi \rangle - \frac{\mathrm{i}}{\hbar} \langle \Psi | \hat{H} \hat{P}_{\mathrm{var}} \hat{H} | \Psi \rangle
= 0.$$
(2.53)

In the following sections, different methods derived from the TDVP will be presented.

2.4.2 Expansion in a Finite Time-Independent Basis

In a numerical simulation, the simplest way to represent the wave packets χ_{α} from equation (2.39) is *via* an expansion over a finite, time-independent basis. To understand the main features and limitations of this approach, we start from a one-dimensional wave packet, expanded as

$$\chi_{\alpha}(q,t) = \sum_{m=1}^{N} A_{m}^{(\alpha)}(t) \psi_{m}(q),$$
(2.54)

where $A_m^{(\alpha)}(t)$ are the complex-valued expansion coefficients, and ψ_m are the basis functions, assumed to be orthonormal $\langle \psi_m | \psi_n \rangle = \delta_{mn}$.

The application of the TDVP for a generic diabatic Hamiltonian in the form of equation (2.40) gives the equations of motion

$$\dot{A}_{m}^{(\alpha)}(t) = -\frac{\mathrm{i}}{\hbar} \sum_{n=1}^{N} \langle \psi_{m} | \hat{T} | \psi_{n} \rangle A_{n}^{(\alpha)}(t) - \frac{\mathrm{i}}{\hbar} \sum_{\beta=1}^{N_{\mathrm{S}}} \sum_{n=1}^{N} \langle \psi_{m} | W_{\alpha\beta}(q) | \psi_{n} \rangle A_{n}^{(\beta)}(t). \tag{2.55}$$

The equations are linear in the parameters and therefore can be solved efficiently with great accuracy, using specific iterative algorithms, such as the Lanczos or Chebyshev methods [40, 41]. It is easy to prove that the norm and energy of the wavefunction are conserved (provided that the Hamiltonian is time-independent), as expected from the results of section 2.4.1.

The choice of basis functions $\psi_m(q)$ typically depends on the type of motion one needs to describe (small amplitude vibrations, dissociation, angular or torsional motions, etc.). For computational efficiency, one should choose functions for which the matrix elements $\langle \psi_m | \hat{T} | \psi_n \rangle$ and $\langle \psi_m | W_{\alpha\beta}(q) | \psi_n \rangle$ can be evaluated analytically. For the integrals involving the kinetic energy operator, which has a standard expression, this is not a problem, because analytic expressions are available, e.g., between eigenfunctions of the harmonic oscillator, as well as for many other quantum models. The same is true for the evaluation of matrix elements of harmonic potentials $W_{\alpha\beta}(q)$.

For arbitrary, anharmonic potentials, a more convenient choice is to choose an orthonormal basis set made of functions which are strongly localized at specific values of the coordinate q_m , so that the potential matrices can be approximated as diagonal, $\langle \psi_m | W_{\alpha\beta}(q) | \psi_n \rangle \approx W_{\alpha\beta}(q_m) \delta_{mn}$, and can be readily evaluated. This type of basis defines a so-called discrete variable representation (DVR), whereby the nuclear wavefunction is represented on a grid of points, and can be obtained by an orthogonal transformation between the delocalized basis functions. For example, the so-called harmonic oscillator DVR is formed by diagonalizing the operator q in the basis of the harmonic oscillator eigenstates [42]; the same transformation is applied to the matrix of the kinetic energy operator. Equidistant grids, which define the exponential DVR or sine DVR, can be obtained in a similar way starting from particle-in-a-box eigenfunctions [42, 43].

As mentioned above, the equations of motion in the form of equation (2.55) are perfectly valid even when the diabatic potentials $W_{\alpha\beta}$ are time-dependent. This can be used to model the interaction with an electromagnetic field explicitly [44–46] or to incorporate the time-dependent variations of the electronic Hamiltonian due to the fluctuations of a surrounding environment [22].

The curse of dimensionality

The linear parameterization of equation (2.54) is easy to implement, but is limited to low-dimensional problems, due to an exponential scaling with respect to the

number of coordinates. Indeed, for a multi-dimensional quantum dynamical problem with f coordinates, equation (2.54) takes the form

$$\chi_{\alpha}(q_1, q_2, ..., q_f, t) = \sum_{m_1=1}^{N_1} \sum_{m_2=1}^{N_2} \cdots \sum_{m_f=1}^{N_f} A_{m_1 m_2 ... m_f}^{(\alpha)}(t) \psi_{m_1}^{(1)}(q_1) \psi_{m_2}^{(2)}(q_2) \cdots \psi_{m_f}^{(f)}(q_f)
= \sum_{\mathbf{m}} A_{\mathbf{m}}^{(\alpha)}(t) \psi_{\mathbf{m}}(\mathbf{q}),$$
(2.56)

where the multi-index $\mathbf{m} = (m_1, ..., m_f)$ has been introduced. The coefficients for each electronic state are now stored in a tensor with f indices, i.e., the total number of coefficients is $N_S \times N_1 N_2 \cdots N_f$, which is also the formal number of rows and columns of the Hamiltonian matrix. Hereafter, we refer to the use of the ansatz of equation (2.56) as the "standard method".

This exponential scaling is an example of the curse of dimensionality, typical of methods for quantum dynamics, that limits the use of the standard method presented here to low-dimensional problems. Consider, as an example, a quantum dynamical problem with 8 degrees of freedom and 2 electronic states; using a grid of N=20 points for each degree of freedom make $2 \cdot 20^8$ complex coefficients per time step: the storage of the coefficient vector in double precision would take about 760 GB of memory.

This example illustrates why the standard parametrization of equation (2.56) is practically used only for relatively low-dimensional systems. However, the efficient numerical implementation of this approach often relies on techniques of tensor operations, which are also used in more sophisticated methods.

Basics of tensor algebra

Let us consider a lower-dimensional quantum dynamical problem, say 6 degrees of freedom for two electronic states, as previously. The same conditions as before are used: 20 points for each of the two electronic states. However, this time, the number of degrees of freedom is reduced to 6 instead of 8. Storing the coefficient vector would take less than 2 GB, which is quite a large value, but certainly fits in the memory of modern computers.

On the other hand, one has to consider the storage of the Hamiltonian matrix, which in this example contains formally $\left(2\cdot 20^6\right)^2$ matrix elements. Assuming a real Hamiltonian, the storage of the whole matrix would take something of the order of 10^5 TB of memory, which is prohibitive. However, in most cases, it is not necessary to form and store the full Hamiltonian matrix. In particular, this is true when the Hamiltonian has a sum-of-products (SOP) form:

$$\hat{H}_{\alpha\beta} = \hat{T} + W_{\alpha\beta}(\mathbf{q})
= \sum_{r} K_{r}^{(\alpha\beta)} \hat{h}_{r,1}^{(\alpha\beta)}(q_{1}) \hat{h}_{r,2}^{(\alpha\beta)}(q_{2}) \cdots \hat{h}_{r,f}^{(\alpha\beta)}(q_{f}),$$
(2.57)

where the operators $\hat{h}_{r,\kappa}^{(\alpha\beta)}(q_{\kappa})$ are one-dimensional.

Note that the kinetic energy operator already has the form of equation (2.57). In the cases where the harmonic approximation is used, the potential also has the desired form, and the same is true for generic anharmonic polynomial potentials and many more cases.

For the SOP form, the Hamiltonian matrix elements are given as

$$H_{\mathbf{mn}}^{(\alpha\beta)} = \left\langle \psi_{\mathbf{m}} \middle| \hat{H}_{\alpha\beta} \middle| \psi_{\mathbf{n}} \right\rangle$$

$$= \sum_{r} K_{r}^{(\alpha\beta)} \left\langle \psi_{m_{1}} \middle| \hat{h}_{r,1}^{(\alpha\beta)} \middle| \psi_{n_{1}} \right\rangle \cdots \left\langle \psi_{m_{f}} \middle| \hat{h}_{r,f}^{(\alpha\beta)} \middle| \psi_{n_{f}} \right\rangle$$

$$= \sum_{r} K_{r}^{(\alpha\beta)} H_{r,1,m_{1},n_{1}}^{(\alpha\beta)} \cdots H_{r,f,m_{f},n_{f}}^{(\alpha\beta)},$$
(2.58)

i.e., in matrix form, the Hamiltonian becomes a sum of Kronecker products,

$$\mathbf{H}^{(\alpha\beta)} = \sum_{r} K_r^{(\alpha\beta)} \mathbf{H}_{r,1}^{(\alpha\beta)} \otimes \cdots \otimes \mathbf{H}_{r,f}^{(\alpha\beta)}.$$
 (2.59)

This has a computational advantage. For a Hamiltonian in the SOP form, one does not need to store the full $\mathbf{H}^{(\alpha\beta)}$ matrices, but only the small $N \times N$ $\mathbf{H}^{(\alpha\beta)}_{r,\kappa}$ matrices. In our example, each of these matrices takes only ≈ 3 kB of memory, therefore, it is affordable to store even thousands of them. Moreover, if the DVR basis is used, the matrices related to potential terms are diagonal, so that only their diagonals need to be stored.

In summary, in quantum dynamical simulations where the wave packet is represented on high-dimensional direct-product coordinate grids, the construction of model PES in the sum-of-products form is critical for computational efficiency.

It is useful to understand what this implies in the numerical wave packet propagation. The coefficient vectors for each electronic state $A_{m_1m_2...m_f}^{(\alpha)}$ are mathematically rank-f tensor, which contains N^f elements; we can think of them as " $N \times N \times N \times \cdots$ " matrices. Solving the equations of motion of the type of equation (2.55) involves computing products like $\mathbf{H}^{(\alpha\beta)}\mathbf{vec}\left(\mathbf{A}^{(\beta)}\right)$ to evaluate the derivative $\dot{\mathbf{A}}^{(\alpha)}$. Here, $\mathbf{vec}\left(A^{(\beta)}\right)$ is the vectorization of the tensor \mathbf{A} , i.e., a reshaping of the tensor in the form of a column vector with N^f entries. Typically, this is achieved by ordering the elements of the tensor in a well-defined way, called the colexicographic order.

Using equation (2.59), the computation of $\mathbf{H} \cdot \mathbf{vec}(\mathbf{A})$ (electronic superscripts are omitted for simplicity) involves summing the results of the multiplication of Kronecker products of "small matrices" by the coefficient tensor. To this end, one useful operation that can be straightforwardly implemented in computer codes is the *matricisation* along the κ -th mode $\mathbf{Mat}_{\kappa}(\mathbf{A})$, which converts the tensor into a $N \times N^{f-1}$ matrix, where each row is associated with a different value of m_{κ} and the columns are ordered colexicographically. The inverse operation to the matricisation $\mathbf{Mat}_{\kappa}^{-1}$, called *tensorization*, reconstructs the rank-f tensor, *i.e.* $\mathbf{A} = \mathbf{Mat}_{\kappa}^{-1}(\mathbf{Mat}_{\kappa}(\mathbf{A}))$.

Using the matricisation, the products $\mathbf{H} \cdot \mathbf{vec}(\mathbf{A}) = \mathbf{H}_{r,1} \otimes \cdots \otimes \mathbf{H}_{r,f} \cdot \mathbf{vec}(\mathbf{A})$ are readily evaluated. It is sufficient to make a loop over the different modes and, at each step, overwrite the \mathbf{A} tensor with the tensor obtained by multiplying the small matrix $\mathbf{H}_{r,\kappa}$ by the κ -mode matricisation of \mathbf{A} , and transform back via tensorization,

$$\mathbf{A} \longrightarrow \mathbf{Mat}_{1}^{-1} (\mathbf{H}_{r,1} \mathbf{Mat}_{1}(\mathbf{A})) \longrightarrow \mathbf{Mat}_{2}^{-1} (\mathbf{H}_{r,2} \mathbf{Mat}_{2}(\mathbf{A}))$$

$$\longrightarrow \cdots \longrightarrow \mathbf{Mat}_{f}^{-1} (\mathbf{H}_{r,f} \mathbf{Mat}_{f}(\mathbf{A}))$$

$$= \mathbf{H}_{r,1} \otimes \mathbf{H}_{r,2} \otimes \cdots \otimes \mathbf{H}_{r,f} \mathbf{A}.$$
(2.60)

This is computationally very efficient. The cost for the direct $\mathbf{H} \cdot \mathbf{vec}(\mathbf{A})$ multiplication (provided that we have enough memory to store the \mathbf{H} matrix) scales as $O(N^{2f})$. Conversely, the evaluation performed using equation (2.60) scales as $O(fN^{f+1})$, which for large f and N is a huge speedup.

2.4.3 Mitigating the Curse of Dimensionality: The Multi-Configurational Time-Dependent Hartree Method

In equation (2.56), the shape of the wavefunction along the mode q_{κ} is expressed using a *static* basis set made of the functions $\psi_{m_{\kappa}}^{(\kappa)}(q_{\kappa})$. In the DVR, these functions are associated with grid points, and large grids are needed to be able to describe complex and large amplitude motions that the wave packet might undergo during its time evolution. This leads to the computationally undesirable N^f dependence.

In 1990, Meyer, Manthe, and Cederbaum introduced a way to significantly mitigate the curse of dimensionality by showing that, at a given time, the wave packet can be expanded over an effective smaller basis set in such a way that the dimensionality of the coefficient tensor is significantly reduced [47]. The effective basis set is time-dependent and needs to be constructed on the fly. This scheme gives rise to the multi-configurational time-dependent Hartree (MCTDH) approach [42], where the nuclear wavefunctions are given by the ansatz

$$\chi_{\alpha}(q_{1},...,q_{f},t) = \sum_{j_{1}=1}^{n_{1}^{(\alpha)}} \cdots \sum_{j_{f}=1}^{n_{f}^{(\alpha)}} B_{j_{1}...j_{f}}^{(\alpha)}(t) \varphi_{j_{1}}^{(\alpha,1)}(q_{1},t) \cdots \varphi_{j_{f}}^{(\alpha,f)}(q_{f},t)
= \sum_{\mathbf{i}} B_{\mathbf{j}}^{(\alpha)}(t) \Phi_{\mathbf{j}}^{(\alpha)}(\mathbf{q},t),$$
(2.61)

where $\mathbf{j} = (j_1, ..., j_f)$ is a multi-index. This expression is similar to that of the standard method of equation (2.56), with the important difference that here both the coefficients $B_{\mathbf{j}}^{(\alpha)}(t)$ and the configurations $\Phi_{\mathbf{j}}^{(\alpha)}(\mathbf{q}, t)$ are time-dependent. Each configuration is a Hartree product of the so-called single-particle functions (SPFs), which are the effective basis functions that describe the dynamics of individual degrees of freedom.

Note that, according to equation (2.61), different sets of SPFs are used for the different electronic states $|\alpha\rangle$. This is called "multi-set" formalism in the MCTDH literature [48]. Alternatively, one can use the same SPFs for the different electronic states ("single-set" formalism). The SPFs are, in turn, expanded in the primitive basis used in equation (2.56),

$$\varphi_{j_{\kappa}}^{(\alpha,\kappa)}(q_{\kappa},t) = \sum_{m_{\kappa}=1}^{N_{\kappa}} C_{j_{\kappa}m_{\kappa}}^{(\alpha,\kappa)}(t) \psi_{m_{\kappa}}^{(\kappa)}(q_{\kappa}). \tag{2.62}$$

The number of SPFs for a given mode and electronic state $n_{\kappa}^{(\alpha)}$ is typically fixed in advance and is a convergence parameter for the calculation.

The central idea and the power of the MCTDH method is the following approximate tensor decomposition of the original coefficient tensor:

$$A_{m_1...m_f}^{(\alpha)}(t) \approx \sum_{j_1=1}^n \cdots \sum_{j_f=1}^n B_{j_1...j_f}^{(\alpha)}(t) C_{j_1m_1}^{(\alpha,1)}(t) \cdots C_{j_fm_f}^{(\alpha,f)}(t), \qquad (2.63)$$

where, for simplicity, the same number of SPFs n is used for the different modes. The decomposition is sketched diagrammatically in figure 2.6b. The total number of parameters needed to describe the total wavefunction is $N_{\rm S} \times \left(n^f + f \times nN\right)$. For a large number of modes (high f) and $n \ll N$ the number of parameters drops significantly. To follow up with the example in section 2.4.2, consider a system with 2 electronic states, 8 modes, and 20 primitive basis functions per mode; this makes $2 \times 20^8 = 5.12 \cdot 10^{10}$ complex parameters to define the full wavefunction (≈ 760 GB in double precision), making the calculation prohibitive. With MCTDH, it is not uncommon to use, on average, 4–5 SPFs per mode, taking n=5, we would have $2 \times \left(5^8 + 8 \times 5 \times 20\right) = 7.83 \cdot 10^5$ parameters, which take about 11 MB of memory: the calculation becomes doable on a laptop!

Due to the exponential scaling with respect to f, it is clear from this example that the lower the ratio n/N the higher the computational gain. This is why in practice, the number of SPFs is carefully tuned for each mode and electronic state, so to keep the value of $n_{\kappa}^{(\alpha)}$ the smallest as possible. On the other hand, using too few SPFs makes the approximation of equation (2.63) less accurate, therefore, a balance between accuracy and computational feasibility needs to be found. Fortunately, as explained below, there are ways to understand whether one is doing a too severe approximation, and therefore $n_{\kappa}^{(\alpha)}$ should be increased.

One remark still needs to be made, before describing how the MCTDH parameters evolve in time. The decomposition of equation (2.63) is invariant under unitary transformations of the form

$$\widetilde{C}_{j_{\kappa}m_{\kappa}}^{(\alpha,\kappa)} = \sum_{l=1}^{n} U_{j_{\kappa}l} C_{lm_{\kappa}}^{(\alpha,\kappa)},
\widetilde{B}_{...j_{\kappa-1}j_{\kappa}j_{\kappa+1}...}^{(\alpha)} = \sum_{l=1}^{n} U_{j_{\kappa}l}^{*} B_{...j_{\kappa-1}j_{\kappa+1}...}^{(\alpha)},$$
(2.64)

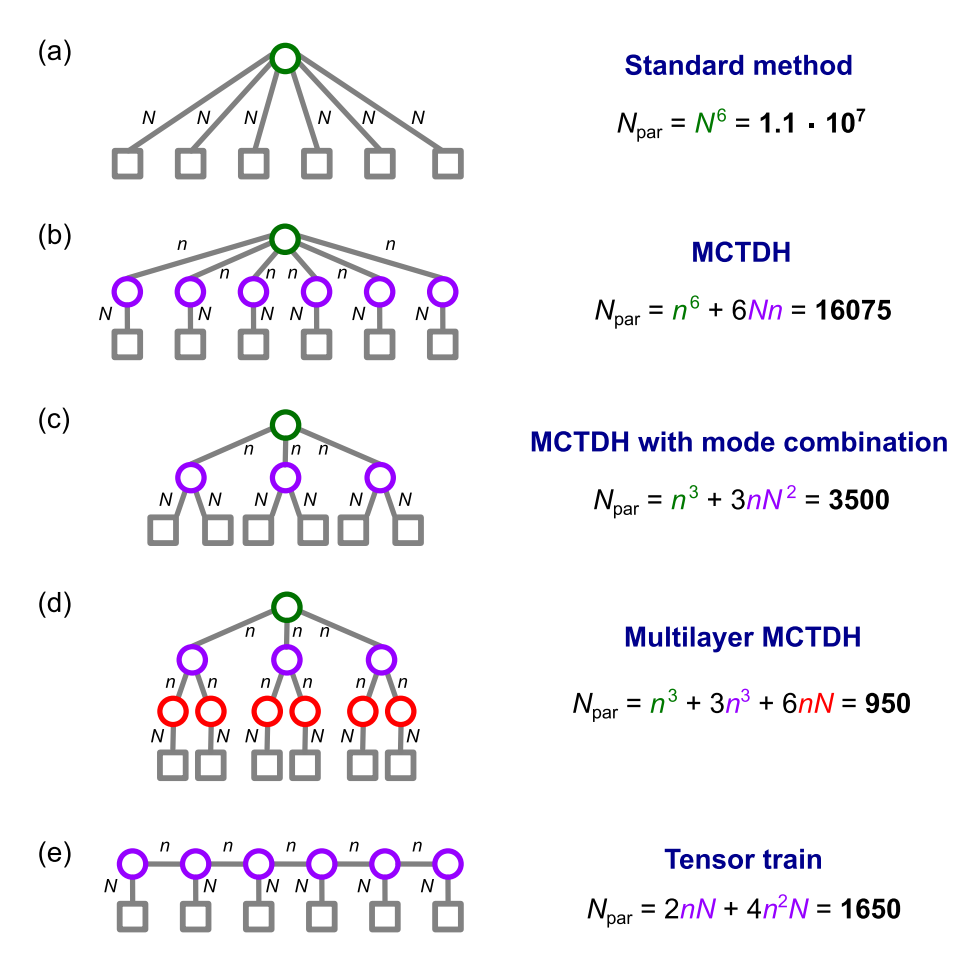


FIG. 2.6 – Different tensor representations for a 6-dimensional nuclear wavefunction. The squares represent primitive one-dimensional basis functions, such as DVR grid points. The circles represent tensors of time-dependent coefficients, for which the number of dimensions is given by the number of legs, and the size of each dimension is reported near the leg. For each type of representation, the total number of parameters $N_{\rm par}$ is reported. This value can be simply calculated by summing the product of the dimensions of each circle. In these examples, the number of parameters is calculated by taking n=5 and N=15.

where **U** is a unitary matrix, *i.e.* $\mathbf{U}^{\dagger}\mathbf{U} = \mathbf{U}\mathbf{U} = 1$. This implies that some redundancies exist between the B and C parameters. To eliminate such redundancies, the C coefficients are propagated in such a way as to satisfy the following condition for each mode:

$$\left\langle \varphi_{j}^{(\alpha\kappa)} \middle| \frac{\partial \varphi_{l}^{(\alpha\kappa)}}{\partial t} \right\rangle = \frac{\mathrm{i}}{\hbar} \left\langle \varphi_{j}^{(\alpha\kappa)} \middle| \hat{G}_{\kappa}^{(\alpha)} \middle| \varphi_{l}^{(\alpha,\kappa)} \right\rangle, \tag{2.65}$$

where $\hat{G}_{\kappa}^{(\alpha)}$ is a Hermitian gauge operator with energy units, which can be chosen arbitrarily. The most common choice is to set $\hat{G}_{\kappa}^{(\alpha)}=0$ for all modes. It is immediate to verify that the gauge condition of equation (2.65) guarantees that the orthonormality condition $\langle \varphi_{j}^{(\alpha,\kappa)} | \varphi_{l}^{(\alpha,\kappa)} \rangle = \delta_{jl}$ is conserved over time.

Equations of motion

In order to solve the time-dependent Schrödinger equation using the ansatz of equation (2.61), we need to find the equations of motion for the coefficient tensor **B** and the SPFs $\varphi_j^{(\kappa)}(q_{\kappa},t)$ (or, equivalently, the coefficients $C_{jm}^{(\alpha,\kappa)}(t)$). The best convergence towards the exact result is obtained by using the time-dependent variational principle, introduced in section 2.4.1.

In order to apply equation (2.48), we need to identify the partial derivatives of the wavefunction ansatz with respect to the variational parameters. The derivatives with respect to the $B_i^{(\alpha)}$ coefficients give trivially the respective configurations,

$$\frac{\partial |\Psi, t\rangle}{\partial B_{\mathbf{i}}^{(\alpha)}} = |\alpha\rangle \Phi_{\mathbf{j}}(\mathbf{q}, t). \tag{2.66}$$

The partial functional derivative with respect to a SPF of a given mode gives the single-hole functions,

$$\frac{\delta|\Psi,t\rangle}{\delta\varphi_l^{(\alpha,\kappa)}} = |\alpha\rangle \widetilde{\Phi}_l^{(\alpha,\kappa)}(q_1,...,q_{\kappa-1},q_{\kappa+1},...,q_f,t). \tag{2.67}$$

The comparison with equation (2.61) shows that the single particle functions are defined as

$$\widetilde{\Phi}_{l}^{(\alpha,\kappa)}(q_{1},...,q_{\kappa-1},q_{\kappa+1},...,q_{f},t)
= \sum_{j_{1}=1}^{n_{1}^{(\alpha)}} \cdots \sum_{j_{\kappa-1}=1}^{n_{\kappa-1}^{(\alpha)}} \sum_{j_{\kappa+1}=1}^{n_{\kappa+1}^{(\alpha)}} \cdots \sum_{j_{f}=1}^{n_{f}^{(\alpha)}} B_{j_{1}...j_{\kappa-1}lj_{\kappa+1}..j_{f}}^{(\alpha)}(t)
\times \varphi_{j_{1}}^{(\alpha,1)}(q_{1},t) \cdots \varphi_{j_{\kappa-1}}^{(\alpha,\kappa-1)}(q_{\kappa-1},t) \varphi_{j_{\kappa+1}}^{(\alpha,\kappa+1)}(q_{\kappa+1},t) \cdots \varphi_{j_{f}}^{(\alpha,f)}(q_{f},t).$$
(2.68)

Note that, as the name says, they are functions of f-1 coordinates.

At this stage, the TDVP gives a clear strategy to find the equations of motion: evaluate the formal (approximate) time derivative of the MCTDH ansatz as,

$$|\dot{\Psi}\rangle_{\rm approx} = \sum_{\alpha=1}^{N_{\rm S}} |\alpha\rangle\dot{\chi}_{\alpha}(\mathbf{q}, t),$$
 (2.69)

with

$$\dot{\chi}_{\alpha}(\mathbf{q},t) = \sum_{\mathbf{j}} \dot{B}_{\mathbf{j}}^{(\alpha)} \Phi_{\mathbf{j}}^{(\alpha)} + \sum_{\kappa=1}^{f} \sum_{j=1}^{n_{\kappa}^{(\alpha)}} \dot{\phi}_{j}^{(\alpha,\kappa)}(q_{\kappa},t) \widetilde{\Phi}_{l}^{(\alpha,\kappa)}(q_{1},...,q_{\kappa-1},q_{\kappa+1},...,q_{f},t),$$
 (2.70)

set up equation (2.48) as

$$\left\langle \Phi_{\mathbf{j}}^{(\alpha)} \middle| \dot{\chi}_{\alpha} + \frac{\mathrm{i}}{\hbar} \sum_{\beta} \hat{H}_{\alpha\beta} \chi_{\beta}(t) \right\rangle,$$
 (2.71a)

$$\left\langle \widetilde{\Phi}_{j}^{(\alpha,\kappa)} \middle| \dot{\chi}_{\alpha} + \frac{\mathrm{i}}{\hbar} \sum_{\beta} \hat{H}_{\alpha\beta} \chi_{\beta}(t) \right\rangle,$$
 (2.71b)

and carry out all the algebra. The full derivation can be found in the Ref. [42]. Below, we simply report the final equations of motion for the multi-set formalism and the commonly used gauge condition $\left\langle \varphi_{j}^{(\alpha,\kappa)} \middle| \dot{\varphi}_{l}^{(\alpha,\kappa)} \right\rangle = 0$.

Replacing equation (2.70) into equation (2.71a) yields the differential equation for the **B** tensor,

$$\dot{B}_{\mathbf{j}}^{(\alpha)} = -\frac{\mathrm{i}}{\hbar} \sum_{\beta=1}^{N_{\mathrm{S}}} \sum_{\mathbf{l}} \left\langle \Phi_{\mathbf{j}}^{(\alpha)} \middle| \hat{H}_{\alpha\beta} \middle| \Phi_{\mathbf{l}}^{(\beta)} \right\rangle B_{\mathbf{l}}^{(\beta)}. \tag{2.72}$$

The equations of motion for the SPFs are found by replacing equations (2.70) and (2.72) into equation (2.71b). A somewhat tedious derivation [42] yields

$$\dot{\boldsymbol{\varphi}}_{j}^{(\alpha,\kappa)} = -\frac{\mathrm{i}}{\hbar} \left(1 - \hat{\boldsymbol{P}}^{(\alpha,\kappa)} \right) \sum_{\beta=1}^{N_{\mathrm{S}}} \sum_{l=1}^{n_{\kappa}^{(\beta)}} \left[\left(\boldsymbol{\rho}^{(\alpha,\kappa)} \right)^{-1} \hat{\mathbf{H}}^{(\alpha\beta,\kappa)} \right]_{jl} \boldsymbol{\varphi}_{l}^{(\beta,\kappa)}, \tag{2.73}$$

where

$$\hat{P}^{(\alpha,\kappa)} = \sum_{j=1}^{n_{\kappa}^{(\alpha)}} \left| \varphi_{j}^{(\alpha,\kappa)} \right\rangle \left\langle \varphi_{j}^{(\alpha,\kappa)} \right| \tag{2.74}$$

is the projector onto the space of the SPFs; the operator $1 - \hat{P}^{(\alpha,\kappa)}$ constrains the time variations of the SPFs to the space orthogonal to the current effective basis set.

 $\rho^{(\alpha,\kappa)}$ is the reduced *density matrix* for the mode κ and the electronic state α in the basis of the SPFs, and its matrix elements are formally given as overlaps between single-hole functions³

$$\rho_{jl}^{(\alpha,\kappa)} = \left\langle \widetilde{\mathbf{\Phi}}_{j}^{(\alpha,\kappa)} \middle| \widetilde{\mathbf{\Phi}}_{l}^{(\alpha,\kappa)} \right\rangle. \tag{2.75}$$

Finally $\hat{\mathbf{H}}^{(\alpha\beta,\kappa)}$ is the matrix of the mean fields,

$$\hat{H}_{jl}^{(\alpha\beta,\kappa)} = \left\langle \widetilde{\Phi}_{j}^{(\alpha,\kappa)} \middle| \hat{H}^{(\alpha\beta)} \middle| \widetilde{\Phi}_{l}^{(\alpha,\kappa)} \right\rangle. \tag{2.76}$$

Note that the integration is performed over f-1 degrees of freedom, therefore the mean fields are operators in the space of the κ -th mode.

In summary, equations (2.72) and (2.73) define the MCTDH algorithm. Some interesting features of this approach are worth noting:

- Both the evaluation of the mean fields and the Hamiltonian matrix $\left\langle \Phi_{\mathbf{j}}^{(\alpha)} \middle| \hat{H}^{(\alpha\beta)} \middle| \Phi_{\mathbf{l}}^{(\beta)} \right\rangle$ from equation (2.72) requires multi-dimensional integrations. For problems with a large number of modes, such integrations would be impossible without the use of a SOP form for the Hamiltonian, as for the standard method. This is one of the limitations of the MCTDH method, in addition to the general problem that the whole potential energy surfaces need to be known before performing the quantum dynamical simulation⁴. On the other hand, for Hamiltonians in SOP form, the integrations can be conveniently carried out using a sequence of matricisation-multiplication-tensorisation akin to that of equation (2.60). The difference is that the "small" \mathbf{H} matrices are built in the basis of the SPFs and not in the primitive basis.
- The general theory of the time-dependent variational principle (section 2.4.1) involves the inversion of a matrix \mathbf{M} , which has the same size as the number of variational parameters, which can be huge for the MCTDH ansatz. However, the special form of the wavefunction allows us to perform such matrix inversion partially analytically. The only numerical inversion left over in equation (2.71b) is that of the density matrices $\boldsymbol{\rho}^{(\alpha,\kappa)}$, which are however small $\left(n_{\kappa}^{(\alpha)} \times n_{\kappa}^{(\alpha)}\right)$, Hermitian and positive-defined, therefore relatively easy to invert.
- One of the advantages of MCTDH is that the equations of motion for the B coefficients and the SPFs are relatively weakly coupled. Indeed, it turns out that it is convenient for each time step to propagate the different sets of parameters separately, each time keeping the non-propagated parameters fixed. This is the idea behind the so-called constant mean field algorithm [49], which allows relatively large step sizes at a negligible loss of accuracy. For example, in equation (2.71a), the quantities $\left\langle \Phi_{\bf j}^{(\alpha)} | \hat{H}^{(\alpha\beta)} | \Phi_{\bf l}^{(\beta)} \right\rangle$ can be kept constant (only for a given step size!) while the B parameters are propagated; this makes the problem linear and allows the use of fast integrators such as the Lanczos scheme.
- One problem related to the inversion of $\rho^{(\alpha,\kappa)}$ is that some of its eigenvalues tend to vanish when some of B coefficients are small (this is typically the case at the beginning of the simulation), and the inverse $(\rho^{(\alpha,\kappa)})^{-1}$ becomes singular and makes the equations of motion numerically ill-conditioned. The workaround is to replace the density matrix with a regularised version. From time to time, different regularisation schemes are proposed in the literature [50],

 $^{^4}$ A workaround to avoid the need of a sum-of-product form for the potential is the *correlated DVR* scheme [U. Manthe, *J. Chem. Phys.* **105**, 6989 (1996)], which is however limited to maximum 15–20 degrees of freedom.

the most common approach being to replace the density matrix as $\rho^{(\alpha,\kappa)} \longrightarrow \rho^{(\alpha,\kappa)} + \varepsilon \exp(-\rho^{(\alpha,\kappa)}/\varepsilon)$, where ε is a small constant. This type of regularisation is generally useful in quantum dynamical approaches based on the TDVP, which often leads to equations of motion where possibly singular matrices need to be inverted.

• In its standard version, the MCTDH method is not "black-box". For example, the user needs to choose the primitive basis and the number of SPFs for each mode. Whether $n_{\kappa}^{(\alpha)}$ is large enough can be understood by diagonalizing the density matrices, which have unit trace. If the lowest of the eigenvalues of $\rho^{(\alpha,\kappa)}$ is smaller than a certain threshold $(10^{-2}-10^{-3}$ depending on the application) then the dimension of the SPF basis is deemed sufficient; if not, it has to be increased. To this end, it is worth mentioning that novel algorithms have been recently proposed to automate the construction of the MCTDH wavefunction on-the-fly [51].

Mode combination and multi-layer MCTDH

A powerful way to use the MCTDH machinery is to work in an intermediate representation between MCTDH and the standard method. The idea is that SPFs do not necessarily need to be one-dimensional. Instead, one can group the degrees of freedom into *combined modes* $\mathbf{q}_1 = (q_{1,1}, q_{1,2}, ...), \mathbf{q}_2 = (q_{2,1}, q_{2,2}, ...),$ etc., so that each combined mode is associated with a set of SPFs,

$$\chi_{\alpha}(\mathbf{q}_{1},...,\mathbf{q}_{f},t) = \sum_{j_{1}=1}^{n_{1}^{(\alpha)}} \cdots \sum_{j_{\ell}=1}^{n_{f}^{(\alpha)}} B_{j_{1}...j_{f}}^{(\alpha)}(t) \varphi_{j_{1}}^{(\alpha,1)}(\mathbf{q}_{1},t) \cdots \varphi_{j_{f}}^{(\alpha,f)}(\mathbf{q}_{f},t). \tag{2.77}$$

The SPFs, in turn, are expanded into a one- or multi-dimensional direct product basis. This form of MCTDH potentially provides a more compact representation compared to using one-dimensional functions directly. To see why, let us follow up on the previous example: we have 2 electronic states and 8 physical modes and primitive bases with 20 grid points. In the basic form of MCTDH, using 5 SPFs per mode, we would get $\approx 8 \cdot 10^5$ complex parameters (≈ 12 MB) to propagate in time. Combining the eight modes into 4 effective particles, and using still 10 SPFs per particle gives $2 \times \left(10^4 + 4 \times 10 \times 20^2\right) = 52000$ parameters (≈ 800 kB). It is clear that mode combination can be extremely helpful, especially when the effective particle combines modes that are strongly correlated between them (e.g., tuning and coupling modes at a conical intersection), but are weakly correlated with the remaining modes, allowing for a smaller number of SPFs to be used.

Note that the MCTDH equations of motion remain formally identical if combined modes are used. In this sense, equation (2.77) is the most general ansatz for the MCTDH wavefunction. A tensor tree illustrating the structure of an MCTDH wavefunction with mode combination is shown in figure 2.6c.

The use of combined modes suggests a further way to make the wavefunction more compact, reducing the number of variational parameters. Consider the SPFs of a two-dimensional mode for the single-set formalism $\varphi_i^{(\kappa)}(q_{\kappa,1}, q_{\kappa,2}, t)$. It is possible to

apply the MCTDH strategy to treat each SPF. To do so, they must be expanded into "level 2" SPFs,

$$\varphi_{j}^{(\kappa)}(q_{\kappa,1}, q_{\kappa,2}, t) = \sum_{l_{1}=1}^{n_{\kappa,1}} \sum_{l_{2}=1}^{n_{\kappa,2}} \widetilde{B}_{j,l_{1}l_{2}}^{(\kappa)}(t) \widetilde{\varphi}_{l_{1}}^{(\kappa,1)}(q_{\kappa,1}, t) \widetilde{\varphi}_{l_{2}}^{(\kappa,2)}(q_{\kappa,2}, t), \tag{2.78}$$

which are, in turn, represented on the primitive basis. The structure of the wavefunction can be represented compactly using the tree diagram of figure 2.6d. Such nested application of the MCTDH ansatz is denoted "2-layer MCTDH", and allows us to further decompose the B tensor in the same way we originally decomposed the A tensor (see equation (2.63)). This leads to a further reduction of the number of variational parameters and gives us the possibility to treat systems with higher dimensionality.

Indeed, for systems with dozens or even hundreds of modes, we can expand the MCTDH tree with further layers. This is the idea of multi-layer MCTDH (ML-MCTDH), a methodology that, together with few other approaches, represents the state-of-the-art for high-dimensional quantum wave packet simulations, and has allowed simulating quantum systems with 100–1000 modes. As an example, figure 2.7 shows a calculation performed on a stack of five tetrathiophene chains, which includes 13 electronics and 78 modes [52]. The equations of motion for ML-MCTDH were originally derived by Wang and Thoss [53] using the TDVP and, layer-by-layer, have the same form of the MCTDH equations (2.71a) and (2.71b).

The difficulty of using ML-MCTDH is that the user is left with the choice of the number of SPFs in each layer, which is more tedious than in standard MCTDH. Moreover, for high-dimensional systems, different structures of the tensor tree can lead to substantially different computational costs. Intense investigation is being carried out to find optimal and automated ways to construct ML-MCTDH trees [54].

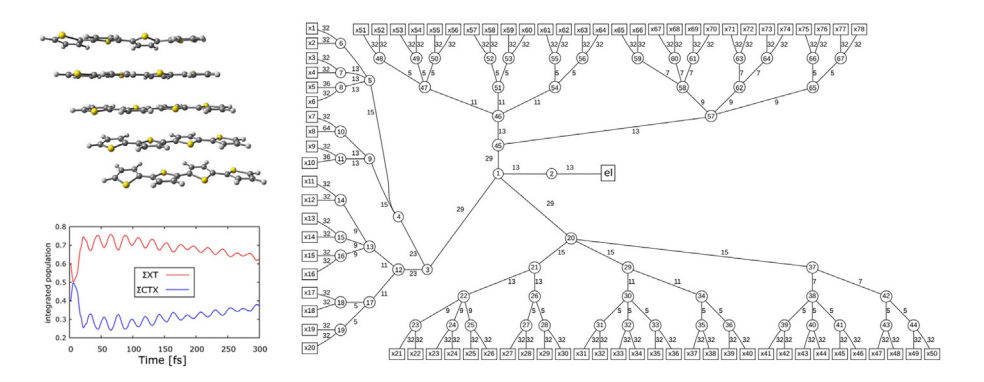


FIG. 2.7 — Multilayer MCTDH simulation of the coherent interplay between excitonic (XT) and charge-transfer (CT) states in an aggregate of polythiophene, taken from Ref. [51]. The calculation is performed using a linear vibronic coupling model that includes 13 electronic states (5 XT and 8 CT states) and 78 vibrational modes. The tensor tree used to construct the wavefunction is shown in the right panel. The simulated populations of the XT and CT states are shown in the lower left panel.

2.4.4 An Alternative Tensor Decomposition: Tensor Trains

Let us suppose that we want to study the dynamics of a polymeric chain of chromophores, with nearest-neighbor interaction, accounting for one quantum coordinate for each chromophore. A physically and computationally reasonable way is to order the modes in a chain-like fashion and correlate the neighboring modes explicitly. A wavefunction ansatz that corresponds to this structure is

$$\chi_{\alpha}(q_{1},...,q_{f},t) = \sum_{j_{1}=1}^{n_{1}^{(\alpha)}} \cdots \sum_{j_{f-1}=1}^{n_{f-1}^{(\alpha)}} \varphi_{j_{1}}^{(\alpha,1)}(q_{1},t) \varphi_{j_{1}j_{2}}^{(\alpha,2)}(q_{2},t) \varphi_{j_{2}j_{3}}^{(\alpha,3)}(q_{3},t) \\
\cdots \varphi_{j_{f-2}j_{f-1}}^{(\alpha,f-1)}(q_{f-1},t) \varphi_{j_{f-1}}^{(\alpha,f)}(q_{f-1},t),$$
(2.79)

where the single-particle functions are represented in the primitive basis,

$$\varphi_{jj'}^{(\alpha,\kappa)}(q_{\kappa},t) = \sum_{m=1}^{N_{\kappa}} C_{jj'm}^{(\alpha,\kappa)}(t) \psi_m(q_{\kappa}). \tag{2.80}$$

The comparison with equation (2.56) shows that the ansatz of equation (2.79) defines the following tensor decomposition

$$A_{m_1...m_f}^{(\alpha)}(t) \approx \sum_{j_1=1}^{n_1^{(\alpha)}} \cdots \sum_{j_{f-1}=1}^{n_{f-1}^{(\alpha)}} C_{j_1 m_1}^{(\alpha,1)}(t) C_{j_1 j_2 m_2}^{(\alpha,2)}(t) C_{j_2 j_3 m_3}^{(\alpha,3)}(t) \cdots C_{j_{f-1} m_f}^{(\alpha,f)}(t), \qquad (2.81)$$

which is denoted as tensor train or matrix product states [55]. In theoretical physics, tensor trains underlie the techniques introduced to renormalize the reduced density matrix of a single site in a one-dimensional lattice [56]. Therefore, in the literature, methods based on tensor trains are also referred to as density matrix renormalization group (DMRG) techniques.

Despite having a structure closely related to a one-dimensional lattice, upon increasing the value of the so-called bond order $n_{\kappa}^{(\alpha)}$ the tensor train decomposition can be made exact. Indeed, this approach has been successfully applied to model the excitonic dynamics in multichromophoric systems that do not have a chain structure [57, 58], converging to essentially the same results obtained using multilayer MCTDH [58].

In terms of computational resources, it is easy to see that the tensor train ansatz eliminates the exponential scaling. For a system with $N_{\rm S}$ electronic states, f degrees of freedom, a bond order of n and a primitive N-dimensional basis, we have $N_{\rm S} \times (2nN + (f-1)n^2N)$ variational parameters, *i.e.*, a linear dependence on the number of modes.

Before presenting the equations of motion, it needs to be pointed out that, similar to the MCTDH ansatz, the decomposition of equation (2.79) is not unique, therefore, there is a gauge freedom. Indeed, it is easy to see that unitary transformations of the form

$$\widetilde{\varphi}_{j_{\kappa-1}j_{\kappa}}^{(\alpha,\kappa)} = \sum_{l=1}^{n_{\kappa}^{(\alpha)}} \varphi_{j_{\kappa-1}l}^{(\alpha,\kappa)} U_{lj_{\kappa}}$$

$$\widetilde{\varphi}_{j_{\kappa}j_{\kappa+1}}^{(\alpha,\kappa+1)} = \sum_{l=1}^{n_{\kappa}^{(\alpha)}} \varphi_{lj_{\kappa+1}}^{(\alpha,\kappa+1)} U_{lj_{\kappa}}^{*}$$
(2.82)

leaves the wavefunction invariant. One way to fix the gauge is to adopt the so-called *left-canonical form*, enforcing (for $\kappa < f$) the condition

$$\sum_{j=1}^{n_{\kappa-1}^{(\alpha)}} \left\langle \varphi_{jl}^{(\alpha,\kappa)} \middle| \frac{\partial \varphi_{jl'}^{(\alpha,\kappa)}}{\partial t} \right\rangle = 0, \tag{2.83}$$

which guarantees the conservation of the left-orthogonality $\sum_{j} \left\langle \phi_{jl}^{(\alpha,\kappa)} \middle| \phi_{jl'}^{(\alpha,\kappa)} \right\rangle = \delta_{ll'}$.

Once the gauge is fixed, one can derive the equations of motion for the tensor-train ansatz. We do not report the full derivation, but just set up the problem and report the final equations of motion. The variations are performed with respect to the SPFs $\varphi_{jj'}^{(\alpha,\kappa)}$ (or, equivalently, their expansion coefficients). Using equation (2.79), the approximate time derivative of the molecular wavefunction is readily evaluated as

$$\begin{aligned} |\dot{\Psi}\rangle_{\text{approx}} &= \sum_{\alpha=1}^{N_{S}} |\alpha\rangle \dot{\chi}_{\alpha}(\mathbf{q}, t), \\ \dot{\chi}_{\alpha}(\mathbf{q}, t) &= \sum_{\kappa=1}^{f} \sum_{j=1}^{n_{\kappa-1}^{(\alpha)}} \sum_{j'=1}^{n_{\kappa}^{(\alpha)}} L_{j}^{(\alpha, \kappa)}(q_{1}, ..., q_{\kappa-1}, t) \dot{\varphi}_{jj'}^{(\alpha, \kappa)}(q_{\kappa}, t) R_{j'}^{(\alpha, \kappa)}(q_{\kappa+1}, ..., q_{f}, t), \end{aligned}$$
(2.84)

where $L_{j}^{(\alpha,\kappa)}$ and $R_{j'}^{(\alpha,\kappa)}$ are the left and right components of the *single-hole function* complementary to the SPF $\varphi_{jj'}^{(\alpha,\kappa)}$. Due to the gauge condition of equation (2.83), the left components are orthonormal, $\left\langle L_{j}^{(\alpha,\kappa)} \left| L_{j'}^{(\alpha,\kappa)} \right\rangle = \delta_{jj'}$, whereas the right components are not,

$$\left\langle R_j^{(\alpha,\kappa)} \middle| R_{j'}^{(\alpha,\kappa)} \right\rangle = S_{jj'}^{(\alpha,\kappa)}.$$
 (2.85)

Using the time-dependent variational principle, the variations with respect to the SPFs lead to the system of equations

$$\left\langle L_{j}^{(\alpha,\kappa)} R_{j'}^{(\alpha,\kappa)} \middle| \dot{\Psi}_{\text{approx}} + \frac{i}{\hbar} \hat{H} \Psi \right\rangle = 0. \tag{2.86}$$

The solution of these equations is rather tedious. The final equations of motion have the form [59, 60]

$$\frac{\partial \varphi_j^{(\alpha,f)}}{\partial t} = -\frac{\mathrm{i}}{\hbar} \sum_{R=1}^{N_{\mathrm{S}}} \sum_{l=1}^{n_{f-1}^{(\alpha)}} \left\langle L_j^{(\alpha,f)} \middle| \hat{H}^{(\alpha\beta)} \middle| L_l^{(\beta,f)} \right\rangle \varphi_l^{(\beta,f)},\tag{2.87}$$

$$\frac{\partial \varphi_{jj'}^{(\alpha,\kappa)}}{\partial t} = -\frac{\mathrm{i}}{\hbar} \sum_{\beta=1}^{N_{\mathrm{S}}} \sum_{l,l',l'',l'''} \left(\delta_{jl} - \hat{P}_{jl}\right) \left[\mathbf{S}^{(\alpha,\kappa)}^{(\alpha,\kappa)}\right]_{j'l'} \left\langle L_{l}^{(\alpha,\kappa)} R_{l'}^{(\alpha,\kappa)} \middle| \hat{H}^{(\alpha\beta)} \middle| L_{l''}^{(\beta,\kappa)} R_{l'''}^{(\beta,\kappa)} \right\rangle \varphi_{l''l'''}^{(\beta,\kappa)}$$

$$(2.88)$$

which, similar to the MCTDH equations (2.71b), contain mean fields operators, and "projector-like" operators

$$\hat{P}_{jl}^{(\alpha,\kappa)} = \sum_{i=1}^{n_{\kappa}^{(\alpha)}} \left| \varphi_{ji}^{(\alpha,\kappa)} \right\rangle \left\langle \varphi_{jl}^{(\alpha,\kappa)} \right|. \tag{2.89}$$

All the integrals can be evaluated using the matricisation/tensorization procedures introduced before. Note that the equations of motion involve the inverse of the overlap matrix between the right components of the single-hole functions. Alternative so-called "sweeping algorithms", based on the *mixed-canonical form* of the tensor-train ansatz (instead of the left-canonical form used here), avoid the need of forming and inverting the **S** matrices [60].

This means that the tensor-train method, or time-dependent DMRG, does not eliminate the need to construct the Hamiltonian operator into a sum-of-products form. Despite that, this method has the potential to overcome the exponential dependence on the number of degrees of freedom, which multilayer MCTDH mitigates but not eliminates completely.

In the context of molecular photophysics, tensor trains are relatively recent techniques and have been mostly applied to Frenkel exciton or linear vibronic coupling models of supramolecular assemblies. However, their use is rapidly increasing, and applications to more sophisticated model Hamiltonians, along with more efficient codes, are expected in the coming years.

2.4.5 Towards Direct Dynamics: Variational Multi-Configurational Gaussian Wave Packets

The standard method introduced in section 2.4.2 involves the definition of direct product multi-dimensional grids to represent the wavefunction. When the number of coordinates becomes large, not only does the size of these grids grow exponentially, but we get a larger and larger number of grid points which are inaccessible, simply because the potential at these points is too high.

Indeed, in many problems in photochemistry and photophysics, the wave packets explore a rather limited region of the coordinate space. In 1975, Heller used this fact to introduce moving Gaussian wave packets (GWPs) as a basis to perform quantum dynamical simulations [61]. In his formulation, the center of the GWPs follows classical Hamiltonian trajectories, whereas the Gaussian width accounts for quantum uncertainty. Alternatively, a full quantum mechanical prescription can be adopted, determining the wave packet dynamics according to the TDVP. This gives rise to the so-called variational multiconfigurational Gaussian (vMCG) approach [62], which is a special case of a more general method (see below), first introduced by Burghardt, Meyer, and Cederbaum [63]. Classically moving GWPs are described in section 2.5.

In the vMCG method, the ansatz for the wavefunction is

$$\chi_{\alpha}(\mathbf{q},t) = \sum_{j=1}^{N^{(\alpha)}} B_j^{(\alpha)} G_j^{(\alpha)} \Big(\mathbf{q}; \mathbf{\Delta}, \boldsymbol{\xi}_j^{(\alpha)}(t), \boldsymbol{\eta}_j^{(\alpha)}(t) \Big), \tag{2.90}$$

where G_i is a multi-dimensional Gaussian wave packet,

$$G_{j}^{(\alpha)}\left(\mathbf{q};\boldsymbol{\Lambda},\boldsymbol{\xi}_{j}^{(\alpha)}(t),\boldsymbol{\eta}_{j}^{(\alpha)}(t)\right) = \exp\left[\sum_{\kappa=1}^{f} \left(-\frac{q_{\kappa}^{2}}{2\Delta_{\kappa}^{2}} + \boldsymbol{\xi}_{j,\kappa}^{(\alpha)}(t)q_{\kappa}\right) + \boldsymbol{\eta}_{j}^{(\alpha)}(t)\right]. \tag{2.91}$$

The parameters defining the GWPs are:

- The width matrix Δ , here taken as real, diagonal, independent of the specific GWP, and kept *frozen* as a function of time. In a more general approach (but computationally unfavourable), the Gaussian widths are allowed to change in time; in this case, the GWPs are denoted as *thawed Gaussians*.
- The time-dependent $\boldsymbol{\xi}_{j}^{(\alpha)}$ vectors, which are f-dimensional and contain complex parameters, related to the expectation values of the positions $\bar{\mathbf{q}}_{j}^{(\alpha)}$ and momenta $\bar{\mathbf{p}}_{j}^{(\alpha)}$ of the GWP as

$$\bar{\mathbf{q}}_{j}^{(\alpha)} = \mathbf{\Lambda}^{2} \operatorname{Re} \left(\mathbf{\xi}_{j}^{(\alpha)} \right), \tag{2.92a}$$

$$\bar{\mathbf{p}}_{j}^{(\alpha)} = \hbar \operatorname{Im}\left(\boldsymbol{\xi}_{j}^{(\alpha)}\right). \tag{2.92b}$$

The parameters $\xi_{j,\kappa}^{(\alpha)}$ are propagated in time according to equations derived from the TDVP.

• The phases $\eta_j^{(\alpha)}(t)$, which are also time-dependent, but redundant with the coefficients $B_j(t)$. Due to this redundancy, in typical implementations, these parameters are kept real and propagated in such a way as to guarantee that the GPWs remain normalized.

GWPs provide a compact way to represent a high-dimensional wavefunction, because the only quantities that effectively need to be propagated in time are the $\xi_j^{(\alpha)}$ vectors, which contain f complex parameters, and the coefficient $B_j^{(\alpha)}$. For a problem with $N_{\rm S}$ electronic states, N GWPs per state and f modes, the vMCG wavefunction is constructed from $N_{\rm S}N(f+1)$ parameters, therefore, the exponential scaling is overcome. The vMCG method is also at the core of the so-called Davydov ansätze, typically used for dynamics driven by Frenkel exciton Hamiltonians [64].

The steps to derive the equations of motion for the parameters B and ξ are the same as in the previous section. As before, we only set up the problem and report the final result; the full derivation can be found in the references [62].

The approximate time derivative of the molecular wave function is given, for the vMCG ansatz, as

$$\begin{aligned} |\dot{\Psi}\rangle_{\text{approx}} &= \sum_{\alpha=1}^{N_{\text{S}}} |\alpha\rangle \dot{\chi}_{\alpha}(\mathbf{q}, t) \\ &= \sum_{\alpha=1}^{N_{\text{S}}} \sum_{j=1}^{N^{(\alpha)}} \left(\dot{B}_{j}^{(\alpha)} G_{j}^{(\alpha)}(\mathbf{q}, t) + B_{j}^{(\alpha)} \dot{G}_{j}^{(\alpha)}(\mathbf{q}, t) \right) \\ &= \sum_{\alpha=1}^{N_{\text{S}}} \sum_{j=1}^{N^{(\alpha)}} \left(\left(\dot{B}_{j}^{(\alpha)} + \dot{\eta}_{j}^{(\alpha)} \right) G_{j}^{(\alpha)}(\mathbf{q}, t) + B_{j}^{(\alpha)} \sum_{\kappa=1}^{f} \frac{\partial G_{j}^{(\alpha)}}{\partial \xi_{j,\kappa}^{(\alpha)}} \right). \end{aligned}$$
(2.93)

As stated above, and clear from the equation, the parameter $\eta_j^{(\alpha)}$ is redundant with $B_j^{(\alpha)}$ and therefore is simply kept real and propagated, so as to keep the GWPs normalized.

Applying the TDVP to the variations with respect to $B_j^{(\alpha)}$ and $\xi_{j,\kappa}^{(\alpha)}$ gives the equations

$$\left\langle G_j^{(\alpha)} \middle| \dot{\Psi}_{\text{approx}} + \frac{\mathrm{i}}{\hbar} \hat{H} \Psi \right\rangle = 0,$$
 (2.94a)

$$\left\langle \frac{\partial G_j^{(\alpha)}}{\partial \xi_{j,\kappa}^{(\alpha)}} \middle| \dot{\Psi}_{approx} + \frac{i}{\hbar} \hat{H} \Psi \right\rangle = 0.$$
 (2.94b)

Replacing equations (2.90) and (2.93) into equation (2.94a), the equations of motion for the GWP coefficients are obtained,

$$\mathbf{S}^{(\alpha)} \frac{\partial \mathbf{B}^{(\alpha)}}{\partial t} = -\frac{\mathrm{i}}{\hbar} \sum_{\beta=1}^{N_{\mathrm{S}}} \left(\mathbf{H}^{(\alpha\beta)} - \mathrm{i}\hbar \delta_{\alpha\beta} \mathbf{\tau}^{(\alpha)} \right) \mathbf{B}^{(\beta)}, \tag{2.95}$$

where **B** is the (column) vector of the coefficients, and the matrices $\mathbf{S}^{(\alpha)}$, $\mathbf{H}^{(\alpha\beta)}$ and $\mathbf{\tau}^{(\alpha)}$ are evaluated as

$$S_{jl}^{(\alpha)} = \left\langle G_j^{(\alpha)} \middle| G_l^{(\alpha)} \right\rangle, \tag{2.96a}$$

$$H_{jl}^{(\alpha\beta)} = \left\langle G_j^{(\alpha)} \middle| \hat{H}^{(\alpha\beta)} \middle| G_l^{(\beta)} \right\rangle, \tag{2.96b}$$

$$\tau_{jl}^{(\alpha)} = \left\langle \left. G_j^{(\alpha)} \right| \dot{G}_l^{(\alpha)} \right\rangle. \tag{2.96c}$$

The equations of motion for the GWPs centers are obtained, after some algebra, by replacing equations (2.90), (2.93) and (2.95) into equation (2.94b). Defining the vectors $\boldsymbol{\xi}^{(\alpha)} = \left(\boldsymbol{\xi}_1^{(\alpha)}, \boldsymbol{\xi}_2^{(\alpha)}, \ldots\right)$, one obtains the following expression

$$\mathbf{C}^{(\alpha)} \frac{\partial \boldsymbol{\xi}^{(\alpha)}}{\partial t} = \mathbf{Y}^{(\alpha)}, \tag{2.97}$$

where the matrix $\mathbf{C}^{(\alpha)}$ and the vector $\mathbf{Y}^{(\alpha)}$ are defined as

$$C_{j\kappa,l\mu}^{(\alpha)} = \left\langle \frac{\partial G_{j}^{(\alpha)}}{\partial \xi_{j,\kappa}^{(\alpha)}} \middle| 1 - \hat{P}^{(\alpha)} \middle| \frac{\partial G_{l}^{(\alpha)}}{\partial \xi_{l,\mu}^{(\alpha)}} \right\rangle B_{j}^{(\alpha)*} B_{l}^{(\alpha)}, \tag{2.98a}$$

$$Y_{j\kappa}^{(\alpha)} = -\frac{\mathrm{i}}{\hbar} \sum_{\beta=1}^{N_{\mathrm{S}}} \sum_{l=1}^{N(\beta)} \left\langle \frac{\partial G_{j}^{(\alpha)}}{\partial \xi_{j,\kappa}^{(\alpha)}} \middle| \left(1 - \hat{P}^{(\alpha)} \right) \hat{H}^{(\alpha\beta)} \middle| G_{l}^{(\beta)} \right\rangle B_{j}^{(\alpha)*} B_{l}^{(\beta)}, \tag{2.98b}$$

and the projector on in the basis of GWPs is defined as

$$\hat{P}^{(\alpha)} = \sum_{i,l=1}^{N^{(\alpha)}} \left| G_j^{(\alpha)} \right\rangle \left[\left(\mathbf{S}^{(\alpha)} \right)^{-1} \right]_{il} \left\langle G_l^{(\alpha)} \right| \tag{2.99}$$

Now that we have the equations of motion for the vMCG ansatz, a few facts are worth noting:

- One of the advantages of the vMCG method is that it is almost "black-box":
 only the number of GWPs for each electronic state needs to be chosen by the
 user. In particular, one does not need to define a primitive basis: the Gaussians
 move where the dynamics brings them, without the need for an underlying
 coordinate grid.
- In principle, the dynamics can be converged to the exact solution of the time-dependent Schrödinger equation upon increasing the number of GWPs. However, in complex molecular problems, e.g., dynamics at conical intersections, the more flexible MCTDH ansatz of section 2.4.3 typically converges much faster. Nevertheless, the vMCG approach usually provides a solution that is accurate enough for comparisons with experiments, fully accounting for quantum effects in the nuclear motion [60].
- The expression for the $\mathbf{C}^{(\alpha)}$ matrix, equation (2.98a), seems complicated, but its evaluation is in practice fast, because it is based on the analytic formulas for Gaussian moments.
 - Equations (2.95) and (2.98b) are also relatively easy to evaluate, provided that the matrix elements of the Hamiltonian operator between Gaussians (or Gaussian derivatives) are analytic. Fortunately, many analytic expressions for Gaussian integrals are available. Note that for the vMCG method, there is no computational necessity for the SOP form for the potentials. For example, a potential energy surface given as a sum of Gaussians is not necessarily in SOP form, but the integrals required for the vMCG equations are still analytic.
- One way to simplify the evaluation of Hamiltonian integrals is to exploit the fact that the GWPs are relatively well localized in space; therefore, for potential terms, one does not need to know the full surface, but only a local

approximation in the vicinity of the GWPs. For example, one can use a local harmonic approximation (LHA)

$$\langle G_j | V(\mathbf{q}) | G_l \rangle \approx \left\langle G_j \middle| V_{jl} + \mathbf{g}_{jl}^T \cdot \left(\mathbf{q} - \overline{\mathbf{q}}_{jl} \right) + \frac{1}{2} \left(\mathbf{q} - \overline{\mathbf{q}}_{jl} \right)^T \mathbf{M}_{jl} \left(\mathbf{q} - \overline{\mathbf{q}}_{jl} \right) \middle| G_l \right\rangle, \quad (2.100)$$

where the energy V_{jl} , gradient \mathbf{g}_{jl} and force constants \mathbf{M}_{jl} are evaluated at some intermediate points $\overline{\mathbf{q}}_{il}$ between the positions of the Gaussians G_i and G_l .

Note that the LHA eliminates the need to know the whole potential energy surface in advance, therefore, the vMCG method has the appealing feature of being usable on-the-fly, *i.e.*, computing the potential energy surface during the wave packet evolution [62]. However, the LHA leads to the formal breakdown of the conservation of energy, a fundamental property that should be carefully checked during the simulation.

• Finally, we come to the main drawbacks of the vMCG method. Solving for the time derivatives in the equations (2.95) and (2.97) involve inverting the matrices $\mathbf{S}^{(\alpha)}$ and $\mathbf{C}^{(\alpha)}$. This leads to two types of complications. First, the $\mathbf{C}^{(\alpha)}$ matrix can get large for high-dimensional problems: for 20 degrees of freedom and 50 GWPs, we get a 1000×1000 matrix to invert. Formally, one does not need to compute the inverse, but any method to solve the linear system of equation (2.97) scales anyhow as the third power of the size of $\mathbf{C}^{(\alpha)}$; moreover, similar to the ρ matrices in MCTDH, this matrix might become singular when the coefficients of some Gaussians are small, and the propagation of the Gaussian parameters becomes ill-conditioned.

The second problem occurs when two GWPs approach each other during the dynamics. In this case, it is the overlap matrix $\mathbf{S}^{(\alpha)}$ to become singular, and this makes both equations (2.95) and (2.97) are ill-conditioned.

Over the past decades, various techniques have been developed to regularize the equations of motion [65, 66]. However, experience shows that a universal solution to ensure numerically stable vMCG propagation for systems with more than a few dozen modes has yet to be found.

Combining MCTDH with Gaussian wave packets: The G-MCTDH scheme

In many problems of molecular photochemistry and photophysics, it is possible to identify a small set of *primary modes* that undergo a rather complex dynamics, whereas the remaining intra- or inter-molecular motions (*secondary modes*) behave as a nearly harmonic bath. Examples of primary modes could be the dominant reaction coordinates in a photochemical process, or the tuning and coupling modes in a conical intersection.

A practical option to model these types of problems quantum mechanically is to adopt an MCTDH description combining flexible SPFs for the primary modes and GWPs for the secondary modes. This gives rise to the hybrid Gaussian/MCTDH (G-MCTDH) ansatz [63],

$$\chi_{\alpha}(\mathbf{q},t) = \sum_{\mathbf{j}} B_{\mathbf{j}}^{(\alpha)} \prod_{\kappa=1}^{p} \varphi_{j_{\kappa}}^{(\alpha,\kappa)}(\mathbf{q}_{\kappa},t) \prod_{\kappa=p+1}^{f} G_{j_{\kappa}}^{(\alpha,\kappa)} \left(\mathbf{q}_{\kappa}, \boldsymbol{\xi}_{j_{\kappa}}^{(\alpha,\kappa)}(t)\right). \tag{2.101}$$

In this approach, the dynamics along the first p combined modes \mathbf{q}_{κ} , which are associated with the primary modes, is described by fully flexible SPFs. The less complex motion of the secondary modes is represented by variational Gaussian wave packets. Both the MCTDH and the vMCG methods can be viewed as limiting cases of G-MCTDH.

The equations of motion for the G-MCTDH ansatz can be found in the Refs. [67] and [68]. Briefly, the equations for the coefficients and the standard SPFs are the same as in conventional MCTDH, see equations (2.71a) and (2.71b); those for the Gaussian parameters resemble those of the vMCG ansatz, see equation (2.97).

In the cases where the bath behaves nearly classically, the G-MCTDH method requires a low number of GWPs, therefore, it is competitive with the most sophisticated multilayer-MCTDH scheme. This is especially true when the bath modes are strongly correlated: using tensor networks, one might need a large number of SPFs to capture the correlation; in contrast, Gaussian wave packets can describe a high-dimensional combined mode, thus describing the inter-mode correlation in a good effective way [68].

2.5 Numerical Methods: Quantum-Classical Approximations

2.5.1 Gaussian Wave Packets Moving Classically

As discussed in section 2.4.5, Gaussian wave packets are a convenient way to account for nuclear quantum effects using a compact wavefunction ansatz. However, the rigorous application of the vMCG scheme has three main drawbacks: (i) to be accurate in the evaluation of the Hamiltonian matrix elements, the potential energy surfaces need to be precalculated; (ii) the Gaussian positions and momenta, embedded in the $\boldsymbol{\xi}_j^{(\alpha)}$ vector [see equations (2.92a) and (2.92b)], follow non-classical trajectories that require a potentially large matrix inversion to be computed; (iii) the overlap matrix $\mathbf{S}^{(\alpha)}$, defined in equation (2.96a), becomes singular when two GWPs approach each other, making the numerical propagation ill-conditioned.

There is a simple way to solve these three problems in one shot: let the GWPs follow classical trajectories! To this end, it is convenient to express the GWP in such a way that the position and momenta are explicit,

$$G_{j}^{(\alpha)}(\mathbf{q},t) = \left(\frac{1}{\pi\Delta^{2}}\right)^{\frac{1}{4}} \exp\left[-\sum_{\kappa=1}^{f} \left(-\frac{\left(q_{\kappa} - \bar{q}_{j,\kappa}^{(\alpha)}(t)\right)^{2}}{\Delta^{2}} + \frac{\mathrm{i}}{\hbar} \bar{p}_{j,\kappa}^{(\alpha)}(t)\left(q_{\kappa} - \bar{q}_{j,\kappa}^{(\alpha)}\right)\right)\right],$$
(2.102)

and follow classical Hamilton trajectories,

$$\frac{\partial \bar{q}_{j,\kappa}^{(\alpha)}}{\partial t} = \frac{\partial H^{(\alpha\alpha)}(\mathbf{q}, \mathbf{p})}{\partial \bar{p}_{j,\kappa}^{(\alpha)}},$$
(2.103a)

$$\frac{\partial \bar{p}_{j,\kappa}^{(\alpha)}}{\partial t} = -\frac{\partial H^{(\alpha\alpha)}(\mathbf{q}, \mathbf{p})}{\partial \bar{q}_{j,\kappa}^{(\alpha)}},$$
(2.103b)

where $H^{(\alpha\alpha)} = T(\mathbf{p}) + V_{\alpha}(\mathbf{q})$ is the classical Hamiltonian associated with the adiabatic potential energy surface α . The choice of the adiabatic representation allows us to compute energies and forces on the fly using quantum chemistry codes. This is not possible in the diabatic picture, unless we have a strategy to construct the diabatic states from single-point electronic structure data. Moreover, many algorithms developed for classically moving GWPs rely on the adiabatic representation. In many works, classically moving GWPs are also denoted as trajectory basis functions (TBFs) [69].

Classical trajectories solve the problems mentioned above: (i) they can be calculated using single points gradients, therefore the entire PES is not needed; (ii) no matrix inversion is required to compute the trajectories; (iii) two TBFs initially located at different positions and momenta will never overlap perfectly (Liouville's theorem), therefore the $\mathbf{S}^{(\alpha)}$ matrix is never singular.

It is possible to apply the time-dependent variational principle to the multi-configurational Gaussian ansatz of equation (2.90), assuming that the GWPs move along predefined classical trajectories. The equations of motion for the coefficients have the same form as equation (2.95), with the only difference that the $\tau^{(\alpha)}$ matrix is evaluated using the classical derivatives $\dot{G}_j^{(\alpha)}$ instead of the quantum mechanical ones. The Hamiltonian matrix elements $\left\langle \left. G_j^{(\alpha)} \right| \hat{H}^{(\alpha\beta)} \right| \left. G_l^{(\beta)} \right\rangle$ can be evaluated either exactly, if the global PESs are available, or using the local harmonic – or even linear or zeroth-order – approximation.

Another formalism to introduce quantum mechanical coupling between classically moving Gaussians is based on the properties of the *coherent states*, and it is the basis for the *coupled coherent states* method developed by Child and Shalashilin [70]. In principle, this approach converges to the exact quantum mechanical result upon increasing the number of Gaussians. Of course, the convergence is slower as compared to the vMCG method, where the GWP trajectories are variationally optimized. However, one gains a significant speedup in the propagation (different Gaussians can be propagated in parallel), and for many observables, the accuracy is good enough.

2.5.2 Spawning Techniques for Trajectory Basis Functions

The use of trajectory basis functions allows us to eliminate many of the numerical difficulties of the vMCG method. One issue that is left is how to make the method

fully "black box" so that the user does not need to choose the number of TBFs in advance. This problem has been addressed by Martínez and coworkers [71, 72], who introduced a spawning algorithm to increase the number of TBFs when needed. This has been combined with different levels of approximation.

In the *full multiple spawning* method, the molecular wavefunction is set up in the adiabatic representation as a superposition of wave packets, each given as a linear combination of TBFs,

$$\Psi(\mathbf{q},t) = \sum_{r=1}^{N_{\text{in}}} \widetilde{\Psi}_{r}(\mathbf{q},t)$$

$$= \sum_{r=1}^{N_{\text{in}}} \sum_{\alpha=1}^{N_{\text{S}}} \sum_{j=1}^{N_{r}^{(\alpha)}} |\alpha(\mathbf{q})\rangle B_{rj}^{(\alpha)}(t) G\left(\mathbf{q}; \bar{\mathbf{q}}_{rj}^{(\alpha)}(t), \bar{\mathbf{p}}_{rj}^{(\alpha)}(t)\right)$$

$$= \sum_{r=1}^{N_{\text{in}}} \sum_{\alpha=1}^{N_{\text{S}}} \sum_{j=1}^{N_{r}^{(\alpha)}} |\alpha(\mathbf{q})\rangle B_{rj}^{(\alpha)}(t) G_{rj}^{(\alpha)}(\mathbf{q},t)$$
(2.104)

where the geometry dependence of the adiabatic electronic states is explicitly indicated. In equation (2.104) $G(\mathbf{q}; \bar{\mathbf{q}}, \bar{\mathbf{p}})$ indicates a TBF centered at the phase point $(\bar{\mathbf{q}}, \bar{\mathbf{p}})$, and the same Gaussian width is assumed for all TBFs, for simplicity. The double subscript "rj" seems redundant at this stage, but will be motivated below; the first subscript denotes one of the specific initial wave packet, the second one runs over the TBFs used to expand each wave packet. Denoting as $\mathbf{B}^{(\alpha)}$ the vector of coefficients for the state α , its equations of motion can be derived from the TDVP and are the same as in the vMCG method of section 2.4.5,

$$\mathbf{S}^{(\alpha)} \frac{\partial \mathbf{B}^{(\alpha)}}{\partial t} = -\frac{\mathrm{i}}{\hbar} \sum_{\beta=1}^{N_{\mathrm{S}}} \left(\mathbf{H}^{(\alpha\beta)} - \mathrm{i}\hbar \delta_{\alpha\beta} \mathbf{\tau}^{(\alpha)} \right) \mathbf{B}^{(\beta)}, \tag{2.105}$$

where $S_{rj,r'j'}^{(\alpha)} = \left\langle G_{jr}^{(\alpha)} \middle| G_{j'r'}^{(\alpha)} \right\rangle$ and $\tau_{jr,j'r'}^{(\alpha)} = \left\langle G_{jr}^{(\alpha)} \middle| \dot{G}_{j'r'}^{(\alpha)} \right\rangle$ and the time derivatives are evaluated from equations (2.102), (2.103a) and (2.103b). In the adiabatic representation, the Hamiltonian matrix takes the form (rectilinear coordinates are assumed)

$$H_{rj,r'j'}^{(\alpha\beta)} = \delta_{\alpha\beta} \left\langle G_{jr}^{(\alpha)} \middle| \hat{T} + V_{\alpha}(\mathbf{q}) \middle| G_{j'r'}^{(\alpha)} \right\rangle + \sum_{i=1}^{f} \left\langle G_{jr}^{(\alpha)} \middle| \hbar D_{\kappa}^{(\alpha\beta)}(\mathbf{q}) \frac{\partial}{\partial q_{\kappa}} + F_{\kappa}^{(\alpha\beta)}(\mathbf{q}) \middle| G_{j'r'}^{(\beta)} \right\rangle,$$
(2.106)

where $V_{\alpha}(\mathbf{q})$ are the adiabatic potential energy surfaces, and $D_{\kappa}^{(\alpha\beta)}(\mathbf{q})$ and $F_{\kappa}^{(\alpha)}(\mathbf{q})$ are the derivative and scalar couplings, introduced in section 2.2.2. In most applications the scalar couplings are neglected.

It is clear from equation (2.106) that the nonadiabatic couplings induce mixing between the TBFs evolving in two different adiabatic surfaces, leading to more complex nuclear wavefunctions. Therefore, the idea of making the number of TBFs adaptive is to generate a new Gaussian $G_{rl}^{(\beta)}$ in the state β whenever the TBF $G_{rl}^{(\alpha)}$ in

the state α reaches a molecular geometry where the derivative couplings are large. This process is denoted *spawning* and is activated at propagation times t_0 , when the norm of the derivative coupling vector $|\mathbf{D}^{(\alpha\beta)}|$ or its projection on the velocity vector $|\mathbf{D}^{(\alpha\beta)} \cdot \dot{\mathbf{q}}_{rj}^{(\alpha)}|$ exceeds a certain threshold. At this point:

• The B coefficients are frozen, and the TBF $G_{rj}^{(\alpha)}$ is propagated from t_0 to t_1 in the state α until a maximum derivative coupling is reached. At this stage, a new TBF $G_{rl}^{(\beta)}$ is generated at the same position and with a momentum $\bar{\mathbf{p}}_{rl}^{(\beta)} = \bar{\mathbf{p}}_{rj}^{(\alpha)} - s\mathbf{D}^{(\alpha\beta)}$, where s is defined so as to impose energy conservation

$$T(\bar{\mathbf{p}}_{rl}^{(\beta)}) + V_{\beta}(\mathbf{q}_{rj}^{(\alpha)}) = T(\bar{\mathbf{p}}_{rj}^{(\alpha)}) + V_{\alpha}(\mathbf{q}_{rj}^{(\alpha)}). \tag{2.107}$$

In the cases where the constraint cannot be satisfied, the position of the spawned TBF is also adjusted with a steepest descent algorithm. Note that, after the spawing, the number of TBFs in the r branch increases by one, $N_r^{(\beta)} \to N_r^{(\beta)} + 1$.

- The "child" TBF created in the β state is back-propagated from t_1 to t_0 .
- The propagation is resumed from t_0 , and dynamics of the B coefficients is reactivated.

More details about the FMS algorithms can be found in Ref. [73].

The ab initio multiple spawing approximation

The FMS method is an excellent starting point to design algorithms to simulate nonadiabatic molecular dynamics while computing the potential energy surfaces and nonadiabatic couplings on the fly. However, implementing these simulations in a computationally efficient way requires, at present, two additional approximations, which define the *ab initio multiple spawning method (AIMS)* [72]:

1. Scalar nonadiabatic couplings, usually small and hard to compute *ab initio*, are neglected. The other Hamiltonian matrix elements are evaluated using the so-called saddle-point approximation of order zero, *i.e.*, as

$$\left\langle \left. G_{jr}^{(\alpha)} \right| V_{\alpha}(\mathbf{q}) \right| G_{j'r'}^{(\alpha)} \right\rangle \approx \left. V_{\alpha} \left(\bar{\mathbf{q}}_{jr,j'r'} \right) \left\langle \left. G_{jr}^{(\alpha)} \right| G_{j'r'}^{(\alpha)} \right\rangle, \tag{2.108a}$$

$$\left\langle G_{jr}^{(\alpha)} \middle| D_{\kappa}^{(\alpha\beta)}(\mathbf{q}) \frac{\partial}{\partial q_{\kappa}} \middle| G_{j'r'}^{(\alpha)} \right\rangle \approx D_{\kappa}^{(\alpha\beta)} \left(\bar{\mathbf{q}}_{jr,j'r'} \right) \left\langle G_{jr}^{(\alpha)} \middle| \frac{G_{j'r'}^{(\alpha)}}{\partial q_{\kappa}} \right\rangle, \tag{2.108b}$$

where $\bar{\mathbf{q}}_{jr,j'r'}$ is the midpoint between the positions of the two Gaussians, $\bar{\mathbf{q}}_{jr,j'r'} = (\bar{\mathbf{q}}_{jr} + \bar{\mathbf{q}}_{j'r'})/2$. This approximation allows us to perform the dynamics simulation without the need to know the entire surface in advance.

2. The initial wave packets $\widetilde{\Psi}_r$ of equation (2.104) are propagated independently. In practice, one samples an initial distribution of Gaussians, for

example using Wigner sampling, and lets them evolve and spawn their "children" independently. This is called the *independent first-generation* approximation, and is justified by the assumptions that the initially generated TBFs rapidly spread out in configuration space after photoexcitation.

The AIMS method has been successfully applied to a number of problems in molecular photochemistry [74]. Note, however, that he above approximations – especially the number 2 – formally prevent the AIMS method from converging to the exact result when the initial TBFs are decoupled.

2.5.3 Fully Independent Trajectories: The Surface Hopping Approach

From the computational viewpoint, the most efficient approaches for nonadiabatic molecular dynamics are those based on classical (*i.e.*, independent) trajectories from a given ensemble, because they can be launched in parallel in multi-core computing infrastructures. As explained in section 2.5.4, the use of independent trajectories is the essence of the classical limit of quantum mechanics, therefore, it is intrinsically an approximation. The question, still not completely solved, is: what is the best way to do this approximation?

Many (many!) different methods have been proposed to address this problem. In a few words, there are two main aspects that one needs to define, and that distinguish one method from the other [79]: (i) What are the classical equations of motion that govern the trajectory dynamics? (ii) How do we aggregate the data from the ensemble of trajectories to reconstruct the electronic populations and coherences?

To answer the question (i) we need to define a potential energy surface. One possible strategy is to define some time-dependent potential, by averaging the PESs of the different electronic states. This led to the so-called *Ehrenfest method*, or similar related approaches. These types of approximation are described in section 2.5.5.

The other possibility is to use trajectories that, at each time, evolve on a specific PES. Radiationless transitions are mimicked by letting the trajectory "hop" between the surface of one state to another. This strategy defines the *surface hopping* methods for nonadiabatic photochemistry. Conceptually, these methods can be viewed as a simplification of the AIMS method, whereby the TBF hops to another electronic state, instead of spawing a new child.

The most popular algorithm for surface hopping is the so-called "fewest-switches" approach introduced by Tully [76]. In this approach, the nuclear coordinates follow classical trajectories, indexed by the superscript (r), governed by the PES of one specific adiabatic state γ_t that is *active* at the given time,

$$\dot{q}_{\kappa}^{(r)} = \frac{\partial H^{(\gamma_t)}}{\partial p_k^{(r)}}, \quad \dot{p}_{\kappa}^{(r)} = -\frac{\partial H^{(\gamma_t)}}{\partial q_{\kappa}}, \tag{2.109}$$

where $H^{(\gamma_t)} = T(\mathbf{p}) + V_{\gamma_t}(\mathbf{q})$ is the classical Hamiltonian of the active state. Due to the hops, the active state can change over time. The electronic wavefunction is

expanded in the adiabatic basis as $|\Psi_{\rm el}\rangle = \sum_{\alpha=1}^{N_{\rm S}} C_{\alpha}(t) |\alpha(\mathbf{q}(t))\rangle$ and the expansion coefficients follow the time-dependent Schrödinger equation,

$$\frac{\mathrm{d}C_{\alpha}^{(r)}}{\mathrm{d}t} = -\frac{\mathrm{i}}{\hbar} \sum_{\beta=1}^{N_{\mathrm{S}}} \left[\delta_{\alpha\beta} V_{\beta} \left(\mathbf{q}^{(r)} \right) - \mathbf{D}^{(\alpha\beta)} \left(\mathbf{q}^{(r)} \right) \cdot \dot{\mathbf{q}}^{(r)} \right] C_{\beta}(t)^{(r)}. \tag{2.110}$$

With this setup, we can imagine two different ways to compute electronic time-dependent populations. One is to evaluate the fraction of trajectories that are evolving in each electronic state at a given time $N_{\alpha}(t)$. The other way is to use the quantum mechanical definition, based on the electronic coefficients, and the two ways should be approximately equivalent, *i.e.*

$$\frac{N_{\alpha}(t)}{N_{\text{traj}}} \approx \frac{1}{N_{\text{traj}}} \sum_{r=1}^{N_{\text{traj}}} \left| C_{\alpha}(t)^{(r)} \right|^2. \tag{2.111}$$

The criterion of Tully's surface hopping is to minimize the number of state switches while approximately satisfying the consistency relation given by equation (2.111). To this end, when the quantum mechanical population of the active state gets reduced, a hopping may occur. The hopping probability per unit time can be found to be [76]

$$p_{\alpha \to \beta} = \max \left\{ 0, \frac{2\mathbf{D}^{(\alpha\beta)}(\mathbf{q}^{(r)}) \cdot \dot{\mathbf{q}}^{(r)} \operatorname{Re}\left[C_{\alpha}^{(r)*}(t)C_{\beta}^{(r)}(t)\right]}{\left|C_{\alpha}^{(r)}(t)\right|^{2}} \right\}.$$
(2.112)

The introduction of a hopping probability defines a stochastic propagation, *i.e.*, the trajectories are not uniquely determined by the initial conditions. At each time step, one needs to compute the derivative coupling vector, evaluate the hopping probability, and choose whether the trajectory hops or not, by comparing $p_{\alpha \to \beta}$ with a random number.

If the hop occurs, the momentum \mathbf{p} is rescaled (typically along the direction of the derivative coupling) to ensure energy conservation, as for the FMS method, see equation (2.107). The only difference is that, when the hop terminates in a higher adiabatic state, and there is not enough energy left for the kinetic terms, the hop is aborted ("frustrated hop") and the momentum is reversed.

Tully's surface hopping algorithm has been combined with almost all common electronic structure methods developed for excited states, and has revealed itself to be accurate in a number of studies. Its main limitation is a poor description of the electronic decoherence, i.e., the loss of overlap between wave packets associated with different PES. This phenomenon is due to the strong coupling between electronic and nuclear dynamics in the regions of large nonadiabatic couplings and cannot be described by a single trajectory. Therefore, surface hopping methods are generally found to be overcoherent, and the results need to be empirically corrected [77].

2.5.4 The Phase Space View on Nuclear Quantum Effects

In section 2.5.1, we introduced – without any particular justification – the trajectory basis functions as a means to describe quantum dynamics using classical trajectories, and emphasised that the difference with the Gaussian wave packets used in the vMCG method, which, in contrast, follow quantum mechanical trajectories. Indeed, there are different ways to retrieve classical Hamiltonian trajectories as a limit of quantum mechanics. One aspect of this limit is the need to connect the Hilbert space, which contains coordinate or momentum dependent functions, with the phase space, which describes distributions dependent on both coordinates and momenta.

One elegant way to retrieve the classical limit of quantum mechanics is the use of the *phase space formulation* introduced in the 1940s by Groenewold and Moyal. This is an alternative formulation of quantum mechanics, self-standing and equivalent to the Hilbert space formulation, which makes use of phase space distributions just as in classical mechanics. A complete account of this subject is well beyond the purpose of this chapter. However, it is worth reporting the main results of the theory to understand what we are neglecting when we use classical instead of quantum mechanics. More details can be found in Ref. [78] and, at an introductory level, Ref. [79].

Suppose that we want to describe a quantum dynamical system governed by a single potential energy surface. In standard Hilbert space quantum mechanics, we would make use of a high-dimensional wavefunction $\chi(\mathbf{q},t)$. The equivalent quantity in the phase space is the Wigner function, connected to the Hilbert space wavefunction as

$$W(\mathbf{q}, \mathbf{p}, t) = \frac{1}{(\pi \hbar)^f} \int d\mathbf{s} \chi^*(\mathbf{q} - \mathbf{s}, t) e^{-2\frac{\mathbf{i}}{\hbar} \mathbf{s} \cdot \mathbf{p}} \chi(\mathbf{q} + \mathbf{s}, t).$$
 (2.113)

Note that here the momentum \mathbf{p} is not an operator, but a variable, exactly as \mathbf{q} is. The Wigner function has the nice property of delivering the expectation value of a quantum observable $\Omega_{qu}(\hat{\mathbf{q}},\hat{\mathbf{p}})$ via phase space integration of the corresponding classical observable $\Omega_{cl}(\mathbf{q},\mathbf{p})$

$$\langle \chi | \Omega_{qu}(\hat{\mathbf{q}}, \hat{\mathbf{p}}) | \chi \rangle = \int d\mathbf{q} d\mathbf{p} \Omega_{cl}(\mathbf{q}, \mathbf{p}) W(\mathbf{q}, \mathbf{p}).$$
 (2.114)

Usually (but not always!), the quantum and classical operators have the same functional expression. In particular, this is true for purely \mathbf{p} - and \mathbf{q} -dependent observables, as well as their sum, such as the Hamiltonian $H(\mathbf{q}, \mathbf{p}) = T(\mathbf{p}) + V(\mathbf{q})$. Equation (2.114) tells us that the Wigner function behaves as a probability distribution in the phase space. However, a purely quantum mechanical signature is that, in small regions of the phase space, $W(\mathbf{q}, \mathbf{p})$ can be negative, therefore it is often referred to as quasi-probability.

A useful property is that if two Hilbert space wavefunctions χ_n and χ_m are orthogonal, the corresponding Wigner functions W_n and W_m also are. More in general, one can derive the equation

$$\int d\mathbf{q} \int d\mathbf{p} W_n(\mathbf{q}, \mathbf{p}) W_m(\mathbf{q}, \mathbf{p}) = \frac{\left| \langle \chi_n | \chi_m \rangle \right|^2}{(2\pi\hbar)^f}, \qquad (2.115)$$

which allows us to compute state populations using projections, as for the conventional Hilbert space formulation.

The Wigner function evolves in time according to the Moyal equation,

$$\frac{\partial W}{\partial t} = -\frac{\mathrm{i}}{\hbar} (H \star W - W \star H), \tag{2.116}$$

where the \star -product is defined by the operator

$$\star \equiv \exp\left(\frac{i\hbar}{2}\hat{\Lambda}\right)$$

$$= \exp\left[\frac{i\hbar}{2}\sum_{\kappa=1}^{f} \left(\frac{\overleftarrow{\partial}}{\partial q_{\kappa}}\frac{\overrightarrow{\partial}}{\partial p_{\kappa}} - \frac{\overleftarrow{\partial}}{\partial p_{\kappa}}\frac{\overrightarrow{\partial}}{\partial q_{\kappa}}\right)\right],$$
(2.117)

which is always interposed between two phase space functions, and the arrows indicate the factor that gets differentiated. Equation (2.116) seems complicated, but can be simplified by expanding the exponential of the \star -product in Taylor series. The classical limit is obtained for $\hbar \to 0$, which coincides with the first order expansion $\star \approx 1 + \frac{i\hbar}{2}\hat{\Lambda}$,

$$\frac{\partial W}{\partial t} \approx -\frac{\mathrm{i}}{\hbar} \left[H \left(1 + \frac{\mathrm{i}\hbar}{2} \hat{\Lambda} \right) W - W \left(1 + \frac{\mathrm{i}\hbar}{2} \hat{\Lambda} \right) H \right] + O(\hbar^2)
= \sum_{i}^{f} \left(\frac{\partial V}{\partial q_{\nu}} \frac{\partial W}{\partial p_{\nu}} - \frac{\partial T}{\partial p_{\nu}} \frac{\partial H}{\partial q_{\nu}} \right) + O(\hbar^2),$$
(2.118)

i.e., the classical Liouville equation! This equation contains only first-order derivatives. It is immediate to see that, due to this fact, it can be solved by expanding $W(\mathbf{q}, \mathbf{p})$ as an ensemble of independent trajectories, formally represented as Dirac delta functions,

$$W_{\rm cl}(\mathbf{q}, \mathbf{p}) = \frac{1}{N_{\rm traj}} \sum_{r=1}^{N_{\rm traj}} \delta\left(\mathbf{q} - \mathbf{q}^{(r)}(t)\right) \delta\left(\mathbf{p} - \mathbf{p}^{(r)}(t)\right), \tag{2.119}$$

where $\mathbf{q}^{(r)}(t)$ and $\mathbf{p}^{(r)}(t)$ follow Hamilton's equations.

The lowest order correction to classical mechanics is obtained as

$$\frac{\partial W}{\partial t} \approx -\frac{\mathrm{i}}{\hbar} \left[H \left(1 + \frac{\mathrm{i}\hbar}{2} \hat{\Lambda} - \frac{\hbar^2}{8} \hat{\Lambda}^2 - \frac{\mathrm{i}\hbar^3}{48} \hat{\Lambda}^3 \right) W - W \left(1 + \frac{\mathrm{i}\hbar}{2} \hat{\Lambda} - \frac{\hbar^2}{8} \hat{\Lambda}^2 - \frac{\mathrm{i}\hbar^3}{48} \hat{\Lambda}^3 \right) H \right] + O(\hbar^4)$$

$$= \sum_{\kappa=1}^{f} \left(\frac{\partial V}{\partial q_{\kappa}} \frac{\partial W}{\partial p_{\kappa}} - \frac{\partial T}{\partial p_{\kappa}} \frac{\partial H}{\partial q_{\kappa}} \right) + \frac{\hbar^2}{24} \sum_{\kappa,\mu,\nu=1}^{f} \frac{\partial^3 V}{\partial q_{\kappa} \partial q_{\mu} \partial q_{\nu}} \frac{\partial^3 W}{\partial p_{\kappa} \partial p_{\mu} \partial p_{\nu}} + O(\hbar^4). \tag{2.120}$$

This equation is definitely much worse, and, as such, not much of practical use (it is as difficult to solve as the time-dependent Schrödinger equation – or even more difficult). However, there are some interesting features that emerge:

- The classical limit is clearly obtained as $\hbar \to 0$. Since the prefactor in the correction term is $\hbar^2/24$, it is also clear that the quantum corrections are small unless strong anharmonicities are present. For harmonic potentials, the classical Liouville equation gives the exact quantum mechanical dynamics.
- High-order corrections to equation (2.120) scale as \hbar^4 and therefore are small and can be safely neglected in most cases. The truncation of equation (2.120) is exact for at most quartic potentials.
- Equation (2.120) involves summations over the degrees of freedom, therefore, it suggests that it is possible to include quantum corrections only for a few selected modes. This gives rise to the quantum-classical Liouville equation (QCLE) [80] (see section 2.5.5).
- The presence of cubic derivatives has the effect that the independent trajectories ansatz of equation (2.119) cannot be used to solve equation (2.120) exactly. The solution of the equation or the QCLE typically involves the propagation of coupled trajectories to account for quantum mechanical coupling.

Despite being uncommon, the phase space formulation of quantum mechanics is certainly a useful tool to explore new possibilities to design novel methods for quantum dynamics. In particular, when classical trajectories are used, Moyal's equation allows one to understand which terms are discarded and how large they could be.

2.5.5 Mapping Discrete Electronic States to Phase Space Variables

The phase space formulation of quantum mechanics gives a precise definition of the classical limit of quantum mechanics, which allows simulations in terms of independent trajectories, as well as the identification of the most important corrections. It is interesting to apply this procedure to nonadiabatic molecular dynamics problems, which involve multiple nuclear wavefunctions associated with different electronic states. However, the Wigner function is defined in equation (2.113) via an integral over a continuous coordinate variable s. In contrast, the whole formalism derived by the group Born–Oppenheimer approximation relies on a discrete set of electronic states. How can we get a phase space picture for the electronic space and, eventually, take the classical limit?

One possible way is to use the so-called bosonization technique developed by Schwinger [81]. This formalism establishes an exact mapping between a system with $N_{\rm S}$ discrete levels and the singly excited states of a $N_{\rm S}$ -dimensional isotropic harmonic oscillator. The formal steps are the following:

• Consider the $N_{\rm S}$ -dimensional oscillator defined by the Hamiltonian $\hat{H}_{\rm HO} = \frac{1}{2} \sum_{\alpha=1}^{N_{\rm S}} \left(P_{\alpha}^2 + X_{\alpha}^2\right)$, where P_{α} and X_{α} are dimensionless coordinates and momenta. This oscillator has $N_{\rm S}$ eigenstates with one vibrational quantum, whose wavefunctions are

$$\psi_{\alpha}(\mathbf{X}) = \left(\frac{4}{\pi}^{N_{S}}\right)^{\frac{1}{4}} X_{\alpha} \exp\left(-\frac{1}{2}\mathbf{X}^{T}\mathbf{X}\right). \tag{2.121}$$

• The singly excited states are mapped to the discrete electronic levels, $|\alpha\rangle \longleftrightarrow \psi_{\alpha}(\mathbf{X})$. The corresponding wigner functions can be evaluated from equation (2.113) as

$$W_{\alpha}(\mathbf{X}, \mathbf{P}) = \frac{1}{\pi^{N_{S}}} \exp\left(-\mathbf{X}^{T}\mathbf{X} - \mathbf{P}^{T}\mathbf{P}\right) \left(2X_{\alpha}^{2} + 2P_{\alpha}^{2} - 1\right)$$

$$\equiv W_{00}(\mathbf{X}, \mathbf{P}) \left(2X_{\alpha}^{2} + 2P_{\alpha}^{2} - 1\right). \tag{2.122}$$

This defines the phase space representation of the electronic states.

• The electronic operators $|\alpha\rangle\langle\beta|$ are mapped to operators between the singly excited harmonic oscillator levels as

$$|\alpha\rangle\langle\beta|\longleftrightarrow\hat{a}_{\alpha}^{\dagger}\hat{a}_{\beta},$$
 (2.123)

where $\hat{a}_{\beta} = (\hat{X}_{\beta} + i\hat{P}_{\beta})/\sqrt{2}$ and $\hat{a}_{\alpha}^{\dagger} = (\hat{X}_{\alpha} - i\hat{P}_{\alpha})/\sqrt{2}$ are annihilation and creation operators for the Schwinger oscillators β and α , respectively. In the Hilbert space (Schrödinger representation), the momentum operator is defined as usual $\hat{P}_{\alpha} = -i\partial/\partial X_{\alpha}$.

With these definitions, the mapping from the discrete to the continuous space is *exact*! This means that, instead of solving the usual time-dependent Schrödinger equation

$$\frac{\partial |\Psi, t\rangle}{\partial t} = -\frac{\mathrm{i}}{\hbar} \sum_{\alpha, \beta=1}^{N_{\mathrm{S}}} |\alpha\rangle H^{(\alpha\beta)}(\hat{\mathbf{q}}, \hat{\mathbf{p}}) \langle \beta | \Psi, t \rangle, \tag{2.124}$$

we can solve the mapped equation

$$\frac{\partial \Psi(\mathbf{q}, \mathbf{X}, t)}{\partial t} = -\frac{i}{\hbar} \sum_{\alpha, \beta = 1}^{N_{S}} \hat{a}_{\alpha}^{\dagger} \hat{a}_{\beta} H^{(\alpha\beta)}(\hat{\mathbf{q}}, \hat{\mathbf{p}}) \Psi(\mathbf{q}, \mathbf{X}, t)$$

$$= -\frac{i}{\hbar} \left(\frac{1}{2} \hat{\mathbf{X}}^{T} \mathbf{H}(\hat{\mathbf{q}}, \hat{\mathbf{p}}) \hat{\mathbf{X}} + \frac{1}{2} \hat{\mathbf{P}}^{T} \mathbf{H}(\hat{\mathbf{q}}, \hat{\mathbf{p}}) \hat{\mathbf{P}} \right) \Psi(\mathbf{q}, \mathbf{X}, t), \tag{2.125}$$

and the results of the calculations will be exactly the same (provided that we map the initial state consistently). Here, it is assumed that the electronic Hamiltonian matrix set in the diabatic representation is real and symmetric, $H^{(\alpha\beta)} = H^{(\beta\alpha)}$.

Of course, solving equation (2.125) is as difficult as solving equation (2.124). The potential advantage that we can get from Schwinger's model is that we can easily write down the equivalent of equation (2.125) in the phase space using equations (2.116) and (2.117),

$$\frac{\partial W(\mathbf{q}, \mathbf{p}, \mathbf{X}, \mathbf{P}, t)}{\partial t} = -\frac{\mathrm{i}}{\hbar} \left(H e^{\frac{\mathrm{i}\hbar}{2} \hat{\Lambda}_{\mathbf{q}\mathbf{p}}} e^{\frac{\mathrm{i}\hbar}{2} \hat{\Lambda}_{\mathbf{X}\mathbf{P}}} W - W e^{\frac{\mathrm{i}\hbar}{2} \hat{\Lambda}_{\mathbf{q}\mathbf{p}}} e^{\frac{\mathrm{i}\hbar}{2} \hat{\Lambda}_{\mathbf{X}\mathbf{P}}} H \right), \tag{2.126}$$

and take the classical limit by truncating the exponential operators at the first order.

If we do this procedure only for the nuclear variables, i.e. $e^{\frac{i\hbar}{2}\hat{\Lambda}_{qp}} \approx 1 + \frac{i\hbar}{2}\hat{\Lambda}_{qp}$ we obtain, after some calculus, the quantum-classical Liouville equation [80],

$$\frac{\partial W}{\partial t} = H \hat{\Lambda}_{\mathbf{qp}} W + \frac{1}{\hbar} H \hat{\Lambda}_{\mathbf{XP}} W - \frac{1}{8} H \hat{\Lambda}_{\mathbf{qp}} \hat{\Lambda}_{\mathbf{XP}}^2 W, \qquad (2.127)$$

which still does not allow a solution in terms of independent trajectories. To reach this situation, we must neglect the last term in equation (2.127) to obtain the classical Liouville equation in the mapping representation,

$$\frac{\partial W}{\partial t} = \sum_{\kappa=1}^{f} \left(\frac{\partial H}{\partial q_{\kappa}} \frac{\partial W}{\partial p_{\kappa}} - \frac{\partial H}{\partial p_{\kappa}} \frac{\partial W}{\partial q_{\kappa}} \right) + \sum_{\alpha=1}^{N_{S}} \left(\frac{\partial H}{\partial X_{\alpha}} \frac{\partial W}{\partial P_{\alpha}} - \frac{\partial H}{\partial P_{\alpha}} \frac{\partial W}{\partial X_{\alpha}} \right). \tag{2.128}$$

Here $W(\mathbf{q}, \mathbf{p}, \mathbf{X}, \mathbf{P}, t)$ is the classical-like distribution function, which also depends on the electronic phase space variables \mathbf{X} and \mathbf{P} , and $H(\mathbf{q}, \mathbf{p}, \mathbf{X}, \mathbf{P})$ is the Meyer-Miller-Stock-Thoss~(MMST)~Hamiltonian~[82, 83], which in the diabatic representation takes the form

$$H_{\text{MMST}}(\mathbf{q}, \mathbf{p}, \mathbf{X}, \mathbf{P}) = \frac{1}{2} \mathbf{X}^{T} (T(\mathbf{p})\mathbf{1} + \mathbf{V}(\mathbf{q}))\mathbf{X} + \frac{1}{2} \mathbf{P}^{T} (T(\mathbf{p})\mathbf{1}_{N_{S}} + \mathbf{V}(\mathbf{q}))\mathbf{P}, \quad (2.129)$$

where $T(\mathbf{p})$ is the classical nuclear kinetic energy, $\mathbf{1}_{N_{\mathrm{S}}}$ is the $N_{\mathrm{S}} \times N_{\mathrm{S}}$ identity matrix, and $\mathbf{V}(\mathbf{q})$ is an electronic Hamiltonian matrix in the diabatic representation.

Many different mapping approaches

Equation (2.128) can be viewed as the classical limit of the coupled nuclear-electronic time-dependent Schrödinger equation. This equation is the basis of many different methods to simulate nonadiabatic dynamics, which cannot be exhaustively reviewed here. The reason why different methods can be derived from just one equation is that we have taken the classical limit for the electronic motion, therefore, we have lost key properties of the full quantum mechanical problem. Therefore, we are left with some ambiguities, for which different solutions – in principle equally legitimate – can be proposed.

One key ambiguity is the definition of the identity operator for the electronic space. Quantum mechanically, we have the completeness relation $\hat{1} = \sum_{\alpha} |\alpha\rangle\langle\alpha|$. The phase space expression of the left-hand side gives simply 1. The right-hand side, using equation (2.123), would give $\hat{1}\longleftrightarrow (\mathbf{X}^T\mathbf{X}+\mathbf{P}^T\mathbf{P})/2-N_S/2$. This inconsistency is irrelevant if exact quantum mechanics, or the quantum classical Liouville equation, is used. However, in the classical limit, the results change if one uses one or the other form.

In a number of tests and investigations, it has been found that, often a better agreement with full quantum calculations is obtained by treating the identity operator, as far as possible, as 1 [84]. To this end, the diabatic MMST Hamiltonian is defined as

$$\hat{H}_{\text{MMST}} = T(\mathbf{p}) + V_0(\mathbf{q}) + \frac{1}{2} \mathbf{X}^T \overline{\mathbf{V}}(\mathbf{q}) \mathbf{X} + \frac{1}{2} \mathbf{P}^T \overline{\mathbf{V}}(\mathbf{q}) \mathbf{P},$$
 (2.130)

where $V_0(\mathbf{q}) = \frac{1}{N_S} \text{Tr}[\mathbf{V}(\mathbf{q})]$ is the average potential and the residual electronic Hamiltonian $\overline{\mathbf{V}}(\mathbf{q}) = \mathbf{V}(\mathbf{q}) - V_0(\mathbf{q})\mathbf{1}$ is made traceless. The classical equations of motion used for the independent trajectory simulations read

$$\dot{q}_{\kappa} = \frac{\partial T(\mathbf{p})}{\partial p_{\kappa}},$$
 (2.131a)

$$\dot{p}_{\kappa} = -\frac{\partial V_0(\mathbf{q})}{\partial q_{\kappa}} - \frac{1}{2} \mathbf{X}^T \frac{\partial \overline{\mathbf{V}}(\mathbf{q})}{\partial q_{\kappa}} \mathbf{X} - \frac{1}{2} \mathbf{P}^T \frac{\partial \overline{\mathbf{V}}(\mathbf{q})}{\partial q_{\kappa}} \mathbf{P}, \tag{2.131b}$$

$$\dot{\mathbf{X}} = \frac{1}{\hbar} \overline{\mathbf{V}}(\mathbf{q}) \mathbf{P}, \tag{2.131c}$$

$$\dot{\mathbf{P}} = -\frac{1}{\hbar} \overline{\mathbf{V}}(\mathbf{q}) \mathbf{X}. \tag{2.131d}$$

Upon solution of the equations of motion, electronic populations can be computed using classical phase space averages. In particular, the population of the electronic state β , given that the dynamics are initiated in state α , is approximated as⁵

$$P_{\beta \leftarrow \alpha}(t) = \text{Tr}\left[e^{\frac{i}{\hbar}\hat{H}t}|\beta\rangle\langle\beta|e^{-\frac{i}{\hbar}\hat{H}t}|\alpha\rangle\langle\alpha|\hat{\rho}_{\text{nuc}}\right]$$

$$\approx \int F'_{\beta\beta}(\mathbf{X}_{t}, \mathbf{P}_{t})F_{\alpha\alpha}(\mathbf{X}_{0}, \mathbf{P}_{0})W_{\text{nuc}}(\mathbf{q}_{0}, \mathbf{p}_{0})d\mathbf{q}_{0}d\mathbf{p}_{0}d\mathbf{X}_{0}d\mathbf{P}_{0},$$
(2.132)

where the subscripts "0" and "t" indicate the time at which the phase space variables are evaluated, and $F_{\alpha\alpha}$ and $F'_{\beta\beta}$ are electronic projection observables (classical projectors).

As mentioned before, given that the classical approximation is used, different choices are possible for the projectors. For example, one can exploit the projective property expressed by equation (2.115) and use the Wigner function of the singly-excited oscillator states, given by equation (2.122). Another option is to evaluate the population using the phase space expression of the operator $\hat{a}_{\alpha}^{\dagger}\hat{a}_{\alpha}\longleftrightarrow (X_{\alpha}^2+P_{\alpha}^2-1)/2$. A more recent, theoretically justified technique involves constraining the value of $\mathbf{X}^T\mathbf{X}+\mathbf{P}^T\mathbf{P}$ to one fixed value for each trajectory.

Below, we report the choices associated with different methods, which are among the most popular approaches used for mapping [75]:

 $[\]overline{}^5$ In the quantum mechanical formula $\hat{\rho}_{\rm nuc}$ is the initial nuclear density matrix, which, in general, is given as a statistical ensemble of pure states $\hat{\rho}_{\rm nuc} = \sum_n p_n |\chi_n\rangle \langle \chi_n|$. In this case the initial Wigner function is also the average of the Wigner functions computed for the individual states of the mixture, $W_{\rm nuc}({\bf q},{\bf p}) = \sum_n p_n \, W_n({\bf q},{\bf p})$.

• Linearized semiclassical initial value representation (LSC-IVR) [85]

$$F_{\alpha\alpha}(\mathbf{X}_0, \mathbf{P}_0) = W_{00}(\mathbf{X}_0, \mathbf{P}_0) \Big(2X_{\alpha,0}^2 + 2P_{\alpha,0}^2 - 1 \Big),$$
 (2.133a)

$$F'_{\beta\beta}(\mathbf{X}_t, \mathbf{P}_t) = (2\pi)^{N_S} W_{00}(\mathbf{X}_t, \mathbf{P}_t) \left(2X_{\beta, t}^2 + 2P_{\beta, t}^2 - 1 \right). \tag{2.133b}$$

• Poisson bracket mapping equation (PBME) [86]

$$F_{\alpha\alpha}(\mathbf{X}_0, \mathbf{P}_0) = W_{00}(\mathbf{X}_0, \mathbf{P}_0) \left(2X_{\alpha,0}^2 + 2P_{\alpha,0}^2 - 1 \right),$$
 (2.134a)

$$F'_{\beta\beta}(\mathbf{X}_t, \mathbf{P}_t) = \frac{X_{\beta,t}^2 + P_{\beta,t}^2}{2} + \frac{2 - \mathbf{X}_t^T \mathbf{X}_t - \mathbf{P}_t^T \mathbf{P}_t}{2N_S}.$$
 (2.134b)

Note that equation (2.134b) can be derived from the identity $|\alpha\rangle\langle\alpha| = |\alpha\rangle\langle\alpha| + 1/N_S - 1/N_S\sum_{\beta}|\beta\rangle\langle\beta|$.

• "Single unity" approach for linearized semiclassical dynamics [87]

$$F_{\alpha\alpha}(\mathbf{X}_0, \mathbf{P}_0) = \frac{X_{\alpha,0}^2 + P_{\alpha,0}^2}{2} + \frac{2 - \mathbf{X}_0^T \mathbf{X}_0 - \mathbf{P}_0^T \mathbf{P}_0}{2N_S},$$
 (2.135a)

$$F'_{\beta\beta}(\mathbf{X}_t, \mathbf{P}_t) = W_{00}(\mathbf{X}_t, \mathbf{P}_t) \Big(2X_{\beta,t}^2 + 2P_{\beta,t}^2 - 1 \Big).$$
 (2.135b)

• Spin mapping (SM) [88]

$$F_{\alpha\alpha}(\mathbf{X}_0, \mathbf{P}_0) = \mathcal{N} \left[\frac{X_{\alpha,0}^2 + P_{\alpha,0}^2}{2} + \frac{2 - \mathbf{X}_0^T \mathbf{X}_0 - \mathbf{P}_0^T \mathbf{P}_0}{2N_{\mathrm{S}}} \right] \delta \left(\mathbf{X}_0^T \mathbf{X}_0 + \mathbf{P}_0^T \mathbf{P}_0 - \overline{R}^2 \right),$$
(2.136a)

$$F'_{\beta\beta}(\mathbf{X}_t, \mathbf{P}_t) = \frac{X_{\beta,t}^2 + P_{\beta,t}^2}{2} + \frac{2 - \mathbf{X}_t^T \mathbf{X}_t - \mathbf{P}_t^T \mathbf{P}_t}{2N_S}.$$
 (2.136b)

Here, the constants \mathcal{N} and \overline{R} are fixed so that at the initial time $P_{m \leftarrow m}(t=0) = 1$ and the initial distribution is normalized. These conditions give $\overline{R}^2 = 2\sqrt{N+1}$ and $\mathcal{N} = N_{\rm S}!/(\pi^{N_{\rm S}}\overline{R}^{2N_{\rm S}-2})$.

• Ehrenfest dynamics

$$F_{\alpha\alpha}(\mathbf{X}_0, \mathbf{P}_0) = \mathcal{N} \left[\frac{X_{\alpha,0}^2 + P_{\alpha,0}^2}{2} + \frac{2 - \mathbf{X}_0^T \mathbf{X}_0 - \mathbf{P}_0^T \mathbf{P}_0}{2N_{\mathrm{S}}} \right]$$

$$\times \delta(\mathbf{X}_0^T \mathbf{X}_0 + \mathbf{P}_0^T \mathbf{P}_0 - 2) \delta(X_{\alpha,0}^2 + P_{\alpha,0}^2 - 2),$$
(2.137a)

$$F'_{\beta\beta}(\mathbf{X}_t, \mathbf{P}_t) = \frac{X_{\beta,t}^2 + P_{\beta,t}^2}{2} + \frac{2 - \mathbf{X}_t^T \mathbf{X}_t - \mathbf{P}_t^T \mathbf{P}_t}{2N_S}.$$
 (2.137b)

Which method is better? Experience shows that there is not always a clear answer [75, 89]. Despite being very efficient, these methods need to be benchmarked against converged quantum dynamics to properly understand how to choose a specific mapping method on a case-by-case basis. Furthermore, the computational implementation of these approaches is limited [75]. Nevertheless, there is a lot of room for improvement, because the approximations used to derive mapping-based approaches are clear, and it is also relatively straightforward to understand how these methods can be extended to simulate nonlinear spectroscopic observables.

One typical weak point, common to all these methods, is that they employ some average potential, as evident from equation (2.131b). This might be a rather bad approximation when the potential energy surfaces are well separated in energy, and is a problem that does not occur in the surface hopping approach, which, however, cannot be rigorously derived as the classical limit of quantum mechanics.

Indeed, an interesting recent developments involve the combination of mapping approaches with trajectory surface hopping [90–92]. These techniques have the potential of merging the best of the two methods, but, being new methodologies, additional benchmarks and tests are needed. Moreover, as for all methods based on independent trajectories, overcoherence is an issue and needs to be corrected in an ad hoc.

2.5.6 Quantum-Classical Approaches vs. Numerically Exact Quantum Dynamics

To conclude the overview on different methods for nonadiabatic molecular dynamics, a comparison is shown below between results obtained by numerically exact quantum dynamical simulation and quantum-classical methods. To this end, the simulations are performed with different methods using exactly the same molecular vibronic couplings models, which include two electronic states. Quantum mechanical calculations are performed using the MCTDH method as implemented in the Quantics package [93], whereas quantum-classical results are obtained by plugins recently implemented in the PySurf code [75, 94].

All five mapping approaches of section 2.5.5 are tested. Among surface hopping methods, a comparison is made between the fewest switches (FSSH) method [76] described in section 2.5.3, Landau–Zener surface hopping (LZSH) [95], and the mapping-inspired approach of Ref. [91] (MISH).

Three examples of photoinduced molecular processes are considered. Details of these simulations can be found in Ref. [75].

• The $B_{2u} \longrightarrow B_{3u}$ internal conversion in pyrazine is studied using a four-dimensional linear vibronic coupling model (see section 2.2.5)⁶.

⁶This is the model used by Worth *et al.* [*J. Chem. Phys.* **105**, 4412 (1996)] including the modes v_{10a} , v_{6a} , v_1 and v_{9a} .

In figure 2.8, the time-dependent population of the initially unpopulated $B_{3\rm u}$ state is plotted as a function of time, as resulting from different types of simulations. Exact quantum mechanical results, to be regarded as a reference, are shown with a black line. At short times, all quantum-classical methods underestimate by $\approx 5\%$ the extent of population transfer, and, in this case, the LSC-IVR and the Ehrenfest methods perform particularly worse. In contrast, surface hopping approaches are rather accurate. In particular, the FSSH method predicts the correct diabatic populations at long times.

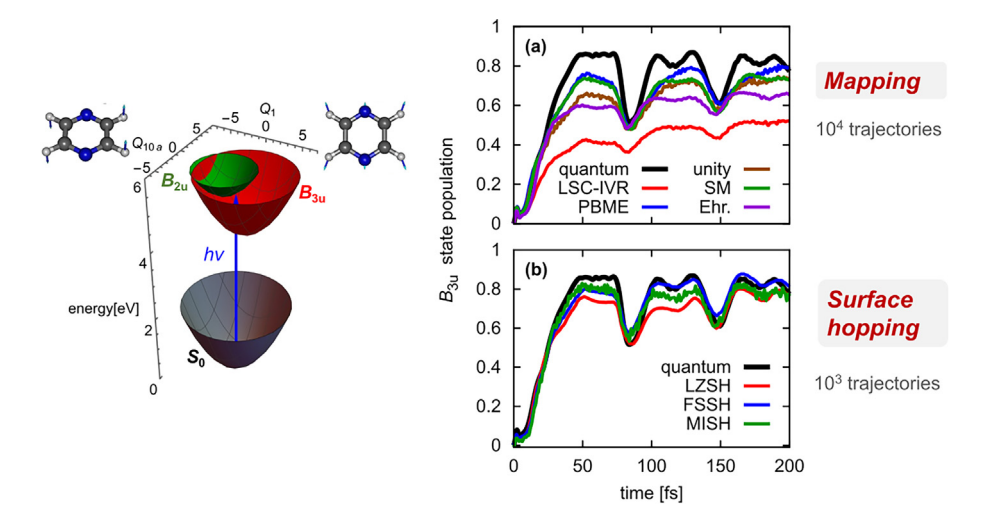


Fig. 2.8 – Simulation of the $B_{2u} \longrightarrow B_{3u}$ internal conversion in pyrazine performed by exact quantum dynamics (MCTDH), mapping approaches (a), and surface-hopping methods (b). The initial wave packet is Gaussian and located in the B_{2u} diabatic surface.

- The $B_{2u} \longrightarrow B_{2g}$ internal conversion of butatriene following the photoionization to the B_{2u} state is simulated using a full-dimensional (18-modes) quadratic vibronic coupling model [96]. The population of the B_{2g} state, calculated with different quantum-classical methods, is plotted as a function of time in figure 2.9. In contrast to the pyrazine model, the prediction of surface-hopping methods is slightly inaccurate on the long time scale, except for the MISH approach. Mapping approaches generally overestimate the B_{2g} population, with the exception of the LSC-IVR and Ehrenfest methods. Interestingly, these are the worst-performing approaches in the case of pyrazine.
- The cis-trans photoisomerization of the protonated Schiff base PSB3, a prototype for the retinal chromophore, is studied using a three-mode anharmonic diabatic model [12]. The three coordinates are a bond length alternating vibration (r), a dihedral torsion (θ) that connects the cis and trans structures of PSB3, and a hydrogen out-of-plane wagging mode (ϕ) . Figure 2.10 depicts the quantum yield for the cis—trans isomerization as a function of time,

computed using different quantum-classical methods as well as quantum mechanically. In this case, surface hopping methods are rather accurate in the short time (before ≈ 100 fs) but tend to overestimate the quantum yield at longer times. Mapping approaches also predict too large values for the yield, with the exception of the PBME approach.

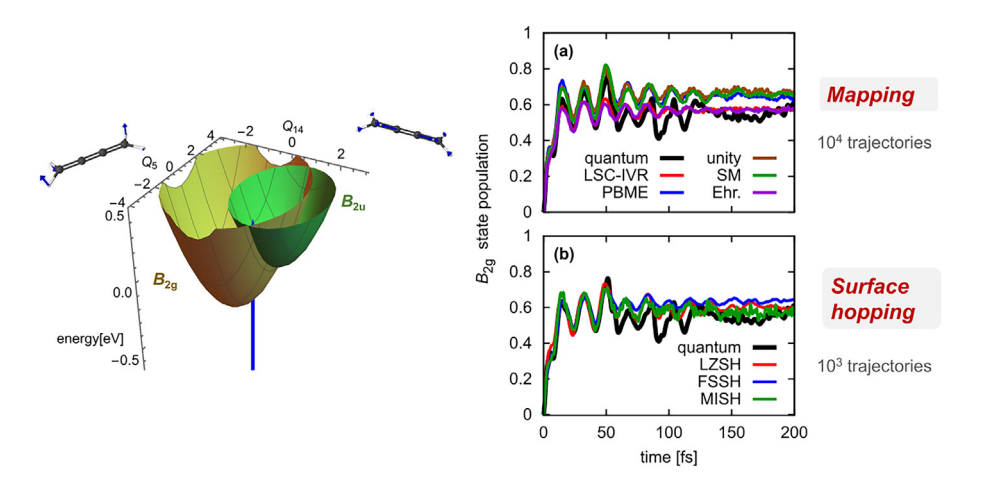


Fig. 2.9 – Simulation of the $B_{2u} \longrightarrow B_{2g}$ internal conversion of butatriene following the photoionization to the B_{2u} state performed by exact quantum dynamics (MCTDH), mapping approaches (a), and surface-hopping methods (b). The initial wave packet is Gaussian and located in the B_{2u} diabatic surface.

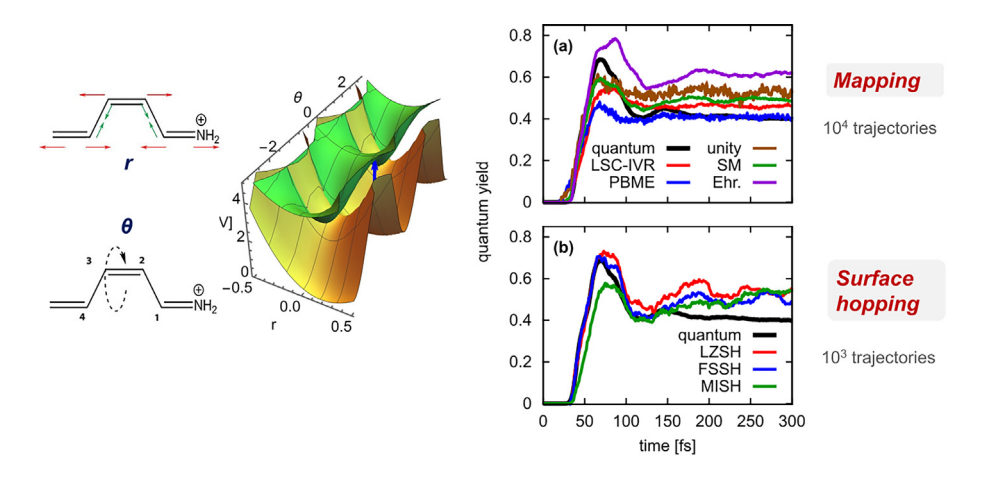


Fig. 2.10 – Simulation of the cis-trans photoisomerization of the retinal chromophore performed by quantum dynamics, mapping approaches (a) and surface-hopping methods. The initial wave packet is Gaussian and located in the upper (green) diabatic surface.

2.5.7 What Else Do We Have?

The literature about nonadiabatic molecular dynamics is rich in ideas to get the most accurate description of photoinduced phenomena without resorting to full quantum mechanical simulations. Rather than reviewing all existing approaches in detail, we have chosen to focus on the key conceptual ideas used to develop approximate quantum-classical methods. Many other methods found in the literature can be understood by using such concepts.

However, to complete the picture, it is useful to provide a list of references to other interesting methodologies – most of them still under development – not covered in this chapter. These are:

- The multi-configurational Ehrenfest method [97, 98], where the wave packets are constructed as a combination of Gaussians that evolve along Ehrenfest mean-field trajectories, instead of being guided by state-specific potentials.
- Many different approaches for the approximate solution of the quantum-classical Schrödinger equation [80, 99–101].
- The partial linearized density matrix [101] and the forward-backward methods [103], which add a correction to the classical limit of mapping approaches.
- The coupled trajectories approach derived from the exact factorization of the molecular wavefunction [104]. The underlying theory is based on a molecular wavefunction ansatz, alternative to the Born-Huang expansion of equation (2.5), where both the electronic and nuclear wavefunctions are time-dependent.

Acknowledgements. D. P. wishes to thank the participants and the organizers of the Summer School "Quantum Dynamics and Spectroscopy of Functional Molecular Materials and Biological Photosystems" in Les Houches (2023) for making the school lively, stimulating, and enjoyable.

References

- Cederbaum L. S. (2008) Born-Oppenheimer approximation and beyond for time-dependent electronic processes, J. Chem. Phys. 128, 124101.
- [2] Gatti F., Lasorne B., Meyer H.-D., Nauts A. (2017) Applications of quantum dynamics in chemistry. Springer International Publishing, Cham, pp. 127–166.
- [3] Cederbaum L. S. (2004) Conical intersections (W. Domcke, D. R. Yarkony, H. Köppel, Eds). World Scientific, Chapter 1, pp. 3–40.
- [4] Penfold T. J., Gindensperger E., Daniel C., Marian C. M. (2018) Spin-vibronic mechanism for intersystem crossing, Chem. Rev. 118, 6975.
- [5] Faraji S., Picconi D., Palacino-González E. (2024) Advanced quantum and semiclassical methods for simulating photoinduced molecular dynamics and spectroscopy, WIREs Comput. Mol. Sci. 14, e1731.
- [6] Reiter S., Keefer D., de Vivie-Riedle R. (2020) Quantum chemistry and dynamics of excited states. John Wiley & Sons, Ltd, Chapter 11, p. 355.
- [7] Persico M., Granucci G. (2018) Photochemistry: A modern theoretical perspective. Springer International Publishing, Cham, pp. 141–177.

- [8] Cave R. J., Stanton J. F. (2016) A simple quasi-diabatization scheme suitable for spectroscopic problems based on one-electron properties of interacting states, *J. Chem. Phys.* 144, 054110.
- [9] Hoyer C. E., Parker K., Gagliardi L., Truhlar D. G. (2016) The DQ and DQΦ electronic structure diabatization methods: Validation for general applications, J. Chem. Phys. 144, 194101.
- [10] Picconi D. (2022) Quantum dynamics of the photoinduced charge separation in a symmetric donor-acceptor-donor triad: The role of vibronic couplings, symmetry and temperature, J. Chem. Phys. 156, 184105.
- [11] Picconi D., Grebenshchikov S. Y. (2018) Photodissociation dynamics in the first absorption band of pyrrole. I. Molecular Hamiltonian and the Herzberg-Teller absorption spectrum for the ${}^{1}A_{2}(\pi\sigma^{*}) \leftarrow \widetilde{X}^{1}A_{1}(\pi\pi)$ transition, J. Chem. Phys. 148, 104103.
- [12] Marsili E., Farag M. H., Yang X., De Vico L., Olivucci M. (2019) Two-state, three-mode parametrization of the force field of a retinal chromophore model, J. Phys. Chem. A 123, 1710–1719.
- [13] Fumanal M., Plasser F., Mai S., Daniel C., Gindensperger E. (2018) Interstate vibronic coupling constants between electronic excited states for complex molecules, J. Chem. Phys. 148, 124119.
- [14] Green J. A., Asha H., Santoro F., Improta R. (2021) Excitonic model for strongly coupled multichromophoric systems: The electronic circular dichroism spectra of guanine quadruplexes as test cases, J. Chem. Theor. Comput. 17, 405–415.
- [15] Wolf T. J. A. et al. (2017) Probing ultrafast $\pi \pi^*/n\pi^*$ internal conversion in organic chromophores via K-edge resonant absorption, Nat. Comm. 8, 29.
- [16] Crespo-Hernández C. E., Cohen B., Hare P. M., Kohler B. (2004) Ultrafast excited-state dynamics in nucleic acids, Chem. Rev. 104, 1977–2020.
- [17] Mohamadzade A., Nenov A., Garavelli M., Conti I., Ullrich S. (2023) Double thionated pyrimidine nucleobases: Molecular tools with tunable photoproperties, J. Am. Chem. Soc. 145, 11945–11958.
- [18] Picconi D., Barone V., Lami A., Santoro F., Improta R. (2011) The interplay between ππ*/nπ* excited states in gas-phase thymine: A quantum dynamical study, ChemPhysChem 12, 1957–1968.
- [19] Picconi D., Avila Ferrer F. J., Improta R., Lami A., Santoro F. (2013) Quantum-classical effective-modes dynamics of the ππ* → nπ* decay in 9H-adenine. A quadratic vibronic coupling model, Faraday Discuss. 163, 223–242.
- [20] Mayer D. et al. (2022) Following excited-state chemical shifts in molecular ultrafast x-ray photoelectron spectroscopy, Nat. Comm. 13, 198.
- [21] Mondelo-Martell M., Brey D., Burghardt I. (2022) Quantum dynamical study of inter-chain exciton transport in a regioregular P3HT model system at finite temperature: HJ vs H-aggregate models, J. Chem. Phys. 157, 094108.
- [22] Palacino-González E., Jansen T. L. C. (2023) Modeling the effect of disorder in the two-dimensional electronic spectroscopy of poly-3-hexyltiophene in an organic photovoltaic blend: A combined quantum/classical approach, J. Phys. Chem. C 127, 6793.
- [23] Brey D., Burghardt I. (2024) Coherent transient localization mechanism of interchain exciton transport in regioregular P3HT: A quantum-dynamical study, J. Phys. Chem. Lett. 15, 1836.
- [24] Hestand N. J., Spano F. C. (2018) Expanded theory of H- and J-molecular aggregates: The effects of vibronic coupling and intermolecular charge transfer, Chem. Rev. 118, 7069.
- [25] Aster A., Bornhof A.-B., Sakai N., Matile S., Vauthey E. (2021) Lifetime broadening and impulsive generation of vibrational coherence triggered by ultrafast electron transfer, J. Phys. Chem. Lett. 12, 1052.
- [26] Adolphs J., Müh F., Madjet M. E. A., Renger T. (2007) Calculation of pigment transition energies in the FMO protein, *Photosynth. Res.* 95, 197.
- [27] Strich R., Faraji S., Palacino-González E. (2025) Extending quantum coherence lifetimes in nonadiabatic dissipative molecular systems with chirped pulses. Submitted.

- [28] Renger T., Müh F. (2013) Understanding photosynthetic light-harvesting: A bottom up theoretical approach, Phys. Chem. Chem. Phys. 15, 3348–3371.
- [29] Dereka B., Koch M., Vauthey E. (2017) Looking at photoinduced charge transfer processes in the IR: Answers to several long-standing questions, Acc. Chem. Res. 50, 426–434.
- [30] Binder R., Lauvergnat D., Burghardt I. (2018) Conformational dynamics guides coherent exciton migration in conjugated polymer materials: First-principles quantum dynamical study, *Phys. Rev. Lett.* 120, 227401.
- [31] Grebenshchikov S. Yu., Picconi D. (2017) Fano resonances in the photoinduced H-atom elimination dynamics in the πσ* states of pyrrole, Phys. Chem. Chem. Phys. 19, 14902– 14906.
- [32] Picconi D. (2021) Nonadiabatic quantum dynamics of the coherent excited state intramolecular proton transfer of 10-hydroxybenzo[h]quinoline, *Photochem. Photobiol. Sci.* 20, 1455–1473.
- [33] Child M. S., Bernstein R. B. (2003) Diatomic interhalogens: Systematics and implications of spectroscopic interatomic potentials and curve crossings, J. Chem. Phys. 59, 5916–5925.
- [34] Kobayashi Y., Chang K. F., Zeng T., Neumark D. M., Leone S. R. (2019) Direct mapping of curve-crossing dynamics in IBr by attosecond transient absorption spectroscopy, *Science* 365, 79–83.
- [35] Domcke W., Yarkony D. R. (2012) Role of conical intersections in molecular spectroscopy and photoinduced chemical dynamics. Annu. Rev. Phys. Chem. 63, 325–352.
- [36] Mukamel S. (1999) Principles of nonlinear optical spectroscopy. Oxford University Press.
- [37] Tannor D. J. (2018) Introduction to quantum mechanics: A time-dependent perspective. University Science Books.
- [38] Heller E. J. (1981) The semiclassical way to molecular spectroscopy, Acc. Chem. Res. 14, 368–375.
- [39] Heller E. J. (2018) The semiclassical way to dynamics and spectroscopy. Princeton University Press, Princeton.
- [40] Tal-Ezer H., Kosloff R. (1984) An accurate and efficient scheme for propagating the time dependent Schrödinger equation, J. Chem. Phys. 81, 3967–3971.
- [41] Park T. J., Light J. C. (1986) Unitary quantum time evolution by iterative Lanczos reduction, J. Chem. Phys. 85, 5870–5876.
- [42] Beck M., Jäckle A., Worth G., Meyer H.-D. (2000) The multiconfiguration time-dependent Hartree (MCTDH) method: A highly efficient algorithm for propagating wavepackets, *Phys. Rep.* 324, 1–105.
- [43] Colbert D. T., Miller W. H. (1992) A novel discrete variable representation for quantum mechanical reactive scattering via the S-matrix Kohn method, J. Chem. Phys. 96, 1982–1991.
- [44] Palacino-González E., Gelin M. F., Domcke W. (2017) Theoretical aspects of femtosecond double-pump single-molecule spectroscopy. II. Strong-field regime, *Phys. Chem. Chem. Phys.* 19, 32307.
- [45] Soh J. H., Jansen T. L. C., Palacino-González E. (2024) Controlling the nonadiabatic dynamics of the charge-transfer process with chirped pulses: Insights from a double-pump time-resolved fluorescence spectroscopy scheme, J. Chem. Phys. 160, 024110.
- [46] Picconi D., Burghardt I. (2020) Time-resolved spectra of I2 in a krypton crystal by G-MCTDH simulations: Nonadiabatic dynamics, dissipation and environment driven decoherence, Faraday Discuss. 221, 30.
- [47] Meyer H.-D., Manthe U., Cederbaum L. (1990) The multi-configurational time-dependent Hartree approach, Chem. Phys. Lett. 165, 73–78.
- [48] Worth G. A., Meyer H., Cederbaum L. S. (1996) The effect of a model environment on the S2 absorption spectrum of pyrazine: A wave packet study treating all 24 vibrational modes, J. Chem. Phys. 105, 4412–4426.
- [49] Beck M., Meyer H.-D. (1997) An efficient and robust integration scheme for the equations of motion of the multiconfiguration time-dependent Hartree (MCTDH) method, Z. Phys. D -Atoms Mol. Clusters 42, 113–129.
- [50] Meyer H.-D., Wang H. (2018) On regularizing the MCTDH equations of motion, J. Chem. Phys. 148, 124105.

- [51] Mendive-Tapia D., Meyer H.-D. (2020) Regularizing the MCTDH equations of motion through an optimal choice on-the-fly (i.e., spawning) of unoccupied single-particle functions, J. Chem. Phys. 153, 234114.
- [52] Popp W., Polkehn M., Binder R., Burghardt I. (2019) Coherent charge transfer exciton formation in regionegular P3HT: A quantum dynamical study, J. Phys. Chem. Lett. 10, 3326– 3332.
- [53] Wang H., Thoss M. (2003) Multilayer formulation of the multiconfiguration time-dependent Hartree theory, J. Chem. Phys. 119, 1289–1299.
- [54] Mendive-Tapia D., Meyer H.-D., Vendrell O. (2023) Optimal mode combination in the multiconfiguration time-dependent Hartree method through multivariate statistics: Factor analysis and hierarchical clustering, J. Chem. Theor. Comput. 19, 1144–1156.
- [55] Oseledets I. V. (2011) Tensor-train decomposition, SIAM J. Sci. Comput. 33, 2295–2317.
- [56] White S. R. (1992) Density matrix formulation for quantum renormalization groups, Phys. Rev. Lett. 69, 2863–2866.
- [57] Borrelli R., Gelin M. F. (2021) Finite temperature quantum dynamics of complex systems: Integrating thermo-field theories and tensor-train methods, WIREs Comput. Mol. Sci. 11, e1539.
- [58] Dorfner M. F. X., Brey D., Burghardt I., Ortmann F. (2024) Comparison of matrix product state and multiconfiguration time-dependent Hartree methods for nonadiabatic dynamics of exciton dissociation, J. Chem. Theor. Comput. 20, 8767.
- [59] Haegeman J., Cirac J. I., Osborne T. J., Pižorn I., Verschelde H., Verstraete F. (2011) Time-dependent variational principle for quantum lattices, *Phys. Rev. Lett.* 107, 070601.
- [60] Ren J., Li W., Jiang T., Wang Y., Shuai Z. (2022) Time-dependent density matrix renormalization group method for quantum dynamics in complex systems, WIREs Comput. Mol. Sci. 12, e1614.
- [61] Heller E. J. (1975) Time-dependent approach to semiclassical dynamics, J. Chem. Phys. 62, 1544–1555.
- [62] Worth G. A., Robb M. A., Burghardt I. (2004) A novel algorithm for non-adiabatic direct dynamics using variational Gaussian wavepackets, Faraday Discuss. 127, 307–323.
- [63] Burghardt I., Meyer H.-D., Cederbaum L. S. (1999) Approaches to the approximate treatment of complex molecular systems by the multiconfiguration time-dependent Hartree method, J. Chem. Phys. 111, 2927–2939.
- [64] Zhao Y., Sun K., Chen L., Gelin M. (2022) The hierarchy of Davydov's Ansätze and its applications, WIREs Comput. Mol. Sci. 12, e1589.
- [65] Richings G., Polyak I., Spinlove K., Worth G., Burghardt I., Lasorne B. (2015) Quantum dynamics simulations using Gaussian wavepackets: The vMCG method, *Int. Rev. Phys. Chem.* 34, 269–308.
- [66] Joubert-Doriol L. (2022) Variational approach for linearly dependent moving bases in quantum dynamics: Application to Gaussian functions, J. Chem. Theor. Comput. 18, 5799.
- [67] Burghardt I., Nest M., Worth G. A. (2003) Multiconfigurational system-bath dynamics using Gaussian wave packets: Energy relaxation and decoherence induced by a finite-dimensional bath, J. Chem. Phys. 119, 5364–5378.
- [68] Picconi D., Cina J. A., Burghardt I. (2019) Quantum dynamics and spectroscopy of dihalogens in solid matrices. I. Efficient simulation of the photodynamics of the embedded I₂Kr₁₈ cluster using the G-MCTDH method, J. Chem. Phys. 150, 064111.
- [69] Curchod B. F. E., Martínez T. J. (2018) Ab initio nonadiabatic quantum molecular dynamics, Chem. Rev. 118, 3305.
- [70] Shalashilin D. V., Child M. S. (2004) The phase space ccs approach to quantum and semiclassical molecular dynamics for high-dimensional systems, *Chem. Phys.* 304, 103–120, towards Multidimensional Quantum Reaction Dynamics.
- [71] Martínez T. J., Ben-Nun M., Levine R. D. (1996) Multi-electronic-state molecular dynamics: A wave function approach with applications, J. Phys. Chem. 100, 7884–7895.

- [72] Ben-Nun M., Quenneville J., Martínez T. J. (2000) Ab initio multiple spawning: Photochemistry from first principles quantum molecular dynamics, J. Phys. Chem. A 104, 5161–5175.
- [73] Ben-Nun M., Martínez T. J. (2002) Adv. Chem. Phys. John Wiley & Sons, Ltd, pp. 439-512.
- [74] Curchod B. F. E. (2020) Quantum chemistry and dynamics of excited states. John Wiley & Sons, Ltd, Chapter 14, pp. 435–467.
- [75] Picconi D., Menger M. F. S. J., Palacino-González E., Salazar E. X., Faraji S. (2025) Implementation of quantum-classical mapping approaches for nonadiabatic molecular dynamics in the PySurf package, Phys. Chem. Chem. Phys., Accepted Manuscript, DOI: 10.1039/D5CP01194A.
- [76] Tully J. C. (1990) Molecular dynamics with electronic transitions, J. Chem. Phys. 93, 1061– 1071.
- [77] Granucci G., Persico M. (2007) Critical appraisal of the fewest switches algorithm for surface hopping, J. Chem. Phys. 126, 134114.
- [78] Zachos C. K., Fairlie D. B., Curtright T. L. (2005) Quantum mechanics in phase space. World Scientific.
- [79] Case W. B. (2008) Wigner functions and Weyl transforms for pedestrians, Am. J. Phys. 76, 937–946.
- [80] Kapral R., Ciccotti G. (1999) Mixed quantum-classical dynamics, J. Chem. Phys. 110, 8919–8929.
- [81] Schwinger J. (1965) Quantum theory of angular momentum (L. C. Biedenharn, H. V. Dam, Eds). Academic, New York.
- [82] Meyer H., Miller W. H. (1979) A classical analog for electronic degrees of freedom in nonadiabatic collision processes, J. Chem. Phys. 70, 3214–3223.
- [83] Stock G., Thoss M. (1997) Semiclassical description of nonadiabatic quantum dynamics, Phys. Rev. Lett. 78, 578–581.
- [84] Saller M. A. C., Kelly A., Richardson J. O. (2020) Improved population operators for multi-state nonadiabatic dynamics with the mixed quantum-classical mapping approach, Faraday Discuss. 221, 150–167.
- [85] Sun X., Wang H., Miller W. H. (1998) Semiclassical theory of electronically nonadiabatic dynamics: Results of a linearized approximation to the initial value representation, J. Chem. Phys. 109, 7064-7074.
- [86] Kim H., Nassimi A., Kapral R. (2008) Quantum-classical Liouville dynamics in the mapping basis, J. Chem. Phys. 129, 084102.
- [87] Saller M. A. C., Kelly A., Richardson J. O. (2019) On the identity of the identity operator in nonadiabatic linearized semiclassical dynamics, J. Chem. Phys. 150, 071101.
- [88] Runeson J. E., Richardson J. O. (2019) Spin-mapping approach for nonadiabatic molecular dynamics, J. Chem. Phys. 151, 044119.
- [89] Liu Z., Lyu N., Hu Z., Zeng H., Batista V. S., Sun X. (2024) Benchmarking various nonadiabatic semiclassical mapping dynamics methods with tensor-train thermo-field dynamics, J. Chem. Phys. 161, 024102.
- [90] Mannouch J. R., Richardson J. O. (2023) A mapping approach to surface hopping, J. Chem. Phys. 158, 104111.
- [91] Runeson J. E., Manolopoulos D. E. (2023) A multi-state mapping approach to surface hopping, J. Chem. Phys. 159, 094115.
- [92] Lawrence J. E., Mannouch J. R., Richardson J. O. (2024) A size-consistent multi-state mapping approach to surface hopping, J. Chem. Phys. 160, 244112.
- [93] Worth G. (2020) Quantics: A general purpose package for quantum molecular dynamics simulations, Comp. Phys. Comm. 248, 107040.
- [94] Menger M. F. S. J., Ehrmaier J., Faraji S. (2020) Pysurf: A framework for database accelerated direct dynamics, J. Chem. Theor. Comput. 16, 7681–7689.
- [95] Belyaev A. K., Lebedev O. V. (2011) Nonadiabatic nuclear dynamics of atomic collisions based on branching classical trajectories, Phys. Rev. A 84, 014701.

- [96] Cattarius C., Worth G. A., Meyer H.-D., Cederbaum L. S. (2001) All mode dynamics at the conical intersection of an octa-atomic molecule: Multi-configuration time-dependent Hartree (MCTDH) investigation on the butatriene cation, J. Chem. Phys. 115, 2088–2100.
- [97] Shalashilin D. V. (2010) Nonadiabatic dynamics with the help of multiconfigurational Ehrenfest method: Improved theory and fully quantum 24D simulation of pyrazine, J. Chem. Phys. 132, 244111.
- [98] Römer S., Burghardt I. (2013) Towards a variational formulation of mixed quantum-classical molecular dynamics, Mol. Phys. 111, 3618–3624.
- [99] Horenko I., Salzmann C., Schmidt B., Schütte C. (2002) Quantum-classical Liouville approach to molecular dynamics: Surface hopping Gaussian phase-space packets, J. Chem. Phys. 117, 11075–11088.
- [100] Donoso A., Martens C. C. (2002) Classical trajectory-based approaches to solving the quantum Liouville equation, Int. J. Quant. Chem. 90, 1348–1360.
- [101] Roman E., Martens C. C. (2007) Independent trajectory implementation of the semiclassical Liouville method: Application to multidimensional reaction dynamics, J. Phys. Chem. A 111, 10256–10262.
- [102] Huo P., Coker D. F. (2011) Communication: Partial linearized density matrix dynamics for dissipative, non-adiabatic quantum evolution, J. Chem. Phys. 135, 201101.
- [103] Hsieh C.-Y., Kapral R. (2012) Nonadiabatic dynamics in open quantum-classical systems: Forward-backward trajectory solution, J. Chem. Phys. 137, 22A507.
- [104] Min S. K., Agostini F., Gross E. K. U. (2015) Coupled-trajectory quantum-classical approach to electronic decoherence in nonadiabatic processes, *Phys. Rev. Lett.* 115, 073001.

Chapter 3

Open Quantum System Simulation of Time and Frequency Resolved Spectroscopy

Tobias Kramer*

Institute for Theoretical Physics, Department of Quantum and Classical Dynamics, Johannes Kepler Universität Linz, Austria

*e-mail: tobias.kramer@jku.at

Abstract

The dynamics of excitonic energy transfer in molecular complexes triggered by interaction with laser pulses offer a unique window into the underlying physical processes. The absorbed energy moves through the network of interlinked pigments and, in photosynthetic complexes, reaches a reaction center. The efficiency and time scale depend not only on the excitonic couplings but are also affected by the dissipation of energy to vibrational modes of the molecules. An open quantum system description provides a suitable tool to describe the involved processes and connects the decoherence and relaxation dynamics to measurements of the time-dependent polarization.

3.1 Introduction

This lecture note reviews how to perform detailed calculations of the dynamics in open quantum systems with applications to energy transfer in light-harvesting complexes. The approach relies on the Frenkel exciton description of excitonic energy transfer. For an introduction to the Frenkel exciton picture from a molecular theory perspective, we refer to the monograph by May and Kühn [1], as well as other relevant materials from this book, in particular chapters 5 and 6.

DOI: 10.1051/978-2-7598-3760-1.c003 © The authors, 2025 Section 3.2 reviews the open quantum system approach and in section 3.3, we compare different solution methods. Section 3.4 describes the computation of optical spectra, while section 3.5 reviews the ensemble averages required to compare with experimental data. As a well-studied light-harvesting complex with a known atomistic structure, we focus exemplary calculations in section 3.6 on the Fenna-Matthews-Olson (FMO) complex. Its structure model, derived from experimental observations on crystallized complexes, is detailed in the seminal works by Olson et al. [2] and Fenna and Matthews [3]. Parameters for the corresponding Frenkel exciton model have been derived by Adolphs and Renger [4].

3.2 Open Quantum System Dynamics

To describe the dynamics of an electronic excitation in an LHC, the concept of an open quantum system is employed. A comprehensive introduction to open quantum system dynamics can be found in [5], and a concise overview of the notation applicable to LHC is provided in [1]. For the purpose of defining the fundamental quantities of interest, this section closely follows the approach outlined in [6, 7]. The photosynthetic complex, which interacts with light, is described using the Frenkel exciton model. In this model, the system is characterized by the Hamiltonian given by equation (1):

$$H(t) = H_{\rm g} + H_{\rm ex} + H_{\rm bath} + H_{\rm ex-bath} + H_{\rm field}(t). \tag{1}$$

The first term, denoted as $H_{\rm g} = \varepsilon_0 |0\rangle\langle 0|$, represents the ground state Hamiltonian with a ground state energy of ε_0 . The second term, $H_{\rm ex}$, incorporates the excitation energies of each pigment and the inter-pigment couplings. Additionally, the vibrational modes of each pigment are introduced through the inclusion of $H_{\rm bath}$. In this model, the vibrations are linearly coupled to the excitons $via\ H_{\rm ex-bath}$. When expressed in bra-ket notation, the excitonic Hamiltonian $H_{\rm ex}$ is formulated for a system comprising $N_{\rm sites}$ pigments (referred to as sites) as follows in the site basis $(H_{\rm ex}^{\rm site})$:

$$H_0^{\rm site} = \sum_{m=1}^{N_{\rm sites}} \varepsilon_m^0 |m\rangle\langle m| + \sum_{n \neq m} J_{mn} |m\rangle\langle n|, \quad H_{\rm ex}^{\rm site} = H_0^{\rm site} + \sum_{m=1}^{N_{\rm sites}} \sum_{v=1}^{V_m} \lambda_{m,v} |m\rangle\langle m|. \quad (2)$$

The site energy $\varepsilon_m = \varepsilon_m^0 + \sum_{v=1}^{V_m} \lambda_{m,v}$ consists of the zero phonon energy ε_m^0 plus the reorganization energy $\sum_v \lambda_{m,v}$. The inter-site couplings are denoted by J_{mn} . The vibrational states of the pigments are described by $B = \sum_m V_m$ independent baths, where several baths can be assigned to the same pigment to either represent a more complex spectral density or to describe states representing two excitons at different sites. Non-diagonal (site $m \neq n$) couplings between a state $|m\rangle\langle n|$ and baths are not considered here. The V_m baths are represented by a Hamiltonian $H_{\text{bath},m,v} = \sum_i \hbar \omega_{m,v,i} (b_{m,v,i}^{\dagger} b_{m,v,i} + \frac{1}{2})$ which consist of harmonic oscillators with frequencies $\omega_{m,v,i}$. The bosonic creation and annihilation operators $b_{m,v,i}$ are specified for each

pigment m. Finally, the linear coupling to the excitons is written in terms of the linear displacement of each bath mode $(b_{m,v,i}^{\dagger} + b_{m,v,i})$:

$$H_{\text{ex-bath}} = \sum_{m} |m\rangle\langle m| \otimes \sum_{v} \sum_{i} \hbar \omega_{m,v,i} d_{mvi} (b_{m,v,i}^{\dagger} + b_{m,v,i}), \tag{3}$$

Here, d_{mvi} denotes the coupling strength, which for a continuous spectrum of oscillator frequencies is expressed as the spectral density of vibrational modes

$$J_{m,v}(\omega) = \pi \sum_{i} \hbar^{2} \omega_{mvi}^{2} d_{mvi}^{2} \delta(\omega - \omega_{mvi}). \tag{4}$$

The spectral density is also connected to the reorganization energy

$$\lambda_{m,v} = \int_0^\infty \frac{J_{m,v}(\omega)}{\pi \omega} d\omega. \tag{5}$$

The Liouville-von Neumann equation describes the dynamics of an open quantum system in terms of the full (system and bath) density matrix $\rho^{\text{total}}(t)$:

$$\frac{\partial}{\partial t} \rho^{\text{total}}(t) = -\frac{\mathrm{i}}{\hbar} [H(t), \rho^{\text{total}}(t)]. \tag{6}$$

For the description of the excitonic degrees of freedom and the optical response of the system to light pulses, the vibrational degrees of freedom are traced out. The remaining reduced density matrix $\rho(t)$ becomes

$$\rho(t) = \text{Tr}_{\text{bath}} \left[\rho^{\text{total}}(t) \right]. \tag{7}$$

The reduced density matrix is, in general, evolving in a non-unitary fashion, in contrast to the total density matrix.

3.3 Exact vs. Approximate Solution

The density matrix of an isolated system (*i.e.*, without coupling to vibrations) undergoes coherent dynamics. Decoherence and relaxation is brought into the system dynamics by the specifics of the coupling to vibrational modes, which affects the system dynamics. We use a parametrization of the vibrational modes introduced in [8] and implemented in [9] and [7, 10]. To describe a frequency-dependent vibrational bath, we use a superposition of (shifted) Drude-Lorentz peaks assigned to each site:

$$J_{m}(\omega) = \sum_{v=1}^{V_{m}} \left(\frac{\lambda_{m,v} \omega v_{m,v}}{\left(\omega - \Omega_{m,v}\right)^{2} + v_{m,v}^{2}} + \frac{\lambda_{m,v} \omega v_{m,v}}{\left(\omega + \Omega_{m,v}\right)^{2} + v_{m,v}^{2}} \right). \tag{8}$$

Here, $v_{m,v}^{-1}$ denotes the inverse bath correlation time, and the parameter $\Omega_{m,v}$ shifts the peak position of the spectral density and allows one to vary the pure dephasing and relaxation processes while maintaining the reorganization energy $\lambda_{m,v}$ [6, 8].

There are several methods available to evolve a reduced density matrix of a system linearly coupled to a bath, as given by equation (2), to various degrees of

approximation. For arbitrary coupling λ , the solution requires numerical methods, such as the Hierarchical Equation Of Motion (HEOM) [11, 12]. The HEOM method serves as the standard reference for comparing with other methods, including the quasi-adiabatic path integral QUAPI [13] and various stochastic methods. A Mathematica implementation of HEOM is available online at [14] as a reference implementation for demonstrating the algorithm. We discuss high-performance implementations of HEOM in section 3.6, which are suitable for computing quantum dynamics and optical response functions in larger systems (up to 100 sites).

3.3.1 Weak Coupling Limit: Redfield Equations

To explore the dynamics of the coupled system, it is useful to consider first only a weak system-bath coupling (small λ compared to the eigenenergy differences). In this limit, the Redfield equation provides a suitable approximation (a concise derivation can be found in [15, 16]). When a system is coupled to a thermal environment, it eventually reaches an equilibrium state where both the system and the environment share a common temperature. The timescale for thermalization is inversely proportional to the relaxation rate. The Redfield approach reveals that, in the case of weak coupling, the relaxation rate depends on the spectral density value at the energy difference between two energy eigenstates. Under weak coupling conditions, the system and environment can be considered as forming a product state, with entanglement considered as a negligible perturbation (Born approximation).

The Redfield tensor R is commonly expressed in the energy representation, which is connected to the site representation through the diagonalizing matrix A:

$$H^{\text{exc}} = AH^{\text{site}}A^{T}.$$
 (9)

In the energy basis, the matrix H^{exc} only has diagonal entries, with $i = 1, ..., N_{\text{sites}}$ representing the eigenenergies $E_i = \hbar \omega_i$. The Redfield tensor is then entirely determined by the (in general site dependent) bath correlation function $C_m(\omega)$, which in turn depends on the spectral density (as described below):

$$R_{\mu\nu\mu'\nu'} = \Gamma_{\mu\nu\mu'\nu'} + (\Gamma_{\mu\nu\mu'\nu'})^* - \delta_{\nu\nu'} \sum_{\kappa=1}^{N_{\text{sites}}} \Gamma_{\mu\kappa\kappa\mu'} - \delta_{\mu\mu'} \sum_{\kappa=1}^{N_{\text{sites}}} \Gamma_{\nu\kappa\kappa\nu'}, \tag{10}$$

$$\Gamma_{\mu\nu\mu'\nu'} = \frac{1}{\hbar^2} \sum_{m=1}^{N_{\text{sites}}} A_{\mu m} A_{\nu m} A_{\mu' m} A_{\nu' m} C_m (\omega_{\nu'} - \omega_{\mu'}), \tag{11}$$

The Fourier transform of the bath correlation function at temperature T $(\beta = 1/(k_B T))$ is given by

$$C_m(t) = \frac{1}{\pi} \int_0^\infty d\omega J_m(\omega) \left[n(\omega, \beta) e^{i\omega t} + (n(\omega, \beta) + 1) e^{-i\omega t} \right]$$
 (12)

$$= \frac{1}{\pi} \int_{-\infty}^{\infty} d\omega J_m(\omega) n(\omega, \beta) e^{i\omega t}, n(\omega, \beta) = 1/(e^{\beta\hbar\omega} - 1).$$
 (13)

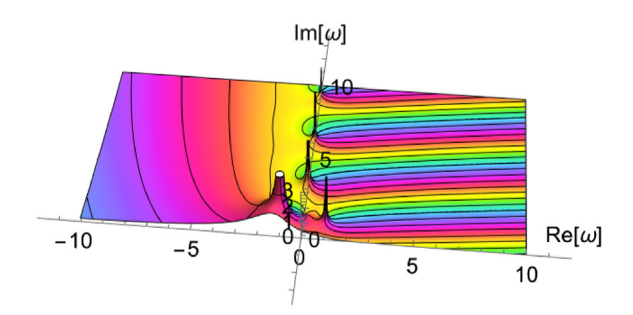


Fig. 3.1 – Visualization of the integrand $c(\omega) = J(\omega)n(\omega,\beta)e^{i\omega t}$ of $C(t) = \int_{-\infty}^{\infty} c(\omega)d\omega$ in the complex ω plane in the domain $-10 < \Re\omega < 10$ and $0 < \Im\omega < 10$. To obtain C(t), the integration path along the real ω -axis is deformed and closed by a semi-circular contour in the positive imaginary ω -plane. This new path encloses an infinite number of poles, which yield the result of the integration by a sum of the residues at the poles, multiplied by $2\pi i$.

The integrand of equation (13) is depicted in figure 3.1. For the spectral density in equation (8), it is expressed in terms of the Digamma function F (we surppress the index m for compactness):

$$C(\omega) = -\frac{i\lambda\hbar}{2} \left[\frac{v_{+}(-\omega + iv_{-})\cot(\frac{1}{2}\beta v_{+}\hbar) + iv_{-}(v + i\omega_{+})\cot(\frac{1}{2}\beta v_{-}\hbar) - 2(v^{2} + iv\omega + \Omega^{2})}{\Omega^{2} + (v + i\omega)^{2}} + \frac{iv_{+}(v^{2} + \omega_{+}^{2})F(\frac{\beta v_{+}\hbar}{2\pi} + 1)}{\pi(v - i\omega_{-})(v^{2} + \omega_{+}^{2})} + \frac{iv_{-}(v_{+}^{2} + \omega^{2})F(\frac{\beta v_{-}\hbar}{2\pi} + 1) - iv_{+}(\Omega^{2} + (v - i\omega)^{2})F(1 - \frac{\beta v_{+}\hbar}{2\pi})}{\pi(v - i\omega_{-})(v^{2} + \omega_{+}^{2})} + \frac{2v\omega(\frac{1}{v^{2} + \omega_{+}^{2}} + \frac{1}{v^{2} + \omega_{-}^{2}})F(1 + \frac{i\beta\omega\hbar}{2\pi})}{\pi} + \frac{v_{-}F(1 - \frac{\beta v_{-}\hbar}{2\pi})}{\pi(-\omega + iv_{-})} \right],$$
(14)

$$v_{\pm} = v \pm i\Omega \tag{15}$$

$$\omega_{+} = \omega \pm i\Omega \tag{16}$$

The last relation can be computed by using the residues theorem for C(t) and by performing the Fourier transformation $(t \to \omega)$ term by term. The Redfield tensor is then evaluated in terms of $C(\omega)$ values, and the time evolution of the density matrix elements $\rho_{\mu\nu}$ in the energy representation of the exciton Hamiltonian (2) is a solution to the following differential full Redfield equation:

$$\frac{\partial \rho_{\mu\nu}^{\text{exc}}(t)}{\partial t} = -\mathrm{i}(\omega_{\mu} - \omega_{\nu})\rho_{\mu\nu}^{\text{exc}}(t) + \sum_{\mu'=1}^{N_{\text{states}}} \sum_{\nu'=1}^{N_{\text{states}}} R_{\mu\nu,\mu'\nu'}\rho_{\mu'\nu'}^{\text{exc}}(t). \tag{17}$$

The first term in equation (17) represents the coherent evolution governed by the diagonalized Hamiltonian, while the second term accounts for decoherence and relaxation resulting from the coupling to the baths. To simplify the equations further, we can use the secular Redfield approximation. In this approximation, all entries that do not satisfy the condition $(\omega_{\mu} - \omega_{\nu}) = (\omega_{\mu'} - \omega_{\nu'})$ are set to zero. This approximation is employed to address the violation of positive definiteness in the density matrix that can occur at low temperatures when using the full Redfield equations. A detailed comparison of the dynamics obtained using the full and secular Redfield equations is presented in [7].

To compare the results with the reduced density matrix obtained from HEOM in the site basis, we need to transform the Redfield density matrix from the energy basis back to the site representation:

$$\rho_{\text{Redfield}}^{\text{site}}(t) = A^T \rho_{\text{Redfield}}^{\text{exc}}(t) A. \tag{18}$$

3.3.2 Strong Coupling Limit: Förster Energy Transfer and Rate Equations

The Redfield description relies on a weak coupling between the system and bath (λ small compared to eigenenergy differences). In the opposite case, for a very strong coupling, Förster theory provides an alternative approach to compute the quantum dynamics. The Förster expression for the rate **R** in site basis reads [17]

$$R_{m,n}^{\text{F\"{o}rster}} = 2|J_{mn}|\Re\left[\int_0^\infty dt F_m^*(t) A_n(t)\right],\tag{19}$$

with

$$A_n(t) = \exp[-i(\epsilon_n^0 + \lambda_n)t - g_n(t)], \tag{20}$$

$$F_m^*(t) = \exp[+\mathrm{i}(\epsilon_m^0 - \lambda_m)t - g_m(t)],\tag{21}$$

$$g_m(t) = -\frac{1}{2\pi} \int_{-\infty}^{\infty} d\omega \frac{J_m(\omega)}{\omega^2} (1 + \coth(\beta \hbar \omega/2)) (e^{-i\omega t} + i\omega t - 1).$$
 (22)

The Förster rate is therefore determined by the overlap of absorption (A) and emission (F) spectra of the monomers, computed using the lineshape function g(t) [18]. The lineshape function is, in turn, given as double integral of the bath correlation function C(t) [19]

$$g(t) = \int_0^t d\tau_1 \int_0^{\tau_1} d\tau_2 C(\tau_2).$$
 (23)

The last relation connects the spectral density of a monomeric unit to the absorption spectrum at very low temperatures *via* the lineshape function. An experimental determination of the spectral density of the FMO complex from fluorescence

line-narrowing measurements is performed in [20]. The population dynamics in Förster theory is then given by

$$\rho_{mm}(t) = \rho_{mm}(0)e^{\mathbf{K}t},\tag{24}$$

$$K_{\alpha\alpha} = -\sum_{\gamma=1, \gamma \neq \alpha}^{N} R_{\gamma\alpha}^{\text{F\"{o}rster}}, \tag{25}$$

$$K_{\alpha\beta} = R_{\alpha\beta}^{\text{F\"{o}rster}}, (\alpha \neq \beta)$$
 (26)

For the shifted Drude Lorentz spectral density (8), an analytic expression for the bath-correlation and lineshape function can be computed using *Mathematica*:

While Redfield and Förster theories correspond respectively to the limiting cases of weak or strong coupling of the system to the thermal environment, the HEOM method developed by Kubo and Tanimura [11] provides the connection between

both regimes and, in addition, covers both limits [16]. Within HEOM, the time evolution of the reduced density matrix is described by a system of interlinked differential equations comprising $N_{\rm matrices}$ auxiliary density matrices σ_u of dimensions $N_{\rm states} \times N_{\rm states}$. The auxiliary density matrices (also referred to auxiliary density operators (ADO)) are put in separate layers with a specific depth index D. The matrices in different layers are connected by vertices with +-upward and --downward connecting links.

$$\frac{\mathrm{d}\sigma_u}{\mathrm{d}t} = -\frac{\mathrm{i}}{\hbar}[H, \sigma_u] + \sum_{\text{baths}} A\sigma_u + \sum_{\text{baths}} B\sigma_{u_+} + \sum_{\text{baths}} C\sigma_{u_-}.$$
 (27)

Explicit expressions for the operators A, B, C are given in [21] and [7], equations (12)–(36). The number of matrices in each layer increases with the layer depth D, whereas the top-layer contains as unique member the reduced density matrix σ_0 . The layer links are the result of a series expansion of the exponentially decaying bath correlation function and thus contains with increasing depth increasingly higher derivatives. The HEOM depth has to be carefully chosen to guarantee a converged result. For the parameters encountered in the FMO complex this implies that only the first few layers are required (D=2-3) at T=300 K [7]. For lower temperatures or a stronger system-bath coupling, the total number of matrixes increases and is given by

$$N_{\text{matrices}} = \binom{MB+D}{MB},\tag{28}$$

where B denotes the number of vibrational baths B, and M the number of Matsubara modes M [7]. In practise this large number of matrices limits the HEOM method for computing exciton dynamics to systems with less than 100 pigments. A detailed comparison of Förster theory with HEOM in the Photosystem I complex [22] shows that the aggregated transfer times from the A-B branch within the Förster theory (9 ps) differ from the exact HEOM results in the presence of a mixture of small and large intersite couplings (17 ps).

3.3.3 Decoherence, Dephasing, and Relaxation Dynamics

Any initial coherence, which is expressed by an off-diagonal element of the density matrix in the energy representation, decays over a timescale determined by the decoherence rate $\gamma_{\rm decoh}$. The decoherence rate is set by two contributions $\gamma_{\rm decoh} = \gamma_{\rm pd} + \gamma_{\rm r}/2$, the pure dephasing rate $\gamma_{\rm pd}$ determined by the slope of the spectral density as it approaches $\omega \to 0$ and the relaxation rate $\gamma_{\rm r}$, given by the value of the spectral density at the difference of eigenenergies. For a two-site system, where each site is coupled to an independent bath at temperature T,

$$H_{\text{exciton}} = \begin{pmatrix} -\epsilon/2 & d/2 \\ d/2 & \epsilon/2 \end{pmatrix}, \tag{29}$$

the respective rates are ([23], section 21.4.2):

$$\begin{split} \gamma_{\rm r} &\approx \frac{d^2 J(\omega) {\rm coth}(\hbar\omega/(2k_BT))}{2(\epsilon^2+d^2)}\big|_{\omega=\sqrt{\epsilon^2+d^2}}, \\ \gamma_{\rm pd} &= \frac{\epsilon^2 J(\omega) {\rm coth}(\hbar\omega/(2k_BT))}{2(\epsilon^2+d^2)}\big|_{\omega\to 0}. \end{split}$$

An illustrative example is provided by a dimer, which is coupled to an environment. By choosing the form of the spectral density, one can fix the thermalization rate, while at the same time, the dephasing rate can be vastly different. This is demonstrated in figure 3.2, reprinted from [6]. For computing transport, the thermalization rate sets the timescale of how fast energy is transferred towards a thermal equilibrium state. Secular Redfield theory would predict a faster equilibration for a stronger coupling to the vibrational states (i.e., for increasing λ), while the non-perturbative methods (i.e., HEOM) show that there exists an optimal value for λ which supports the fastest thermalization (see [24–27]). Increasing λ prolongs the thermalization process again, as illustrated in figure 3.3. For comparison, also the full Redfield result is shown. The good agreement between secular Redfield and HEOM obtained for small reorganization energies relies on error compensation effects. Modified Redfield theory, by the inclusion of multi-phonon relaxation processes, is also able to describe this effect via rate equations, see, e.g., figure 2 in [17], but does not capture the dynamics of the coherences.

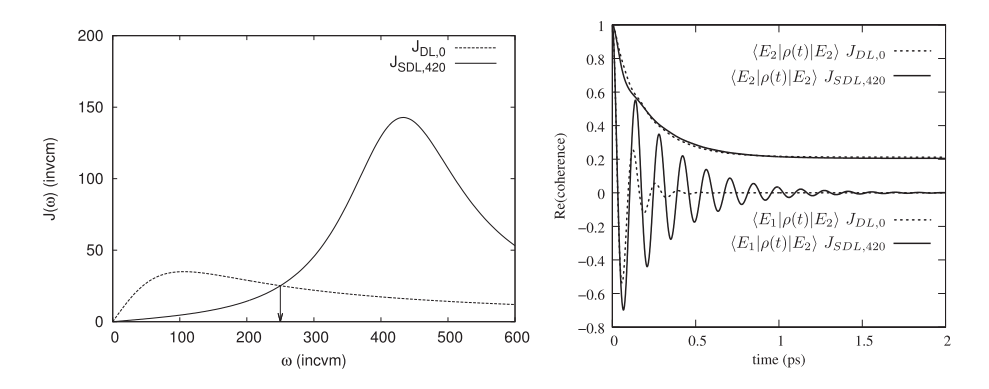


FIG. 3.2 – Left panel: Spectral density $J_{\text{DL},0}$ (unshifted Drude-Lorentz form, $\lambda=35~\text{cm}^{-1}$ and $v^{-1}=50~\text{fs}$) and $J_{\text{SDL},420}$ (shifted Drude-Lorentz peak, $\Omega=420~\text{cm}^{-1}$, $\lambda=35~\text{cm}^{-1}$ and $v^{-1}=50~\text{fs}$). The arrow indicates the difference of eigenenergies of a two-site system $H_{\text{ex}}=\begin{pmatrix} -75&100\\100&75 \end{pmatrix}\text{cm}^{-1}$, whereby construction both spectral densities have the same value. Right panel: Relaxation of the diagonal element $\langle E_2|\rho(t)|E_2\rangle$ to the thermal state (upper non-oscillatory graphs) and damped oscillations of the off-diagonal coherence $\text{Re}(\langle E_1|\rho(t)|E_2\rangle)$ at T=277~K. While both spectral densities give very similar relaxation rates, the off-diagonal coherence is much prolonged for $J_{\text{SDL},420}$ due to its small slope toward $\omega\to 0$. Reprinted from [6], figure 8, with the permission of AIP Publishing.

3.4 Computing Optical Spectra

The spectral density of the vibrational modes $J(\omega)$ directly influences the line widths computed for optical spectra. To model the creation of an exciton through optical excitation of the molecular complex, we introduce the interaction between an external electric field and the dipole moments of the molecules. This interaction is represented by the dipole operator [28]:

$$H_{\text{field}}(t) = -\sum_{p} \mathbf{e}_{p} \cdot \widehat{\boldsymbol{\mu}} E_{p}(\mathbf{r}, t). \tag{30}$$

Here, \mathbf{e}_p is the unit vector in the Cartesian electric field component $E_p(\mathbf{r}, t)$, and the dipole matrix operator is given by $\hat{\mathbf{\mu}} = \hat{\mathbf{\mu}}^+ + \hat{\mathbf{\mu}}^-$, where

$$\widehat{\mu}^{+} = \sum_{a=1}^{N_{\text{sites}}} \mathbf{d}_{a} |a\rangle\langle 0|, \tag{31}$$

$$\widehat{\mu}^{-} = \sum_{a=1}^{N_{\text{sites}}} \mathbf{d}_{a} |0\rangle\langle a|, = (\widehat{\mu}^{+})^{\dagger}.$$
(32)

To facilitate calculations, we decompose the real part of the time-varying electric field amplitude $E(\mathbf{r},t)=E^+(\mathbf{r},t)+E^-(\mathbf{r},t)$ into two complex amplitudes, where $E_p^-(\mathbf{r},t)=(E_p^+(\mathbf{r},t))^*$ and

$$E^{+}(\mathbf{r},t) = \tilde{E}(t-t_c)e^{\mathrm{i}(\omega_c t - \mathbf{k} \cdot \mathbf{r})}.$$
 (33)

In this expression, $\tilde{E}(t)$ represents the pulse envelope centered around time t_c , ω_c is the carrier frequency, and $\varphi = \mathbf{k} \cdot \mathbf{r}$ denotes the phase of the laser pulse. Using the rotating-wave approximation (RWA), the complex-valued electric field is combined with the respective excitation and de-excitation parts of the dipole operator [28, 29], reflecting energy conservation, that is, the excitation/de-excitation of the system is related to an annihilation/creation of a photon:

$$H_{\text{field}}(t) = -\sum_{p} \mathbf{e}_{p} \cdot [\widehat{\boldsymbol{\mu}}^{+} E_{p}^{-}(\mathbf{r}, t) + \widehat{\boldsymbol{\mu}}^{-} E_{p}^{+}(\mathbf{r}, t)]. \tag{34}$$

To obtain the optical spectra, we examine the time-dependent optical response of the molecular complex, specifically the non-linear polarization P(t) induced by a single or a combination of weak probe laser pulses. The time-dependent polarization is given by:

$$P(t) = \text{Tr}_{\text{system}}(\text{Tr}_{\text{bath}}(\rho_{\text{total}}(t))\widehat{\mu}^+), \quad \rho_{\text{total}}(t=0) = |0\rangle\langle 0| \otimes \rho_{\text{bath}}$$
 (35)

$$= \operatorname{Tr}_{\text{system}}(\rho(t)\widehat{\mu}^{+}), \qquad \qquad \rho(t) = \operatorname{Tr}_{\text{bath}}(\rho_{\text{total}}(t)), \qquad (36)$$

where $\rho(t)$ represents the time-evolved reduced density matrix following the time-dependent Hamiltonian (1). For weak laser pulses, the polarization function can be expanded in powers of the electric field [30] and written as a convolution of the electric field with the response function $S^{(n)}(t_n, \ldots, t_1)$ or calculated using a non-perturbative approach.

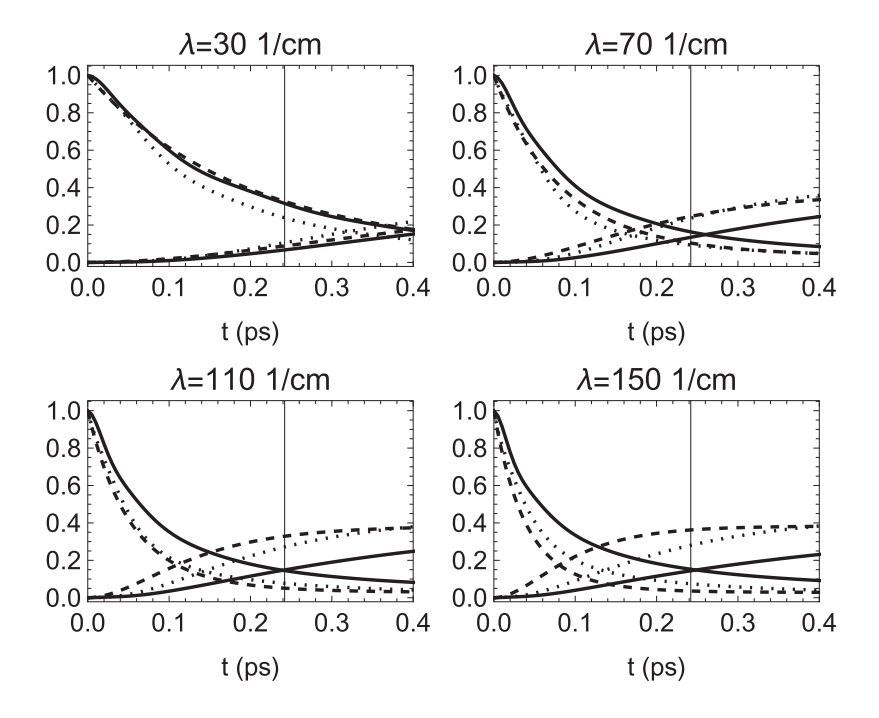


Fig. 3.3 – Quantum dynamics starting from the highest eigenstate of the FMO Hamiltonian [4] to the thermal state for various reorganization energies λ at T=277 K. Solid line: HEOM method (exact) population in exciton basis of the highest and lowest eigenstate populations, dashed line: secular Redfield theory, dotted line: full Redfield. HEOM shows there exists an optimal value of $\lambda \approx 110$ cm⁻¹ for the fastest thermalization (as seen by the crossing of the populations of both states, vertical line), while in the secular Redfield approximation (not applicable at strong couplings), a higher coupling always increases the thermalization rate.

A spectrometer records for a linear absorption spectrum the sum of the incoming electric field of the laser E_0 and the polarization-induced field E_{signal} via its absolute value after performing a Fourier transform:

$$I(\omega) = \left| \int_0^\infty dt e^{i\omega t} (E_0(t) + E_{\text{signal}}(t)) \right|^2 \propto I_0(\omega) + 2\Re \left[E_0(\omega) E_{\text{signal}}(\omega) \right]. \tag{37}$$

This expression neglects the weaker quadratic term due to the signal alone. To compute the spectra, the dipole operator, which accounts for the charge redistribution in the presence of an external electric field in each molecule of the complex, must be specified. For short pulses, it is a $(N_{\text{sites}} + 1) \times (N_{\text{sites}} + 1)$ dimensional matrix, as shown in equation (31). For a specific cartesian component p, it reads:

$$\widehat{\mu}_{p}^{+} = \sum_{m=1}^{N_{\text{sites}}} \mathbf{e}_{p} \cdot \mathbf{d}_{m} | m \rangle \langle 0 |.$$
(38)

For long enough pulses or multiple short pulses, it is possible to excite an additional exciton, necessitating the extension of the dipole representation to include two

exciton states. This enlarges the Hamiltonian and dipole matrix to $N_{\rm states}$ entries [31, 32]:

$$N_{\text{states}} = 1 + N_{\text{sites}} + [N_{\text{sites}}(N_{\text{sites}} - 1)]/2. \tag{39}$$

3.4.1 Linear Absorption Spectra

To compute the optical spectra, it is useful to employ the Fourier transform of the time evolution of the dipole correlation function, as described by [33] and earlier references therein. The Fourier transform allows us to obtain frequency-dependent spectra from the time-dependent trace.

First, we consider the linear absorption spectra, which result from a short initial excitation and can be obtained by Fourier transforming the dipole–dipole correlation function. To account for rotational averaging, we include the sum over polarization directions \mathbf{e}_p (as discussed in section 3.5). The linear absorption spectra $\langle \mathrm{LA}(\omega) \rangle_{\mathrm{rot}}$ is then expressed as:

$$\langle \mathrm{LA}(\omega) \rangle_{\mathrm{rot}} = \mathrm{Re} \sum_{p} \int_{0}^{\infty} \mathrm{d}t \exp(\mathrm{i}\omega t) \mathrm{Tr}[\widehat{\mu}_{p}(t)\widehat{\mu}_{p}(0)\rho(0)].$$
 (40)

Here, the dipole operators $\hat{\mu}_p(t)$ are calculated in the interaction picture [30], and the trace is taken over the system part only, as the trace over the environment is already considered in the reduced density matrix. At finite temperatures, the presence of decoherence and relaxation towards the thermal state results in a decay of the time-dependent polarization, which, in the frequency domain, corresponds to a finite line width. After the polarization vanishes, one can increase the range of time propagation by padding the time series of the polarization with zeroes to longer times. This increases the sampling of the frequency-resolved spectra.

3.4.2 Two-Dimensional Electronic Spectroscopy (2DES)

While the pure dephasing rate $\gamma_{\rm pd}$ determines the width of a single spectral line in the absorption spectra, the thermalization rate $\gamma_{\rm r}$ determines the time scale towards equilibrium of an initially excited state. Two-dimensional electronic spectroscopy (2DES) allows one to track the excitonic energy transfer and to investigate the energetic arrangement of site (pigment) energies.

This is achieved by a pump-probe setup involving a total of four pulses (including the signal pulse) and by scanning over a central interval (the time delay T_2) to observe the energy transfer. Formally, 2DES reveals the third-order non-linear response function, involving three commutators of the dipole operator acting at specific times $t_0=0$, t_1 , t_2 and a fourth dipole operator acting at t_3 representing the signal. In between the dipole operations, the reduced density matrix is propagated from $t_0=0$ to t_3 in $N_{\rm steps}$. The time traces of the response function in the first T_1 and last T_3 interval around the central interval are transformed to the frequency domain with two Fourier transforms $T_1 \to \omega_1$, $T_3 \to \omega_3$ [30, 34]. To obtain the 2DES in the $\omega_1 - \omega_3$ plane requires obtaining

first a time-dependent data set in the t_1, t_2 -plane for all times $t_i = i\Delta t$, with $i = 0, ..., N_{\text{steps}}$ and time-step Δt . The computation is performed for equidistantly spaced times $T_1 = 0, \Delta t, ..., t_1$ and $T_3 = 0, \Delta t, ..., (t_3 - t_2)$. This requirement increases the computational overhead by a factor N_{steps} compared to the calculation of absorption spectra. In the impulsive limit, the 2D spectra can be separated by an expansion in terms of products of the electric field of the different pulses with varying \mathbf{k} vectors. A separation into rephasing $(-\mathbf{k}_1 + \mathbf{k}_2 + \mathbf{k}_3)$ and non-rephasing directions $(+\mathbf{k}_1 - \mathbf{k}_2 + \mathbf{k}_3)$ results in three rephasing pathways and three non-rephasing pathways [30, 34] representing ground state bleaching (GB), stimulated emission (SE), and excited state absorption (ESA). In terms of the dipole operators at distinct times, the rephasing pathways are given by

$$S_{\text{GB,RP}}(T_3, T_2, T_1 | p_0, p_1, p_2, p_3) = +i \text{Tr}[\widehat{\mu}_{p_3}^-(t_3) \widehat{\mu}_{p_2}^+(t_2) \rho_0 \widehat{\mu}_{p_0}^-(0) \widehat{\mu}_{p_1}^+(t_1)]$$
(41)

$$S_{\text{SE,RP}}(T_3, T_2, T_1 | p_0, p_1, p_2, p_3) = +i \text{Tr}[\widehat{\mu}_{p_3}^-(t_3) \widehat{\mu}_{p_1}^+(t_1) \rho_0 \widehat{\mu}_{p_0}^-(0) \widehat{\mu}_{p_2}^+(t_2)]$$
(42)

$$S_{\text{ESA,RP}}(T_3, T_2, T_1 | p_0, p_1, p_2, p_3) = -i \text{Tr}[\widehat{\mu}_{p_3}^-(t_3) \widehat{\mu}_{p_2}^+(t_2) \widehat{\mu}_{p_1}^+(t_1) \rho_0 \widehat{\mu}_{p_0}^-(0)], \quad (43)$$

and the non-rephasing pathways are given by

$$S_{\text{GB,NR}}(T_3, T_2, T_1 | p_0, p_1, p_2, p_3) = +i \text{Tr}[\widehat{\mu}_{p_3}^-(t_3) \widehat{\mu}_{p_2}^+(t_2) \widehat{\mu}_{p_1}^-(t_1) \widehat{\mu}_{p_0}^+(0) \rho_0]$$
(44)

$$S_{\text{SE,NR}}(T_3, T_2, T_1 | p_0, p_1, p_2, p_3) = +i \text{Tr}[\widehat{\mu}_{p_3}(t_3) \widehat{\mu}_{p_0}^+(0) \rho_0 \widehat{\mu}_{p_1}^-(t_1) \widehat{\mu}_{p_2}^+(t_2)]$$
(45)

$$S_{\text{ESA,NR}}(T_3, T_2, T_1 | p_0, p_1, p_2, p_3) = -i \text{Tr}[\widehat{\mu}_{p_3}^-(t_3) \widehat{\mu}_{p_3}^+(t_2) \widehat{\mu}_{p_0}^+(0) \rho_0 \widehat{\mu}_{p_1}^-(t_1)]. \tag{46}$$

When working with a sequence of laser pulses with different relative polarizations, it is necessary to adjust the electric field polarizations p_0 , p_1 , p_2 , and p_3 accordingly. The ESA pathways access the two-exciton manifold [31, 32], which increases the number of states to propagate from $1+N_{\rm sites}$ to $N_{\rm states}=1+N_{\rm sites}+N_{\rm sites}(N_{\rm sites}-1)/2$ and increases the time required to compute the commutator and the bath interactions considerably. To obtain time- and frequency-resolved two-dimensional spectra for a specific delay time $T_2=(t_2-t_1)$, the third-order response function

$$S(T_3 = t_3 - t_2, T_2, T_1 = t_1) = S_{RP} + S_{NR}$$
 (47)

is computed separately for the three rephasing (RP) and non-rephasing (NR) pathways. The resulting spectra are then Fourier transformed with different signs of ω_1 , according to:

$$S_{\text{RP}}(\omega_3, T_2, \omega_1) = \int_0^\infty dT_1 \int_0^\infty dT_3 e^{-iT_1\omega_1 + iT_3\omega_3} S_{\text{RP}}(T_3, T_2, T_1)$$
(48)

$$S_{\rm NR}(\omega_3, T_2, \omega_1) = \int_0^\infty dT_1 \int_0^\infty dT_3 e^{+iT_1\omega_1 + iT_3\omega_3} S_{\rm NR}(T_3, T_2, T_1). \tag{49}$$

3.5 Ensemble Averages

3.5.1 Isotropic Average

In typical experiments, the ensemble of randomly oriented molecules is measured with respect to the laser direction and polarization plane. For linear spectroscopy, which records the first-order response function, rotational averaging is achieved by considering three representative electric fields along the Cartesian unit vectors:

$$e_1 = \{1, 0, 0\}, e_2 = \{0, 1, 0\}, e_3 = \{0, 0, 1\}.$$
 (50)

In two-dimensional spectra, rotational averaging becomes more involved due to the four dipole interactions involved. For laser pulses that share the same polarization plane, a set of ten representative electric field directions along the vertices of a dodecahedron suffices [32].

However, for more complex polarization sequences, up to twenty-one electric field combinations need to be considered. This tensorial averaging is implemented as follows [35, 36]

$$\langle S(T_3, T_2, T_1) \rangle_{\text{rot}} = \sum_{k=1}^{3} \sum_{l=1}^{3} \sum_{m=1}^{3} \sum_{n=1}^{3} C_{klmn} S(T_3, T_2, T_1 | p_{0,k}, p_{1,l}, p_{2,m}, p_{3,n}).$$
 (51)

To perform the tensorial average, for each dipole interaction (i = 0, 1, 2, 3) and each pigment, a specific Cartesian component k (k = 1, 2, 3) of the dipole moment is selected:

$$\widehat{\mu}_{p_{i,k}}^{+} = \sum_{a=1}^{N_{\text{sites}}} \mathbf{e}_k \cdot \mathbf{d}_a |a\rangle\langle 0|$$
 (52)

$$\widehat{\mu}_{p_{i,k}}^{-} = \sum_{a=1}^{N_{\text{sites}}} \mathbf{e}_k \cdot \mathbf{d}_a |0\rangle\langle a|.$$
 (53)

The factors C_{klmn} are determined by

$$C_{klmn} = \delta_{kl}\delta_{mn}[4(\mathbf{f}_0 \cdot \mathbf{f}_1)(\mathbf{f}_2 \cdot \mathbf{f}_3) - (\mathbf{f}_0 \cdot \mathbf{f}_2)(\mathbf{f}_1 \cdot \mathbf{f}_3) - (\mathbf{f}_0 \cdot \mathbf{f}_3)(\mathbf{f}_1 \cdot \mathbf{f}_2)]/30$$

$$+ \delta_{km}\delta_{ln}[4(\mathbf{f}_0 \cdot \mathbf{f}_2)(\mathbf{f}_1 \cdot \mathbf{f}_3) - (\mathbf{f}_0 \cdot \mathbf{f}_1)(\mathbf{f}_2 \cdot \mathbf{f}_3) - (\mathbf{f}_0 \cdot \mathbf{f}_3)(\mathbf{f}_1 \cdot \mathbf{f}_2)]/30$$

$$+ \delta_{kn}\delta_{lm}[4(\mathbf{f}_0 \cdot \mathbf{f}_3)(\mathbf{f}_1 \cdot \mathbf{f}_2) - (\mathbf{f}_0 \cdot \mathbf{f}_1)(\mathbf{f}_2 \cdot \mathbf{f}_3) - (\mathbf{f}_0 \cdot \mathbf{f}_2)(\mathbf{f}_1 \cdot \mathbf{f}_3)]/30,$$
(54)

where \mathbf{f}_i represents the unit vector of the electric field perpendicular to the propagation direction of the *i*th pulse p_i . Symmetry considerations reduce the $3^4 = 81$ C_{klmn} terms to a maximum of 21 non-zero terms, which are further reduced for specific polarization sequences. The C_{klmn} values for two exemplary polarization sequences, all parallel (all pulses have the same polarization) and double-crossed (each pair of pulses has the polarization rotated by 90°), are listed in table 3.1.

Tab. 3.1 – C_{klmn} coefficients for isotropic averaging of the $\langle 0^{\circ}, 0^{\circ}, 0^{\circ}, 0^{\circ} \rangle$ and $\langle 45^{\circ}, -45^{\circ}, 90^{\circ}, 0^{\circ} \rangle$ polarization sequences.

(k,l,m,n)	$C_{klmn} \langle 0^{\circ}, 0^{\circ}, 0^{\circ}, 0^{\circ} \rangle$
(1,1,2,2), (1,1,3,3), (1,2,1,2), (1,2,2,1), (1,3,1,3), (1,3,3,1)	+ 1
(2,1,1,2), (2,1,2,1), (2,2,1,1), (2,2,3,3), (2,3,2,3), (2,3,3,2)	$+\frac{1}{15}$
	$+\frac{1}{15}$
(3,1,1,3), (3,1,3,1), (3,2,2,3), (3,2,3,2), (3,3,1,1), (3,3,2,2)	$+\frac{1}{15}$
(1,1,1,1), (2,2,2,2), (3,3,3,3)	
(1,1,1,1), (2,2,2,2), (3,3,3,3)	$+\frac{1}{5}$
(k,l,m,n)	$C_{klmn} \langle 45^{\circ}, -45^{\circ}, 90^{\circ}, 0^{\circ} \rangle$
(1,2,1,2), (1,2,2,1), (1,3,1,3)	+ 1 - 1 + 1
(, , , ,) (, , , ,) (, , , ,)	$+\frac{1}{12}, -\frac{1}{12}, +\frac{1}{12}$
(1,3,3,1), (2,1,1,2), (2,1,2,1)	$-\frac{1}{12}, -\frac{1}{12}, +\frac{1}{12}$
(2,3,2,3), (2,3,3,2), (3,1,1,3)	$\begin{array}{cccc} 12 & 12 & 12 \\ 1 & 1 & 1 \end{array}$
(-,0, -,0,, (-,0, 0, 2)) (0,2, 2,0)	$+\frac{1}{12},-\frac{1}{12},-\frac{1}{12}$
(3,1,3,1), (3,2,2,3), (3,2,3,2)	1 1 1
(9,1,9,1), (9,2,2,9), (9,2,9,2)	$+\frac{1}{12},-\frac{1}{12},+\frac{1}{12}$

3.5.2 Static Disorder

A second type of averaging is required to account for variations in site energies in the molecular ensemble, for instance, caused by slow movement/bending of the complex. The resulting variations of the site energies (inter-site couplings are typically less affected by those modes) require to an average of various realizations of the excitonic Hamiltonian. This variation is termed *static disorder*. In the simplest case, for the absorption spectra of a monomeric unit, this leads to an additional broadening of the spectral line shapes in addition to the thermal line shape function discussed before. For more complex spectra, such as 2DES, the inclusion of static disorder has non-trivial effects on various locations of the 2DES [37].

3.6 Using HEOM for Quantum Dynamics

The hierarchical equations of motions require the propagation of a large (up to 10^6) number of interlinked matrices in parallel. A computationally efficient HEOM implementation [7, 10, 27, 38] distributes the computations across many threads and benefits from many-core processors (either many-core CPUs or GPUs). The distributed memory DM-HEOM [7, 10] tool provides a comprehensive set of applications to compute the time evolution of a density matrix, linear spectra, and two-dimensional spectra. DM-HEOM is distributed as C++/OpenCL source code [39]. A ready-to-run implementation of HEOM using GPUs is provided on the https://nanohub.org simulation platform [9].

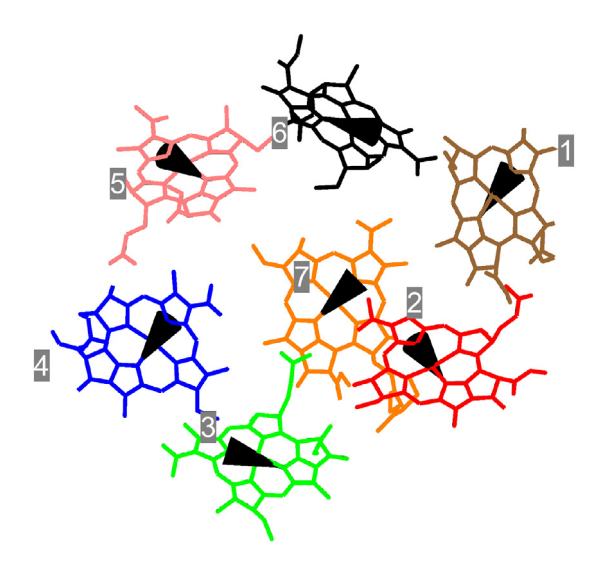


Fig. 3.4 – Monomeric unit of the FMO complex with 7 bacteriochlorophylls with arrows indicating the directions of the transition dipoles. The protein scaffold keeping the bacteriochlorophylls in place is not shown.

3.6.1 Populations and Coherences

The spectral density sets the timescale for the duration of excitonic coherences, as discussed in section 3.3.3. Using HEOM, the conditions for long-lived electronic coherences in the FMO photosynthetic complex have been investigated in [8, 40]. To compute the overall efficiency and transport-time through a network of coupled chromophores requires to additionally consider loss channels, *i.e.* due to radiative decay of the excitons. This has been explored in [6, 27] and shows that from the theoretical models, an intermediate coupling to the bath is preferred to facilitate a the fastest thermalization (see also section 3.3.3).

3.6.2 Two-Dimensional Spectra

The simulation of 2DES signals using equations (41)–(46) and HEOM proceeds by computing the time evolution of the reduced density matrix and the application of the dipole operator at the specific times t_1 , t_2 , and t_3 . Initially the reduced density matrix at t=0 represents a populated ground state $\rho(0) = \sigma_0(0) = |0\rangle\langle 0|$. In addition to the exciton Hamiltonian, the relative transition dipole strengths and directions are also required as input parameters. For the FMO complex, the transition dipoles are directed along the nitrogen atoms NB-ND in the molecular structure (PDB:3ENI) [41]. See also table 1 in [7] and figure 3.4.

Typical 2DES of the Fenna-Matthews-Olson (FMO) complex for the $\langle 0^{\circ}, 0^{\circ}, 0^{\circ}, 0^{\circ}, 0^{\circ} \rangle$ polarization sequence computed using the DM-HEOM method [7, 10] are presented in figure 3.5, upper row. The Hamiltonian and dipole directions used

in the computations can be found in table 1 and equation (77) of Kramer *et al.* [7], respectively. The parameter file for DM-HEOM [7, 10, 39] to generate the upper right panel reads:

```
[program]
```

```
task=two_dimensional_spectra
observations={ (matrix_trace_two_dimensional_spectra,
    fmo_0000_400fs.dat) }
observe_steps=2
```

[filtering]

```
strategy=none
first layer=-1
```

[solver]

```
stepper_type=rk_rk4
step_size=4.e-15
steps=2
track_flows=false
flow filename=
```

[system]

```
ado_depth=3
sites=7
hamiltonian={{1410.000, -87.70000, 5.500000, -5.900000,
6.700000, -13.70000, -9.900000}, {-87.70000, 1530.000,
30.80000, 8.200000, 0.7000000, 11.80000, 4.300000},
{5.500000, 30.80000, 1210.000, -53.50000, -2.200000,
-9.600000, 6.000000}, {-5.900000, 8.200000, -53.50000,
1320.000, -70.70000, -17.00000, -63.30000}, {6.700000,
0.7000000, -2.200000, -70.70000, 1480.000, 81.10000,
-1.300000}, {-13.70000, 11.80000, -9.600000, -17.00000,
81.10000, 1630.000, 39.70000}, {-9.900000, 4.300000,
6.000000, -63.30000, -1.300000, 39.70000, 1440.000}}
```

[baths]

```
max_per_site=1
number=7
coupling={{0}, {1}, {2}, {3}, {4}, {5}, {6}}
lambda={35, 35, 35, 35, 35, 35, 35}
invnu={50, 50, 50, 50, 50, 50, 50}
Omega={0, 0, 0, 0, 0, 0, 0}
matsubaras=1
temperature=100
```

[dipole]

```
Directions={{0.74101, 0.56060, 0.36964}, {0.85714, -0.50378, 0.10733}, {0.19712, -0.95741, 0.21097}, {0.79924, 0.53357, 0.27661}, {0.73693, -0.65576, -0.16406},
```

```
{0.13502, 0.87922, -0.45689}, {0.49511, 0.70834, 0.50310}}

centers={{-0.7410, -0.5606, -0.3696}, {-0.8571, 0.5038, -0.1073},
    {-0.1971, 0.9574, -0.2110}, {-0.7992, -0.5336, -0.2766},
    {-0.7369, 0.6558, 0.1641}, {-0.1350, -0.8792, 0.4569},
    {-0.4951, -0.7083, -0.5031}}

strengths={1,1,1,1,1,1,1}

tensor_prefactors={0.2, 0.066667, 0.066667, 0.066667,
    0.066667, 0.066667, 0.066667, 0.066667,
    0.2, 0.066667, 0.066667, 0.066667, 0.066667,
    0.066667, 0.066667, 0.066667, 0.2}

tensor_components={{0,0,0,0}, {0,0,1,1}, {0,0,2,2}, {0,1,0,1},
    {0,1,1,0}, {0,2,0,2}, {0,2,2,0}, {1,0,0,1}, {1,0,1,0},
    {1,1,0,0}, {1,1,1,1}, {1,1,2,2}, {1,2,1,2}, {1,2,2,1},
    {2,0,0,2}, {2,0,2,0}, {2,1,1,2}, {2,1,2,1}, {2,2,0,0},
    {2,2,1,1}, {2,2,2,2}}
```

[spectra]

```
steps_t_1=200
steps_t_3=200
steps_t_delay=100
pathways={gbnr,senr,esanr,gbrp,serp,esarp}
```

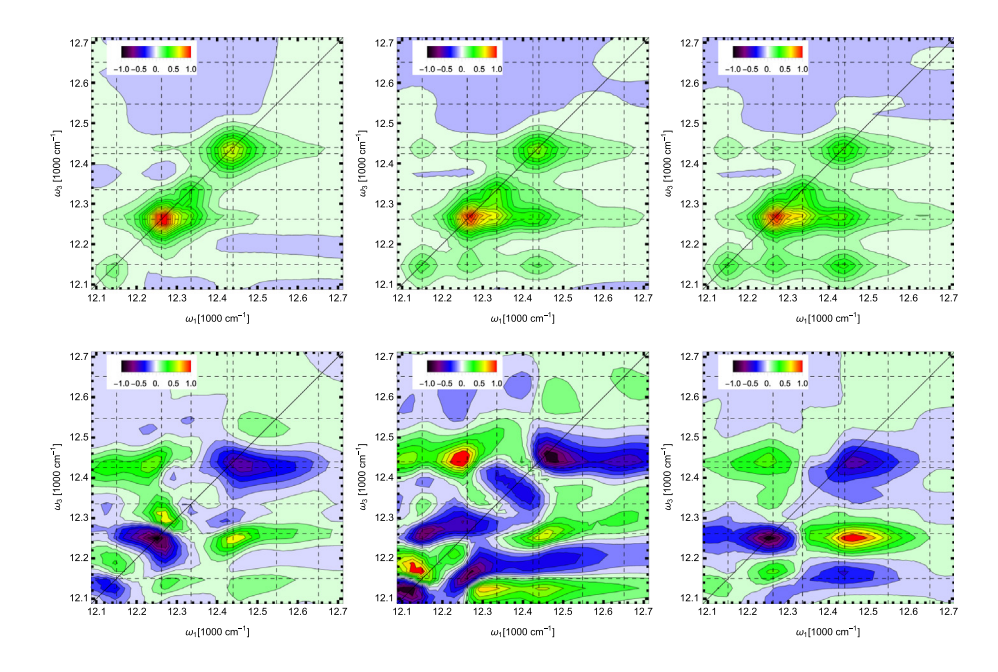


Fig. 3.5 – 2DES (sum of rephasing and non-rephasing pathways) for the FMO complex computed with DM-HEOM from left panels to right panels for increasing delay time $T_2 = \{40, 400, 800\}$ fs at temperature 100 K. Upper row: all parallel polarization $\langle 0^{\circ}, 0^{\circ}, 0^{\circ}, 0^{\circ} \rangle$. Lower row: double-crossed polarization $\langle 45^{\circ}, -45^{\circ}, 90^{\circ}, 0^{\circ} \rangle$. Rotational averaging is performed, static disorder is not considered.

The resulting file contains the third-order nonlinear response function $S(T_1, T_2, T_3)$ for $T_1, T_3 = 0...200 \times 4 \times 10^{-15}$ s and delay time $T_2 = 100 \times 4 \times 10^{-15}$ s (all steps are measured in multiples of step_size). In this example, a total of 6×21 spectra are computed to perform the isotropic ensemble average for all six rephasing and non-rephasing pathways. The energy transfer process shown is revealed from left to right in the upper panels in figure 3.5 by the appearance of off-diagonal peaks below the diagonal line: a lower cross-peak implies a reduced probe (de-excitation) energy as compared to the initial excitation energy: energy has been dissipated to the vibrational modes. The dissipation drives a directional energy flow towards thermal equilibrium, which implies a higher occupation of lower-lying energy states.

This energy transfer is clearly observable in experimental measurements performed by Brixner *et al.* [42], as well as the HEOM computations by Hein *et al.* [32] and Kreisbeck *et al.* [8]. Computed spectra can be separated into contributions from ground state bleaching, stimulated emission, and excited state absorption (see figure 3 in [43] for an illustrative example). The energy flow is not reflected by the ground state bleaching signal, since it requires a population transfer.

In addition to energy decay, Engel et al. [44] and Panitchayangkoon et al. [45] reported the presence of oscillatory amplitudes in the 2DES signals. These oscillations are attributed to a combination of ground-state bleach-induced vibrational modes and electronic coherences. In computed 2DES, these contributions to oscillatory signals can be cleanly separated by a short-time Fourier transform [40]. The electronic coherences are expected to decay on a timescale determined by the combined dephasing and relaxation decoherence time [8] of the two eigenenergies at the location of the cross-peak. In addition to the electronic coherences vibrational peaks in the spectral density are present in 2DES signals, in particular in the ground state bleaching part. This contribution can persist longer than the electronic coherences, and overshadow them [8, 40]. The pure dephasing time is influenced by the slope of the spectral density $J(\omega)$ towards zero frequency, while the relaxation rate is determined by the value of the spectral density at the eigenenergies. Both factors contribute to the decay time, as shown in the supplementary information of Kreisbeck et al. [8] and figure 3.2.

The reorganization energy λ_m , which is related to the spectral density $J_m(\omega)$ of each pigment m, manifests as a downward shift of the diagonal and cross peaks as the delay increases. This shift is consistent with the reorganization energies of approximately 40 cm⁻¹ assigned to the bacteriochlorophylls in the FMO complex by Adolphs *et al.* [4].

Experimental data for different polarization sequences for the FMO complex is presented in [46, 47] and requires corresponding theoretical models for interpretation. While in the all parallel polarization sequence $(\langle 0^{\circ}, 0^{\circ}, 0^{\circ}, 0^{\circ} \rangle)$, all isotropic averaging coefficients are positive numbers, for other polarizations cancellation effects due to alternating signs (see table 3.1) occur. These lead to additional structures in the 2DES [37], and figure 3.5, lower row.

To facilitate analysis and for studying various static disorder configuration, an efficient storage and interpolation of 2DES results is useful. A highly compressed storage uses custom neural networks [48]. Once the neural network has been trained

with an extensive data set of exemplary computations, it generates a 2DES for a specific set of site energies of the Hamiltonian. This approach has been used to simulate 2DES data sets for differently prescribed static disorder distributions for the FMO complex [37].

3.7 Summary

The open quantum system approach provides the required tools for tracking the energy flow in molecular complexes. Only for small or large couplings, simplified descriptions of the density matrix are available, while in general, more accurate quantum propagation methods are required, such as HEOM. These methods come with an additional computational overhead, which requires to use highly optimized numerical algorithms. Compared to the numerical effort to obtain a linear absorption spectra, 2DES calculations increase the run times by $\sim 10^4$ due to the complexity of ensemble averaging and the need to span three-time intervals. The interpretation and analysis of 2DES needs theoretical models to assess the impact of the different pathways and ensemble averages.

Acknowledgements. The further development of numerical methods for describing open quantum systems is funded by the Austrian Science Fund (FWF project "Open quantum dynamics lab") and by the NVIDIA academic hardware donation grant "Simulating branched flow with tensor processing units".

References

- May V., Kühn O. (2004) Charge and energy transfer dynamics in molecular systems. Wiley-VCH, Weinheim. ISBN 3-527-40396-5.
- Olson J. M., Romano C. a. (Jun. 1962) A new chlorophyll from green bacteria, Biochim. Biophys. Acta 59(3), 726-728, DOI: 10.1016/0006-3002(62)90659-5.
- Fenna R. E., Matthews B. W. (Dec. 1975) Chlorophyll arrangement in a bacteriochlorophyll protein from Chlorobium limicola, *Nature* 258(5536), 573–577. DOI: 10.1038/258573a010. 1038/258573a0.
- [4] Adolphs J., Renger T. (Oct. 2006) How Proteins trigger excitation energy transfer in the FMO complex of green sulfur bacteria, *Biophys. J.* 91(8), 2778–2797. DOI: 10.1529/biophysj.105. 079483.
- [5] Carmichael H. J. (1999) Statistical methods in quantum optics 1. Springer Berlin Heidelberg, Berlin, Heidelberg, DOI: 10.1007/978-3-662-03875-8.
- [6] Kramer T., Kreisbeck C. (2014) Modelling excitonic-energy transfer in light-harvesting complexes, AIP Conf. Proc. 1575, 111–135. DOI: 10.1063/1.4861701.
- Kramer T., Noack M., Reinefeld A., Rodríguez M., Zelinskyy Y. (Jun. 2018) Efficient calculation of open quantum system dynamics and time-resolved spectroscopy with distributed memory HEOM (DM-HEOM), J. Comput. Chem. 39(22), 1779. DOI: 10.1002/ jcc.25354.
- [8] Kreisbeck C., Kramer T. (2012) Long-lived electronic coherence in dissipative exciton dynamics of light-harvesting complexes, J. Phy. Chem. Lett. 3(19), 2828–2833. DOI: 10.1021/jz3012029.
- [9] Kreisbeck C., Kramer T. (2014) Exciton dynamics lab for light-harvesting complexes (GPU-HEOM), nanohub. DOI: 10.4231/D3RF5KH7G.

- [10] Noack M., Reinefeld A., Kramer T., Steinke T. (2018) DM-HEOM: A Portable and Scalable Solver-Framework for the Hierarchical Equations of Motion, 2018 IEEE International Parallel and Distributed Processing Symposium Workshops (IPDPSW), best paper award, p. 947. DOI: 10.1109/IPDPSW.2018.00149.
- [11] Tanimura Y., Kubo R. (Jan. 1989) Time evoultion of a quantum system in contact with a nearly Gaussian-Markoffian noise bath, J. Phy. Soc. Japan 58(1), 101–114. DOI: 10.1143/ JPSJ.58.101.
- [12] Tanimura Y., Mukamel S. (1994) Optical Stark spectroscopy of Brownian oscillator in intense fields, J. Phy. Soc. Japan 63, 66–77. DOI: 10.1143/JPSJ.63.66.
- [13] Makri N. (May 1995) Numerical path integral techniques for long time dynamics of quantum dissipative systems, J. Math. Phys. 36(5), 2430–2457. DOI: 10.1063/1.531046.
- [14] Kramer T. (Sep. 2023) Mathematica HEOM Release 1, tobiaskramer/mm-heom. DOI: 10. 5281/zenodo.8309640.
- [15] Ishizaki A., Fleming G. R. (2009) On the adequacy of the Redfield equation and related approaches to the study of quantum dynamics in electronic energy transfer, J. Chem. Phys. 130(23), 234 110–234 110. DOI: 10.1063/1.3155214.
- [16] Ishizaki A., Fleming G. R. (Jun. 2009) Unified treatment of quantum coherent and incoherent hopping dynamics in electronic energy transfer: reduced hierarchy equation approach, J. Chem. Phys. 130(23), 234 111–234 111. DOI: 10.1063/1.3155372.
- [17] Yang M., Fleming G. R. (2002) Influence of phonons on exciton transfer dynamics: Comparison of the Redfield, Forster, and modified Redfield equations, *Chem. Phys.* 275, 355–372. DOI: 10.1016/S0301-0104(01)00540-7.
- [18] Kubo R., Toyozawa Y. (Feb. 1955) Application of the method of generating function to radiative and non-radiative transitions of a trapped electron in a crystal, *Prog. Theor. Phys.* 13 (2), 160–182. DOI: 10.1143/PTP.13.160.
- [19] Knox R. S., Small G. J., Mukamel S. (Jul. 2002) Low-temperature zero phonon lineshapes with various Brownian oscillator spectral densities, *Chem. Phys.* 281(1), 1–10. DOI: 10.1016/S0301-0104(02)00593-1.
- [20] Wendling M., Pullerits T., Przyjalgowski M. A., Vulto S. I. E., Aartsma T. J., Van Grondelle R., Van Amerongen H. (Jun. 2000) Electron-vibrational coupling in the Fenna-Matthews-Olson complex of prosthecochloris aestuarii determined by temperature-dependent absorption and fluorescence line-narrowing measurements, J. Phys. Chem. B 104(24), 5825–5831. DOI: 10.1021/jp000077+.
- [21] Tanimura Y. (Aug. 2006) Stochastic Liouville, Langevin, Fokker-Planck, and Master equation approaches to quantum dissipative systems, J. Phys. Soc. Japan 75(8), 082 001–082 001. DOI: 10.1143/JPSJ.75.082001.
- [22] Kramer T., Noack M., Reimers J. R., Reinefeld A., Rodríguez M., Yin S. (May 2018) Energy flow in the Photosystem I supercomplex: comparison of approximative theories with DM-HEOM, Chem. Phys. 515, 262–271. DOI: 10.1016/j.chemphys.2018.05.028.
- [23] Weiss U. (Mar. 2012) Quantum dissipative systems, 4th edn. World Scientific. DOI: 10.1142/ 8334.
- [24] Plenio M. B., Huelga S. F. (Nov. 2008) Dephasing-assisted transport: quantum networks and biomolecules, New J. Phys. 10(11), 113 019–113 019. DOI: 10.1088/1367-2630/10/11/113019.
- [25] Rebentrost P., Mohseni M., Kassal I., Lloyd S., Aspuru-Guzik A. (2009) Environment-assisted quantum transport, New J. Phys. 11(3), 033 003-033 003. DOI: 10.1088/1367-2630/11/3/ 033003.
- [26] Novoderezhkin V., Marin A., van Grondelle R. (2011) Intra- and inter-monomeric transfers in the light harvesting LHCII complex: the Redfield-Förster picture, *Phys. Chem. Chem. Phys.* 13(38), 17093. DOI: 10.1039/c1cp21079c.
- [27] Kreisbeck C., Kramer T., Rodríguez M., Hein B. (Jul. 2011) High-performance solution of hierarchical equations of motion for studying energy transfer in light-harvesting complexes, J. Chem. Theory Comput. 7(7), 2166–2174. DOI: 10.1021/ct200126d10.1021/ct200126d.
- [28] Chen L., Gelin M. F., Domcke W., Zhao Y. (2015) Theory of femtosecond coherent double-pump single-molecule spectroscopy: application to light harvesting complexes, J. Chem. Phys. 142(16). DOI: 10.1063/1.4919240.

- [29] Gelin M. F., Tanimura Y., Domcke W. (Dec. 2013) Simulation of femtosecond "double-slit" experiments for a chromophore in a dissipative environment, J. Chem. Phys. 139(21), 214 302–214 302. DOI: 10.1063/1.4832876.
- [30] Hamm P., Zanni M. T. (2011) Concepts of 2D spectroscopy. Cambridge University Press, Cambridge.
- [31] Cho M., Vaswani H. M., Brixner T., Stenger J., Fleming G. R. (Jun. 2005) Exciton analysis in 2D electronic spectroscopy, J. Phys. Chem. B 109(21), 10 542–10 556. DOI: 10.1021/ jp050788d.
- [32] Hein B., Kreisbeck C., Kramer T., Rodríguez M. (Feb. 2012) Modelling of oscillations in two-dimensional echo-spectra of the Fenna-Matthews-Olson complex, New J. Phys. 14(2), 023 018–023 018. DOI: 10.1088/1367-2630/14/2/023018.
- [33] Gordon R. (1968) Correlation functions for molecular motion, Advances in magnetic and optical resonance. Academic Press Inc. 3, pp. 1–42. DOI: 10.1016/B978-1-4832-3116-7.50008-4.
- [34] Mukamel S. (1995) Principles of nonlinear optical spectroscopy. Oxford University Press, Oxford.
- [35] Craig D. P., Thirunamachandran T. (1998) Molecular quantum electrodynamics: an introduction to radiation-molecule Interactions. Dover Publications, Mineola, New York.
- [36] Gelin M. F., Borrelli R., Domcke W. (Jul. 2017) Efficient orientational averaging of nonlinear optical signals in multi-chromophore systems, J. Chem. Phys. 147(4), 044 114–044 114. DOI: 10.1063/1.4996205.
- [37] Kramer T., Rodríguez M. (May 2020) Effect of disorder and polarization sequences on two-dimensional spectra of light-harvesting complexes, *Photosynth. Res.* 144(2), 147–154. DOI: 10.1007/s11120-019-00699-6.
- [38] Strümpfer J., Schulten K. (2012) Open quantum dynamics calculations with the hierarchy equations of motion on parallel computers, J. Chem. Theory Comput. 8, 2808–2816. DOI: 10. 1021/ct3003833.
- [39] Noack M., Kramer T. (Sep. 2023) DM-HEOM. DOI: 10.5281/zenodo.8372601.
- [40] Kreisbeck C., Kramer T., Aspuru-Guzik A. (2013) Disentangling electronic and vibronic coherences in two-dimensional echo spectra, J. Phys. Chem. B 117(32), 9380–9385. DOI: 10. 1021/jp405421d10.1021/jp405421d.
- [41] Adolphs J., Müh F., Madjet M. E.-A., Renger T. (Feb. 2008) Calculation of pigment transition energies in the FMO protein, *Photosynth. Res.* 95(2–3), 197–209. DOI: 10.1007/s11120-007-9248-z.
- [42] Brixner T., Stenger J., Vaswani H. M., Cho M., Blankenship R. E., Fleming G. R. (Mar. 2005) Two-dimensional spectroscopy of electronic couplings in photosynthesis, *Nature* 434(7033), 625–628. DOI: 10.1038/nature03429.
- [43] Kramer T., Rodriguez M. (Mar. 2017) Two-dimensional electronic spectra of the photosynthetic apparatus of green sulfur bacteria, Sci. Rep. 7, 45 245–45 245. DOI: 10. 1038/srep45245.
- [44] Engel G. S., Calhoun T. R., Read E. L., Ahn T.-K., Mancal T., Cheng Y.-C., Blankenship R. E., Fleming G. R. (Apr. 2007) Evidence for wavelike energy transfer through quantum coherence in photosynthetic systems, *Nature* 446(7137), 782–786. DOI: 10.1038/nature05678.
- [45] Panitchayangkoon G., Hayes D., Fransted K. a., Caram J. R., Harel E., Wen J., Blankenship R. E., Engel G. S. (Jul. 2010) Long-lived quantum coherence in photosynthetic complexes at physiological temperature, *Proc. Natl. Acad. Sci. U.S.A.* 107(29), 12 766–70. DOI: 10.1073/pnas.1005484107.
- [46] Thyrhaug E., Žídek K., Dostál J., Bína D., Zigmantas D. (May 2016) Exciton structure and energy transfer in the Fenna–Matthews–Olson complex, J. Phys. Chem. Lett. 7(9), 1653–1660. DOI: 10.1021/acs.jpclett.6b00534.
- [47] Thyrhaug E., Tempelaar R., Alcocer M. J. P., Žídek K., Bína D., Knoester J., Jansen T. L. C., Zigmantas D. (Jul. 2018) Identification and characterization of diverse coherences in the Fenna–Matthews–Olson complex, Nat. Chem. 10(7), 780–786. DOI: 10.1038/s41557-018-0060-5.
- [48] Rodríguez M., Kramer T. (Apr. 2019) Machine learning of two-dimensional spectroscopic data, Chem. Phys. 520, 52–60. DOI: 10.1016/j.chemphys.2019.01.002.

Chapter 4

Coherently and Fluorescence-Detected Ultrafast Spectroscopy

Pavel Malý*

Faculty of Mathematics and Physics, Charles University, Prague, Czech Republic

*e-mail: pavel.maly@matfyz.cuni.cz

4.1 Introduction

Ultrafast optical spectroscopy uses multiple short laser pulses to follow photo-induced dynamics with both high spectral and temporal resolution across time scales. In recent decades, the detection of resonant coherent nonlinear signals on a dark background via incoherent observables has become popular in so-called action-detected spectroscopy. Modern nonlinear optical spectroscopy thus includes multi-dimensional variants in various geometries and realizations, as well as the detection of both coherent and incoherent signals. There is a close correspondence between the nonlinear spectra detected by means of nonlinear polarization and by incoherent observables such as fluorescence. Nevertheless, there are profound differences in both practical and fundamental nature, to an extent that makes the techniques partially complementary. In this tutorial, we introduce coherently and action-detected nonlinear spectroscopy experiments on the same footing and directly compare and contrast them both theoretically and in terms of experimental data.

First, we briefly formulate a description of nonlinear spectroscopy using perturbation theory in density matrix formalism, which leads to response functions that accommodate both coherence- and population-based observables. We demonstrate how the state of the perturbed system inherits the phase of the perturbing fields, providing a handle for the isolation of the desired nonlinear signal. We proceed with a direct comparison of the fluorescence- and polarization-based approach on a dimer of squaraine molecules. Going up through the nonlinear orders, we discuss linear absorption, four-wave mixing pump-probe and two-dimensional electronic

DOI: 10.1051/978-2-7598-3760-1.c004 © The authors, 2025 spectroscopy (2DES), and six-wave mixing 2DES spectroscopy. On the example of the dimers, we point out generic similarities and differences between the approaches. We conclude by generalizing and summarizing the results, contrasting the methods, and emphasizing their complementarity.

4.2 Nonlinear Spectroscopy as Measurement of Perturbation Theory

In most cases, laboratory experiments are conducted on volume samples, e.g., solutions with the studied molecular complexes, solid-state samples with grown nanocrystals, etc. The microscopic responses of many microscopic systems then add up to form the overall macroscopic signal.

4.2.1 Microscopic Interaction with Light

At the microscopic level, the electronic system of study interacts with light that perturbs it. We will describe the interaction in the time domain, which is natural to follow the system dynamics. In a quantum description, the dynamics are described by the Liouville—von Neumann equation

$$\frac{d\rho}{dt} = -\frac{i}{\hbar}[H, \rho] - \frac{i}{\hbar}[H_{\text{int}}, \rho]. \tag{1}$$

Here, the system state (which does not need to be a pure quantum-mechanical state) is represented by its density matrix ρ . The dynamics of the system are generated by its Hamiltonian H and the interaction with light is included in $H_{\rm int}$. Concerning the form of $H_{\rm int}$, for most applications and certainly for the purpose of this tutorial, it is customary to make some approximations. First, we will use the dipole approximation, applicable for systems smaller than the wavelength of the excitation light (i.e., not larger than tens of nanometers). In the dipole approximation, the interaction Hamiltonian is $H_{\text{int}} = -\mu \cdot E(t)$, where μ is the dipole moment operator and E(t) is the electric field. Note that both μ and E are vectors, and the interaction is proportional to the projection of the dipole moment to the light polarization. Throughout this lecture, we will suppress the polarization dependence wherever needed, occasionally mentioning it where important. Mathematically, this can be expressed by considering $\mu = \overrightarrow{\mu} \cdot \overrightarrow{e}$, where \overrightarrow{e} is the polarization vector of the electric field. Second, we will employ semiclassical approximation and treat the electric field classically. Quantum optics is a fascinating field that has only recently found proposed applications in spectroscopy with quantum light [1, 2]. However, the experiments are challenging and presently, well behind the theory [3]. In our formulation, we will thus put the E(t) field out of the commutator in equation (1):

$$\frac{d\rho}{dt} = -\frac{i}{\hbar}[H,\rho] + \frac{i}{\hbar}[\mu,\rho]E(t). \tag{2}$$

4.2.2 Perturbative Expansion

An important condition for the interpretation of experiments in terms of single- or n-particle excitations is the validity of perturbation theory in E. In that case, equation (2) can be expanded iteratively in the orders of E, getting [4]

$$\rho^{(n)}(t) = \left(\frac{i}{\hbar}\right)^n \int_0^\infty dt_n \int_0^\infty dt_{n-1} \dots \int dt_1 \mathcal{U}(t_n) [\mu, \dots [\mu, \mathcal{U}(t_1)[\mu, \rho^{\text{eq}}]]] \times E(t - t_n) E(t - t_n - t_{n-1}) \dots E(t - t_n - t_{n-1} - \dots - t_1).$$
(3)

As seen from equation (3), the *n*-th order density matrix consists of a term that contains *n* sequential interactions with the electric field (the commutators with the dipole moment), between which the system propagates freely with propagator $\mathcal{U}(t)$, a superoperator that acts on the whole expression on its right side, evolving both its bra and ket side as in $\mathcal{U}(t)AB = U(t)ABU^{\dagger}(t)$ with U(t) the standard Hilbert space propagator. The zeroth order is the equilibirum density matrix ρ^{eq} , the first-order term includes a single commutator propagating in time t_1 , etc. The key point of this lecture is that the perturbative expansion in $\rho^{(n)}$ can be precisely followed and controlled by using a sequence of laser pulses of defined parameters. A laser pulse with central frequency ω_0 at position r in time t can be described as

$$E_p(t) = E_p^+(t) + E_p^-(t) = A_p(t)e^{-i\omega_0 t + ik_p \cdot r + i\phi_p} + A_p^*(t)e^{i\omega_0 t - ik_p \cdot r - i\phi_p}.$$
 (4)

Here, k_p is the wave vector and ϕ_p is the phase of the pulse, and $A_p(t)$ the slowly varying complex envelope that contains the pulse shape and chirp. The pulse chirp is the frequency-dependent phase of the pulse, which results in different wavelengths arriving at different times, as described in more detail in chapter 1. For future reference, we also separated the electric field into positive frequency $(E^+(t) \propto e^{-i\omega_0 t})$ and negative frequency $(E^-(t) \propto e^{+i\omega_0 t})$ parts. In a time-resolved optical spectroscopy experiment, the E field consists of a sequence of several pulses,

$$E(t) = \sum_{p=1}^{N_{\text{pulses}}} E_p(t) \tag{5}$$

Plugging such pulse train into the perturbative solution equation (3), we get all the possible combinations of interaction:

$$\rho^{(n)}(t) = \sum_{p_1 p_2 \dots p_n} \left(\frac{i}{\hbar}\right)^n \int_0^\infty dt_n \int_0^\infty dt_{n-1} \dots \int dt_1 \mathcal{U}(t_n)[\mu, \dots [\mu, \mathcal{U}(t_1)[\mu, \rho^{\mathrm{eq}}]]].$$

$$E_{p_n}(t-t_n)E_{p_{n-1}}(t-t_n-t_{n-1})\dots E_{p_1}(t-t_n-t_{n-1}\dots-t_1)$$
(6)

Crucially, the state of the system (*i.e.*, the total density matrix), obtains imprinted the phase of each interacting pulse. This phase dependence can then be used to isolate the individual contributions to the total nonlinear signal.

In order to track the perturbed system along its pathway through the Liouville space, it is necessary to keep track of both the bra and ket interactions, including the appropriate parts of the electric field, and of the system evolution. This can be very conveniently achieved by double-sided Feynman diagrams (DSFD) introduced by Shaul Mukamel [4]. To illustrate how this works, let us consider a particular pathway (as given by the commutator sequence), say

$$\rho^{(3)}(t) = \left(\frac{i}{\hbar}\right)^3 \int_0^\infty dt_3 \int_0^\infty dt_2 \int dt_1 \mathcal{U}(t_3) \{\mathcal{U}(t_2) \{\mu \mathcal{U}(t_1) \{|g\rangle\langle g|\mu\}\} \mu\} E_3(t-t_3)$$

$$\times E_2(t-t_3-t_2) E_1(t-t_3-t_2-t_1).$$
(7)

As determined by the sides form which the dipole moments act in the commutators, this pathway goes as $\rho_{gg} \to \rho_{ge} \xrightarrow{t_1} \rho_{ge} \to \rho_{ee} \xrightarrow{t_2} \rho_{ee} \to \rho_{eg} \xrightarrow{t_3} \rho_{eg}$. It is depicted in the form of the double-sided Feynman diagram in figure 4.1.

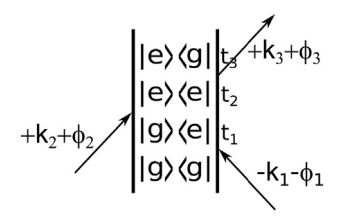


Fig. 4.1 – Example of a double-sided Feynman diagram of the response pathway from equations (7) and (8).

Now, without going into details of the evolution, from the commutator with the system Hamiltonian in equation (2), we can see that the elements of the density matrix oscillate as $\rho_{nm}(t) \propto e^{-i\omega_{nm}t}$. In particular, $\rho_{eg}(t) \propto e^{-i\omega_{eg}t}$ oscillates at the optical frequency of the (quasi-resonant) transition, and so on. Our pathway will thus have an oscillatory factor of $e^{-i\omega_{eg}(t_3-t_1)}$ (because the phase rotates in different directions in t_1 and t_3 , this is called a rephasing pathway). The electric fields on the right-hand side consist of positive and negative frequency terms, $E(t) = E^{+}(t) + E^{-}(t)$, where $E^{+}(t) \propto e^{-i\omega_0 t + ik \cdot r + i\phi}$ and $E^{-}(t) = (E^{+}(t))^*$. As we integrate over the time t_1, \ldots, t_n , there will be terms that oscillate slowly at a frequency difference $(\omega_{eq} - \omega_0)$, and that oscillate rapidly at frequency sum $(\omega_{eq} + \omega)$. Unless we have sub-cycle or very off-resonant pulses, the rapidly oscillating terms cancel out and can be neglected, which is called the rotating wave approximation (RWA). In our pathway, this will leave

$$\rho^{(3)}(t) = \left(\frac{i}{\hbar}\right)^3 (-1)^2 \int_0^\infty dt_3 \int_0^\infty dt_2 \int dt_1 \mathcal{U}(t_3) \{\mathcal{U}(t_2) \{\mu \mathcal{U}(t_1) \{|g\rangle\langle g|\mu\}\} \mu\}$$

$$\times E_3^+(t-t_3) E_2^+(t-t_3-t_2) E_1^-(t-t_3-t_2-t_1).$$
(8)

To keep track of the interactions and corresponding parts of the E field, the DSFDs are defined by a set of rules that allow direct construction of the response pathway from the diagrams. Interactions that excite the system are represented by incoming arrows. When exciting from the right (bra side) or de-exciting from the left (ket side), take E^- part of the field – this is marked by an arrow going from right to left, and for the opposite cases (left to right arrow), take E^+ . A heritage of the commutators with the interaction Hamiltonian, there is an overall minus sign for each interaction from the right. These diagrams can be used not only for spectroscopy, but for any type of perturbation theory on the density matrix. For details, we refer the reader to the book [4]. Using the rules, we can immediately read off that the signal will have a phase signature $-k_1 + k_2 + k_3$ in terms of wave vectors, or $-\phi_1 + \phi_2 + \phi_3$ in terms of pulse phases, and an overall plus sign.

After the n interactions, the system is left to evolve and produce a signal that can be measured. The type of the signal depends on the specific type of spectroscopy. Nevertheless, the expectation value of any observable O can be evaluated using the known system density matrix as

$$\langle O(t) \rangle = \text{Tr}\{O\rho(t)\} = \sum_{n=0}^{\infty} \text{Tr}\{O\rho^{(n)}(t)\} = \sum_{n} \langle O(t) \rangle^{(n)}. \tag{9}$$

We will consider two general types of observables, classified by the element of the density matrix they derive from. We have coherence-based observables, such as polarization, and population-based observables, such as fluorescence. In any case, the local, microscopic nonlinear signals have to be added to form a macroscopically observable signal.

4.2.3 Production of the Overall Macroscopic Signal

4.2.3.1 Polarization

In order to produce a macroscopic signal, the microscopic response from all the perturbed systems has to add up. In a multi-wave mixing experiment, the polarization of each system adds up coherently to a macroscopic overall polarization that gives rise to an additional signal field. The local microscopic polarization is calculated as

$$P(r,t) = \text{Tr}\{\mu\rho(t)\},\tag{10}$$

i.e., the observable is the dipole moment operator [4]. The local nonlinear polarizations add up to from the macroscopic signal field propagating through the sample according to the wave equation (from Maxwell equations),

$$-\nabla^2 E(r,t) + \frac{n^2}{c^2} \frac{\partial^2 E(r,t)}{\partial t^2} = -\frac{1}{\varepsilon_0 c^2} \frac{\partial^2 P(r,t)}{\partial t^2}.$$
 (11)

Here, the linear polarization has already been taken into account by a (complex) refractive index n. The nonlinear polarization is, according to the equations above, expanded perturbatively in the orders of interaction with the electric field as

$$P(r,t) = \sum_{n>1} P^{(n)}(r,t) = \sum_{n>1} \sum_{s} P_s^{(n)}(t) e^{ik_s r - i\omega_s t + i\phi_s} + \text{c.c.}$$
(12)

Here, s denotes the particular signal, distinguished by its frequency $\omega_s = \pm \omega_1 \pm \omega_2 ... \pm \omega_n$, wave vector $k_s = \pm k_1 \pm k_2 ... \pm k_n$ (vector sum) and phase $\phi_s = \pm \phi_1 \pm \phi_2 ... \pm \phi_n$, c.c. denotes complex conjugate.

Assuming a slowly varying envelope, we can solve equation (11) along the propagation through the sample of thickness l, for details, see the book by Mukamel [4]. We obtain

$$E_s(l,t) = i \frac{2\pi}{n(\omega_s)c} \omega_s l e^{i(k_s - k_s')l/2} \operatorname{sinc}\left(\left(k_s - k_s'\right)l/2\right) P_s(t) e^{ik_s'l - i\omega_s t + i\phi_s} + \text{c.c.}$$
(13)

A reader familiar with nonlinear optics (see, e.g., the book by Robert Boyd [5]) immediately recognizes the phase matching in the approximation of a non-depleted pump (see chapter 1). For reasonably large interaction length l, the sinc function acts as a delta function and selects a signal wave vector very close to the combination of the wave vectors of the pulses so that we can set $k'_s = k_s$. We thus have

$$E_s(t) \propto i \frac{\omega_s}{n(\omega_s)c} P_s(t) e^{ik_s l - i\omega_s t + i\phi_s} + \text{c.c.}$$
 (14)

The macroscopic electric field can, in principle, be detected, but it is very weak and, moreover, we are interested in its phase as well. It is thus more customary to use a so-called heterodyne detection, where the signal field is mixed with a reference field (which can be an additional pulse or one of the original pulses). This field is traditionally called a local oscillator, E_{LO} , and the detected intensity is

$$I_{\text{det}}(t) \propto |E_s(t) + E_{\text{LO}}|^2 = I_s(t) + I_{\text{LO}}(t) + 2\text{Re}\{E_{\text{LO}}^-(t)E_s^+(t)\}.$$
 (15)

The signal field itself is very weak and can be neglected in comparison to the other two terms. The intensity of the LO can be subtracted in a differential measurement, leaving us with the last phase-sensitive heterodyne measurement. As is apparent from this construction, with heterodyne detection of the macroscopic signal field, we have direct access to the complex nonlinear polarization field. We will discuss the quantity

$$E_s^{(n)} \propto i \int_{-\infty}^{\infty} dt_n \int_{-\infty}^{\infty} dt_{n-1} \dots \int_{-\infty}^{\infty} dt_1 S_{\text{coh}}^{(n)}(t_n, \dots, t_1) E(t - t_n) \times E(t - t_n - t_{n-1}) \dots E(t - t_n - t_{n-1} - \dots - t_1),$$
(16)

where

$$S_{\text{coh}}^{(n)}(t_n, \dots, t_1) = \left(\frac{i}{\hbar}\right)^n \theta(t_n) \dots \theta(t_1) \operatorname{Tr} \{\mu \mathcal{U}(t_n)[\mu, \dots[\mu, \mathcal{U}(t_1)[\mu, \rho^{\text{eq}}]]]\}.$$
 (17)

Since the dipole moment operator is off-diagonal, the trace in equation (10) selects elements of the density matrix off-diagonal in the electronic state manifolds. That is why the polarization is sometimes called a coherence-based signal. This terminology is somewhat confusing since it does not immediately correspond to the coherence properties of the generated field. At this point, we note that when the polarization of

light is considered, the response function gains an index for each of the dipole moments, and the indices sum with the corresponding components of the electric fields: $S_{ijkl...}E_jE_kE_l...$ The pulse polarization thus allows further selection of response pathways. This dependence is exploited in a range of applications, from anisotropy spectra to cross-peak-specific 2DES. A detailed description of polarization control is, however, out of the scope of this lecture, and we refer the reader to, e.g., the book by Minhaeng Cho [6].

4.2.3.2 Fluorescence

Apart from the coherent polarization, other observables can be measured in nonlinear spectroscopy. A prominent, popular example is spontaneous emission from the excited state, also termed luminescence or fluorescence, dependent on the particular research field. The fluorescence from the excited state $|i\rangle$ is proportional to its population $\langle i|\rho(t)|i\rangle$ by a radiative decay rate Γ_i :

$$FL(t) = Tr \left\{ \sum_{i \in \text{excited}} |i\rangle \Gamma_i \langle i| \rho(t) \right\}.$$
 (18)

Explicitly, the nonlinear fluorescence of the n-th order can be written as

$$FL^{(n)}(t) = \int_{-\infty}^{\infty} dt_n \int_{-\infty}^{\infty} dt_{n-1} \dots \int_{-\infty}^{\infty} dt_1 S_{\text{incoh}}^{(n)}(t_n, \dots, t_1) \times E(t - t_n) E(t - t_n - t_{n-1}) \dots E(t - t_{n-1} - \dots - t_1),$$
(19)

where the incoherent response function now reads

$$S_{\text{incoh}}^{(n)}(t_n, \dots, t_1) = \left(\frac{i}{\hbar}\right)^n \theta(t_n) \dots \theta(t_1) \operatorname{Tr} \left\{ \sum_{i \in \text{excited}} |i\rangle \Gamma_i \langle i| \mathcal{U}(t_n)[\mu, \dots[\mu, \mathcal{U}(t_1)[\mu, \rho^{\text{eq}}]]] \right\}.$$
(20)

Being an incoherent observable, the fluorescence from the (detected part of) the interaction region of the sample is simply added up to form the total signal. Since the nonlinear fluorescence signal depends only on the relative pulse phase differences, the spatial extent of the emissive region is not of crucial importance. This applies to the dependence on the inter-pulse delays as well, with the exception of the emission time, which starts counting from the interaction with the last pulse. While this moment can be different for different parts of the sample, the practical path length difference is on the order of tens of micrometers, corresponding to about 100 fs overall emission time smearing. Since the typical emission times are on the picosecond to nanosecond timescale and the emission is, in most cases, time-integrated anyway, the spatial extent of the signal is thus of no importance. As a side note, this would change if thicker samples (mm and more) were used and the emission was time-gated with ps resolution, which is possible with current technology. Since the emission comes from the excited-state populations (diagonal elements), this type of spectroscopy is sometimes called population-based.

4.2.3.3 Polarization vs. Fluorescence Response

The expressions for the nonlinear polarization signal, equation (16), and nonlinear fluorescence, equation (19), can be directly compared. In both cases, the signal depends on an n-th order response function to the perturbation by n interactions with the electric field. To find the corresponding system response, we have to look for the length of the pathways the system takes through the Liouville space. These are determined by the number of dipole moment operators present in the expressions for the response function, equations (17) and (20). In the coherent nonlinear polarization response (17), there is the additional dipole moment from the polarization that does not come from interaction with the incoming field. Thus, to have the same Liouville-space length, one needs one more interaction with light in the incoherent response (20). In an n+1 – wave mixing experiment, we therefore have $S_{\text{coh}}^{(n)}$ response for the polarization (n waves in, one wave out), and $S_{\text{incoh}}^{(n+1)}$ response for the fluorescence (n+1) waves in, fluorescence out). The structure of the response functions is very similar and they can indeed even be expressed by a generalized response function [7]. The fluorescence-detected response has, however, several additional features that lead to some more or less profound differences. First, there is the additional commutator with the dipole moment. This leads to the presence of an additional (ESA-type) pathway in the response, with an interesting interpretation that includes multiple excited states for nonlinear fluorescence. Second, there are the parts connected to the emission of the incoherent signal, namely, the weighting of the states by their emissive rate Γ_i and the time evolution $\mathcal{U}(t_n)$ during signal emission. Under emission-time integration, this leads to the weighting of the response pathways by the emission quantum yield of the end states (quantum yield means what fraction of the excited population is radiated in the form of spontaneous emission). In addition, the weighting can be controlled by time-gating the detected signal [8].

4.2.4 Signal Separation by Phase and Wave Vector

After the interaction with the laser pulses, the system is in a state that can be described as

$$\rho(t) = \sum_{n=0}^{\infty} \rho^{(n)}(t). \tag{21}$$

Importantly, this state is a superposition of the system that does not interact with the pulses at all (n = 0), interacts once with one of the pulses, etc. The observables are determined by this state via equation (9). Since this is linear in the density matrix, the perturbative expansion translates into a combination of nonlinear signals.

A macroscopic polarization gives rise to a propagating electric field E_s in the sample,

$$E_s(t) = \sum_s E_s^{(n)}(t),$$
 (22)

with $E_s^{(n)}(t)$ described in equation (16). At the same time, all excited parts of the sample emit linear and nonlinear fluorescence,

$$FL(t) = \sum_{n} FL^{(n)}(t), \qquad (23)$$

with $FL^{(n)}(t)$ described in equation (19).

The task of the experimenter is to isolate the wanted nonlinear response of the particular order and particular type from the total signal, which is practically always dominated by the linear response. To this end, the dependence of the signal on the pulse phase and/or wave vectors is utilized.

Both in population-based and coherence-based techniques, the nonlinear signal generated at each spatial point in the sample inherits the relative phase combination of the interacting pulses, see equations (14), (19). Specifically, each interaction with a pulse p at position r_0 brings a factor of $\pm (k_p \cdot r_0 + \phi_p)$. In the case of the nonlinear polarization, the signal constructively adds up along the phase-matching wave vector combinations (see equation (13)). In this way, the sample performs the (partial) signal separation by itself. While the n-th order nonlinear signal contains all combinations of n interactions with the interacting pulses, these will end up at different positions in the phase space (or the k space). The different k vectors get separated spatially by signal propagation after the sample, so they can be easily isolated. For incoherent observables such as fluorescence, the contributions have to be separated manually utilizing their phase dependence. By varying the pulse phases continuously (phase modulation) or in discrete steps (phase cycling), the phase space points can be isolated in Fourier space by a Fourier transformation. Phase cycling (or, in principle, even modulation) can be used in coherently detected spectroscopy as well, in combination with phase matching, for additional signal selection. We will elaborate on the phase cycling approach in the examples below.

4.2.4.1 Problem of Higher-Order Nonlinearities

A problem of the signal separation by the phase signature is that for each phase $\phi_s = \alpha \phi_1 + \beta \phi_2 + \ldots$, there exists a higher-order contribution with two more interactions with the pulses with the same phase, namely $\phi_{ho} = \phi_s + \phi_i - \phi_i$, where ϕ_i is the phase obtained by an interaction with any of the pulses. Since this higher-order signal has precisely the same phase signature as the desired lower-nonlinearity one, it cannot be separated by phase cycling or phase matching. Under specific circumstances, one can, however, count combinatorically the number of such contributing pathways and determine the relative contribution [9].

4.3 Wave Mixing on a Heterodimer

So far, our formulation has been completely general, not restricted to any particular system, experimental geometry, or studied system. In the following, we demonstrate

the coherence- and population-based spectroscopy side by side on a dimer of coupled squaraine molecules.

4.3.1 Squaraine Dimers with Increasing Coupling

The basic properties of the squaraine dimers are introduced in figure 4.2. They consist of squaraine A and squaraine B molecules (figure 4.2D), linked by a spacer of increasing length. Dissolved in toluene, these dimers assume an almost linear arrangement of their transition dipoles [11] so that we do not need to consider the polarization dependence of the orientationally averaged response. The energy gap ΔE between the transitions at the two monomers is about 1300 cm⁻¹. Due to the electronic coupling between the monomers, the excitons become partially delocalized between the monomers. As apparent from the absorption spectrum in figure 4.2A, there is a relatively strong (Huang–Rhys factor about 0.15) vibrational mode at 1220 cm⁻¹, quasi-resonant with the energy gap between the monomers (see, e.g., the small peak on the dSQAB-3 lineshape around 14 950 cm⁻¹). This will lead to some vibronic mixing effects [12, 13].

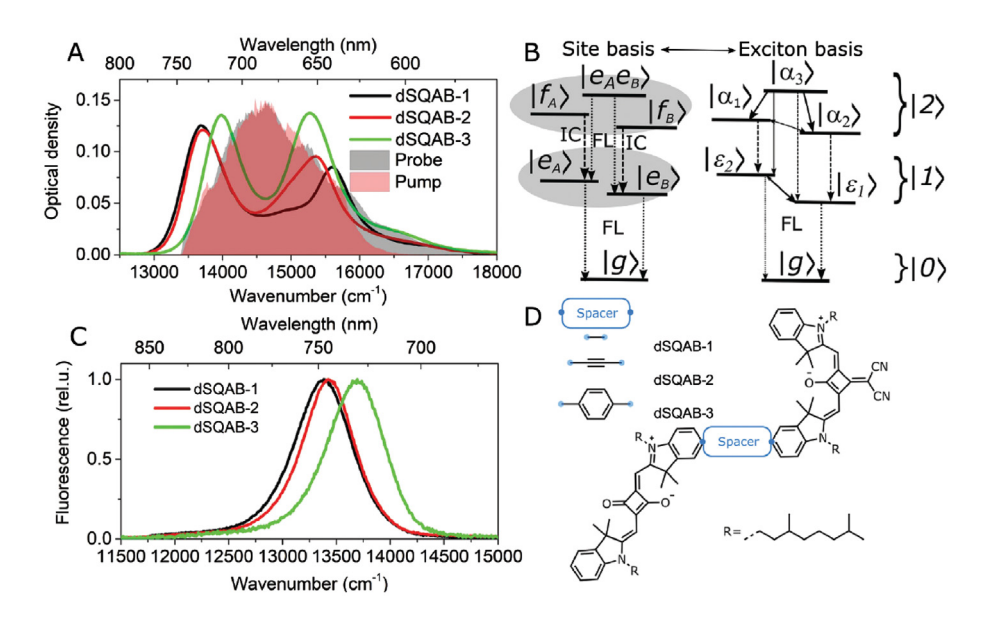


Fig. 4.2 – Squaraine dimers, adapted from Ref. [10]. A. Absorption spectra and laser spectra. B. Electronic states in diabatic (left) and adiabatic (right) basis. C. Fluorescence emission spectra. D. Dimer chemical structure describes the increasing length of the spacer.

However, for the purpose of demonstration, we will explicitly treat the electronic states only and keep all vibrational modes in the environmental bath, including this underdamped mode and the quasi-continuum of the overdamped solvent modes.

The spectroscopy of an electronic dimer is nicely described in, e.g., Ref. [14]. In the electronic dimer, the state mixing is given by the mixing angle

$$\tan 2\vartheta = \frac{2J}{\Lambda E},\tag{24}$$

where J is the coupling. Due to the head-to-tail arrangement of the transition dipoles, the coupling is indeed J-type, i.e., negative, and increases in magnitude from -350 cm^{-1} for the longest spacer (dSQAB-3) to -450 cm^{-1} (dSQAB-2) to -650 cm^{-1} with the shortest spacer (dSQAB-1) [10, 11]. The increasing coupling is visible in the absorption spectrum, the increasing splitting of the two peaks (arising predominantly from the two monomers), and in the oscillator strength redistribution from the higher-energy to the lower-energy peak. Note that, because of the large energy gap, the oscillator strength redistribution is still not very large, in contrast to what happens, e.q., in J aggregates with superradiant lowest states [14, 15]. In the emission spectrum (figure 4.2C), the gradual shift to lower-energy states is visible as well. In figure 4.2B, the state structure is shown, both on the site (diabatic) basis and on the excitonic (adiabatic) basis. We have the ground state $|q\rangle$, one-exciton states in manifold $|1\rangle$, and a two-exciton state together with some higher excited states of the squaraine monomers in manifold $|2\rangle$. From the kinematic perspective, we are interested in the properties of the electronic states: the exciton delocalization, energies of the optical transitions, and coupling of the delocalized excitons to the environmental vibrations. From the dynamical perspective, there is energy transfer from the higher-energy to the lower-energy single-exciton state, often studied in, e.g., solar energy context. The energy transfer from the two-exciton state to the higher states, followed by rapid internal conversion to the single-exciton states is together called exciton—exciton annihilation since it leads to a loss of one excitation. In the squaraine dimers, all of the mentioned relaxation processes occur on timescales of several tens of femtoseconds. Further dynamics that can be explored but will be omitted in this tutorial is vibronic beating, i.e., oscillatory dynamics of the electron-vibrational wavepacket. The timescale for the oscillations and their decay is picoseconds. Finally, we have radiative and non-radiative excited-state decay to the ground state, occurring on a timescale of several nanoseconds. We will now look at how these properties can be extracted with the help of coherence- and population-based spectroscopy.

4.3.2 Two-Wave Mixing: Linear Absorption

As an introduction, it is useful to first briefly consider common linear absorption experiments. Which order of perturbation theory is that? In the language of our description, it depends on what type of signal we detect. The most common way of measuring absorption is to illuminate the sample with white light and compare how much passes through (intensity $I(\omega)$) compared to a reference without the sample (intensity I_0), with the light spectrum dispersed by a spectrograph. That is, one measures the absorption coefficient $\alpha(\omega)$ according to the Beer–Lambert law,

$$-\log \frac{I(\omega)}{I_0(\omega)} = \alpha(\omega) d, \tag{25}$$

where d is the thickness of the sample. In this case, we measure the linear polarization of the sample (see figure 4.3 top).

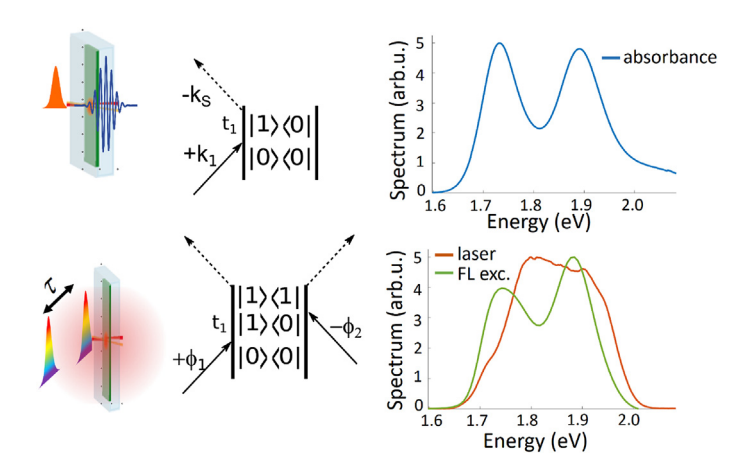


Fig. 4.3 – Linear absorption. Top: Coherent polarization picture. Bottom: Fluorescence-detected excitation picture. Spectra correspond to the dSQAB-3 dimer introduced in figure 4.2. Left column: excitation pulses, sample response. Middle column: DSFD of the corresponding response pathways. Right: obtained spectra. Note: the coherently detected absorption (blue) was measured in transmission and already divided by the spectrally dependent intensity. The fluorescence excitation spectrum (green) is still multiplied by the laser spectrum (orange).

According to equation (10),

$$P^{(1)}(t) = \text{Tr}\Big\{\mu\rho^{(1)}(t)\Big\}. \tag{26}$$

Together with equation (6), this reads

$$P^{(1)}(t) = \int_{-\infty}^{\infty} dt_1 S_{\text{coh}}^{(1)}(t_1) E(t - t_1) = \frac{i}{\hbar} \int_{0}^{\infty} dt_1 \text{Tr}\{\mu \mathcal{U}(t_1)[\mu, \rho^{\text{eq}}]\} E(t - t_1).$$
 (27)

The commutator leads to two expressions that correspond to two Liouville-space pathways. Since these two pathways are complex-conjugate of each other, we can write

$$P^{(1)}(t) = \frac{i}{\hbar} \int_0^\infty dt_1 \text{Tr} \{ \mu \mathcal{U}(t_1) \mu \rho^{\text{eq}} \} E^+(t - t_1) + \text{c.c.}$$
 (28)

Here, only the positive-frequency part of the E field survives since the other term oscillates fast under the integration (RWA). The pathway before the c.c. is shown in figure 4.3 top.

In order to obtain the absorption spectrum, the light has to be spectrally dispersed by, e.g., a prism or grating spectrometer. This corresponds to making a

Fourier transformation in t. Since the Fourier transform of a convolution is a multiplication, we have

$$P^{(1)}(\omega) = S_{\text{coh}}^{(1)}(\omega)E(\omega). \tag{29}$$

Here we can directly compare with $D(\omega) = \varepsilon_0 E(\omega) + P(\omega) = \varepsilon_0 (1 + \chi(\omega)) E(\omega) = \varepsilon_0 \varepsilon_r E(\omega)$, identifying the linear response $S_{\text{coh}}^{(1)}(\omega)$ with the susceptibility. In the experiment, we compare the field on the spectrometer with minus without the sample, isolating the second term. Since for complex refractive index $\tilde{n}^2 = \varepsilon_r = 1 + \chi(\omega)$, $k = \tilde{n} \frac{\omega}{c}$, $E^+(r) \propto e^{ikr}$ and absorption coefficient is defined from $I = I_0 e^{-\alpha(\omega)r}$, we can immediately relate the absorption coefficient to the imaginary part of $S_{\text{coh}}^{(1)+}(\omega)$,

$$\alpha(\omega) = \frac{\omega}{nc} \operatorname{Im} \left\{ S^{(1)+}(\omega) \right\} = \frac{\omega}{\hbar nc} \operatorname{Re} \int_0^\infty dt_1 e^{i\omega t_1} \left\{ \operatorname{Tr} \left\{ \mu \mathcal{U}(t_1) \mu \rho^{eq} \right\} \right\}. \tag{30}$$

The coherent linear response pathway is shown in figure 4.3 top, with the emission of coherent polarization with wave vector $k_s = k_1$ indicated by a dashed arrow.

A second way to measure absorption is to excite the sample with light and measure its spontaneous emission, which is proportional to the excited state population (see figure 4.3 bottom). Variation of emission intensity with the frequency of excitation light then provides information about the absorption spectrum, in this case, called the excitation spectrum. According to equation (19), we have for the fluorescence

$$FL^{(2)}(t) = \int_{-\infty}^{\infty} dt_2 \int_{-\infty}^{\infty} dt_1 S_{\text{incoh}}^{(2)}(t_2, t_1) E(t - t_2) E(t - t_2 - t_1).$$
 (31)

Integrating over the emission time, we get

$$\operatorname{FL}^{(2)} = \frac{1}{\hbar^2} \int_{-\infty}^{\infty} dt \int_{0}^{\infty} dt_2 \int_{0}^{\infty} dt_1 \operatorname{Tr} \left\{ \sum_{i \in \text{excited}} |i\rangle \Gamma_i \langle i| \mathcal{U}(t_2)[\mu, \mathcal{U}(t_1)[\mu, \rho^{\text{eq}}]] \right\}$$

$$\times E(t - t_2) E(t - t_2 - t_1).$$
(32)

Note that these are also effectively two pathways only: since they have to end up in the excited state to produce emission, the dipole moments have to act from opposite sides. As before, the pathways are complex and conjugate to each other, producing an overall real population. One of the pathways is depicted in figure 4.3 bottom.

In order to vary the excitation spectrum, one can use quasi-monochromatic light and scan the wavelength. Alternatively, way more useful in time-resolved spectroscopy, a pair of pulses can be used with variable delay τ , determining the spectrum interferometrically by a Fourier transformation. In this case, we have

$$\operatorname{FL}^{(2)}(\omega) = \int_{-\infty}^{\infty} d\tau e^{i\omega\tau} \frac{1}{\hbar^2} \int_{-\infty}^{\infty} dt \int_{0}^{\infty} dt_2 \int_{0}^{\infty} dt_1 \operatorname{Tr} \left\{ \sum_{i \in \text{excited}} |i\rangle \Gamma_i \langle i|\mathcal{U}(t_2)\mu\mathcal{U}(t_1)\mu\rho^{\text{eq}} \right\}$$

$$\times A^*(t - t_2) A(t - t_2 - t_1 + \tau) e^{-i\omega_0(\tau - t_1)} + \text{c.c.}$$
(33)

Here, we have already separated the response to the two complex-conjugated pathways and kept only the opposite-frequency parts of the electric fields since the other terms rapidly oscillate and cancel under integration. Furthermore, we have omitted the terms that interact twice with one of the pulses since these do not oscillate with the delay τ and produce a constant background for our measurement. Carrying out the F.T. over τ (substituting for $\tau = t - t_2 - t_1 + \tau$), we get

$$\operatorname{FL}^{(2)}(\omega) = A(\omega - \omega_0) \frac{1}{\hbar^2} \int_{-\infty}^{\infty} dt \int_0^{\infty} dt_2 \int_0^{\infty} dt_1 \operatorname{Tr} \left\{ \sum_{i \in \text{excited}} |i\rangle \Gamma_i \langle i| \mathcal{U}(t_2) \mu \mathcal{U}(t_1) \mu \rho^{\text{eq}} \right\}$$

$$\times A^*(t - t_2) e^{-i(\omega - \omega_0)(t - t_2)} e^{i\omega t_1} + \text{c.c.}$$
(34)

Now, we can perform the F.T. over t (substituting $t - t_2$). Since t_2 remains in the excited-state decay only, we can integrate over that as well, getting the FL quantum yields Q_i . We thus have

$$\operatorname{FL}^{(2)}(\omega) = |A(\omega - \omega_0)|^2 \frac{2}{\hbar^2} \operatorname{Re} \left\{ \int_0^\infty dt_1 \operatorname{Tr} \left\{ \sum_{i \in \text{excited}} |i\rangle Q_i \langle i| \mu \mathcal{U}(t_1) \mu \rho^{\text{eq}} \right\} e^{i\omega t_1} \right\}.$$
(35)

This expression (35) can be directly compared to the expression (30). The incoherent second-order response pathway is indicated in figure 4.3 bottom, with fluorescence emission indicated by the two dashed arrows. The fluorescence excitation spectrum looks different from the absorption because of the additional multiplication by the laser spectrum $|A(\omega - \omega_0)|^2$ in equation (35) compared to equation (30). Same as in equation (25), one can divide by the known laser spectrum to obtain the absorption spectrum. In practice, it can be surprisingly difficult to measure precisely the same spectrum that is absorbed, and small errors lead to large discrepancies in the division, especially at the spectral edges. In a coupled dimer, the excited-state populations rapidly equilibrate in a quasi-stationary state (according to Boltzmann distribution at a given temperature), and this state then radiates with a single effective fluorescence quantum yield [8]. Due to this separation of timescales and inevitable excitation relaxation to the lowest excited state, the excitation spectrum should directly correspond to the absorption one. The situation is different when multiple relaxation pathways are present for different states, in which case is the contribution of their respected peaks weighted by the specific quantum yields. This is useful since the comparison of fluorescence excitation and absorption spectrum then reports on, for example, energy transfer efficiency – a measurement often used in photosynthetic light-harvesting complexes.

4.3.3 Four-Wave Mixing

4.3.3.1 General Description

In centrosymmetric samples such as randomly oriented molecules in solution, the even nonlinear order polarization vanishes. The lowest-order nonlinear spectroscopy is thus four-wave mixing (FWM).

We have third-order nonlinear coherent polarization

$$P^{(3)}(t) = \left(\frac{i}{\hbar}\right)^{3} \int_{0}^{\infty} dt_{3} \int_{0}^{\infty} dt_{2} \int_{0}^{\infty} dt_{1} \operatorname{Tr} \{\mu \mathcal{U}(t_{3})[\mu, \mathcal{U}(t_{2})[\mu, \mathcal{U}(t_{1})[\mu, \rho^{\text{eq}}]]]\}$$

$$\times E(t - t_{3}) E(t - t_{3} - t_{2}) E(t - t_{3} - t_{2} - t_{1})$$
(36)

In fluorescence, the corresponding order of nonlinearity is the fourth:

$$FL^{(4)}(t) = \left(\frac{i}{\hbar}\right)^{4} \int_{0}^{\infty} dt_{4} \int_{0}^{\infty} dt_{3} \int_{0}^{\infty} dt_{2} \int_{0}^{\infty} dt_{1}$$

$$\times Tr \left\{ \sum_{i \in \text{excited}} |i\rangle \Gamma_{i}\langle i| \mathcal{U}(t_{4})[\mu, \mathcal{U}(t_{3})[\mu, \mathcal{U}(t_{2})[\mu, \mathcal{U}(t_{1})[\mu, \rho^{\text{eq}}]]]] \right\}$$

$$\times E(t - t_{4}) E(t - t_{4} - t_{3}) E(t - t_{4} - t_{3} - t_{2}) E(t - t_{4} - t_{3} - t_{2} - t_{1}).$$
(37)

These expressions are completely general and can be used for many types of four-wave mixing experiments. Here, we will focus on the most basic and widespread experiments, *i.e.*, pump-probe (also known as transient absorption, TA), and its multi-dimensional variant two-dimensional electronic spectroscopy (2DES) [16, 17]. Both of these experiments can be described by the same train of excitation pulses: first comes a pair of pulses delayed by time delay τ , exciting the system. This delay needs to be phase-stable. In TA or transient grating experiment, we have $\tau = 0$. Then, we wait for delay time T called waiting or population time, during which the perturbed system evolves. Finally, the spectrum of the system has to be probed. This is done in the same way as in the linear absorption section above. That is, in the coherence-based approach, a single pulse creates a nonlinear polarization oscillating in time t, whose spectrum is to be detected, while in the population-based approach, a pair of pulses is used with their delay t interferometrically scanned to produce the spectrum. In the coherently-detected spectroscopy, we thus have a pulse train

$$E_{\text{C-2DES}}(t, T, \tau) = A_3(t)e^{-i\omega_0 t + ik_3 \cdot r + i\phi_3} + A_2(t+T)e^{-i\omega_0(t+T) + ik_2 \cdot r + i\phi_2} + A_1(t+T+\tau)e^{-i\omega_0(t+T+\tau) + ik_1 \cdot r + i\phi_1} + \text{c.c.}$$
(38)

For the action-detected experiment, we have one more pulse:

$$E_{\text{F-2DES}}(t', t, T, \tau) = A_4(t') e^{-i\omega_0 t' + ik_4 \cdot r + i\phi_4} + A_3(t' + t) e^{-i\omega_0 (t' + t) + ik_3 \cdot r + i\phi_3}$$

$$+ A_2(t' + t + T) e^{-i\omega_0 (t' + t + T) + ik_2 \cdot r + i\phi_2}$$

$$+ A_1(t' + t + T + \tau) e^{-i\omega_0 (t' + t + T + \tau) + ik_1 \cdot r + i\phi_1} + \text{c.c.}$$

$$(39)$$

In both cases, we chose the last pulse to be centered at zero time, *i.e.*, the signal emission begins immediately after the action of the last pulse. We emphasize at this point that for a transient grating experiment, we have $\tau = 0$, and for a pump–probe (TA) experiment, we have $\tau = 0$ and $k_1 = k_2$. While coherently-detected transient grating is relatively common, the fluorescence-detected variant has not, to our knowledge, been realized yet.

In the nonlinear signal expressions (36) and (37), the times t_1, t_2, \ldots are positive, *i.e.*, the response follows the perturbation, respecting causality. When we neglect

pulse overlap in time (which is not always possible), we can, therefore, take the first interaction to be with pulse 1, the second with pulse 2, etc. This leads to

$$P^{(3)}(t, T, \tau) = \left(\frac{i}{\hbar}\right)^{3} \int_{0}^{\infty} dt_{3} \int_{0}^{\infty} dt_{2} \int_{0}^{\infty} dt_{1} \operatorname{Tr}\{\mu \mathcal{U}(t_{3})[\mu, \mathcal{U}(t_{2})[\mu, \mathcal{U}(t_{1})[\mu, \rho^{\text{eq}}]]]\}$$
(40)

$$E_3(t-t_3)E_2(t+T-t_3-t_2)E_1(t+T+\tau-t_3-t_2-t_1)$$
(41)

and

$$FL^{(4)}(t', t, T, \tau) = \left(\frac{i}{\hbar}\right)^{4} \int_{0}^{\infty} dt_{4} \int_{0}^{\infty} dt_{3} \int_{0}^{\infty} dt_{2} \int_{0}^{\infty} dt_{1}$$

$$\times Tr \left\{ \sum_{i \in \text{excited}} |i\rangle \Gamma_{i} \langle i| \mathcal{U}(t_{4})[\mu, \mathcal{U}(t_{3})[\mu, \mathcal{U}(t_{2})[\mu, \mathcal{U}(t_{1})[\mu, \rho^{\text{eq}}]]]] \right\}$$

$$\times E_{4}(t' - t_{4}) E_{3}(t' + t - t_{4} - t_{3}) E_{2}(t' + t + T - t_{4} - t_{3} - t_{2})$$

$$\times E_{1}(t' + t + T + \tau - t_{4} - t_{3} - t_{2} - t_{1}). \tag{42}$$

The expressions (40) and (42) can be used for the evaluation of the total signal, broken into the individual response pathways. For interpretation, it is very useful to consider pulses shorter than any electronic dynamics except the optical frequency oscillations (impulsive limit), in which case the slowly-varying envelopes can be taken as 'physical' delta functions, $A(t) \approx \delta(t)$. In this case, we get rid of the integrations and obtain directly the response with $t_1 = \tau$, $t_2 = T$, $t_3 = t$, $t_4 = t'$. We therefore measure signals directly proportional to the response, sampled in the inter-pulse delay times:

$$P^{(3)}(t,T,\tau) \propto \text{Tr}\{\mu \mathcal{U}(t)[\mu,\mathcal{U}(T)[\mu,\mathcal{U}(\tau)[\mu,\rho^{\text{eq}}]]]\}$$
(43)

and

$$\operatorname{FL}^{(4)}(t',t,T,\tau) \propto \operatorname{Tr} \left\{ \sum_{i \in \operatorname{excited}} |i\rangle \Gamma_i \langle i| \mathcal{U}(t')[\mu,\mathcal{U}(t)[\mu,\mathcal{U}(|T)[\mu,\mathcal{U}(\tau)[\mu,\rho^{\operatorname{eq}}]]]] \right\}. \tag{44}$$

While the dependence of $\mathrm{FL}^{(4)}$ on t' opens up the possibility of gating, we will consider the following time-integrated detection $\mathrm{FL}^{(4)}(t,T,\tau) = \int_0^\infty dt' \mathrm{FL}^{(4)}(t',t,T,\tau)$, getting

$$\operatorname{FL}^{(4)}(t, T, \tau) \propto \sum_{i \in \operatorname{avcited}} \operatorname{Tr}\{|i\rangle Q_i \langle i| [\mu, \mathcal{U}(t)[\mu, \mathcal{U}(|T)[\mu, \mathcal{U}(\tau)[\mu, \rho^{\operatorname{eq}}]]]]\}, \tag{45}$$

where Q_i is the quantum yield of state i.

4.3.3.2 Signal Selection by Phase Matching and Phase Cycling

As we demonstrated when introducing the double-sided Feynman diagrams above, the individual Liouville-space pathways contain various combinations of the positive- and negative-frequency parts of the electric fields of the excitation pulses. In the coherently-detected case, the individual contributions will have different wave vectors. There is, e.g., a contribution with a wave vector $-k_1 + k_1 + k_1$ that travels along pulse one and would be hard to isolate from the linear signal. There are, however, other contributions as well that travel in other directions. Here, we will focus on the contribution with wave vector $-k_1 + k_2 + k_3$. In the incoherently-detected spectroscopy, the contributions cannot be distinguished by spatial propagation. However, we can still distinguish them by their (relative) phase signature. The phase signature that corresponds to the wave vector combination above is $-\phi_1 + \phi_2 + \phi_3 - \phi_4$. The wave vector can be selected by choosing the wave vector of the local oscillator. The phase dependence is used in phase cycling or phase modulation approach. In phase modulation, the excitation beams are phase-modulated at slightly different frequencies (for typical Ti:sapphire 80 MHz repetition rate, the frequency differences are typically around 10 kHz), typically by acousto-optical modulators [18-21]. A lock-in detection is then used to isolate the appropriate phase combination. The advantage of lock-in detection is that it suppresses the slow, low-frequency noise (1/f) noise in lock-in speak, pink or flicker noise) at the same time. Phase modulation is typically used with MHz laser repetition rate systems. For kHz laser repetition rate systems, the phase can be cycled discretely on a shot-to-shot basis, typically using a pulse shaper [10, 18, 22, 23]. An excellent paper on phase cycling is by Howe-Siang Tan [24]. Briefly, for a phase signature $\alpha \phi_1 + \beta \phi_2 + \gamma \phi_3 + \delta \phi_4$ (we have $[\alpha, \beta, \gamma, \delta] = [-1, 1, 1, -1]$ for our contribution), one can (denoting $\phi_{nm} = \phi_n - \phi_m$) isolate the contribution by

$$FL_{\beta,\gamma,\delta}^{(4)} = \frac{1}{LMN} \sum_{l=0}^{L-1} \sum_{m=0}^{M-1} \sum_{n=0}^{N-1} e^{-il\beta_L^{2\pi}} e^{-im\gamma_M^{2\pi}} e^{-in\delta_N^{2\pi}} FL^{(4)}$$

$$\times \left(\phi_{21} = l \frac{2\pi}{L}, \phi_{31} = m \frac{2\pi}{M}, \phi_{41} = n \frac{2\pi}{N} \right).$$
(46)

The technique is called phase cycling because the complex unit cycle in phase space is separated into L, M, and N points uniformly, the inter-pulse phases are cycled along these points, and the measured fluorescence signals are added with the complex weights. The number of points is chosen such that the discrete Fourier Transformation can distinguish between the desired orders of nonlinearity (signals with coefficient β and $\beta + pL$ where p is an integer get aliased (overlap)). For standard four-wave mixing, to suppress the lower-order contributions, one can use L = M = N = 3, i.e., $1 \times 3 \times 3 \times 3$ phase cycling.

When we stay with the $-k_1 + k_2 + k_3$, respectively $-\phi_1 + \phi_2 + \phi_3 - \phi_4$ contribution, there are three types of pathways that constitute the signal. These are depicted in figure 4.4, with the curly arrows indicating signal emission. As is apparent from the C-2DES and F-2DES comparison, the additional commutator has here more profound consequences than in the linear experiment. First, the excited-state absorption (ESA) type pathway has the same sign as the GSB and SE type pathways. And second, there is an additional response pathway of the ESA type (ESA2), with an opposite sign, ending in a double-excited state. What are the

consequences for the interpretation of the overall signal? We will illustrate this in the particular example of our squaraine dimer.

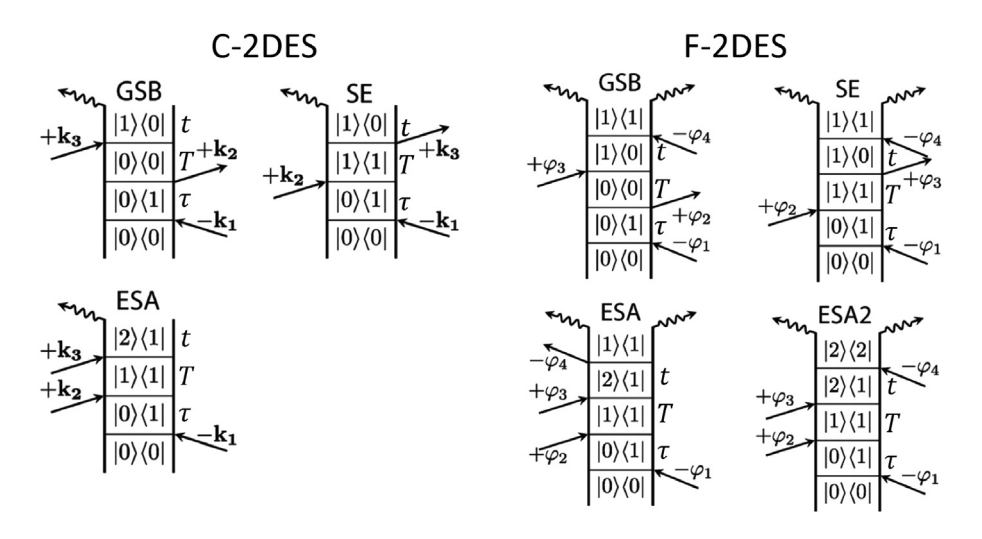


Fig. 4.4 – Liouville-space pathways for coherently (C-) and fluorescence (F-) detected 2DES. Adapted from Ref. [10].

4.3.3.3 Experimental Setup

We will be comparing the coherently and fluorescence-detected experiments under practically identical conditions. We have already invested some effort in formulating their description in an unified way, facilitating direct comparison. Experimentally, we used a setup at Würzburg University, sketched in figure 4.5. It is a typical kHz pulse repetition rate laser system, with MHz Ti:Sapphire oscillator as a seed for an amplifier with about 35 fs, 1 kHz, 4 mJ pulses (Spectra Physics). To broaden the spectrum, the pulses are attenuated to about 1.5 mJ and broadened in an Ar or Ne filled 1 m long hollow core fiber (Ultrafast Innovations). The pulse chirp after the fiber can be compensated by chirped mirrors, part of the beam is split off by a wedge, delayed by a delay stage (Newport), and used as a probe. The rest of the pulses are pre-compressed by a GRISM (prism pair with engraved gratings) compressor and shaped by the Dazzler Acousto-Optical Programmable Dispersive Filter (AOPDF, Fastlite)). The shaper is used both for pulse compression, spectral shaping, and generation of pulse sequences. The pulses are overlapped in a sample cell (Starna) through which the sample flows. The nonlinear polarization signal is detected in the same direction as the probe beam, overlapping them on a CCD spectrometer (Princeton instruments) working shot-to-shot in line mode. The fluorescence is collected by an objective and detected by an avalanche photodiode (Laser Components), not in the photon counting mode but resolved in the APD response time, digitized by a digitizer card (Teledyne) and integrated on the fly.

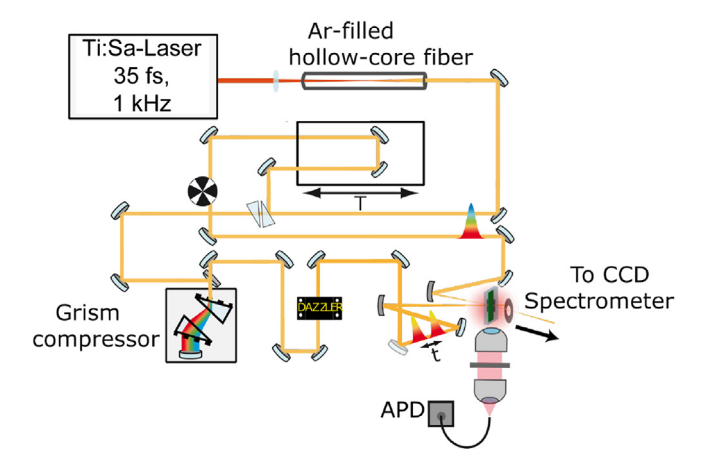


Fig. 4.5 – Setup at University of Würzburg used for the measurements directly comparing coherently and fluorescence-detected spectra. Adapted from Ref. [10].

4.3.3.4 Four-Wave Mixing: Transient Absorption

First, we compare coherently detected (*i.e.*, standard) pump–probe (C-PP) and fluorescence-detected pump–probe (TA) spectroscopy (developed by us) of the most weakly coupled squaraine dimer (dSQAB-3). The measured data as well as calculated maps are presented in figure 4.6. The pump-probe is measured in a very standard way, recording the signal self-heterodyned with the probe field and performing pumped/unpumped differential acquisition. The coherently-detected data are evaluated as TA:

$$\text{C-PP}^{(3)}(\omega, T) = -\log \frac{I_{\text{pumped}}}{I_{\text{unpumped}}} \approx \frac{2\text{Re}\left\{E_{pr}^{-} \cdot E^{(3)+}(\omega, T, 0)\right\}}{I_{pr}}.$$
 (47)

Here, we used the approximation $\log(1+x) \approx x$ and neglected $I_{\rm sig}$. In reality, we measure not two but four combinations of the pump and probe pulses to isolate and subtract the pump scatter (if any) and background contributions: $-\log\frac{I_{\rm pumped}-I_{\rm background}}{I_{\rm unpumped}-I_{\rm background}}$. Note, however, that only the incoherent part of the scatter can be subtracted in this way, leaving the potential scatter-probe interference ripples on top of the TA spectrum. A single pump and single probe pulses are used of highly similar spectra and duration (around 12 fs, spectrally covering the two main transitions of the dimer).

For the fluorescence-detected variant, The experimental setup is kept as it is, but the probe pulse now serves as the pump, while the pump pulse is shaped into a pulse pair (by the Dazzler AOPDF) that is used as a probe. Compared to the linear absorption section above, we can see that this is really a direct analog of transient absorption and should be, thus perhaps, called transient excitation spectroscopy. The fluorescence from the spot of pulse overlap in the sample is collected by

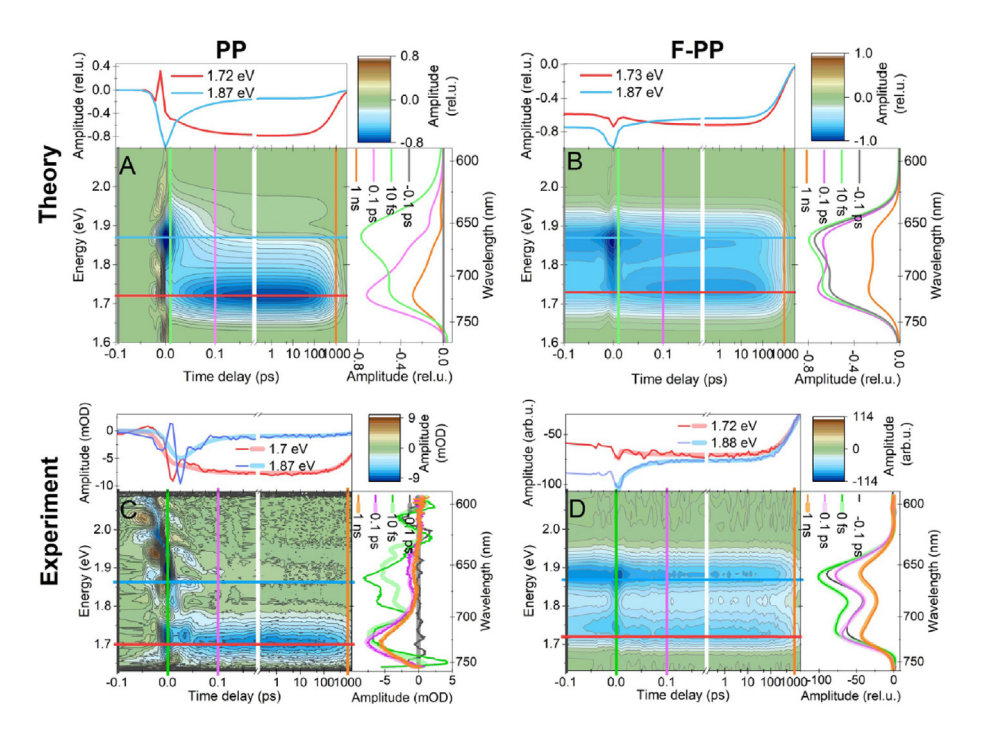


Fig. 4.6 – Coherently (left) and fluorescence-detected (right) transient absorption. Shown is theoretical non-perturbative calculation (top) and experiment (bottom). Adapted from Ref. [26].

a $10\times$ objective perpendicular to the beams, coupled to a multimode fiber, and recorded time-integrated by the avalanche photodiode. The F-PP data are calculated as

$$F-PP^{(4)}(\omega, T) = \int_0^\infty dt e^{i\omega t} \{ FL_{Pu+Pr}(t, T) - FL_{Pr}(t) \}$$

$$\propto \int_0^\infty dt e^{i\omega t} \int_0^\infty dt' FL^{(4)}(t', t, T, 0).$$
(48)

Note, that the Fourier transform (in practice discrete, carried out after subtraction of the average signal value over t) isolates the oscillatory component of the measured fluorescence in t, i.e., the part probed by the probe pulse pair, eliminating the fluorescence from the pump beam only. The fluorescence from the probe pulses alone is measured with the pump beam blocked and subtracted. In case one has perfectly phase-stable pump and probe beams, using 2×2 phase cycling on the probe pulse pair is recommended to get rid of coherence between the pump and the probe. A natural choice of geometry for F-PP would be single-beam, all-collinear. However, slightly non-collinear is fine as well, as we use here to facilitate comparison. Using pulse-shaper for the double-pulse scan allows one to scan the delay in a

(partially) rotating frame to save acquisition time [10]. However, any phase-stable way, such as an interferometer, would do.

In both cases, the pump and probe are delayed by a mechanical delay line to access delays up to nanoseconds with femtosecond precision (the shaper can reach only a couple of picoseconds). To maintain the symmetry between the experiments, we use the same intensity for the pump and probe beams, making sure to stay in the perturbative regime. This can be checked by fluorescence intensity scaling linearly both with the pump and the probe intensities. The sample is flown through a standard 200 μ m flow cell, tilted at an angle to allow collection of fluorescence.

In the calculation, we follow the experimental procedure. That is, we solve equation (2) non-perturbatively in the system-field interaction, using Redfield theory for the interaction with the vibrational bath [25] (see chapter 3). We use finite 12 fs Gaussian pulses and vary the delays and pulse amplitudes same as in the experiment. The only difference is for the coherently-detected pump-probe, as we do not solve signal propagation and thus do not have phase matching. We use simple 1×2 phase cycling of the probe pulse instead. As can be seen from the good correspondence between the theory and experiment in figure 4.6, our description of the experiment is quantitatively sufficient not to distinguish between the measurement and calculation in our discussion. Let us discuss the shape of the transient maps and the difference between the two approaches. It is characteristic for the field that we use a non-perturbative approach for calculations (straightforward treatment of finite pulses, automatically includes all possible interactions with the pulses etc.), and perturbative language of response pathways for interpretation.

Unsurprisingly, the transient spectra feature two peaks at the positions of the two absorption peaks (see figure 4.2). The upper-energy peak decays rapidly with population relaxation to the lower-energy state. While this applies to both C-PP and F-PP, in C-PP, the upper peak disappears completely since the SE from the upper transition shifts to the lower one, and the upper transition is not bleached anymore (the SQA squaraine is in its ground state). In contrast, in F-PP the seeming bleach of the upper transition remains. As a result, the population transfer is much more pronounced in C-PP. This is a general difference between the techniques that can be understood either at the response pathway level or at the conceptual level. At the diagram level, we will think on a collective state basis. There, in C-PP, the GSB-type pathway through the upper transition is canceled by the ESA-type pathway with population relaxation in the waiting time. This causes the peak to disappear. This cancellation cannot happen in F-PP, since the ESA pathway has the same sign. All this depends on the contribution of the ESA2 pathway with the opposite sign, ending in the two-exciton manifold. In case the double-excited state would produce two photons, the ESA2 + ESA pathways act together as the standard ESA pathway in C-PP, and one recovers the standard C-PP. However, and this is the case almost for all connected molecular systems, two excitons will sooner meet and undergo exciton-exciton annihilation (EEA) than the emission can occur. In the dimer the separation of timescales is

extreme, since the EEA takes about 30 fs, while emission takes 3 ns. One of the two excitations is therefore lost, the photon yield of the ESA2 pathway is precisely the same as that of the ESA pathway, and they cancel each other out. The GSB-type pathway involving the upper transition thus remains until the molecules recover by relaxation back to ground state. On the conceptual level, one can understand the F-PP as the amount of fluorescence caused by the probe, modified by the presence of the pump. When the pump has excited the system, the probe absorption will not always lead to fluorescence. This is because 1) the probe can induce stimulated emission of the pump-induced excitation (same as in C-PP), 2) the system is already bleached by the pump (this would be the standard ground-state bleach known from C-PP), or 3) the pump-induced excitation can annihilate the one induced by the probe. The latter is why the bleach of both transitions remains as long as the pump excitation lives in the system, since the upper transition can absorb the probe, but does not produce more fluorescence as long as there already is an excitation in the system. From this point of view, it is also easy to see the reason for the presence of a signal before time zero, i.e., in the situation when the probe comes before the pump. While the probe always finds the system in the ground state, the following pump can decrease the system excitation due to stimulated emission or EEA. As an important side note, it is important to reverse the direction of the probe pulse pair scanning when measuring before time zero (pulse needs to be scanned to earlier times, while after time zero the pulse is scanned to later times). Writing down the response pathways for systems with perfect EEA, we find for T < 0 two pathways in both of which the ground-state absorption is probed, and for T > 0 one pathway probing ground state bleach and one the stimulated emission. In other words, for T < 0, there is the bleach-type absorption spectrum only, while for T > 0, there is also SE by the probe. This can even be utilized, since subtracting half of the negative time transient map from the positive time isolates the SE-type pathways, reporting on the excited-state dynamics. We verified this on the squaraine dimers and mCherry fluorescent proteins, isolating the dynamic Stokes shift [26]. The full extent of the applicability of this approach has not yet been explored. In both techniques the signal lives with the excited state lifetime, which is around 3 ns.

Another consequence of the additional ESA2 pathway is the absence of ESA for complete EEA (in case of ESA into doubly excited states) and rapidly relaxing higher excited states (in case of ESA into these). In the pathway language, this is because the two pathways cancel out. The physical intuition is that as long as ESA does not lead to more emission, it will not be visible in the signal.

Next to these fundamental differences, there are practical differences as well. First, since F-PP arises from the resonant excitation only, it does not suffer from off-resonant processes such as cross-phase modulation, stimulated Raman scattering, etc., together comprising the so-called coherent artifact (CA). Note that in our case of a strong probe, the CA is unusually strong as well, exacerbating the situation. In practice, however, the CA is still often the problem preventing access to the early-time behavior, even for short pulses. F-PP is thus excellent for short-time dynamics. Another difference is that, due to the type of acquisition, the C-PP is

implicitly divided by the probe spectrum, while the F-PP remains multiplied by the laser spectrum. While this does not influence the dynamics, it does change the spectral shape. Division by the laser spectrum to correct is possible, but introduces noise, especially at the edges of the spectrum. For a detailed description of F-PP and its comparison with C-PP on diverse samples, we refer the reader to Ref. [26]. Now, we proceed with 2DES.

4.3.3.5 Four-Wave Mixing: 2DES

We have seen already both in the linear absorption (excitation spectra) and in the F-PP (transient excitation) that a double-pulse scan can be used to obtain spectral resolution for two interactions with the electric field. In the fluorescence-detected version of the TA, we used the double-pulse scan to get the spectrum along the probe axis. In the pump-probe, both coherently and fluorescence-detected, we do have two interactions with the pump pulse. It is, therefore, straightforward to replace the pump pulse with a double pulse to spectrally resolve the excitation process as well. This leads to the 2D electronic spectroscopy (2DES) in the pump-probe geometry. We thus still have $k_1 = k_2 = k_{Pu}$, $k_3 = k_{Pr}$, but now we do not set $\tau = 0$ anymore. We can use the same experimental setup as before, figure 4.5. For the C-2DES, we use the probe pulse and make the Dazzler produce the pump pulse pair. For F-2DES, we now make all four pulses using the Dazzler shaper in an all-collinear geometry. In C-2DES, the signal is isolated the same as in C-PP (self-heterodyned, the probe field acts as the LO, producing an inherently absorptive spectrum without phasing). The delay τ between the pump pulses is scanned, and discrete FT leads to the result

$$C-2DES(\omega_t, T, \omega_\tau) = \int d\tau e^{i\omega_\tau \tau} PP^{(3)}(\omega_t, T, \tau).$$
(49)

In F-2DES, we drop the differential acquisition, and proceed with full $1 \times 3 \times 3 \times 3$ phase cycling of all pulses. The absorptive spectrum is then obtained by adding the rephasing ($[\alpha, \beta, \gamma, \delta] = [-1, 1, 1, -1]$) and non-rephasing ($[\alpha, \beta, \gamma, \delta] = [1, -1, 1, -1]$) contributions, with the usual ω_{τ} axis flip for one of them (typically rephasing) to obtain positive frequencies [27]. We have

$$F-2DES_{[\alpha,\beta,\gamma,\delta]}(\omega_{t}, T, \omega_{\tau})$$

$$= \int dt e^{i\omega_{t}t} \int d\tau e^{\pm i\omega_{\tau}\tau} \sum_{l=0}^{2} \sum_{m=0}^{2} \sum_{n=0}^{2} e^{-il\beta\frac{2\pi}{3}} e^{-im\gamma\frac{2\pi}{3}} e^{-in\delta\frac{2\pi}{3}}$$

$$\times \int dt' FL^{(4)} \left(t', t, T, \tau, \phi_{21} = l\frac{2\pi}{3}, \phi_{31} = m\frac{2\pi}{3}, \phi_{41} = n\frac{2\pi}{3}\right),$$
(50)

where the + in the τ F.T. applies for non-rephasing and - for rephasing part.

In the theoretical description, we exactly follow the experiment, same as in the case of PP, only now we also scan the time interval between the first pair of pulses. The 2D spectra taken at T=30 fs are shown in figure 4.7. Once again, the correspondence between the experiment and theory is good enough to compare the techniques only.

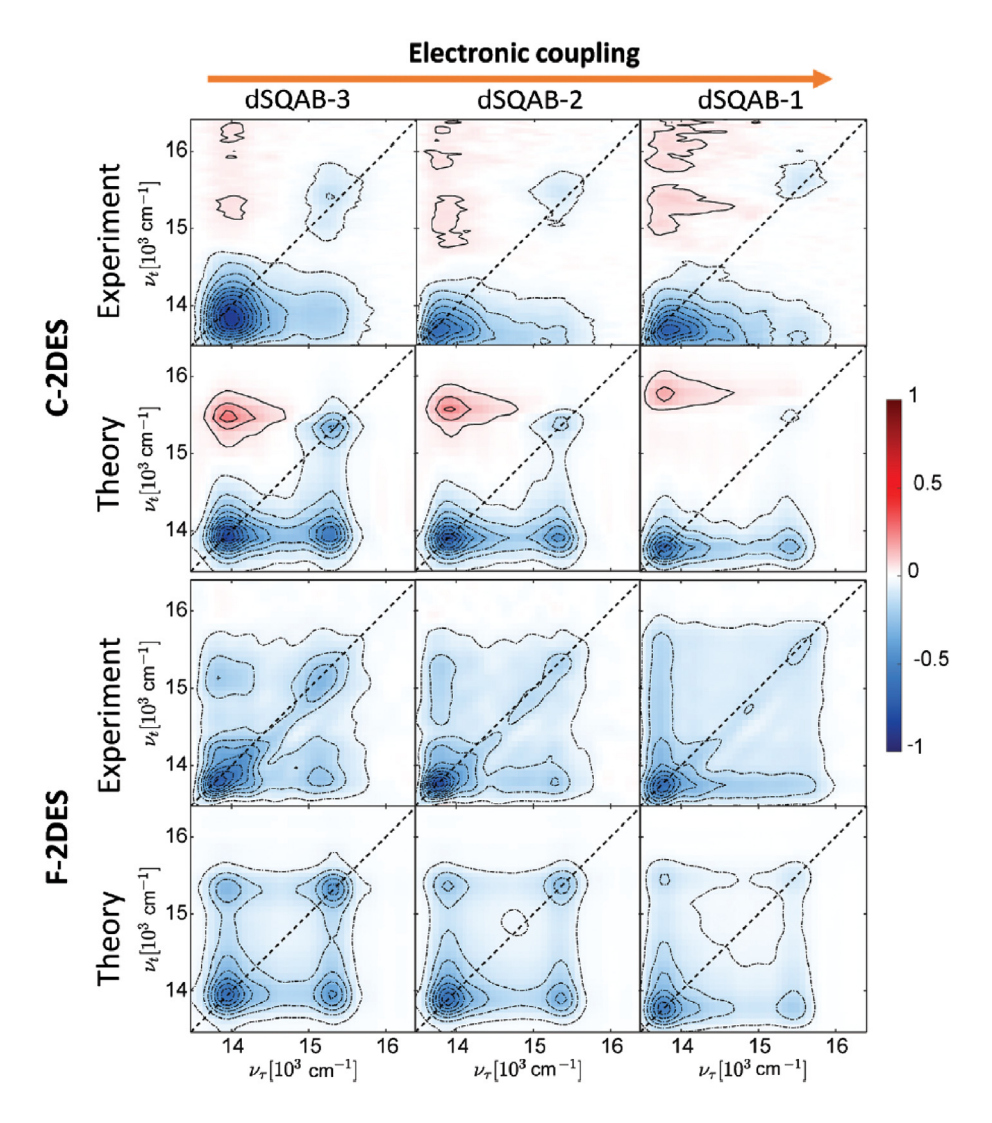


Fig. 4.7 – Coherently (C-, top) and Fluorescence- (F-, bottom) detected Two-dimensional electronic spectra (2DES) of squaraine dimers with decreasing spacer length, *i.e.*, increasing coupling (left to right). Shown is always theoretical calculation (top rows) and experimental data (bottom rows). Spectra are taken at T = 30 fs. Adapted from Ref. [10].

The spectra feature two diagonal peaks, at the position of the two absorption peaks of the dimers, see figure 4.2. With increasing electronic coupling the peaks split from each other by excitonic splitting, and the lower peak becomes relatively more prominent due to J-type coupling leading to oscillator strength redistribution. Note that because of the additional two interactions with the electric field, the peak amplitude is proportional to $|\mu|^4$ instead of $|\mu|^2$ as in linear absorption. The oscillator

strength differences are thus much more pronounced. There are also cross peaks in the 2D spectra at the frequencies of the two transitions, indicating spectral correlations between them. The most striking feature is the opposite sign of the upper cross peak, which is positive (in our convention) in C-2DES and negative in F-2DES. In C-2DES, it is well known that the magnitude of the cross-peaks at T=0 reflects the extent of excitonic delocalization. Moreover, the sign of the cross-peaks is determined by the coupling sign, with a negative upper cross-peak indicating negative coupling ([10] and references therein). This is visible considering the response pathways on a collective-state basis, where the balance of ESA and GSB-type pathways reflects the redistribution of the oscillator strength that scales with the coupling [8]. In case of no coupling, the transition from state $q \to A$ and $B \to AB$ have the same strength. This is broken with increasing delocalization, with the extreme of complete delocalization resulting in one of the $g \to A, A \to AB$ and $q \to B, B \to AB$ pathways to the double excited state being suppressed and the other one enhanced. In C-2DES, the T=0 cross peaks thus report on excitonic coupling and resulting delocalization, as can be seen from the relative magnitude of the cross peaks (normalized to the total volume of the peaks) increasing with the electronic coupling (dSQAB-3 with weakest coupling to dSQAB-1 with strongest coupling) [10]. With time evolution, the lower cross-peak magnitude increases due to population relaxation from the higher to the lower excited state (SE pathway). Since the relaxation is very fast, especially in the dSQAB-1 dimer, and the pulses are of finite length (12 fs pulses, about 25 fs fastest relaxation), it already starts happening close to T=0. It is, therefore, easier to look at the upper cross-peak magnitude. This, however, works only when there is no intrinsic ESA to higher excited states, as is the case of the squaraines, where the higher excited states lie well below the double excited state.

Interestingly, in F-2DES the cross peak magnitude does not increase with the electronic couping. In fact, the cross peak amplitude actually somewhat decreases with the coupling strength, as predicted by theory [8, 10]. Clearly, the cross peaks in F-2DES, i.e., spectral correlations, do not originate from the delocalization. What is then their cause? It can be shown both conceptually and in the language of Feynman diagrams that the transitions are correlated by EEA. In C-2DES, the cross peaks reflect delocalization because it breaks the cancellation between the ESA and GSB-type pathways. In F-2DES, the ESA-type pathway has the same sign as the GSB and thus cannot cancel it, so, as in the F-PP, it all depends on the contribution of the ESA2 pathway. If we do get two photons from the double excited state, the ESA + ESA2 pathways act as the standard ESA, and the F-2DES spectrum will look the same as the C-2DES. However, in the case of efficient EEA, the ESA and ESA2 pathways cancel each other, and we are left with the GSB and SE, where the former leads to T – independent cross peaks. The physical origin of these cross-peaks in EEA can be understood by considering very weak (i.e., quasi-independent)molecules, with a possibility of EEA. In case of no EEA, the 2D spectral signals from both molecules reach the detector independently, so we get the total spectrum being the sum of the two. Crucially, this includes the situation when photons from both of the excited molecules reach the detector. However, if the EEA is present, it decreases the photons from both molecules since one of the two excitations does not survive.

This nonlinearity therefore introduces correlation between the transitions at the otherwise independent molecules. We note here that some coupling between the molecules is necessary for the EEA to happen, so in this sense, the cross peaks still do indicate that. However, even indirect coupling (via a third molecule) is enough. Moreover, we see that any type of nonlinearity that introduces a correlation between the signals from the two molecules will lead to a spectral correlation. An example would be, e.g. the nonlinearity of the detector, which has, in practice, the same effect. This is very dangerous since most sensitive detectors tend to be nonlinear over a larger range, and in phase cycling, a large dynamic range is required. The necessity to subtract large linear signals to isolate weak nonlinear contribution makes the experiment fragile to such kind of nonlinearities and resulting artifacts.

Apart from the cross peak presence, F-2DES shares all the advantages of F-PP: there is no coherent artifact, so dynamics close to time zero are more easily accessible. In this context, note that the techniques are still sensitive to finite pulse overlap effects. An example of pulse overlap manifesting in an artificial signal is given, e.g., in the SI of Ref. [10]. The close relation between the PP and 2DES is easily formalized in a so-called projection-slice 'theorem' [27]. This states nothing more than the property of Fourier transformation that by integrating over ω_{τ} , one obtains the response at $\tau = 0$. The absorptive C-2DES (F-2DES) spectra as shown in figure 4.7, integrated over ω_{τ} , thus produce precisely the C-PP (F-PP) transient maps in figure 4.6 (for dSQAB-3). The correspondence with TA means that all effects discussed for C/F-PP above, such as less pronounced relaxation due to the always present ground-state bleach in F-PP, apply to C/F-2DES as well.

Another rather mundane difference worth mentioning is that, in this geometry, the F-2DES has the laser spectrum imprinted along both axes, while in C-2DES in pump-probe geometry, the spectrum is implicitly divided by the probe spectrum along ω_t . An experimenter would expect the spectra to be merely multiplied by the pump spectrum along ω_{τ} , and, optionally, dependent on the acquisition scheme, by the probe spectrum along ω_t . At least, this is exactly what happens when measuring the excitation spectrum interferometrically. Here in 2DES, however, the situation is a bit more subtle. It is possible to show, by carrying out the Fourier transformations in equations (40) and (42) sequentially, that under the conditions of 1) the same pulse shape within the first and second pulse pair, 2) negligible pulse overlap effect and 3) $\omega_T \to 0$ (no oscillations in waiting time), the spectral multiplication is indeed the result (see appendix in Ref. [10]). Since the typical laser spectrum decreases towards the edges, the peaks are 'pulled' inside, resulting in shifted peak positions. This is important to consider when trying to read off the peak positions. When conditions 1) and 2) apply but there are oscillations in T, it is still possible to correct the 3D $P^{(3)}(\omega_t, \omega_T, \omega_\tau)$ or $\mathrm{FL}^{(4)}(\omega_t, \omega_T, \omega_\tau)$ in full Fourier domain, to obtain the $S_{\text{coh}}^{(3)}(\omega_t, \omega_T, \omega_\tau)$ or $S_{\text{incoh}}^{(4)}(\omega_t, \omega_T, \omega_\tau)$. It is thus, at least in principle since this has not been tried to my knowledge, possible to isolate directly the response function. Such response function could then be used to compare to theory without the need of calculating dynamics with finite pulses, and also to predict other FWM experiments.

4.3.3.6 Six-Wave Mixing: 2DES

The main motivation for measurements of even higher orders of nonlinearity is the option to observe the dynamics and energies of multiple excitations [28]. The natural extension is to consider two more interactions with the excitation pump pulses, keeping the total number of pulses the same. Experimentally (and theoretically), the step from four-wave mixing to six-wave mixing is thus easy. In the coherentlydetected case, one keeps the probe weak, increases somewhat the intensity of the pump, and scans τ with two times finer steps, fine enough to sample the oscillations at the frequency given by the two-exciton energy. The 3rd and 5th-order spectra can then be distinguished by their position along the ω_{τ} axis. As a word of caution, the fact that one sees the 5th order spectrum directly implies that the seemingly 3rd order spectrum will include fifth-order contribution as well, typically in form of annihilation dynamics [9]. In the fluorescence-detected case, higher-order phase cycling is to be used. In case of all pulses with the same amplitude, $1 \times 5 \times 5 \times 5$ phase cycling is advisable. We note that action-detected spectroscopy with the unequal intensity of pulses, e.g., with weaker probe pulse pair, has not been explored so far, although this would decrease the number of necessary phase cycling steps (e.g., from $1 \times 5 \times 5 \times 5 = 125$ to $1 \times 5 \times 3 \times 3 = 45$, i.e., almost three-fold faster measurement). The acquired FWM and SWM 2D spectra of dSQAB-3 at T=30 fs are shown in figure 4.8. Clearly, the structure of the 2D spectra is very different from the one-exciton case. Along the excitation frequency ω_{τ} , we have now only a single, significantly broadened peak, at the two-exciton frequency. Along the detection frequency we still have two peaks at the position of the two transitions. The main peak has opposite sign to the FWM case, which comes from the additional $\left(\frac{i}{\hbar}\right)^2$ factor in the perturbation theory. The sign of the upper peak is negative in C-2DES, and positive in F-2DES, a result of the different balance of pathways. A detailed analysis of the higher-order spectra gets involved due to the large number of pathways. A general aspect, however, seems to be that the main peak rises with the timescale of EEA (about 30 fs) in C-2DES, while in F-2DES the peaks are present from T=0. The coherently-detected version thus seems better suited for the measurement of EEA [29]. On the other hand, the fluorescence-detected version can provide cleaner information about peak energies at T=0 and thus, e.g., bi-exciton interaction energies [28].

4.4 Overview: Fluorescence vs. Polarization

Finally, now that we have compared the fluorescence and coherence-based approaches, we are in the position to contrast their features. As we have shown in our unified description, the n-th order nonlinear polarization probes the same type of response as n+1-th order nonlinear fluorescence. Despite this correspondence, the spectra in general look quite different. All the differences essentially boil down to the signal being emitted for a relatively long time spontaneously in the case of fluorescence detection, in contrast to the practically immediate coherent polarization response to the pulse sequence. During the signal emission, effects such as diverse

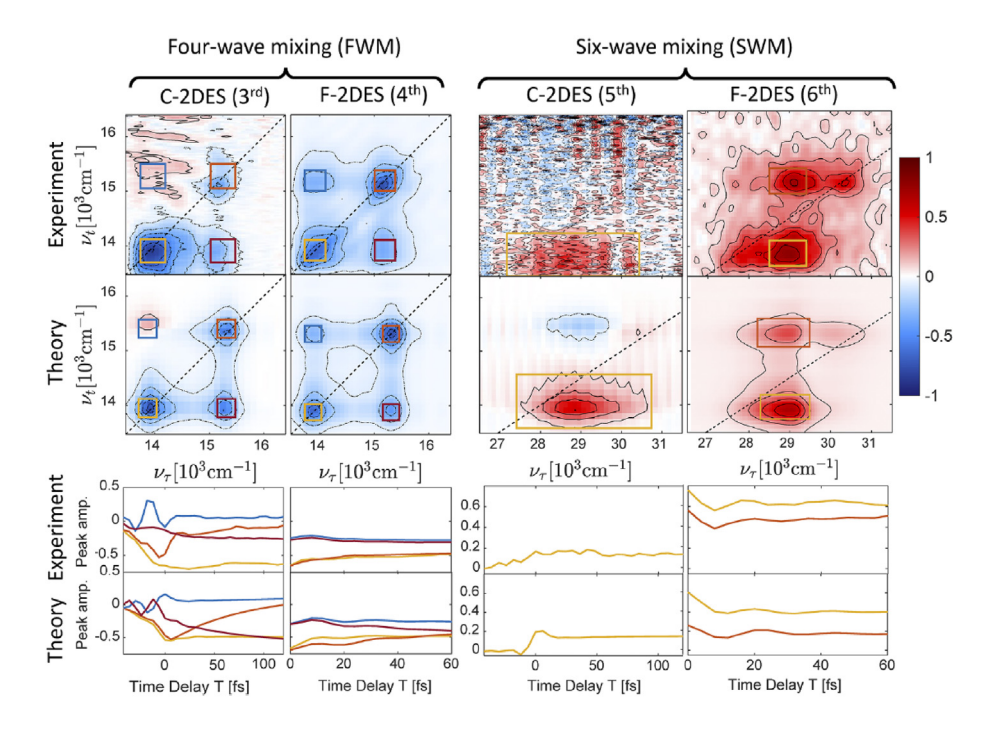


Fig. 4.8 – Direct comparison of coherently (C-) and fluorescence (F-) detected four-wave mixing (left) and six-wave mixing (right) 2DES of squaraine dimers with the longer spacer (dSQAB-3). Adapted from Ref. [7].

quantum yield for different states, presence of dark states, or exciton-exciton annihilation lowering the emission of two-exciton states will contribute to the signal. As a result, in F-2DES and F-PP the ESA-type pathways are suppressed. This results in a lack of photo-induced spectra, the presence of bleach-type peaks even after energy relaxation, and the presence of cross-peaks in F-2DES that result from EEA and not from delocalization. The bleach presence is a serious drawback in large systems with energetically close sites, where it can obscure the relatively small SE reporting on excited state dynamics [30]. What is also suppressed in fluorescence detection is coherent artifact and dark product states, including photo-damaged sample. Fluorescence detection is in principle more sensitive and much more easily applicable in the microscope, to the point that it allows TA measurement on single molecules [31]. In C-2DES and especially C-PP, the high nonlinear orders are extracted more easily, with less experimental effort, than in fluorescence-based counterparts. Moreover, the rise of the 5th order coherent polarization signal follows the EEA, which is not the case of the fluorescence-detected variant. The coherently detected approach is thus better suitable for the measurement of multi-excitonic states, exciton interaction such as EEA, exciton long-range diffusion, etc. Recently, we have even developed a (phase-cycling-inspired) approach to measure high-order multi-excitonic signals in TA [32]. From the experimental side, the coherent

techniques are very well implementable using (tens of) kHz systems with shot-to-shot measurement. The fluorescence-based techniques benefit from higher repetition rates in the MHz regime, and higher sensitivity due to the detection against the dark background. This makes them well-suited for microscopy [21] and even single-molecule spectroscopy [31]. The techniques are thus, both experimentally and theoretically, to a degree complementary.

Acknowledgements. Many thanks to the participants and organizers of the 2023 Les Houches summer school and workshop for the great hikes and stimulating discussions. The author also thanks to all his past and present ultrafast colleagues who contributed to the results mentioned here.

References

- [1] Mukamel S., Freyberger M., Schleich W., Bellini M., Zavatta A., Leuchs G., Silberhorn C., Boyd R.W., Sánchez-Soto L.L., Stefanov A., Barbieri M., Paterova A., Krivitsky L., Shwartz S., Tamasaku K., Dorfman K., Schlawin F., Sandoghdar V., Raymer M., Marcus A., Varnavski O., Goodson T., Zhou Z.-Y., Shi B.-S., Asban S., Scully M., Agarwal G., Peng T., Sokolov A.V., Zhang Z.-D., Zubairy M.S., Vartanyants I.A., del Valle E., Laussy F. (March 2020) Roadmap on quantum light spectroscopy, J. Phys. B: At. Mol. Opt. Phys. 53(7), 072002. Publisher: IOP Publishing.
- Ishizaki A. (August 2020) Probing excited-state dynamics with quantum entangled photons: correspondence to coherent multidimensional spectroscopy, J. Chem. Phys. 153(5), 051102.
- [3] Landes T., Raymer M.G., Allgaier M., Merkouche S., Smith B.J., Marcus A.H. (June 2021) Quantifying the enhancement of two-photon absorption due to spectral-temporal entanglement, *Opt. Express* **29**(13), 20022–20033. Publisher: Optica Publishing Group.
- [4] Mukamel S. (1995) Principles of nonlinear optical spectroscopy, 1st edn. Oxford University Press, New York.
- [5] Boyd R.W. (April 2008) Nonlinear optics, 3rd edn. Academic Press, Burlington.
- 6] Cho M. (June 2009) Two-dimensional optical spectroscopy. CRC Press, Boca Raton, FL.
- [7] Malý P., Mueller S., Lüttig J., Lambert C., Brixner T. (October 2020) Signatures of exciton dynamics and interaction in coherently and fluorescence-detected four- and six-wave-mixing two-dimensional electronic spectroscopy, J. Chem. Phys. 153(14), 144204.
- [8] Malý P., Mančal T. (September 2018) Signatures of exciton delocalization and exciton-exciton annihilation in fluorescence-detected two-dimensional coherent spectroscopy, J. Phys. Chem. Lett. 9, 5654-5659.
- [9] Lüttig J., Rose P.A., Malý P., Turkin A., Bühler M., Lambert C., Krich J.J., Brixner T. (June 2023) High-order pump-probe and high-order two-dimensional electronic spectroscopy on the example of squaraine oligomers, J. Chem. Phys. 158(23), 234201.
- [10] Malý P., Lüttig J., Mueller S., Schreck M.H., Lambert C., Brixner T. (2020) Coherently and fluorescence-detected two-dimensional electronic spectroscopy: direct comparison on squaraine dimers, Phys. Chem. Chem. Phys. 22(37), 21222–21237.
- [11] Röhr M.I.S., Marciniak H., Hoche J., Schreck M.H., Ceymann H., Mitric R., Lambert C. (April 2018) Exciton dynamics from strong to weak coupling limit illustrated on a series of squaraine dimers, J. Phys. Chem. C 122(15), 8082–8093.
- [12] Malý P., Somsen O.J.G., Novoderezhkin V.I., Mančal T., van Grondelle R. (May 2016) The role of resonant vibrations in electronic energy transfer, ChemPhysChem 17(9), 1356–1368.
- [13] Bennett D.I.G., Malý P., Kreisbeck C., van Grondelle R., Aspuru-Guzik A. (May 2018) Mechanistic regimes of vibronic transport in a heterodimer and the design principle of incoherent vibronic transport in phycobiliproteins, J. Phys. Chem. Lett. 9(10), 2665–2670.

- [14] Pisliakov A.V., Mančal T., Fleming G.R. (June 2006) Two-dimensional optical three-pulse photon echo spectroscopy. II. Signatures of coherent electronic motion and exciton population transfer in dimer two-dimensional spectra, J. Chem. Phys. 124(23), 234505.
- [15] Brixner T., Hildner R., Köhler J., Lambert C., Würthner F. (August 2017) Exciton transport in molecular aggregates – from natural antennas to synthetic chromophore systems, Adv. Energy Mater. 7(16), 1700236.
- [16] Brixner T., Mančal T., Stiopkin I.V., Fleming G.R. (June 2004) Phase-stabilized two-dimensional electronic spectroscopy, J. Chem. Phys. 121(9), 4221–4236.
- [17] Valkunas L., Abramavicius D., Mančal T. (2013) Molecular excitation dynamics and relaxation, 1st edn. WILEY-VCH, Weinheim.
- [18] Tian P., Keusters D., Suzaki Y., Warren W.S. (June 2003) Femtosecond phase-coherent two-dimensional spectroscopy, Science 300(5625), 1553–1555.
- [19] Tekavec P.F., Dyke T.R., Marcus A.H. (November 2006) Wave packet interferometry and quantum state reconstruction by acousto-optic phase modulation, J. Chem. Phys. 125(19), 194303.
- [20] Tekavec P.F., Lott G.A., Marcus A.H. (2007) Fluorescence-detected two-dimensional electronic coherence spectroscopy by acousto-optic phase modulation, J. Chem. Phys. 127 (21), 214307.
- [21] Tiwari V., Matutes Y.A., Gardiner A.T., Jansen T.L.C., Cogdell R.J., Ogilvie J.P. (December 2018) Spatially-resolved fluorescence-detected two-dimensional electronic spectroscopy probes varying excitonic structure in photosynthetic bacteria, Nat. Commun. 9(1), 4219.
- [22] Wagner W., Li C., Semmlow J., Warren W. (May 2005) Rapid phase-cycled two-dimensional optical spectroscopy in fluorescence and transmission mode, Opt. Express 13(10), 3697–3706.
- [23] Draeger S., Roeding S., Brixner T. (February 2017) Rapid-scan coherent 2D fluorescence spectroscopy, Opt. Express 25(4), 3259–3267.
- [24] Tan H.-S. (2008) Theory and phase-cycling scheme selection principles of collinear phase coherent multi-dimensional optical spectroscopy, J. Chem. Phys. 129(12), 124501.
- [25] May V., Kühn O. (2004) Charge and energy transfer dynamics in molecular systems, 2nd edn. Wiley-VCH Verlag GmbH.
- [26] Malý P., Brixner T. (August 2021) Fluorescence-detected pump-probe spectroscopy, Angew. Chem. Int. Ed. 60(34), 18867–18875.
- [27] Hamm P., Zanni M. (February 2011) Concepts and methods of 2D infrared spectroscopy, 1st edn. Cambridge University Press, New York.
- [28] Lüttig J., Mueller S., Mal\u00ed P., Krich J.J., Brixner T. (August 2023) Higher-order multidimensional and pump-probe spectroscopies, J. Phys. Chem. Lett. 14(33), 7556-7573.
- [29] Heshmatpour C., Malevich P., Plasser F., Menger M., Lambert C., Šanda F., Hauer J. (September 2020) Annihilation dynamics of molecular excitons measured at a single perturbative excitation energy, J. Phys. Chem. Lett. 11(18), 7776–7781.
- [30] Bolzonello L., Bruschi M., Fresch B., van Hulst N.F. (December 2023) Nonlinear optical spectroscopy of molecular assemblies: what is gained and lost in action detection? J. Phys. Chem. Lett. 14(50), 11438–11446. Publisher: American Chemical Society.
- [31] Fersch D., Malý P., Rühe J., Lisinetskii V., Hensen M., Würthner F., Brixner T. (June 2023) Single-molecule ultrafast fluorescence-detected pump-probe microscopy, J. Phys. Chem. Lett. 14(21), 4923–4932.
- [32] Malý P., Lüttig J., Rose P.A., Turkin A., Lambert C., Krich J.J., Brixner T. (April 2023) Separating single-from multi-particle dynamics in nonlinear spectroscopy, *Nature* 616(7956), 280–287.

Chapter 5

Light Harvesting in Photosynthesis: From Structure to Function

Thomas Renger*

Institute of Theoretical Physics, Johannes Kepler University Linz, Austria *e-mail: thomas.renger@jku.at

5.1 Overview

This chapter provides an introduction into the structure-based description of light harvesting in photosynthesis. A first important aspect of this description is the derivation of an effective Hamiltonian, termed Frenkel exciton Hamiltonian, from first principles and its structure-based parameterization by combining quantum chemical/electrostatics/molecular mechanics methods, as will be discussed in section 5.2. A second aspect concerns the development of dynamical theories, using the Frenkel exciton Hamiltonian, to describe optical spectra and excitation energy transfer, discussed in section 5.3 together with applications to the Fenna-Matthews-Olson (FMO) protein. As an example, we will consider light-harvesting and trapping of excitation energy by primary charge transfer in the core of green sulfur bacteria (figure 5.1), which will be studied in section 5.4. In the final section 5.5 of this chapter, we will discuss similarities and differences between photosynthetic pigment-protein complexes (PPCs) and organic solar cells (OSCs). The latter are studied in detail in chapter 6.

5.2 Frenkel Exciton Hamiltonian and Parameterization

In the spirit of the Born-Oppenheimer approximation [4], we first solve the electronic problem for fixed nuclear coordinates and, in a second step, add the kinetic energy of nuclei and the electron-vibrational coupling. To obtain the electronic eigenstates we divide the molecular aggregate into building blocks that are defined

DOI: 10.1051/978-2-7598-3760-1.c005 © The authors, 2025

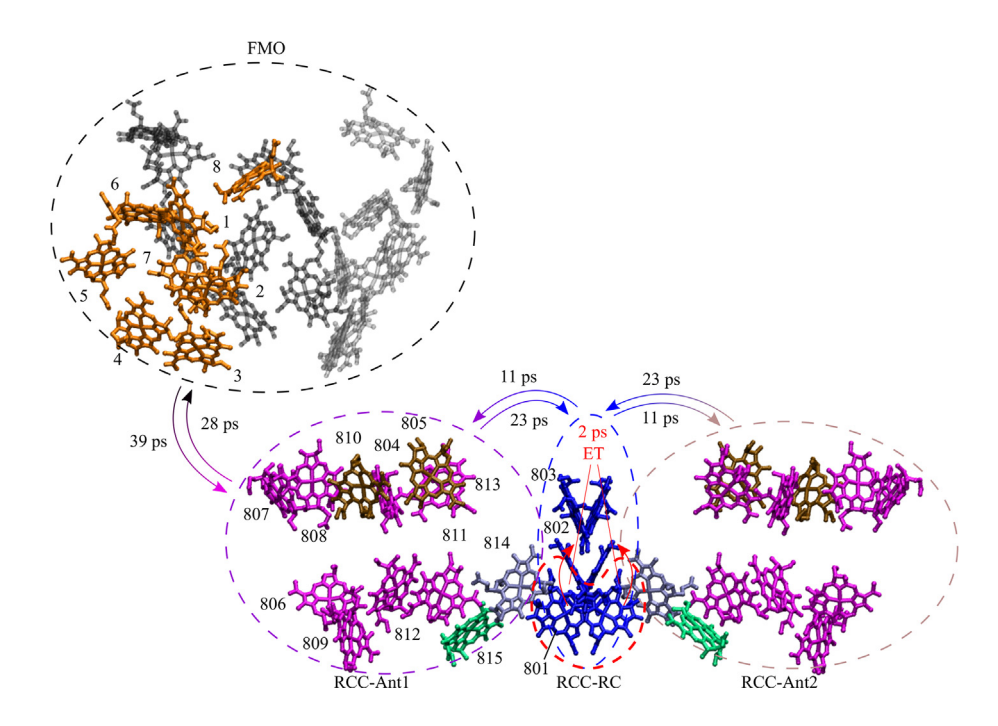


FIG. 5.1 – Arrangements of bacteriochlorophyll (BChl) a pigments in Fenna Matthews Olson (FMO)/ reaction center complex (RCC) supercomplexes in the core of green sulfur bacteria [1, 2], as viewed parallel to the photosynthetic membrane. The membrane-embedded RCC consists of two core antenna complexes (RCC-Ant1 and RCC-Ant2) and the reaction center (RCC-RC). The protein is omitted for clarity. Pigments 802 and 803 in the RC are chlorophyll (Chl) a. Pigments colored in the same way belong to the same exciton domain, introduced in section 5.3. The dashed lines encircle certain compartments, identified in a minimal model of light-harvesting, that also reveals the time constants of energy transfer between the different compartments, as explained in detail in section 5.4. The red dashed line in the center encircles the primary electron donors (BChl a 801) in the reaction center (RC). After excitation energy transfer to the RC, electrons are transferred from the excited state of the primary donors with a time constant of 2 ps to the neighboring primary electron donors (Chl a 802) in the two symmetric branches of the RC, depicted in blue. Figure adopted from Ref. [3].

such that electron exchange between different building blocks is small and can be neglected. In a pigment-protein complex (PPC), the chromophores, in good approximation, form their own building blocks. In this case, as will be discussed in the following, the wavefunction of the complex may be expanded with respect to Hartree products of wavefunctions of the isolated building blocks, and the eigenstates of the aggregate can be obtained by diagonalizing a Frenkel exciton Hamiltonian. The latter contains in the diagonal the local transition energies of the complex which are shifted, e.g., by electrostatic, inductive, and dispersive interactions between the chromophores and their environment, and in the off-diagonal, the excitonic couplings that couple excited states, which are localized at different

chromophores. Once we have determined the electronic states at the equilibrium positions of nuclei in the electronic ground state, we will expand the resulting Frenkel exciton Hamiltonian for small displacements of nuclei from their equilibrium positions and add the kinetic energy of nuclei to obtain a complete Hamiltonian that can be used for quantum dynamical studies of excitation energy transfer and optical spectra, discussed in section 5.3.

5.2.1 Electronic Degrees of Freedom

We start with the general electronic Hamiltonian of the PPC that depends parametrically on the nuclear positions R

$$H = \sum_{i} \frac{\hat{\mathbf{p}}_{i}^{2}}{2m_{e}} + V(\mathbf{r}_{i}, \dots, \mathbf{r}_{N_{e}}, R), \tag{1}$$

where $\hat{\mathbf{p}}_i = -i\hbar\nabla_i$ denotes the momentum of the *i*th electron (with mass $m_{\rm e}$, and $V(\mathbf{r}_i, \dots, \mathbf{r}_{N_{\rm e}}, R)$ contains the Coulomb couplings between electrons, electrons, and nuclei and between nuclei. Here, R denotes the equilibrium position of nuclei in the electronic ground state.

In the next step, we divide the Hamiltonian into building blocks characterized by the fact that there is no electron exchange between different building blocks.

$$H = \sum_{a} H_a + \frac{1}{2} \sum_{a,b}^{a \neq b} V_{ab} = H_0 + V, \tag{2}$$

where

$$H_a = \sum_{i} \frac{\hat{\mathbf{p}}_{ia}^2}{2m_e} + V(\mathbf{r}_1^{(a)}, \dots, \mathbf{r}_{N_a}^{(a)}, R) + \hat{T}_n^{(a)}$$
(3)

is the Hamiltonian of the isolated building block a and V_{ab} contains the Coulomb couplings between different building blocks a and b

$$V_{ab} = \sum_{i,j} \frac{e^2}{|\mathbf{r}_i^{(a)} - \mathbf{r}_j^{(b)}|} - \sum_{I,j} \frac{Z_I e^2}{|\mathbf{R}_I^{(a)} - \mathbf{r}_j^{(b)}|} - \sum_{i,J} \frac{Z_J e^2}{|\mathbf{r}_i^{(a)} - \mathbf{R}_J^{(b)}|} + \sum_{I,J} \frac{Z_I Z_J e^2}{|\mathbf{R}_I^{(a)} - \mathbf{R}_J^{(b)}|}, \quad (4)$$

where $\mathbf{r}_{k}^{(c)}$ and $\mathbf{R}_{K}^{(c)}$ are the spatial coordinates of the kth electron and Kth nucleus, respectively, of building block c.

The eigenfunctions of the Hamiltonian H_a of the isolated building block a are denoted as $\varphi_{n_a}^{(a)}(\mathbf{r}_1^{(a)},\cdots\mathbf{r}_{N_a}^{(a)})$ with corresponding eigenenergies $E_{n_a}^{(a)}$. Hence, the eigenstates of the Hamiltonian $H_0 = \sum_a H_a$ in equation (2) are products of the eigenfunctions of the building blocks

$$\varphi_{\mathbf{n}}(\mathbf{r}_{1},...,\mathbf{r}N_{e}) = \langle \mathbf{r}_{1},...,\mathbf{r}N_{e}|n_{1}n_{2}n_{3}\cdots n_{N}\rangle
= \prod_{a=1}^{N} \varphi_{n_{a}}^{(a)}(\mathbf{r}_{1}^{(a)},...,\mathbf{r}_{N_{a}}^{(a)})$$
(5)

and we have

$$H_0|\mathbf{n}\rangle = E_n|\mathbf{n}\rangle$$
 (6)

with the eigenenergy

$$E_{\mathbf{n}} = \sum_{a} E_{n_a}^{(a)}.\tag{7}$$

Note that a simple product of eigenfunctions in equation (5) is sufficient since there is no electron exchange between different building blocks.

Since the states $|\mathbf{n}\rangle$ form a complete basis in the Hilbert space of the complex, we can expand the eigenstate $|\psi_M\rangle$ of the total Hamiltonian H (equation (2)) in this basis

$$|\psi_M\rangle = \sum_{n_1 \cdots n_N} c_{n_1 \cdots n_N}^{(M)} |n_1 \cdots n_N\rangle = \sum_{\mathbf{n}} c_{\mathbf{n}}^{(M)} |\mathbf{n}\rangle. \tag{8}$$

In the following, we will use the variational principle to determine the coefficients $c_{\mathbf{n}}^{(M)}$ According to this principle, the expectation value $\langle \psi_M | H | \psi_M \rangle$ becomes minimal for the true eigenfunction of H. As a constraint of the minimization, we require a normalization of the wavefunction $|\psi_M\rangle$, that is, $\langle \psi_M | \psi_M \rangle = 1 = \sum_{\mathbf{k}} (c_{\mathbf{k}}^{(M)})^2$. We introduce Lagrangian multipliers λ_M and minimize the expression

$$\Lambda = \langle \psi_M | H | \psi_M \rangle - \lambda_M \left\{ \sum_{\mathbf{k}} (c_{\mathbf{k}}^{(M)})^2 - 1 \right\}. \tag{9}$$

We will consider real-valued eigenfunctions $|\mathbf{n}\rangle$ and $|\psi_M\rangle$ and, hence, all coefficients $c_{\mathbf{k}}^{(M)}$ are real and we have $\langle \mathbf{n}|H|\mathbf{m}\rangle = \langle \mathbf{m}|H|\mathbf{n}\rangle$. As a minimum condition, we have

$$\partial/\partial c_{\mathbf{n}}^{(M)} \Lambda = 0 \tag{10}$$

which, using equation (8), leads to the following eigenvalue problem

$$c_{\mathbf{n}}^{(M)}(\langle \mathbf{n}|H|\mathbf{n}\rangle - \lambda_{M}) + \sum_{\mathbf{k}}^{\mathbf{k}\neq\mathbf{n}} c_{\mathbf{k}}^{(M)}\langle \mathbf{n}|H|\mathbf{k}\rangle = 0$$
(11)

where the diagonal matrix elements are given as

$$\langle \mathbf{n}|H|\mathbf{n}\rangle = \langle \mathbf{n}|\sum_{a} H_{a} + \frac{1}{2} \sum_{a,b}^{a \neq b} \hat{V}_{ab}|\mathbf{n}\rangle$$

$$= \sum_{a} E_{n_{a}}^{(a)} + \frac{1}{2} \sum_{a,b}^{a \neq b} V_{n_{a}n_{b},n_{a}n_{b}}^{(ab)}$$
(12)

and the off-diagonal matrix elements are

$$\langle \mathbf{n}|H|\mathbf{k}\rangle = \frac{1}{2} \sum_{a,b}^{a\neq b} V_{n_a n_b, k_a k_b}^{(ab)}, (\mathbf{k} \neq \mathbf{n}), \tag{13}$$

where $\mathbf{k} \neq \mathbf{n}$ means that n_a and n_b should not simultaneously be k_a and k_b , respectively. Note that the Lagrangian multiplier λ_M is identified as the eigenenergy of $|\psi_M\rangle$ in equation (11).

The matrix element of the inter-building block Coulomb coupling $V_{n_a n_b, m_a m_b}^{(ab)}$ is obtained from the following integral over the electronic coordinates of building blocks a and b

$$V_{n_a n_b, m_a m_b}^{(ab)} = \int d\mathbf{r}_1^{(a)} \cdots d\mathbf{r}_{N_a}^{(a)} \int d\mathbf{r}_1^{(b)} \cdots d\mathbf{r}_{N_b}^{(b)}$$

$$\times \varphi_{n_a}^{(a)}(\mathbf{r}_1^{(a)}, \cdots \mathbf{r}_{N_a}^{(a)}) \varphi_{n_b}^{(b)}(\mathbf{r}_1^{(b)}, \cdots \mathbf{r}_{N_b}^{(b)})$$

$$\times \hat{V}_{ab} \varphi_{m_a}^{(a)}(\mathbf{r}_1^{(a)}, \cdots \mathbf{r}_{N_a}^{(a)}) \varphi_{m_b}^{(b)}(\mathbf{r}_1^{(b)}, \cdots \mathbf{r}_{N_b}^{(b)})$$

$$(14)$$

and contains the inter-building block Coulomb couplings \hat{V}_{ab} given above (equation (4)).

By using Pauli's principle for the exchange of electrons and renaming integration variables, the above high-dimensional integral can be simplified to [5]

$$V_{n_{a}n_{b},m_{a}m_{b}}^{(ab)} = \int d\mathbf{r}_{a} \int d\mathbf{r}_{b} \frac{\rho_{m_{a},n_{a}}^{(a)}(\mathbf{r}_{a})\rho_{m_{b},n_{b}}^{(b)}(\mathbf{r}_{b})}{|\mathbf{r}_{a} - \mathbf{r}_{b}|}$$

$$-\delta_{n_{b},m_{b}} \sum_{J} \int d\mathbf{r}_{a} \frac{eZ_{J}\rho_{m_{a},n_{a}}^{(a)}(\mathbf{r}_{a})}{|\mathbf{r}_{a} - \mathbf{R}_{J}^{(b)}|}$$

$$-\delta_{n_{a},m_{a}} \sum_{I} \int d\mathbf{r}_{b} \frac{eZ_{I}\rho_{m_{b},n_{b}}^{(a)}(\mathbf{r}_{b})}{|\mathbf{r}_{b} - \mathbf{R}_{I}^{(a)}|}$$

$$-\delta_{n_{a},m_{a}}\delta_{n_{b},m_{b}} \sum_{I,J} \frac{e^{2}Z_{I}Z_{J}}{|\mathbf{R}_{I}^{(a)} - \mathbf{R}_{J}^{(b)}|},$$

$$(15)$$

where the one-particle densities $\rho_{m_a,n_a}^{(a)}(\mathbf{r}_a)$ and $\rho_{m_b,n_b}^{(b)}(\mathbf{r}_b)$ of the electrons in building block a and b, respectively, were introduced according to

$$\rho_{m,n}(\mathbf{r}) = e \int d\mathbf{r}_2 \cdots d\mathbf{r}_N \phi_m(\mathbf{r}, \mathbf{r}_2, \dots, \mathbf{r}_N) \phi_n(\mathbf{r}, \mathbf{r}_2, \dots, \mathbf{r}_N), \tag{16}$$

which for m=n is the electronic charge density of the mth molecular state and for $m \neq n$ is the transition density between the mth and the nth electronic state. Whereas the charge density has a classical analog, the transition density is a quantum mechanical quantity related below to the excitonic coupling leading to a delocalization of excited states over different pigments (building blocks). Note also that the first moment of the transition density is the transition dipole moment, which characterizes the system-field interaction in dipole approximation.

Examining the eigenvalue problem in equation (11), it is seen that the off-diagonal matrix element $\langle \mathbf{n}|H|\mathbf{k}\rangle$ couples different electronic states $|\mathbf{n}\rangle$ and $|\mathbf{k}\rangle$.

A considerable mixing of these states only occurs if the absolute magnitude of the difference in respective diagonal elements $|\langle \mathbf{n}|H|\mathbf{n}\rangle - \langle \mathbf{k}|H|\mathbf{k}\rangle|$ is not much larger than this coupling. We leave it as an exercise to the reader to diagonalize a 2 × 2 matrix and investigate the eigenvectors obtained for different ratios between the difference in diagonal elements and the off-diagonal element.

With this relation in mind and taking into account that any Coulomb matrix element $V_{n_a n_b, m_a m_b}^{(ab)}$ is small (meV) compared to the difference between the first excited state of a building block and its ground state, $E_1^{(a)} - E_0^{(a)}$ (eV), we may well neglect any mixing of the ground state of the PPC with any excited state, by setting $\langle \mathbf{n}|H|0\rangle = 0$ for $\mathbf{n} \neq 0$. This approximation is known as the Heitler-London approximation [6]. In this case, the ground state of the aggregate reads

$$|\psi_0\rangle = |0, \dots, 0\rangle \tag{17}$$

with energy

$$E_0 = \sum_{a} E_0^{(a)} + \frac{1}{2} \sum_{ab} V_{00,00}^{(ab)}, \tag{18}$$

that contains the sum of ground state energies $E_0^{(a)}$ of isolated building blocks and the electrostatic coupling $V_{00,00}^{(ab)}$ between the ground state charge densities of different building blocks. The states next higher in energy are those in which one building block is in its first excited state, whereas all the remaining building blocks of the PPC are in their electronic ground state. Such a state is termed a localized 1-exciton state of the complex. Since the protein starts to absorb at much higher energies than the pigments, no mixing of the excited pigment states with states involving excited protein building blocks needs to be considered. Thus, we obtain the following eigenvalue problem for the 1-exciton states $|m\rangle = \varphi_1^{(m)} \prod_a^{a\neq m} \varphi_0^{(a)}$ in which all building blocks are in their electronic ground state, except for pigment m, which is in its first excited state

$$c_m^{(M)} \left\{ E_1^{(m)} + \sum_{a}^{a \neq m} \left(E_0^{(a)} + V_{10,10}^{(m,a)} \right) + \frac{1}{2} \sum_{a,b}^{a \neq m,b \neq m} V_{00,00}^{(a,b)} - \lambda_M \right\} + \sum_{k}^{k \neq m} c_k^{(M)} V_{10,01}^{(k,m)} = 0.$$

$$(19)$$

Three types of matrix elements need to be considered: the Coulomb coupling $V_{10,10}^{(m,a)}$ between the charge density of the excited state of pigment m and the ground state charge density of the remaining building blocks of the PPC (including pigments and the protein), the ground state charge density coupling $V_{00,00}^{(a,b)}$ between the remaining building blocks of the PPC, and the Coulomb coupling $V_{10,01}^{(k,m)}$ between the ground-to-excited state transition densities of the pigments. Note that k in equation (19) runs over all pigments, whereas a also includes the building blocks of the protein.

If we are interested in the transition energies between the ground state $|\psi_0\rangle$ and the one-exciton states $|\psi_M\rangle$, we may subtract from the diagonal elements of the above matrix the energy E_0 of the ground state (equation (18)), resulting in

$$c_m^{(M)}\{E_m - E_M\} + \sum_{k=0}^{(k \neq m)} c_k^{(M)} V_{km} = 0,$$
 (20)

with the local transition energy (site energy) of pigment m

$$E_m = E_1^{(m)} - E_0^{(m)} + \sum_{a} \left(V_{10,10}^{(m,a)} - V_{00,00}^{(m,a)} \right)$$
 (21)

that is given as the transition energy $E_1^{(m)}-E_0^{(m)}$ of the isolated pigment m and the difference in charge density coupling $V_{10,10}^{(m,a)}$ of the excited state of pigment m with the ground state charge density of the environment and the ground state charge density coupling $V_{00,00}^{(m,a)}$. The eigenenergy

$$E_M = \lambda_M \tag{22}$$

corresponds to the transition energy between the ground state $|\psi_0\rangle$ and the delocalized one-exciton state $|\psi_M\rangle$, which determines the position of optical lines observed in spectroscopy, and

$$V_{km} = V_{10\ 01}^{(k,m)} \tag{23}$$

is the Coulomb coupling between the transition densities of pigments k and m. The latter is termed excitonic coupling. Hence, the singly excited states of the PPC may be seen as eigenstates of the following Frenkel exciton Hamiltonian

$$H_{\rm ex} = \sum_{m} E_m |m\rangle\langle m| + \sum_{m,k}^{m \neq k} V_{km} |m\rangle\langle k|, \tag{24}$$

which contains a diagonal matrix elements the site energies E_m (equation (21)) and in the off-diagonal the excitonic couplings V_{km} (equation (23)).

Moreover, our derivation of the exciton Hamiltonian provides us with a minimal model for the calculation of its parameters. As equation (21) suggests, the site energy E_m of pigment m is obtained from the transition energy $E_1^{(m)} - E_0^{(m)}$ of this pigment in vacuum and the difference in charge density coupling between the excited and the ground state of the pigment with the remaining building blocks of the PPC (including other pigments and the protein parts). The excitonic couplings V_{km} (equation (23)) are obtained from the Coulomb interaction between transition densities of the pigments.

In the derivation of the Frenkel exciton Hamiltonian, discussed above, we have neglected the inter-building block Coulomb coupling between strongly off-resonant states (Heitler-London approximation). These interactions can, however, in principle, be included in perturbation theory, where the transition energy shift

$$\Delta E_m = E_m - (E_1^{(m)} - E_0^{(m)}) = \sum_n \Delta E_m^{(n)}$$
 (25)

is sorted with respect to the power n of the inter-building block Coulomb coupling. The first-order contribution

$$\Delta E_m^{(1)} = \sum_{a} \left(V_{10,10}^{(m,a)} - V_{00,00}^{(m,a)} \right) \tag{26}$$

was already obtained using the variational principle approach used above. The next higher-order contribution

$$\Delta E_m^{(2)} = \Delta E_m^{\text{ind}} + \Delta E_m^{\text{disp}} \tag{27}$$

contains the inductive and dispersive site energy shifts [7]. The inductive contribution reads

$$\Delta E_m^{\text{ind}} = -\sum_{k}^{k \neq m} \sum_{c}^{c \neq 0} \frac{|V_{10,1c}^{(m,k)}|^2 - |V_{00,0c}^{(m,k)}|^2}{E_c^{(k)} - E_0^{(k)}} - \sum_{k}^{k \neq m} \left(\sum_{n}^{n \neq 1} \frac{|V_{10,n0}^{(m,k)}|^2}{E_1^{(m)} - E_n^{(m)}} - \sum_{n}^{n \neq 0} \frac{|V_{00,n0}^{(m,k)}|^2}{E_0^{(m)} - E_n^{(m)}}\right).$$
(28)

The first line contains the Coulomb coupling between the transition density $\rho_{0c}^{(k)}$ of the kth building block and the charge density of the excited state $\rho_{11}^{(m)}$ and the ground state $\rho_{00}^{(m)}$ of pigment m, and in the second line we have the Coulomb coupling between the ground state charge density $\rho_{00}^{(k)}$ of k and the transition densities $\rho_{0n}^{(m)}$ and $\rho_{1n}^{(m)}$ of m. The sums over the transition densities with the respective energy denominators can be interpreted as electronic polarizations [8–10]. Hence the first line contains the difference in polarization of the environment by the excited and the ground state charge density of the pigment. The second line contains the difference in polarizations of the excited and ground state of the pigment by the ground state charge density of the environment.

The dispersive site energy shift in equation (27) reads

$$\Delta E_m^{\text{disp}} = -\sum_{k}^{k \neq m} \sum_{c}^{c \neq 0} \left(\sum_{n}^{n \neq 1} \frac{|V_{10,nc}^{(m,k)}|^2}{E_n^{(m)} - E_1^{(m)} + E_c^{(k)} - E_0^{(k)}} - \sum_{n}^{n \neq 0} \frac{|V_{00,nc}^{(m,k)}|^2}{E_n^{(m)} - E_0^{(m)} + E_c^{(k)} - E_0^{(k)}} \right)$$
(29)

and contains the Coulomb coupling between transition densities of the pigment and the environment. These transition density couplings can be interpreted as the difference in van der Waals-type couplings between the excited and the ground state of the pigment.

In the charge density coupling (CDC) method [11], the local transition energy of the chromophore m is approximated by including the first-order corrections explicitly. Screening effects of this charge density Coulomb coupling, arising from

higher-order coupling terms in the perturbation series, are included by an effective dielectric constant ϵ_{eff} . The local transition energy E_m is then given as

$$E_m = E_0 + \frac{1}{\epsilon_{\text{eff}}} \sum_{I,J} \frac{(q_I^{(m)}(1,1) - q_I^{(m)}(0,0)) q_J^{(k)}(0,0)}{|\mathbf{R}_I^{(m)} - \mathbf{R}_I^{(k)}|}.$$
 (30)

Here, E_0 denotes a reference energy that will be assumed to be the same for the same type of chromophore. Dispersive and inductive site energy shifts are assumed to be site-independent and, therefore, can be included in the constant E_0 .

5.2.1.1 Higher-Order Corrections to the Excitonic Couplings-The Poisson-TrEsp Method

In order to describe contributions from higher excited states of the environment to the excitonic coupling between pigments, we consider a homodimer with equal site energies $E_1 = E_2 = E_0$ and excitonic coupling $V_{12}^{(0)}$. In this case, the delocalized eigenstates (exciton states) are obtained as

$$|\pm\rangle = \frac{1}{\sqrt{2}}(|1\rangle \pm |2\rangle),$$
 (31)

with energies $E_{\pm}^{(0)} = E_0 \pm V_{12}^{(0)}$. Now, we switch on the excitonic coupling to the off-resonant high-energy transitions between the ground state and the cth excited state of the environmental building blocks k

$$\hat{V} = \sum_{k} \sum_{c} \left(V_{10,0c}^{(1,k)} |1\rangle \langle k, c| + V_{10,0c}^{(2,k)} |2\rangle \langle k, c| \right) + h.c., \tag{32}$$

where "h.c." denotes the hermitian conjugate and $|k,c\rangle$ denotes a singly excited state, where the environmental site k is in its cth excited state and all other building blocks are in their electronic ground state. In second-order perturbation theory the following energies are obtained for the exciton states $|\pm\rangle$

$$E_{\pm} = E_{\pm}^{(0)} + \sum_{k} \sum_{c} \frac{\left| \langle \pm | V | k, c \rangle \right|^{2}}{E_{\pm}^{(0)} - E_{c}^{(k)}}$$

$$= E_{0} \pm V_{12}^{(0)} + \frac{1}{2} \sum_{k,c} \frac{V_{10,0c}^{(1,k)} V_{0c,10}^{(1,k)} + V_{10,0c}^{(2,k)} V_{0c,10}^{(2,k)} \pm V_{10,0c}^{(1,k)} V_{0c,10}^{(2,k)} \pm V_{10,0c}^{(2,k)} V_{0c,10}^{(1,k)}}{E_{0} \pm V_{12}^{(0)} - E_{c}^{(k)}}.$$
(33)

Taking into account that $E_0 \pm V_{12}^{(0)} - E_c^{(k)} \approx E_0 - E_c^{(k)}$, the difference between perturbed exciton energies becomes

$$E_{+} - E_{-} = 2V_{12}^{(0)} + 2\sum_{k,c} \frac{V_{10,0c}^{(1,k)} V_{0c,10}^{(2,k)}}{E_{0} - E_{c}^{(k)}},$$
(34)

where we have also used the fact that the eigenfunctions of all states are assumed to be real-valued. Identifying the perturbed excitonic coupling V_{12} as half the splitting between eigenstates results in

$$V_{12} = V_{12}^{(0)} + \sum_{k} V_{12}^{(k)}, \tag{35}$$

where $V_{12}^{(0)}$ is the direct excitonic coupling between the pigments and

$$V_{12}^{(k)} = \sum_{c} \frac{V_{10,0c}^{(1,k)} V_{0c,10}^{(2,k)}}{E_0 - E_c^{(k)}}$$
(36)

contains a superexchange-type contribution involving excitonic couplings to off-resonant states of the environmental building block k. $V_{10,0c}^{(n,k)} = V_{0c,10}^{(n,k)}$ is the Coulomb coupling between the transition density of the $0 \to 1$ transition of pigment n and the transition density of the $0 \to c$ transition of the building block k reading

$$V_{10,0c}^{(n,k)} = \int d\mathbf{r}_n \int d\mathbf{r}_k \frac{\rho_{10}^{(n)}(\mathbf{r}_n)\rho_{0c}^{(k)}(\mathbf{r}_k)}{|\mathbf{r}_k - \mathbf{r}_n|}$$

$$\approx \sum_{I,J} \frac{q_I^{(n)}(1,0)q_J^{(k)}(0,c)}{|\mathbf{R}_I^{(n)} - \mathbf{R}_J^{(k)}|}.$$
(37)

In the second line of the above equation, we have approximated the integral by a sum over pairwise Coulomb interactions between atomic transition charges, introduced in the Transition charges from the Electrostatic Potential (TrEsp) method [5]. These charges are obtained from a fit of the electrostatic potential of the ab-initio transition density. Applying a dipole approximation to the environmental building block k results in

$$V_{10,0c}^{(n,k)} = \sum_{I} \frac{q_I^{(n)}(1,0)\mathbf{d}_{0c}^{(k)} \cdot (\mathbf{R}_I^{(n)} - \mathbf{R}_k)}{|\mathbf{R}_I^{(n)} - \mathbf{R}_k|^3},$$
(38)

with the transition dipole moment $\mathbf{d}_{0c}^{(k)}$ of the $0 \rightarrow c$ transition

$$\mathbf{d}_{0c}^{(k)} = \sum_{I} q_J^{(k)}(0, c) \mathbf{R}_J^{(k)} \tag{39}$$

of building block k with center coordinate R_k . With the above approximations the environmental mediated excitonic coupling $V_{12}^{(k)}$ in equation (36), can be expressed as

$$V_{12}^{(k)} = \frac{1}{2} \sum_{I,J} q_I^{(1)}(1,0) q_J^{(2)}(0,1) \frac{\left(\mathbf{R}_J^{(2)} - \mathbf{R}_k\right) \hat{\alpha}_k(-E_0) \left(\mathbf{R}_k - \mathbf{R}_I^{(1)}\right)}{\left|\mathbf{R}_J^{(2)} - \mathbf{R}_k\right|^3 \left|\mathbf{R}_I^{(1)} - \mathbf{R}_k\right|^3},$$
(40)

where we introduced the polarizability tensor of the kth building block at energy E_0 with Cartesian components

$$(\alpha(-E_0))_{ij} = 2\sum_{c} \frac{\left(\mathbf{d}_{0c}^{(k)}\right)_i \left(\mathbf{d}_{0c}^{(k)}\right)_j}{E_c^{(k)} - E_0}.$$
(41)

With this polarizability tensor, equation (40) can be interpreted in the following way. The transition charge $q_L^{(1)}(1,0)$ of pigment 1 creates a field

$$\mathbf{E}_{I} = q_{I}^{(1)}(1,0) \left(\mathbf{R}_{k} - \mathbf{R}_{I}^{(1)} \right) / |\mathbf{R}_{I}^{(1)} - \mathbf{R}_{k}|^{3}, \tag{42}$$

which induces a dipole moment in the kth environmental building block

$$p_k = \hat{\alpha}_k(-E_0)\mathbf{E}_I,\tag{43}$$

that interacts with the partial charge $q_J^{(2)}(0,1)$ at position $\mathbf{R}_J^{(2)}$ of monomer 2 via the dipole potential

$$\phi_{p_k}(\mathbf{R}_J^{(2)}) = \mathbf{p}_k \Big(\mathbf{R}_J^{(2)} - \mathbf{R}_k\Big) / |\mathbf{R}_J^{(2)} - \mathbf{R}_k|^3.$$
(44)

Noting that the polarizability tensor $\hat{\alpha}_k(\hbar\omega)$ is related to the dynamic polarizability $\hat{\alpha}_k^{\text{dyn}}(\hbar\omega)$, that describes the polarization by a field of frequency ω by [8–10]

$$\hat{\alpha}_k^{\text{dyn}}(\hbar\omega) = \frac{1}{2}(\hat{\alpha}_k(\hbar\omega) + \hat{\alpha}_k(-\hbar\omega)) \approx \frac{1}{2}\hat{\alpha}_k(-\hbar\omega), \tag{45}$$

we can identify the polarization in equation (40) as a fast (optical) polarization of the environment, which takes care of the fact that an electronic excitation energy transfer event does not leave any time for a slow polarization of the environment.

The above derivation is exploited in the Poisson-TrEsp method [10, 12, 13]. In this method, the protein/solvent environment is described by a homogeneous dielectric of optical dielectric constant ϵ . The transition charges of the pigments are placed in molecule-shape cavities with $\epsilon = 1$ inside the cavities and $\epsilon = n^2$, with the (average) refractive index n outside. The electrostatic potential of the transition density of chromophore m, $\phi_m^{1,0}(r)$ is obtained by solving a Poisson equation

$$\nabla \left(\epsilon(\mathbf{r}) \nabla \phi_m^{(1,0)}(\mathbf{r}) \right) = -4\pi \sum_I q_I^{(m)}(1,0) \delta(\mathbf{r} - \mathbf{R}_I^{(m)}), \tag{46}$$

where $\epsilon(\mathbf{r})$ equals one if \mathbf{r} points into a cavity and n^2 otherwise. The coupling between chromophores m and n is then obtained as

$$V_{mn} = \sum_{I} \phi_m^{(1,0)}(\mathbf{R}_J^{(n)}) q_J^{(n)}(1,0). \tag{47}$$

An uncertainty in the calculation of couplings is the absolute magnitude of the transition charges which can vary substantially for different quantum chemical methods used to calculate the transition density. Fortunately the shape of the transition density is often very similar. Therefore, the magnitude can be scaled by a constant factor that is obtained by comparing the first moment of the transition density, that is the transition dipole moment, with the experimental vacuum transition dipole moment. The latter can be extrapolated from dipole strengths measured in different solvents (The values for different types of chlorophylls and bacteriochlorophylls can be found in Ref. [14]).

By comparing the couplings obtained with Poisson-TrEsp with those obtained in vacuum, directly from the TrEsp charges, an empirical screening factor $f_{mn}^{\text{appr}}(R_{mn}, \kappa_{mn})$ can be inferred, such that the couplings may be approximated as

$$V_{mn} \approx f_{mn}^{\text{appr}}(R_{mn}, \kappa_{mn}) \sum_{I,J} \frac{(q_I^{(m)}(1,0) q_J^{(n)}(0,1)}{|\mathbf{R}_I^{(m)} - \mathbf{R}_J^{(n)}|}.$$
 (48)

Whereas previous works suggested an exponential distance dependence of the screening factor [15, 16] or a rather constant screening factor [17], a recent investigation of excitonic couplings in photosystem I trimers found an improved approximation of the screening effects using a function [10]

$$f_{mn}^{\text{appr}}(R_{mn}, \kappa_{mn}) = 0.60 + 39.6\Theta(|\kappa_{mn}| - 1.17) \exp\{-0.56R_{mn}/\text{Å}\}$$
 (49)

containing the orientation factor κ_{mn} of the dipole-dipole interaction

$$\kappa_{mn} = \overrightarrow{e}_m \cdot \overrightarrow{e}_n - 3(\overrightarrow{e}_m \cdot \overrightarrow{e}_{mn})(\overrightarrow{e}_n \cdot \overrightarrow{e}_{mn}), \tag{50}$$

where \overrightarrow{e}_m and \overrightarrow{e}_n are unit vectors that are oriented along the transition dipole moments $\overrightarrow{\mu}_m$ and $\overrightarrow{\mu}_n$ of pigments m and n, respectively, and the unit vector \overrightarrow{e}_{mn} is oriented along the center-to-center vector $\overrightarrow{R}_m - \overrightarrow{R}_n$ between these pigments. The Heaviside step function

$$\Theta(|\kappa_{mn}| - 1.17) = \begin{cases} 1 & |\kappa_{mn}| \ge 1.17 \\ 0 & \text{else} \end{cases}$$
 (51)

ensures that the screening factor depends exponentially on distance for in-line-type geometries ($|\kappa_{mn}| \ge 1.17$) and is constant for sandwich-like geometries ($|\kappa_{mn}| < 1.17$).

5.2.2 Vibrational Degrees of Freedom

So far we have discussed how the electronic degrees of freedom can be treated by the Frenkel exciton Hamiltonian introduced above. We have considered the equilibrium position of nuclei in the electronic ground state of the complex for the definition of the Frenkel exciton Hamiltonian. In order to include the nuclear degrees of freedom, we will consider small displacements of nuclei from their equilibrium positions and add the kinetic energy of nuclei in the following. The Frenkel exciton Hamiltonian is expanded into a Taylor series for small displacements of nuclei around their equilibrium position

$$H_{mn} \approx H_{mn}^{(0)} + \sum_{J} (\nabla_{J} H_{mn}|_{0}) \cdot (\mathbf{R}_{J} - \mathbf{R}_{J}^{(0)}),$$
 (52)

where $H_{mn}^{(0)} = H_{mn}(\{R\}_0)$ denotes the exciton Hamiltonian at the equilibrium position of nuclei in the electronic ground state of the aggregate $\{R\} = \{R_0\}$, the sum runs over all atoms J of the complex and $(\nabla_J H_{mn}|_0)$ denotes the gradient of the Hamiltonian with respect to the three Cartesian coordinates of nucleus J, taken at $\{R\} = \{R_0\}$. We introduce mass-weighted normal coordinates $q_{\xi}(t)$ via

$$R_J - R_J^{(0)} = M_J^{-1/2} \sum_{\xi} A_J^{(\xi)} q_{\xi}, \tag{53}$$

with the mass M_J of nucleus J, and $\mathbf{A}_J^{(\xi)}$ contains the contribution of nucleus J to the eigenvector of normal mode ξ . The normal coordinates q_{ξ} are related to dimensionless coordinates $Q_{\xi} = C_{\xi} + C_{\xi}^{\dagger}$ with the creation and annihilation operators of vibrational quanta C_{ξ}^{\dagger} and C_{ξ} , respectively by $q_{\xi} = (\hbar/2\omega_{\xi})^{1/2}Q_{\xi}$ [4]. Hence, equation (52) may be expressed as

$$H_{mn} \approx H_{mn}^{(0)} + \sum_{\xi} g_{\xi}(m, n) \hbar \omega_{\xi} Q_{\xi}, \tag{54}$$

where the dimensionless exciton-vibrational coupling constants $g_{\xi}(m, n)$ have been introduced as

$$g_{\xi}(m,n) = \omega_{\xi}^{-3/2} (2\hbar)^{-1/2} \sum_{J} M_{J}^{-1/2} \mathbf{A}_{J}^{(\xi)} \cdot (\nabla_{J} H_{mn}|_{0}).$$
 (55)

Two requisites for the calculation of the above coupling constants are the performance of a normal mode analysis in the electronic ground state of the complex and the calculation of the gradients of the Frenkel exciton Hamiltonian. Whereas for isolated chromophores a quantum chemical normal mode analysis is possible, for whole aggregates one has to rely on classical molecular mechanics approaches. However, also a combination of the two is possible since the diagonal elements of H_{mn} , that is the local excitation energies E_m in equation (21) also contains a contribution of the isolated chromophores $E_1^{(m)} - E_0^{(m)}$ that depends solely on the intramolecular nuclear degrees of freedom. Therefore, in the spirit of the derivation of the Frenkel exciton Hamiltonian above, the coupling constants $g_{\xi}(m,n)$ may be grouped into intra-molecular and inter-molecular coupling constants

$$g_{\xi}(m,n) = \delta_{m,n} g_{\xi}^{(\text{intra})} + g_{\xi}^{(\text{inter})}(m,n), \tag{56}$$

where the intramolecular coupling constants are identical for identical chromophores and contain the influence of intramolecular electron-vibrational coupling, and the intermolecular coupling constants comprise the effect of the modulation of inter-building block Coulomb coupling by the nuclear dynamics on the diagonal and off-diagonal elements of H_{mn} . Note that we neglect the mixing between interand intramolecular vibrational modes because of the different energies of their vibrational quanta.

The complete Hamiltonian governing the coupled exciton-vibrational motion also includes the vibrational Hamiltonian, which, in terms of the normal modes introduced above, is a sum over independent harmonic oscillator modes ξ with normal mode frequencies ω_{ξ} . Hence, the total Hamiltonian of the aggregate reads

$$H = \sum_{m,n} \left(H_{mn}^{(0)} + \sum_{\xi} g_{\xi}(m,n) \hbar \omega_{\xi} Q_{\xi} \right) |m\rangle\langle n| + \sum_{\xi} \frac{\hbar \omega_{\xi}}{4} \left(P_{\xi}^{2} + Q_{\xi}^{2} \right), \tag{57}$$

where the dimensionless momentum $P_{\xi} = i(C_{\xi} - C_{\xi}^{\dagger})$ [4] was used in the harmonic oscillator Hamiltonian. The above Hamiltonian can be treated fully quantum mechanically to derive, e.g., expressions for the lineshape function of optical transitions or rate constants of excitation energy transfer. All these expressions are related to the spectral density of the exciton-vibrational coupling

$$J_{mnkl}(\omega) = \sum_{\xi} g_{\xi}(m, n) g_{\xi}(k, l) \delta(\omega - \omega_{\xi})$$
 (58)

that contains the exciton-vibrational coupling constants introduced above and the normal mode frequencies ω_{ξ} . Taking into account that the intra- and intermolecular modes have different frequencies, the spectral density can be expressed as a sum of intra- and intermolecular contributions

$$J_{mnkl}(\omega) = \delta_{m,n} \delta_{n,k} \delta_{k,l} J^{(\text{intra})}(\omega) + J_{mnkl}^{(\text{inter})}(\omega), \tag{59}$$

with

$$J^{(\text{intra})}(\omega) = \sum_{\xi} \left(g_{\xi}^{(\text{intra})} \right)^2 \delta(\omega - \omega_{\xi}), \tag{60}$$

and

$$J_{mnkl}^{(\text{inter})}(\omega) = \sum_{\xi} g_{\xi}^{(\text{inter})}(m,n) g_{\xi}^{(\text{inter})}(k,l) \delta(\omega - \omega_{\xi}). \tag{61}$$

The intermolecular spectral density contains information about the modulation of excitonic couplings, transition energies and also about correlations in the modulations of those quantities, whereas such effects in the intramolecular spectral density are neglected because of the local nature of the latter.

5.2.3 Parameterization of the FMO Protein

Application of the above parameterization to the FMO protein revealed the following results:

• The electrostatic pigment-protein coupling creates a site energy funnel in the FMO protein such that the pigments that are closer to the outer antenna are blue-shifted and those closer to the reaction center complex (RCC) are red-shifted [11, 18, 19]. These calculations provided a structure-based explanation of some of

the earlier fits of site energies [12, 20–22]. Based on these fits and earlier linear dichroism spectra of isolated FMO proteins and membrane fragments with FMO proteins attached [23], the relative orientation of the FMO protein with respect to the RCC has been predicted in 2006 [12]. The first experimental verification of this orientation was provided based on chemical labeling and mass spectrometry [24]. Recently, the first high-resolution cryo-electron microscopy studies of the FMO-RCC supercomplex were reported [1, 2], which also provided evidence that the pigments, identified as low-energy sites earlier, are closest to the RCC. Concerning the effect of electrostatic pigment-protein coupling, it was found that the electric field of the backbone of two alpha helices in the neighborhood of BChl 3 in the FMO protein and a hydrogen bond between a tyrosine residue and the 3-acetyl group of BChl 3 are the main contributors to the red shift of this pigment. The latter prediction has been recently verified by site-directed mutagenesis experiments [25].

- Based on Poisson-TrEsp calculations of the excitonic coupling and vacuum dipole strength of the pigments extrapolated from an analysis of absorption spectra in different solvents [14], an effective dipole strength of 30 D² was inferred [12] to be used in calculations of inter-pigment excitonic couplings. The excitonic couplings had been found to be critical for the fit of site energies, and an unusually low effective dipole strength was inferred from a fit of optical spectra [20]. The Poisson-TrEsp calculations [12] explained this value quantitatively.
- The calculation of the spectral density of the FMO protein revealed a one-order-of-magnitude smaller Huang-Rhys factor for the fluctuations of the

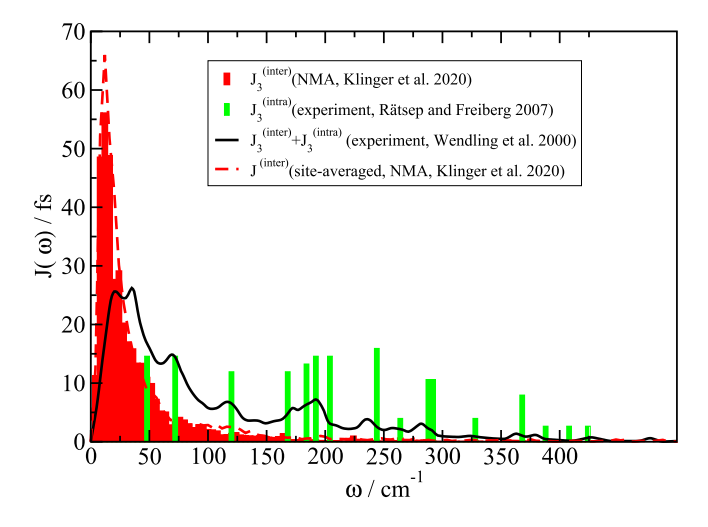


FIG. 5.2 – Comparison between the intermolecular spectral density $J_{33}(\omega)$ of low-energy pigment BChl 3 (red bars) obtained from an NMA [26], the intrapigment part of the spectral density $J_{\text{intra}}(\omega)$ extracted from experiment [27] (green bars), and the overall spectral density of the lowest exciton state in the FMO protein, extracted from fluorescence line narrowing spectra (black line) [28]. For comparison, the intermolecular spectral density averaged over all sites is also shown (dashed red line). Figure adapted from Ref. [26].

excitonic couplings as compared to that of the site energies [13]. In addition, correlations in site energy fluctuations at low vibrational frequencies were found in different pigments in the same [13] as well as in different monomeric subunits of the FMO trimer [26]. The intermolecular contribution $J_3^{(\text{inter})}(\omega) = J_{3333}^{(\text{inter})}(\omega)$ of the site energy fluctuations of the low-energy site 3 obtained from a NMA [26] is compared in figure 5.2 to experimental data [27, 28]. The calculated spectral density is larger than the experimental one at very low frequencies and smaller at intermediate and high frequencies. The deviations at small and intermediate frequencies could be due to the harmonic approximations, and the deviations at high frequencies are due to contributions from intramolecular vibrational modes of the pigments. The site-averaged intermolecular contribution to the site energy modulation (dashed line in figure 5.2) is very similar to the spectral density $J_3^{(\text{inter})}(\omega)$ of the low-energy site 3.

5.3 Quantum Dynamics

Taking into account the fact that the modulation of excitonic couplings is negligibly small compared to that of the site energies [13] (see above), we arrive at the following Frenkel exciton Hamiltonian

$$H = \sum_{m} \left(E_{m} + \sum_{\xi} g_{\xi}(m) \hbar \omega_{\xi} Q_{\xi} \right) |m\rangle\langle m| + \sum_{m,n} V_{mn} |m\rangle\langle n| + \sum_{\xi} \frac{\hbar \omega_{\xi}}{4} \left(P_{\xi}^{2} + Q_{\xi}^{2} \right), \tag{62}$$

where E_m and V_{mn} are the site energy of pigment m and the excitonic coupling between pigments m and n, taken at the equilibrium position of nuclei in the electronic ground state. To find the eigenstates of the above Hamiltonian and the resulting exciton-vibrational dynamics is a non-trivial task. To get some first insights we use the completeness relation $1 = |0\rangle\langle 0| + \sum_m |m\rangle\langle m|$ and introduce potential energy surfaces of localized excited states $|m\rangle$ by rewriting the above Hamiltonian as

$$H = \sum_{m} \left(\tilde{E}_{m} + \sum_{\xi} \frac{\hbar \omega_{\xi}}{4} (Q_{\xi} + 2g_{\xi}(m))^{2} \right) |m\rangle\langle m| + \sum_{m,n} V_{mn} |m\rangle$$

$$+ \sum_{\xi} \frac{\hbar \omega_{\xi}}{4} \left(P_{\xi}^{2} + Q_{\xi}^{2} \right) |0\rangle\langle 0| + T_{\text{nuc}},$$
(63)

with the kinetic energy of nuclei $T_{\text{nuc}} = \sum_{\xi} \frac{\hbar \omega_{\xi}}{4} P_{\xi}^2$ and the minimum energy of the PES (at $Q_{\xi} = -2g_{\xi}(m)$), $\tilde{E}_m = E_m - E_{\lambda}(m)$, where

$$E_{\lambda}(m) = \sum_{\xi} \hbar \omega_{\xi} g_{\xi}^{2}(m) \tag{64}$$

is the reorganization energy of the local exciton-vibrational coupling of site m. If this reorganization energy is much larger than the excitonic coupling, i.e., $E_{\lambda}(m) > |V_{mn}|$ in good approximation, localized excited, states are excited and the nuclei relax in the PES of these excited states, releasing the reorganization energy $E_{\lambda}(m)$. Energy transfer between these localized excited states can be described by standard Förster theory [4, 7].

In the limit of very strong excitonic couplings, that is, $E_{\lambda}(m) < < |V_{mn}|$, delocalized excited states $|M\rangle = \sum_{m} c_{m}^{(M)} |m\rangle$ are excited, where the coefficients $c_{m}^{(M)}$ follow from the eigenvectors of the exciton matrix defined above and the lowest eigenenergy E_{M} of a delocalized state is lower than the E_{m} of a localized excited state an amount that is in the order of the nearest neighbor excitonic coupling. Qualitatively speaking, the system tries to minimize the free energy after optical excitation. In the case of strong excitonic couplings, the excitons created after light excitation relaxes between different delocalized excited states, and this relaxation can be described by using perturbation theory in the local exciton-vibrational coupling, as done in Redfield theory [7].

In photosynthetic pigment-protein complexes, the theory is challenged by the fact that the nearest neighbor excitonic couplings V_{mn} are in the same order of magnitude as the local reorganization energies of exciton-vibrational coupling. Hence, there is no obvious small parameter that can be used for perturbation theory. Numerically exact methods have been developed to deal with this situation, such as the hierarchical equation of motion (HEOM) approach [29–31] (see chapter 3), the density matrix renormalization group/polynomial transformation approach [32, 33], path integral methods [34–37], the multi-configurational time-dependent Hartree (MCTDH) method [38] (see chapter 2) and polaron transformation techniques [39]. Here, we will follow a different strategy and transform the Frenkel exciton Hamiltonian in equation (62) into the exciton basis, defined at the equilibrium position of nuclei in the electronic ground state. The resulting Hamiltonian reads

$$H = \sum_{M} \left(E_{M} + \sum_{\xi} g_{\xi}(M, M) \hbar \omega_{\xi} Q_{\xi} \right) |M\rangle \langle M|$$

$$+ \sum_{M,N} g_{\xi}(M, N) \hbar \omega_{\xi} Q_{\xi} |M\rangle \langle N| + \sum_{\xi} \frac{\hbar \omega_{\xi}}{4} \left(P_{\xi}^{2} + Q_{\xi}^{2} \right),$$
(65)

where the exciton-vibrational coupling constant $g_{\xi}(M, N)$ in the exciton basis

$$g_{\xi}(M,N) = \sum_{m} c_{m}^{(M)} c_{m}^{(N)} g_{\xi}(m)$$
 (66)

now contains diagonal (M = N) as well as off-diagonal $(M \neq N)$ contributions. Interestingly, the off-diagonal contributions are smaller than the diagonal ones, as was revealed, e.g., by a normal mode analysis of the spectral density of the FMO protein [13] (figure 5.3).

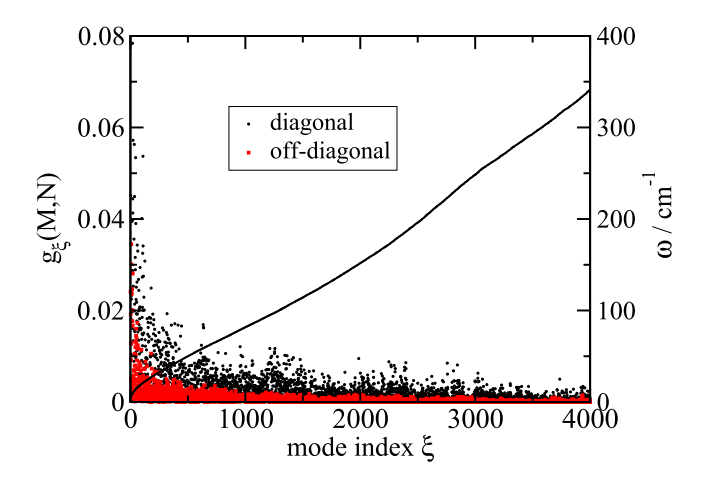


FIG. 5.3 – Coupling constants $g_{\xi}(M, N)$ of exciton-vibrational coupling of delocalized exciton states of the monomeric subunit of the FMO protein, obtained from equation (66), using the microscopic coupling constants $g_{\xi}(m, n)$ from the NMA as a function of normal mode index ξ for the first 4000 normal modes. The black solid line shows the corresponding normal mode frequencies ω_{ξ} . Figure taken from Ref. [13].

The diagonal elements can be used to construct potential energy surfaces of the exciton states, as was shown above for the localized excited states (equation (63)), and is illustrated in figure 5.4.

The off-diagonal elements of the exciton-vibrational coupling couple different excitonic PES and give rise to exciton relaxation. Expressions for the lineshape function $D_M(\omega)$ for the optical transition between the ground state and exciton state $|M\rangle$ have been derived using an exact treatment of the diagonal elements of the exciton vibrational coupling and different levels of perturbation theory for the off-diagonal elements. The general expression for the lineshape function reads

$$D_M(\omega) = \Re \int_0^\infty dt e^{i(\omega - \tilde{\omega}_M)t} e^{G_M(t) - G_M(0)} e^{-t/\tau_M}, \tag{67}$$

where the diagonal part of the exciton-vibrational coupling is contained in the function $G_M(t)$

$$G_M(t) = \int_0^\infty d\omega J_{MM}(\omega) \{ (1 + n(\omega)) e^{-i\omega t} + n(\omega) e^{i\omega t} \}, \tag{68}$$

with the spectral density

$$J_{MM}(\omega) = \sum_{\xi} g_{\xi}^{2}(M, M)\delta(\omega - \omega_{\xi}), \tag{69}$$

the exciton relaxation-induced lifetime broadening

$$\tau_M^{-1} = \sum_{N}^{N \neq M} \Re\{f_{MN}\},\tag{70}$$

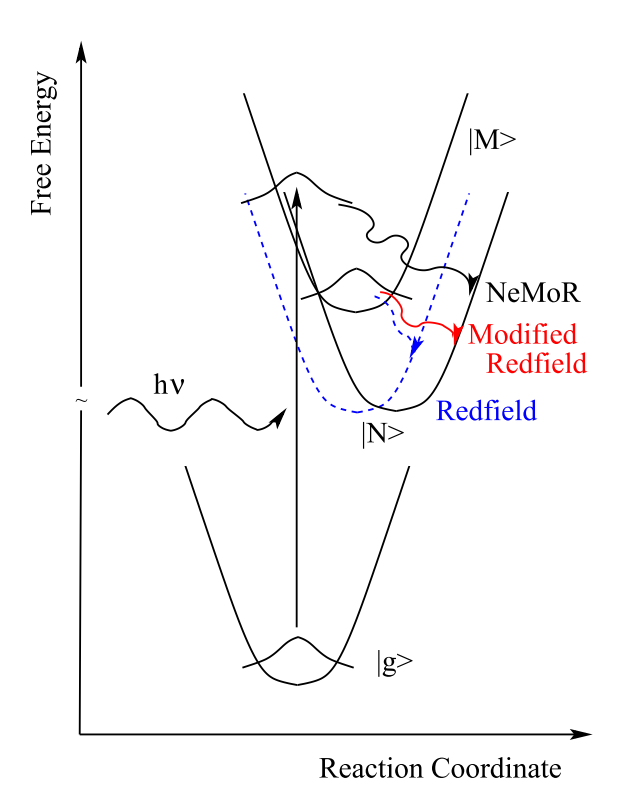


FIG. 5.4 – Illustration of free energy surfaces of exciton states and inter-surface transfer as described by Redfield theory [40], Modified Redfield theory [41], and Non-equilibrium Modified Redfield (NeMoR) theory [42, 43]. After optical excitation of the Mth exciton state, in Redfield and Modified Redfield theory, the inter-free energy surface coupling giving rise to exciton relaxation is treated by assuming that the nuclei are relaxed in the initial exciton state. Redfield theory, in addition, neglects the mutual displacement of free energy surfaces of exciton states along the nuclear coordinate (reaction coordinate) axis. The present NeMoR theory takes into account the finite nuclear relaxation time and the mutual displacements of free energy surfaces of exciton states. Figure taken from Ref. [42].

and the transition frequency

$$\tilde{\omega}_M = \omega_M - E_{\lambda}(M) + \Im\{f_{MN}\} \tag{71}$$

containing the reorganization energy $E_{\lambda}(M) = \sum_{\xi} \hbar \omega_{\xi} g_{\xi}^{2}(M, M)$ of the PES of the Mth exciton state. Equations (70) and (71) contain the real and imaginary parts, respectively of the function f_{MN} reading [42]

$$f_{MN} = \int_0^\infty dt e^{i\omega t} \operatorname{tr}_{\text{vib}} \left\{ U_M^{\dagger}(t) V_{MN} U_N(t) V_{NM} W_{\text{eq}}(g) \right\}, \tag{72}$$

where the inter-PES coupling V_{MN} contains the off-diagonal elements of the exciton-vibrational coupling

$$V_{MN} = \sum_{\xi} g_{\xi}(M, N) \hbar \omega_{\xi} Q_{\xi}, \tag{73}$$

the time-evolution operators $U_M^{\dagger}(t)$ and $U_N(t)$ of the vibrational degrees of freedom in the PES of the Mth and Nth exciton state, respectively, and the equilibrium statistical operator $W_{eq}(g)$ of the vibrations in the electronic ground state.

Different approximations of the function f_{MN} in equation (72) exist, as illustrated in figure 5.4. In Redfield theory [40], the mutual shift between the PES of exciton states $|M\rangle$ and $|N\rangle$ are neglected by setting $U_N(t) = U_M(t)$. In addition, it is assumed that after optical excitation of the state $|M\rangle$ the nuclei relax instantaneously in the PES of this state, prior to exciton relaxation. In this case, the equilibrium operator $W_{eq}(g)$ of the vibrations in the electronic ground state can be replaced by that of the exciton state $|M\rangle$, $W_{eq}(g) \approx W_{eq}(M)$. The inverse lifetime τ_M^{-1} in equation (70) is obtained as

$$\tau_M^{-1} = \frac{1}{2} \sum_{N}^{N \neq M} k_{M \to N}^{\text{Redf}},$$
(74)

with the Redfield rate constant

$$k_{M \to N}^{\text{Redf}} = 2\pi\omega_{MN}^2 (J_{MN}(\omega_{MN})(1 + n(\omega_{MN}) + J_{MN}(\omega_{NM})n(\omega_{NM})),$$
 (75)

that contains the spectral density

$$J_{MN}(\omega) = \sum_{\xi} g_{\xi}^{2}(M, N)\delta(\omega - \omega_{\xi}), \tag{76}$$

with the off-diagonal elements of the exciton-vibrational coupling. Please note that this spectral density can be expressed by the spectral densities of the local-exciton-vibrational coupling, using equation (66), as

$$J_{MN}(\omega) = \sum_{m} \left(c_{m}^{(M)}\right)^{2} \left(c_{m}^{(N)}\right)^{2} J_{m}(\omega) + \sum_{m,n}^{m \neq n} c_{m}^{(M)} c_{m}^{(N)} c_{n}^{(N)} c_{n}^{(N)} J_{mn}(\omega), \tag{77}$$

where

$$J_m(\omega) = \sum_{\xi} g_{\xi}^2(m)\delta(\omega - \omega_{\xi})$$
 (78)

contains the fluctuation of the site energy of pigment m and

$$J_{mn}(\omega) = \sum_{\xi} g_{\xi}(m)g_{\xi}(n)\delta(\omega - \omega_{\xi})$$
 (79)

describes the correlations in the fluctuations of the site energies of pigment s m and n.

In modified Redfield theory [41] the mutual displacement between the PES of exciton states $|M\rangle$ and $|N\rangle$ is taken into account, and vibrational relaxation is assumed to be fast by approximating $W_{eq}(g) \approx W_{eq}(M)$. In non-equilibrium modified Redfield theory [42, 43] the finite relaxation time of nuclei is taken into account by evaluating the full expression for f_{MN} in equation (72). Application to the water-soluble chlorophyll-binding protein (WSCP) revealed only very minor differences between the different theories, within reasonable parameter ranges [42]. It should, however, be noted that the very high-frequency intramolecular modes, outside of the range in which exciton relaxation occurs, were not included in this study. A word of caution is needed here. These very high-frequency intramolecular modes have small Franck-Condon factors. Therefore, the interpigment excitonic coupling involving excitations of these modes is small, and slight perturbations by the environment will destroy any delocalization effects of the exciton-vibrational wavefunction. Such dynamic localization effects are difficult to describe theoretically. However, non-perturbative approaches exist now [44, 45] that provide support for an implicit treatment of these localization effects [46, 47]. In this treatment, the high-frequency intramolecular vibronic transitions are treated as localized excitations and delocalization is only allowed for the 0-0 transition, including the low-frequency part of the spectral density.

A problem, related in spirit, occurs if there are pigments that are only weakly coupled to other pigments that form strongly coupled exciton domains, or if there is weak inter-domain excitonic coupling. Working with perturbation theory in the exciton basis of the whole complex could lead to an artificial exciton delocalization involving weakly coupled pigments. Consider, for example, a molecule in Les-Houches (France) and another one in Telluride (USA), 8600 km apart. If both have the same transition energy, their exciton matrix has equal diagonal elements and hence, the exciton states will be delocalized since the off-diagonal elements (the excitonic couplings) are not exactly zero. In reality, however, the slightest perturbation will bring the two molecules out of resonance and the excited states will be localized. Such a dynamic localization is difficult to describe explicitly, requiring a non-perturbative approach. Again an implicit treatment of the dynamic localization effects can be applied by introducing domains of strongly coupled pigments, in which the exciton wavefunction is allowed to delocalize, and treating the inter-domain excitonic coupling in second-order perturbation theory [30, 48, 49].

The standard generalized Förster theory rate constant for excitation energy transfer between an exciton state $|M_a\rangle$ in domain a and exciton state $|N_b\rangle$ in domain b reads [48]

$$k_{M_a \to N_b}^{GF} = \frac{2\pi}{\hbar^2} |V_{M_a N_b}|^2 \int d\omega D_{N_b}(\omega) D'_{M_a}(\omega), \tag{80}$$

where the excitonic coupling between the two exciton states,

$$V_{M_a N_b} = \sum_{m_a, n_b} c_{m_a}^{(M_a)} c_{n_b}^{(N_b)} V_{m_a n_b}$$
(81)

contains the exciton coefficients of these states and the individual inter-domain excitonic couplings $V_{m_a n_b}$ between pigments m_a and n_b in domains a and b,

respectively. The functions $D_{N_b}(\omega)$ and $D'_{M_a}(\omega)$ in equation (80) are the absorption and emission lineshape functions, respectively, of these exciton states. The absorption lineshape function is given in equation (67) by setting $M = N_b$, and the emission lineshape function $D'_M(\omega)$ is obtained from equation (67) by setting $M = M_a$ and by changing the sign of the first exponent on the r.h.s. $(e^{i(\omega-\tilde{\omega}_M)t} \to e^{-i(\omega-\tilde{\omega}_M)t})$. In addition, we have neglected the small off-diagonal frequency shift in equation (71), that is, we approximate $\tilde{\omega}_M$ by $\omega_M - E_{\lambda}(M)$.

The above rate constant has been extended to include correlations in site energy fluctuations between pigments in different exciton domains [26]. In this case, the rate constant reads

$$k_{M_a \to N_b}^{GF} = \frac{|V_{M_a N_b}|^2}{\hbar^2} \int_{-\infty}^{\infty} e^{i(\tilde{\omega}_{M_a} - \tilde{\omega}_{N_b})t} e^{G_{M_a}(t) - G_{M_a}(0)} e^{G_{N_b}(t) - G_{N_b}(0)} e^{-t(1/\tau_{M_a} + 1/\tau_{N_b})} \times e^{G_{M_a N_b}(t) - G_{M_a N_b}(0)},$$
(82)

where the first line formally resembles the standard result in equation (80) and the function $G_{M_aN_b}(t)$ in the second line reading

$$G_{M_aN_b}(t) = \int_0^\infty d\omega J_{M_aN_b}(\omega) \{ (1 + n(\omega)) e^{-i\omega t} + n(\omega) e^{i\omega t} \}$$
 (83)

contains the spectral density

$$J_{M_a N_b}(\omega) = \sum_{m_a, n_b} \left(c_{m_a}^{(M_a)} \right)^2 \left(c_{n_b}^{(N_b)} \right)^2 J_{m_a n_b}(\omega), \tag{84}$$

which is non-zero only if there are correlations in site energy fluctuations of pigments in different domains, that is, if $J_{m_a n_b}(\omega)$ is non-zero.

5.3.1 Energy Transfer in the FMO Protein

Application of the quantum dynamic theories to the FMO protein, using the parameterization given above, resulted in the following insights:

- Correlations in site energy fluctuations have practically no influence on exciton relaxation within the FMO monomer [13] as well as excitation energy transfer between different FMO monomers [26].
- The site-dependence of the Huang-Rhys factor is not critical for exciton relaxation and transfer. Exciton relaxation in the monomeric subunit of the FMO proteins occurs on a sub-ps timescale and excitation energy transfer between the subunits takes about 10 ps [26], in agreement with transfer times inferred from 2D electronic [50] and hole-burning spectroscopy [51], respectively.
- The semiclassical limits of Redfield [52, 53] and generalized Förster [26, 53] theories reveal that in a world where electrons move according to the laws of quantum mechanics and nuclei behave classically, that is, without taking notice of the coordinate/momentum uncertainty principle, exciton relaxation in the monomeric subunit of FMO would lead to equal population of all exciton states,

i.e., the principle of detailed balance assuring a preferential population of low-energy states would be violated, whereas this principle would be fulfilled for the transfer between different monomeric subunits of the FMO protein. The different behavior is explained by the difference in the relative strength of excitonic coupling and nuclear reorganization energies [53].

5.4 Light-Harvesting Efficiency of the Core of Green Sulfur Bacteria

Finally, we want to discuss a recent application of the parameterization of the Frenkel exciton Hamiltonian derived above and the dynamical theory of optical spectra and excitation energy transfer to calculate the light-harvesting efficiency of the FMO protein-reaction center core complex (FMO-RCC) supercomplex of green sulfur bacteria [3]. Green sulfur bacteria (GSB) are able to survive under extremely low light conditions, as in the neighborhood of black smokers or 100 m below the surface of the black sea. Whereas all other photosynthetic organisms organize a couple of hundred pigments in their light-harvesting antennae per reaction center (RC), the number of antenna pigments is one order of magnitude larger in GSB. Most of these antenna pigments are self-organized in the chlorosomes, from where the excitation energy is transferred through the baseplate and the FMO protein to the RCC. Recently the first high-resolution cryo-electron microscopy (cryo-EM) structural models of the FMO-RCC supercomplex were reported [1, 2]. These structures provided the basis for the calculations of the light-harvesting efficiency (LHE) which are summarized below. Details are given in a recent publication [3]. First, the Frenkel exciton Hamiltonian has been parameterized.

The excitonic couplings have been obtained using the Poisson-TrEsp method described above. A site-independent spectral density of the site energy fluctuations has been used, obtained from experimental fluorescence line narrowing spectra of the FMO protein [28]. The neglect of the modulation in excitonic couplings and the neglect of correlations in site energy fluctuations, as well as the assumption of a site-independent Huang-Rhys factor, have been justified above [13, 26]. The site energy calculations using the structure-based CDC method did not result in values that were able to reproduce the experimental optical spectra of the FMO and RCC subunits. Therefore, a genetic algorithm [12] has been applied to determine the site energies from a fit of the optical spectra of the FMO and RCC subunits. The resulting optical spectra of the FMO protein and the RCC are compared in figure 5.5 with the experimental data, revealing very reasonable agreement. The optimal site energies for the FMO protein agree very well with those obtained earlier [11, 18, 19] from calculations based on the crystal structure of this complex. It seems that the crystal structure of the FMO protein has reached a high enough resolution for meaningful electrostatic calculations, whereas the cryo-EM model still needs some refinement. So far, there is no crystal structure available for the RCC, and hence, no independent verification of the fitted site energies of this complex is possible.

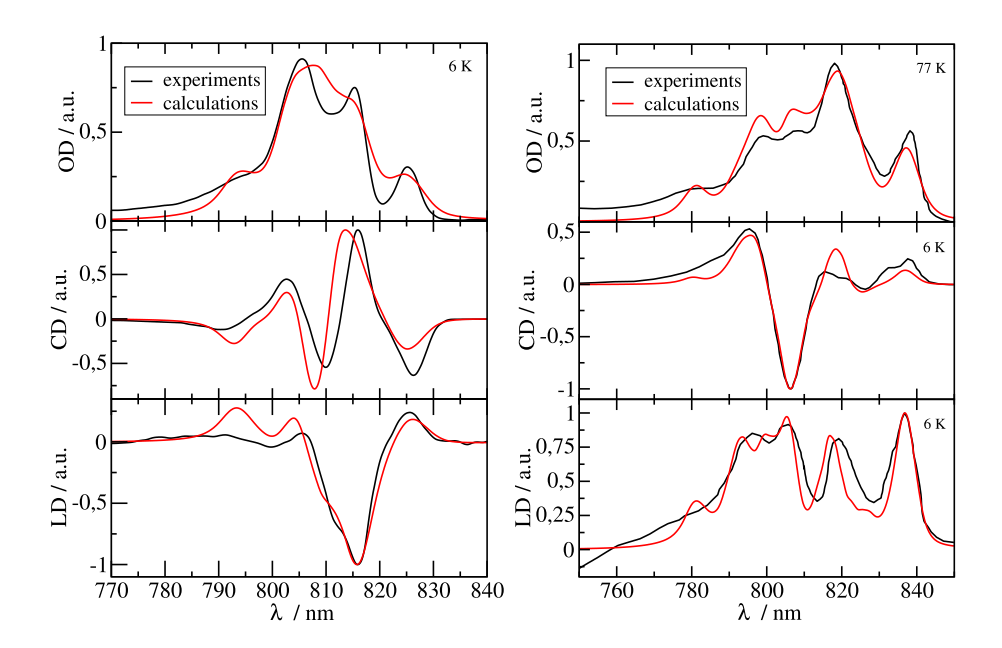


Fig. 5.5 – **Left:** Comparison of measured [21] (black lines) and calculated [3] (red lines) absorption (upper part), circular dichroism (middle part) and linear dichroism (bottom part) spectra of the FMO protein, all at cryogenic temperatures (T=6 K). **Right:** Same as left, but for the RCC and temperatures given in the right upper corners. Experimental spectra taken from [54] (absorption) and [55] (linear and circular dichroism). Figure adopted from Ref. [3].

With the parameters, determined above, the rate constants $k_{M_a \to N_a}^{\text{Redf}}$ (equation (75)) of intradomain exciton relaxation and $k_{M_a \to N_b}^{\text{GF}}$ (equation (80)) of inter-domain transfer can be calculated. These rate constants enter the following master equations for the populations of exciton states

$$\frac{\mathrm{d}}{\mathrm{d}t}P_{M_{a}}^{(a)}(t) = -\sum_{N_{a}}^{N_{\mathrm{pig}}^{(a)}} \left(k_{M_{a}\to N_{a}}^{\mathrm{Redf}}P_{M_{a}}^{(a)}(t) - k_{N_{a}\to M_{a}}^{\mathrm{Redf}}P_{N_{a}}^{(a)}(t)\right)
-\sum_{b,b\neq a}^{N_{\mathrm{dom}}} \sum_{N_{b}}^{N_{\mathrm{pig}}^{(b)}} \left(k_{M_{a}\to N_{b}}^{\mathrm{GF}}P_{M_{a}}^{(a)}(t) - k_{N_{b}\to M_{a}}^{\mathrm{GF}}P_{N_{b}}^{(b)}(t)\right)
-(k_{M_{a}\to\mathrm{ET}} + k_{M_{a}\to\mathrm{FL}})P_{M_{a}}^{(a)}(t)$$
(85)

where $N_{\rm dom}$ is the number of domains, $N_{\rm pig}^{(a)}$ and $N_{\rm pig}^{(b)}$ are the number of pigments in domains a and b respectively. The third line of the above equation contains the sinks of the excitation energy. If an exciton reaches the RC, it can be irreversibly trapped by primary electron transfer, described by the rate constant $k_{M_a \to \rm ET}$, which is given as

$$k_{M_a \to \text{ET}} = \frac{1}{\tau_{\text{ET}}} \delta_{a,\text{RC}} \left(\left| c_{P_A}^{(M_{\text{RC}})} \right|^2 + \left| c_{P_B}^{(M_{\text{RC}})} \right|^2 \right).$$
 (86)

Here, $\left|c_{\mathrm{P_A}}^{(M_{\mathrm{RC}})}\right|^2$ and $\left|c_{\mathrm{P_B}}^{(M_{\mathrm{RC}})}\right|^2$ are the probabilities to find the primary electron donors $\mathrm{P_A}$ and $\mathrm{P_B}$ in the central special pair formed by BChls a 801 of the two branches of the RC (figure 5.1) excited in state $|M_{\mathrm{RC}}\rangle$ and τ_{ET} is the intrinsic inverse rate constant of primary electron transfer $\mathrm{P^*(Chl}~a~802) \to \mathrm{P^+(Chl}~a~802)^-$. Due to the fortuitous circumstance that the primary electron donor is a Chl a, whereas all antenna pigments are BChl a, the RC can be selectively excited and the decay of excited states measured. Neerken et~al.~[56] reported a fastest decay constant of 1.5 ps, which most likely reflects primary electron transfer. In our simulations, we take $\tau_{\mathrm{ET}}=2$ ps as a conservative estimate.

The LHE is limited by the losses due to fluorescence (including non-radiative decays of excited states) described by the rate constant

$$k_{M_a \to \mathrm{FL}} = \frac{1}{\tau_{\mathrm{FL}}} \frac{\left| \boldsymbol{\mu}_{M_a} \right|^2}{\left| \boldsymbol{\mu}_{\mathrm{BChl}} \right|^2},\tag{87}$$

where $|\mu_{\rm BChl}|^2$ is the dipole strength of an isolated BChl a pigment and $|\mu_{M_a}|^2$ is that of exciton state $|M_a\rangle$. $\tau_{\rm FL}$ is the intrinsic fluorescence lifetime of BChl a, which is about 2 ns. This time sets the clock for light-harvesting. Every exciton that reaches the RC within this time has a high chance of being converted into a charge-separated state. The population of the latter, denoted as $P_+(t)$, is obtained from

$$P_{+}(t) = \sum_{M_{\rm RC}} k_{M_{\rm RC} \to \rm ET} \int_{0}^{t} d\tau P_{M_{\rm RC}}^{(\rm RC)}(\tau). \tag{88}$$

Due to the inhomogeneous distribution of pigments in the FMO-RCC supercomplex, we expect certain bottlenecks in the light-harvesting. As discussed above, exciton relaxation within the monomeric subunit of the FMO protein is at least an order of magnitude faster than intermonomer transfer. Hence, it is possible to assume that the exciton states within a domain are in quasi-thermal equilibrium before interdomain transfer occurs, that is,

$$P_{M_a}^{(a)} \approx f_{M_a} P_a(t), \tag{89}$$

with the Boltzmann factor

$$f_{M_a} = \frac{e^{-\hbar\omega_{M_a}/k_b T}}{\sum_{N_a} e^{-\hbar\omega_{N_a}/k_b T}}.$$
 (90)

Inserting the above approximation (equation (89)) into the master equation (equation (85)) and performing a sum over M_a , using $\sum_{M_a} f_{M_a} = 1$ results in a master equation for the domain populations $P_a = \sum_{M_a} P_{M_a}$

$$\frac{\mathrm{d}}{\mathrm{d}t} P_{a}(t) = -\sum_{b,b\neq a}^{N_{\text{dom}}} (k_{a\to b} P_{a}(t) - k_{b\to a} P_{b}(t)) -(k_{a\to \mathrm{FT}} + k_{a\to \mathrm{FL}}) P_{a}^{(a)}(t), \tag{91}$$

with the rate constant $k_{a\rightarrow b}$ of inter-domain exciton transfer

$$k_{a \to b} = \sum_{M_a, N_b} f_{M_a} k_{M_a \to N_b}^{GF} \tag{92}$$

and those of primary electron transfer and fluorescence

$$k_{a \to \text{ET}} = \frac{1}{\tau_{\text{ET}}} \delta_{a, \text{RC}} \sum_{M_{\text{R}C}} f_{M_{R_c}} \left(\left| c_{\text{P}_{\text{A}}}^{(M_{\text{RC}})} \right|^2 + \left| c_{\text{P}_{\text{B}}}^{(M_{\text{RC}})} \right|^2 \right)$$
 (93)

and

$$k_{a \to \text{FL}} = \frac{1}{\tau_{\text{FL}}} \sum_{M_a} f_{M_a} \frac{\left| \boldsymbol{\mu}_{M_a} \right|^2}{\left| \boldsymbol{\mu}_{\text{BChl}} \right|^2}, \tag{94}$$

respectively. The population $P_{+}(t)$ of the charge-separated state then follows as

$$P_{+}(t) = k_{\mathrm{R}C \to \mathrm{ET}} \int_{0}^{t} d\tau P_{\mathrm{R}C}(\tau). \tag{95}$$

The next level of coarse-graining can be obtained by combining certain domains into larger compartments and assuming fast equilibration within these compartments. The energy transfer rate constant between two such compartments I and J is given as

$$k_{I \to J} = \sum_{a,b}^{a \in I, b \in J} \sum_{M_a, N_b} f_{I,M_a} k_{M_a \to N_b}^{GF}$$
(96)

with the Boltzmann factor

$$f_{I,M_a} = \frac{e^{-\hbar\omega_{M_a}/k_b T}}{\sum_{a \in I} \sum_{N_a} e^{-\hbar\omega_{N_a}/k_b T}}.$$
 (97)

On the basis of a comparison of the different levels of coarse-graining, described above, one can search for a minimal model that still captures the main characteristics, in particular the light-harvesting efficiency, of the most detailed description. As a measure, the population of excited states $P_{\rm exc}(t)$ obtained from a sum over all excited state populations as well as the populations of the charge-separated state $P_{+}(t)$, obtained in the different models, will be compared. As an initial condition, incoherent transfer from the baseplate to the FMO-protein is taken into account, as described in detail in Ref. [3].

In figure 5.6, the populations $P_{\text{exc}}(t)$ and $P_{+}(t)$ are compared for different levels of coarse-graining. In the full model (equation (85)), about 95% of the initial excitations are converted into a charge-separated state. Very similar kinetics are obtained by assuming fast intradomain exciton equilibration (equation (91)) and also within a 5-compartment model, consisting of the FMO-protein, RCC-Ant1, RCC-RC, RCC-Ant2, and the charge-separated state P_{+} . Assuming, in addition, fast exciton equilibration in the whole RCC, as in the 3-compartment model results in noticeable deviations from the results obtained in the more detailed models.

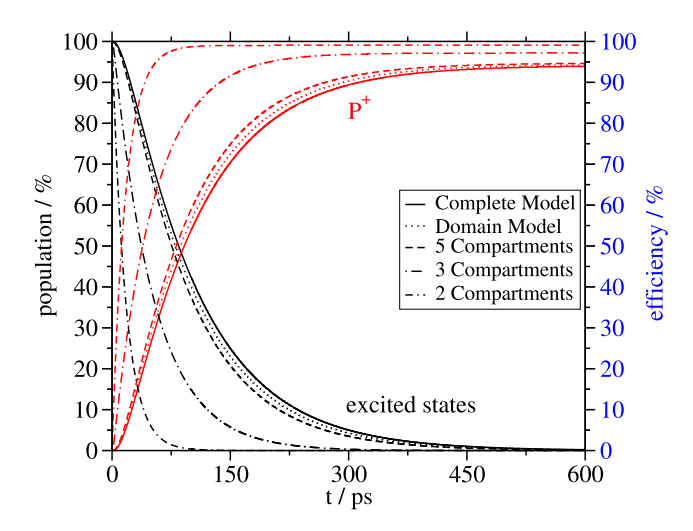


Fig. 5.6 – Populations of charge-separated state P⁺ (red lines) and excited states (black lines) of the FMO-RCC supercomplex obtained using different levels of coarse-graining, as described in the text and the figure legend. Figure adopted from Ref. [3].

These deviations show that the transfer between the core antenna subunits (RCC-Ant1 and RCC-Ant2) and the RC are a bottleneck of the overall light-harvesting process. According to the 5-compartment model the transfer RCC-Ant1/2 \rightarrow RC occurs with a time constant of 23 ps. Interestingly, the reverse reaction (RC \rightarrow RCC-Ant1/2) takes only 11 ps. This difference reflects the different number of pigments in the antenna subunits and the RC giving rise to an entropic contribution to the free energy difference that is reflected in the rate constants.

In the 3-compartment model, which assumes fast exciton equilibration in the whole FMO-RCC supercomplex, additional deviations occur, suggesting that a second light-harvesting bottleneck is the transfer between the FMO protein and the RCC, occurring with 39 ps in forward and 28 ps in backward direction. In summary, the minimal model of light-harvesting is the 5-compartment model, the time constants of which are given in figure 5.1.

Finally, we want to investigate how the LHE depends on different factors, in particular, the site energy funnel in the FMO protein that is supposed to guide the excitons to the RCC [11, 12, 18], the quantum nature of the vibrations that guarantees the preferential equilibrium population of low-energy exciton states in the domains [52, 53] and the timescale of primary electron transfer in the RC. The influence of these different factors is investigated in figure 5.7. Inverting the site energy funnel in the FMO protein has some influence on the kinetics but barely influences the LHE. The funnel is shallow and the 2 ns fluorescence lifetime is large enough that it can still be out-competed by the excitation energy transfer to the RCC at room temperature. Ironically, the site energy funnel has been used to predict the relative orientation of the FMO-protein relative to the RCC [12]. The present

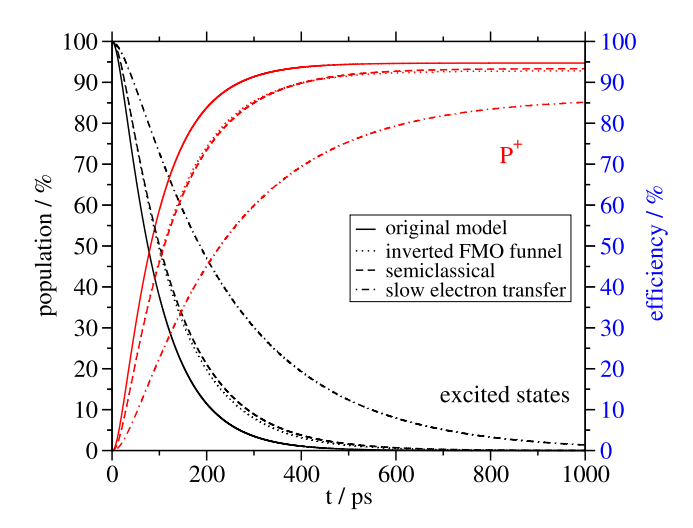


Fig. 5.7 – Populations of charge-separated state P⁺ (red lines) and excited states (black lines) of the FMO-RCC supercomplex obtained by using different parameters for the site energies in the FMO protein or the time constant of primary electron transfer and different theories for the vibrational motion, as described in the text and the figure legend. Figure adopted from Ref. [3].

calculations suggest that this prediction, although it turned out to be correct [57], was somewhat fortuitous, since the LHE does not depend critically on it. Note, however, that this site energy funnel was found to be important for photoprotection [3]. In the presence of molecular oxygen, the excitation energy of the low-energy BChl 3 is quenched by a nearby Cys residue, a quenching that occurs on a similar time-scale as the transfer to the RCC and, therefore, has a large impact on the LHE, protecting the RC from excitation energy that could lead to damage at the secondary electron acceptors (the iron-sulfur clusters).

Very similar results as for the inverted site energy funnel of the FMO protein are obtained if the motion of nuclei is described classically (the dashed lines in figure 5.7). In this case, the principle of detailed balance is still valid for the transfer between different exciton domains [26, 53], just within the exciton domains there is no correct exciton equilibration [52, 53], similar to the inverted site energy funnel in the FMO protein. Interestingly, the largest influence on the LHE comes from the time constant of primary electron transfer. Slowing down this time constant by a factor of 10 (from 2 to 20 ps) results in a 10% reduction of the LHE (dashed-dotted lines in figure 5.7). A fast primary electron transfer is needed to catch every exciton that reaches the RC, before it can escape back to the antenna, an escape that is promoted by the entropic factor, discussed above, giving rise to faster outward than inward transfer (figure 5.1).

5.5 Photosynthetic Light Conversion as a Blueprint for Organic Solar Cells?

Finally, we want to discuss similarities and differences between photosynthetic pigment-protein complexes (PPC) and organic solar cells (for introduction to organic solar cells (OSC), see chapter 6). Both use organic molecules for light harvesting and charge separation. Whereas PPCs have a well-defined structure, OSCs self-organize in a more random way in two inter-penetrating phases of donor and acceptor molecules. An electron-hole pair (exciton) created by light absorption in one phase will be transferred to the interface between the two phases, where it will separate, the electron being transferred in the acceptor phase and the hole in the donor phase. Only two different molecules are needed in OSCs, whereas PPCs utilize proteins to fine-tune the energetics of the system and to hold the pigments at optimal distances for efficient energy transfer in the light-harvesting antennae and electron transfer in the RC. The main photosynthetic pigment in cyanobacteria and plants is chlorophyll, which due to its planar ring-structure (enforced by the delocalization of π electrons) is rather rigid leading to a rather weak coupling of electronic excitations to intramolecular vibrational modes. The pigments in PPCs are non-covalently bound to proteins and the distances between pigments in light-harvesting antennae are kept large enough to avoid electron exchange effects, as coupling to charge transfer states, that could lead to quenching of excited states, which would limit the light-harvesting efficiency (LHE). OSCs contain a polymer phase, where the spectroscopic units are not so easily identified. Strong couplings between π electrons and intra and intermolecular vibrations of the polymer occur, where the low-frequency vibrations involve torsional degrees of freedom that limit the delocalization of excited states to certain segments of the polymer between which the excitation energy is transferred, much like in PPCs. Whereas in PPCs, these spectroscopic units are more or less static, in OSCs, they are changing in time. Moreover, the relatively large coupling to intramolecular vibrations in OSCs leads to additional dynamic localization effects of the exciton wavefunction. Coupling to intramolecular charge transfer states in the polymer has to be taken into account, as well as a modulation of this short-range as well as the long-range excitonic coupling by the intra and intermolecular vibrations. Non-perturbative methods, as the multi-configurational time-dependent Hartree method (MCTDH-see also chapter 2) are needed to describe this rich electron-vibrational dynamics, whereas in PPCs one can often obtain a qualitatively correct picture by simpler theories, as described above. In both cases, OSC and PPC, one has to find the right parameterization of the Frenkel-exciton (charge transfer) Hamiltonian. A simplification in the case of PPCs, is that this parameterization needs to be done only once, since the structural changes are small enough to be described by harmonic oscillator models. In case of OSCs, larger variations of the parameters during the exciton and electron transfer dynamics need to be taken into account. A rough characterization of the 3D structure (morphology) of the organic solar cell is sufficient, since the structural variations anyway have to be taken into account explicitly in the theory. In the case of PPCs, a high-resolution structural model provides a representative structure that

can be used in dynamic models of excitation energy and charge transfer. Without such a model, mostly obtained by X-ray crystallography or in recent years more and more by cryo-EM, a parameterization of the Hamiltonian would be practically impossible, because of the complexity of the system. The exact 3D structure of the complex is needed in order to evaluate the electrostatic pigment-protein coupling that tunes the local excitation energies of the pigments and the redox properties of the RC. A PPC can use the different properties of the 20 naturally occurring amino acids for this tuning. Our calculations, presented above, seem to suggest that the exact values for the site energies are not so important for a high LHE, because the RC is only a shallow trap and excitation energy transfer to the RC is fast compared to the fluorescence lifetime. There are, however, situations, where a switch from a light-harvesting into a quenching mode of the PPC is needed in order to protect the RC from receiving too much excitation energy. In the FMO protein of green sulfur bacteria it was found that this quenching is most efficient at the low-energy sites [3]. In this case, the presence of oxygen switches the FMO protein from a light-harvesting into a photoprotective mode. In the light-harvesting apparatus of higher plants and cyanobacteria, the decisive factor for this transition is the intensity of sunlight. In response to high light, a conformational change of the PPC opens the dissipative channels for the excitation energy. The microscopic mechanisms are not yet understood in detail. One likely candidate is the mixing of excited and intermolecular charge transfer states. In OSCs, such mixing is always present, and diabatization schemes have been developed to parameterize the Frenkel exciton charge transfer Hamiltonian in an efficient way (see chapter 6). These schemes are expected to be helpful also in the study of PPCs.

A more delicate tuning of cofactor properties concerns the photosynthetic reaction center. Whereas there are many different light-harvesting complexes in photosynthesis, nature has organized all photosynthetic reaction centers in a very similar way. There is a central chlorophyll or bacteriochlorophyll dimer and two membrane-spanning branches of cofactors. Electron transfer occurs downhill in free energy between neighboring cofactors along both (in type I RCs) or along one branch (type II RCs). The free energy differences are caused by electrostatic pigment-protein coupling and also by utilizing chemically different cofactors. Due to this, stepwise and downhill electron transfer recombination reactions can be suppressed, and, hence, charge separation is very efficient. The high oxidation power allowing the type II RC of photosystem II in plants and cyanobacteria to split water, was found to be created mainly by electrostatic pigment-protein coupling [58, 59]. OSCs do not have proteins for redox tuning and also do not utilize additional molecules for stabilizing the charge-separated state. Nevertheless, the electron-hole pairs can be separated at the interface. The exact microscopic mechanism is still a matter of discussions in the literature, but chapter 6 suggests that non-trivial dynamic effects involving donor-acceptor coherences and ultrafast charge transfer are exploited for efficient charge separation. After the initial charge separation, the motion of the charge carriers (electrons in the donor phase and holes in the acceptor phase) depends even more strongly than that of the excitons on the nuclear dynamics, because of the larger electron-vibrational coupling and the dominance of short-range effects that are very sensitive to structural variations. In photosynthesis,

a qualitatively correct picture is obtained by applying standard non-adiabatic electron transfer theory for nearest neighbor electron transfer in the RC. However, there are experimental reports of slow nuclear relaxation processes in photosynthetic RCs [60–62], whereas the standard theories assume nuclear relaxation processes are fast compared to the charge transfer. In addition, many of the kinetic details of primary photosynthetic charge transfer, in particular in photosystems I and II of higher plants and cyanobacteria are still unknown [59]. It could well be that a complete picture of primary photosynthetic charge transfer requires new theories and experiments. In that respect, the photosynthetic community can learn from the theoretical developments in the field of OSCs that can deal with scenarios, where the vibrations are much more than a heatbath of harmonic oscillators.

Acknowledgments. Financial support by the Austrian Science Fund (FWF) through grants P33155-NBL, I6484-N, and I6313-N is gratefully acknowledged.

References

- Chen J.-H., Wu H., Xu C., Liu X.-C., Huang Z., Chang S., Wang W., Han G., Kuang T., Shen J.-R., Zhang X. (2020) Architecture of the photosynthetic complex from a green sulfur bacterium, *Science* 370(6519), eabb6350.
- [2] Xie H., Lyratzakis A., Khera R., Kountantou M., Welsch S., Michel H., Tsiotis G. (2023) Cryo-em structure of the whole photosynthetic reaction center apparatus from the green sulfur bacterium Chlorobaculum tepidum, Proc. Natl. Acad. Sci. U.S.A. 120(5), e2216734120
- [3] Klinger A., Lindorfer D., Müh F., Renger T. (2023) Living on the edge: light-harvesting efficiency and photoprotection in the core of green sulfur bacteria, *Phys. Chem. Chem. Phys.* 25, 18698–18710.
- [4] May V., Kühn O. (2011) Charge and energy transfer dynamics in molecular systems: a theoretical introduction. Wiley-VCH, Berlin.
- [5] Madjet M.E., Abdurahman A., Renger T. (2006) Intermolecular coulomb couplings from ab initio electrostatic potentials: application to optical transitions of strongly coupled pigments in photosynthetic antennae and reaction centers, J. Phys. Chem. B 110, 17268–17281.
- Bakalis L., Knoester J. (1997) Optical properties of one-dimensional exciton systems: beyond the Heitler-London approximation, J. Chem. Phys. 106, 6964-6976.
- [7] Renger T., Müh F. (2013) Understanding photosynthetic light-harvesting: a bottom up theoretical approach, Phys. Chem. Chem. Phys. 15, 3348–3371.
- [8] Atkins P.W., Friedman R.S. (2005) Molecular quantum mechanics. Oxford University Press.
- [9] Slama V., Müh F., Renger T., Mancal T. (2023) Role of environmental dynamic polarizability in static excited state properties of embedded molecular systems: Application to disordered fluorographene systems, J. Phys. Chem. C 127, 381–392.
- [10] Eder M., Renger T. (2024) A simple expression for the screening of excitonic couplings between chlorophylls as inferred for photosystem I trimers, Int. J. Mol. Sci. 25, 9006.
- [11] Adolphs J., Müh F., Madjet M.E., Renger T. (2008) Calculation of pigment transition energies in the FMO protein: from simplicity to complexity and back, *Photosynth. Res.* 95, 197–209.
- [12] Adolphs J., Renger T. (2006) How proteins trigger excitation energy transfer in the FMO complex of green sulfur bacteria, Biophys. J. 91, 2778–2797.
- [13] Renger T., Klinger A., Steinecker F., Schmidt am Busch M., Numata J., Müh F. (2012) Normal mode analysis of the spectral density of the Fenna-Matthews-Olson light-harvesting protein: how the protein dissipates the excess energy of excitons, J. Phys. Chem. B 116, 14565–14580.

- [14] Knox R.S., Spring B.Q. (2003) Dipole strengths in the chlorophylls, Photochem. Photobiol. 77 (5), 497–501.
- [15] Scholes G.D., Curutchet C., Mennucci B., Cammi R., Tomasi J. (2007) How solvent controls electronic energy transfer and light harvesting, J. Phys. Chem. Lett. 111, 6978–6982.
- [16] Curutchet C., Scholes G.D., Mennucci B., Cammi R. (2007) How solvent controls electronic energy transfer and light harvesting: toward a quantum-mechanical description of reaction field and screening effects, J. Phys. Chem. B 111, 13253-13265.
- [17] Renger T., Müh F. (2012) Theory of excitonic couplings in dielectric media, Photosynth. Res. 111, 47–52.
- [18] Müh F., Madjet M.E., Adolphs J., Abdurahman A., Rabenstein B., Ishikita H., Knapp E.W., Renger T. (2007) α-helices direct excitation energy flow in the Fenna-Matthews-Olson protein, Proc. Natl. Acad. Sci. USA 104, 16862–16867.
- [19] Schmidt am Busch M., Müh F., Madjet M.E., Renger T. (2011) The eighth bacteriochlorophyll completes the excitation energy funnel in the FMO protein, J. Phys. Chem. Lett. 2, 93–98.
- [20] Louwe R.J.W., Vrieze J., Hoff A.J., Aartsma T.J. (1997) Toward an integral interpretation of the optical steady-state spectra of the FMO-complex of *Prosthecochloris aestuarii*. 2. Exciton simulations, *J. Phys. Chem. B* 101, 11280–11287.
- [21] Vulto S.I.E., de Baat M.A., Louwe R.J.W., Permentier H.P., Neef T., Miller M., van Amerongen H., Aartsma T.J. (1998) Exciton simulations of optical spectra of the FMO complex from the green sulfur bacterium *Chlorobium tepidum* at 6 K, *J. Phys. Chem. B* 102 (47), 9577–9582.
- [22] Wendling M., Przyjalgowski M.A., Gülen D., Vulto S.I.E., Aartsma T.J., van Grondelle R., van Amerongen H. (2002) The quantitative relationship between structure and polarized spectroscopy in the FMO complex of *Prosthecochloris aestuarii*: refining experiments and simulations, *Photosynth. Res.* 71, 99–123.
- [23] Melkonzernov A.N., Olson J.M., Li Y.-F., Allen J.P., Blankenship R.E. (1998) Orientation and excitonic interactions of the Fenna-Matthews-Olson bacteriochlorophyll a protein in membranes of the green sulfur bacterium Chlorobium tepidum, Photosynth. Res. 56, 315–328.
- [24] Wen J., Zhang H., Gross M.L., Blankenship R.E. (2011) Native electrospray mass spectrometry reveals the nature and stoichiometry of pigments in the FMO photosynthetic antenna protein, *Biochemistry* 50, 3502–3511.
- [25] Saer R.G., Stadnytskyi V., Magdaong N.C., Goodson C., Savikhin S., Blankenship R.E. (2017) Probing the excitonic landscape of the *Chlorobaculum tepidum* Fenna-Matthews-Olson (FMO) complex: a mutagenesis approach, *Biochim. Biophys. Acta* 1858, 288–296.
- [26] Klinger A., Lindorfer D., Müh F., Renger T. (2020) Normal mode analysis of spectral density of FMO trimers: intra- and intermonomer energy transfer, J. Chem. Phys. 153(21), 215103.
- [27] Rätsep M., Freiberg A. (2007) Electron-phonon and vibronic couplings in the FMO bacteriochlorophyll a antenna complex studied by difference fluorescence line narrowing, J. Lumin. 127, 251–259.
- [28] Wendling M., Pullerits T., Przyjalgowski M.A., Vulto S.I.E., Aartsma T.J., van Grondelle R., van Amerongen H. (2000) Electron-vibrational coupling in the Fenna-Matthews-Olson complex of *Prosthecochloris aestuarii* determined by temperature-dependent absorption and fluorescence line-narrowing measurements, J. Phys. Chem. B 104, 5825–5831.
- [29] Ishizaki A., Tanimura Y. (2005) Quantum dynamics of system strongly coupled to low-temperature colored noise bath: reduced hierarchy equations approach, J. Phys. Soc. Jap. 74, 3131–3134.
- [30] Kreisbeck C., Kramer T., Aspuru-Guzik A. (2014) Scalable high-performance algorithm for the simulation of exciton dynamics. Application to the light-harvesting complex II in the presence of resonant vibrational modes, J. Chem. Theory Comput. 10, 4045–4054.
- [31] Tanimura Y. (2020) Numerically "exact" approach to open quantum dynamics: the hierarchical equations of motion (HEOM), J. Chem. Phys. 153, 020901.
- [32] Chin A.W., Rivas A., Huelga S.F., Plenio M.B. (2010) Exact mapping between system-reservoir quantum models and semi-infinite discrete chains using orthogonal polynomials, J. Math. Phys. 51, 092109.

- [33] Prior J., Chin A.W., Huelga S.F., Plenio M.B. (2010) Efficient simulation of strong system-environment interactions, Phys. Rev. Lett. 105, 050404.
- [34] Huo P., Coker D.F. (2010) Iterative linearized density matrix propagation for modeling coherent excitation energy transfer in photosynthetic light harvesting, J. Chem. Phys. 133, 184108
- [35] Nalbach P., Braun D., Thorwart M. (2011) Exciton transfer dynamics and quantumness of energy transfer in the Fenna-Matthews-Olson complex, Phys. Rev. E 84, 041926.
- [36] Moix J.M., Zhao Y., Cao J. (2012) Equilibrium-reduced density matrix formulation: influence of noise, disorder, and temperature on localization in excitonic systems, *Phys. Rev. B* 85, 115412.
- [37] Kundu S., Dani R., Makri N. (2022) Tight inner ring architecture and quantum motion of nuclei enable efficient energy transfer in bacterial light harvesting, Science Adv. 8, eadd0023.
- [38] Beck M.H., Jäckle A., Worth G.A., Meyer H.-D. (2000) The multiconfiguration time-dependent Hartree (MCTDH) method: a highly efficient algorithm for propagating wavepackets, Phys. Rep. 324, 1–105.
- [39] Zhao Y. (2023) The hierarchy of Davydov's Ansätze: from guesswork to numerically "exact" many-body wave functions, J. Chem. Phys. 158, 080901.
- [40] Renger T., Marcus R.A. (2002) On the relation of protein dynamics and exciton relaxation in pigment-protein complexes: an estimation of the spectral density and a theory for the calculation of optical spectra, J. Chem. Phys. 116, 9997–10019.
- [41] Schröder M., Kleinekathöfer U., Schreiber M. (2006) Calculation of absorption spectra for light-harvesting systems using non-Markovian approaches as well as modified Redfield theory, J. Chem. Phys. 124, 084903.
- [42] Dinh T.-C., Renger T. (2016) Lineshape theory of pigment-protein complexes: how the finite relaxation time of nuclei influences the exciton relaxation-induced lifetime broadening, J. Chem. Phys. 145, 034105.
- [43] Seibt J., Mancal T. (2017) Ultrafast energy transfer with competing channels: non-equilibrium Förster and modified Redfield theories, J. Chem. Phys. 146, 174109.
- [44] Reppert M. (2020) Delocalization effects in chlorophyll fluorescence: nonperturbative line shape analysis of a vibronically coupled dimer, J. Phys. Chem. B 124, 10024–10033.
- [45] Caycedo-Soler F., Mattioni A., Lim J., Renger T., Huelga S.F., Plenio M.B. (2022) Exact simulation of pigment-protein complexes unveils vibronic renormalization of electronic parameters in ultrafast spectroscopy, *Nature Comm.* 13, 2912.
- [46] Renger T., Madjet M.E., Knorr A., Müh F. (2011) How the molecular structure determines the flow of excitation energy in plant light-harvesting complex II, J. Plant Physiol. 168, 1497–1509.
- [47] Müh F., Renger T. (2012) Refined structure-based simulation of plant light-harvesting complex II: linear optical spectra of trimers and aggregates, *Biochim. Biophys. Acta* 1817, 1446–1460.
- [48] Raszewski G., Renger T. (2008) Light harvesting in photosystem II core complexes is limited by the transfer to the trap: can the core complex turn into a photoprotective mode? J. Am. Chem. Soc. 130, 4431–4446.
- [49] Amarnath K., Bennett D.I.G., Schneider A., Fleming G. (2016) Multiscale model of light harvesting by photosystem II in plants, Proc. Natl. Acad. Sci. USA 113, 1156–1161.
- [50] Thyrhaug E., Zidek K., Dostal J., Bina D., Zigmantas D. (2016) Exciton structure and energy transfer in the Fenna-Matthews-Olson complex, J. Phys. Chem. Lett. 7, 1653–1660.
- [51] Matsuzaki S., Zazubovich V., Rätsep M., Hayes J.M., Small G.J. (2000) Energy transfer kinetics and low energy vibrational structure of the three lowest energy Q_y-states of the Fenna-Matthews-Olson antenna complex, J. Phys. Chem. B 104, 9564–9572.
- [52] Cao J., Cogdell R.J., Coker D.F., Duan H.-G., Hauer J., Kleinekathöfer U., Jansen T.L.C., Mancal T., Miller R.J.D., Ogilvie J.P., Prokhorenko V.I., Renger T., Tan H.-S., Tempelaar R., Thorwart M., Thyrhaug E., Westenhoff S., Zigmantas D. (2020) Quantum biology revisited, Sci. Adv. 6, eaaz4888.
- [53] Renger T. (2021) Semiclassical modified Redfield and generalized Förster theories of exciton relaxation/transfer in light-harvesting complexes: the quest for the principle of detailed balance, J. Phys. Chem. B 125, 6406–6416.

- [54] He G., Niedzwiedzki D.M., Orf G.S., Zhang H., Blankenship R.E. (2015) Dynamics of energy and electron transfer in the FMO-reaction center core complex from the phototrophic green sulfur bacterium *Chlorobaculum tepidum*, J. Phys. Chem. B 1190(26), 8321–8329.
- [55] Permentier H.P., Schmidt K.A., Kobayashi M., Akiyama M., Hager-Braun C., Neerken S., Miller M., Amesz J. (2000) Composition and optical properties of reaction centre core complexes from the green sulfur bacteria Prosthecochloris aestuarii and Chlorobium tepidum, Photosynth. Res. 640(1), 27–39.
- [56] Neerken S., Schmidt K.A., Aartsma T.J., Amesz J. (1999) Dynamics of energy conversion in reaction center core complexes of the green sulfur bacterium *Prosthecochloris aestuarii* at low temperature, *Biochemistry* 38(40), 13216–13222.
- [57] Wen J., Zhang H., Gross M.L., Blankenship R.E. (2009) Membrane orientation of the FMO antenna protein from *Chlorobaculum tepidum* as determined by mass spectrometry-based footprinting, *Proc. Natl. Acad. Sci. USA* 106, 6134–6139.
- [58] Ishikita H., Saenger W., Biesiadka J., Loll B., Knapp E.-W. (2006) How photosynthetic reaction centers control oxidation power in chlorophyll pairs P680, P700, and P870, Proc. Natl. Acad. Sci. U.S.A. 103, 9855–9860.
- [59] Renger T. (2018) Photoinduced electron transfer in the reaction centers, Light harvesting in photosynthesis (R. Croce, R. van Grondelle, H. van Amerongen, I. van Stokkum, Eds). CRC Press, pp. 399–435.
- [60] Kriegl J.M., Nienhaus G.U. (2004) Structural, dynamic, and energetic aspects of long-range electron transfer in photosynthetic reaction centers, Proc. Natl. Acad. Sci. U.S.A. 101, 123– 128.
- [61] Wang H., Lin S., Allen J.P., Williams J.C., Blankert S., Laser C., Woodbury N.W. (2007) Protein dynamics control the kinetics of initial electron transfer in photosynthesis, *Science* 316, 747–750.
- [62] Wohri A.B., Katona G., Johansson L.C., Fritz E., Malmerberg E., Andersson M., Vincent J., Eklund M., Cammarata M., Wulff M., Davidsson J., Groenhof G., Neutze R. (2010) Light-induced structural changes in a photosynthetic reaction center caught by Laue diffraction, Science 328, 630–633.

Chapter 6

Organic Photovoltaics – Excitons at Work

Irene Burghardt*

Institute for Physical and Theoretical Chemistry, Goethe University Frankfurt, Max-von-Laue-Straße 7, 60438 Frankfurt am Main, Germany *e-mail: burghardt@chemie.uni-frankfurt.de

6.1 Introduction

Molecular materials for organic photovoltaics (OPV) applications [1, 2] offer vast flexibility in designing optimal components for the elementary excitations (*i.e.*, excitons) and the transport of emerging charge carriers (*i.e.*, electrons and holes). OPV device materials are thin, lightweight, flexible, and semi-transparent, combining various advantages over established photovoltaic materials. Since the advent of organic photovoltaics, efficiencies have risen significantly, and power conversion efficiencies (PCE) well above 10% are now feasible [3]. The PCE represents the ratio between the input optical power and the resulting electrical power – for comparison, silicon-based devices exhibit PCE values around 25%. In general, the PCE threshold is defined by a detailed balance limit, *i.e.*, the Shockley–Queisser limit [4, 5].

In the first OPV generation between 2000 and 2005, fullerene-based materials were at the forefront, exemplified by donor-acceptor (DA) combinations involving poly(3-hexyl-thiophene) (P3HT) as donor material and fullerene-based acceptors, e.g., [6,6]-phenyl-C₆₁ butyric acid methyl ester (PCBM). The P3HT:PCBM blend made PCEs around 6% feasible, benefitting from the so-called bulk heterojunction (BHJ) technology [5, 6], which led to a breakthrough in producing materials where donor and acceptor domains were optimally mixed. At a later stage, starting around 2010, donor materials were improved, achieving PCEs of around 10%. Finally, since around 2018, new non-fullerene acceptor (NFA) materials have taken the stage [6, 7]. In particular, the PM6:Y6 combination [8, 9] shown in figure 6.1a has reached PCEs above 15%, promising that the 20% threshold will soon be reached [3]. From today's vantage point, NFA materials have doubtlessly led to a renaissance of

DOI: 10.1051/978-2-7598-3760-1.c006 © The authors, 2025

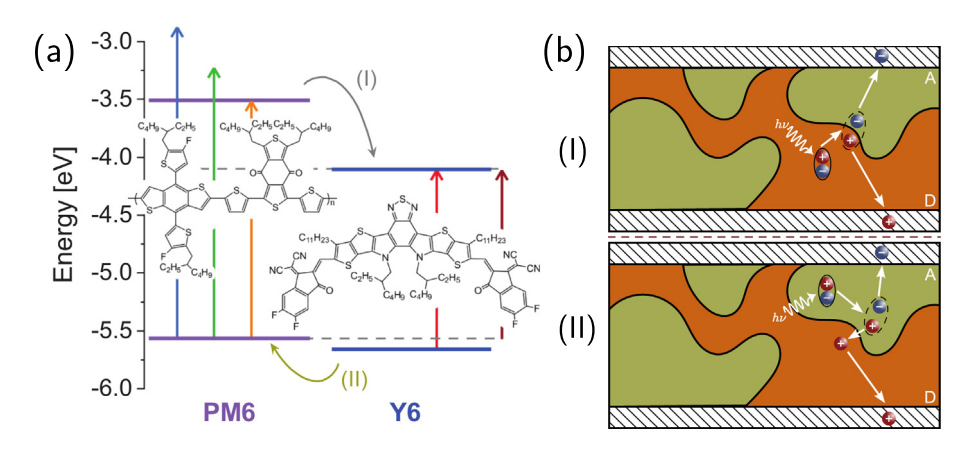


Fig. 6.1 – (a) Chemical structure of the non-fullerene acceptor Y6 and the donor species PM6 (representation from Ref. [9]) along with energy levels measured by cyclic voltammetry [8]. Curved arrows indicate two channels for carrier generation, via electron transfer (channel I) or hole transfer (channel II). (b) Schematic illustration of charge separation at a donor-acceptor interface: The first pathway (I), generally considered the dominant mechanism in OPV materials, involves exciton migration to the DA interface followed by electron transfer to the acceptor domain, while the second pathway (II) involves generation of an exciton in the acceptor domain, followed by break-up of the exciton in the acceptor domain (i.e., creation of a charge transfer exciton), and finally hole transfer to the donor domain. In the Y6:PM6 material, pathway (I) involves a significant driving force, while pathway (II) proceeds in a barrierless way.

the field. In parallel, different types of materials and alternative strategies were exploited, especially perovskite-based PV cells [10], dye-sensitized PV [11], as well as singlet fission [12] as a mechanism of carrier multiplication, and single-component photovoltaics [13], to name but a few active research avenues.

Despite the progress made during the past 20 years, the optimization of OPV materials and the identification of structure-function relations remain challenging, given the complexity of the elementary conversion steps. While energy gap criteria were mainly advocated in the past, more detailed analysis has highlighted the role of exciton transport towards the DA interface, along with the nanoscale morphology, nonradiative energy losses, as well as the ubiquitous presence of vibronic (electron-phonon) coupling effects. In fact, vibronic coupling can be both beneficial and detrimental, to the point that the suppression of vibronic coupling has been proposed as an optimization strategy [14].

In this chapter, we give an overview of the elementary steps relevant to organic photovoltaics and discuss their theoretical and computational treatment. A focus is placed on the construction of suitable lattice Hamiltonians and on the role of ultrafast conversion events requiring a quantum dynamical treatment [15]. While the examples that are discussed mainly relate to fullerene-based materials, the basic strategies can be transposed to new NFA materials.

Another aspect that is touched upon in this chapter relates to the similarities and differences as compared with biological light-harvesting systems (see chapter 5). The latter also involve a combination of exciton transport and exciton dissociation, achieved with extremely high efficiencies. Indeed, suggestions for the design of bio-organic semiconductors have been put forward [16, 17].

The remaining sections are organized as follows: section 6.2 sketches out the elementary steps in OPVs, section 6.3 summarizes the computational strategy that we employed in our recent work, combining vibronic lattice Hamiltonians and quantum dynamics, and section 6.4 presents two case studies illustrating the role of quantum coherence in exciton dissociation and exciton transport. Section 6.5 gives a brief perspective on two-dimensional electronic spectroscopy, and section 6.6 concludes with a discussion.

6.2 Key Elementary Steps

The fundamental mechanism of charge generation in OPV devices differs significantly from inorganic semiconductors. In contrast to the latter, the elementary excitations (excitons) in OPV materials are essentially of Frenkel type [18], i.e., tightly bound electron-hole (e-h) pairs resulting from local molecular excitations. In contrast, inorganic semiconductors exhibit Wannier–Mott type [19] excitons with an extended e-h radius; these excitons are weakly bound since the electron-hole attraction is screened by a large dielectric constant.

For this reason, charge separation -i.e., e-h pair dissociation - is a stepwise process in OPV materials. As sketched out in the upper panel of figure 6.1b, excitons migrate to the donor-acceptor interface, where initial charge separation generates bound interfacial CT states, i.e., e-h pairs that experience strong Coulombic attraction as a consequence of the low dielectric screening of organic materials. Subsequently, the interfacial CT state breaks up and generates free carriers, i.e., electrons (e) and holes (h), that are collected at the electrodes.

As illustrated in figure 6.1, the PM6:Y6 material [6, 8, 9] is thought to also exhibit an alternative pathway, shown in the lower panel of figure 6.1b. This pathway exhibits the initial excitation of e-h pairs in the acceptor domain, followed by a break-up of the exciton in the acceptor domain, preceding hole transfer to the donor material. This second pathway proceeds in a barrierless fashion in PM6:Y6, and is, hence, thought to be favored in this highly efficient material. Indeed, most efficient NFA materials are characterized by small interfacial energy offsets and yet lead to highly efficient charge separation – contrary to expectations based on the first-generation materials.

Turning to a microscopic perspective, figure 6.2 illustrates that the creation of long-range charge-separated (CS) states from the initial CT state results from overcoming an effective Coulomb barrier to charge separation (see panel a). This barrier typically varies between 0.2 eV and 0.5 eV, exceeding the thermal energy by a factor of 10 or more (noting that $k_BT = 0.026$ eV at room temperature), and depends on the local microelectrostatics as well as charge delocalization effects.

As can be inferred from figure 6.2b, the interfacial CT state tends to be predominantly populated and long-lived, but CS states potentially appear on ultrafast time scales, too. In the case illustrated in figure 6.2b, two key factors are at play [20]: First, the effective Coulomb barrier is lowered by charge delocalization, and second, the initial charge separation generates a significant amount of vibronic excess energy. The conditions under which CS states can arise on (ultra-)short time scales have been extensively addressed in the literature. However, other factors can affect the charge separation efficiency, notably the nonradiative decay to the ground state, both from the initial exciton and from the interfacial CT state.

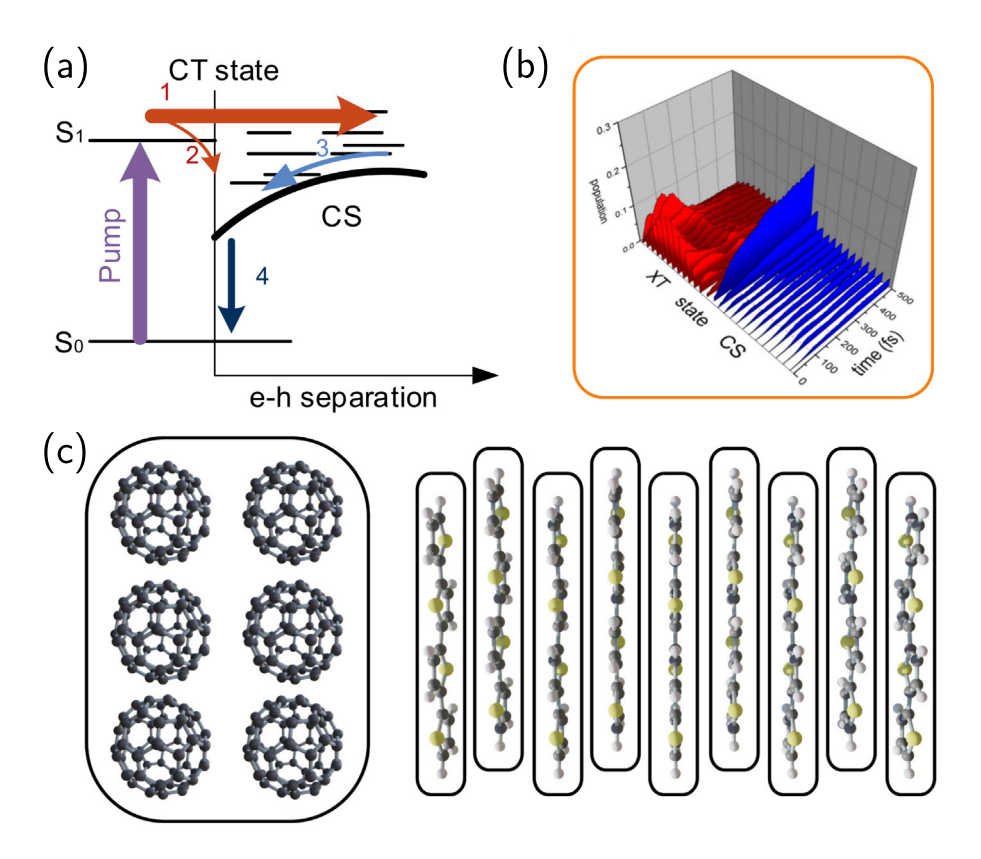


Fig. 6.2 – (a) Illustration of the formation of charge-separated states: Initial excitation (1) can lead to direct transfer to the interfacial CT state (2), but vibronic excess energy could also entail the excitation of long-range charge-separated (CS) states that partially decay to the interfacial CT state (3, 4). (b) Simulation results from Ref. [20], to be discussed in detail in section 6.4.1, showing time-evolving populations of excitonic (XT) and charge-separated (CS) states. At the center, the $CS_1 \equiv CT$ state is shown, which accumulates population with time, while the remaining CS states are weakly populated. (c) Lattice model of a regioregular P3HT:PCBM type interface underlying the calculations shown in (b). Each oligothiophene (OT) unit corresponds to a lattice site, while the fullerene domain is subsumed into an effective acceptor particle [20, 21].

Finally, we note that in photosynthetic light-harvesting complexes (see chapter 5), the electron and hole are generally even closer than in OPV materials. Charge separation in the reaction center is achieved by step-wise electron transfer along a chain of well-defined cofactors with decreasing free energy of the transferred electron. In this way, recombination reactions are suppressed, and within less than a nanosecond, the electron and the hole are separated by the thickness of the photosynthetic membrane (30 Å) with nearly 100% quantum efficiency [22].

In section 6.4.1, we will return in some detail to the model of a regioregular P3HT:PCBM junction as depicted in figure 6.2. Furthermore, section 6.4.2 will show simulations of the exciton migration process that leads to the initial encounter with the DA interface.

6.3 Theoretical Approaches

The atomistic modeling of OPV materials is challenging, both on the electronic structure and dynamics side. Multiple excited electronic states are involved, typically belonging to excitonic and charge-separated manifolds whose spatial delocalization is highly sensitive to electronic couplings and vibronic effects. While kinetic descriptions, notably relying on the kinetic Monte-Carlo (KMC) approach, are viable on longer time scales, simulations of the elementary steps in OPV materials require a time-dependent quantum description of both electrons and nuclei.

To date, theoretical and computational approaches that capture quantum dynamical effects on (ultra-)short time scales essentially fall into two classes. The first class of methods consists of lattice Hamiltonians adapted to homogeneous or heterogeneous molecular aggregates, combined with quantum master equations, e.g., the Hierarchical Equations of Motion (HEOM) [23, 24], or alternatively wavefunction-based propagation schemes, e.g., using the Multi-Configuration Time-Dependent Hartree (MCTDH) method [15, 25, 26] or else path-integral based approaches. The second class of methods consists of ab initio molecular dynamics (AIMD) [27] and non-adiabatic excited-state molecular dynamics (NA-ESMD) [28, 29] simulations. Here, standard quantum-classical dynamical techniques like mean-field Ehrenfest dynamics and surface hopping are often employed; these, however, suffer from various drawbacks that may hamper the interpretation of the elementary transfer mechanisms within the coupled manifolds of excitonic states [30, 31]. As an alternative, more sophisticated quantum-classical techniques [32, 33] or else combinations of atomistic and kinetic descriptions have been proposed, e.g., the multichromophoric FRET (MC-FRET) approach [34] and the delocalized kinetic Monte Carlo (dKMC) scheme [35]. Whether or not the more approximate propagation schemes are valid strongly depends on the molecular material under study.

In this chapter, we report on advances in the full quantum treatment of the elementary events in typical DA materials, relying on first-principles parametrized vibronic lattice Hamiltonians and multiconfigurational quantum dynamics treatments of MCTDH type. In the present section, an outline is given of the construction of the relevant lattice Hamiltonians (section 6.3.1) and strategies for reducing the system dimensionality (section 6.3.2), along with a brief perspective on the quantum dynamical approach (section 6.3.3).

6.3.1 First-Principles Parametrized Lattice Hamiltonians

Given that the lattice Hamiltonians mentioned above should accommodate both Frenkel-type excitations and charge-separated states, we employ a general electron-hole (e-h) quasi-particle picture, including charge separation effects [36–38]. While our discussion is restricted to the single-excitation picture, the approach can be generalized to multi-exciton states and singlet fission [39–41]. Importantly, the parametrization of these Hamiltonians can be fully or partially based on electronic structure calculations.

6.3.1.1 Electron-Hole Lattice Models

Following Refs. [36–38], delocalized molecular excitations in molecular aggregates can be described as superpositions of e-h quasi-particle states $|v_e\mu_h\rangle \equiv |v\mu\rangle$ representing an electron located at the site $v_e \equiv v$ and a hole located at the site $\mu_h \equiv \mu$. Localized e-h states correspond to Frenkel excitonic (XT) configurations, $|XT_n\rangle = |v = n, \mu = n\rangle$ (with n = 1, ..., N for an N-site lattice), while charge transfer exciton (CTX) configurations of type $|CTX_{n,n'}\rangle = |v = n, \mu = n'\rangle$ correspond to spatially separated e-h pairs, $n \neq n'$. In DA systems where a net charge transfer occurs between donor and acceptor species, one often refers to the interfacial charge transfer state as the CT state. Charge-separated (CS) states then denote states with increasing e-h separation (see figure 6.2a).

A general aggregate Hamiltonian in the *e-h* the basis takes the following form [38], including vibronic coupling terms, *i.e.*, diagonal and/or off-diagonal elements that carry a dependence on the vibrational coordinates,

$$\widehat{H}(\widehat{\mathbf{x}}) = \sum_{\nu\mu} \sum_{\nu'\mu'} \widehat{H}_{\nu\mu,\nu'\mu'}(\widehat{\mathbf{x}}) |\nu\mu\rangle\langle\nu'\mu'| \tag{1}$$

where $\hat{\mathbf{x}} = \{\hat{x}_i\}$ denotes a set of vibrational coordinates (also referred to as phonon modes in the following). The Hamiltonian elements $\hat{H}_{\nu\mu,\nu'\mu'}$ can be written as a sum over an electronic part (\hat{H}^{el}) , a vibrational or phonon part (\hat{H}^{ph}) , and a vibronic coupling, or electron-phonon part $(\hat{H}^{\text{e-ph}})$,

$$\widehat{H}_{\nu\mu,\nu'\mu'}(\widehat{\mathbf{x}}) = \widehat{H}^{\mathrm{el}}_{\nu\mu,\nu'\mu'} + \widehat{H}^{\mathrm{e-ph}}_{\nu\mu,\nu'\mu'}(\widehat{\mathbf{x}}) + \widehat{H}^{\mathrm{ph}}(\widehat{\mathbf{x}})$$
(2)

Further, the electronic Hamiltonian is composed of an electronically diagonal on-site part $(\widehat{H}^{\text{on-site}})$ and an off-diagonal coupling part $(\widehat{H}^{\text{coup}})$,

$$\widehat{H}_{\nu\mu,\nu'\mu'}^{\text{el}} = \delta_{\nu\nu'}\delta_{\mu\mu'}\,\widehat{H}_{\nu\mu,\nu'\mu'}^{\text{on-site}} + (1 - \delta_{\nu\nu'}\delta_{\mu\mu'})\,\widehat{H}_{\nu\mu,\nu'\mu'}^{\text{coup}}$$
(3)

The electronic coupling part typically comprises both energy and charge transfer contributions, *i.e.*, Frenkel-type excitonic couplings, as well as transfer integrals that couple charge-separated configurations to Frenkel configurations and among each other.

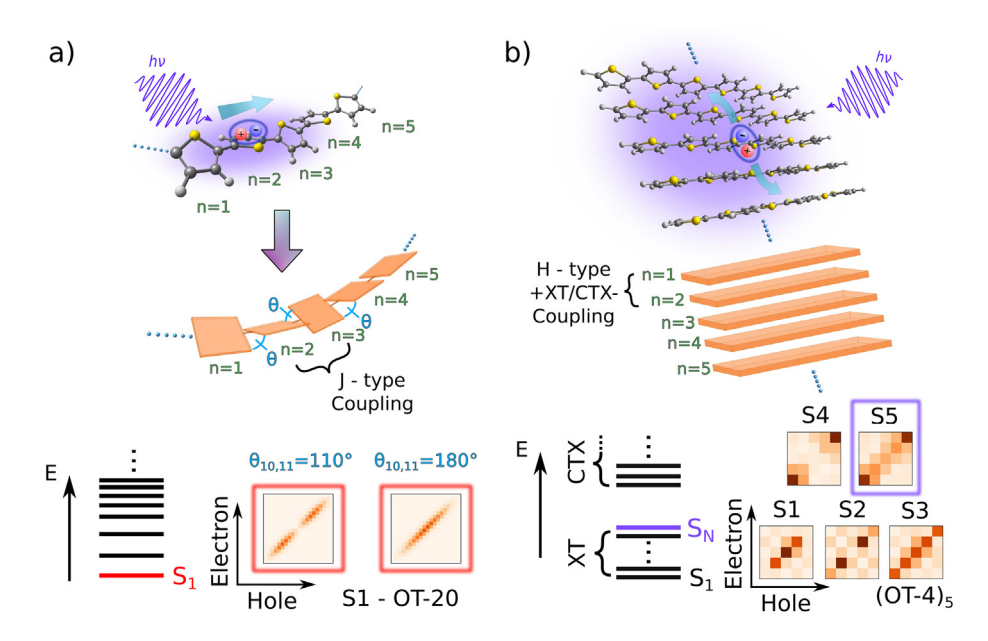


Fig. 6.3 – Translation between supermolecular electronic structure results and the fragment-based Hamiltonian of equations (1)–(3). (a) Oligothiophene chain which is mapped onto a monomer representation of aromatic rings, conforming to a J-aggregate model. The bright oligomer state (S_1) is the lowest state of the excitonic manifold. As can be inferred from the e-h map (bottom), the S_1 electronic density is a sensitive function of the torsional coordinates (here, the $\theta_{10,11}$ torsion at the center of an OT-20 oligomer). The near-diagonal character of the e-h map reflects that a Frenkel model holds to a good approximation. (b) Stacked (OT-n)₅ assembly, which is mapped onto an e-h model containing significant admixtures of CTX states. Similarly to an H-aggregate, the bright state (S_5) is found at the top of the modified XT manifold, but the electronic density is concentrated at the edges of the lattice, see the e-h map (bottom). Adapted with permission from Ref. [15]. Copyright 2021 Annual Reviews.

6.3.1.2 Construction of Lattice Hamiltonians from Electronic Structure Data

The Hamiltonian of equations (1)–(3) encodes a fragment-based representation that is highly suitable to describe both local excitations and charge separation effects in molecular aggregates. However, the connection to direct treatment of these aggregate systems using electronic structure methods is not necessarily straightforward. The latter usually rely on an *adiabatic*, *supermolecular* representation, while the Hamiltonian of equations (1)–(3) employs a *diabatic*, *site-based* picture. The term diabatic refers to an electronic basis with well-defined properties, *e.g.*, in terms of the site-based *e-h* distribution.

To translate electronic structure information to the Hamiltonian of equations (1)–(3), suitable *diabatization* procedures [21, 42–45] are required. Various such diabatization schemes are applicable, including fit procedures as typically employed

for linear and higher-order vibronic coupling Hamiltonians [42], determination of selected coupling elements [43], wavefunction-based diabatization schemes [46, 47], or analogous TDDFT-based approaches [21, 44, 45]. In future developments, we expect that machine learning approaches, e.g., based on neural network fitting, will be used extensively, possibly in combination with the lattice models addressed here.

Figure 6.3 illustrates the translation between a supermolecular perspective and the diabatic e-h lattice representation, for excitation energy transfer (EET) in an oligothiophene chain (panel a) and, analogously, inter-chain EET in a regioregular oligothiophene assembly (panel b). In the latter case, charge transfer excitons (CTX) coexist with Frenkel excitons. From the vantage point of the Frenkel exciton picture, the oligomer chains can be interpreted as J-aggregates [48], exhibiting a head-to-tail alignment of the monomer transition dipoles, while the stacked species correspond to H-aggregates with face-to-face orientation (or, from an alternative viewpoint, HJ-aggregates [48–50] composed of individual repeat units as building blocks). In the case shown in panel (b), the H-aggregate picture is significantly modified, though, since CTX states arise upon photoexcitation [49, 51].

6.3.2 Vibronic Coupling Effects

The manifestations of vibronic coupling effects are ubiquitous in molecular assemblies and organic functional materials. Vibronic coupling leads to deexcitation by internal conversion and stabilization of local excitations (excitons) by self-trapping [52, 53], but also enhances transport by fluctuations [54, 55] and vibronic resonance effects [56]. Many of these effects necessitate a molecular-level description in terms of wavepacket dynamics on multiple potential energy surfaces (PESs), rather than a conventional rate theory approach.

Hence, the construction of approximate PESs for molecular aggregates is of paramount importance. Here, we address two representative PES construction schemes that are subsequently employed in the examples presented in the case studies of section 6.4. The first scheme relates to a multi-state linear vibronic coupling (LVC) model [42, 57], which employs first-principles computed vibronic couplings and the related spectral densities (SDs) [58]. The second scheme is tailored to a more detailed description of anharmonic potentials and is based upon PES cuts from electronic structure calculations [59, 60]. These two schemes are illustrated in figure 6.4 and will be discussed in some detail in the following.

6.3.2.1 Linear Vibronic Coupling Models for Multi-Chromophoric Systems

Within the LVC approximation, a shifted harmonic oscillator (HO) model is used to approximate the molecular PESs, usually adopting a basis of ground-state normal modes (NMs). Despite its simplicity, the LVC model accounts for the most important types of excited-state topologies and encompasses both avoided crossings and conical intersections [42, 61]. Furthermore, the LVC Hamiltonian coincides with various model Hamiltonians from solid-state physics, notably the Frenkel-Holstein (FH) Hamiltonian and its generalization in terms of vibronic lattice Hamiltonians in an e-h basis.

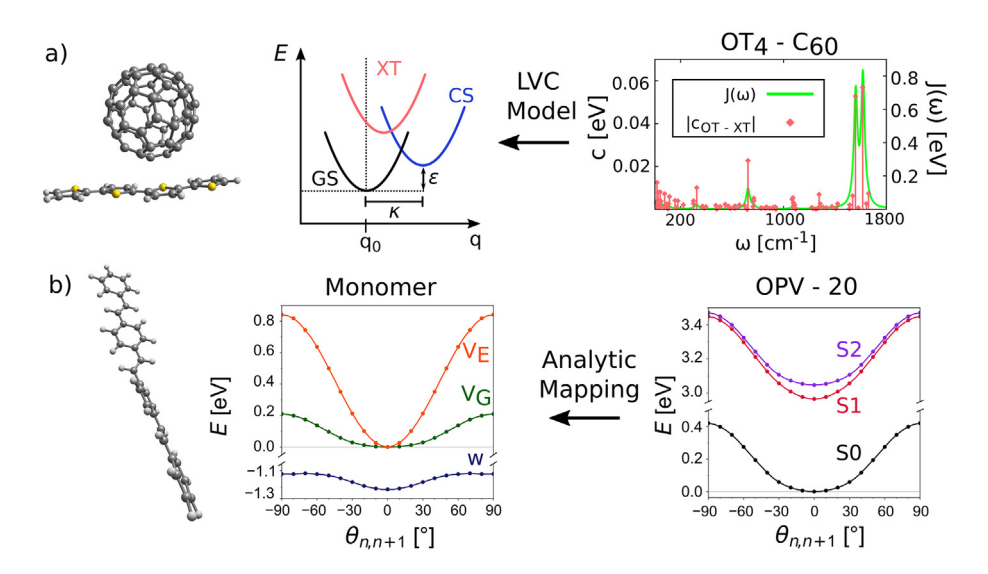


FIG. 6.4 – Approximate molecular potentials that appear in the vibronic lattice Hamiltonians of section 6.3.2: (a) LVC model, which translates state-specific vibronic couplings $\{c_n\}$ (r.h.s.) to a shifted HO model (center), here shown for an OT:fullerene aggregate. (b) Analytic mapping procedure which translates oligomer PESs (r.h.s.) to monomer potentials $\{v_G, v_E\}$ and the excitonic coupling $\{w\}$ (center), according to a generalized Frenkel-Holstein model. Adapted with permission from Ref. [15]. Copyright 2021 Annual Reviews.

We now outline the construction of a fragment-based LVC model for multi-chromophoric systems [57], as sketched in figure 6.4a. Each fragment, denoted monomer M_n in the following, is associated with a subset of normal modes \boldsymbol{q}_{M_n} , referred to as local normal modes (local NMs). Intermolecular modes can be included separately, such that the main aim is to accurately account for the local NM space. The full normal mode space is therefore spanned by a combination of N sets of local NMs, $\hat{\mathbf{q}}^T = (\hat{\mathbf{q}}_{M_1}^T, \hat{\mathbf{q}}_{M_2}^T, \dots, \hat{\mathbf{q}}_{M_{N-1}}^T, \hat{\mathbf{q}}_{M_N}^T)$. With this convention, the zeroth-order vibrational Hamiltonian is given as follows, using mass and frequency weighted coordinates,

$$\widehat{H}^{\text{ph}} = \frac{1}{2} \left(\widehat{\mathbf{p}}^T \boldsymbol{\omega} \widehat{\mathbf{p}} + \widehat{\mathbf{q}}^T \boldsymbol{\omega} \widehat{\mathbf{q}} \right) \tag{4}$$

where $\boldsymbol{\omega}$ is a diagonal frequency matrix in the local NM representation, $(\boldsymbol{\omega})_{ij} = \delta_{ij}\omega_i$. Vibronic interactions are defined within a shifted HO approximation for N_s electronic states $|\mathbf{X}_s\rangle$ and $N_{\rm ph}$ phonon modes,

$$\widehat{H}^{\text{e-ph}} = \sum_{s=1}^{N_s} \sum_{j=1}^{N_{\text{ph}}} c_{s,j} \widehat{q}_j |X_s\rangle \langle X_s| = \sum_{s=1}^{N_s} \boldsymbol{c}_s^T \widehat{\mathbf{q}} |X_s\rangle \langle X_s|$$
 (5)

The state-specific vibronic couplings $\{c_{s,j}\}$, $j = 1, ..., N_{ph}$, are computed from Franck-Condon gradients for every state of interest (or, alternatively, by

excited-state geometry optimization, from which the displacement of the respective minima can be obtained). Even though all normal modes are taken to be local – *i.e.*, localized on a given molecular fragment – the vibronic couplings may be non-local: *e.g.*, in the case of CTX states, modes $\widehat{\mathbf{q}}_{M_n}$ belonging to the *n*th fragment also couple to the (n+1)st and (n-1)st fragment, due to the delocalized nature of the CTX states.

Assuming that the frequency distribution of the vibrational modes is dense, it is natural to characterize the influence of the vibrations on the electronic subsystem in terms of a spectral density (SD), or its discretized representation. Due to the non-local part of the electron-phonon coupling, *correlated* fluctuations appear, which are included in a $N_s \times N_s$ dimensional SD matrix J with elements

$$J_{ss'}(\omega) = \frac{\pi}{2} \sum_{j=1}^{N_{\rm ph}} c_{s,j} c_{s',j} \delta(\omega - \omega_j)$$
 (6)

Spatially correlated fluctuations can have different origins: Notably, local modes can couple to delocalized electronic states (as discussed above), or else delocalized modes – typically of intermolecular type – can couple simultaneously to several local excitations [62–64]. Correlated fluctuations have been conjectured to slow down decoherence and favor coherent transfer processes, even though this aspect remains controversial [64].

In the case of photosynthetic light-harvesting complexes the main function of the exciton-vibrational coupling is the dissipation of excess energy of the exciton during relaxation and transport [65]. Although correlations in site energy fluctuations were found [66], these occur for such small vibrational frequencies that they have practically no influence on exciton relaxation. Moreover, artificially creating correlations at higher vibrational frequencies was found to lead to long-lived coherences, but, at the same time, to a suppression of exciton relaxation [66].

6.3.2.2 Effective-Mode Reduction Schemes

For extended molecular assemblies, the full normal-mode space quickly becomes prohibitively large. In view of a quantum dynamical treatment, it is, therefore, of key importance to reduce the dimensionality of the vibrational subspace while preserving the features of the dynamics. To this end, we employ an effective-mode reduction scheme [56, 57, 67, 68] that generates a reduced set of *collective* modes that couple to the electronic subsystem.

To see how the effective-mode scheme works, we consider the vibronic interaction term of equation (5). First-layer effective modes (FLEMs) \hat{Q}_s are constructed to subsume the state-specific vibronic couplings of equation (5) into a single collective coordinate per electronic state,

$$\widehat{H}^{\text{e-ph}} = \sum_{s}^{N_s} \overline{c}^s \widehat{Q}_s |X_s\rangle \langle X_s| \quad \text{with} \quad \widehat{Q}_s = \frac{1}{\overline{c}^s} \boldsymbol{c}_s^T \widehat{\mathbf{q}}$$
 (7)

where \overline{c}^s is a normalization constant. In the next step, the primary FLEMs $\widehat{\boldsymbol{Q}}_s$ are orthogonalized. Subsequently, a full-dimensional coordinate transformation is built, $\widehat{\mathbf{Q}} = \mathbf{T}\widehat{\mathbf{q}}$, whose first row is defined by equation (7). This transformation generates the FLEMs along with $(N_{\rm ph} - N_s)$ residual modes. The latter couple to the FLEMs and, therefore, exert an indirect influence on the electronic subsystem.

In the transformed representation, the phonon part of the Hamiltonian, \widehat{H}^{ph} of equation (4), takes the form

$$\widehat{H}^{\text{ph}} = \frac{1}{2} \left(\widehat{\mathbf{P}}^T \mathbf{\Omega} \widehat{\mathbf{P}} + \widehat{\mathbf{Q}}^T \mathbf{\Omega} \widehat{\mathbf{Q}} \right)$$
 (8)

where a non-diagonal form of the frequency matrix arises, $\Omega = \mathbf{T}\boldsymbol{\omega}\mathbf{T}^T$. As a result, bilinear couplings emerge, which can be cast, e.g., in a band-diagonal form, yielding a hierarchical electron-phonon model [57, 68].

By truncating this hierarchical representation and re-diagonalizing the Ω matrix, a series of approximate LVC models can be defined. In practice, mode reduction by factors 5–10, as compared with the original NM space, is possible while preserving an accurate picture of the dynamics on short time scales.

6.3.2.3 Analytic Mapping Procedure: Anharmonic Potentials

The LVC model, in conjunction with a local NM basis, is generally well suited for situations where the electronic coupling between monomer species is comparatively weak, as in many OPV aggregates and in photosynthetic systems (see chapter 5). This approach can be augmented by including a dependence on the electronic coupling of intermolecular modes. However, the investigation of transfer processes between strongly coupled monomers requires a different strategy. An example of the latter situation, to be discussed below (section 6.4.2), is intra-chain EET in conjugated polymers (see also figure 6.3a). In this case, the monomer basis is taken to refer to individual repeat units, with large electronic couplings between neighboring units – typically of the order of 1 eV. Besides the difficulty of carrying out suitable diabatization procedures adapted to the monomer basis, anharmonic large-amplitude motions – notably, torsional motions – are an important feature that needs to be accounted for.

For these reasons, we describe here an approach, sketched in figure 6.4b, that is based on PES cuts – in 1D or multi-D – generated by electronic structure calculations for oligomer species [59, 60]. These are converted into a vibronic lattice Hamiltonian of generalized Frenkel–Holstein [52, 69] type, set up in a monomer basis as described above. The mapping procedure of Ref. [59] is an analytic protocol based on the solution to an inverse eigenvalue problem that works in a pointwise fashion and provides an *exact* mapping of adiabatic PESs onto a generalized FH model. While the method is restricted to homo-oligomers, it can be selectively applied, *e.g.*, to the donor domain of DA systems.

As just mentioned, the e-h basis of equation (1) is here assumed to be restricted to Frenkel excitonic species of a homo-oligomer,

$$\widehat{H}(\widehat{\mathbf{x}}, \widehat{\mathbf{y}}) = \sum_{n,n'} \widehat{H}_{n,n'}(\widehat{\mathbf{x}}, \widehat{\mathbf{y}}) |XT_n\rangle \langle XT_{n'}|$$
(9)

where two types of modes are included, i.e., site-local modes $\hat{\mathbf{x}} = \{\hat{x}_n\}$ and site-correlated modes $\hat{\mathbf{y}} = \{\hat{y}_{n,n+1}\}$, where the latter are assumed to couple to neighboring sites. Differently from other approaches that separate the elements of the exciton Hamiltonian into electronic and vibronic parts (see section 6.3.1.1), the Hamiltonian is here formulated from the outset in terms of coordinate-dependent diabatic potential functions,

$$\widehat{H}_{n,n'}(\widehat{\mathbf{x}},\widehat{\mathbf{y}}) = \delta_{n,n'}\left(\widehat{T}(\widehat{\mathbf{p}}_x,\widehat{\mathbf{p}}_y) + \widehat{H}_n^{\text{on-site}}(\widehat{\mathbf{x}},\widehat{\mathbf{y}})\right) + (\delta_{n',n+1} + \delta_{n',n-1})\widehat{H}_{n,n'}^{\text{coup}}(\widehat{\mathbf{x}},\widehat{\mathbf{y}})$$
(10)

Here, the on-site part takes the following form,

$$\widehat{H}_{n}^{\text{on-site}}(\widehat{\mathbf{x}}, \widehat{\mathbf{y}}) = \widehat{V}_{0}(\widehat{\mathbf{x}}, \widehat{\mathbf{y}}) + \widehat{\Delta}_{n}(\widehat{x}_{n}, \widehat{y}_{n-1,n}, \widehat{y}_{n,n+1})$$
(11)

with the ground-state potential

$$\widehat{V}_0(\widehat{\mathbf{x}}, \widehat{\mathbf{y}}) = \sum_{l=1}^N \widehat{v}_G(\widehat{x}_l, \widehat{y}_{l-1,l}, \widehat{y}_{l,l+1})$$
(12)

and the difference potential

$$\widehat{\Delta}_{n}(\widehat{x}_{n},\widehat{y}_{n-1,n},\widehat{y}_{n,n+1}) = c_{\mathcal{E}} + \widehat{v}_{\mathcal{E}}(\widehat{x}_{n},\widehat{y}_{n-1,n},\widehat{y}_{n,n+1}) - \widehat{v}_{\mathcal{G}}(\widehat{x}_{n},\widehat{y}_{n-1,n},\widehat{y}_{n,n+1})$$
(13)

where $c_{\rm E}$ is the constant excitation energy of a single monomer and $\hat{v}_{\rm G}$ and $\hat{v}_{\rm E}$ are ground-state and excited-state monomer potentials, respectively. Further, the excitonic couplings of equation (10) are given as nearest-neighbor couplings,

$$\widehat{H}_{n,n'}^{\text{coup}}(\widehat{\mathbf{x}},\widehat{\mathbf{y}}) = \delta_{n',n-1}\widehat{w}(\widehat{x}_{n-1},\widehat{x}_n,\widehat{y}_{n-1,n}) + \delta_{n',n+1}\widehat{w}(\widehat{x}_n,\widehat{x}_{n+1},\widehat{y}_{n,n+1})$$
(14)

The monomer functions \hat{v}_G , \hat{v}_E , and \hat{w} , are now determined analytically, for a specified geometry $(\hat{\mathbf{x}}, \hat{\mathbf{y}})$ from a set of adiabatic oligomer potentials (specifically the lowest-lying S_1 and S_2 PESs in the case of J-aggregates), along with the ground-state potential S_0 . Hence, the input of the analytic mapping procedure consists of a set of electronic structure data points, as indicated in figure 6.4b. The procedure returns the monomer potentials and coupling that are subsequently fitted to a suitable functional form. No a priori assumption is made about the specific functional form of the potentials, and the characteristic scaling behavior of oligomer potentials as a function of system size is automatically accounted for.

This method, which can be understood as a *diabatization-by-ansatz*, illustrates that it is highly desirable to directly encode PES information into a vibronic lattice Hamiltonian whose diagonal and off-diagonal elements are flexible functions of all coordinates. Future work in this direction would likely draw on machine learning

approaches, e.g., neural network schemes, that perform a more general and robust mapping onto the desired form of the Hamiltonian.

6.3.3 Multiconfigurational Quantum Dynamics

While numerically exact quantum dynamical treatments often turn out prohibitive for the relevant system sizes, recent advances in quantum dynamical simulations based on tensor network schemes have enabled significant progress, notably using efficient multiconfigurational methods of the Multiconfiguration Time-Dependent Hartree (MCTDH) [25, 70, 71] family. In particular, the hierarchical multi-layer (ML-MCTDH) approach [26, 72–74] permits the treatment of tens to hundreds of electronic states and vibrational degrees of freedom. Matrix Product States (MPS) are another type of tensor network scheme that is rising in popularity [75, 76]. Based on these methods, ensembles of wavefunction realizations in the full electronic-vibrational space can be obtained, which are subsequently used to derive observable properties.

Details of these methods are presented in chapters 2 and 7. In the simulations reported in section 6.4, the ML-MCTDH approach was used throughout. We refer to the original publications for details of the numerical applications.

6.4 Coherent Effects in Exciton Dynamics: Case Studies

In this section, two case studies are considered: First, exciton dissociation at a regioregular donor-acceptor interface of P3HT:PCBM type (section 6.4.1), and second, exciton transport in a P3HT donor domain (section 6.4.2).

6.4.1 Exciton Dissociation at Donor-Acceptor Interfaces

Here, we consider a lattice Hamiltonian describing exciton dissociation at a typical polymer: fullerene heterojunction [77, 78], by combining a stacked OT assembly with a fullerene-type acceptor moiety placed in a face-on position, as shown in figure 6.2c. Within a minimal set-up, a single coarse-grained acceptor site is included, subsuming the effect of multiple fullerene species [20, 21, 79]. As a result, the Coulomb barrier to charge separation is reduced, facilitating free carrier generation [21, 80].

Within the e-h basis introduced above, Frenkel excitonic configurations arise, $|\mathrm{XT}_n\rangle$, $n=1,\ldots,N$, along with charge separated (CS) configurations, $|\mathrm{CS}_n\rangle=|v,\mu=v+n\rangle$, where the e-h separation is given as $|v-\mu|=n$. With a single effective acceptor site that is assigned the position v=0, the hole position varies between $\mu=1$ and $\mu=N$. The $|\mathrm{CS}_1\rangle$ state corresponds to the interfacial charge-transfer state (often denoted $|\mathrm{CT}\rangle$ state), whereas the remaining $|\mathrm{CS}_n\rangle$ states feature an increasing e-h distance n. With N=13, the system comprises 26 electronic states, along with 108 effective phonon modes that were constructed as detailed in section 6.3.2.1.

In the Hamiltonian $\hat{H} = \hat{H}^{el} + \hat{H}^{e-ph} + \hat{H}^{ph}$, the electronic part reads as follows,

$$\widehat{H}^{\text{el}} = \widehat{H}^{\text{on-site}} + \widehat{H}^{\text{coup}}_{\text{XT}} + \widehat{H}^{\text{coup}}_{\text{XT},\text{CS}} + \widehat{H}^{\text{coup}}_{\text{CS}}$$
(15)

where the on-site Hamiltonian $\widehat{H}^{\text{on-site}}$ is given as

$$\widehat{H}^{\text{on-site}} = \sum_{n=1}^{N} \left(\epsilon^{XT} |XT_n\rangle \langle XT_n| + \epsilon_n^{CS} |CS_n\rangle \langle CS_n| \right)$$
(16)

The on-site energies of the Frenkel excitonic states $|XT_n\rangle$, denoted ϵ^{XT} , are identical (in the absence of disorder), while the on-site energies of the charge-separated states, ϵ_n^{CS} , are determined by an effective Coulomb barrier [20, 21]. The coupling part of the Hamiltonian, in turn, comprises the conventional Frenkel-type coupling between neighboring $|XT_n\rangle$ states (here, j=0.09 eV),

$$\widehat{H}_{\mathrm{XT}}^{\mathrm{coup}} = j \sum_{n=1}^{N} (|\mathrm{XT}_n\rangle \langle \mathrm{XT}_{n+1}| + \mathrm{h.c.})$$
 (17)

as well as the coupling between CS states mediated by hole transfer ($t_h = -0.12 \text{ eV}$),

$$\widehat{H}_{\mathrm{CS}}^{\mathrm{coup}} = t_h \sum_{n=1}^{N-1} (|\mathrm{CS}_n\rangle \langle \mathrm{CS}_{n+1}| + \mathrm{h.c.})$$
(18)

along with the interfacial coupling ($\lambda = 0.2 \text{ eV}$) between the $|\text{XT}_1\rangle$ state and the interfacial $|\text{CS}_1\rangle$ state (*i.e.*, the so-called CT state),

$$\widehat{H}_{XT,CS}^{\text{coup}} = \lambda(|XT_1\rangle\langle CS_1| + \text{h.c.})$$
(19)

In Ref. [79], this model was expanded such as to include charge-separated $|CTX\rangle$ states in the donor domain, leading to additional exciton dissociation channels (similarly to the pathway shown in the lower panel of figure 6.1b).

Figure 6.5 shows the electronic eigenstates obtained for this Hamiltonian at the Franck-Condon reference geometry (panel a), along with the dynamical evolution for two different initial conditions, *i.e.*, the initial bright exciton state of the H-aggregate (panel b) and a localized state at the interface (panel c).

From the eigenstate analysis of figure 6.5a, we can infer that the Frenkel excitonic and charge-separated manifolds predominantly interact through a highly localized, stable interfacial state, i.e., the $|CS_1\rangle$ state (equivalently denoted $|CT\rangle$). However, if the initial photoexcitation entails significant excess energy, as is the case for the high-energetic bright state of the H-aggregate type donor domain (see figure 6.5a), internal conversion within the excitonic manifolds also entails partial mixing with delocalized charge-separated states.

These observations are borne out in the quantum dynamical simulations shown in figure 6.5b and c. Two different initial conditions are considered, *i.e.*, an initial bright exciton state at the upper band edge of the Frenkel manifold (figure 6.5b) and an initial localized state at the interface (figure 6.5c). The time evolution starting from the bright exciton state reflects the progressive energy loss due to internal

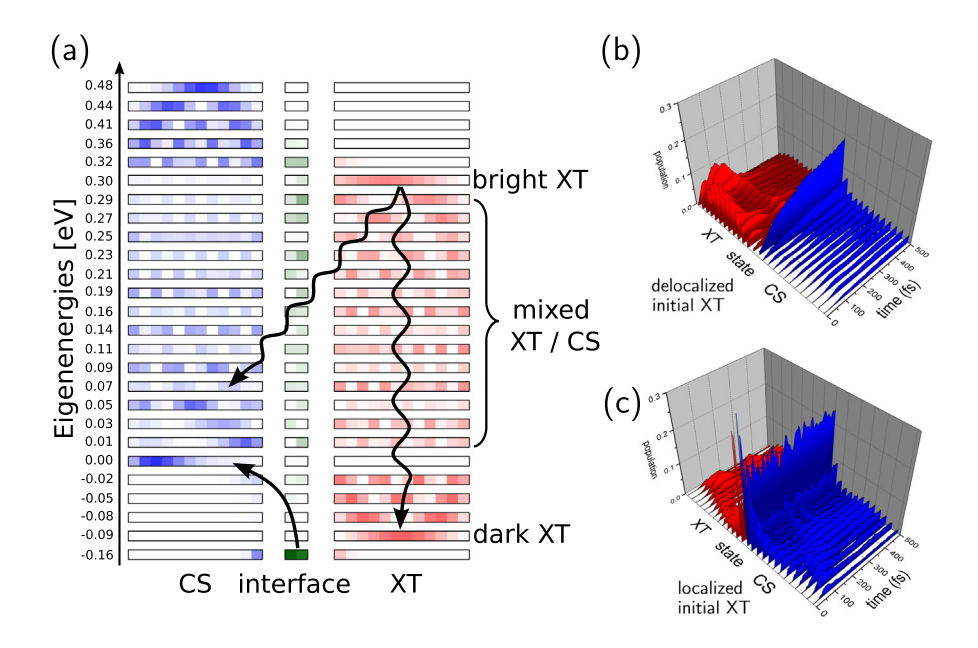


Fig. 6.5 – (a) Electronic eigenstate analysis based upon $\hat{H}^{\rm el}$ of equation (15), at the ground state reference geometry. The effective barrier [20, 21] exhibits a height of around 0.28 eV. The resulting eigenvalues are indicated along the ordinate. The abscissa defines a series of N=26 e-h basis state pertaining to the CS manifold (i.e., CS_n , $n=2,\ldots,13$ from left to right, shown in blue), the subset of interfacial states (i.e., $CS_1 \equiv CT$ and XT_1 , shown in green), and the XT manifold (i.e., XT_n , $n=2,\ldots,13$, from left to right, shown in red). The squared eigenvector coefficients are represented as a density profile. The low-energy interfacial state mainly corresponds to a superposition of CS₁ and XT₁ states, while higher-energy CS and XT states also mix to some extent. The bright XT state of the donor H aggregate is found at the upper band edge around 0.3 eV, while the lowest-energy dark XT state is found at -0.09 eV. For a bright-state initial condition, internal conversion within the donor excitonic manifold followed by relaxation to the interfacial states occurs, along with partial conversion into CS states (see arrows indicating these pathways). (b) Dynamical evolution starting from the delocalized bright exciton state, showing that a build-up of the interfacial charge-separated state (CS₁ \equiv CT) occurs, along with a gradual population of long-range charge-separated states. (c) Dynamical evolution starting from the localized interfacial exciton XT₁, giving rise to an immediate population of the interfacial charge-separated state and a larger population of long-range charge-separated states. Adapted with permission from Ref. [20]. Copyright 2015 American Chemical Society.

conversion, leading to a predominant population of the interfacial $|CS_1\rangle$ state as time proceeds. In the case of the localized initial condition, the interfacial state is immediately populated. In both cases, long-range charge separated states arise to a significant extent, which is due to the reduced barrier height (around 0.28 eV, due to delocalization effects as explained in Ref. [21]).

The above analysis shows that delocalization and internal conversion within the coupled excitonic and charge-separated manifolds can tune ultrafast charge separation at a typical donor-acceptor interface, especially if vibronic excess energy is present. This is in line with experimental observations, e.g., for P3HT:PCBM, showing that charge-separated states can be generated on ultrafast time scales. However, other materials exhibit slow and "cold" charge separation, exemplified by the highly ordered DA material that we investigated in Refs. [81, 82] by a combination of quantum dynamical and KMC simulations. The different regimes of interfacial charge separation and their relation to the PCE have been extensively and controversially discussed in the literature [6, 21, 83–88].

6.4.2 Intra-Chain Exciton Diffusion

Complementary to the previous section, where it was assumed that the initial exciton was localized close to the interface, we now consider a quantum dynamical description of exciton diffusion in a regioregular P3HT-type system. In Refs. [50, 62, 89], we considered both intra-chain and inter-chain diffusion, and we focus on the former case here. Since the intra-chain diffusion process depends strongly on the low-frequency torsional modes that generate thermal fluctuations, the description of the vibronic coupling part of the Hamiltonian has to be refined such as to include anharmonic potentials, as shown in figure 6.4b. To this end, the mapping procedure described in section 6.3.2.3 is employed. Furthermore, thermal fluctuations have to be included explicitly in the dynamical treatment, which was realized in Refs. [50, 62, 89] by a stochastic mean-field approach such as to generate an ensemble of wavefunction realizations. Initial conditions of a set of bath oscillators at finite temperatures are sampled by a Monte Carlo procedure over a thermal Wigner distribution.

The Hamiltonian takes the form of equation (9) on the basis of Frenkel configurations, $|XT_n\rangle$, n = 1, ..., N, with N = 20 monomer sites,

$$\widehat{H}(\widehat{\mathbf{x}}, \widehat{\mathbf{y}}, \widehat{\boldsymbol{\theta}}) = \sum_{n,n'=1}^{N} \widehat{H}_{n,n'}(\widehat{\mathbf{x}}, \widehat{\mathbf{y}}, \widehat{\boldsymbol{\theta}}) |XT_n\rangle \langle XT_{n'}| + \widehat{H}_{\text{bath}}(\widehat{\mathbf{b}}) \widehat{1}$$
(20)

where an external bath Hamiltonian, represented by a finite set of bath oscillators $\hat{\mathbf{b}} = {\hat{b}_j}$, acts on the torsional mode(s). The elements of the excitonic Hamiltonian read as follows (see equation (10)),

$$\widehat{H}_{n,n'}(\widehat{\mathbf{x}},\widehat{\mathbf{y}},\widehat{\boldsymbol{\theta}}) = \delta_{n,n'}\left(\widehat{T}(\widehat{\mathbf{p}}_{x},\widehat{\mathbf{p}}_{y},\widehat{\mathbf{p}}_{\theta}) + \widehat{H}_{n}^{\text{on-site}}(\widehat{\mathbf{x}},\widehat{\mathbf{y}},\widehat{\boldsymbol{\theta}})\right) + (\delta_{n',n+1} + \delta_{n',n-1})\widehat{H}_{n,n'}^{\text{coup}}(\widehat{\mathbf{x}},\widehat{\mathbf{y}},\widehat{\boldsymbol{\theta}})$$
(21)

where the kinetic energy operator $\widehat{T} = \widehat{\mathbf{p}}^T \mathbf{G} \widehat{\mathbf{p}}$ with the metric tensor \mathbf{G} is computed in curvilinear coordinates [53], and the on-site and coupling Hamiltonians, $\widehat{H}_n^{\text{on-site}}$ and $\widehat{H}_{n,n'}^{\text{coup}}$, are defined as in equations (11) and (14). As explained in section 6.3.2.3, all components of the Hamiltonian are expressed in terms of monomer potentials and couplings that fully account for anharmonicities, as illustrated in figure 6.4b.

In figure 6.6, individual realizations of stochastic exciton motion at T=300 K for a N=20 site oligomer under the above Hamiltonian are illustrated. The exciton is seen to move as an exciton-polaron, dressed by local-mode displacements that arise within the first tens of femtoseconds [53]. This polaronic state remains in a coherent superposition, despite the vibronic interactions. Torsional motions

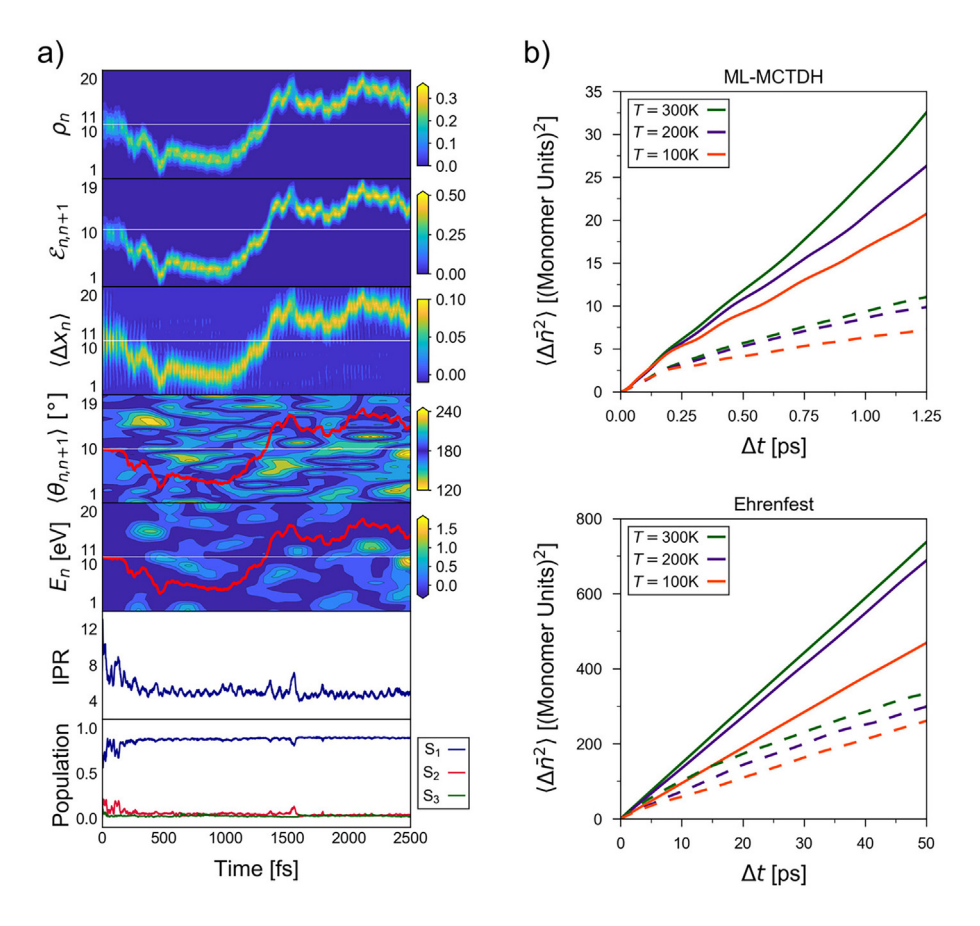


FIG. 6.6 – ML-MCTDH simulation results for an OT-20 system at finite temperature. (a) A single realization is shown at T=300 K. Top to bottom: excitonic site populations ρ_n ; bipartite entanglement $\mathcal{E}_{n,n+1}$, expectation values of the high-frequency modes relative to their ground-state equilibrium positions $\langle \Delta x_n \rangle$; expectation values of the torsions $\langle \theta_{n,n+1} \rangle$ with mean position of the exciton overlaid in red; torsional contribution to the on-site energies E_n with mean position of the exciton overlaid in red; inverse participation ratio; adiabatic populations of the S_n , $n=1,\ldots,3$, states. (b) MSDs obtained for the OT-20 system at different temperatures, i.e., T=100 K, 200 K, 300 K, with PBCs (full lines) and without PBCs (dashed lines). Upper panel: ML-MCTDH results on a time scale of 1.25 ps, lower panel: mean-field Ehrenfest dynamics results on a time scale of 50 ps. Adapted from Ref. [15] with permission from Annual Reviews.

trigger an exciton displacement because the spatial extension of the exciton depends sensitively on these soft modes, which can induce and remove conjugation breaks (see figure 6.3a). Therefore, the torsional dynamics act as a *dynamical barrier* to exciton displacement. In turn, the presence of the exciton induces planarization of the torsions in the excited state. This process proceeds nearly adiabatically in the oligothiophene chain shown here, but significant non-adiabatic effects can be observed in systems that exhibit weaker excitonic coupling and polaronic effects [60, 90]. This also includes the case of interchain exciton transport, where a transient localization mechanism is prevalent [50, 62].

As also demonstrated in figure 6.6, diffusion coefficients are computed based on the mean-squared displacement (MSD). In general, the following expression applies [50, 91],

$$\langle \Delta n^2 \rangle (\Delta t) = (MN_{\Delta t})^{-1} \left\langle \sum_{t=0}^{t_f - \Delta t} \sum_{n,n'} \rho_n(t) \rho_{n'}(t + \Delta t) (n' - n)^2 \right\rangle$$
 (22)

where a combined time and ensemble average are considered. The above expression takes into account the delocalized nature of the excitonic wave function. A simplified form of this expression, which was employed in figure 6.6b, results when referring to the mean exciton position,

$$\langle \Delta \bar{n}^2 \rangle (\Delta t) = (M N_{\Delta t})^{-1} \left\langle \sum_{t=0}^{t_{\bar{t}} - \Delta t} (\bar{n}(t + \Delta t) - \bar{n}(t))^2 \right\rangle$$
 (23)

In general, the MSD relates to the diffusion coefficient as D via $\langle \Delta n^2 \rangle (\Delta t) = 2D\Delta t^{\alpha}$ for a one-dimensional system, where $\alpha = 1$ for normal diffusion, $\alpha < 1$ for subdiffusive processes, and $\alpha > 1$ for superdiffusive processes. In the simulations shown in figure 6.6, diffusive behavior is observed for periodic boundary conditions, while subdiffusive behavior appears for a confined lattice. Diffusion coefficients of the order of $D \sim 10^{-2}$ cm² s⁻¹ are observed, in comparison to typical experimental values around $D \sim 10^{-3}$ cm² s⁻¹, mainly due to the neglect of static disorder.

6.5 Brief Excursion to 2D Electronic Spectroscopy

Regarding the spectroscopic observation of the elementary steps discussed above, 2DES has taken a prominent role in recent years (see chapter 4). In line with experimental observations of coherent exciton transport, we have examined in Ref. [92] how the vibronic signatures of exciton migration translate to 2DES signals [93–98]. In the implementation of Ref. [92], we simplified the treatment of the previous section such as to account for an individual "fluctuation event" induced by a single torsional mode, similar to Ref. [53].

As further detailed in chapters 4 and 8, the 2DES pulse sequence describes a third-order, or four-wave mixing (4WM) experiment, like the simpler two-pulse pump-probe (PP) experiment. In 2DES, the first pulse of the PP experiment is essentially replaced by two pulses with a time delay τ , denoted coherence time, which

enables frequency resolution of the excitation. Similar to the PP experiment, this is followed by the waiting (or population) time T, placed between the second and third pulse in the 2DES experiment. Signal detection occurs in the time t following the third pulse. For a single spectrum, the signal is detected for a fixed waiting time T and varying coherence time τ . Fourier transformation in the τ and t domains leads to a two-dimensional frequency-frequency correlation map. This map yields information on couplings between different electronic states, through the emergence of cross peaks, as well as their optical accessibility through the relative intensities of the peaks. Spectra recorded for different waiting times T reveal characteristic beatings of the signals.

In our implementation of Ref. [92], we used the Equation-of-Motion Phase-Matching Approach (EOM-PMA) [99], where the relevant third-order polarization is obtained from a set of auxiliary wavefunctions which are propagated in parallel and yield the polarization in the following form [99],

$$\mathcal{P}^{(3)}(t) = \langle \bar{\psi}_{12^{\dagger}3^{\dagger}}(t) | \widehat{\mu} | \psi_{12^{\dagger}3^{\dagger}}(t) \rangle - \langle \bar{\psi}_{13^{\dagger}}(t) | \widehat{\mu} | \psi_{12^{\dagger}}(t) \rangle - \langle \bar{\psi}_{13^{\dagger}}(t) | \widehat{\mu} | \psi_{13^{\dagger}}(t) \rangle$$

$$(24)$$

where the subscript indices of the ket and bra wavefunctions indicate which pulses these auxiliary wavefunctions experience. The bra wavefunctions are marked by an overbar for clarity.

Figure 6.7 reports on 2DES maps that illustrate the effect of torsional excited-state reorganization at T=0 K, for a single active torsion [92]. For reference, figure 6.7a illustrates the adiabatic energies relative to the ground state as a function of time, showing that energy relaxation takes place due to torsional planarization. The time scale of planarization, around 400–600 fs, is consistent with experimental observations. Figure 6.7b shows 2DES maps for the indicated values of the mixing time T. At T=0, a prominent diagonal peak is visible, whose position corresponds to the S_1 (and S_2) states at the initial, twisted geometry of an OT-20 oligomer. This peak shows a deformation which indicates that a frequency change as a function of the torsional evolution is taking place during the detection interval (see panel a). Moving to the final panel, at T=350 fs, we discern a cross-peak whose frequency corresponds to ($\omega_{\tau} = 1.88 \text{ eV}, \omega_{t} = 1.79 \text{ eV}$), such that the S_1 (and S_2) frequency during the coherence time is correlated with the S_1 frequency of the planarized system during the detection time. The vertical distance between the diagonal peak at T=0 fs and the off-diagonal cross-peak at T=350 fs corresponds to the torsional reorganization energy indicated by an arrow, generating a spectral red shift around 0.08 eV. In a realistic system, a number of torsional modes act in a concerted fashion, giving rise to a significant value of the reorganization energy.

Figure 6.7c-d show integrated absorption and emission spectra which have been obtained by integration over the ω_t domain (in the case of the absorption spectrum) and by integration over the ω_{τ} domain (in the case of the emission spectrum). Here, the red shift due to torsional planarization, and its gradual emergence between T=0 fs and T=350 fs is clearly visible.

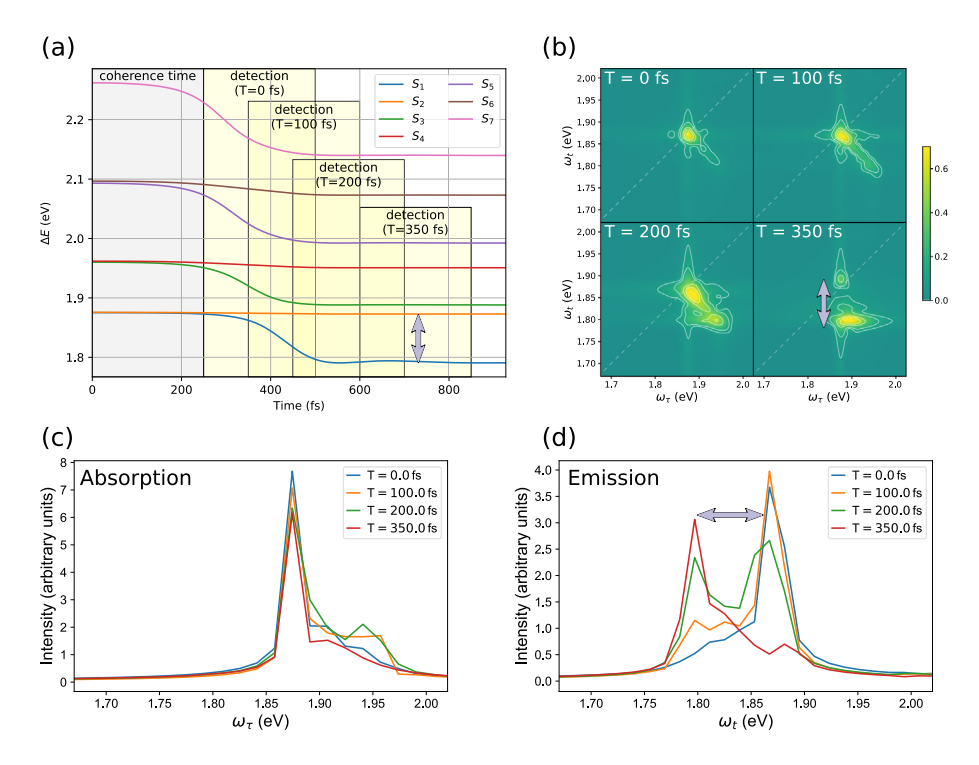


Fig. 6.7 – 2D electronic spectra for exciton dynamics of an OT-20 model system including a single torsional mode [92]; absolute values are shown. The carrier frequencies of all pulses were fixed at $\omega_j = 1.87$ eV, j = 1, ..., 3. (a) Evolution of the adiabatic energies of the S_n , n = 1, ..., 7, states relative to the ground state (S_0) , i.e., $\Delta E = E_{S_n} - E_{S_0}$, during the coherence time $(\tau = 250 \text{ fs})$, variable mixing times (T) and the detection time (t = 250 fs) whose start is shifted depending on T, as indicated by the yellow-shaded areas. The vertical arrow indicates the reorganization energy of the torsional mode, around $\Delta = 0.08$ eV. (b) 2DES signals for different waiting times, see the discussion in the text. At T = 350 fs, planarisation has occurred, and a cross-peak exhibits a redshift consistent with the reorganisation energy shown in (a). (c) Absorption spectrum obtained by integration over the ω_t domain. (d) Emission spectrum obtained by integration over the ω_t domain, highlighting the red shift shown in (b). Reproduced from Ref. [92] with permission from the Royal Society.

In the full model system studied in Ref. [92], we further included an effective high-frequency mode, *i.e.*, a "polaronic" mode that dynamically adapts to the time-evolving (de)localization of the exciton. Similarly to the experimental observations Refs. [96, 100, 101], a prominent vibronic fine structure is observed, underscoring that the exciton undergoes non-stationary trapping. Remarkably, due to the weak temperature dependence of the relevant polaronic mode(s), high-frequency oscillatory signatures persist even in thin films of P3HT [96, 100]. Hence, while the study of Ref. [92] addresses a minimal model, it reflects nonetheless the key features of the dynamical process in a realistic system.

6.6 Discussion and Outlook

The theoretical and computational treatment of elementary events in organic photovoltaics is challenging, due to the intricate interplay among site-to-site electronic couplings, exciton and charge delocalization, and vibronic coupling effects, along with the local nanostructure and molecular packing. Time-resolved spectroscopies have shown that coherent effects can play a significant role in these molecular materials, despite the large number of degrees of freedom. As a result, standard kinetic treatments are not applicable on the shortest time scales, and quantum dynamical approaches are called for.

In this chapter, we have illustrated that first-principles parametrized lattice Hamiltonians, together with efficient quantum dynamics in many dimensions, provide a viable route to describe charge separation at donor-acceptor junctions as well as exciton transport. Electron-hole lattice models, including vibronic interactions, encompass a range of transfer phenomena, from exciton transport represented by the Frenkel-Holstein Hamiltonian to multi-state models for exciton dissociation at donor-acceptor junctions.

Multiconfigurational methods of the MCTDH type are especially well suited to treat highly correlated exciton dynamics in the presence of strong vibronic couplings and anharmonic vibrations. This includes temperature-dependent effects, notably exciton diffusion driven by fluctuations of low-frequency soft modes, e.g., ring-torsions. Related methods like matrix product states and non-Markovian reduced-dynamics approaches like the HEOM scheme provide alternative routes and are discussed in several chapters of this volume (see chapters 2 and 3).

The sequential exciton migration and exciton dissociation steps in OPVs are obviously analogous to similar processes in biological light harvesting systems (see chapter 5). This raises the intriguing possibility of designing bio-inspired OPV materials that would benefit from the outstanding efficiency of their biological counterparts. While this concept is not straightforward to put into practice because of the limited stability of the relevant building blocks -e.g., chlorophylls - outside of their native environment [16], future developments in this direction are obviously expected.

As for exciton transport, very recent experiments have shown that highly efficient exciton diffusion can be achieved in nanofiber materials [63, 102], possibly opening an avenue towards tailored energy flow. At the same time, it is interesting to note that nature has found many ways to collect light energy, as demonstrated by the large variety of light-harvesting antennae. In contrast, all known photosynthetic reaction centers are structurally very similar. In photosynthetic systems, the key apparently lies in the fine tuning of redox properties and intermolecular couplings for the electron transfer step. Similar optimization strategies might apply to OPV materials.

Regarding the recent improvements in OPVs, largely due to NFA materials, many issues regarding the elementary conversion steps remain open [6]. Notably, the fact that the most efficient materials necessitate a negligible driving force as compared with the first-generation materials, has not been fully understood. As a result,

establishing design rules that connect the microscopic level to device performance remain a major challenge. Once such design rules are established and connected to recent progress in machine learning [103, 104], exciting prospects can be expected for the rational design of OPV materials.

Acknowledgements. We thank D. Brey, W. Popp, R. Binder, M. Polkehn, and H. Tamura for their contributions to the work reported in this chapter. D. Brey is acknowledged for providing the graphics of figure 6.1b. Comments and suggestions by T. Renger are highly appreciated.

References

- Brabec C., Scherf U., Dyakonov V. (2011) Organic photovoltaics: Materials, device physics, and manufacturing technologies. Wiley-VCH, Weinheim.
- Köhler A., Bässler H. (2015) Electronic processes in organic semiconductors: An introduction. Wiley-VCH, Weinheim.
- [3] Tamai Y. (2022) Aggregate 3, e280.
- [4] Shockley W., Queisser H. J. (1961) J. Appl. Phys. 32, 510.
- [5] Scharber M., Sariciftci N. (2013) Prog. Polymer Sci. 38, 1929.
- [6] Zhang G. et al. (2022) Chem. Revs. 122, 14180.
- [7] Chatterjee S., Jinnai S., Ie Y. (2021) J. Mater. Chem. A 9, 18857.
- [8] J. Yuan et al. (2019) Joule 3, 1140.
- [9] Perdigón-Toro L. et al. (2020) Adv. Mater. 32, 1906763.
- [10] Green M., Ho-Baillie A., Snaith H. (2014) Nat. Photon. 8, 506.
- [11] Ren Y. et al. (2023) Nature 613, 60.
- [12] Smith M. B., Michl J. (2013) Annu. Rev. Phys. Chem. 64, 361.
- [13] Price M. B. et al. (2022) Nat. Commun. 13, 2827.
- [14] Jiang Y., Li Y., Liu F. (2022) Nat. Commun. 14, 5079.
- [15] Popp W., Brey D., Binder R., Burghardt I. (2021) Annu. Rev. Phys. Chem. 72, 591.
- [16] Cavinato L. M., Fresta E., Ferrara S., Costa R. D. (2021) Adv. Energ. Mater. 11, 2100520.
- [17] Richtar J. et al. (2018) Molecules 23.
- [18] Frenkel J. (1931) Science 37, 17.
- [19] Wannier G. H. (1937) Phys. Rev. 52, 191–197.
- [20] Huix-Rotllant M., Tamura H., Burghardt I. (2015) J. Phys. Chem. Lett. 6, 1702.
- [21] Tamura H., Burghardt I. (2013) J. Am. Chem. Soc. 135, 16364.
- [22] Renger T. (2018) Photoinduced electron transfer in the reaction centers, Molecular mechanisms of photosynthesis (R. E. Blankenship, Ed.). CRC Press, pp. 327–358.
- [23] Chen L., Zhao Y., Tanimura Y. (2015) J. Phys. Chem. Lett. 6, 3110.
- [24] Kato A., Ishizaki A. (2018) J. Phys. Chem. Lett. 121, 026001.
- [25] Beck M. H., Jäckle A., Worth G. A., Meyer H. D. (2000) Phys. Rep. 324, 1.
- [26] Wang H. (2015) J. Phys. Chem. A 119, 7951.
- [27] Zhang X., Li Z., Lu G. (2011) Phys. Rev. B 84, 235208.
- [28] Nelson T., Fernandez-Alberti S., Roitberg A. E., Tretiak S. (2013) Phys. Chem. Chem. Phys. 15, 9245.
- [29] Nelson T. R. et al. (2020) Chem. Rev. 120, 2215.
- [30] Parandekar P. V., Tully J. C. (2005) J. Chem. Phys. 122, 094102.
- [31] Parandekar P. V., Tully J. C. (2006) J. Chem. Theory Comput. 2, 229.
- [32] Chen L., Borelli R., Zhao Y. (2017) J. Phys. Chem. A 121, 8757.
- [33] Chen L., Gelin M. F., Shalashilin D. V. (2019) J. Chem. Phys. 151, 244116.
- [34] Jang S., Newton M. D., Silbey R. J. (2004) Phys. Rev. Lett. 92, 218301.
- [35] Balzer D., Kassal I. (2023) J. Phys. Chem. Lett. 14, 2155.
- [36] Merrifield R. E. (1961) J. Chem. Phys. 34, 1835.
- [37] Mukamel S., Tretiak S., Wagersreiter T., Chernyak V. (1997) Science 277, 781.

- [38] Polkehn M., Eisenbrandt P., Tamura H., Burghardt I. (2018) Int. J. Quant. Chem. 118.
- [39] Bardeen C. J. (2014) Annu. Rev. Phys. Chem. 65, 127.
- [40] Smith M. B., Michl J. (2013) Annu. Rev. Phys. Chem. 64, 361.
- [41] Tamura H., Huix-Rotllant M., Burghardt I., Olivier Y., Beljonne D. (2015) Phys. Rev. Lett. 115, 107401.
- [42] Köppel H., Domcke W., Cederbaum L. S. (1984) Adv. Chem. Phys. 57, 59.
- [43] Hsu C.-P. (2009) Acc. Chem. Res. 42, 509.
- [44] Grofe A., Qu Z., Truhlar D. G., Li H., Gao J. (2017) J. Chem. Theory Comput. 13, 1176.
- [45] Green J. A., Yaghoubi Jouybari M., Asha H., Santoro F., Improta R. (2017) J. Chem. Theory Comput. 17, 4660–4674.
- [46] Li S. L., Truhlar D. G., Schmidt M. W., Gordon M. S. (2015) J. Chem. Phys. 142, 064106.
- [47] Blancafort L., Voityuk A. A. (2014) J. Chem. Phys. 140, 095102.
- [48] Spano F. C., Silva C. (2014) Ann. Rev. Phys. Chem. 65, 477.
- [49] Hestand N. J., Spano F. C. (2017) Acc. Chem. Res. 50, 341.
- [50] Mondelo-Martell M., Brey D., Burghardt I. (2022) J. Chem. Phys. 157, 094108.
- [51] Popp W., Polkehn M., Burghardt I. (2020) J. Phys. Chem. Lett. 10, 3326.
- [52] Barford W. (2013) Electronic and optical properties of conjugated polymers, 2nd edn. Oxford, Clarendon.
- [53] Binder R., Lauvergnat D., Burghardt I. (2018) Phys. Rev. Lett. 120, 227401.
- [54] Rebentrost P., Mohseni M., Kassal I., Lloyd S., Aspuru-Guzik A. (2009) New J. Phys. 11, 033003.
- [55] Plenio M. B., Huelga S. F. (2008) New J. Phys. 10, 113019.
- [56] Hughes K. H., Christ C. D., Burghardt I. (2009) J. Chem. Phys. 131, 124108.
- [57] Popp W., Polkehn M., Hughes K. H., Martinazzo R., Burghardt I. (2019) J. Chem. Phys. 150, 244114.
- [58] Weiss U. (2008) Quantum dissipative systems, 3rd edn. World Scientific Singapore.
- [59] Binder R., Römer S., Wahl J., Burghardt I. (2014) J. Chem. Phys. 141, 014101.
- [60] Binder R., Bonfanti M., Lauvergnat D., Burghardt I. (2020) J. Chem. Phys. 152, 204119.
- [61] Green J. A., Brey D., Razgatlioglu L., Ali B., Błasiak B., Burghardt I. (2024) J. Chem. Theor. Comput. 20, 8127.
- [62] Brey D., Burghardt I. (2024) J. Phys. Chem. Lett. 15, 1836.
- [63] Carta A. et al. (2024) J. Phys. Chem. Lett. 15, 2697.
- [64] Jang S. J., Mennucci B. (2018) Rev. Mod. Phys. 90, 035003.
- [65] Cao J. et al. (2020) Sci. Adv. 6, eaaz4888.
- [66] Renger T. et al. (2012) J. Phys. Chem. B 116, 14565–14580.
- [67] Cederbaum L. S., Gindensperger E., Burghardt I. (2005) Phys. Rev. Lett. 94, 113003.
- [68] Tamura H., Ramon J. G. S., Bittner E. R., Burghardt I. (2008) Phys. Rev. Lett. 100, 107402.
- [69] Holstein T. (1959) Ann. Phys. (N. Y.) 8, 325.
- [70] Meyer H.-D., Manthe U., Cederbaum L. S. (1990) Chem. Phys. Lett. 165, 73.
- [71] Manthe U., Meyer H.-D., Cederbaum L. S. (1992) J. Chem. Phys. 97, 3199.
- [72] Wang H., Thoss M. (2003) J. Chem. Phys. 119, 1289.
- [73] Manthe U. (2018) J. Chem. Phys. 128, 164116.
- [74] Vendrell O., Meyer H.-D. (2011) J. Chem. Phys. 134, 044135.
- [75] Yao Y., Xie X., Ma H. (2011) Phys. Rev. E 84, 030102R.
- [76] Dorfner M., Brey D., Burghardt I., Ortmann F. (2024) J. Chem. Theory Comput. 20, 8767.
- [77] Sariciftci N. S., Smilowitz L., Heeger A. J., Wudl F. (1992) Science 258, 1474.
- [78] Brabec C. J. et al. (2001) Chem. Phys. Lett. 340, 232.
- [79] Polkehn M., Tamura H., Burghardt I. (2018) J. Phys. B: At. Mol. Opt. Phys. 51, 014003.
- [80] Kahle F. et al. (2018) J. Phys. Chem. C 122, 21792.
- [81] Brey D., Popp W., Budakoti P., D'Avino G., Burghardt I., J. Phys. Chem. C 125, 25030 (2021).
- [82] D'Avino G., Hegger R., Brey D., Budakoti P., Mery S., Burghardt I. (2022) J. Phys. Chem. C 126, 9762.
- [83] Baranovskii S. D., Wiemer M., Nenashv A. V., Jansson F., Gebhard F. (2012) J. Phys. Chem. Lett. 3, 1214.

- [84] Nenashev A. V. et al. (2011) Phys. Rev. B: Condens. Matter Mater. Phys. 84, 035210.
- [85] Arkhipov V. I., Heremans P., Bässler H. (2003) Appl. Phys. Lett. 82, 4605.
- [86] Vandewal K. et al. (2014) Nat. Mater. 13, 63.
- [87] Athanasopoulos S. et al. (2019) Adv. Energy Mater. 9, 1900814.
- [88] Köhler A., Bässler H. (2015) Phys. Chem. Chem. Phys. 17, 28451.
- [89] Binder R., Burghardt I. (2020) Faraday Discuss. 221, 406.
- [90] Binder R., Bonfanti M., Lauvergnat D., Burghardt I. (2020) J. Chem. Phys. 152, 204119.
- [91] Maiolo F. D., Brey D., Binder R., Burghardt I. (2020) J. Chem. Phys. 153, 184107.
- [92] Brey D., Binder R., Martinazzo R., Burghardt I. (2022) Faraday Discuss. 237, 148.
- [93] Mukamel S. (2000) Annu. Rev. Phys. Chem. 51, 691.
- [94] Ginsberg N. S., Cheng Y. C., Fleming G. R. (2009) Acc. Chem. Res. 42, 1352.
- [95] Collini E., Scholes G. D. (2009) Science 323, 369.
- [96] De Sio A. et al. (2016) Nature Comm. 7, 13742.
- [97] Sio A. D. et al. (2018) Eur. Phys. J. B 91, 236.
- [98] Brixner T., Hildner R., Köhler J., Lambert C., Würthner F. (2017) Adv. Energy Mater. 7, 1700236.
- [99] Krčmář J., Gelin M. F., Egorova D., Domcke W. (2014) J. Phys. B: At. Mol. Opt. Phys. 47, 124019.
- [100] De Sio A., Lienau C. (2017) Phys. Chem. Chem. Phys. 19, 18813.
- [101] Song Y., Hellmann C., Stingelin N., Scholes G. D. (2015) J. Chem. Phys. 142, 212410.
- [102] Sneyd A. J. et al. (2021) Sci. Adv. 7, eabh4232.
- [103] Li M., Dai L., Hu Y. (2022) ACS Energ. Lett. 7, 3204.
- [104] Eibeck A. et al. (2021) ACS Omega 6, 23764.

Chapter 7

Computational Exercise: Introduction to Quantum Dynamical Simulations

Dominik Brey* and James A. Green**

Institute of Physical and Theoretical Chemistry, Goethe University Frankfurt, Max-von-Laue-Str. 7, Frankfurt, 60438, Germany

This chapter serves as an accompaniment to the computational exercises contained within the Jupyter notebook LesHouches_QD.ipynb, aimed at illustrating the basics of numerical quantum dynamics. The notebook as well as installation instructions can be found at www.doi.org/10.5281/zenodo.15033674. The computational exercises rely on Python3.10 but should work with higher versions as well.

The chapter is structured as follows: Section 7.1 introduces conventions used in this chapter. Section 7.2 shows the theoretical background to solve the time dependent Schrödinger equation in this chapter. For this, we focus on the split-operator formalism. Further theoretical background is introduced in subsequent sections where necessary. Section 7.3 introduces the first system: a one-dimensional system with a single electronic state that models a carbonyl vibration. Section 7.4 continues with a similar system to illustrate imaginary time propagation as a means to obtain suitable initial conditions. Section 7.5 extends the theory to multiple electronic states and introduces the concept of density matrices. Section 7.6 introduces autocorrelation functions as an intermediate to power spectra. Section 7.7 applies the theory for multi-state systems to an excitonic dimer, and finally, section 7.8 concludes.

7.1 Conventions in this Chapter

While all necessary code can be found in the accompanying Jupyter notebook, this chapter also contains code snippets for illustration. These are marked as follows:

^{*}e-mail: brey@theochem.uni-frankfurt.de

^{**}e-mail: green@chemie.uni-frankfurt.de

```
1 #This is a code snippet
2 n = 5
3 for i in range(n):
4 print(i)
```

Also mirroring the notebook, various boxes can be found in the chapter: Throughout the text, questions to you can be found as:



These are meant for you to pause and ponder before proceeding. In contrast to the notebook, the answers are given right after.

At the end of sections, tasks are given in these boxes:



where, as for the questions, the solution is given right after. You are nevertheless encouraged to try the tasks yourself in the notebook.

The answers to questions and solutions to tasks are given in boxes like this:



Finally, at the end of sections, there is a conclusion box that summarizes the most important findings:



7.1.1 Initial Conditions

While all simulations will, in principle, take place right after a photo-excitation, we will not model the excitation itself. Rather, we assume an instantaneous Franck-Condon excitation to create a "doorway state". Formally, we create this

¹A doorway state is, in general, a state that connects a small manifold of simple states (here the ground state) with a large manifold of complex states (here the excited states), see, e.g., Ref. [1].

"doorway state" via an instantaneous electric dipole interaction of the ground state wave function with an electric field as $\hat{\mu}\Psi_0$, where Ψ_0 is the lowest ground state eigenfunction and $\hat{\mu}$ is the transition dipole moment operator [2].

In practice, this means that we will construct ground-state wave functions and put them in excited state potentials.

7.1.2 Atomic Units

For all simulations it is important to take care of unit consistency. This reduces the risk of neglecting conversion factors.

In quantum dynamical simulations, it is common to work in atomic units, and we will do the same in this chapter. Atomic units are built relative to the following four physical constants [3, 4]:

- elementary charge: e
- electron mass: m_e
- Planck constant/ 2π : \hbar
- Coulomb constant: $4\pi\epsilon_0$

which are all set to have a value of 1. Analytical expressions will still show the \hbar . Important derived units are then the units of

- energy: $m_e e^4/\left(\left(4\pi\epsilon_0\right)^2\hbar^2\right)$ in "Hartree" $(E_{\rm h})$
- distance: $(4\pi\epsilon_0)\hbar^2/(m_e e^2)$ in "bohr" (a_0)
- time: $\hbar^3 (4\pi\epsilon_0)^2 / (m_e e^4) = \hbar / E_h$ in "atomic time units" (atu)

Conversion factors from

- femtoseconds to atomic time units (1 fs ≈ 41.341 atu)
- wavenumbers to electron volt $(1 \, \mathrm{cm}^{-1} \approx 1/8065.5 \, \mathrm{eV})$
- electron volt to Hartree (1eV $\approx 1/27.2114 E_h$)
- Angstrom to Bohr (1 Å $\approx 1.889 a_0$)

are declared as variables to make conversion easier.

```
1 fs2atu = 41.341374575751
2 invcm2eV = 1.0/8065.5
3 eV2Eh = 1.0/27.2114
4 A2a0 = 1.88973
```

7.1.3 Python Packages

A few external Python packages are imported to help with the calculations. These are numpy for general calculations and Fourier transformation, matplotlib for plotting and scipy for matrix diagonalization and integration.

- 1 # import the relevant python packages
- 2 import numpy as np # for general math and FT
- 3 import scipy.linalg as scla # for matrix diagonalization
- 4 import scipy.integrate as scpi # for integration
- 5 import scipy.special as scps # for Hermite polynomials
- 6 import matplotlib.pyplot as plt # for plotting

7.2 Solving the Time-Dependent Schrödinger Equation

At the center of quantum dynamics lies the time-dependent Schrödinger equation

$$i\hbar \frac{\partial}{\partial t} \psi(t) = \hat{H}(t)\psi(t)$$
 (1)

where we have the time derivative of the wave function on the left-hand side and the Hamiltonian acting on the wave function on the right-hand side. Solving this equation for a given Hamiltonian \hat{H} and given initial condition $\psi(t_0)$ yields the time evolution of the corresponding system.

The formal solution of the time-dependent Schrödinger equation is [5–7]

$$\psi(t) = \hat{U}(t, t_0)\psi(t_0) \tag{2}$$

with the time evolution operator (or propagator) $\hat{U}(t, t_0)$ that propagates the initial wave function at time t_0 up to time t. When equation (2) is inserted into the time-dependent Schrödinger equation (equation (1)), we get

$$i\hbar \frac{\partial}{\partial t} \hat{U}(t, t_0) \psi(t_0) = \hat{H}(t) \hat{U}(t, t_0) \psi(t_0). \tag{3}$$

And since this equation needs to hold for any initial wave function $\psi(t_0)$, the propagator itself must satisfy it as well

$$i\hbar \frac{\partial}{\partial t} \hat{U}(t, t_0) = \hat{H}(t)\hat{U}(t, t_0). \tag{4}$$

Integrating both sides from t_0 to t gives

$$\hat{U}(t, t_0) - \hat{U}(t_0, t_0) = -\frac{i}{\hbar} \int_{t_0}^{t} \hat{H}(\tau) \hat{U}(\tau, t_0) d\tau$$
 (5)

which, upon noting that $\hat{U}(t_0, t_0)$ has to be the identity operator $\hat{1}$, finally gives an equation for the propagator

$$\hat{U}(t, t_0) = \hat{1} - \frac{i}{\hbar} \int_{t_0}^{t} \hat{H}(\tau) \, \hat{U}(\tau, t_0) d\tau.$$
 (6)

This equation can be solved iteratively by plugging it into itself to give

$$\hat{U}(t, t_0) = \hat{1} + \sum_{n=1}^{\infty} \left(-\frac{\mathrm{i}}{\hbar} \right)^n \int_{t_0}^t \mathrm{d}\tau_n \int_{t_0}^{\tau_n} \mathrm{d}\tau_{n-1} \cdots \int_{t_0}^{\tau_2} \mathrm{d}\tau_1 \hat{H}(\tau_n) \hat{H}(\tau_{n-1}) \dots \hat{H}(\tau_1)$$
 (7)

which is also called positive time-ordered exponential and denoted

$$\hat{U}(t, t_0) = \exp_+\left(-\frac{\mathrm{i}}{\hbar} \int_{t_0}^t \hat{H}(\tau) d\tau\right). \tag{8}$$

7.2.1 Numerical Perspective

Since we will perform numerical propagations of wave functions, it might be more instructive to look at the propagator as a series of small time steps, *i.e.*, we divide our time interval from t_0 to t into N equal segments $\delta t = t_n - t_{n-1}$, so that $N\delta t = t - t_0$. Equation (2) can then be rewritten as

$$\psi(t) = \hat{U}(t, t_n) \,\hat{U}(t_n, t_{n-1}) \dots \hat{U}(t_1, t_0) \psi(t_0) \tag{9}$$

and the propagator from t_{n-1} to t_n can be approximated from equation (7), with a sufficiently small δt , as

$$\hat{U}(t_n, t_{n-1}) \approx \hat{1} - \frac{\mathrm{i}}{\hbar} \hat{H}(t_n) \delta t. \tag{10}$$

This is the infinitesimal evolution operator. The total evolution operator is then the product of those infinitesimal operators.

We will focus on time-independent Hamiltonians in this chapter, for which we can then write

$$\hat{U}(t, t_0) = \prod_{n=1}^{N} \hat{U}(t_n, t_{n-1}) = \left(1 - \frac{i}{\hbar} \hat{H} \delta t\right)^{N}$$
(11)

and, since

$$\lim_{N \to \infty} \left(1 + \frac{a}{N} \right)^N = \exp(a),\tag{12}$$

we have

$$\hat{U}(t, t_0) = \exp\left(-\frac{\mathrm{i}}{\hbar}\hat{H}(t - t_0)\right) \tag{13}$$

as the final result for the propagator. Note that you can, in practice, approximate the propagator of a time-dependent Hamiltonian as a series of short time-step propagations of time-independent Hamiltonians as long as the time dependence of the Hamiltonian is sufficiently small in the given time step.

7.2.1.1 Split Operator Formalism

Equation (13) can be used to construct the propagator for any given (time-independent) Hamiltonian to then propagate an initial wave function of choice. An advantage of this approach is that, in principle, the propagator of a Hamiltonian can be constructed once and then applied to any initial condition.

Our simulations will occur in time steps $\Delta t = t - t_0$. To simplify the construction of the propagator, we will partition the Hamiltonian into a kinetic and potential part, $\hat{H} = \hat{T} + \hat{V}$, so that

$$\hat{U}(\Delta t) \equiv \hat{U}(t, t_0) = \exp\left(-i(\hat{T} + \hat{V})\frac{\Delta t}{\hbar}\right). \tag{14}$$

We will use a grid representation [8, 9] of the Hamiltonian and wave function so that

$$\hat{U}(\Delta t) \equiv \exp\left(-i\left(-\frac{\hbar}{2m}\frac{\partial^2}{\partial x^2} + V(x)\right)\frac{\Delta t}{\hbar}\right)
= \exp\left(-i\left(\frac{p^2}{2m} + V(x)\right)\frac{\Delta t}{\hbar}\right).$$
(15)

The potential part is, in all cases in this chapter, multiplicative. The kinetic part, however, would require us to calculate the second-order derivative of the wave function. To avoid this, we exploit that the kinetic part is multiplicative in momentum space and that position and momentum are a Fourier pair so that it is easy to switch between the two.

The idea is then to separate the propagation of the potential energy and kinetic energy. The potential energy will be propagated in position space. For the propagation of the kinetic energy, we transform to momentum space. A first idea might be to do the separation with a perturbative approach like

$$\hat{U}(\Delta t) \approx \hat{1} - i \frac{\Delta t}{\hbar} (\hat{T} + \hat{V}).$$
 (16)

With this, however, \hat{U} is no longer a unitary operator. We would like to retain the unitary nature of \hat{U} since then, the norm of the wave function is conserved as

$$\langle \psi(\Delta t) | \psi(\Delta t) \rangle = \langle \psi(0) | \hat{U}^{\dagger}(\Delta t) \hat{U}(\Delta t) | \psi(0) \rangle = \langle \psi(0) | \psi(0) \rangle. \tag{17}$$

A way to separate the propagator into parts while retaining its nature of a unitary transformation is in analogy to the classical exponential law

$$\hat{U}(\Delta t) = \underbrace{\exp\left(-i\hat{T}\frac{\Delta t}{\hbar}\right)}_{\hat{U}_{T}(\Delta t)} \underbrace{\exp\left(-i\hat{V}\frac{\Delta t}{\hbar}\right)}_{\hat{U}_{V}(\Delta t)} + \mathcal{O}(\Delta t^{2}). \tag{18}$$

This is the Lie-Trotter splitting [10] and it is only exact if the two operators commute. The operators for kinetic and potential energy, in general, do not commute so that an error proportional to the square of the time step accrues.

Another approach compared to equation (18) is the so-called Strang splitting [11]:

$$\hat{U}(\Delta t) = \underbrace{\exp\left(-i\hat{V}\frac{\Delta t}{2\hbar}\right)}_{\hat{U}_{V}(\Delta t/2)} \underbrace{\exp\left(-i\hat{T}\frac{\Delta t}{\hbar}\right)}_{\hat{U}_{T}(\Delta t)} \underbrace{\exp\left(-i\hat{V}\frac{\Delta t}{2\hbar}\right)}_{\hat{U}_{V}(\Delta t/2)} + \mathcal{O}(\Delta t^{3})$$
(19)

which only accrues an error proportional to the cube of the time step. At first glance, this is more costly compared to equation (18) since the potential part needs to be propagated twice. This is, however, offset since we can choose a larger time step to achieve the same accuracy.

Both equations (18) and (19) are special cases of the Lie-Suzuki-Trotter decomposition [12, 13] (first and second order, respectively). For higher numerical accuracy, one can either go to higher orders or use a smaller time step. If the (nested) commutators between operators are easily accessible, one can also employ the Baker-Campbell-Hausdorff formula [14–16], but this is out of scope for this chapter.

By comparing equations (13) and (18) or (19), we can see that the propagator for the Hamiltonian is now successfully rewritten in terms of propagators for the potential and kinetic energy, \hat{U}_V and \hat{U}_T respectively.

With the propagator of equation (19), the algorithm for the propagation is then

- 1. Define the position grid $x \equiv \{x_i\}$ and corresponding momentum grid $p \equiv \{p_i\}$
- 2. Construct the kinetic energy $\hat{T} \equiv T(p)$, the potential energy $\hat{V} \equiv V(x)$ and the initial wavefunction ψ_0
- 3. Choose the final time t_f and a sufficiently small time step Δt
- 4. Construct the propagators for kinetic energy \hat{U}_T and potential energy \hat{U}_V
- 5. Propagate the wave function with $\hat{U}_V(\Delta t/2)$
- 6. Perform a Fourier transformation to momentum space
- 7. Propagate the wave function with $\hat{U}_T(\Delta t)$
- 8. Back-transform to position space
- 9. Propagate the wave function with $\hat{U}_V(\Delta t/2)$
- 10. Repeat steps 5–9 until the final time is reached

Of course, we can already calculate expectation values with the wave functions during the propagation.

Keep in mind that this is by far not the only way to solve the time-dependent Schrödinger equation. The split operator formalism is a flexible tool but is limited in terms of system size. For simulations with more than a few degrees of freedom, one would employ algorithms like the Multiconfiguration Time-Dependent Hartree (MCTDH) method [17]. More details on these methods can be found in chapter 2.

7.3 Single-State Systems

We will start with a simple one-dimensional model system with a single electronic state. Be warned that some parameters are chosen poorly at first to illustrate problems that might occur in larger simulations, where checking everything is not as straightforward anymore.

In this first model, we simulate the dynamics of an isolated carbonyl (C=O) vibration upon photo-excitation. The model features a harmonic potential with a frequency $\omega = 1750.0 \,\mathrm{cm}^{-1}$ and reduced mass $m = 37000.0 \,m_e$. The active

coordinate x is the change in distance between the carbon and oxygen atoms, hence the ground state equilibrium position is set to x = 0.0 as reference. With the given frequency ω , we can expect a periodicity $T \approx 19$ fs.

In the calculation, we only simulate the excited state and assume a Franck-Condon excitation, *i.e.*, we put the ground state wave packet in the excited state potential without an explicit interaction with any electric field. Furthermore, we assume that the frequency of oscillation does not change in the excited state, whereas the equilibrium position is shifted to $x_0 = 0.2 a_0$. Our Hamiltonian is thus

$$H = \frac{p^2}{2m} + \frac{1}{2}m\omega^2(x - x_0)^2 = \frac{p^2}{2m} + \frac{1}{2}m\omega^2(x - 0.2)^2.$$
 (20)

The situation is sketched in figure 7.1.

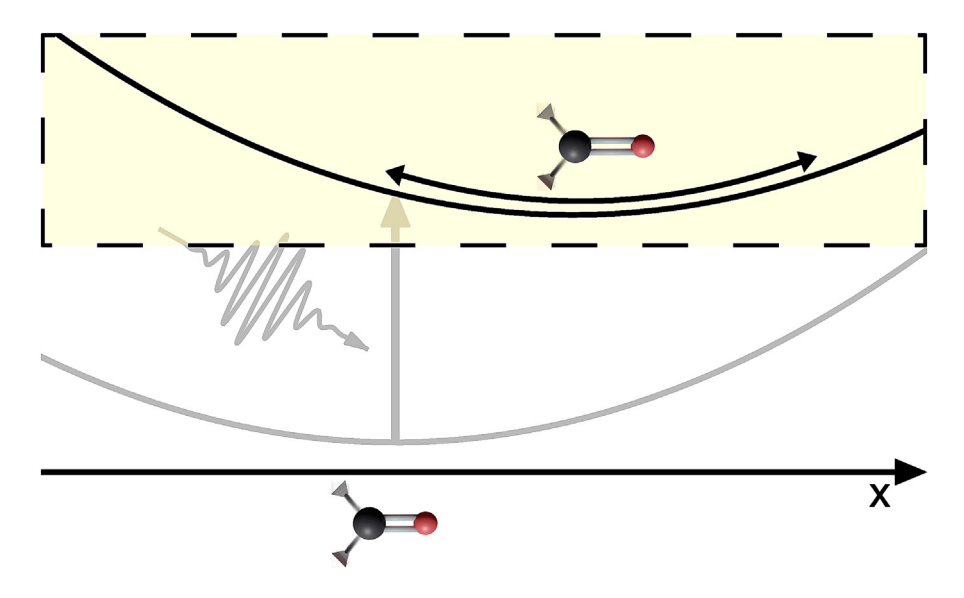


Fig. 7.1 – Sketch of the 1D model. The box marks the active part of the system that is simulated. The initial photoexcitation is indicated but not part of the simulation.

To prepare the system for numerical simulations, we define the key parameters for the potential:

- 1 # define the parameters as given in the text and convert to atomic units
- 2 w = 1750.0*invcm2eV*eV2Eh
- 3 m = 37000.0

and create a discretized grid $x \equiv \{x_1, x_2, ..., x_N\}$ of the position space:

- 1 # define the position grid of the simulation
- 2 N = 128 # number of grid points
- 3 x = np.linspace(-0.2, 0.4, N) # grid
- 4 dx = np.abs(x[1]-x[0]) # grid spacing

Position and momentum are a Fourier pair. With this in mind, we can construct our momentum grid *via* Fourier transformation from our position grid.

- 1 # define the corresponding momentum grid via Fourier transformation
- 2 p = np.fft.fftfreq(N, dx) * 2 * np.pi

We should keep in mind that the grid spacing in position space defines the maximum value in the momentum grid. In turn, the maximum value in the position grid defines the grid spacing in momentum space. Especially the first relation is important and can be written as

$$p_{\text{max}} = \frac{\hbar}{2\Lambda x}.\tag{21}$$

If the resolution in position space is not high enough, we cannot represent the momentum, and hence the kinetic energy, adequately.

With the previously defined parameters m and ω as well as the position grid x, we can define the potential:

- 1 # define the excited state potential: a shifted harmonic oscillator
- 2 V = 0.5 * m * w * * 2 * (x-0.2) * * 2

Question 3.1

We have defined the coordinate grid in the interval $[-0.2, 0.4] a_0$. Why is this grid definition problematic for this simulation?



Answer to question 3.1

The minimum of the harmonic potential is at $0.2 a_0$, the starting position is at $0.0 a_0$. For a classical harmonic oscillator, we would expect a periodic evolution from $0.0 a_0$ over $0.2 a_0$ to $0.4 a_0$ and back. Our grid is defined up to $0.4 a_0$, which would be sufficient for a classical particle. We are, however, dealing with a wave function that has a finite width. As such, the wave function will reach the end of the grid, i.e., "crash into a wall".



Now, we define the initial wave function, centered at 0, as the (analytic) first eigenfunction of a quantum harmonic oscillator. With mass m, frequency ω , and $\alpha = m\omega/2$, this is

$$\psi_0(x) = \sqrt[4]{\frac{m\omega}{\pi}} \exp\left(-\frac{m\omega}{2}x^2\right) = \sqrt[4]{\frac{2\alpha}{\pi}} \exp\left(-\alpha x^2\right). \tag{22}$$

We will learn a way to get the non-analytic lowest eigenfunction of an arbitrary potential in the next section.

```
1  # prepare array of complex numbers
2  psi = np.zeros((len(x)), dtype=np.complex_)
3
4  alpha = m*w/2.0
5  # fill the array with the lowest analytical eigenfunction
6  psi[:] = np.sqrt(np.sqrt(2.0*alpha/np.pi))*np.exp(-alpha*x**2)
```

After defining the potential and initial wave function, it is a good idea to plot both. The result is shown in figure 7.2 and as expected.

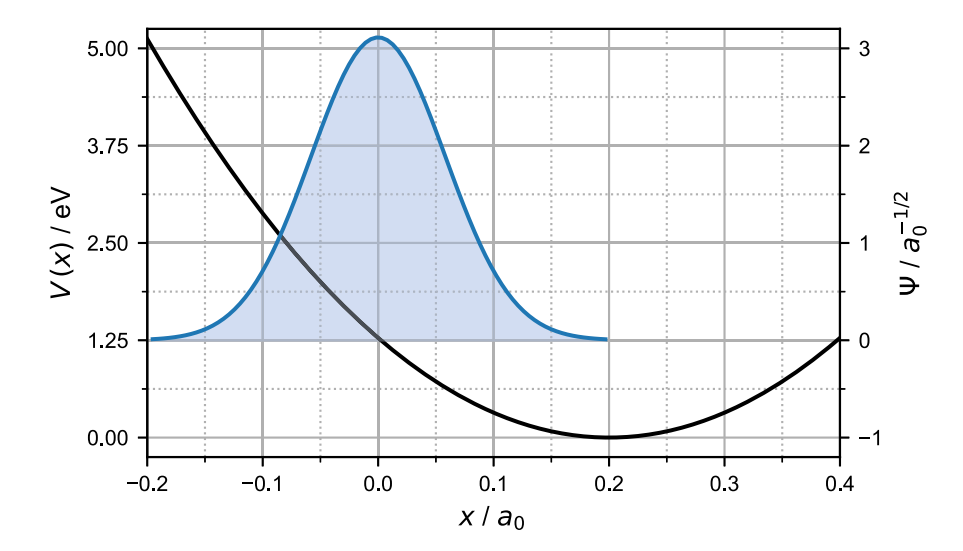


Fig. 7.2 – The harmonic potential and initial wave function on the discretized grid for the C=O model are shown in black and blue, respectively.

Next, we define our simulation time. We want to simulate 60 fs, *i.e.*, a little over three periods, with a time step of 0.005 fs.

```
1 t_f = 60 # final time in fs
2 dt = 0.005 # time step in fs
3 # number of timesteps is final time/timestep
4 # +1 because we want to include the first timestep (0)
5 timesteps = int(np.ceil(t_f/dt))+1
6
7 # and convert to atomic time units for the propagators
8 dt *= fs2atu
```

We also need to define our propagator for the potential energy in position space

```
1 U_V = np.exp(-1j*V*dt/2.0)
```

and for the kinetic energy in momentum space

```
1 U_T = np.exp(-1j*(p**2/(2*m))*dt)
```

And finally, we write our propagation routine

```
for step in range(timesteps):
    psi[:] = U_V[:]*psi[:] # propagate potential energy

psi[:] = np.fft.fft(psi[:]) # transform to momentum space

psi[:] = U_T[:]*psi[:] # propagate kinetic energy

psi[:] = np.fft.ifft(psi[:]) # transform back to position space

psi[:] = U_V[:]*psi[:] # propagate potential energy
```

We should take a look at a few parameters to gauge the reliability of the calculation. These include the norm (or the squared norm) and the total energy of the system. Both should be conserved since we are dealing with a time-independent Hamiltonian and a closed quantum system. Furthermore, the wave function has to be contained in the pre-defined grid at all times. To test this, we can take a look at the grid end populations, *i.e.*, the density of the wave function on the first and last grid points. These grid ends should not (or only marginally) be populated. Otherwise, we might experience an unphysical momentum reversal at the end of the grid. Lastly, it might be a good idea to take a look at the position expectation value.

To understand how we calculate these values, let us recall what to do with a wave function in continuous position space. The density distribution function $P_{\rho}(x)$ is given as

$$P_{\rho}(x) = \psi^*(x)\psi(x) \equiv |\psi\rangle\langle\psi| \tag{23}$$

and the position expectation value can be calculated with $P_{\rho}(x)$ as

$$\langle x \rangle = \int_{-\infty}^{\infty} x P_{\rho}(x) \mathrm{d}x.$$
 (24)

Similarly, the squared norm ρ is the integral over $P_{\rho}(x)$

$$\rho = \int_{-\infty}^{\infty} P_{\rho}(x) dx. \tag{25}$$

The total energy is the expectation value of the Hamiltonian.

$$E = \langle H \rangle = \int_{-\infty}^{\infty} \psi^{*}(x) H(x) \psi(x) dx$$

$$= \int_{-\infty}^{\infty} \psi^{*}(x) T(x) \psi(x) dx + \int_{-\infty}^{\infty} \psi^{*}(x) V(x) \psi(x) dx$$

$$= \int_{-\infty}^{\infty} \psi^{*}(x) T(x) \psi(x) dx + \int_{-\infty}^{\infty} V(x) P_{\rho}(x) dx$$

$$= \left(\int_{-\infty}^{\infty} \phi^{*}(p) \phi(p) dp \right)^{-1} \int_{-\infty}^{\infty} \phi^{*}(p) \frac{p^{2}}{2m} \phi(p) dp + \langle V \rangle$$
(26)

where $\phi(p)$ is the wave function in momentum space.

210

We can now rewrite equations (23)–(26) for a discretized grid $x \equiv \{x_1, x_2, ..., x_N\}$. For this, we introduce the grid density

$$\rho(x_i) = \psi^*(x_i)\psi(x_i)\Delta x \tag{27}$$

to replace the density distribution function. $\rho(x_1)$ and $\rho(x_N)$ are then the grid-end populations.

The position expectation value, equation (24), is written as

$$\langle x \rangle = \sum_{i=1}^{N} x_i \rho(x_i) \tag{28}$$

and the squared norm, equation (25), is

$$\rho = \sum_{i=1}^{N} \rho(x_i). \tag{29}$$

Finally, the energy expectation value, equation (26), becomes

$$E = \langle H \rangle = \left(\sum_{i=1}^{N} \phi^{*}(p_{i})\phi(p_{i})\right)^{-1} \sum_{i=1}^{N} \frac{p_{i}^{2}}{2m} \phi^{*}(p_{i})\phi(p_{i}) + \sum_{i=1}^{N} V(x_{i})\rho(x_{i}).$$
(30)

The results from employing equations (27)–(30) are shown in figure 7.3. Since we are not interested in the total energy at this point but in the energy conservation, we plot the difference to the initial value in μeV . As a rule of thumb, this should be no larger than about 0.01 μeV but this depends on the system under study.

Question 3.2

Before you plot the results: what would you expect the position expectation value to look like? Compare with the actual result.



Answer to question 3.2

The system is an initially displaced harmonic oscillator with a periodicity of $T \approx 19 \,\text{fs}$. One would expect regular oscillations starting at $0.0 \,a_0$, going up to $0.4 \,a_0$ and returning to $0.0 \,a_0$ at multiples of T.



From figure 7.3, we can see problems with the simulation. As mentioned earlier, in "exact" quantum dynamics for closed systems and a time-independent Hamiltonian, both the squared norm and total energy should be conserved. While the squared norm is conserved, the total energy has excursions in regular intervals. The grid ends are also highly populated and indicate that the chosen grid is too small. Lastly, the position expectation value looks regular but has

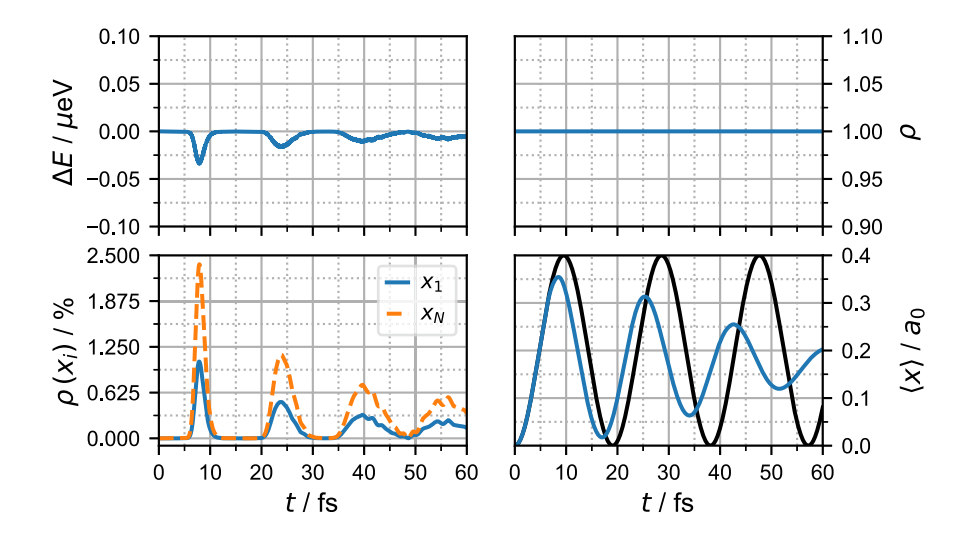


Fig. 7.3 – Different values can be used to gauge the reliability of a simulation. Top left: change in total energy compared to the initial time. Top right: the squared norm of the wave function. Bottom left: population of the first (blue line) and last (orange line) grid point. Bottom right: position expectation value (blue line) and expected result for a regular oscillation (black line).

(i) the wrong periodicity and (ii) experiences damping, which should not happen in the current model.

For this one-dimensional system, we can also plot the wave function at different points in the dynamics. These are shown in figure 7.4. At t=T/3, the wave packet reaches the end of the grid and starts to get compressed. Part of the wave packet is wrapped around to the other side of the grid. This is connected to the Fourier transformations that are used during the propagation. From this point on, the wave packet starts to behave unphysically. One would expect that the absolute value of the wave packet is identical to the initial wave packet at integer multiples of the period for an unperturbed harmonic oscillator. With the current grid, however, the system is not in an unperturbed harmonic potential but a harmonic potential augmented by an infinitely high barrier at the grid edges. This effective potential, together with the potential that was supposed to describe the system, is shown in figure 7.5.

Of course, the parameters were chosen in a way to illustrate the problems that can arise when defining a system for numerical simulations. Larger grids, both in terms of higher grid ends and lower grid spacing, can improve the numerical accuracy but also take more computational effort so that a balance has to be found. In the task, you can repeat the simulations with parameters that are better suited for the system.

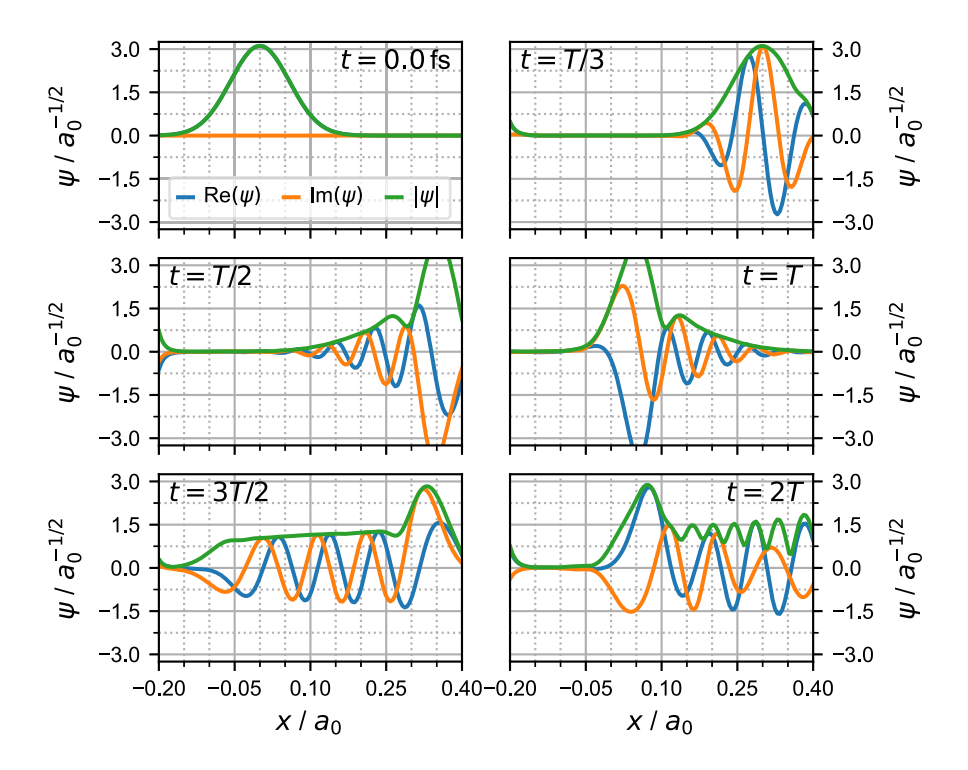
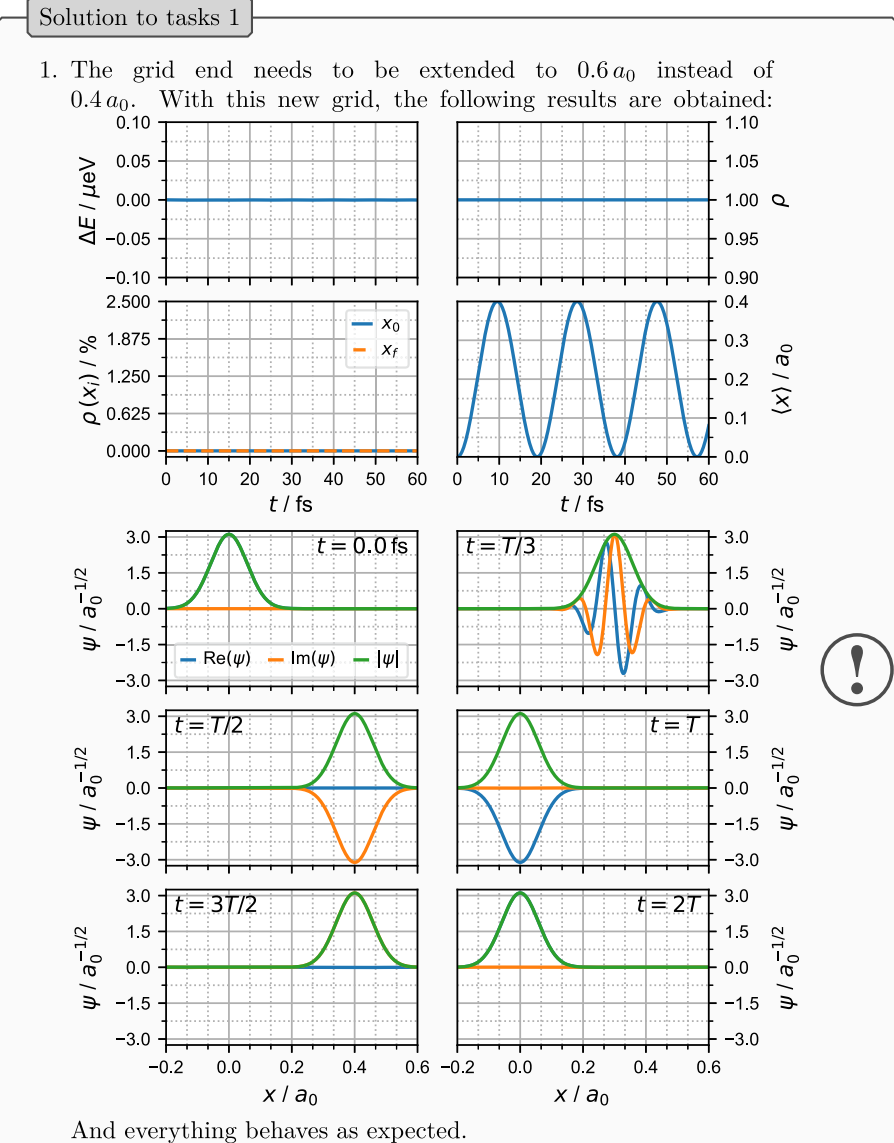


Fig. 7.4 – Real and imaginary parts as well as absolute value of the wave function for the C=O model with the initial grid definition at different times during the dynamics. At t = T/3, the wave packet reaches the grid end.

Tasks 1

- 1. Repeat the calculation with a more sensible definition of the grid and plot the
 - position expectation value
 - total energy
 - norm
 - grid-end populations
 - time-dependent wavefunction
- 2. Play around with the grid (number of grid points, values of grid ends) to understand how they influence the results.





And everything behaves as expected.

2. Larger grid ends with the same number of points corresponds to a larger grid spacing, *i.e.*, lower maximum momentum. Conversely, increasing the number of grid points leads to a lower grid spacing *i.e.*, higher maximum momentum. The more grid points are used the higher the computational effort.

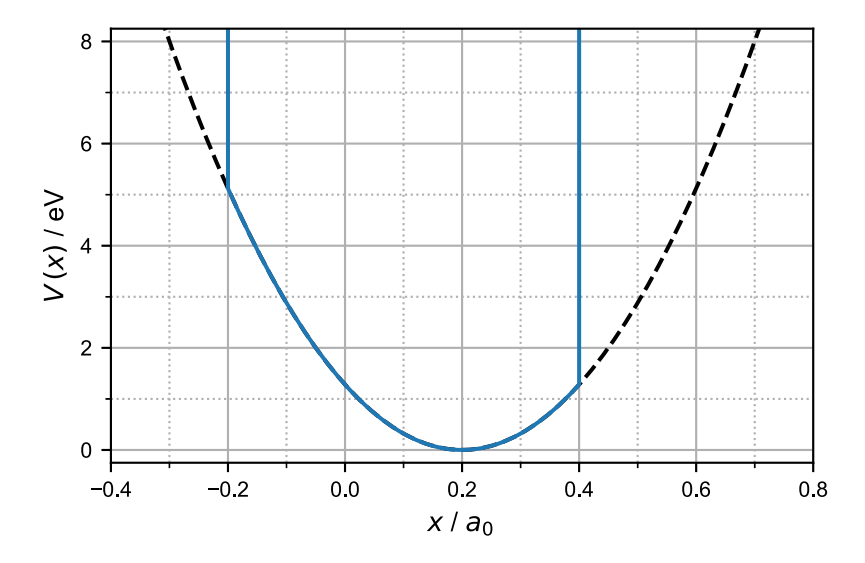


Fig. 7.5 – The dashed black line shows the harmonic potential that was supposed to describe the system. The blue line shows the effective potential that is implemented due to the finite grid.

Conclusion 1

Always check key parameters after a simulation. These include norm, total energy, and grid end populations. If one of them indicates that something might be wrong, carefully check all your input parameters. A common source for errors is the grid, which one would like to make as small as possible. It is always a balance between speed and accuracy!



7.4 Imaginary Time Propagation

In the calculations up to this point, and for the following calculations as well, we assume an instantaneous Franck-Condon excitation. That is, we set the lowest electronic ground state eigenfunction (ground state equilibrium) in the electronic excited state potential(s). So far, we manually set the initial wave function to be the lowest ground state eigenfunction. For a harmonic potential, this is easy to do: the analytic eigenfunctions are known. For potentials that are obtained from electronic structure calculations and fitted to a different functional form, this might not be the case. One possibility is to numerically calculate the eigenfunctions, choose the lowest one, and set it as the initial condition. An alternative approach is imaginary time propagation (ITP). In this approach, an initial guess for the eigenfunction is taken and then propagated in negative imaginary time [17, 18]. This is convenient to set up

with the propagation routines that are used here since it only requires two modifications.

Let us recall the time-dependent Schrödinger equation

$$i\hbar \frac{\partial}{\partial t} \psi(t) = \hat{H}\psi(t)$$
 (1 revisited)

and let us further recall that the formal solution of this equation is

$$\psi(t) = \hat{U}(t, t_0)\psi(t_0)$$
 (2 revisited)

and with a time-independent Hamiltonian the time evolution operator (propagator) is

$$\hat{U}(t, t_0) = \exp\left(-\frac{\mathrm{i}}{\hbar}\hat{H}(t - t_0)\right).$$
 (13 revisited)

We now express our initial wave function $\psi(t_0)$ in the basis of the (time-independent) eigenfunctions φ_n of the Hamiltonian \hat{H} with $\hat{H}\varphi_n = E_n\varphi_n$:

$$\psi(t_0) = \sum_n c_n \varphi_n \tag{31}$$

so that

$$\psi(t) = \hat{U}(t, t_0)\psi(t_0) = \sum_n c_n \exp\left(-\frac{\mathrm{i}(t - t_0)}{\hbar}E_n\right)\varphi_n. \tag{32}$$

By setting $t_0 = 0$ and substituting $t = -i\tau$, we get

$$\tilde{\psi}(\tau) = \sum_{n} c_n \exp\left(-\frac{\tau}{\hbar} E_n\right) \varphi_n. \tag{33}$$

The coefficients of the eigenfunctions are subject to an exponential decay, and the decay constant is the associated eigenenergy. That is, the higher the energy of the eigenfunction, the faster the contribution disappears.

Two points become immediately clear from this:

- 1. Since we actively remove components from the wave function, we need to re-normalize regularly
- 2. In the limit of infinite time, we arrive at the lowest eigenstate that is part of the initial wave function

The first point can be avoided by introducing the (now time-dependent) energy expectation value as a Lagrange parameter in the time-dependent Schrödinger equation [17], but we will not do this in this chapter.

Following the second point, we will only arrive at the lowest eigenfunction if it is not orthogonal to the initial guess. Most likely, the initial wave function will have at least some contribution of the lowest eigenfunction (if not by design or

chance, then by numerical inaccuracies!) so that this is the wave function obtained after the ITP.

A more practical concern is that the ITP could take a long time in cases where the two lowest eigenstates are close in energy. Let us assume that all population is initially distributed in the lowest two eigenfunctions. We further assume that the lowest eigenstate has a reference energy $E_0 = 0$ and the second eigenstate has an energy $E_1 = \Delta E$, so that the wave function is

$$\psi(\tau) = c_0 \varphi_0 + c_1 \exp\left(-\frac{\tau}{\hbar} \Delta E\right) \varphi_1. \tag{34}$$

For a normalized wave function, we have $c_1 = \sqrt{1 - c_0^2}$. The (re-normalized) density in the lowest eigenfunction is then

$$\rho_0(c_0^2, \tau \Delta E/\hbar) \equiv \frac{c_0^2}{c_0^2 + (1 - c_0^2) \exp(-2\frac{\tau}{\hbar} \Delta E)}$$
 (35)

and depends on c_0^2 and $\tau \Delta E/\hbar$. Plotting this shows that $\tau \Delta E/\hbar \approx 10$ is a good rule of thumb so that the wave function is almost completely the lowest eigenfunction, see figure 7.6.

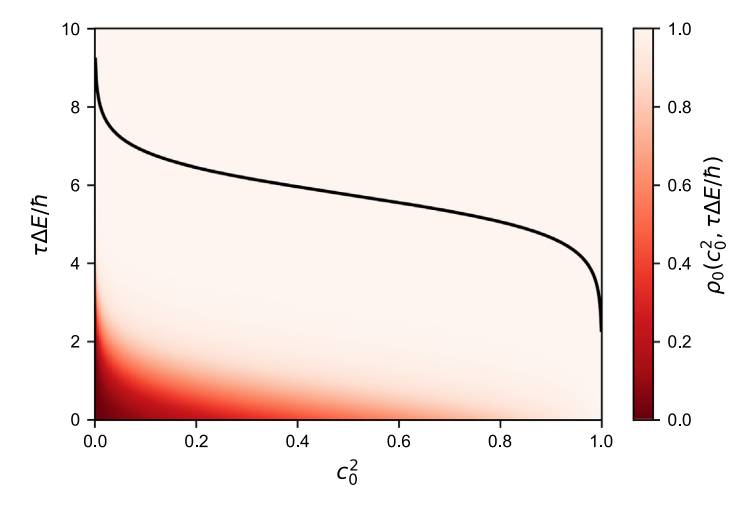


Fig. 7.6 – Population of the lowest eigenfunction for different initial partitions of the two lowest eigenfunctions and different relaxation lengths, following equation (35). The solid black line indicates a 99.999% population of the lowest eigenfunction.

To test the ITP, we now want to describe the carbonyl vibration from the previous section with an anharmonic potential. Following a Taylor expansion of an arbitrary anharmonic potential, this can be done by adding a cubic term (or even higher orders) as an anharmonic correction.

$$V(x) = \frac{1}{2}kx^2 + \gamma x^3. {36}$$

This anharmonic correction can be obtained from electronic structure calculations. For demonstration purposes, we will obtain γ from a third-order Taylor expansion of a Morse potential

$$V_{\text{Morse}}(x) = D\left(1 - \exp\left(-\sqrt{\frac{k}{2D}}x\right)\right)^2 \tag{37}$$

with the same harmonic force constant k as in section 7.3 and a dissociation energy D of 743 kJ mol⁻¹, representative of a carbonyl bond. Note that we could also use the Morse potential directly.

The Morse potential, third-order Taylor expansion, and the harmonic potential from section 7.3 are shown in figure 7.7. As expected, the difference is larger at greater distances from the minimum position.

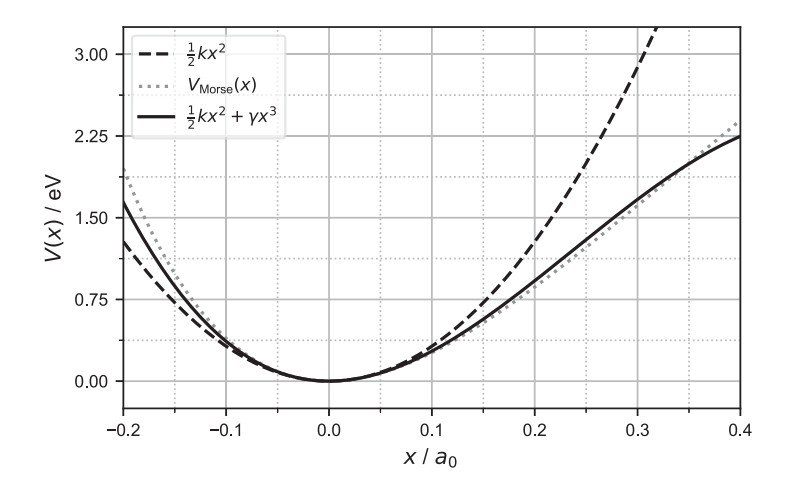


Fig. 7.7 – Harmonic potential from section 7.3 (black dashed line), Morse potential (grey dotted line), and the resulting third-order Taylor expansion (solid line).

We do not know the analytical eigenfunctions for the anharmonic potential we have created. Given the similarity around the minimum, it is probably similar to the harmonic eigenfunction, and this would be a reasonable initial condition for the ITP. We can assume that the lowest vibrational eigenstates are close to the harmonic states so that the energetic difference between the two lowest eigenstates is $\Delta E \approx 1750 \, \mathrm{cm}^{-1}$. Following our rule of thumb, we should thus propagate for 30 fs to ensure that we end in the lowest eigenfunction.

For demonstration and to emphasize the application of ITP to create the lowest eigenfunction of a potential from any guess (as long as it fits on the grid), we will start with a guess that is not close to the lowest eigenfunction. Namely, $\psi(x, t_0) = 2 \exp(-0.5\alpha|x - 0.2|)$. Note that this wave function is neither centered at the minimum of the potential nor is it normalized.

Setting up the numerical propagation is identical to the previous section. The only differences, besides the changed potential and initial wave function, are that the time step is now a negative imaginary number and that during the propagation, the wave function needs to be renormalized:

```
for step in range (timesteps):
2
        # calculate norm
 3
       norm = np.dot(np.conj(psi),psi) *dx
 4
        # renormalize
 5
       psi[:] /= np.sqrt(norm)
 6
7
       psi[:] = U V[:]*psi[:] # propagate potential energy
 8
 9
       psi[:] = np.fft.fft(psi[:]) # transform to momentum space
10
       psi[:] = U T[:]*psi[:] # propagate kinetic energy
11
       psi[:] = np.fft.ifft(psi[:]) # transform back to position space
12
13
       psi[:] = U_V[:]*psi[:] # propagate potential energy
```

Here, the renormalization is done in every time step, but this could also only be done every *n*th step to save on computational costs.

The initial wave function, the anharmonic potential, and the resulting wave function after ITP are shown in figure 7.8. This wave function could now be used to create a doorway state, like in the previous section.

ITP can also be used for other applications. It can be used as part of the calculation of thermalized systems, where an ensemble of initial wave functions with random phases is first propagated in imaginary time for $\tau = \hbar/(2k_BT)$ to create initial states for the dynamics [19, 20]. Another application is in the simulation of solids via the quantum diffusion Monte Carlo approach [21].

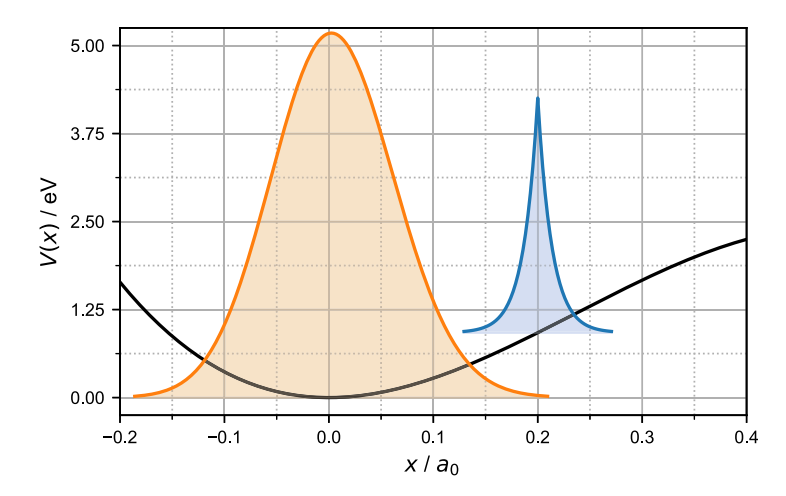


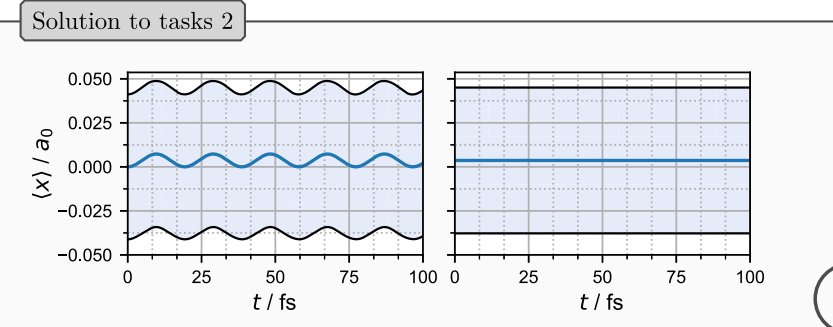
Fig. 7.8 – Anharmonic potential (black), initial guess for the wave function (blue), and eigenfunction after ITP (orange).

Tasks 2

 Take the anharmonic potential and put a reasonable guess for the wave function as the initial condition. Propagate the wave function and plot the position expectation value and standard deviation.



2. Now do an imaginary time propagation of your guess first and then propagate the resulting wave function. How do the position expectation value and standard deviation look?





The zeroth order guess of taking the lowest eigenfunction of the harmonic potential (left hand side) shows oscillations for the position expectation value. The standard deviation (shaded blue area) stays constant, i.e., the shape and width of the guess are already correct. When doing an imaginary time propagation first (right-hand side), neither the position expectation value nor the standard deviation change over time. This shows that an eigenstate of the potential was created.

Conclusion 2

Imaginary time propagations are propagations in negative imaginary time. They yield the lowest eigenfunction of the Hamiltonian (that is part of the initial guess) and can be used to prepare initial conditions.



7.5 Multiple Electronic States

So far, we have been looking at systems with only one electronic state. Often, when going to larger molecules or materials, multiple electronic states are of interest, so we want to extend our computational treatment to reflect this. Adding more electronic states makes the propagation more demanding, both in terms of setting up the calculations as well as running them.

For calculations with multiple electronic states, the system can be described in an adiabatic or (quasi-)diabatic basis. For this chapter, it is sufficient to distinguish the two by the type of coupling between the electronic states (assuming that the states *are* coupled):

- in the adiabatic basis, the matrix description of \hat{V} is diagonal; that of \hat{T} is not
- ullet in the diabatic basis, the matrix description of \hat{T} is diagonal; that of \hat{V} is not

In practice, one often favours the diabatic basis for quantum dynamical simulations as the adiabatic representation can become numerically unstable for high-dimensional non-adiabatic quantum dynamics. A reason for this is the divergence of the derivative (kinematic) type couplings when the potential energy surfaces of different states come close. Another advantage of the diabatic representation is that the states have a well-defined electronic character. With this in mind, we will also use the diabatic representation in this chapter. The adiabatic and diabatic representation are more extensively discussed in chapter 2.

To set up a simulation with multiple electronic states, the potential on each grid point needs to be described by a matrix rather than a single point. For the propagators this means that we need to calculate the exponential of a matrix. For this, we can either use a perturbative approach (cf. equation (16)), or we can transform to the eigenbasis, calculate the exponential and transform back. For accuracy and since we will need the eigenbasis for other things as well, we will use the latter approach in this chapter.

7.5.1 Density Matrix

When dealing with multiple electronic states, the wave function can be written as the sum of products of a vibrational and an electronic part

$$\Psi(x) = \sum_{n=1}^{M} c_n \psi_n(x) |n\rangle \tag{38}$$

where $|n\rangle$ denotes the electronic state and c_n is an expansion coefficient. From equation (38), we can, in analogy to equation (23) for single-state wave functions, write the density distribution function for this multi-state wave function as the density tensor

$$P_{\rho}(x) = |\Psi\rangle\langle\Psi| = \sum_{n,m}^{M} c_n \psi_n(x) |n\rangle\langle m| c_m^* \psi_m^*(x) = \sum_{n,m}^{M} \psi_m^*(x) \psi_n(x) c_m^* c_n |n\rangle\langle m|. \quad (39)$$

We can obtain the reduced electronic density matrix from the density tensor as

$$\rho = \operatorname{Tr}_x \{ P_{\rho}(x) \} = \sum_{n,m} c_m^* c_n |n\rangle \langle m| = \sum_{n,m} \rho_{nm} |n\rangle \langle m|$$
(40)

where Tr_x is the trace over the vibrational part. The trace of ρ is the squared norm.

So far, we have been looking at the density matrix for a single multi-state wave function, i.e., a pure state. It is straightforward to extend the density matrix picture to an ensemble of N multi-state wave functions, a so-called mixed state, as

$$P_{\rho}^{\text{mixed}} = \sum_{n=1}^{N} p_n |\Psi_n\rangle \langle \Psi_n| = \sum_{n=1}^{N} p_n P_{\rho,n}$$
(41)

where p_n is the probability that the system is in the state described by wave function $|\Psi_n\rangle$. This extension makes it convenient to use the density matrix picture to describe ensembles, e.g., to account for inhomogeneous broadening, dephasing, or temperature effects. The main drawback of density matrices is that the propagation is more cumbersome than the propagation of wave functions. An easy way to think about this is with the number of elements in a matrix. An electronic wave function with 20 states would have 20 entries in the vector representation. The corresponding density matrix has 400 elements. This enables the use of computationally more demanding Hamiltonians or the treatment of larger systems within the wave function picture.

For this chapter, we will stay in the wave function picture for the calculation of dynamics but use the reduced electronic density matrix to analyse the results. Complementary, chapter 8 uses the density matrix picture for the calculation of (non-linear) spectroscopic signals.

Taking a closer look at the reduced electronic density matrix (equation (40)) for a two-state system

$$\rho = \sum_{n,m}^{2} c_{m}^{*} c_{n} |n\rangle\langle m| = \begin{pmatrix} |c_{1}|^{2} & c_{1} c_{2}^{*} \\ c_{1}^{*} c_{2} & |c_{2}|^{2} \end{pmatrix}$$
(42)

we can identify the diagonal elements as the state populations. The off-diagonal elements are coherences and can be used to differentiate a coherent superposition from a statistical mixture. To illustrate this point, let us take a look at the difference between the reduced electronic density matrix for a coherent superposition of purely electronic wave functions and the one for a corresponding mixed state. We start with the coherent superposition

$$|\Psi\rangle = \frac{1}{\sqrt{2}}(|1\rangle + |2\rangle). \tag{43}$$

By employing equation (40), we can calculate the reduced electronic density matrix as

$$\rho = \sum_{n=1}^{2} \frac{1}{2} |n\rangle\langle m| = \begin{pmatrix} 0.5 & 0.5 \\ 0.5 & 0.5 \end{pmatrix}, \tag{44}$$

where we can see the coherent nature reflected in the non-zero off-diagonal elements.

Conversely, the mixed state is a 1:1 mixture of wave functions that are completely located on either state $|1\rangle$ or state $|2\rangle$, *i.e.*, we have $|\Psi_1\rangle = |1\rangle$ and

 $|\Psi_2\rangle = |2\rangle$ with $p_1 = p_2 = 0.5$. Following equations (40) and (41), the density matrices are

$$\rho_1 = \begin{pmatrix} 1.0 & 0.0 \\ 0.0 & 0.0 \end{pmatrix}, \quad \rho_2 = \begin{pmatrix} 0.0 & 0.0 \\ 0.0 & 1.0 \end{pmatrix} \Rightarrow \rho^{\text{mixed}} = \begin{pmatrix} 0.5 & 0.0 \\ 0.0 & 0.5 \end{pmatrix}. \tag{45}$$

As we can see, the off-diagonal elements are strictly zero for a statistical mixture. As a side note, the coherence of a pure state also vanishes when all population is in one state; since then, it is no longer a coherent superposition of states.

7.6 Autocorrelation Function

The autocorrelation function C(t) of the excited state wave function $|\Psi\rangle$ is given as

$$C(t) = \langle \Psi(0) | \Psi(t) \rangle \tag{46}$$

and is related to the first-order polarization and thus the linear absorption spectrum.

To understand this relation, we will start with the power spectrum $\sigma(E)$ of the system:

$$\sigma(E) = \langle \Psi | \delta(E - \hat{H}) | \Psi \rangle. \tag{47}$$

If the eigenfunctions φ_n of the system Hamiltonian \hat{H} and the corresponding energies E_n ($\hat{H}\varphi_n = E_n\varphi_n$) are known, they can be used as a basis, so that

$$|\Psi\rangle = \sum_{n} c_n |\varphi_n\rangle \tag{48}$$

with $c_n = \langle \varphi_n | \Psi \rangle$. With the basis of eigenfunctions, we also have the completeness relation

$$\hat{1} = \sum_{n} |\varphi_n\rangle\langle\varphi_n| \tag{49}$$

and the power spectrum of the system can be obtained by inserting equation (49) into equation (47):

$$\sigma(E) = \sum_{n,m} \langle \Psi | \varphi_n \rangle \langle \varphi_n | \delta(E - \hat{H}) | \varphi_m \rangle \langle \varphi_m | \Psi \rangle$$

$$= \sum_{n,m} c_n^* c_m \delta(E - E_m) \delta_{n,m}$$

$$= \sum_n |c_n|^2 \delta(E - E_n).$$
(50)

The power spectrum is thus peaked at the eigenenergies of the system. The peaks are weighted by the contribution of the corresponding eigenfunction to the total wave function.

Rather than projecting onto all eigenfunctions and calculating the corresponding eigenenergies, we can employ the Fourier representation of the δ function

$$\delta(E - \hat{H}) = \frac{1}{2\pi} \int_{-\infty}^{\infty} \exp\left(\frac{\mathrm{i}}{\hbar} (E - \hat{H})t\right) \mathrm{d}t \tag{51}$$

to get

$$\sigma(E) = \frac{1}{2\pi} \int_{-\infty}^{\infty} \left\langle \Psi \middle| \exp\left(\frac{i}{\hbar} (E - \hat{H})t\right) \middle| \Psi \right\rangle dt$$

$$= \frac{1}{2\pi} \int_{-\infty}^{\infty} \exp\left(\frac{i}{\hbar} Et\right) \left\langle \Psi \middle| \exp\left(-\frac{i}{\hbar} \hat{H} t\right) \middle| \Psi \right\rangle dt$$

$$= \frac{1}{2\pi} \int_{-\infty}^{\infty} \exp\left(\frac{i}{\hbar} Et\right) \left\langle \Psi \middle| \hat{U}(t, 0) \middle| \Psi \right\rangle dt$$

$$= \frac{1}{2\pi} \int_{-\infty}^{\infty} \exp\left(\frac{i}{\hbar} Et\right) \left\langle \Psi(0) \middle| \Psi(t) \right\rangle dt$$

$$= \frac{1}{2\pi} \int_{-\infty}^{\infty} \exp\left(\frac{i}{\hbar} Et\right) C(t) dt.$$
(52)

The power spectrum can thus also be obtained from a Fourier transformation of the autocorrelation function [2, 17, 22].

We can exploit some properties of the Hamiltonian and initial wave function to facilitate some calculations.

For a hermitian Hamiltonian, integration over negative time can be avoided since [17]

$$C(-t) = \left\langle \Psi \middle| \exp\left(\frac{\mathbf{i}}{\hbar} \hat{H} t\right) \middle| \Psi \right\rangle$$

$$= \left\langle \exp\left(-\frac{\mathbf{i}}{\hbar} \hat{H} t\right) \Psi \middle| \Psi \right\rangle$$

$$= \left\langle \Psi \middle| \exp\left(-\frac{\mathbf{i}}{\hbar} \hat{H} t\right) \middle| \Psi \right\rangle^*$$

$$= C^*(t)$$
(53)

and thus

$$\int_{-\infty}^{0} \exp\left(\frac{\mathrm{i}}{\hbar} E t\right) C(t) \mathrm{d}t = \int_{0}^{\infty} \exp\left(-\frac{\mathrm{i}}{\hbar} E t\right) C(-t) \mathrm{d}t = \int_{0}^{\infty} \left(\exp\left(\frac{\mathrm{i}}{\hbar} E t\right) C(t)\right)^{*} \mathrm{d}t$$
(54)

so that

$$\sigma(E) = \frac{1}{2\pi} \int_{-\infty}^{0} \exp\left(\frac{\mathrm{i}}{\hbar} E t\right) C(t) dt + \frac{1}{2\pi} \int_{0}^{\infty} \exp\left(\frac{\mathrm{i}}{\hbar} E t\right) C(t) dt$$

$$= \frac{1}{2\pi} \int_{0}^{\infty} \left(\left(\exp\left(\frac{\mathrm{i}}{\hbar} E t\right) C(t) \right)^{*} + \exp\left(\frac{\mathrm{i}}{\hbar} E t\right) C(t) dt \right)$$

$$= \frac{1}{\pi} \operatorname{Re} \int_{0}^{\infty} \exp\left(\frac{\mathrm{i}}{\hbar} E t\right) C(t) dt.$$
(55)

Since we write σ as a function of the energy E in equation (55) it might seem like we can arbitrarily choose the energy resolution of the power spectrum. This is, however,

not true as the autocorrelation function and the power spectrum are linked with a Fourier transformation. Because of this, the resolution (energy spacing) in the power spectrum is defined *via* the highest time in the autocorrelation function and the highest energy *via* the time step. Usually, we want a small energy spacing to better resolve the spectrum, but this would require a longer simulation to get to higher times for the autocorrelation function. However, we can exploit some properties of the autocorrelation function to trade a higher time (better energy resolution) for a higher time step (lower maximal energy):

$$C(t) = \langle \Psi(0) | \Psi(t) \rangle$$

$$= \left\langle \Psi(0) \left| \exp\left(-\frac{i}{\hbar} \hat{H} t\right) \right| \Psi(0) \right\rangle$$

$$= \left\langle \left(\exp\left(-\frac{i}{\hbar} \hat{H}^{\dagger *} \frac{t}{2}\right) \Psi^{*}(0) \right)^{*} \left| \exp\left(-\frac{i}{\hbar} \hat{H} \frac{t}{2}\right) \Psi(0) \right\rangle.$$
(56)

If the initial state $\Psi(0)$ is real and the Hamiltonian is symmetric, then it follows that [17, 23, 24]

$$C(t) = \langle \Psi^*(t/2) | \Psi(t/2) \rangle. \tag{57}$$

With this, we can double our maximal time but also double our time step in the autocorrelation function. Equation (57) is the one that is used in this chapter to calculate the autocorrelation function.

There are two things that we still need to consider:

- 1. From the Fourier transformation, we would get a stick spectrum (assuming C(t) is known for every possible time)
- 2. Unless we have a dissociating state where the autocorrelation function decays to zero at finite time, we introduce artifacts if we do not propagate for infinitely long times

Let us start with the first point. A more realistic line shape, rather than a stick spectrum, can be obtained by taking the finite lifetime of excited states into account. Rather than modelling this lifetime explicitly, we multiply the autocorrelation function with an exponential decay function f(t). The Fourier transformation turns this into a convolution of the power spectrum with a Lorentzian. In this chapter, we use

$$f(t) = \exp\left(-\frac{t}{\tau}\right) \tag{58}$$

where τ is the chosen lifetime of the excited state.

As for the second point, we would need to propagate to infinity, following equation (55). If we have a dissociating state, the autocorrelation function will decrease to zero over time and stay there. As such, the autocorrelation function does not change anymore after this point and we do not introduce any errors by stopping the calculation at this point. In a bound state, however, we will have recurrences of the autocorrelation function. If we arbitrarily stop the propagation at some point t_s (other than infinity) we convolute the power spectrum with a resolution function [17].

This leads to a broadening of the signal and spurious oscillating structures in the spectrum (Gibbs phenomenon).

To remedy this, we can multiply our autocorrelation function with a window or filter function g(t). We require for this function that

i.
$$0 \le g(t) \le 1$$

ii.
$$g(0) = 1$$

iii.
$$q(t_s) = 0$$

There are numerous window functions available, but in this chapter, we will stick to the cosine window function

$$g(t) = \cos\left(\frac{\pi t}{2t_s}\right). \tag{59}$$

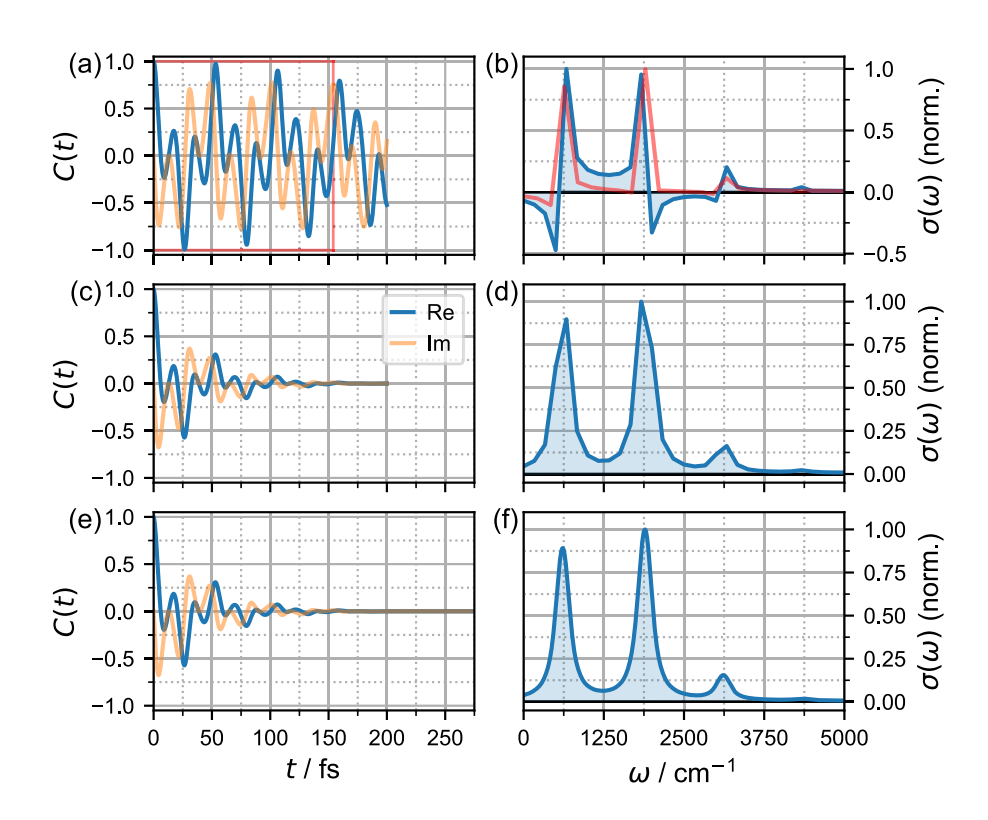


Fig. 7.9 – The left-hand side shows the autocorrelation function, and the right-hand side shows the corresponding normalized power spectrum. (a) and (b) directly from the dynamics until 200 fs. Stopping at this arbitrary point leads to Fourier artifacts in the spectrum. Stopping closer to a multiple of the apparent period of the autocorrelation function (red box in (a)) leads to a spectrum with less artefacts (red line in (b)). (c) and (d) when employing an exponential damping with $\tau = 50$ fs and cosine window function. (e) and (f) with added zero-padding after 200 fs until 2 ps.

For this function, we take advantage of the fact that $t \in [0, t_s]$. In general, one would need to take care of the sign of t and values outside this interval. This can be done by, e.g., taking the absolute value of t or using a Heaviside stepfunction.

Employing such a window function also leads to a line broadening in the spectrum and in turn f(t) can also be seen as a window function.

After employing the window function, we can employ another technique for discrete Fourier transformations: zero-padding. The resolution (energy spacing) in the power spectrum is defined by the maximum time in the autocorrelation function due to the Fourier relation. To increase this resolution, we would need to calculate the dynamics for longer times, which can be prohibitive for demanding calculations. By employing a window function, we ensure that the autocorrelation function is zero at the final time. A common technique is then to add zeros to the end to increase the final time. This padding with zeros leads to an increased resolution but should only be applied when the spectrum is reasonably well-defined without zero-padding. When solving equation (55), this zero-padding can be done by adding zeros to the end of the autocorrelation function or simply by defining the energy axis independently of the underlying Fourier relation to the time axis. A comparison of the autocorrelation functions and corresponding spectra directly from the dynamics, with line broadening and window function applied and with added zero-padding, is shown in figure 7.9.

7.7 Excitonic Dimer

To illustrate the application of reduced electronic density matrices and autocorrelation functions, we will take a look at an excitonic dimer. The system, which is also discussed in chapters 4 and 8, is based on the squaraine dimers studied in Ref. [25]. Figure 7.10 shows the monomers and connectors that are used in this chapter. At first, connector I will be considered, *i.e.*, two uncoupled monomers. Following that, the two monomers will be coupled *via* connector II. In the excitonic dimer model, the connector is realized by the strength of the electronic coupling.

The excitonic dimer model features two singly excited electronic states corresponding to electronic excitations localized on monomer A or B. The excitation energies of the monomers are $E_A = 15240 \,\mathrm{cm}^{-1}$ and $E_B = 13950 \,\mathrm{cm}^{-1}$, respectively. Between the two electronic states is a constant coupling V_1 , which depends on how the two monomers are connected.

A single vibrational degree of freedom with a frequency $\omega = 1220\,\mathrm{cm}^{-1}$ is coupled to both states in the same way. The excited state potential of this vibrational degree of freedom has a Huang-Rhys factor S=0.15 from which the horizontal shift x_0 can be calculated.

The total Hamiltonian is then

$$H = \sum_{n} \left(-\frac{p^2}{2m} + \frac{1}{2} m\omega^2 (x - x_0)^2 + E_n \right) |n\rangle\langle n| + \sum_{n \neq m} V_1 |n\rangle\langle m|$$
 (60)

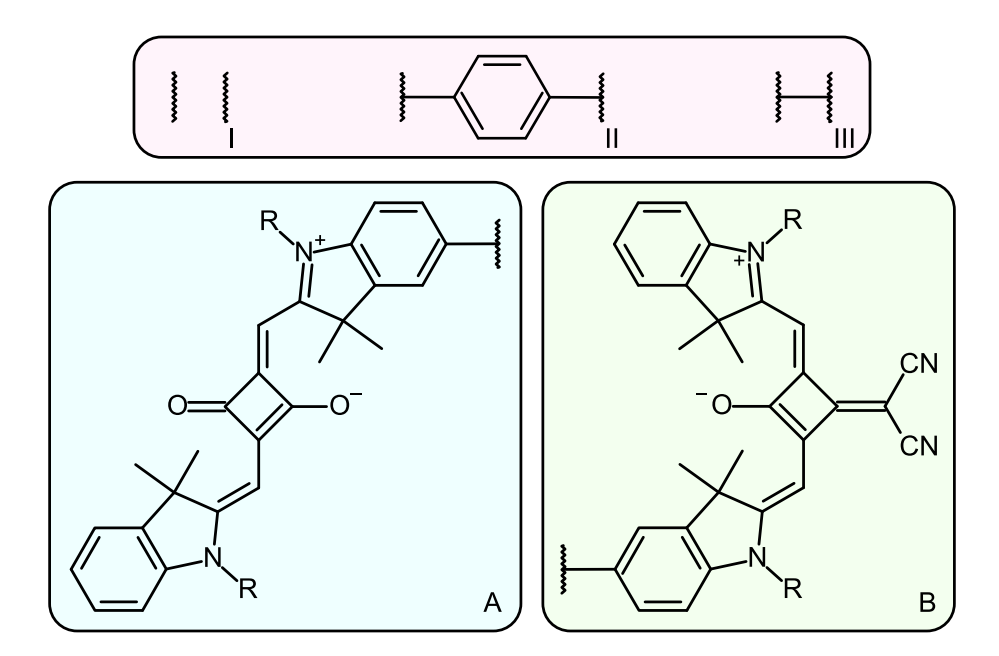


Fig. 7.10 – Monomers A and B form the squaraine dimer with one of the three connectors I, II, or III. The connection point is indicated by squiggly lines. With connector I, the two monomers are uncoupled.

or explicitly in matrix notation

$$H = \left(-\frac{p^2}{2m} + \frac{1}{2}m\omega^2(x - x_0)^2\right) \begin{pmatrix} 1 & 0\\ 0 & 1 \end{pmatrix} + \begin{pmatrix} E_B & V_1\\ V_1 & E_A \end{pmatrix}$$
(61)

where we sorted the diabatic states by energy. Note that we only use the notion of coupled diabatic states for convenience, as it makes it easy to define the system in terms of monomers and a (swappable) linker. In fact, the diabatic states can be transformed into adiabatic states that are uncoupled exactly independently of the coordinate x so that there is no need to work with coupled electronic states. As this is not usually the case, we will continue with the diabatic description for demonstration.

Equation (60) can be rewritten with creation and annihilation operators for the electronic part with

$$a_n^{\dagger} a_n \equiv |n\rangle\langle n| a_n^{\dagger} a_m \equiv |n\rangle\langle m|$$
 (62)

where a_n^{\dagger} is the creation operator of the excited state $|n\rangle$ and a_n the corresponding annihilation operator. Inserting this into equation (60) gives

$$H = \sum_{n} \left(-\frac{p^2}{2m} + \frac{1}{2} m\omega^2 (x - x_0)^2 + E_n \right) a_n^{\dagger} a_n + \sum_{n \neq m} V_1 a_n^{\dagger} a_m$$
 (63)

which can be further rewritten into

$$H = \sum_{n} \left(-\frac{p^2}{2m} + \frac{1}{2} m\omega^2 x^2 + d\omega^2 x + E_{\text{off}} \right) a_n^{\dagger} a_n + \sum_{n \neq m} V_1 a_n^{\dagger} a_m$$
 (64)

with $d = -mx_0$ and $E_{\text{off}} = 0.5m\omega^2 x_0^2 + E_n$. Equation (64) is the form used in chapter 8. The model is sketched in figure 7.11.

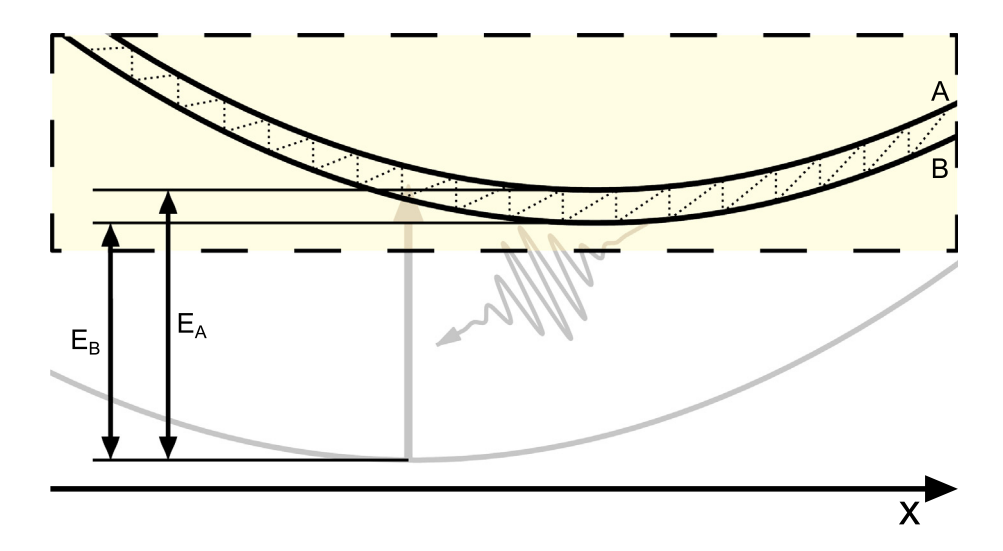


Fig. 7.11 – Sketch of the excitonic dimer model. The box marks the active part of the system that is simulated. The initial photoexcitation is indicated but not part of the simulation. The dotted line shows a potential coupling between the two surfaces for monomers A and B. The excitation energies of the monomers are indicated by black arrows.

To implement the Hamiltonian, we need to connect the Huang-Rhys factor S to the horizontal shift x_0 . For this, we use that both are connected to the reorganization energy λ . The reorganization energy is the difference in energy between the initial energy after Franck-Condon excitation and the minimum of the potential. For our Hamiltonian, this is

$$\lambda = \frac{1}{2}m\omega^2(0 - x_0)^2 - \frac{1}{2}m\omega^2(x_0 - x_0) = \frac{1}{2}m\omega^2x_0^2.$$
 (65)

The Huang-Rhys factor is connected to the reorganization energy as $\lambda = \omega S$, in atomic units. With this,

$$x_0 = \sqrt{\frac{2S}{m\omega}}. (66)$$

The only thing left to define is the mass m, which is unknown. We can estimate the mass or circumvent this by going to mass-weighted coordinates. We will do the latter

in this chapter. For this, we substitute $\sqrt{m}x \to x$. In practice, this is equivalent to setting m = 1.0 in atomic units.

7.7.1 Uncoupled Dimer

For the implementation, we will first use connector I, *i.e.*, the monomers are uncoupled. This corresponds to $V_1 = 0.0$.

```
1  # define the parameters as given in the text and convert to atomic
    units
2  w = 1220.0*invcm2eV*eV2Eh # frequency of vibrational mode
3  eA = 15240.0*invcm2eV*eV2Eh # excitation energy monomer A
4  eB = 13950.0*invcm2eV*eV2Eh # excitation energy monomer B
5  m = 1.0 # mass weighted coordinates -> mass is 1
6  S = 0.15 # Huang-Rhys factor
7  x0 = np.sqrt(2.0*S/(m*w)) # horizontal shift
8  V1 = 0.0 # electronic coupling -> uncoupled monomers
9
10 # also define the number of states
11 num_states = 2
```

The grid points will take on large values, since we are in mass-weighted coordinates.

```
1 # define the position grid of the simulation
2 N = 256 # number of grid points
3 x = np.linspace(-120.0, 120.0, N) # grid
4 dx = np.abs(x[1]-x[0]) # grid spacing
```

The momentum grid is again the Fourier transform of the position grid.

```
1  # define the corresponding momentum grid via Fourier transformation
2  p = np.fft.fftfreq(N, dx) * 2 * np.pi
```

So far this is the same as for a one-state system. The first change comes with the definition of the system potential. Rather than single points, we need to define a potential matrix for each grid point. Furthermore, we also want to calculate the eigenvalues and eigenvectors of these matrices to later build the propagator of the potential.

```
1  # define the excited state potential:
2  # a num_states X num_states matrix for each point in x
3  V = np.zeros((len(x), num_states, num_states))
4
5  # make empty lists for eigenvalues (from _D_iagonalization)
6  D = np.zeros((len(x), num_states), dtype=np.complex_)
7  # and eigenvectors (_U_nitary transformation matrix)
8  U = np.zeros((len(x), num_states, num_states), dtype=np.complex_)
9
```

```
10 # since it is a 2x2 matrix, define all elements by hand
11 # sort by energy, i.e., first monomer B, then A
12 pot[:,0,0] = 0.5*m*w**2*(x-x0)**2 + eB
13 pot[:,1,1] = 0.5*m*w**2*(x-x0)**2 + eA
14 pot[:,0,1] = pot[:,1,0] = V1
15
16 # calculate eigenvalues and eigenvectors for every grid point
17 for grid_idx in range(len(x)):
18 D[grid_idx], U[grid_idx] = scla.eigh(V[grid_idx,:,:])
```

Remember that the coupling V_1 is currently set to zero. This essentially means that we propagate two independent states that are still described by one wave function.

Now we define the initial wave function, centered at 0, as the analytic first eigenfunction of a quantum harmonic oscillator with correct mass and frequency (equation (22)). We also need to define the initial populations, from which we calculate the expansion coefficients of the wave function, cf equation (38).

```
# prepare array of complex numbers
 1
   # now a vector for each grid point
   psi = np.zeros((len(x), num states), dtype=np.complex )
 4
 5 alpha = m*w/2.0
 6 # create ground state wave function
   # this is the lowest analytical eigenfunction of the HO
 8
   psi 0 = \text{np.sqrt}(\text{np.sqrt}(2.0*\text{alpha/np.pi}))*\text{np.exp}(-\text{alpha*}(x)**2)
 9
10 # create array of initial populations
11 pop 0 = np.zeros(num states)
12 # set first population to 50%
13 pop 0[0] = 0.5
14 # second population is 100% minus first population
15 pop 0[1] = 1.0-pop 0[0] #0.5
16
17 # make sure that populations are normalized
18 pop 0 /= np.sum(pop 0)
19
20 # set initial wavefunction as ground state wave function
21 # weighted by square root of initial population of states
22 psi[:,0] = psi 0.copy()*np.sqrt(pop 0[0])
23 psi[:,1] = psi 0.copy()*np.sqrt(pop 0[1])
```

Next, we define our simulation time. We want to simulate 100 fs with a time step of 0.005 fs.

```
1 t_f = 100 # final time in fs
2 dt = 0.005 # time step in fs
3 # number of timesteps is final time/timestep
4 # +1 because we want to include the first timestep (0)
5 timesteps = int(np.ceil(t_f/dt))+1
```

```
6
7 # and convert to atomic time units for the propagators
8 dt *= fs2atu
```

We also want to calculate the reduced electronic density matrix and the autocorrelation function. To reduce the computational cost, we only do so every 20th time step, *i.e.*, every 0.1 fs.

```
# every 20th step, to store results
2
   writeInterval = 20
 3
 4
   # define a 'time grid' for the timesteps when we store results
 5
   # this is useful for plotting
 6 t axis = np.arange(0, timesteps*np.abs(dt), np.abs(dt)*
   writeInterval)
7
   # number of times we store results; to create lists of values to store
8
   tpoints = len(t axis)
 9
10
   # define empty lists for reduced electronic density matrix
   densmat = np.zeros((tpoints, num states, num states), dtype=np.
   complex )
   # and for autocorrelation function
12
   auto = np.zeros((tpoints, num states), dtype=np.complex )
```

To define the propagator for the potential energy, we calculate the exponential of the matrix in the eigenbasis and transform it back. Note that this is not strictly necessary right now, since the electronic coupling is set to zero. We are thus already in the eigenbasis. But since we will include electronic coupling later on, it makes sense to write the propagator with the transformation in mind. The propagator is thus

$$\hat{U}_{V}(\Delta t/2) = \underline{U} \exp\left(-i\underline{D}\frac{\Delta t}{2\hbar}\right)\underline{U}^{\dagger}$$
(67)

with

$$\underline{VU} = \underline{UD}. \tag{68}$$

 \underline{D} is a matrix that has the eigenvalues of the potential matrix \underline{V} as diagonal entries. \underline{U} is the corresponding eigenvector matrix and describes the unitary transformation to the eigenbasis. For the implementation, we need to do this for every grid point.

```
1  # prepare an array for the potential energy propagator.
2  # dimensions are: 1. number of grid points, 2./3. number of states
3  # data type should be complex
4  U_V = np.zeros((len(x), len(D[0]), len(D[0])), dtype=np.complex_)
5
6  # loop over all grid points
7  for grid_idx in range(len(x)):
8  # exponential of potential energy matrix in eigenbasis
9  diag pot = np.diag(np.exp(-1.0j*D[grid idx]*dt/2.0))
```

```
# transform back to get propagator
U_V[grid_idx,:,:] = np.matmul(U[grid_idx], np.matmul
(diag_pot, np.conj(U[grid_idx]).T))
```

The propagator for the kinetic energy is unchanged compared to the case with only one electronic state since the kinetic energy operator is identical for all electronic states.

```
1 U_T = np.exp(-1j*(p**2/(2*m))*dt)
```

Finally, we write our propagation routine

```
for step in range (timesteps):
 2
        # every nth step, store results
 3
       if step%writeInternal==0:
 4
          # print out progress
 5
          print("Step {:d} of {:d}".format(step, timesteps), end="\r")
 6
          # calculate relative time step for storing results
 7
          rel step = step//writeInterval
 8
 9
          # prepare list for density tensor
10
          densTensor = np.zeros((len(x), num states, num states),
    dtype=np.complex )
11
          # go through all grid points and calculate outer product of psi
        for grid idx in range (len (x)):
12
            densTensor[grid idx] = np.outer(np.conj(psi[grid idx]),
13
    psi[grid idx])
14
        # trace out grid for reduced electronic density matrix
15
       densmat[rel step] = np.sum(densTensor, axis=0)*dx
16
17
        # go through all states and calculate autocorrelation function
18
       for n in range (num states):
19
           auto[rel step, n] = np.dot(psi[:,n], psi[:,n])*dx
20
21
     # on each grid point, matrix product for potential energy
    propagator
22
    for grid idx in range (len (x)):
23
       psi[grid idx,:] = np.matmul(U V[grid idx,:,:], psi
    [grid idx,:])
24
     # element wise multiplication of kinetic energy propagator
25
26
     # for all states identical
27
     psi[:,:] = np.fft.fft(psi[:,:], axis=0)
28
    psi[:,:] = U T[:,np.newaxis]*psi[:,:]
29
    psi[:,:] = np.fft.ifft(psi[:,:], axis=0)
30
31
     # on each grid point, matrix product for potential energy propagator
32
    for grid idx in range (len(x)):
33
       psi[grid idx,:] = np.matmul(U V[grid idx,:,:], psi
    [grid idx,:])
```

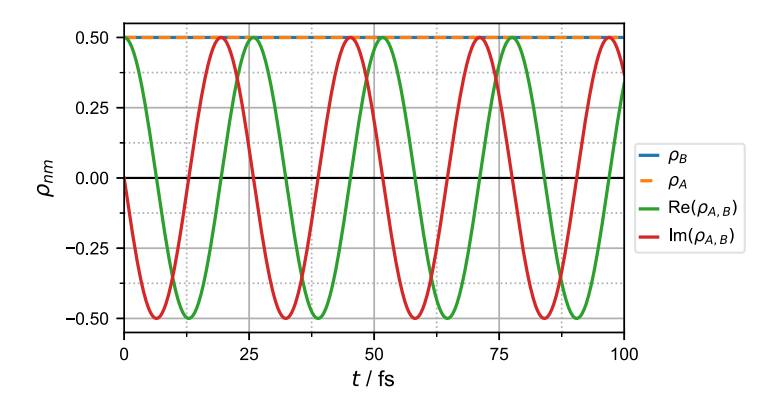


Fig. 7.12 – Populations and coherence for the uncoupled dimer. The populations for both states (blue line for monomer B, orange line for monomer A) remain at their initial value. The real and imaginary parts of the coherence (green and red line, respectively) oscillate with a period corresponding to the energetic difference between the two states.

After the propagation, we can take a look at the state populations and coherences. These are shown in figure 7.12. The populations remain constant for both states, as expected for an uncoupled system. The coherence oscillates with a period of about 26 fs. To understand this behaviour, we can take a look at the time evolution of the reduced electronic density matrix.

To this end, we first rewrite the Hamiltonian from equation (60) as

$$H = \begin{pmatrix} H_0 + E_B & 0\\ 0 & H_0 + E_A \end{pmatrix} \tag{69}$$

and the wave function as

$$\Psi(x) = \psi(x)(c_A|A\rangle + c_B|B\rangle) = \sum_{n=1}^{\infty} d_n \varphi_n(x)(c_A|A\rangle + c_B|B\rangle)$$
 with $H_0 \varphi_n(x) = \varepsilon_n \varphi_n(x)$. The time-dependent wave function is then

$$\Psi(x,t) = \sum_{n=1}^{\infty} d_n \exp\left(-\frac{\mathrm{i}}{\hbar}(\varepsilon_n + E_A)t\right) \varphi_n(x) c_A |A\rangle + \sum_{n=1}^{\infty} d_n \exp\left(-\frac{\mathrm{i}}{\hbar}(\varepsilon_n + E_B)t\right) \varphi_n(x) c_B |B\rangle$$

$$= \sum_{n=1}^{\infty} d_n \exp\left(-\frac{\mathrm{i}}{\hbar}\varepsilon_n t\right) \varphi_n(x) \left(\exp\left(-\frac{\mathrm{i}}{\hbar}E_A t\right) c_A |A\rangle + \exp\left(-\frac{\mathrm{i}}{\hbar}E_B t\right) c_B |B\rangle\right). \tag{71}$$

With this and following equations (38)-(40), we can get the time evolution of the reduced density matrix for our uncoupled system as

$$\rho = \begin{pmatrix}
|c_B|^2 & c_B c_A^* \exp\left(-\frac{\mathrm{i}}{\hbar}(E_B - E_A)t\right) \\
c_B^* c_A \exp\left(-\frac{\mathrm{i}}{\hbar}(E_A - E_B)t\right) & |c_A|^2
\end{pmatrix}$$

$$= \begin{pmatrix}
\rho_B & \rho_{A,B} \exp\left(-\frac{\mathrm{i}}{\hbar}\Delta E t\right) \\
\rho_{A,B} \exp\left(\frac{\mathrm{i}}{\hbar}\Delta E t\right) & \rho_A
\end{pmatrix}. \tag{72}$$

We would thus expect that the populations stay constant and the coherence oscillates with a frequency corresponding to the difference in energy between the two states, $\Delta E = E_A - E_B = 1290 \,\mathrm{cm}^{-1}$, which corresponds to a period of 25.86 fs. This explains the evolution in figure 7.12.

Next, we take a look at the autocorrelation function and corresponding power spectrum. During the propagation, we calculated the autocorrelation function of the individual diabatic states. For the absorption spectrum of the whole system, we first need to construct the full autocorrelation function. With the way the wave function is set up, the individual autocorrelation functions are already weighted by the state populations so that the total autocorrelation function is simply the sum of these individual components. We also define a time axis that is double that of the wave function (cf. equation (57)) and a lifetime τ . With this, we can also define the damping function f(t) of equation (58) and the window function g(t) of equation (59).

```
1 auto_tot = np.sum(auto, axis=1) # C(t) as sum of C_n(t)
2 t = t_axis*2.0 # time axis is doubled in comparison to populations etc.
3 dt_auto = 2.0*dt*writeInterval # time step doubled as well
4 t_s = 2.0*(t_f/fs2atu) # final time as well
5 tau = 50.0 # life time of excited state in fs
6
7 f = np.exp(-t/tau) # equation (58)
8 g = np.cos(np.pi*t/(2*t_s)) # equation (59)
```

Finally, we calculate the power spectrum following equation (55). Since we know the transition energies and, thus, where signals in the spectrum should appear, we can choose the energy axis accordingly and also indicate E_A and E_B .

```
1  C = auto_tot * f * g # apply windowing and damping
2  E = np.linspace(12000, 20000, 4096)/invcm2eV/eV2Eh # energy axis
3  sigma = np.zeros(len(E))
4  for i in range(len(E)):
5     # equation (55)
6     E[i] = np.real(np.sum(np.exp(1.0j*E[i]*t*fs2atu)*C)*dt_auto)/np.pi
7  E = E*invcm2eV*eV2Eh # convert energy to cm-1 for plotting
```

The resulting spectrum is shown in figure 7.13. The signals are, however, not where we would expect. They are shifted to higher energies by 610 cm⁻¹, the zero point energy of the vibrational degree of freedom. When calculating the power spectrum in this way, we implicitly set our reference energy (the (vibronic) ground state) to 0. When we set the transition energies as the state energies, we did not take the zero-point energy of the excited state potentials into account. We thus set the minimum energies to be the transition energies. For the dynamics itself, this does not make a difference since both states are shifted by the same amount; it is a global shift in energy. For the power spectrum, however, we have one zero-point energy, or $\omega/2$, too much energy in the transitions. To have the peaks in the spectrum match the transition energies, we thus need to subtract the zero point energy either by

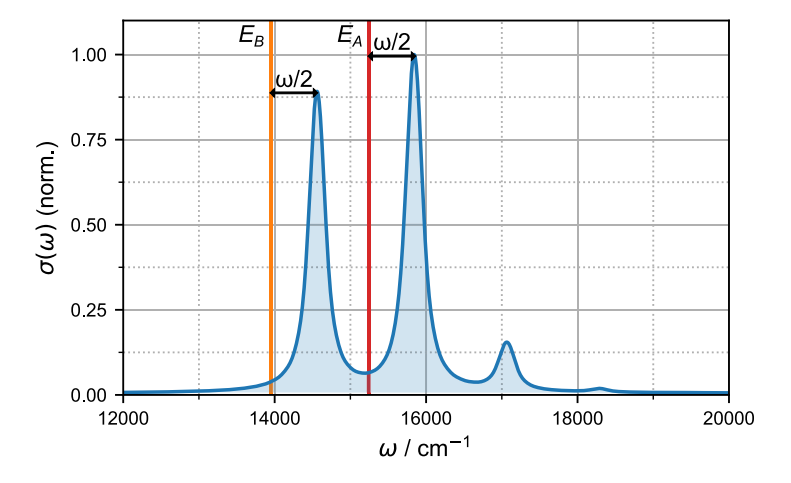
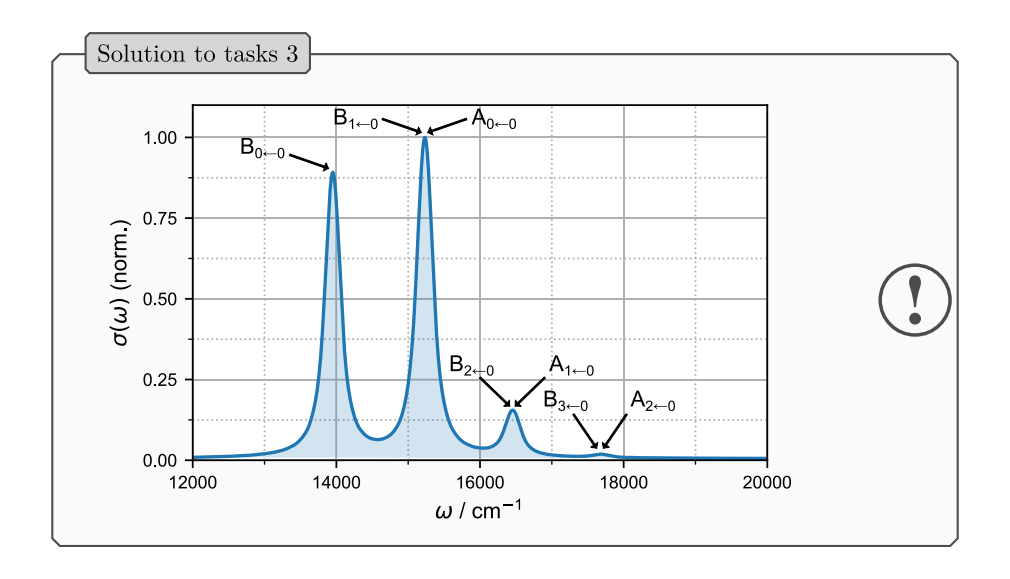


Fig. 7.13 – Power spectrum of the uncoupled dimer. The highest signal is set to 1. The transition energies E_A and E_B are indicated as vertical lines in red and orange, respectively. The spectrum is shifted by half the vibrational frequency in comparison to the transition energies.

reducing the state energies or just during plotting. All future spectra will have this correction already applied.

Tasks 3

Assign all visible peaks to vibronic transitions in the system.



After understanding the peak positions, we also want to take a closer look at the peak intensities. We know that they come from different vibrational levels. And we also know that we can expand our wave function Ψ in the basis of the vibrational eigenstates φ_n as

$$\Psi(x) = \psi(x)(c_A|A\rangle + c_B|B\rangle) = \sum_{n=1}^{\infty} d_n \varphi_n(x)(c_A|A\rangle + c_B|B\rangle)$$
 (70 revisited)

The intensity of the peak that corresponds to the vibrational level φ_n should be linked to the proportion of this vibrational state in the total wave function. So we need to extract the coefficients of the vibrational eigenstates as

$$d_n = \langle \varphi_n | \Psi \rangle = \int_{-\infty}^{\infty} \varphi_n(x) \psi(x) dx \tag{73}$$

Since we are working with harmonic oscillators, we can use the analytical eigenstates and calculate the overlaps. For the first four overlaps, we have

```
d = np.zeros(4) # list of coefficients
2 alpha = m*w/2.0 # alpha to construct HO eigenfunctions
   # reference is unshifted ground state
   GS = np.sqrt(np.sqrt(2.0*alpha/np.pi))*np.exp(-alpha*x**2)
 6 for n in range (len(d)):
7
      # nth vibrational eigenfunction
 8
      phi n = (np.sqrt(np.sqrt(2.0*alpha/np.pi))/
              np.sqrt(2**n*scps.factorial(n))*
 9
10
              scps.eval hermite(n, np.sqrt(2.0*alpha)*(x-x0))*
11
              np.exp(-alpha*(x-x0)**2))
12
13
      d[n] = scpi.trapezoid(y=phi n*GS, x=x, dx=dx) # equation (73)
14
      print(d[n]**2) # print squared coefficients: Franck-Condon
   factors
```

The resulting Franck-Condon factors are listed in table 7.1. We can now approximate the spectrum by adding suitably broadened Lorentz functions centered at the vibrational energies and scaled by the corresponding Franck-Condon factors. The result is shown in figure 7.14.

Since we can reconstruct the spectrum, we can explain the peak positions with the vibrational eigenstates and the peak intensities with the Franck-Condon factors.

Tasks 4

Repeat the simulations with different initial population distributions and compare the spectra.



Tab. 7.1 – Franck-Condon factors for the first four vibrational states in the uncoupled dimer.

$0 \leftarrow 0$	$1 \leftarrow 0$	$2 \leftarrow 0$	$3 \leftarrow 0$
86.07%	12.91%	0.97%	0.05%

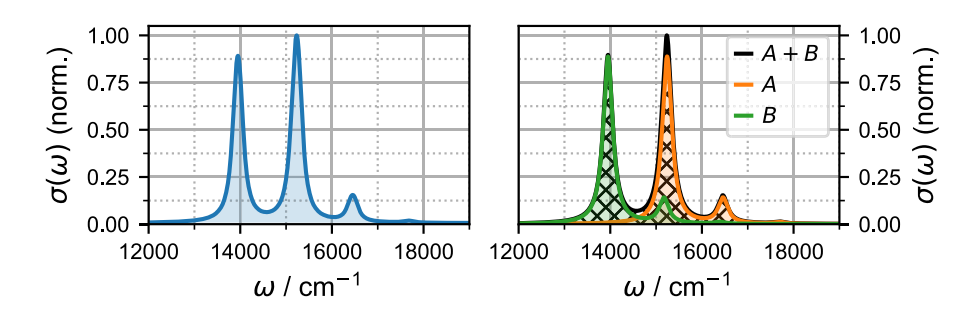
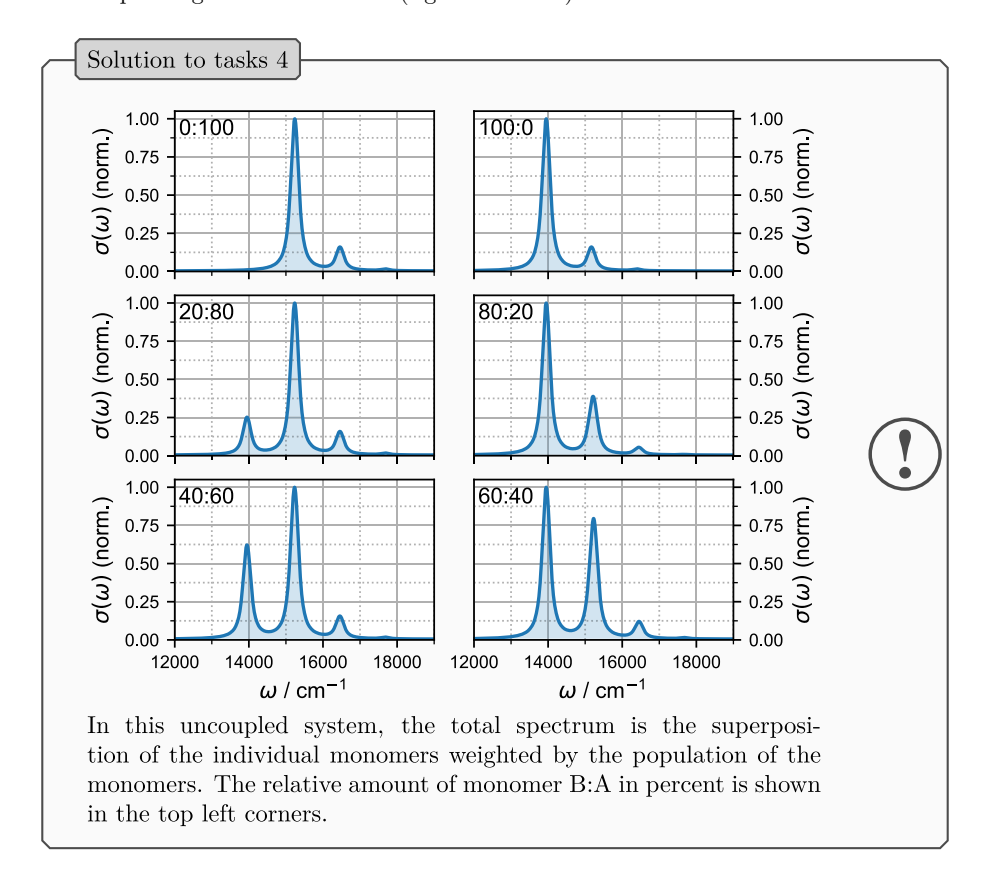


Fig. 7.14 – The power spectrum of the uncoupled dimer (left-hand side) can be reconstructed from signals at the eigenenergies of the monomers weighted by the Franck-Condon factors of the corresponding vibrational states (right-hand side).



Conclusion 3

Power spectra can be obtained from excited state autocorrelation functions. The autocorrelation function can be modified with a window function and exponential decay to remove artifacts and get more realistic line shapes. Peak positions and intensities can be explained with transitions between the vibrational eigenstates of the system.



7.8 Coupled Dimer

After the uncoupled dimer, we will briefly take a look at a coupled dimer by adding a connector between the monomers, starting with connector II. To this end, we set $V_1 = -650.0 \,\mathrm{cm}^{-1}$. Besides this change, the code remains the same and we will directly take a look at the results, starting with the populations and coherence in figure 7.15. Now that the two states are coupled, we can see a population transfer between the monomers. The periodicity of this transfer is connected to the difference in the eigenenergies of the system. Due to the coupling, the difference shifts from $1290 \,\mathrm{cm}^{-1}$ to $1831 \,\mathrm{cm}^{-1}$, corresponding to a period of $18.2 \,\mathrm{fs}$.

In regular intervals, the superposition collapses, and the population can only be found in monomer B. In contrast to the uncoupled dimer, the coherence also periodically vanishes at these points.

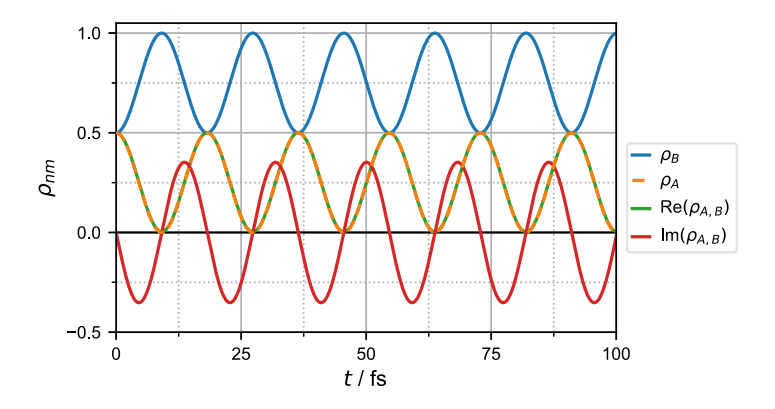


Fig. 7.15 – Populations and coherence for the coupled dimer with connector II. The populations for both states (blue line for monomer B, orange line for monomer A) oscillate, and the superposition periodically collapses to purely monomer B.

Question 7.1

When and why does the coherence reach zero?



Answer to question 7.1

The coherence vanishes when the superposition collapses, i.e., only one monomer is populated. The reason is clear when taking a look at equation (40). When the superposition between the two monomers collapses, all coefficients for the unpopulated state are zero. Thus the off-diagonal elements in the reduced electronic density matrix also have to be zero.



Next, we will take a look at the power spectrum of the coupled dimer, shown in figure 7.16.

Question 7.2

Would you expect to have the peaks in the spectrum at the same positions as before? If not, in what way do you think the spectrum changes and why?



Answer to question 7.2

As we saw in the case of the uncoupled dimer, the signals in the spectrum are related to the eigenenergies of the system. With the coupling, the eigenenergies will change and not correspond to the monomer transition energies anymore so the peaks will shift as well. We would expect the peaks to shift "outwards", i.e., some signals will be red-shifted while others will be blue-shifted.



As expected, the peak positions do not match the monomer transition energies any more but are shifted. To understand the positions, we need to calculate the (vibrational) eigenenergies of the coupled system. Due to the special case of our model, we could directly take the analytical eigenenergies of the harmonic potential and add the electronic eigenenergies to get the vibrational eigenenergies of the whole system. In a more general case of non-adiabatic dynamics, we would first need to calculate the adiabatic electronic potentials and then the vibrational eigenstates for each of these potentials. For illustration purposes, we will pursue this strategy here as well. Luckily, we already have the adiabatic potentials from the construction of the propagator of the potential energy. In addition to the potentials, we also need to define the kinetic energy operator. To do this, we employ finite differencing:

We can think of the wave function on the discretized grid as a vector $\psi(x) = (\psi(x_1), \psi(x_2), \dots, \psi(x_N))$. The second-order central difference as an approximation to the second-order derivative at a grid point x_i is then given as

$$\frac{\mathrm{d}^2}{\mathrm{d}x^2}\psi(x)\bigg|_{x=x_i} \approx \frac{\psi(x_{i-1}) - 2\psi(x_i) + \psi(x_{i+1})}{(\Delta x)^2}$$
(74)

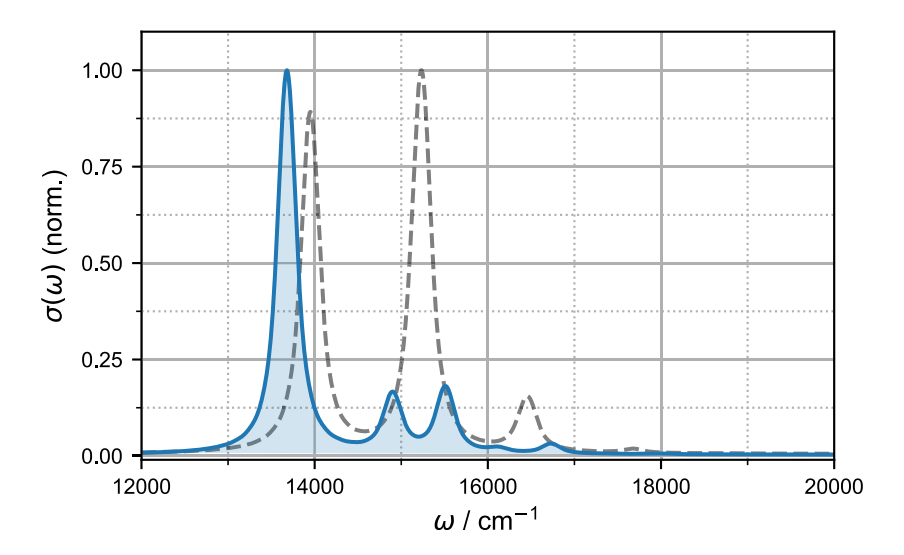


Fig. 7.16 – Power spectrum of the coupled dimer with connector II (blue line). The highest signal is set to 1. For comparison, the power spectrum of the uncoupled dimer is also shown in dashed grev lines.

so that the kinetic energy operator can be expressed as a matrix:

$$T(x)\psi(x) = -\frac{\hbar^2}{2m} \frac{\mathrm{d}^2}{\mathrm{d}x^2} \psi(x) \approx -\frac{\hbar^2}{2m(\Delta x)^2} \begin{pmatrix} -2 & 1 & 0 & \dots & 0 \\ 1 & -2 & 1 & \dots & 0 \\ 0 & 1 & -2 & \dots & 0 \\ \vdots & \vdots & \vdots & \ddots & \vdots \\ 0 & 0 & \dots & 1 & -2 \end{pmatrix} \begin{pmatrix} \psi(x_1) \\ \psi(x_2) \\ \psi(x_3) \\ \vdots \\ \psi(x_N) \end{pmatrix}.$$
(75)

A more rigorous and accurate way to represent the kinetic energy operator is via the "discrete variable representation" that is discussed in chapter 2.

To construct the Hamiltonian matrix, we add the adiabatic potential energy on each grid point as a diagonal matrix to the kinetic energy matrix. The vibrational eigenenergies can then be obtained by diagonalizing this total Hamiltonian matrix.

```
1 # construct finite difference matrix
2 T = (np.eye(len(x))*(-2) # diagonal
3 +np.eye(len(x), k=-1) # first off-diagonal
4 +np.eye(len(x), k=1)) # other first off-diagonal
5
6 # and multiply with prefactor
7 T = (-1.0/(2*m*dx*dx))*T
8
```

```
9 H_1 = T + np.diag(D[:,0]) # add lower adiabatic potential to T
10 eig_1 = scpl.eigvalsh(H_1) # calculate eigenvalues
11
12 H_2 = T + np.diag(D[:,1]) # add upper adiabatic potential to T
13 eig_2 = scpl.eigvalsh(H_2) # calculate eigenvalues
```

When adding the eigenenergies to the plot of the power spectrum, we can again assign the peaks to transitions in the system, see figure 7.17.

We can see that the eigenenergies are shifted away from the uncoupled case. The eigenstates of the lower adiabatic potential are red-shifted in comparison to monomer B, and the eigenstates of the upper adiabatic state are blue-shifted in comparison to monomer A.

Tasks 5

- 1. Repeat the simulations with different initial population distributions and compare the spectra.
 - a) Start with the population distribution of the so-called bright state, which in this case is the lowest electronic eigenstate. How could you get this state?



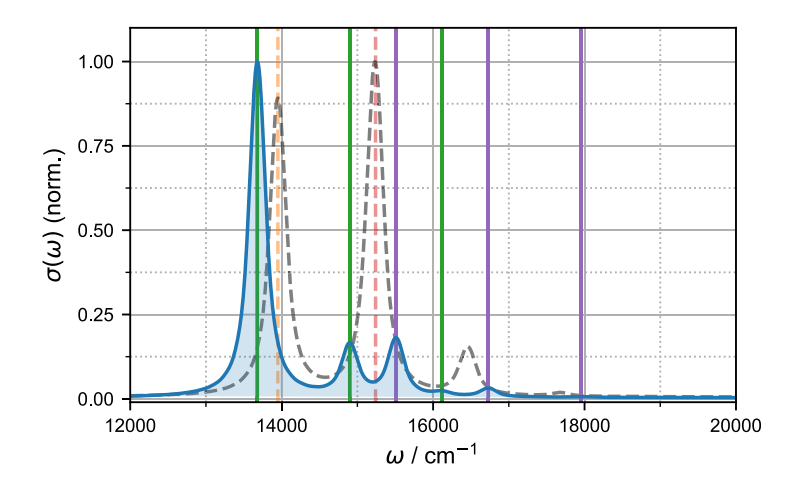
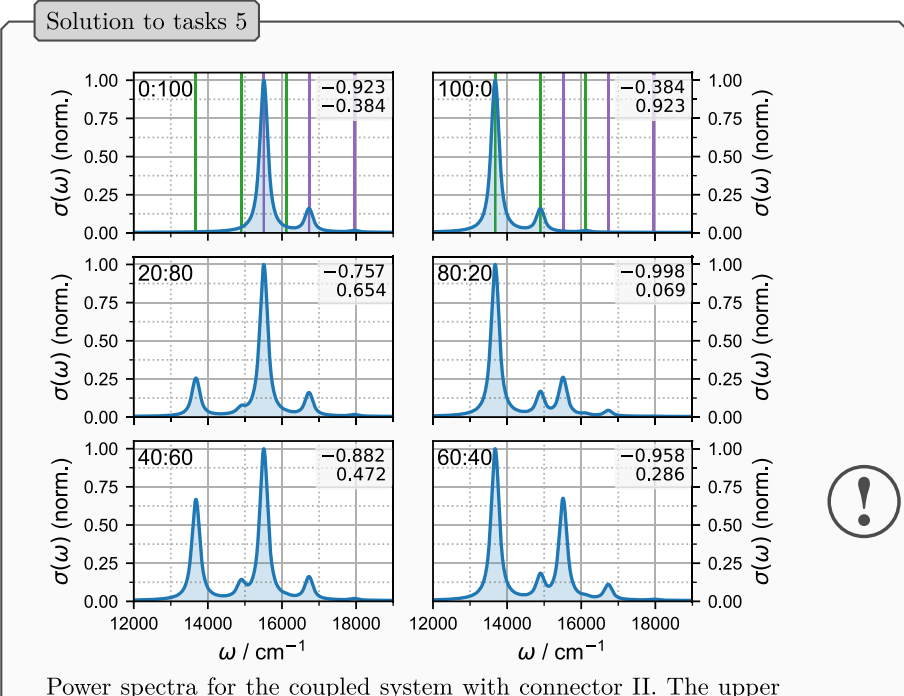


Fig. 7.17 – Power spectrum of the coupled dimer with connector II (blue line). The highest signal is set to 1. The energies corresponding to the first three eigenstates of the lower and upper adiabatic potentials are shown as green and purple lines, respectively. For comparison, the power spectrum of the uncoupled dimer (dashed grey line), as well as E_B (dashed orange line) and E_A (dashed red line) are shown.

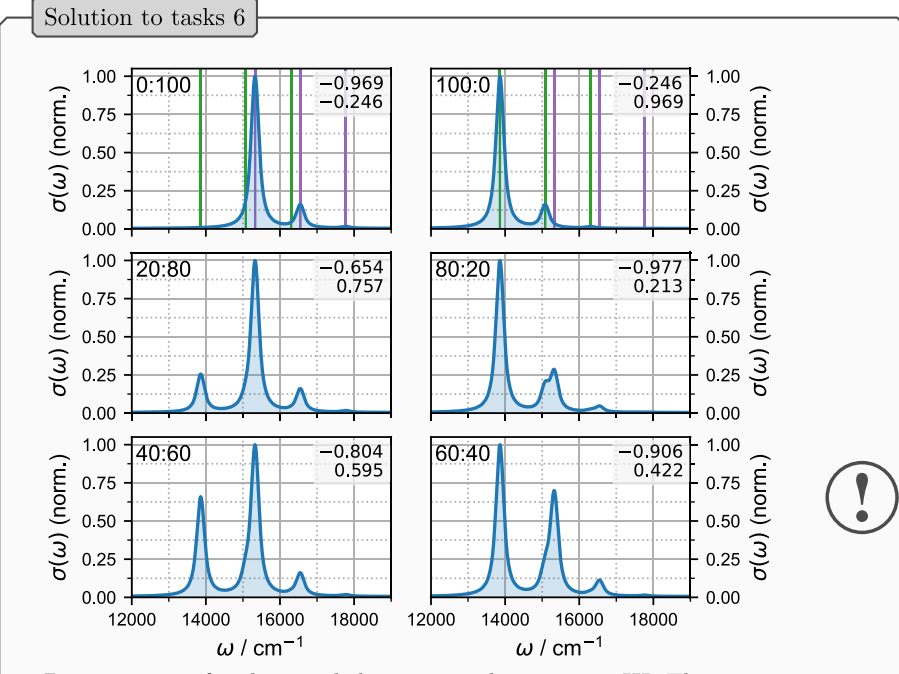


Power spectra for the coupled system with connector II. The upper panels show the spectra for the dark state (left) and bright state (right). These states are obtained by diagonalizing the electronic Hamiltonian matrix and taking the upper and lower eigenfunctions, respectively. Alternatively, we could use ITP with a purely electronic Hamiltonian to get the bright state. The vibronic eigenenergies of the two states are shown as green and purple lines, respectively. The relative amount of eigenstate 1 and 2 in percent are shown in the top left corner. In the top right corner, the coefficients for monomer B and A are shown.

Tasks 6

1. Repeat the simulations with connector III, i.e., a coupling strength of $V_1 = -350\,\mathrm{cm}^{-1}$ and compare with the previous results.





Power spectra for the coupled system with connector III. The upper panels show the spectra for the dark state (left) and bright state (right). These states are obtained by diagonalizing the electronic Hamiltonian matrix and taking the upper and lower eigenfunctions, respectively. Alternatively, we could use ITP with a purely electronic Hamiltonian to get the bright state. The vibronic eigenenergies of the two states are shown as green and purple lines, respectively. The relative amount of eigenstate 1 and 2 in percent are shown in the top left corner. In the top right corner, the coefficients for monomers B and A are shown.

Conclusion 4

In coupled systems, the population can be transferred between different states. The periodicity is connected to the difference in the eigenenergies of the states. Signals in spectra of coupled systems are shifted in comparison to the monomer spectra. This can manifest as a red- or blue shift. To understand the peak positions, one has to look at the adiabatic vibronic eigenstates.



7.9 Final Remarks

This chapter presented the basics of quantum dynamical simulations within the split-operator formalism. This includes the formal solution of the time-dependent Schrödinger equation with propagators and setting up a numerical calculation for a system with one degree of freedom and one or two electronic states. Furthermore, different parameters to gauge the simulations were introduced: energy and norm conservation, as well as grid-end populations.

The generation of initial conditions from imaginary time propagations and how to calculate position expectation values, state populations, coherences, and autocorrelation functions were covered.

The connection between autocorrelation functions and the power spectrum of the system, as well as how to modify the autocorrelation function in a sensible way to get a more realistic and better-resolved spectrum was introduced. The analysis of the resulting linear spectra in terms of peak positions and intensities was demonstrated.

Keep in mind that all of these topics were only an introduction to quantum dynamical simulations. Some details that apply to more complex systems were intentionally left out for brevity. For quantum dynamical simulations with more than a few degrees of freedom, you will need to go to other methods, like MCTDH, but the same principles still apply.

We hope that you enjoyed this brief primer and found value in the numerical examples. We encourage you to return to the other chapters in the book after completing the notebook of this chapter. Try to make connections between the more theoretical aspects and this more practical introduction. Maybe you also know someone else who might be interested in or benefit from this chapter or the school, in which case: let them know.

References

- Feshbach H., Kerman A., Lemmer R. (1967) Ann. Phys. 41, 230–286. DOI 10.1016/0003-4916 (67)90235-7.
- [2] Heller E. J. (1981) Acc. Chem. Res. 14, 368–375. DOI 10.1021/ar00072a002.
- [3] Hartree D. R. (1928) Math. Proc. Camb. Philos. Soc. 24, 89-110. DOI 10.1017/ S0305004100011919.
- [4] McWeeny R. (1973) Nature 243, 196–198. DOI 10.1038/243196a0.
- [5] Kosloff R. (1988) J. Phys. Chem. 92, 2087–2100. DOI 10.1021/j100319a003.
- [6] Mukamel S. (1995) Principles of nonlinear optical spectroscopy. Oxford Univ. Press.
- [7] Tannor D. J. (2007) Introduction to quantum mechanics: a time-dependent perspective. University Science Books, Sausalito, CA.
- [8] Kosloff D., Kosloff R. (1983) J. Comput. Phys. 52, 35–53. DOI 10.1016/0021-9991(83)90015-3.
- [9] Kosloff R. (1996) Dynamics of molecules and chemical reactions (R. E. Wyatt, J. Z. H. Zhang Eds). Marcel Dekker, New York, pp. 185–230.
- [10] Trotter H. F. (1959) Proc. Amer. Math. Soc. 10, 545–551. DOI 10.1090/S0002-9939-1959-0108732-6.
- [11] Strang G. (1968) SIAM J. Numer. Anal. 5, 506-517. DOI 10.1137/0705041.
- [12] Suzuki M. (1976) Commun. Math. Phys. 51, 183-190. DOI 10.1007/BF01609348.

- [13] Hatano N., Suzuki M. (2005) Quantum annealing and other optimization methods (A. Das, B. K. Chakrabarti Eds). Springer Berlin Heidelberg, Berlin, Heidelberg, pp. 37–68. DOI 10.1007/11526216 2.
- [14] Baker H. F. (1905) Proc. London Math. Soc. s2-3, 24-47. DOI 10.1112/plms/s2-3.1.24.
- [15] Campbell J. E. (1903) Introductory treatise on Lie's theory of finite continuous transformation groups. Clarendon Press.
- [16] Hausdorff F. (1906) Ber. Verh. Kgl. Sächs. Ges. Wiss. Leipzig. Math.-phys. Kl. 58, 19–48.
- [17] Beck M., Jäckle A., Worth G., Meyer H.-D. (2000) Phys. Rep. 324, 1–105. DOI 10.1016/S0370-1573(99)00047-2.
- [18] Kosloff R. Tal-Ezer H. (1986) Chem. Phys. Lett. 127, 223-230. DOI 10.1016/0009-2614(86) 80262-7.
- [19] Manthe U., Huarte-Larrañaga F. (2001) Chem. Phys. Lett. 349, 321–328. DOI 10.1016/S0009-2614(01)01207-6.
- [20] Gelman D., Kosloff R. (2003) Chem. Phys. Lett. 381, 129–138. DOI 10.1016/j.cplett.2003. 09.119.
- [21] Foulkes W. M. C., Mitas L., Needs R. J., Rajagopal G. (2001) Rev. Mod. Phys. 73, 33–83. DOI 10.1103/RevModPhys.73.33.
- [22] Schinke R. (1993) Photodissociation dynamics: spectroscopy and fragmentation of small polyatomic molecules. Cambridge University Press.
- [23] Engel V. (1992) Chem. Phys. Lett. 189, 76-78. DOI 10.1016/0009-2614(92)85155-4.
- [24] Manthe U., Meyer H.-D., Cederbaum L. S. (1992) J. Chem. Phys. 97, 9062–9071. DOI 10. 1063/1.463332.
- [25] Malý P., Lüttig J., Mueller S., Schreck M. H., Lambert C., Brixner T. (2020) Phys. Chem. Chem. Phys. 22, 21222–21237. DOI 10.1039/D0CP03218B.

Chapter 8

Computational Exercise: Ultrafast Spectroscopy of Complex Molecular Systems

James A. Green* and Dominik Brey**

Institute of Physical and Theoretical Chemistry, Goethe University Frankfurt, Max-von-Laue-Str. 7, Frankfurt, 60438, Germany

*e-mail: green@chemie.uni-frankfurt.de

8.1 Introduction

This chapter serves as an accompaniment to the computational exercise contained within the Jupyter notebook LesHouches_Spectroscopy.ipynb, aimed at illustrating how one can simulate non-linear spectral signals. In addition to the aim of illustrating how these signals are computed, the exercise will also serve to reinforce the theory, in particular behind 2D electronic spectroscopy, that is contained within the other chapters and lectures presented at the school.

The practical uses a Python package called the ultrafast spectroscopy suite (UFSS) [1-5], chosen due to its ease of use and ease of installation, as well as its speed and instructiveness in performing these calculations, all of which are highly useful for teaching purposes. We are indebted to the authors for making the software freely available, as well as providing a number of Jupyter notebooks on the GitHub page [1], all of which were extremely helpful in creating this practical class. We are in particular thankful to Peter Rose for answering questions on the usage of UFSS and providing some alterations to the code for this practical. The notebook and this chapter can, therefore, also serve as instructions in the use of UFSS, so that you may afterwards use the code yourself. We also hope that the principles can also be transferred to using other codes [6-8], or be used if you desire to write one yourself!

DOI: 10.1051/978-2-7598-3760-1.c008 © The authors, 2025

^{**}e-mail: brey@theochem.uni-frankfurt.de

¹The Jupyter notebook LesHouches_Spectroscopy.ipynb, as well as a Jupyter notebook containing solutions to questions posed in this chapter (LesHouches_Spectroscopy_Completed.ipynb), and installation instructions may be found in the supplementary electronic material, available at: https://doi.org/10.5281/zenodo.14861488.

The chapter will proceed as follows: in section 8.1 a brief background to the theory of light-matter interaction will be presented, as well as its computation in an open-quantum system density matrix based approach. We chose to use density matrices rather than a wavefunction-based approach, as this is typically more commonly encountered when theoretically describing non-linear spectroscopy [9, 10]. Furthermore, this approach allows a more straightforward treatment of dissipation to an environment (open quantum system) and temperature. We note that UFSS can also work in a closed system, wavefunction-based approach, but we do not utilise this in the present chapter or in the practical. Section 8.1 will not be exhaustive but simply provides some basic background information so that the content of the practical can be understood. We refer readers to the other chapters of this volume, and references mentioned in this chapter for further details.

In section 8.2, we describe the numerical setup of the molecular system that we will simulate spectra of. We chose an excitonic dimer consisting of two different squaraine monomers (SQA and SQB), studied by one of the other lecturers, Pavel Malý, in Ref. [11] and discussed in chapter 4. We implement a simplified version of the theoretical treatment employed in that work, consisting of a coupled two-level system, with a ground state $|g\rangle$ and first excited electronic state for each squaraine monomer $|e_A\rangle$ and $|e_B\rangle$, plus a dominant vibrational mode. When both monomers are excited, we also have the possibility of a doubly excited electronic state $|e_A, e_B\rangle$. A schematic of the electronic energy levels in this site-based, diabatic the basis is shown in figure 8.1, as well as the diagonlisation into the excitonic, adiabatic basis. In the reference work, three dimers with different coupling strengths were studied [11]. We choose one for illustrative purposes, and the goal of the reader is to simulate the spectra of another. The non-linear spectra will show signals due to ground state bleaching (GSB), stimulated emission (SE), and excited state absorption (ESA), and this is also schematically shown in figure 8.1.

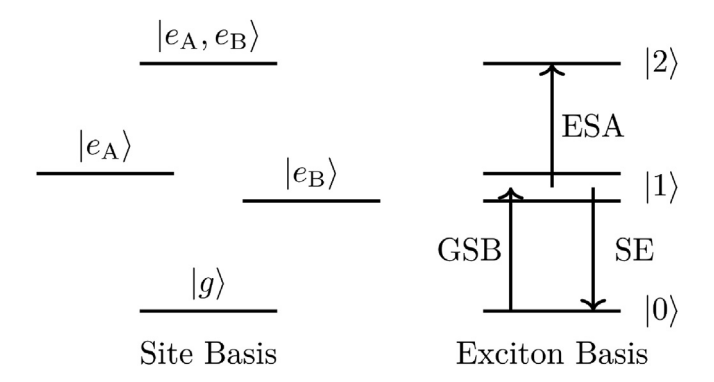


FIG. 8.1 – Schematic of the electronic energy levels of the squaraine dimer (SQAB) studied in this chapter. On the left, the site (diabatic) basis is shown, comprising of a singly excited state for each squaraine monomer, $|e_{\rm A}\rangle$ and $|e_{\rm B}\rangle$, as well as a doubly excited state $|e_{\rm A}, e_{\rm B}\rangle$. On the right-hand side is the diagonalisation of this site basis to the exciton (adiabatic) basis, displaying the 0, 1, and 2 quantum manifolds. The signals that will be observed in the non-linear spectra are also shown, namely ground state bleaching (GSB), stimulated emission (SE), and excited state absorption (ESA).

In section 8.3, we describe how the electric field of a laser pulse with a Gaussian envelope may be defined and how the linear absorption spectrum due to interaction with this Gaussian pulse may be computed. In section 8.4, we illustrate the computation of a signal from perhaps the most commonly encountered non-linear optical spectroscopy, transient absorption. Then, in section 8.5, we illustrate 2D electronic spectroscopy (2DES), a powerful technique for elucidating the dynamics of excitonic systems. Finally, in section 8.6, we demonstrate in more detail the theory of non-linear spectroscopy, particularly 2DES, through the generation of double-sided Feynman diagrams and their use in separating components of a theoretically determined spectral signal.

8.1.1 Background and Theory

When we irradiate a molecular sample, the electric field ϵ of the light will induce a macroscopic electric dipole moment, known as the polarisation P in the sample. For a single weak electric field (*i.e.*, weak laser pulse), the induced polarisation will depend linearly upon the electric field

$$P = \chi \cdot \epsilon \tag{1}$$

where χ is the susceptibility of the material. The polarization acts as a source to generate radiation with angular frequency ω that can be detected and used to measure the absorption of a sample. The detected signal is proportional to the polarization.

For higher electric field strengths, we have a power series expansion of the polarization in terms of the electric field [10, 12]:

$$P = \chi^{(1)} \cdot \epsilon + \chi^{(2)} \cdot \epsilon \cdot \epsilon + \chi^{(3)} \cdot \epsilon \cdot \epsilon \cdot \epsilon + \dots = P^{(1)} + P^{(2)} + P^{(3)} + \dots$$
 (2)

where $\chi^{(1)}$ is the linear susceptibility of the sample, and $\chi^{(n)}$ n > 1 are higher order non-linear susceptibilities. In isotropic media, even order susceptibilities vanish, such that the lowest-order non-linearity is the third order. This third-order non-linear polarization $P^{(3)}$ is measured by transient absorption and 2D electronic spectroscopy. In general, these are known as 4 wave mixing techniques, as 3 interactions with the laser electric field are used to generate $P^{(3)}$ that creates a polarization signal (the fourth wave), which can be detected by another interaction with an incident laser field known as the local oscillator (heterodyne detection).

In order to calculate the polarization, we can turn to perturbation theory, describing the interaction of light with molecular systems by

$$H = H_0 + H'(t) \tag{3}$$

where H_0 is the Hamiltonian of the molecular system, and H'(t) is the interaction with light. In a dipole approximation, this takes the form of the dipole operator of the molecule interacting with the time-dependent electric field of the light

$$H'(t) = -\mu \cdot \epsilon(t). \tag{4}$$

Within a density matrix based picture, we can calculate the nth order polarization via [10]

$$P^{(n)}(t) = \left(-\frac{i}{\hbar}\right)^{n} \int_{0}^{\infty} dt_{n} \int_{0}^{\infty} dt_{n-1} \cdots \int_{0}^{\infty} dt_{1} \epsilon(t-t_{n}) \epsilon(t-t_{n}-t_{n-1}) \cdots \times \epsilon(t-t_{n}-t_{n-1}\cdots -t_{1}) \times \langle \mu(t_{n}+t_{n-1}\cdots +t_{1}) \cdot [\mu(t_{n-1}+\cdots t_{1}), \cdots [\mu(t_{1}), [\mu(0), \rho(-\infty)]] \cdots] \rangle$$
(5)

where the electric fields arrive delayed by times $t_1, ..., t_n$, and the density matrix is the outer product

$$\rho(t) = \sum_{m,n} c_n(t) c_m^*(t) |n\rangle\langle m|.$$
 (6)

The commutators with the dipole operator in equation (5) either raise or lower the ket or bra side of the density matrix by one quantum.

The time dependence of the density matrix may be calculated by a Liouville-von Neumann equation

$$\frac{\mathrm{d}\rho(t)}{\mathrm{d}t} = \frac{-i}{\hbar} (L_0 \rho(t) + L'(t) \rho(t)) \tag{7}$$

where L'(t) is the Liouvilian superoperator of the interaction with light

$$L'(t)\rho(t) = [H'(t), \rho(t)] \tag{8}$$

and L_0 is the Liouvilian superoperator of the molecular system plus environment

$$L_0\rho(t) = [H_0, \rho(t)] + i\hbar D\rho(t). \tag{9}$$

In the above, D is a superoperator that describes dephasing and dissipation to an environment, which in the practical will be described by Redfield theory [13]. We note that this is an approximate approach to describe dephasing and dissipation, and formally exact methods of propagating the density matrix, such as the Hierarchical Equations of Motion (HEOM) described in chapter 3 are possible. The environment itself will be described by a bath of harmonic oscillators, whose frequencies ν follow an overdamped Brownian oscillator spectral density

$$J(v) = 2v\lambda \frac{\gamma}{v^2 + v^2}.$$
 (10)

When the polarization in equation (5) is calculated in the time domain, a Fourier transformation must be performed in order to obtain it in the frequency domain:

$$P^{(n)}(\omega) = \frac{1}{\sqrt{2\pi}} \int_{-\infty}^{\infty} dt e^{i\omega t} P^{(n)}(t). \tag{11}$$

For heterodyne detection, the resulting signal can then be given by the interaction of the polarization with the local oscillator electric field

$$S^{(n)}(\omega) \propto \operatorname{Im}\left[\epsilon_{LO}^*(\omega) \cdot P^{(n)}(\omega)\right]$$
 (12)

The electric field of the jth laser pulse at position r in time t can be expressed by

$$\epsilon_j(t) = A_j(t)e^{-i\omega_j t + ik_j \cdot r + i\phi_j} + A_j^*(t)e^{i\omega_j t - ik_j \cdot r - i\phi_j}$$
(13)

where A(t) is its envelope function, ω_j is its carrier frequency, k_j is its wavevector, and ϕ_j is its phase. We have here both positive and negative carrier frequencies of the field, however, due to the rotating wave approximation (see chapter 4), we will only need to consider one of these terms at a time.

When multiple laser pulses interact and produce polarization in a sample, the direction in which it can be detected k_{sig} will be a function of sums and differences of the wavevectors of the laser pulses, e.g. for 3rd order non-linear polarization

$$k_{\text{sig}} = \pm k_1 \pm k_2 \pm k_3.$$
 (14)

This is known as phase matching, and the direction of k_{sig} is specific to different kinds of non-linear spectroscopy.

The difference between linear absorption and a 4 wave mixing experiment is shown schematically in figure 8.2. For linear absorption, there is a single probe pulse, in the direction $k_{\rm pr}$ that generates a first order polarization $P^{(1)}$ which is detected in the same direction as the probe pulse $k_{\rm sig} = k_{\rm pr}$. The probe pulse acts as a local oscillator, known as self-heterodyned detection. For a 4 wave mixing experiment, three incident beams of light in directions k_1 , k_2 , and k_3 interact with a sample, which then generates a third order polarization $P^{(3)}$ in the sample. This third-order polarization generates an electric field, which is then detected in a direction $k_{\rm sig}$ by a local oscillator. The direction of detection is specific to different kinds of 4-wave mixing experiments, such as transient absorption and 2D electronic spectroscopy, that will be covered in this chapter.

Now that the basic theory is set up, we can proceed with a description of the Jupyter notebook LesHouches_Spectroscopy.ipynb that forms the basis of the practical.

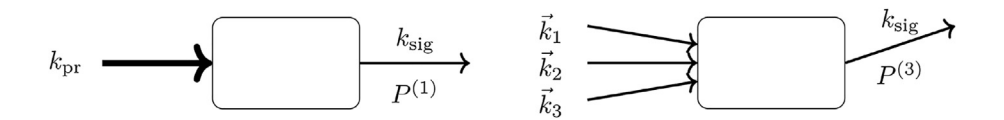


FIG. 8.2 – Schematic showing (left): a linear absorption experiment, where a single probe light pulse with wavevector $k_{\rm pr}$ is incident on the sample, which generates a first-order polarization $P^{(1)}$, detected in the direction of the probe ($k_{\rm sig} = k_{\rm pr}$), and (right): a four-wave mixing experiment where three incident beams of light with wavevectors k_1 , k_2 , and k_3 interact with a sample, which then produces a third order polarization $P^{(3)}$ in the sample that emits an electric field and is detected in the direction $k_{\rm sig}$.

8.2 Setup of System

8.2.1 Setup Notebook and Python Libraries

First, we set up our Jupyter Notebook and import relevant Python libraries that will be used in the practical. The environment used in the practical (from the file les_houches.yml as described in the installation instructions document²) relies on Python 3.10, although in principle, UFSS should work with any version of Python > 3.5. As well as importing ufss, we import numpy (for numerical operations and array handling) and matplotlib (for plotting) using the commonly used aliases np and plt, respectively. We also import the in-built python libraries os (for operating system functions e.g. folder creation) and math (for basic math operation). Finally, we import yaml, for creation of human readable input files for UFSS. You may note that this was also used in the setup of the Python environment (the file les_houches.yml).

```
#Import the relevant python packages
import ufss
import numpy as np
import matplotlib.pyplot as plt
import os
import yaml
import math
```

8.2.2 Define Parameters for System

Now that the relevant packages have been loaded, we can proceed with setting up our molecular Hamiltonian H_0 and dipole operator μ . As mentioned in section 8.1, we consider excitonic dimers consisting of two different squaraine monomers (SQA and SQB), as studied in Ref. [11]. One dimer (henceforth SQAB1 – dimer 1 in the reference work) will be used as an example in the notebook. Another dimer with a different coupling strength will be used in the question set (dimer 3 in the reference work, which will, however, be referred to as SQAB2 below). The electronic states of the dimer may be described as a coupled two-level system, with the general electronic Hamiltonian given by:

$$H_{\rm el} = \sum_{n=1}^{s} e_n a_n^{\dagger} a_n + \sum_{m \neq n} V_{mn} a_m^{\dagger} a_n \tag{15}$$

where s is the total number of coupled two-level systems (s=2 in our example since we have a dimer), e_n is the excitation energy of the monomer, V_{mn} the excitonic coupling, a_n^{\dagger} the creation operator for an excited electronic state $|n\rangle$ (i.e., $|n\rangle = a_n^{\dagger}|g\rangle$

²The electronic supplementary material is available at https://doi.org/10.5281/zenodo.14861488.

where $|g\rangle$ is the ground electronic state), and a_n the respective annihilation operator. In the notebook, we need to define the excitation energies of the SQA and SQB monomers, which in the reference paper [11] are given as 15240 cm⁻¹ for SQA and 13950 cm⁻¹ for SQB. We put these into variables eA and eB, respectively.

```
#Ground to excited state energies of SQA and SQB eA = 15240 eB = 13950
```

The excitonic coupling strength for dimer number 1 is given as $-650~\mathrm{cm}^{-1}$, and we input this into a variable V1

```
#Excitonic coupling between excited states of SQA and SQB for dimer 1 \rm V1 = -650
```

Now that the parameters for the electronic Hamiltonian have been defined, we will input values for the transition dipole moments connecting the ground state and excited states of each of the monomers. In principle, these should be vectors with x, y, and z components; however for simplicity we will just consider that the dipole moments lie parallel to one another and along the direction of the polarization of the electric field, such that we only need to give one number for each. These are input into the variables mua and mub for SQA and SQB, respectively.

Next, we will include a dominant, harmonic, vibrational mode into our model. The Hamiltonian for a set of harmonic vibrations may be given by

$$H_{\rm vib} = \frac{1}{2} \sum_{\alpha=1}^{k} p_{\alpha}^{2} + \Omega_{\alpha}^{2} q_{\alpha}^{2}$$
 (16)

where k is the number of vibrational modes (k=1 in our example), with coordinate q_{α} , momentum p_{α} and vibrational frequency Ω_{α} . This harmonic potential appears in both the ground and excited electronic states. The coupling of the vibrational mode to the excited electronic states is given by

$$H_{\text{el-vib}} = \sum_{\alpha=1}^{k} \sum_{n=1}^{s} \Omega_{\alpha}^{2} d_{\alpha,n} q_{\alpha} a_{n}^{\dagger} a_{n}$$

$$\tag{17}$$

where $d_{\alpha,n}$ is the coupling of the vibrational mode to each two-level system, related to the Huang-Rhys factor by

$$S_{\alpha,n} = \frac{1}{2} \Omega_{\alpha} d_{\alpha,n}^2. \tag{18}$$

Overall, we have a harmonic potential describing the vibrational mode in the ground state and a displaced harmonic oscillator describing the vibration in the excited states. In the notebook, we define the wavenumber of our vibrational mode and the Huang-Rhys factor in the variables Omega and S and give them values from the reference paper of 1220 cm⁻¹ and 0.15, respectively.

```
#Wavenumber of dominant vibrational mode and Huang-Rhys factor S = 0.15
```

The necessary parameters for our molecular Hamiltonian have now been defined, with

$$H_0 = H_{\rm el} + H_{\rm vib} + H_{\rm el-vib}.$$
 (19)

Finally, we need to input parameters for the interaction of the molecular system with the environment, and more specifically, the parameters that describe the spectral density in equation (10). We need to define two parameters: (i) λ , which is the strength of coupling of our molecular system to the environment, and (ii) γ which is a cutoff frequency, above which vibrational frequencies of the environment are less important. We choose similar values again to the reference work, of $\lambda = 200 \text{ cm}^{-1}$ and $\gamma = 666 \text{ cm}^{-1}$, and they are saved into the variables 1_sb and gamma, respectively. As lambda is a keyword used for another purpose in Python, we cannot choose this as a name for our system-bath coupling variable.

```
1_sb = 200
gamma = 666
```

8.2.3 Input to UFSS

Now that we have defined the important parameters for our molecular system plus environment bath, we define a function to input these parameters into a form that UFSS can read.

8.2.3.1 Units

We first need to consider the units in which our Hamiltonian is expressed. Quite often, quantum chemical/dynamical programs work with atomic units; however, in UFSS, units are taken care of implicitly, with frequencies being expressed in multiples of some angular frequency ω_0 and times in units of the inverse of this, ω_0^{-1} . For numerical convenience, we will choose our unit ω_0 to be fixed to the dominant vibrational frequency *i.e.* $\omega_0 = 2\pi c\Omega$, and express all energies in our Hamiltonian as multiples of Ω . The units of time in fs may then be expressed as

$$\omega_0^{-1} = \frac{1 \times 10^{15}}{2\pi c\Omega} \tag{20}$$

where c is the speed of light (given simply as 3×10^{10} cm s⁻¹ in the notebook), and the factor of 2π arises due to the conversion from angular frequency to time. This is expressed in the notebook as

```
inv_omega0 = 1E15/(Omega*2*np.pi*3E10)
print("omega_0^{-1} is equivalent to "+str(inv_omega0)+" fs")
```

with $\omega_0^{-1} \simeq 4.35$ fs, and the value saved in the variable inv_omega0. The corresponding period of the vibrational mode is $T = 2\pi\omega_0^{-1} \simeq 27$ fs.

Next, we can create an input file for UFSS. A function setup_ufss has been created in the notebook for this purpose. It creates a folder whose name you specify, into which an input file simple_params.yaml will be created, containing the parameters and associated keywords required for UFSS. The folder will also subsequently contain information used by the calculations. The routine takes care of converting the energies and couplings into multiples of Ω and setting a temperature of 298 K. The latter is accomplished with the line:

```
'temperature':207/Omega
```

where the value of 207 arises from the fact that $k_{\rm B}T \simeq 207~{\rm cm}^{-1}$ at 298 K. The setup_ufss routine also takes care of setting up the environment bath with the overdamped Brownian oscillator spectral density and dissipation by Redfield theory. Further information on this may be found in Refs. [1] and [2].

The setup_ufss function can be called by passing the parameters we have previously defined, plus the name of a folder, defined in the folder variable.

```
#Define the folder name
folder = 'SQAB1_folder'
#Pass folder name and all previously defined parameters to setup_ufss
setup_ufss(folder,eA,eB,muA,muB,V1,Omega,S,l_sb,gamma)
```

Once the folder and input file have been setup, we call two internal methods of UFSS, HLG.run and DensityMatrices. The former reads the input file and sets up the Liouvillian L_0 within UFSS, while the latter creates an object with this information enclosed, which can subsequently be used to perform the spectroscopy calculations. This object is named sqab1, and will be repeatedly used throughout the rest of the practical.

Task

1.1) Define a new dimer sqab2 which has the same parameters as sqab1, except for an excitonic coupling $V_2=-350~{\rm cm}^{-1}$.



8.3 Ultrafast Laser Pulse and Absorption Spectrum

Now that the molecular system is set up, let us start interacting with light! We want to define an ultrafast laser pulse with a Gaussian envelope of standard deviation σ

$$A(t) = \frac{1}{\sqrt{2\pi\sigma}} e^{-t^2/2\sigma^2} \tag{21}$$

We will choose a pulse with full-width half maximum (FWHM) of 12 fs. The relationship between FWHM and the standard deviation σ is

$$FWHM = 2\sqrt{2\ln(2)}\sigma \tag{22}$$

In the notebook we implement the conversion from FWHM in fs to σ in units of ω_0^{-1} :

```
def fwhm to sigma (fwhm fs):
 "'This function converts from a full width half maximum (FWHM)
 of a Gaussian in fs, to a standard deviation of the Gaussian in
 units of omega 0^{-1}
 Parameters
 _____
 fwhm fs: FWHM of a Gaussian in fs
 Returns
 _____
 sigma: standard deviation of the Gaussian in units of omega 0^{-1}
  ,,,
 #Convert from fs to omega 0^{-1}
 fwhm = fwhm fs/inv omega0
 #Calculate standard deviation sigma
 sigma = fwhm/(2*np.sqrt(2*np.log(2)))
 return sigma
```

This function can be called as follows

```
sigma = fwhm_to_sigma (12)
```

which results in a value of $\sigma \simeq 1.17 \ \omega_0^{-1}$, *i.e.*, we have a Gaussian pulse with a standard deviation ~ 5 fs.

In order to numerically define this Gaussian envelope, we need to create an array of values of t. We will use an array of 1001 points, equally spaced on the interval $t = [-20\sigma, 20\sigma]$

```
#Number of time points
Nt = 1001
#Vector of 1001 time points from -20*sigma to 20*sigma
t = np.linspace (-20*sigma, 20*sigma, num = Nt)
```

The envelope itself can be defined by the gaussian function in UFSS, passing the times and standard deviation σ as parameters

```
A = ufss.gaussian (t, sigma)
```

Next, we would like to set our laser pulse to have a carrier frequency ω_c , such that our electric field in the time domain will be defined as:

$$\epsilon(t) = A(t)e^{i\omega_c t} \tag{23}$$

where for the moment we will ignore the phase and wavevector, as we are only dealing with a single pulse in this section.

We will use a pulse centered at $\omega_c = 14700 \text{ cm}^{-1}$, which we write in the notebook as a multiple of Ω

```
#Set carrier frequency in multiples of Omega
omega_c = 14700/Omega
```

An array for the electric field $\epsilon(t)$ can, therefore be written as

```
epsilon = A*np.exp(1j*omega_c*t)
```

where the symbol 1 is how an imaginary number is written in Python.

We can plot what this laser pulse looks like in the frequency domain by a Fourier transformation from the time domain, which is implemented *via* the signals.SignalProcessing.ft1D function in UFSS. This function takes as arguments the time array and the electric field array. It returns an array of frequencies, which we save into the laser_w variable, and the electric field in the frequency domain, which we save in the epsilon_w variable.

```
laser_w, epsilon_w = ufss.signals.SignalProcessing.ft1D (t, epsilon)
```

Experimentally, detectors will not measure the electric field directly, but instead its intensity, i.e.

$$I(\omega) = |\epsilon(\omega)|^2. \tag{24}$$

This is calculated in the notebook in the cell

```
I_w = np.abs (epsilon_w) **2
```

Now let us plot both the real part of the electric field and its detected intensity. In the plot, since we wrote our carrier frequency in a multiple of Ω , we must multiply our laser frequency array by Ω to return to units of cm⁻¹

```
laser_w_cm = laser_w*Omega
```

We can also normalise the electric field and its intensity

```
epsilon_w_norm = np.real(epsilon_w)/np.max(np.real(epsilon_w))
I_w_norm = I_w/np.max(I_w)
```

The resulting plot is executed with the command

and shown in figure 8.3, with the electric field in the dashed line and its intensity plotted with a solid line. Notice that the measured intensity is narrower than the field itself by a factor of $\sqrt{2}$.

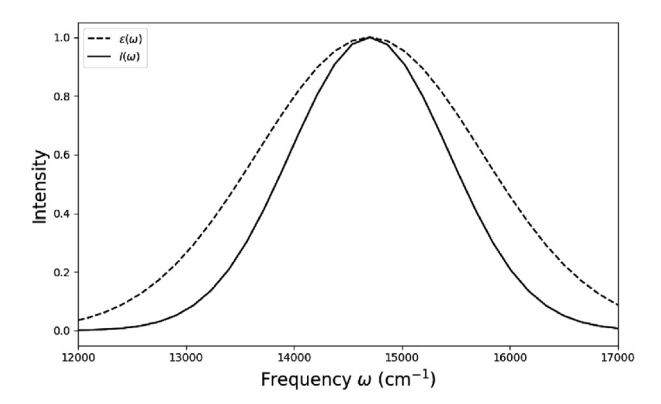


Fig. 8.3 – Electric field (dashed line) and its intensity (solid line) in the frequency domain due to a Gaussian laser pulse of FWHM=12 fs.

Task

2.1) Change the pulse duration by passing different FWHM values on the line sigma = fwhm_to_sigma(12), and see how it affects the width of the pulse in the frequency domain.



Solution to task

Due to the properties of the Fourier transform, you should notice that when the electric field is narrower in the time domain, it becomes wider in the frequency domain, and *vice-versa*.



8.3.1 Absorption Spectrum

Now, let us calculate the absorption spectrum that would be obtained from the interaction of our laser pulse with the molecular system we defined in section 8.2. A routine is included in the notebook for this, calculate_linear_absorption so that it is straightforward to recalculate an absorption spectrum with a change of parameters. We will describe some components of this routine below.

In order for UFSS to read the laser field and compute its interaction with our molecular system, we need to use the set_efields routine, which takes as arguments the time array, envelope function, carrier frequency, and phase discrimination condition. We will pass the first three variables as arguments to the linear absorption function, while the latter point we have not yet considered but will become important when we consider multiple pulses later in the chapter. For now, we will simply set it equal to '+'. This is implemented within the calculate_linear_absorption function as:

```
 \begin{tabular}{ll} \#Set the electric fields for interaction with molecular system in UFSS \\ spec_obj.set_efields([t],[A],[center],['+']) \end{tabular}
```

Since UFSS is primarily intended for the computation of non-linear spectra with multiple pulses, it requires a set of pulse delays and times with the set_pulse_delays routine. For now, we only have one arriving at t=0, so we pass an empty array to this routine

```
#Make an empty pulse delay for linear absorption
spec_obj.set_pulse_delays ([])
```

For the spectral signal itself, a time grid upon which it is calculated is set by the line

```
#Set a time grid for the signal that will be returned
spec_obj.set_t(0.1)
```

Internally, UFSS calculates the maximum time upon which to evaluate the signal by dividing the passed value by 6.91, *i.e.* 6.91/0.1 = 69.1 ω_0^{-1} . The reason 6.91 is used is because, assuming the signal decays exponentially, $e^{-6.91} = 0.001$, *i.e.*, the maximum time to evaluate the signal should be until it has decayed to 0.1%. Unless you have a priori knowledge about the slowest optical dephasing time in your system, setting this parameter may require some trial and error to get a properly resolved signal. In the workbook, it should not be necessary to alter this parameter.

The routine calculates the polarization in the x, y, and z directions and then averages. For our example, only the x direction will contribute since we defined the dipole moments only in the x direction.

The calculate_linear_absorption function can be called by passing the object created by the Density Matrices routine of UFSS (in the example case, sqab1), the time array, envelope function and carrier frequency, and it returns the spectral signal which we save in a variable la

```
%% capture
#Calculate linear absorption signal from our routine
la = calculate_linear_absorption (sqab1,t,A,omega_c)
```

Since, by default, UFSS will print a lot of information into the notebook; we use the ipython command %%capture at the beginning of the cell to suppress output.

The values of the frequencies on which the spectral signal is computed are stored in the w item of the sqab1 object, and we can copy them to a new array:

```
#Extract the frequency array
w = sqab1.w.copy()
```

UFSS returns these frequencies centered at $\omega = 0$, so we must shift by the carrier frequency ω_c before plotting the spectrum. We must also remember to multiply by Ω , since our Hamiltonian was set up in multiples of this for numerical convenience. Both of these features are achieved with the following:

```
w_cm = (w+omega_c) *Omega
```

The signal returned is complex-valued, and we only wish to plot the real part of it. So we use the np.real command to extract this. We can also normalise the linear absorption signal by dividing by its maximal value, which is obtained with the np.max command

```
la_norm = np.real(la)/np.max(np.real(la))
```

Finally, the spectrum and the exciting laser pulse are plotted as shown in figure 8.4. Red vertical lines have been added at the positions of the vibronic peaks *via* the commands

```
ax.axvline (13533, color='red')
ax.axvline (14800, color='red')
```

Task

2.2) As we did in task 2.1), change the pulse duration by passing different values on the sigma = fwhm_to_sigma(12) line, and recalculate the absorption spectrum. How does it change?



2.3) Using the sqab2 dimer object you defined in task 1.1), compute and plot the linear absorption spectrum. In the plot, add two vertical lines passing through the two most intense vibronic peaks.

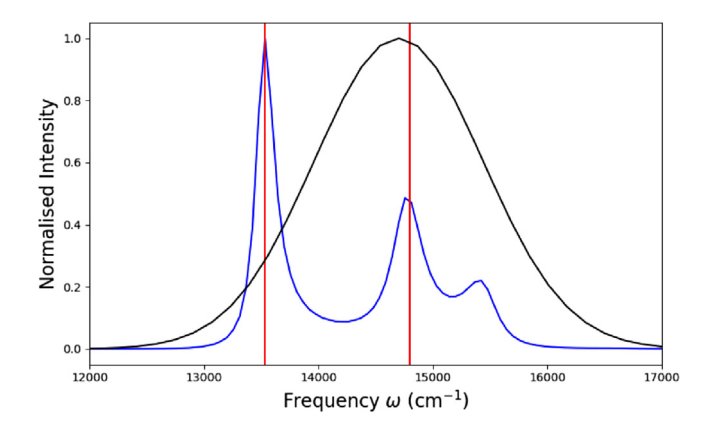


Fig. 8.4 – Ultrafast linear absorption signal (blue) of the SQAB1 dimer due to an exciting Gaussian laser pulse with FWHM of 12 fs (black). Positions of the main peaks indicated with red vertical lines.

Conclusion

Conclusion from task 2.2: When calculating the linear absorption signal with an ultrafast laser pulse, the intensity of the signal is weighted by the pulse. We note that this is not a "true" linear absorption spectrum, since that is a fingerprint of the molecular system, insensitive to the incident light field. We could remove the dependence on the incident electric field by dividing the signal by the intensity.

$$\mathsf{Abs}(\omega) = \frac{S(\omega)}{I(\omega)} \tag{25}$$



This is implemented in the workbook and shown in the code block below. We define a new array for the electric field intensity from the sqab1 object, via the get_local_oscillator() routine, in order to have the same array dimensions as the signal. A mask is also implemented, setting the intensity to 1 in places where it is small, to ensure we do not have division by very small numbers. The resulting linear absorption spectrum is shown in figure 8.5.

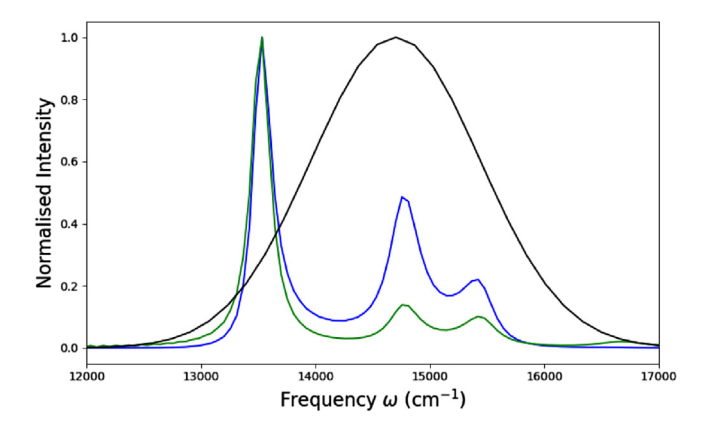


Fig. 8.5 – Ultrafast linear absorption signal (blue) of the SQAB1 dimer due to an exciting Gaussian laser pulse with FWHM of 12 fs (black), with the intensity normalised linear absorption spectrum in green.

8.3.2 Inhomogeneous Broadening

Spectral peaks typically have some width associated with them and are not perfectly sharp lines. The broadening of the lines can be separated into two components: homogeneous broadening and inhomogeneous broadening.

Homogeneous broadening arises from three sources:

- 1. Population relaxation (time constant T_1). Transitions have a finite lifetime associated with them, and this uncertainty in time gives rise to an uncertainty in the energy that is the same for all molecules in the system.
- 2. Pure dephasing (time constant T_2^*). A dynamic effect in which memory of the phase of oscillation of a molecule is lost as a result of intermolecular interactions that randomize the phase.

3. Orientational relaxation (τ_{or}) An ensemble averaged dephasing effect associated with the randomization of the initial dipole orientations.

Population and orientational relaxation are exponential, and so give rise to a Lorentzian line shape, however pure dephasing is not necessarily exponential. These sources of homogeneous broadening are already accounted for in our model.

Inhomogeneous broadening arises due to the fact that each molecule is in a slightly different environment, and hence, the electronic transitions all have slightly different energies due to interactions with this environment. This gives rise to a Gaussian broadening of the absorption spectrum. We can mimic this effect in UFSS by first setting up a number of different molecular Hamiltonians with slightly different energy levels according to a Gaussian distribution and then computing absorption spectra for each and averaging. This is implemented in the notebook in two routines: 1) setup_inhom that sets up the requisite molecular Hamiltonians with energy levels offset according to a Gaussian distribution, as well as calculating the weights of the subsequent spectra for these molecular Hamiltonians, and 2) inhomogeneous broadening that calculates the spectra and averages.

We can define a standard deviation for the inhomogeneous broadening, specified in the notebook, as $200~{\rm cm}^{-1}$

```
broad = 200
```

Then, a list of separate calculation objects containing the molecular Hamiltonians with Gaussian distributions of energy levels may be obtained by calling the setup_inhom routine and saved in sqab1_inhom. This routine also returns the weights of the spectra that will be subsequently calculated and saves them in the weights list. The number of different calculations is set to 11 in the workbook, which is too small for practical purposes, and typically, tens to hundreds of different spectra should be calculated. However, this small number will allow the subsequent calculations to be carried out quickly while still observing the inhomogeneous broadening of the spectra.

The function to calculate the inhomogeneously broadened spectrum can then be called, passing as parameters the previously defined calculate_linear_absorption function, the sqab1_inhom list, the weights for the averaging, the carrier frequency of our laser field, as well as the other named parameters required by calculate_linear_absorption, i.e. the time array and envelope function. The spectral signal is returned by this function, and saved into the la_broadened variable.

The corresponding frequencies are obtained by using the w.copy() command on the first element of the sqab1_inhom list

```
w = sqab1_inhom[0].w.copy()
```

The resulting spectrum can now be plotted by once more shifting this frequency array by omega_c, multiplying by Omega, and normalising the signal. The result is illustrated in figure 8.6, noticing how the higher energy vibronic peaks are now no longer distinct.

Task

- 2.4) Test different values for the broadening parameter broad and see how it affects the absorption spectrum.
- 2.5) Compute and plot an inhomogeneously broadened absorption spectrum for sqab2.



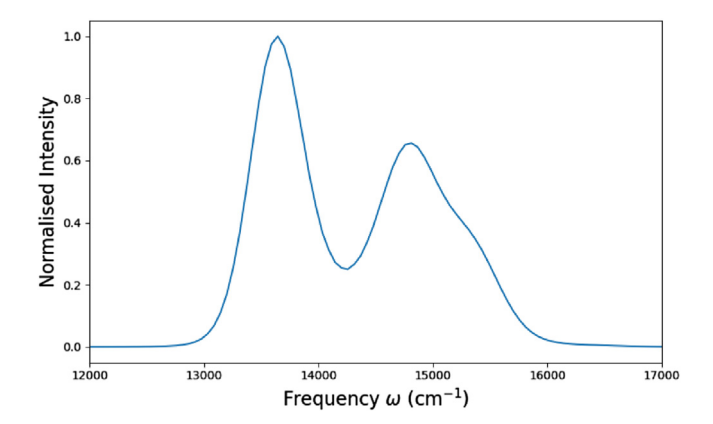


Fig. 8.6 – Linear absorption spectrum (blue) of the SQAB1 dimer, with inhomogeneously broadened transitions due to a Gaussian distribution of electronic transitions with standard deviation 200 cm⁻¹.

8.4 Transient Absorption

Transient absorption spectroscopy is conducted by a pump laser pulse that excites a sample and a probe laser pulse that measures the change in absorption of the sample after a time delay. It is perhaps the most straightforward of the 3rd order non-linear spectroscopies, with the generated 3rd-order polarisation being detected in the same direction as the probe laser pulse, which acts as a local oscillator. In terms of the phase-matching condition, the resultant wavevector of the detected third-order

polarization k_{sig} can be expressed in terms of the wavevectors of the pump k_{pu} and probe k_{pr} pulses as:

$$k_{\rm sig} = -k_{\rm pu} + k_{\rm pu} + k_{\rm pr} \tag{26}$$

Therefore, the electric field of the pump pulse is actually providing two wavevectors simultaneously in the positive and negative directions so that the resultant k_{sig} is in the direction of the probe, which is used as the local oscillator for detection. Despite only using pump and probe pulses, transient absorption is still formally a 4 wave mixing technique (three waves to generate the third-order polarization in the direction k_{sig} , which then emits an electric field in this direction and detected using the local oscillator).

Let's now illustrate how we can compute this within UFSS. This is implemented in the calculate_transient_absorption function in the notebook. For simplicity, we have chosen the pump and probe pulses to have the same Gaussian profile and carrier frequency. Important points to note in this function are as follows: similar to the previously illustrated linear absorption routine, the electric fields and phase matching condition must be set within the UFSS through the set_efields routine. The parameters passed to this routine are the time array, envelope function and central carrier frequencies, in this case each of them is multiplied by 4 since we have 4 electric fields we need to define, and ['-','+','+'] sets the phase matching condition, equivalent to $-k_{pu} + k_{pr}$.

```
spec_obj.set_efields([t]*4,[A]*4,[c]*4,['-','+','+'])
```

Then, the code sets the delay time for the pulses. Only two variables are passed: time 0 for the pump pulse and a sequence of delay times for the probe pulse.

```
spec_obj.set_pulse_delays([np.array([0]),delay_times])
```

Next, all the pulses are defined to have x direction polarization – i.e., in the same direction as our dipole moments.

```
spec_obj.set_polarization_sequence(['x']*4)
```

The final two lines of the routine perform an isotropic averaging of the spectral signal – assuming a random distribution of molecules in the laboratory frame.

```
#Makes an object for the isotropically averaged signal
iso = ufss.signals.FWMIsotropicAverage(spec_obj,['x']*4)
#Perform the isotropic averaging
signal = iso.averaged_signal(return_signal = True)
```

The returned signal is of the form $S^{(3)}(t_{\text{pump}}, t_{\text{probe}}, \omega_{\text{probe}})$, and therefore given as a 3-dimensional numpy array. The first dimension is equal to the dimension of the pump times passed to spec_obj.set_pulse_delays (i.e., 1D, as we only have a pump at time 0), the second dimension is equal to that of delay_times, while the

third dimension is equal to the dimension of the probe detection frequencies that exist in the spec_obj.w method, which is worked out internally by UFSS.

With the routine explained, let us compute transient absorption spectra using it. First, let us define an array for the probe delays, from 0 to 30 in units of ω_0^{-1} such that it corresponds in fs to delay times from 0 to ~ 130 fs.

```
probe_t = np.arange(0,30,1)
```

Now, we can call our transient absorption function, and save the resulting signal into the array ta. The parameters passed to it are the sqab1 object, the standard deviation of the laser fields sigma, carrier frequency omega_c, and the array of probe times probe_t. As with the linear absorption example in the previous section, we can get an array of the detection frequencies with the sqab1.w.copy() command.

```
ta = calculate_transient_absorption(sqab1, sigma, omega_c, probe_t)
w = sqab1.w.copy()
```

Now, we will plot this transient absorption signal. In contrast to linear absorption, where we only had two dimensions to plot (signal and frequency), with transient absorption we now have a third dimension – time. To visualise this, we will make use of a colour map, where delay time appears on the x-axis, detection frequency on the y-axis, and the signal intensity is given a colour. UFSS has a ufss.signals.plot2D function that takes care of this for us, we just need to pass the x and y values, the signal, and an optional argument that states we only want to plot the real part of the signal.

Before calling this ufss.signals.plot2D function however, let us take care of the units: delay times of the probe converted to fs, and frequencies shifted and converted to ${\rm cm}^{-1}$

```
#Convert probe delay times to fs
probe_t_fs = probe_t*inv_omega0

#Convert detection frequency to cm-1
w_cm = (w+omega_c)*Omega
```

Now we can plot the signal.

Technical note: As mentioned above, the transient absorption signal ta is a 3-dimensional array, and plot2D requires a 2-dimensional array for the signal. However, the first array index only has a size of 1, so we can "slice" the array at this point with the command ta[0,:,:] (Python starts indexing at "0"). The result is shown in figure 8.7.

```
ufss.signals.plot2D(probe_t_fs,w_cm,ta[0,:,:],part='real')
```

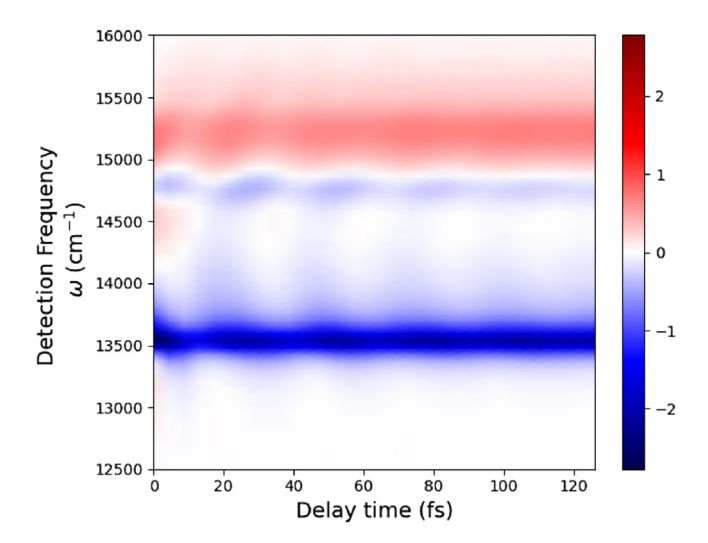


Fig. 8.7 – Transient absorption spectrum of the SQAB1 dimer as a function of probe delay time and detection frequency.

Task

3.1) Compute and plot the transient absorption spectrum for sqab2. What is the difference between the two spectra?



8.4.1 Peak Monitoring

A common way to gain insight into the dynamical process being explored by pump-probe spectroscopy is to monitor the intensity of the peaks and how they change as a function of time. We can also do this theoretically by plotting time-dependent cuts through the signal at approximately the energies from peaks in the absorption spectrum ($f_1 = 13533 \, \mathrm{cm}^{-1}$ and $f_2 = 14800 \, \mathrm{cm}^{-1}$). To do this, we need to first find out what index in the frequency array w these wavenumbers correspond to. We can work this out by adding the carrier frequency to the w array, and then subtracting either f_1 or f_2 . After this procedure, the element in the w array closest to 0 is located in the index we want, which can be found using the np.argmin command. The two indices are obtained below:

```
#Get wavenumbers in multiples of Omega
f1=13533/Omega
f2=14800/Omega
#Get the index they appear in the detection frequency array w
ind1 = np.argmin(np.abs(w+omega_c-f1))
ind2 = np.argmin(np.abs(w+omega_c-f2))
```

Then, one can extract the intensity of the signal at these frequencies, as the detection frequency corresponds to the third dimension in the ta array.

```
#Extract TA signal at 13533 cm-1
y1 = np.real(ta[0,:,ind1])
#Extract TA signal at 14800 cm-1
y2 = np.real(ta[0,:,ind2])
```

A plot of these extracted intensities is shown in figure 8.8, and we can notice oscillations due to coherences.

Question

Are the coherences due to vibrational or electronic coherences, or both? Could you think how to make a model with purely vibrational or purely electronic coherences?



Solution to question

Resolving vibrational from electronic coherences is often a difficult challenge experimentally [14]. In this example, following analysis of the eigenvectors of the excitonic states from the diagonalisation of the vibronic Hamiltonian in chapter 7, we see that the two lowest excitonic states contributing to these bands contain a mixture of electronically excited and vibrationally excited components. Therefore, these oscillations correspond to vibronic coherences. This could also be interpreted based on the fact that the energy gap between the monomeric electronic states is of similar energy to the vibrational mode.



If we wanted to observe a purely vibrational coherence, we could create a monomer model, while if we wanted to observe a purely electronic coherence, we could remove the vibrational mode.

Task

3.2) Make cuts through your transient absorption signal for sqab2 at the wavenumbers of the two main peaks in your absorption spectrum.



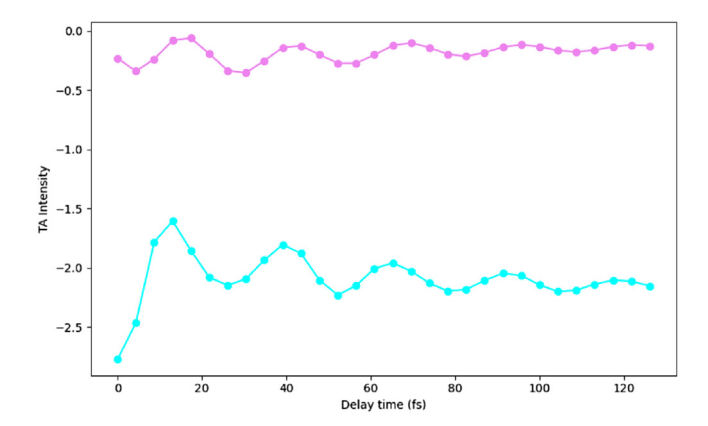


Fig. 8.8 – Time dependence of transient absorption peaks at $13533~{\rm cm}^{-1}$ (cyan) and $14800~{\rm cm}^{-1}$ (violet) of the SQAB1 dimer.

8.5 2D Electronic Spectroscopy (2DES)

8.5.1 Rephasing, Non-Rephasing and Absorptive Spectra

2DES consists of a sequence of three ultrafast laser pulses interacting with a sample, separated by times t_1 , t_2 , and t_3 , which generate the third-order polarization $P^{(3)}$ in the sample that is detected by a fourth laser beam (the local oscillator). This pulse sequence is illustrated in figure 8.9.

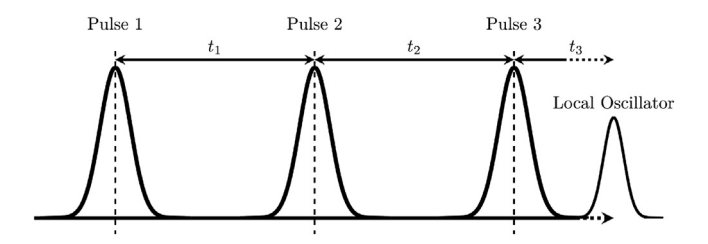


Fig. 8.9 – Pulse sequence for a 2DES experiment.

The resulting signal generated by the third-order polarization is then plotted as a function of the excitation frequency ω_1 , which is the Fourier transform of t_1 (also known as the coherence time), and the detection frequency ω_3 , which is the Fourier transform of t_3 (also known as the detection time). The evolution of these 2D maps is followed along t_2 , which is known as the delay or population time, and during this time the molecular system evolves. Therefore t_2 reports on the excited and ground state dynamics of the system.

The signal is typically detected in so called "rephasing" and "non-rephasing" directions, where the phase-matched wavevectors of the detected signal are respectively:

$$k_{\rm r} = -k_1 + k_2 + k_3 \tag{27}$$

and

$$k_{\rm nr} = +k_1 - k_2 + k_3 \tag{28}$$

The signals in these directions are complex-valued, and typically, they contain both absorptive and dispersive contributions, making the bands broad and difficult to interpret. Commonly, the real parts of the rephasing and non-rephasing signals are summed, obtaining the "purely absorptive" or "total" signal, which yields sharper peaks that are easier to interpret.

In the notebook, routines are defined to calculate the rephasing and non-rephasing signals in UFSS, calculate_2DES_r and calculate_2DES_nr respectively. These routines resemble that of calculate_transient_absorption, although there are some differences:

- The set_efields method is passed the rephasing and non rephasing phase matching conditions $(k_r = ['-', '+', '+'])$ and $k_{nr} = ['+', '-', '+']$.
- The set_pulse_delays method now contains an array of t_1 times rather than 0 as in the pump probe case.
- The electric field envelopes are defined on a much smaller grid (M = 51 and from -5σ to $+5\sigma$) in order to speed up the calculations.
- In order to return the full, complex signal we set spec_obj.return_complex_signal = True.

The returned signal is of the form $S^{(3)}(t_1, t_2, \omega_3)$, and therefore a 3-dimensional array, similar to the transient absorption case. However, the first dimension of the array is now not equal to 1 but equal to the size of the array of t_1 times. The second dimension of the array is equal to the size of the t_2 array, while the third-dimension is equal to the size of the ω_3 array.

The defined routines automatically set t_1 and ω_3 , and we only need to define the population time array t_2 . We choose an array from 0 to 30, in steps of 3 and units of ω_0^{-1} such that it corresponds in fs to delay times from 0 to ~ 130 fs, in steps of ~ 13 fs.

```
#Delay times
t2 = np.arange(0,30,3)
#Also write the array in fs
t2_fs = t2*inv_omega0
```

Now, we calculate the rephasing and nonrephasing signals using these routines. We also obtain the coherence times t_1 directly from UFSS with the all_pulse_delays[0] element of our sqab1 object, as well as the detection frequency w_3 from the w element of our sqab1 object. These are stored in the variables tlr and tlnr, and w3r and w3nr for the rephasing and nonrephasing spectra, respectively.

```
#Calculate the rephasing spectrum

tdes_r = calculate_2DES_r(sqab1, sigma, omega_c, delay_times=t2)
#Obtain the coherence times

tlr = sqab1.all_pulse_delays[0].copy()
#Obtain the detection frequencies
w3r = sqab1.w.copy()

#Calculate the non-ephasing spectrum
tdes_nr = calculate_2DES_nr(sqab1, sigma, omega_c, delay_times=t2)
#Obtain the coherence times
tlnr = sqab1.all_pulse_delays[0].copy()
#Obtain the detection frequencies
w3nr = sqab1.w.copy()
```

Since our obtained signals tdes_r and tdes_nr are of the form $S^{(3)}(t_1, t_2, \omega_3)$, but we would like to plot $S^{(3)}(\omega_1, t_2, \omega_3)$, we must Fourier transform over the times t_1 in order to obtain the signal in terms of the excitation frequencies ω_1 .

To do this, we can utitlise the Fourier transform methods built into UFSS. We require the signals.SignalProcessing.ft1D method for the rephasing spectrum, and the signals.SignalProcessing.ift1D method for the non-rephasing spectrum. It is necessary to use the inverse Fourier transform for the latter due to the sign change associated with k_1 for the non-rephasing spectrum relative to the rephasing one. We implement two functions ft_rephasing and ft_nonrephasing to calculate these Fourier transforms, which return an array of excitation frequencies ω_1 (saved in the notebook as w1r and w1nr for the rephasing and non-rephasing signals, respectively), as well as the signal as a function of ω_1 , t_2 , and ω_3 (saved in the notebook as tdes_r_ft and tdes_nr_ft for the rephasing and non-rephasing signal, respectively).

```
wlr, tdes_r_ft = ft_rephasing(tdes_r,tlr)
wlnr, tdes_nr_ft = ft_nonrephasing(tdes_nr,tlnr)
```

Now, we can plot the spectra as a function of ω_1 and ω_3 . This is implemented in the plot_2des function in the notebook, which can be called by passing $S^{(3)}(\omega_1, t_2, \omega_3)$, ω_1 and ω_3 , as well as the laser carrier frequency and Ω . The routine also optionally takes as an argument an integer index for the population time t_2 . By default it is set to 0, which would correspond to the first element of the t2 array we defined above. We can also optionally control the range of the colorbar for the signal intensity through the vmax argument. Part of the implementation is shown below:

```
def plot_2des (signal,w1,w3,omega_c,Omega,t2_ind=0,vmax='max'):
    """ This function plots 2D spectra

Parameters
-----
signal : 2DES signal as a function of w1, t2 and w3
w1 : Array of excitation frequencies
```

```
wЗ
        : Array of detection frequencies
omega c : Carrier frequency of the laser pulses
        : Vibrational wavenumber which the Hamiltonian
Omega
                  is written in multiples of
t2 ind (optional): Integer index of t2 delay times.
                    Default is 0, i.e. first t2 time.
vmax (optional)
                   : Maximum value for colourbar.
                    Default is maximum signal intensity.
** ** **
#Shift by carrier frequency and multiply by Omega
w1 cm = (w1 + omega c) * Omega
w3 cm = (w3 + omega c) * Omega
#Make the plot
ufss.signals.plot2D(w1_cm, w3_cm, signal[:,t2_ind,:],
                  part='real', vmax=vmax)
```

As with the transient absorption case, we make use of the plot2D function in UFSS within the plot_2des function. Here, the x and y axes are the excitation frequency ω_1 and detection frequency ω_3 , respectively. As previous, we must shift by the carrier frequency and multiply by Ω . The 2DES rephasing and non-rephasing spectra for an initial population time ($t_2 = 0$) are shown in figure 8.10.

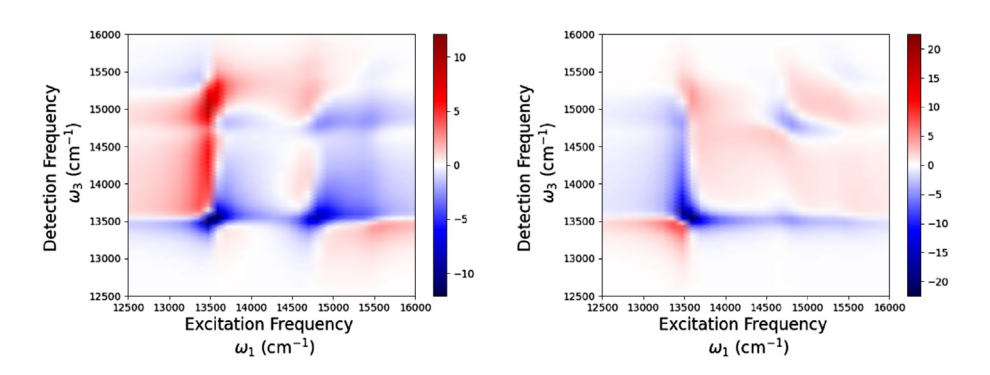


Fig. 8.10 – Real part of the rephasing (left) and non-rephasing (right) spectra for an initial population time ($t_2 = 0$) for SQAB1.

UFSS follows the experimental convention that ground-state bleaching and stimulated emission are shown as negative signals and excited state absorption is shown with a positive signal. This comes from the historical pump probe convention that signals are measured as an absorption difference relative to the absorption before photoexcitation.

As was mentioned earlier in this section, the bands are particularly broad, which we can observe in figure 8.10. So instead we will plot the purely absorptive spectra,

by summing the rephasing and non-rephasing signals and then plotting the real part of this sum

```
#Sum the rephasing and nonrephasing signals
tdes_abs_ft = tdes_r_ft + tdes_nr_ft
#Plot the real part of the absorptive signal
plot_2des(tdes_abs_ft,wlr,w3r,omega_c,Omega)
```

The result of this is shown in figure 8.11, where it can be seen we have much more clearly defined peaks, with ground state bleaching/stimulated emission signals in blue on the diagonal and lower right off-diagonal, and excited state absorption in the upper left off-diagonal.

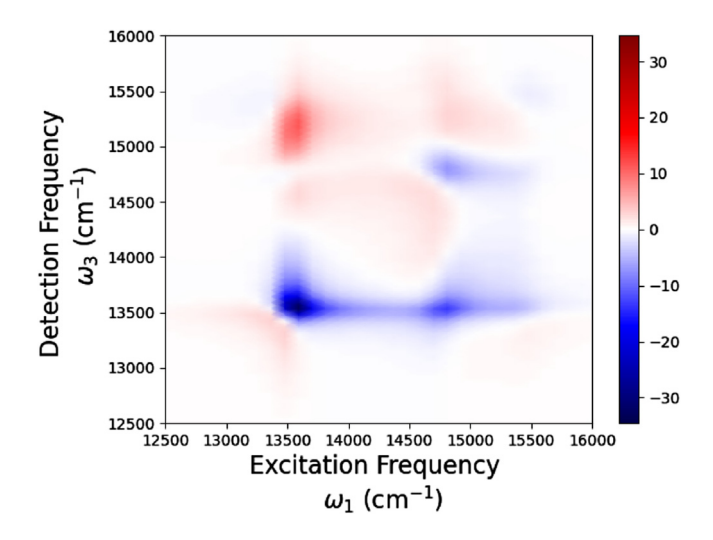


Fig. 8.11 – Total absorptive 2D electronic spectrum for an initial population time ($t_2 = 0$) for SQAB1.

Question

What extra information do we get in the 2DES signal, compared to the transient absorption signal?



Solution to question

We have two pump pulses delayed by the coherence time t_1 in 2DES, as opposed to two pump pulses arriving simultaneously in transient absorption, so we can resolve the spectrum over the excitation frequency as well as the detection frequency. This gives rise to the appearance of cross peaks in 2DES that are indicative of energy transfer and would be overlapping with the diagonal ones in transient absorption.



Task

4.1) Plot how the absorptive spectrum changes as a function of the population time, by passing an integer parameter to the optional t2_ind argument of plot_2des. This will range from 0 to 9 as we defined our delay time array to have 10 points, and Python indexing starts from 0. We should also pass a numerical value to the optional vmax argument to set the colorbar scale to be the same on every plot e.g. plot_2d_absorptive(tdes_r_ft,tdes_nr_ft,w3r,w1r,omega_c,0mega,t2_ind=1,vmax=30).



What happens to the intensity of the diagonal peaks as a function of time?

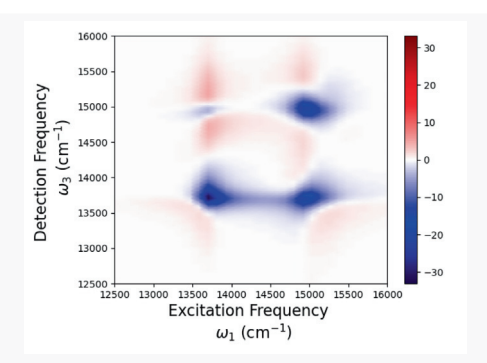
4.2) Generate the rephasing, non-rephasing, and absorptive spectra for sqab2 and plot them.

How is the absorptive spectrum different to that of sqab1?

Solution to task

In the question posed after task 4.1, you should observe a decrease in intensity of the higher energy diagonal peak as a function of time, due to energy transfer to the lower energy state.

In the question posed after task 4.2, you should observe that the spectrum corresponding to SQAB2 has a less intense upper left ESA cross-peak, but more intense lower right cross-peak at $t_2=0$.





As mentioned in chapter 4, the cross peaks at $t_2=0$ should provide a measure of the excitonic coupling strength, with more intense cross peaks indicative of stronger excitonic coupling. However, this is only true of the upper left ESA peak in this example, because the energy transport from upper to lower energy state is already occuring at $t_2=0$ due to the temporal width of the Gaussian pulses, altering the intensity of the lower right cross-peak and meaning it does not provide a direct measure of the excitonic coupling. Furthermore, as seen in the linear absorption spectrum the higher energy peak of SQAB2 is actually composed of two overlapping vibronic transitions, which also results in an increase in the intensity of the lower right cross-peak.

8.5.2 Peak Monitoring

Like with the transient absorption case, it is quite common to monitor the intensity of the peaks as a function of time. We will look at the diagonal peaks at excitation and detection frequencies of $f_1 = 13533$ and $f_2 = 14800$ cm⁻¹, as well as the lower right cross peak, indicative of energy transfer from the higher energy state to the lower. These peaks are highlighted on the left-hand side of figure 8.12.

Similar to the case for transient absorption, we need to calculate the indices in the signal array that f_1 and f_2 will correspond to. These indices are the same as in the ω_1 and ω_3 arrays.

```
indf1w1 = np.argmin(np.abs(w1r+omega_c-f1))
indf1w3 = np.argmin(np.abs(w3r+omega_c-f1))
indf2w1 = np.argmin(np.abs(w1r+omega_c-f2))
indf2w3 = np.argmin(np.abs(w3r+omega_c-f2))
```

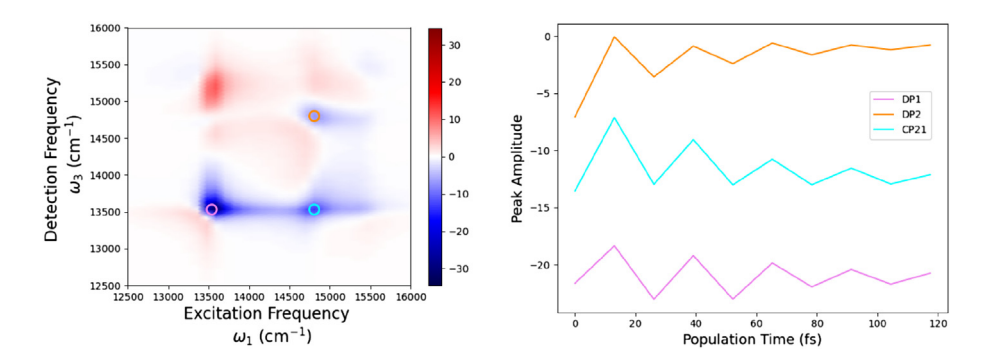


Fig. 8.12 – Highlighted diagonal peaks of the total absorptive spectrum (left) and the time dependence of their intensity (right) for SQAB1.

One can then extract the signal intensities at these points and plot them

with the result shown in the right-hand panel of figure 8.12. We observe a decrease in the intensity of diagonal peak 2 (DP2) and a marginal average increase in the lower right cross peak (CP21) as we have energy transfer from the higher energy state to the lower one. We can also notice again some oscillations due to coherences.



4.3) Extract the intensities of the diagonal and cross peaks from your sqab2 absorptive 2D spectrum.



8.5.3 Inhomogeneous Broadening

2DES can separate homogeneous and inhomogeneous broadening. The width of the peak along the diagonal (from bottom left to top right) corresponds to an inhomogeneous broadening, while the width of the peak along the anti-diagonal (from bottom right to top left) corresponds to homogeneous broadening. This is illustrated in figure 8.13.

Let us observe the effect of inhomogeneous broadening on our computed spectra. Similarly to the linear absorption case, we can utilise the inhomogeneous_broadening routine previously defined, passing it the functions to calculate the 2D

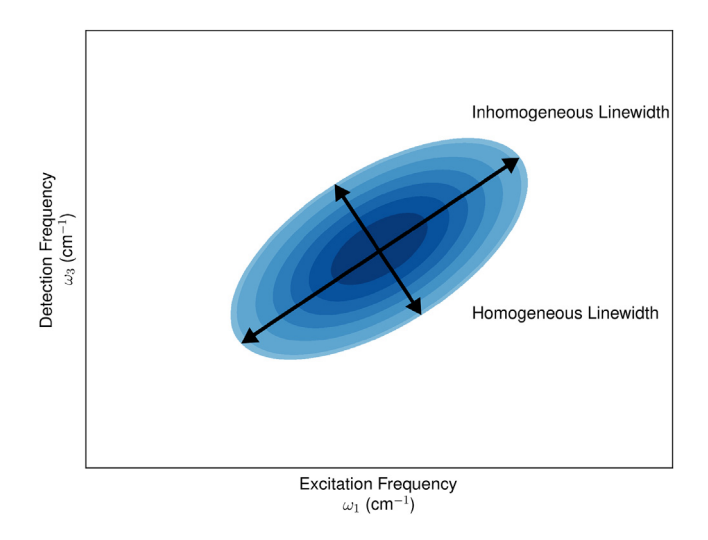


Fig. 8.13 – Illustration of homogeneous and inhomogeneous broadening in 2DES.

spectra, as well as the previously defined $sqab_inhom$ list, weights array, carrier frequency for excitation $omega_c$, and the remaining parameters sigma and a list of population times t_2 . For the latter, we will redefine the t_2 array and only include $t_2 = 0$, as the calculation will take a number of minutes to run:

We can do this for both the rephasing (as shown above) and non-rephasing signals, then sum them up to get the inhomogeneously broadened total absorptive signal, as shown in figure 8.14. In comparison to figure 8.11, we can notice the peaks are elongated along the diagonal.

Task

4.4) Compute the inhomogeneously broadened spectra for sqab2.



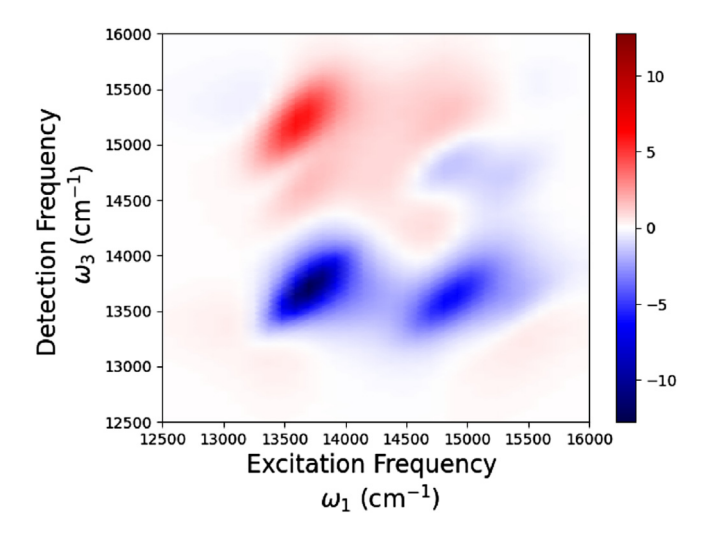


Fig. 8.14 – Inhomogeneously broadened total absorptive 2D electronic spectrum at an initial population time ($t_2 = 0$) for SQAB1.

8.6 Feynman Diagrams

Non-linear spectral signals typically consist of contributions from different sources, such as ground state bleaching (GSB), stimulated emission (SE) and excited state absorption (ESA). As illustrated in the previous section, all of these features can appear in a 2D electronic spectrum. These photochemical pathways can be illustrated through the use of double sided Feynman Diagrams, which illustrate the influence of the laser pulses on the denisty matrix $\rho = |\Psi\rangle\langle\Psi|$ of the system [10]. Feynman Diagrams have the following properties:

- 1. They consist of a pair of parallel vertical lines, with the left hand line representing the ket of the system and the right hand line representing the bra of the system.
- 2. Time evolution proceeds upwards, and interactions with the electric field of the laser are represented by straight arrows.
- 3. Straight arrows pointing towards the bra or ket lines represent an excitation (and so increase the quantum number by 1), straight arrows pointing away from the bra or ket lines represent a de-excitation (and so decrease the quantum number by 1).
- 4. If the arrow points to the right, it represents an electric field with +k wavevector, and if it points to the left, it represents an electric field with -k wavevector.
- 5. The final arrow represents emission of the polarization signal by the system and is typically shown with a different style of arrow (dashed or curved), and by convention is emitted from the ket side. It must also end in a population state (*i.e.*, diagonal element of the density matrix).

6. Each Feynman diagram has a sign $(-1)^n$, where n is the number of interactions from the right (bra side). This is because each time an interaction is from the right in the commutator for the n th-order polarization in equation (5), it carries a minus sign. Since the last interaction is not part of the commutator, it is not counted in this sign-rule.

Example Feynman diagrams for GSB, SE and ESA are shown in figure 8.15. The incident wavevectors sum to $-k_1 + k_2 + k_3$ hence they correspond to the rephasing direction, and the polarization signal emitted is $k_{\text{sig}} = k_r$. Note that UFSS employs the opposite sign convention for the GSB, SE, and ESA signals to that described in the final point of the above list. This will be explained in section 8.6.2.

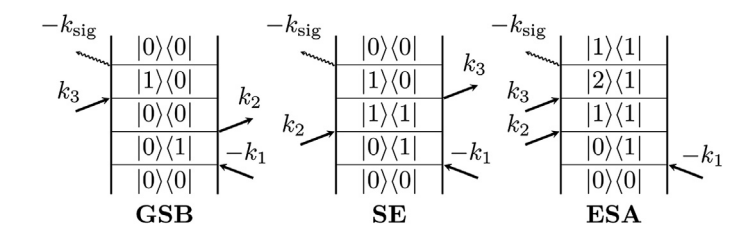


Fig. 8.15 – Example double sided Feynman diagrams in the rephasing direction, showing ground state bleaching (GSB), stimulated emission (SE) and excited state absorption (ESA) for a pair of two-level systems.

In the following section, we will first generate these Feynman diagrams programatically, and then use them to seperate components of the sqab1 2D spectral signal. The questions in this section will only involve the sqab1 object, to save repetition, however you are welcome to seperate the signal of sqab2 as well to compare.

8.6.1 Generating Feynman Diagrams

UFSS contains a class that can generate Feynman diagrams for specific phase-matching conditions and pulse delays, and calculate the spectra using these diagrams. In the following, we will use this to seperate the GSB, SE and ESA components of the 2DES signal.

First let us create an instance of the ufss.DiagramGenerator class, and then call it to make an object with which we will calculate the Feynman diagrams for the rephasing signal.

Now, let us set the phase matching condition to be that of the rephasing signal, *i.e.*, $k_r = -k_1 + k_2 + k_3$

```
tdes_dg_r.set_phase_discrimination(['-','+','+'])
```

For the diagram generator, we need to pass a list of durations for the electric fields. If we use Gaussian pulses with standard deviation σ as previously in the exercise, then the electric fields will have approximately decayed by 5 σ . So we define the duration of the 3 pulses and the local oscillator as:

```
t1 = np.array([-5*sigma,5*sigma])
t2 = np.array([-5*sigma,5*sigma])
t3 = np.array([-5*sigma,5*sigma])
tlo = np.array([-5*sigma,5*sigma])
all_pulse_intervals = [t1,t2,t3,tlo]
```

We then set the efield_times attribute of the tdes_dg_r object equal to this:

```
tdes_dg_r.efield_times = all_pulse_intervals
```

Next, we need to define when these pulses will arrive. To ensure that we have proper time ordering (i.e., pulse 3 arrives when pulse 2 has completely decayed, and pulse 2 arrives when pulse 1 has completely decayed) we will define arrival times separated by $100 \ \omega_0^{-1}$, which is much greater than $5 \ \sigma \sim 6 \omega_0^{-1}$. We also need to define an arrival time for the local oscillator. However this time is irrelevant for the functioning of the code and can be defined to arrive at the same time as pulse 3.

```
arrival_times = [0,100,200,200]
```

Now, we can generate the set of Feynman diagrams associated with the rephasing phase matching condition and time-ordering of the pulses with the get_diagrams method.

```
time_ordered_diagrams_r = tdes_dg_r.get_diagrams(arrival_times)
```

Finally, we can visualise/print the diagrams. In the notebook, the resulting diagrams can only be visualised if you have a TeX distribution installed. This is accomplished as follows:

```
tdes_dg_r.display_diagrams(time_ordered_diagrams_r)
```

UFSS prints only the interaction with the laser fields, and not the emitted signal, with k_1 , k_2 and k_3 denoted as a, b and c, respectively. This is illustrated in figure 8.16.

If you do not have a TeX distribution, you can print the diagrams in a textual format, for example:

```
print(time_ordered_diagrams_r[1])
```

with the output:

```
(('Bu', 0), ('Ku', 1), ('Bd', 2))
```

The numbers 0, 1 and 2 in the output correspond to the first, second and third pulse. "Ku" and "Bu" correspond to arrows pointing towards the ket and bra sides, respectively ("u" signifying we are moving up the density matrix by one quantum), "Kd" and "Bd" correspond to arrows moving away from the ket and bra sides, respectively ("d" signifying we are moving down the density matrix by one quantum). If we were to draw the Feynman diagram according to this output, we would see it would correspond to a SE signal (central panel of figure 8.16).

Task

5.1) Assign the diagrams saved in the time_ordered_diagrams_r array as either GSB, SE or ESA.



5.2) Generate the Feynman diagrams for the non-rephasing signal and assign them.

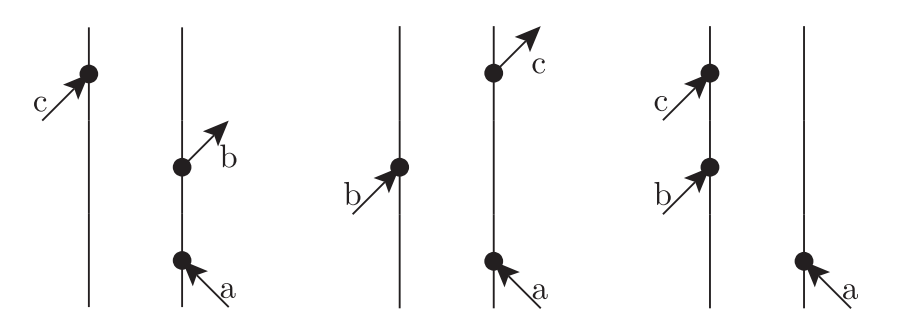


Fig. 8.16 – Feynman diagrams generated by the UFSS code, corresponding to GSB (left), SE (middle) and ESA(right) for the rephasing signal.

8.6.2 Assigning Feynman Diagrams

As well as assigning the diagrams by hand, it is possible to do so programmatically. To do so, we make use of the filter_diagrams_by_excitation_manifold method. This separates the diagrams by the maximum number of quanta in the bra and ket sides after the interaction with the second pulse (i.e., the population state

monitored by 2DES). With 0 quanta in the bra and ket sides after interaction with the second pulse, we have the ground state manifold with the GSB diagram. With a maximum of 1 quantum in the bra and ket sides, we have the singly excited manifold with the SE and ESA diagrams.

Now let us seperate the SE and ESA diagrams. We can do this by filtering by the sign of the signal. As mentioned in the introduction to section 8.6, UFSS employs the opposite convention for the sign to the theoretically derived sign of the polarization, *i.e.*, negative for stimulated emission (and ground state bleaching) and positive for excited state absorption. This is because the convention that UFSS follows is that used in experiment – where the signal is to be interpreted as an intensity change relative to the ground state absorption before photoexcitation. Therefore, when seperating the diagrams with UFSS, we follow this convention.

```
#Define the sign of the SE signal as negative
se_sign = -1
#Extract only the SE Feynman diagram
se_dg_r = tdes_dg_r.filter_diagrams_by_sign(se_esa_dg_r, sign=se_sign)

#Define the ESA signal as positive
esa_sign = 1
#Extract only the ESA Feynman diagram
esa_dg_r = tdes_dg_r.filter_diagrams_by_sign(se_esa_dg_r, sign=esa_sign)
```

As before, one can then print and visualise these diagrams to check that the programmatic assignment is correct.



5.3) Programatically seperate the non-rephasing Feynman diagrams into GSB, SE and ESA components.



8.6.3 Separating Spectral Components by Diagram

Now that we have generated Feynman diagrams and separated them into GSB, SE and ESA, we can use these separated diagrams to generate 2D electronic spectra with only these components. To do this, we will pass the diagrams to our previously

defined calculate_2DES_r function, which had an optional argument to pass Feynman diagrams.

After extracting the t_1 times, ω_3 frequencies, and Fourier transforming over t_1 to get ω_1 as previously, we can plot the GSB-only component of the rephasing signal, as shown in figure 8.17.

We can see that even isolating the GSB component of the rephasing signal, we have positive and negative components. However, for the total absorptive signal (shown in figure 8.18, the answer to the following task 5.6), we have essentially only negative components as may be expected.

Task

- 5.4) Calculate the SE and ESA components of the rephasing spectrum.
- 5.5) Calculate the GSB, SE and ESA components of the non-rephasing spectrum.



5.6) Calculate the GSB, SE and ESA components of the absorptive spectrum.

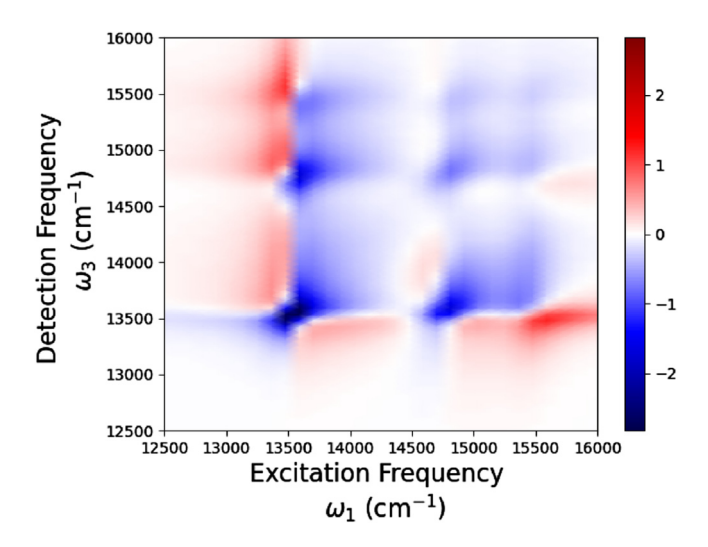


Fig. 8.17 – GSB component of the rephasing 2D electronic spectrum for an initial population time ($t_2 = 0$) for SQAB1.

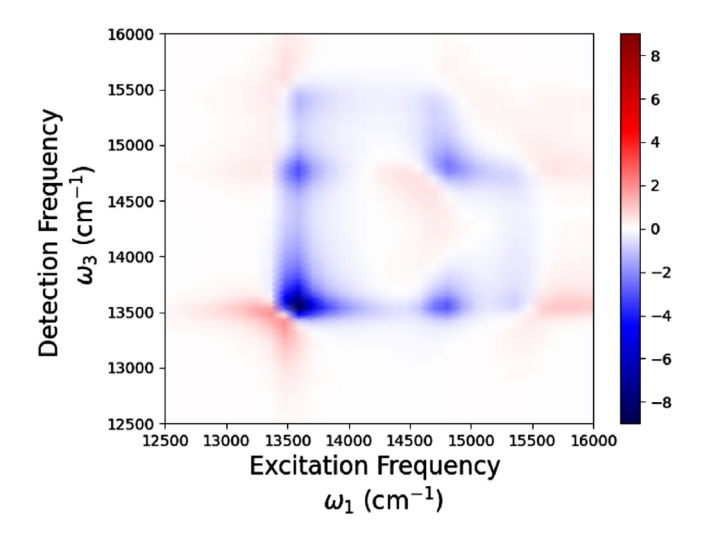


Fig. 8.18 – GSB component of the total absorptive 2D electronic spectrum for an initial population time ($t_2 = 0$) for SQAB1.

8.6.4 Time Ordering

One of the key approximations made in 2DES, both experimentally and theoretically, is that the laser pulses arrive in a time ordered fashion -i.e., laser pulse 3 arrives after laser pulse 2, which arrives after laser pulse 1. However, if the pulses are not strictly ordered in time, we have the possibility of more Feynman diagrams contributing the signal. If we define a set of arrival times where the pulses all overlap, then we have the possibility of 16 rather than 3 Feynman diagrams contributing to the signal. This is shown in the notebook in the following lines:

Now, let us look at the effect on the spectrum if we do not take care of this time ordering of the pulses. The rephasing spectrum computed using the Feynman diagrams from time ordered pulses is shown on the left-hand side of figure 8.19, while that computed using Feynman diagrams with all pulses overlapping is shown on the right-hand side of figure 8.19. While the spectra are quite similar to one another, there are some differences, for example in the intensities of the two spectra. For more complex systems, the differences also could be larger.

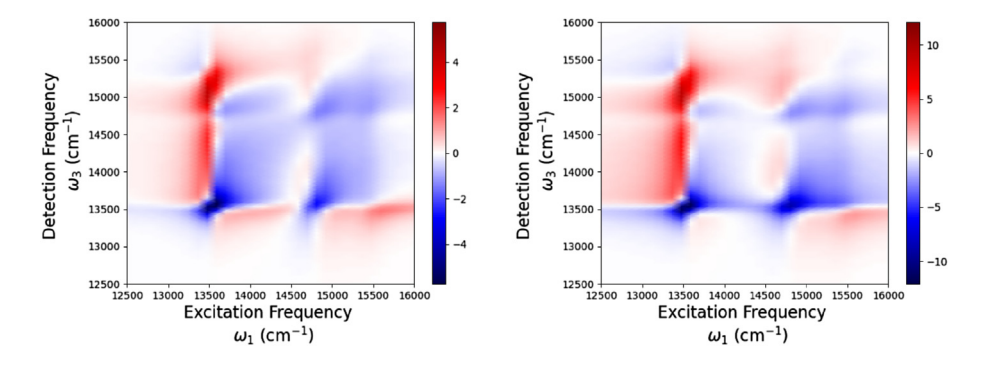


Fig. 8.19 – Rephasing 2D electronic spectra with time ordering of laser pulses (left) and all pulses overlapping in time (right) for SQAB1.

Task

- 5.7) Compute and compare the non-rephasing spectra with overlapping and time ordered pulses.
- 5.8) Compute and compare the absorptive spectra with overlapping and time ordered pulses.



5.9) Edit the arrival_times_overlap array with different numbers of overlapping pulses and recompute the spectra, observing the changes present and number of Feynman diagrams that contribute.

8.7 Where Do We Go From Here?

One can play around with the workbook further, for example, changing the temperature and the parameters for the bath, simulating how the separate GSB, SE and ESA components vary as a function of t_2 etc. One can also use this as a basis to create models for other molecular systems and see how their non-linear spectra look or simulate other non-linear spectra. For example, one can use UFSS to calculate nth-order transient absorption signals, as described in Ref. [15], and 5th-order 2D spectroscopies as described in Ref. [5]. Further examples may also be found in Ref. [2], as well as the UFSS GitHub repository [1]. Happy simulating!

References

- [1] Rose P. A., Krich J. J. Ultrafast spectroscopy suite (ufss). https://github.com/peterarose/ufss.
- [2] Rose P. A. (2022) Algorithms for efficient calculation of nonlinear optical spectra: ultrafast spectroscopy suite and its applications, PhD thesis. University of Ottawa. https://doi.org/10.20381/ruor-27645.

- [3] Rose P. A., Krich J. J. (2019) Numerical method for nonlinear optical spectroscopies: ultrafast ultrafast spectroscopy, *J. Chem. Phys.* **150**(21), 214105.
- [4] Rose P. A., Krich J. J. (2021) Efficient numerical method for predicting nonlinear optical spectroscopies of open systems, J. Chem. Phys. 154(3), 034108.
- Rose P. A., Krich J. J. (2021) Automatic Feynman diagram generation for nonlinear optical spectroscopies and application to fifth-order spectroscopy with pulse overlaps, *J. Chem. Phys.* 154(3), 034109.
- [6] Kreisbeck C., Kramer T. (2013) Exciton dynamics lab for light-harvesting complexes (gpu-heom). http://nanohub.org/tools/gpuheompop.
- [7] Segatta F., Nenov A., Nascimento D. R., Govind N., Mukamel S., Garavelli M. (2021) iSPECTRON: a simulation interface for linear and nonlinear spectra with ab-initio quantum chemistry software, J. Comput. Chem. 42, 644–659. https://doi.org/10.1002/jcc. 26485.
- [8] Jansen T. L. C. (2017) Numerical integration of the schrödinger equation (nise). https://github.com/ghlacour/nise 2017.
- Abramavicius D., Palmieri B., Voronine D. V., Šanda F., Mukamel S. (2009) Coherent multidimensional optical spectroscopy of excitons in molecular aggregates; quasiparticle versus supermolecule perspectives, *Chem. Rev.* 109(6), 2350–2408.
- [10] Mukamel S. (1995) Principles of nonlinear optical spectroscopy. Oxford University Press.
- [11] Malý P., Lüttig J., Mueller S., Schreck M. H., Lambert C., Brixner T. (2020) Coherently and fluorescence-detected two-dimensional electronic spectroscopy: direct comparison on squaraine dimers, Phys. Chem. Chem. Phys. 22, 21222–21237.
- [12] Hamm P. (2005) Principles of nonlinear optical spectroscopy: a practical approach or: Mukamel for dummies. University of Zurich.
- [13] Breuer H.-P., Petruccione F. (2002) The theory of open quantum systems. Oxford University Press.
- [14] Camargo F. V. de A., Grimmelsmann L., Anderson H. L., Meech S. R., Heisler I. A. (2017) Resolving vibrational from electronic coherences in two-dimensional electronic spectroscopy: the role of the laser spectrum, *Phys. Rev. Lett.* 118, 033001.
- [15] Malý P., Lüttig J., Rose P. A., Turkin A., Lambert C., Krich J. J., Brixner T. (2023) Separating single- from multi-particle dynamics in nonlinear spectroscopy, *Nature* 616(7956), 280–287.